UNIVERSIDAD COMPLUTENSE DE MADRID

FACULTAD DE CIENCIAS FÍSICAS
Departamento de Física de la Tierra, Astronomía y Astrofísica II
(Departamento de Astrofísica y Ciencias de la Atmósfera)

TESIS DOCTORAL

Modelado auto-consistente de la emisión de estrellas y polvo en galaxias luminosas en IR a redshift intermedio

Self-consistent modeling of stars and dust emission of IR-bright galaxies at intermediate redshift

MEMORIA PARA OPTAR AL GRADO DE DOCTOR

PRESENTADA POR

Néstor Espino Briones

Directores
Pablo G. Pérez González
Jaime Zamorano Calvo

Madrid, 2016

Modelado auto-consistente de la emisión de estrellas y polvo en galaxias luminosas en IR a redshift intermedio / Self-consistent modeling of stars and dust emission of IR-bright galaxies at intermediate redshift

por

Néstor Espino Briones

Memoria presentada para aspirar al grado de
Doctor en Ciencias Físicas
en la
Universidad Complutense de Madrid
Departamento de Astrofísica y Ciencias de la Atmósfera

Madrid, Noviembre 2015

Dirigida por:

Dr. Pablo G. Pérez González
Profesor Titular
UCM

Dr. Jaime Zamorano Calvo
Profesor Titular
UCM

Modelado auto-consistente de la emisión de estrellas y polvo en galaxias luminosas en IR a redshift intermedio / Self-consistent modeling of stars and dust emission of IR-bright galaxies at intermediate redshift

Néstor Espino Briones

Dedicada a

Mi padre, Herón Espino Domínguez, por todas sus profecias.
Mi madre, Yolanda Briones Franco, que me educó para volar libre.
Mi tía, Raquel Briones Franco, por ser mi segunda madre.
Y , de nuevo, a todos los hermanos que me da el destino.
Ustedes saben quienes son.

Summary

The Spectral Energy Distributions (SEDs) of dusty star-forming galaxies at intermediate redshifts are usually characterized with models that naively assume only one burst (short or extended in time) as representative star formation history (SFH) of the stellar populations of these galaxies, which are obviously much more complex. Moreover, the relation between the optical light attenuation and posterior re-emission at far-infrared (FIR) wavelengths due to dust has been traditionally unappreciated when deriving the physical properties of these objects, such as the stellar mass and star formation rate (SFR).

In this thesis we investigate the stellar properties of a FIR selected sample of 19 star-forming galaxies in the redshift range $0.6 \leq z \leq 1.5$ by analyzing their UV-to-FIR SEDs. The sample is based in three or more FIR detections, one from *Spitzer*-MIPS 70 μm and at least two from PACS and/or SPIRE on *Herschel* observed in the Subaru/XMM-Newton Deep Survey field. These FIR data allow us to accurately determine the total infrared luminosity ($L_{\rm TIR}$, integrated from 8 to 1000 μm) of such (ultra)-luminous infrared galaxies (LIRGs and ULIRGs). The full UV-to-FIR SEDs are fitted to stellar population and dust emission models using codes (Synthesizer and CIGALE) which manage the attenuation of stellar light and dust re-emission with energy balance techniques. We assume a fiducial SFH depicted by a young stellar population on top of an evolved population, each parameterized with a decaying exponential function. We compare the impact on our results of including and excluding the FIR data to constrain the amount of attenuation of stellar light, as well of using this constrain assuming one single stellar population instead of two. Our auto-consistent analysis of the stellar light obscuration and dust emission provides: 1) reliable physical properties of the stellar populations of (U)LIRGs by breaking the age-dust degeneracy; 2) accurate values of the amount of attenuation of stellar light in these galaxies; 3) improved stellar mass and SFR estimations of IR-bright galaxies; 4) estimates of the time spent by galaxies in the (U)LIRG phase, and of the corresponding amount of stellar mass added in this phase; 5) the stellar properties having more impact in the determination of stellar masses and SFRs of IR-bright galaxies; and 6) an evaluation of how *a priori* assumptions and usage

of different codes in the modeling affect the results for the stellar population properties of (U)LIRGs.

Our results are the following ones:

- The $L_{\rm TIR}$ of our sample ranges from 3.0×10^{11} to 5.4×10^{12} $L_{\odot}$, with 5 LIRGs and 14 ULIRGs.

- The omission of the FIR constraint results in an overestimation of the attenuation of the young population with median $\Delta A(V)_{\rm you} = 0.4$ mag. This overestimation translates in an underestimation of the young population ages by a factor of ~ 6 in median.

- Two-population models fit better the observed stellar SED than one-population models. The worst fits with one-population models show an excess of energy at blue wavelengths and a luminosity deficit at $700 - 800$ nm when compared with the observed data. This excess is due to an underestimation of the amount of attenuation, and this deficit is originated by determining population ages < 100 Myr.

- Stellar masses derived from one-population models presenting such excess and deficit are smaller by a factor of 2 compared to those derived with two-population models. Stellar mass values from CIGALE and Synthesizer are similar, $\sim 1 \times 10^{10} - 2 \times 10^{11}$ $M_{\odot}$, with median value $\sim 5 \times 10^{10} M_{\odot}$, in agreement with previous estimations derived for $z > 1$ sub-mm galaxies, and distant red galaxies.

- SED-fit SFRs derived with one-population models present a larger scatter (~ 0.16 dex) than those derived with two-population models (~ 0.11 dex) when compared with $SFR_{\rm UV+IR}$ values. SED-fit SFRs determined with one-population models can be 0.2 dex smaller than those derived with two-population models due to an SFH which is far from constant ($t/\tau > 0.8$) or because the stellar mass is underestimated. The current SFR values from CIGALE and Synthesizer range in $\sim 70 - 2000$ $M_{\odot}$ yr^{-1} and $\sim 70 - 1000$ $M_{\odot}$ yr^{-1}, respectively. We find that SFRs derived from SED fitting are sensitive to the age of the youngest stellar population. The effect can be as large as 60% when comparing populations described by a constant SFH and ages of ~ 100 Myr (the typical assumption when using classical star-formation tracers such as the UV, H_{α} or $L_{\rm TIR}$) with bursts as young as 20 Myr.

- The SFHs for our (U)LIRG sample derived from CIGALE and Synthesizer are characterized by a young population forming stars in a constant rate and there-

fore being responsible of the recent star formation, whereas the old population mostly contributes with stellar mass. Both codes derive similar values for the attenuation of the young population ranging in $\sim 0.5 - 3.5$ mag (with median ~ 2.5 mag). The ages of the young population obtained with both codes are shorter than ~ 400 Myr. The age values are < 100 Myr for 79% and 53% of these (U)LIRGs as derived from Synthesizer and CIGALE, respectively. These values are compatible with estimates of the starburst lifetimes of sub-millimeter galaxies $\sim 100 - 300$ Myr.

- The median SED-fit SFR of our sample is $\sim 230\ M_{\odot}\mathrm{yr}^{-1}$, which is similar to that obtained for SCUBA-2 galaxies. Assuming this median SFR and a lifetime for the starburst phase of 100 Myr imply an addition of stellar mass $\sim 2 \times 10^{10}\ M_{\odot}$ during such phase. This addition corresponds to a fraction of $\sim 40\%$ of the median stellar mass derived for our sample with each code.

In conclusion, we have shown that to derive reliable and accurate stellar population properties of (U)LIRGs at $0.6 < z < 1.5$ is essential to consider the dust FIR emission using a physically-motivated energy-balance approach.

Resumen

Las distribuciones espectrales de energía (SEDs) de galaxias con polvo y formación estelar a desplazamientos al rojo intermedio son caracterizadas usualmente con modelos que asumen un único brote para representar las historia de formación estelar (SFH) de las distintas poblaciones que constituyen estos objetos. Además, la relación entre la atenuación de la emisión estelar en el espectro visible debida al polvo y su posterior re-emisión en el infrarrojo lejano (FIR) ha sido desestimada cuando se determinan las propiedades físicas de estas galaxias, como la masa y la tasa de formación estelar (SFR).

En esta tesis investigamos las propiedades estelares de una muestra de 19 galaxias seleccionadas en el FIR en el intervalo de desplazamiento al rojo $0.6 \leq z \leq 1.5$, analizando su SEDs desde el UV hasta el FIR. La muestra se deriva de objetos con 3 o más medidas fotométricas en el FIR, una tomada a 70 μm con MIPS en *Spitzer* y mínimo otras dos adquiridas con PACS y/o SPIRE en *Herschel* en la región del Subaru/XMM-Newton Deep Survey. Esta fotometría permite estimar de forma precisa la luminosidad total en el IR ($L_{\rm TIR}$, integrada entre 8 y 1000 μm) de estas galaxias brillantes en el IR (LIRGs and ULIRGs). Las SEDs desde el UV hasta el FIR son ajustadas usando modelos de poblaciones estelares y emisión del polvo provenientes de programas (Synthesizer y CIGALE) que conectan usando técnicas de balance energético la atenuación de la emisión estelar debida al polvo y su posterior re-emisión en el FIR. Asumimos una SFH de referencia descrita por una población estelar joven traslapando una población estelar evolucionada, ambas caracterizadas con funciones exponenciales decrecientes. Determinamos el impacto en nuestros resultados cuando se constriñe o no, la atenuación de la emisión estelar usando el método de balance energético, y su efecto en combinación con modelos que asumen una población estelar en lugar de dos. Este análisis con balance energético permite: 1) caracterizar las poblaciones estelares de (U)LIRGs con propiedades físicas robustas determinadas al romper la degeneración edad-polvo; 2) estimar adecuadamente la cantidad de atenuación de la emisión estelar en estas galaxias; 3) mejorar las estimaciones de masa estelar y SFR en (U)LIRGs; 4) calcular el tiempo que transcurren las galaxias en la fase (U)LIRG, y la masa estelar

que se agrega a las galaxias en dicha fase; 5) determinar que propiedades de las poblaciones estelares ejercen mayor impacto en la estimación de masas estelares y SFRs en (U)LIRGs; y 6) evaluar como las suposiciones *a priori* y el uso de programas diferentes en el modelado afectan los resultados en propiedades estelares de (U)LIRGs.

Nuestros resultados son los siguientes:

- La $L_{\rm TIR}$ de estas galaxias va de 3.0×10^{11} a 5.4×10^{12} $L_{\odot}$, siendo 5 LIRGs y 14 ULIRGs.

- La omisión de la constricción FIR produce una sobrestimación promedio de la atenuación de la población joven de $\Delta A(V)_{\rm you} = 0.4$ mag, que produce una subestimación promedio de la edad de la población joven en un factor de ~ 6.

- Los modelos de dos poblaciones ajustan mejor las SED observada que los modelos de una población, ya que los segundos muestran un exceso de energía en la parte azul del espectro y un déficit energético a $700-800$ nm comparando con los datos observados. Dicho exceso se debe a una subestimación de la atenuación, y dicho déficit a la determinación de edades de la población < 100 Myr.

- Las masas estelares derivadas de modelos de una población presentando dichos exceso y déficit son menores en un factor 2 que las masas derivadas con modelos de dos poblaciones. Las masas estelares estimadas con CIGALE y Synthesizer son similares, $\sim 1 \times 10^{10} - 2 \times 10^{11}$ $M_{\odot}$, con valor mediano $\sim 5 \times 10^{10} M_{\odot}$, dichos valores son compatibles con estimaciones para galaxias submilimétricas a $z > 1$ y galaxias rojas distantes.

- SFRs derivadas de los modelos de una población presentan mayor dispersión que las derivadas de modelos de dos poblaciones al compararlas con valores de la estimación típica $SFR_{\rm UV+IR}$. Las SFRs actuales derivadas con CIGALE y Synthesizer abarcan $\sim 70 - 2000$ $M_{\odot}$ yr^{-1} y $\sim 70 - 1000$ $M_{\odot}$ yr^{-1}, respectivamente. Encontramos que SFRs obtenidas del modelado de SEDs son afectadas por la edad de la población más joven. El efecto puede cambiar la estimación hasta en un 60% al comparar resultados obtenidos con una SFH constante modelada con una población de edad ~ 100 Myr (la suposición típica en estimadores de SFR clásicos) con brotes tan jóvenes como 20 Myr.

- Las SFHs más adecuadas para nuestra muestra, determinadas con CIGALE y Synthesizer, están caracterizadas por una población joven formando estrellas a una tasa constante, consecuentemente dominando la formación estelar actual; el aporte de la población vieja es principalmente masa estelar. Ambos programas

obtienen valores similares para la atenuación de la luz de la población joven, en el rango $\sim 0.5 - 3.5$ mag (con mediana ~ 2.5 mag). Las edades de la población joven estimadas con ambos programas son menores a ~ 400 Myr, con valores < 100 Myr para 79% y 53% de estas (U)LIRGs de acuerdo a Synthesizer y CIGALE, respectivamente. Estos valores son compatibles con estimaciones de la duración de brotes intensos en galaxias submilimétricas $\sim 100 - 300$ Myr.

- El valor mediano de la SFR derivada del modelado de SED de nuestra muestra es $\sim 230\ M_{\odot}\mathrm{yr}^{-1}$, compatible con el obtenido para una muestra de galaxias observadas con SCUBA-2. Asumiendo este valor mediano de SFR y una duración de la fase (U)LIRG de 100 Myr, nuestros objetos aumentan su masa estelar en $\sim 2 \times 10^{10}\ M_{\odot}$ en dicha fase. Este aumento se corresponde con un 40% de la masa estelar promedio derivada para nuestra muestra con ambos programas.

Nuestra conclusión es que para derivar propiedades robustas y precisas de las poblaciones estelares en (U)LIRGs a $0.6 < z < 1.5$ es esencial un análisis auto-consistente de la atenuación de la luz estelar y la emisión del polvo en estas galaxias.

Agradecimientos

Esta tesis no hubiera podido se escrita sin el apoyo de la gente que siempre ha confiado en mi, de la gente que me ha aceptado como soy, con mis buenos y mis malos momentos, a todo ellos muchas gracias de verdad...

Contents

Chapter 1

Introduction

1.1 Infrared-bright Galaxies: Historical Remarks

The discovery of infrared-bright galaxies happened five decades ago with the observations of variability in quasars and Seyfert galaxies at infrared (IR) wavelengths by Low and Kleinmann (1968) (see Fig. 1.1), and Kleinmann and Low (1970). Rieke and Low (1972) also reported a population of galaxies with strong IR emission emerging from their nuclei. The IR luminosities of these objects were unusually high when compared with their optical luminosities. In the same study, they also noticed that some of these galaxies hosted compact radio sources with IR fluxes proportional to the radio emission. This fact corroborated the radio-infrared relation, which was first indicated by van der Kruit (1971). This relation produced a debate in order to find if the IR emission from such galaxies was a thermal or non-thermal process. The conclusion was that the IR emission from most of these objects is due to re-radiation of starlight by dust (e.g., Rieke 1978, Rieke and Lebofsky 1979). In the same period, simulations showed that galaxy interactions provoke nuclear activity resulting in violent episodes of star formation (Toomre and Toomre 1972).

The rising interest in IR-bright galaxies[1] brought the first all-sky survey at far-infrared (FIR) wavelengths. This survey was accomplished by the InfraRed Astronomy Sattelite (*IRAS*; Neugebauer et al. 1984), which observed the thermal IR emission of dust (from 1 to 1000 μm) with four filters centered at 12, 25, 60 and 100 μm. *IRAS* detected close to 250,000 extragalactic sources, which had been omitted in optical catalogs. Sanders and Mirabel (1996) summarized some definitions adopted for estimating the broad-band infrared properties of *IRAS* sources. The total infrared luminosity ($L_{\rm TIR}$)

[1]Hereafter, we generalize all galaxies with strong IR emission, therefore selected at IR wavelengths ($\lambda \gtrsim 7$ μm) as IR-bright galaxies.

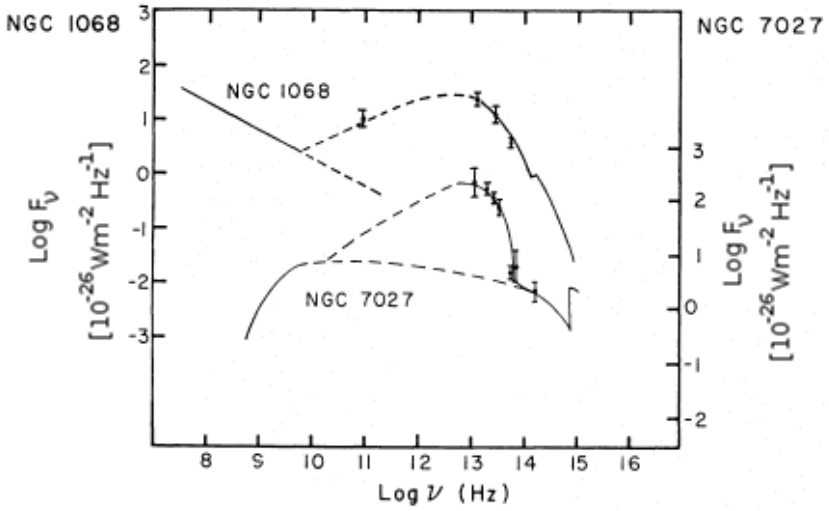

Figure 1.1 : Early infrared measurements from 2 to 22μm of the continua of the Seyfert galaxy NGC 1068 and the planetary nebula NGC 7027.
Credits: Low and Kleinmann (1968)

was considered as the luminosity from 8 to 1000 μm expressed in solar bolometric units ($1\ L_\odot = 3.83 \times 10^{33}$ erg s^{-1}). In addition, IR-bright galaxies were classified by their $L_{\rm TIR}$ as luminous ($L_{\rm TIR} = 10^{11} - 10^{12}\ L_\odot$) and ultra-luminous ($L_{\rm TIR} = 10^{12} - 10^{13}\ L_\odot$), frequently abbreviated as LIRGs and ULIRGs, respectively.

With respect to the origin of the IR luminosity of these sources, it was suggested that the majority of the $L_{\rm TIR}$ of (U)LIRGs is originated by violent star formation events (hereafter, starbursts[2]), but some contribution to this luminosity is due to the activity of galactic nuclei (Sanders and Mirabel 1996).

The first optical imaging surveys of IR-bright galaxies covered an ample range of $L_{\rm TIR}$ (from 10^9 to 10^{12}). Objects with $L_{\rm TIR} < 10^9 L_\odot$ were almost elliptical and lenticular galaxies, with a few spirals. The sources in the range $10^{10} < L_{\rm TIR}/L_\odot < 10^{11}$ were spirals of type Sb or Sc (Rieke and Lebofsky 1986). The galaxies with $L_{\rm TIR} > 10^{11} L_\odot$ are still spirals, but there is an augmenting fraction (up to $\sim 25\%$) of interacting systems (Soifer et al. 1984). This increase in the fraction of interacting galaxies with $L_{\rm TIR}$ was corroborated with the first ULIRGs imaging surveys. Such studies indicated that $70 - 90\%$ of sources with ULIRG (or close-ULIRG) luminosities are big spirals in interaction (e.g., Armus et al. 1987, Melnick and Mirabel 1990). The recent work of Kim et al. (2013) has been devoted to study detailedly the morphological components of these interactions (see Fig. 1.2).

[2]defined as a star-forming episode in a galaxy with a gas depletion timescale that is very short compared to the age of the Universe at the redshift of the galaxy.

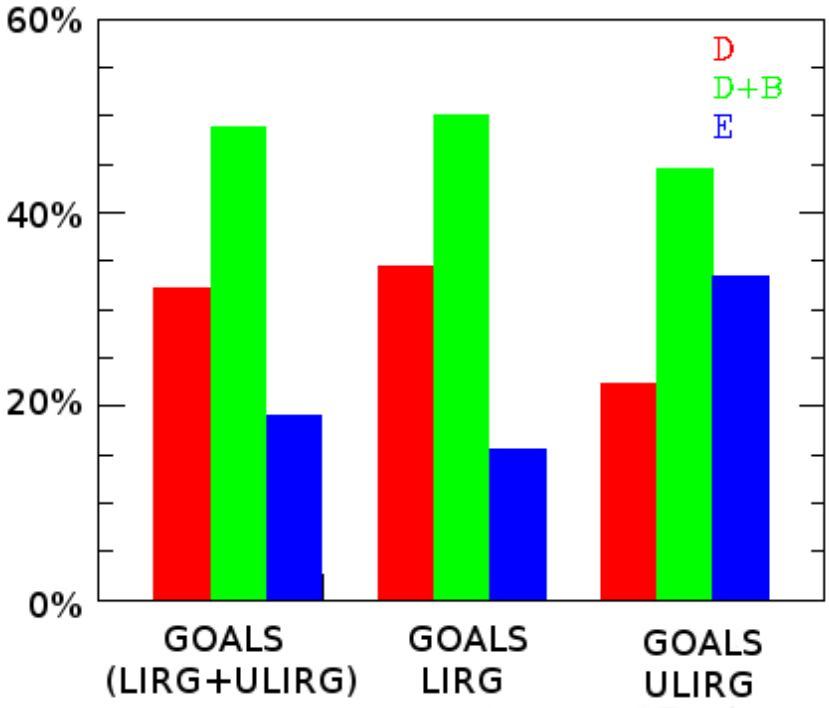

Figure 1.2 : Distribution of the morphological types derived from I-band imaging from the *Hubble Space Telescope* for the Great Observatories All-sky LIRG Survey (GOALS; Armus et al. 2009). From left to right are shown the distribution for all GOALS sources with $L_{\rm TIR} > 2.5 \times 10^{11}\ L_{\odot}$, for GOALS LIRGs, and GOALS ULIRGs. The red, green and blue colors are depicted for disk, disk+bulge, and elliptical structure.
Credits: Kim et al. (2013).

The finding of an increasing number of interacting and/or merging systems when going to higher $L_{\rm TIR}$ conducted to an evolutionary path of IR-bright galaxies. Gas rich galaxy mergers result in starbursts powering an ULIRG, this nuclear violent events of star formation heat the dust of the surrounding cloud, and the AGN appears dissipating the dust envelope (Sanders et al. 1988).

Although *IRAS* detected a couple of galaxies at high redshift (*IRAS* FSC 10214+4724 at $z = 2.86$, Rowan-Robinson et al. 1991; and the Cloverleaf quasar at $z \sim 2.5$, Barvainis et al. 1994), the presence of a noteworthy population of IR-bright galaxies at high redshift was not inferred until the outcome of the results from the Cosmic Background Explorer (*COBE*), launched on November 1989. *COBE* discovered the Cosmic Infrared Background (CIB) radiation by means of the Far Infrared Absolute Spectrometer at $240\ \mu$m (FIRAS, Puget et al. 1996), and with the Diffuse Infrared Background Explorer at 140 and also at $240\ \mu$m (Schlegel et al. 1998). This distant extragalactic IR background light was predicted many years before by Partridge and Peebles (1967).

Surprisingly, when compared with the star formation rate density obtained from the ultraviolet (UV) and optical surveys (Madau et al. 1996), it was noticed that to reach the CIB radiation derived from *COBE*, the star formation rate (SFR) derived from the IR must be at least twice the SFR determined from the UV/optical (Lonsdale et al. 2006). Therefore, the existence of faraway populations of galaxies forming stars in dusty environments was required.

The instrumentation of *COBE* had poor sensitivity to disentangle the galaxy populations that originate the CIB. The first advances in resolving the CIB came with the Infrared Space Observatory (*ISO*, Kessler et al. 1996). Extragalactic surveys were done at 7 and 15 μm with the ISOCAM camera (Cesarsky et al. 1996), and at 90 and 170 μm with ISOPHOT (Kessler et al. 1996), both onboard of *ISO*. Using 15 μm surveys, Elbaz et al. (2002) found a large density of faint IR-bright galaxies. These sources were responsible for $\sim 80\%$ of the CIB measured with *COBE*. The redshift distribution of these objects was found to peak at $z \sim 0.8$. These authors also noticed a correlation between $L_{\rm TIR}$ and the 15 μm luminosity, which is sustained until $z \sim 1$. Utilizing such correlation they claimed that 75% of the ISOCAM sources are LIRGs, and that the comoving density of these LIRGs is at least 40 times larger at $z \sim 1$ than in the local Universe.

Among the results of the 170 μm surveys (e.g., Stickel et al. 1998, Puget et al. 1999), it was found a population of objects selected at this band with *IRAS* counterparts. Using this information, colors between the 170 μm channel and the *IRAS* 60 and 100 μm bands, were derived. Such colors revealed the presence of sources having a dust component with very cold temperature (~ 17 K, Lemke et al. 2001). These objects also present larger dust masses than those estimated in starburst galaxies selected at wavelengths between 12 and 25 μm.

Regarding ULIRGs, the *ISO* program which discovered a large number of these objects was the European Large Area *ISO* Survey (ELAIS, Oliver et al. 2000). Most of such ULIRGs were detected at 15 μm, reaching a fraction of 14% of the whole 15 μm sample (Rowan-Robinson et al. 2004). Many of these ULIRGs have a spectral energy distribution (SED) similar to Arp 220 (see Fig. 1.3), a highly obscured starburst. Some of them being located at the redshift range, $z \sim 2 - 3$.

Then after *ISO*, we have learned that the number of IR-bright galaxies increases with redshift. LIRGs and ULIRGs are a remarkable population at $z \sim 1$ in the context of the global star formation history (SFH) of the Universe.

The IR spatial mission after *ISO* is the *Spitzer Space Telescope* launched in August 2003 (Werner et al. 2004). Among the onboard *Spitzer* instruments, we have the Infrared Array Camera (IRAC, Fazio et al. 2004), and the The Multiband Imag-

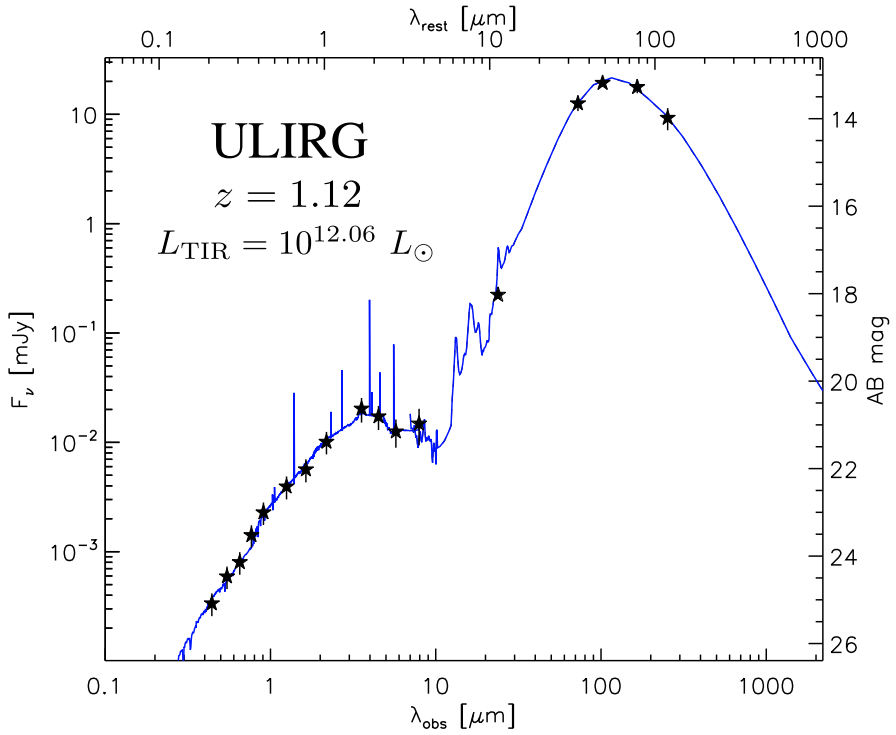

Figure 1.3 : The typical UV-to-FIR SED of an ULIRG. Perceptible features are: the stellar bump at 1.6 μm, the polyciclic aromatic hydrocarbons emitting at $\sim 3 - 14$ μm, and the FIR continuum peaking in this case at ~ 55 μm (all mentioned wavelengths referred to rest-frame).

ing Photometer for Spitzer (MIPS, Rieke et al. 2004). IRAC has four channels that obtain simultaneous broadband imaging at 3.6, 4.5, 5.8 and 8.0 μm. MIPS delivers FIR-wavelength coverage obtaining images at 24, 70 and 160 μm. The instrument was designed to sample the FIR peak due to dust emission (~ 100 μm).

Spitzer has accomplished a series of legacy surveys over several tens of square degrees in order to find large populations of distant (U)LIRGs (e.g., Lonsdale et al. 2003, Le Floc'h et al. 2004, Sanders et al. 2007). Among the results of these *Spitzer* surveys, Rowan-Robinson et al. (2005) have found numerous galaxies with superlative infrared to optical luminosity ratio compared with the average value in the local Universe. These authors also indicate the existence of several cool (U)LIRGs fitted by SEDs resembling spiral galaxies where the dust is heated by the general stellar radiation field rather than starbursts.

Pérez-González et al. (2005) studied a MIPS-24 μm selected sample of star-forming galaxies in the redshift range $0 < z \lesssim 3$. Fitting luminosity functions in several redshift bins in the aforementioned range, they found that the IR cosmic SFR density grows as $(1+z)^4$ from $z = 0$ to $z \sim 0.8$, the slope of this SFR density decreases from $z = 0.8$ to $z \sim 1.2$, but it is still rising. At $1.2 < z \lesssim 3$, the IR SFR density

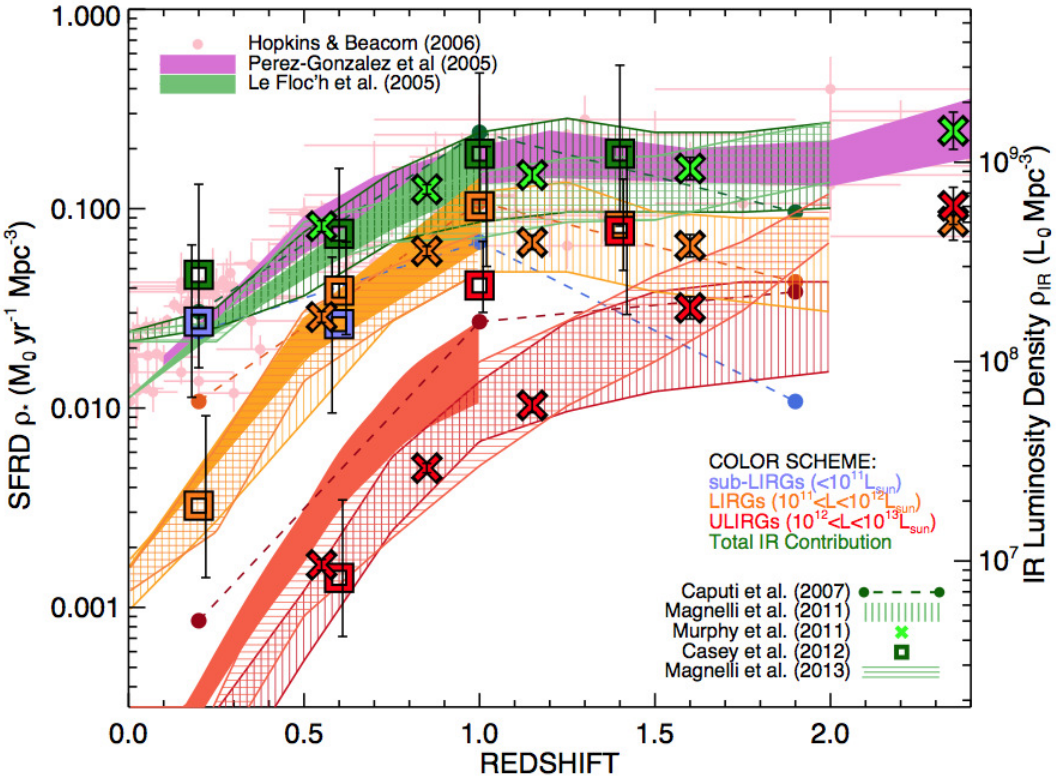

Figure 1.4 : Contributions of IR-bright galaxies to the cosmic star formation and IR luminosity densities estimated by different authors. The color code is: the total IR contribution in *green*, the sub-LIRG population ($L_{\rm TIR} < 10^{11}\ L_\odot$) in *blue*, the LIRG population ($10^{11} < L_{\rm TIR}/L_\odot < 10^{12}$) in *orange*, the ULIRG population ($10^{12} < L_{\rm TIR}/L_\odot < 10^{13}$) in *red*. The authors of each estimate are distinguished by different symbols or line-types as shown (Pérez-González et al. 2005, Le Floc'h et al. 2005, Caputi et al. 2007, Magnelli et al. 2011, 2013, Murphy et al. 2011, Casey 2012). All estimates are based in IR selections except Hopkins and Beacom (2006) which have been corrected for dust attenuation. Notice that not all the derivations are consistent since some $L_{\rm TIR}$s are determined directly from several FIR bands, while others are extrapolations from MIR bands. Nevertheless, all the derivations indicate the small contribution of ULIRGs at $z \sim 0$, and that such contribution become dominant at $z \gtrsim 1.5$.
Credits: Casey et al. (2014).

remains approximately constant (see, Fig. 1.4). In the same work, they pointed out that the (U)LIRG contribution to the SFR density increases unfalteringly from $0 \lesssim z \lesssim 2.5$. Such (U)LIRGs are responsible for half of all newly born stars at $z \sim 1.5$. They also indicated that assuming a nearly flat slope ($\alpha \lesssim -1.3$) of the luminosity function the ULIRG population would become dominant for $z \gtrsim 1.3$. Le Floc'h et al. (2005) have arrived to similar conclusions analyzing a MIPS-24 μm selection in the Chandra Deep Field-South (CDFS) from $z = 0$ to $z \sim 1$. These authors also compare the contribution of the UV (evolving as $(1+z)^{\sim 2.5}$) and IR luminosity, inferring that (U)LIRGs dominate the star formation activity for $z \gtrsim 0.7$. Furthermore, Hopkins and

Beacom (2006) have compiled several results of SFR indicators from the literature in order to derive the global SFR density of the Universe up to $z \sim 6$. They have added the IR SFR density results of Le Floc'h et al. (2005) to correct for obscuration the SFR density obtained from UV measurements to $z \lesssim 1$. They also lean on the IR SFR density findings of Pérez-González et al. (2005) adding a constant value to correct for attenuation the SFR density determined from UV data in $1 < z < 3$. Tresse et al. (2007) studied a spectroscopically selected sample with multi-wavelength photometry to derive the evolution of the SFR density from $z = 0$ to $z = 5$. They compared their UV-derived SFR density, uncorrected from dust attenuation, to the IR SFR density of Pérez-González et al. (2005) and to the dust-corrected H_α-derived SFR density of Tresse et al. (2002) to estimate the amount of attenuation required to retrieve such corrected results from $z = 0$ to $z = 2$. Assuming an average attenuation for the entire galaxy population, they found that the dust obscuration at 1500 Å is $\sim 1.8 - 2$ mag from $z = 0.4$ to $z = 2$. This obscuration diminishes to $\sim 0.9 - 1$ mag from $z = 0$ to $z = 0.4$. They related this attenuation decrease with their finding of early-type galaxies becoming dominant on the B-band luminosity density at $z \sim 0 - 0.4$. This early-type population host small amounts of dust.

Then, the *Spitzer* heritage is a wide mapping of the celestial sky at MIR/FIR wavelengths. In this mapping, thousands of IR-bright galaxies were detected at intermediate and high redshift. The IR mission following *Spitzer* is the *Herschel Space Observatory* launched in May 2009 (Pilbratt et al. 2010). *Herschel* instrumentation includes two cameras which also function as medium resolution spectrometers: The Photodetector Array Camera and Spectrometer (PACS; Poglitsch et al. 2010), and the Spectral and Photometric Imaging Receiver (SPIRE; Griffin et al. 2010). PACS obtains simultaneous images at two bands, 70 μm or 100 μm, and 160 μm. SPIRE carries a three-band imaging photometer operating simultaneously at 250, 350 and 500 μm.

Herschel is the first spatial observatory with an extensive mapping of the sky at sub-millimeter (sub-mm) wavelengths. It has covered several hundreds of square degrees detecting more than a million IR/sub-mm bright galaxies. The PACS imaging photometer was used mainly in two programs: The PACS Evolutionary Probe (PEP; Lutz et al. 2011) and observing the Great Observatories Origin Deep Survey (GOODS) field (GOODS-*Herschel*; Elbaz et al. 2011). These programs were focused on deep observations of blank fields. The SPIRE photometer was utilized primarily for wide-area observations performed for the *Herschel* Multitiered Extragalactic Survey (HerMES; Oliver et al. 2012, and the *Herschel*-ATLAS Survey (Eales et al. 2010). Both surveys also obtained shallow PACS 100 and 160 μm data.

Casey et al. (2012) selected 1594 galaxies with detection in at least one of the 3

SPIRE bands from HerMES fields to do an optical spectroscopic follow-up of these objects. They found spectroscopic redshifts for 767 sources with their redshift distribution peaking at $z = 0.85$, and a fraction of $\sim 95\%$ at $z < 2$. They used FIR detections of each object to estimate directly its $L_{\rm TIR}$. Using these $L_{\rm TIR}$ values, they determined that the contribution of LIRGs to the IR SFR density peaks at $z \sim 1$, and that the ULIRG contribution increases with z, exceeding the LIRG contribution at $z \sim 1.4$ (see Fig. 1.4). These contributions are similar to those derived with 24 μm selected samples (e.g., Pérez-González et al. 2005, Magnelli et al. 2011), but there are also differences (e.g., Le Floc'h et al. 2005 found higher contribution of ULIRGs at $z < 0.5$) suggesting an overestimation in $L_{\rm TIR}$ when derived from $L_{24\mu{\rm m}}$ (see Fig. 1.4).

Magnelli et al. (2013) combined deep PACS observations of GOODS from PEP and GOODS-*Herschel* programs to build photometric catalogs for the 3 PACS bands. Using these catalogs, they derived $L_{\rm TIR}$ values, and then constructed IR luminosity functions down to $L_{\rm TIR} = 10^{11}\ L_{\odot}$ at $z \sim 1$ and $L_{\rm TIR} = 10^{12}\ L_{\odot}$ at $z \sim 2$, respectively. Integrating these luminosity functions they determined that the IR SFR density increases steeply from $z \sim 0$ to $z \sim 1$, and that the slope flattens up to $z \sim 2.3$. LIRGs are responsible for $50 \pm 26\%$ of the IR SFR density at $z \sim 1$, but this contribution diminishes to $30 \pm 20\%$ at $z \sim 2$ where ULIRGs dominate supplying $50 \pm 24\%$ (see Fig. 1.4).

Casey et al. (2014) have summarized the aforementioned IR SFR density findings in Fig. 1.4, which indicates the numerous studies dedicated to point out the importance of (U)LIRG population at $z \gtrsim 0.6$ derived from *Spitzer* and *Herschel* surveys. Moreover, Madau and Dickinson (2014) have compiled data from recent UV (e.g., Cucciati et al. 2012, Bouwens et al. 2012a,b, Schenker et al. 2013) and FIR (e.g., Takeuchi et al. 2003, Magnelli et al. 2011, Gruppioni et al. 2013) SFR density estimations to model the cosmic SFR density at $z \sim 0 - 8$. From these data, they derived that SFR density increases as $\sim (1+z)^{2.7}$ from the local Universe to $z \sim 1.5 - 2$, when the peak of the SFR density happened, at this epoch the Universe was ~ 3.5 Gyr old, and the SFR was 9 times higher than the rate observed presently. Then, the SFR density decreases as $\sim (1+z)^{-2.9}$ at $3 \lesssim z \lesssim 8$. They found a comoving local SFR density value similar to the value it had at $z \sim 7$. They also indicated that that the evolutionary histories of the stellar populations of galaxies and their central black holes present a similar shape, suggesting an evolutionary connection of black holes and their host galaxies.

Regarding the physical process that produces the majority of the $L_{\rm TIR}$ of (U)LIRGs, it is almost accepted that violent star-forming bursts are the main cause, although an Active Galactic Nuclei (AGN) origin is considered too. Starbursts are generated by interactions between gas rich galaxies which are more common in ULIRGs than in

lower luminosity systems. Studying ULIRGs in the local Universe, Farrah et al. (2001) have utilized optical imaging from the *Hubble Space Telescope* (HST). They estimate a fraction of $\sim 90\%$ of interacting systems presenting compact knots, which are thought to have a merger origin.

Studying the merger fraction at high redshift in optical and near infrared (NIR) imaging is difficult due to large amounts of dust generated in galaxy encounters. This dust produce strong attenuation of the stellar light. Nevertheless, Kartaltepe et al. (2007) have used optical imaging from the HST and ground-based optical/NIR data to measure the fraction of galaxies in pairs out to $z \sim 1.2$. They find that $\sim 10\%$ of all bright ($\geq L_V^*$) galaxies are in close pairs at $z \sim 1.2$. They also indicate that the evolution of the pair fraction grows as $(1+z)^3$, implying that at $z \sim 2$, half of all luminous galaxies should be in close pairs. Furthermore, Kartaltepe et al. (2010) have studied the morphology of a MIPS-70 selected sample finding a strong correlation between the major merger fraction and $L_{\rm TIR}$. Their results suggest that at $z < 1$, the major merger fraction is $50-80\%$ in ULIRGs and it is $25-40\%$ for LIRGs. This fraction is smaller, but it is still $30-40\%$ for ULIRGs at $z > 1$.

Respecting AGN activity as the cause of the high $L_{\rm TIR}$ of(U)LIRGs, Brand et al. (2006) have used a 24 μm selected sample including more than 20000 sources to determine the AGN contribution to the MIR emission in (U)LIRGs at $z > 0.6$. They find an increase in the AGN provision to the 24 μm emission, when going to brighter 24 μm flux densities. They estimate a fraction of 9% at $\rm S_{24} = 350$ μJy, growing to $74 \pm 20\%$ at $\rm S_{24} \sim 3$ mJy.

1.2 Cosmological Importance of IR-bright Phases in Galaxy Evolution

The fact of the observed correlation of having an increase in the major merger fraction when reaching higher $L_{\rm TIR}$ values suggests an evolutionary scheme for the utmost luminosity systems (Sanders et al. 1988). In this scheme, the (U)LIRG event comes after two gas-rich disky galaxies encounter and a violent episode of star-formation begins due to the compression and cooling of large amounts of gas. This encounter and the following star formation generate myriads of dust particles which absorb UV/optical radiation from young stars and re-emit such stellar light in MIR/FIR wavelengths throughout the (U)LIRG phase. At the time when the two galaxy nucleus and their respective super massive black hole (SMBH) coalesce an AGN is ignited. This AGN is supported by an accretion disk which bends due to gravitational instabilities producing gas inflows

from the outer parts of the merging system. The (U)LIRG episode is suggested to be of short duration ($\sim$ 300 Myr, see Fig. 1.5), taking into account the finite gas reservoir and the large SFR of the starburst. Once most of the gas is consumed by such starburst, the SMBH commences to blow the residual gas, but it is still dust-enshrouded. Hence, the SMBH resembles an optical quasar when most of the dust has been destroyed. Finally, the system becomes more and more relaxed as the star formation and the quasar activity end due to the exhaustion of gas. The remnant object has the characteristics of an elliptical galaxy with a passive SMBH.

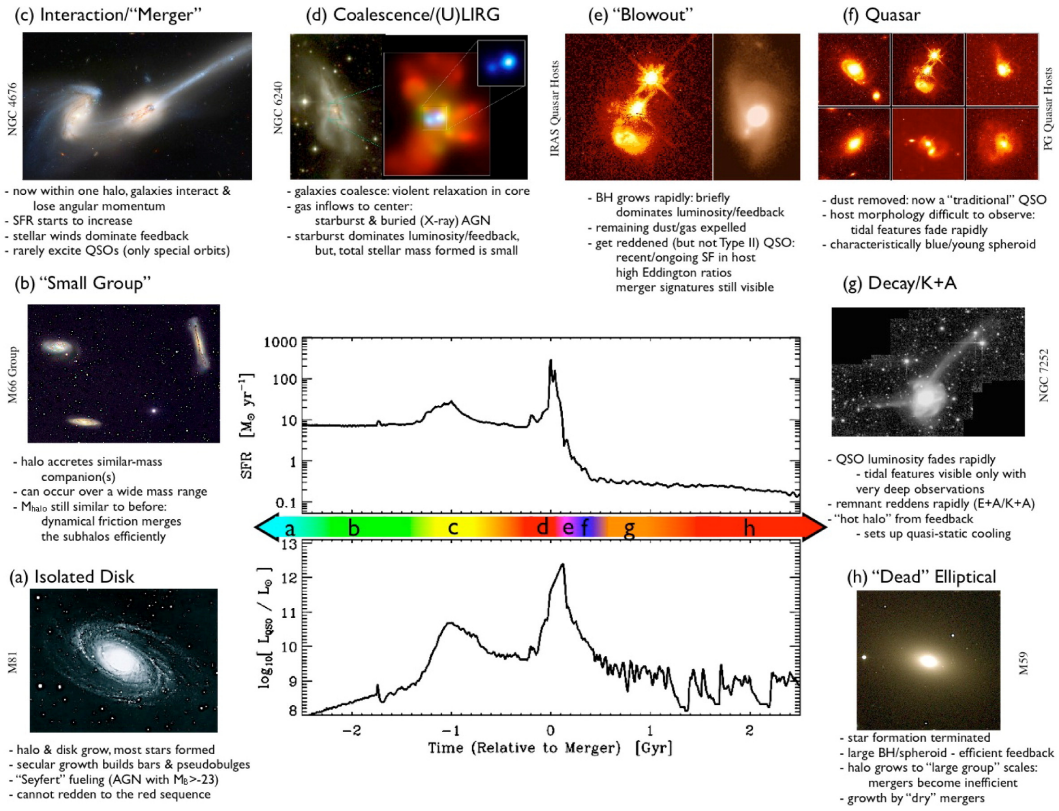

Figure 1.5 : Schematic depiction of the evolutionary phases that a system traverses before and after a major merger of gas rich galaxies. *Credits:* Hopkins et al. (2008).
Image credits: (a) NOAO/AURA/NSF; (b) REU program/NOAO/AURA/NSF; (c) NASA/STScI/ACS Science Team; (d) optical (left): NASA/STScI/R. P. van der Marel & J. Gerssen; X-ray (right): NASA/CXC/MPE/S. Komossa et al; (e) left: J. Bahcall/M. Disney/NASA; right: Gemini Observatory/NSF/University of Hawaii Institute for Astronomy; (f) J. Bahcall/M. Disney/NASA; (g) F. Schweizer (CIW/DTM); (h) NOAO/AURA/NSF.

The aforementioned evolutionary picture is presented in Fig. 1.5, which is replicated from Hopkins et al. (2008). These authors situate the evolutionary scheme in a cosmological framework. By considering starbursts, quasars, and elliptical galaxies as different phases of the same affair, they estimate the cosmological formation rate of the

populations traversing a specific phase, and their evolution with redshift.

Trying to explain the physical processes that produce (U)LIRG luminosities, Kartaltepe et al. (2012) have benefited of the deep PACS 100 and 160 μm observations of GOODS-South from GOODS-*Herschel*, and the HST Wide Field Camera 3 (WFC3) NIR imaging from the Cosmic Assemble Near-infrared Deep Extragalactic Legacy Survey (CANDELS) to study the morphology of 52 ULIRGs at $z \sim 2$. They find that $\sim 70\%$ of these ULIRGs are visually classified as mergers, interactions, and irregular galaxies. They suggest that the final coalescence of a merger may not be necessary to reach ULIRG luminosities at $z \sim 2$, contrary to the situation in the local Universe. Therefore, they give relevance to interactions at different stages, and minor mergers as processes that can trigger high SFRs producing the ULIRG phase in sources at $z \sim 2$. Hence, the evolutionary scheme of a galaxy experiencing a major merger of gas rich disks throughout its lifetime is questioned.

Hung et al. (2013) have used 2085 *Herschel*-selected galaxies at $0.2 < z < 1.5$ in the Cosmological Evolution Survey (COSMOS) field to study the connection between merger fraction and $L_{\rm TIR}$. Using a detailed morphological classification, they find that the fraction of disk galaxies decreases with $L_{\rm TIR}$ up to $z \lesssim 1.5$, and that the fraction of irregular galaxies increases with $L_{\rm TIR}$ out to $z \lesssim 1$. A fraction of $\sim 50\%$ of the sources present signs of interactions for $L_{\rm TIR} > 10^{11.5}\ L_{\odot}$, similar to local LIRGs (but contrary to local ULIRGs, where all sources with $L_{\rm TIR} > 10^{11.5}\ L_{\odot}$ are mergers, Sanders and Mirabel 1996). This suggests that high-redshift ULIRG luminosities can be triggered by other processes different to major mergers.

Consequently, *Herschel* legacy has involved a better determination of $L_{\rm TIR}$ for intermediate and high-redshift IR-bright galaxies based on direct estimations rather than monochromatic extrapolations. *Herschel* surveys have increased the samples of high-redshift IR-bright galaxies allowing a better determination of the evolution of the IR SFR density with cosmic time. *Herschel* and *Spitzer* give us a different picture of high-redshift ULIRGs compared to the local ones. Intermediate and high-redshift ULIRGs are significantly more gas and dust rich (present higher IR surface luminosity density) than local ULIRGs (Rujopakarn et al. 2011).

Considering the impact of the (U)LIRG phase for the cosmic SFR density at $z \gtrsim 0.6$, and the differences between local and medium/high-redshift (U)LIRGs, several natural questions emerge regarding distant (U)LIRGs. How much time a galaxy spends in the (U)LIRG phase? How much stellar mass is added in this phase? How are the stellar populations of these IR-bright galaxies? How much stellar light is attenuated in these dusty objects? What is the role of (U)LIRGs in galaxy evolution?

The answers for such questions reside in the SEDs of these distant (U)LIRGs. The SEDs contain detailed information about the physical properties of galaxies such as: stellar masses, SFRs, SFHs, metallicities, dust content. In order to derive these physical properties from observed SEDs, it is a common practice to use stellar population synthesis and dust emission models.

1.3 Stellar Population Synthesis and Dust Modeling

Stellar population synthesis (SPS) models emulate the different stellar populations that conform a galaxy by means of stellar evolution theory. These populations have a characteristic age and metallicity content yielding to a specific galaxy stellar spectrum. Such stellar radiation is affected by gas emission and dust absorption.

Historically, the (U)LIRG event is related with galaxy interactions yielding gas compression, which results in starbursts. Hence, SFHs including bursts appear as a good choice for IR-bright galaxies. Among the first attempts to model the stellar population of peculiar galaxies we find the work of Larson and Tinsley (1978). In this study, they build stellar population models in order to understand the differences in the color-color diagram $(U-B)$ vs. $(B-V)$ between normal and peculiar galaxies. The models are based on a modified version of the semi-empirical stellar evolution tracks of Tinsley (1972), and a SFH characterized by a decreasing SFR with some optional bursts superimposed at different timescales, and an assumed initial distribution of stellar masses (described by a initial mass function). After deriving synthetic color for their models, they find that the colors of spiral galaxies are compatible with a monotonically decreasing SFR. In the contrary, peculiar galaxies show a large dispersion in colors, which is compatible with short bursts (~ 20 Myr) forming near 5% of the total stellar mass. They indicate that such dispersion is related to tidal interactions, with systems at early stages of interaction presenting the youngest bursts.

Then, these pioneer works modeled different stellar components of a galaxy (e.g., open clusters, groups in an old-disk population) by comparing the position of such components in the Hertzprung-Russell (H-R) diagram with tracks derived from results of the stellar evolution theory. They calibrated their models from these comparisons, building what they called semi-empirical evolutionary tracks. Their models with bursts result from the sum of an old and a young stellar population.

Hence, the stellar light that a galaxy emits can be considered as the sum of the spectra of single stellar populations (SSPs) with different age and chemical composition. A SSP is a population of stars of the same age, and a single metallicity, which spectrum (flux per unit frequency, per unit mass) is produced by the sum of fluxes from individual

stars. Combining the positions in the H-R diagram of stars of different masses with a common age and metallicity an isochrone is formed. These positions are derived from a large grid of tracks which follow the time evolution of stars of a given initial mass and metal content. Several groups have devoted their work to provide consistent evolutionary tracks and isochrones, e.g., Padova (Bertelli et al. 1994, Marigo et al. 2008), BaSTI (Pietrinferni et al. 2004), Geneva (Lejeune and Schaerer 2001).

The initial distribution in mass of the stars forming a SSP is described by the initial mass function (IMF). This IMF is limited between a minimum (commonly determined by the hydrogen burning limit $\sim 0.1\ M_{\odot}$) and maximum stellar mass (typically $\sim 100 - 150\ M_{\odot}$). The IMF is commonly represented by: (1) a power-law (Salpeter 1955), (2) a broken power-law (Kroupa 2001), or (3) a log-normal form (Chabrier 2001).

In order to determine a SSP spectrum, a library of stellar spectra with a large dynamic range in surface gravity ($\log g$), effective stellar temperature ($T_{\rm eff}$), and metallicity (Z) is required. This library should include enough spectra to match the different parameters of the stars that are included in the SSP. There are two approaches to construct stellar libraries: The empirical and the theoretical. Empirical libraries are based on real stars, then, they circumvent uncertainties in stellar opacities and composition of the stellar atmosphere. However, the space of parameters that they cover is biased to Milky Way type stars due to observational restrictions. Examples of empirical libraries covering optical/NIR wavelengths are: Pickles (1998), Indo-US (Valdes et al. 2004), MILES (Sánchez-Blázquez et al. 2006). Contrarily, theoretical libraries can explore a considerable parameter space at high spectral resolution. The main problem that affects theoretical libraries is an incomplete list of atomic an molecular lines. Examples of theoretical libraries include the works of: Kurucz (1992), Westera et al. (2002), Martins et al. (2005).

Therefore, the 3 basic ingredients for SSP modeling are: stellar isochrones, an IMF, and stellar spectral libraries. By combining models of several SSPs with functions that consider the evolution of the metal content and the SFR with time (i.e., the SFH) and a model to account for the attenuation of the stellar spectrum due to dust, we obtain and SPS model. Based on these foundations, several complex SPS models have been developed to interpret the observed UV-to-NIR SEDs of galaxies (e.g., Bruzual and Charlot 1993, Fioc and Rocca-Volmerange 1997, Maraston 2005).

The role of dust in a galaxy is twofold. Dust absorbs the UV-to-NIR light emerging from the stars, and it re-emits such radiation at FIR wavelengths. The attenuation of stellar light due to dust particles depends mainly on the star-dust geometry, dust prop-

erties and dust distribution (homogeneous vs. patchy), and the dust re-emission relies on the interstellar radiation field.

When modeling the SEDs of galaxies, we are interested in the net effect of dust on geometrical star-dust distributions of different complexity. The dust attenuation accounts for stars having different optical depths depending on their location in the galaxy and their age, and for the light scattering into and out different lines of sight. In SPS modeling the shape of the attenuation curve is fixed, common-used attenuation curves comprise, e,g., Calzetti et al. (1994), Charlot and Fall (2000).

Dust emission in the FIR is normally modeled by a modified black body, this modeling assumes that all dust grains are in thermal equilibrium. When considering the MIR wavelengths, it is necessary to take into account emission features from polycyclic aromatic hydrocarbons (PAHs), which are heated stochastically by the interstellar radiation field. There are complex models that consider the different types of dust grains and their associated range of temperatures (e.g., Silva et al. 1998, Piovan et al. 2006, Groves et al. 2008, Popescu et al. 2011). These complex models solve the radiative transfer equation to determine the radiation field over the galaxy, but they include a large number of free parameters and need information about the the star-dust geometry which is normally unknown. Hence, simpler dust-emission models have been created based on such complex ones, commonly known as empirically-based templates. Such templates make use of the complex dust models to fit the observed IR SEDs of galaxies. These templates only depend on one or two parameters, e.g., the Chary and Elbaz (2001) templates are function of the $L_{\rm TIR}$, the Dale and Helou (2002) templates are function of the interstellar radiation field intensity and the dust emissivity. Other simple dust-emission modeling techniques are based on direct fitting of FIR data to modified black body functions (e.g., Blain et al. 2003, Casey 2012).

Conroy (2013) has encapsulated the main aspects of SPS modeling including the absorption and emission processes due to dust in Fig. 1.6. Traditionally, dust absorption an emission are modeled as separated aspects because each feature is influenced by a different property of the galaxy. However, the solutions for such physical properties derived from SPS present degeneracies which depend on several factors among them: the amount of information available to shape the observed SED, and the photometric uncertainties associated to such observations (Gil de Paz and Madore 2002).

An important degeneracy is that found between the age of the stellar population and the dust obscuration. This age-dust degeneracy emerges when the UV-to-NIR spectrum produced by an old, dust-free population cannot be distinguished from that generated by a young, dusty population (Gordon et al. 1997). Notwithstanding, this degeneracy might be broken when UV-to-FIR data are acquired to form a SED. FIR data can help

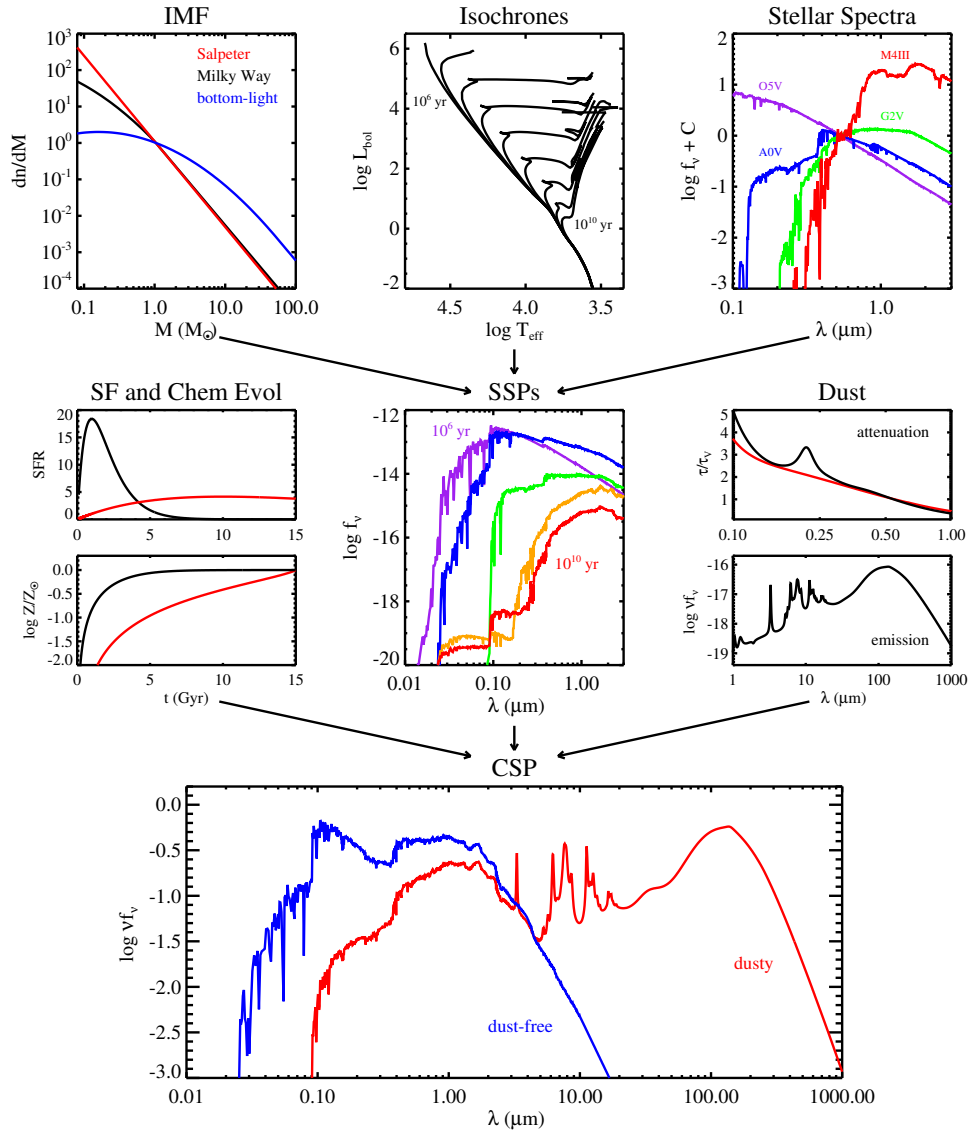

Figure 1.6 : Main aspects of the stellar populations synthesis (SPS) modeling. *Upper panels:* Constituents for emulating single stellar populations (SSPs): an initial mass function (IMF), isochrones for different ages and metal content, and spectra of stars of different types, surface gravities and effective temperatures ($T_{\rm eff}$). *Middle panels:* Elements for SPS and dust modeling: time evolution of star formation rate (SFR) and metallicity (Z), SSPs, and dust-attenuation laws and dust-emission models. *Bottom panel:* UV-to-FIR modeled SED (what Conroy 2013 calls a composite stellar population, CSP) with the blue line depicting the dust-free model, and the red line indicating the spectrum including dust absorption and emission.
Credits: Conroy (2013).

to constrain the attenuation of stellar light if the absorption and emission due to dust are connected in a self-consistent manner (Takagi et al. 1999). An estimation of the energy

emitted by dust can be obtained using FIR data to determine the $L_{\rm TIR}$. Considering that this emitted radiation has the same intensity that the stellar radiation absorbed by dust, i.e., an energy conservation argument, the amount of attenuation of stellar light can be constrained including FIR information in the SED-fitting technique. Such inclusion is named "the FIR prior". By restricting such attenuation we can constrain the age of the stellar population which might be a way to brake the age-dust degeneracy.

(U)LIRGs are bona fide objects to appraise the self-consistent modeling of UV-to-FIR SEDs, and conducting such analysis at the redshift range ($z \gtrsim 0.6$) where these IR-galaxies become dominating the cosmic SFR density is paramount. Benefiting from the large area surveys accomplished with *Spitzer* and *Herschel* in well-observed fields, and from the multi-wavelength data from these fields, now it is possible to carry out such detailed studies (see Fig. 1.7).

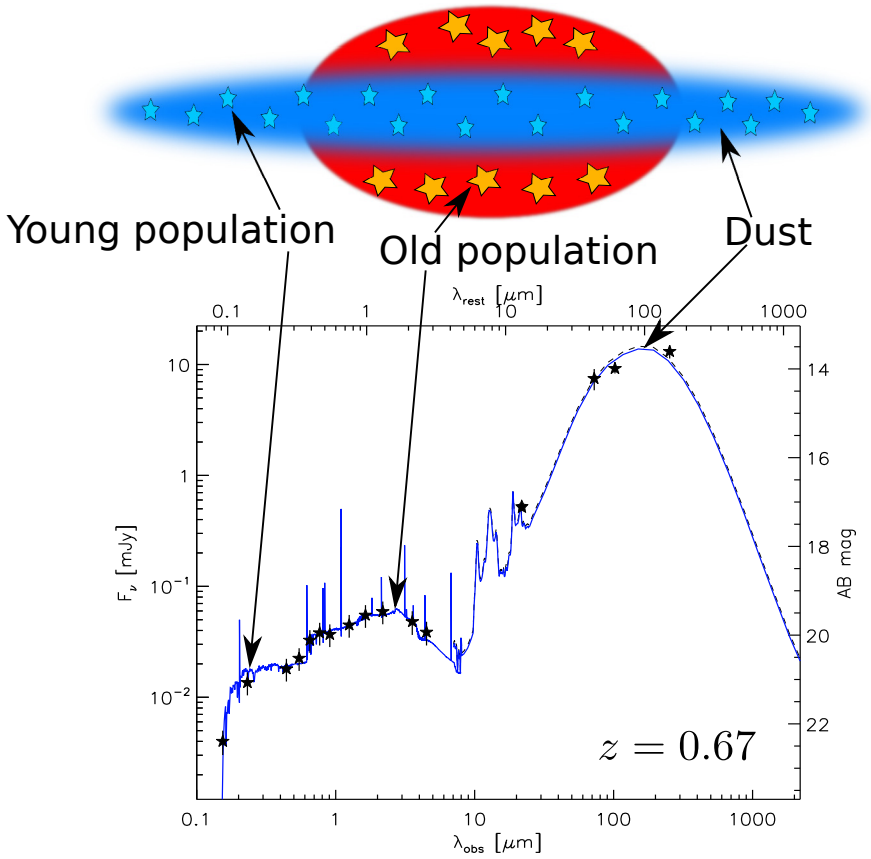

Figure 1.7 : Galaxy cartoon for the UV-to-FIR SED of a LIRG ($L_{\rm TIR} = 3.05 \times 10^{11}$) at $z = 0.67$. The black stars indicate photometric measurements from UV to FIR. The blue solid line depicts the modeled SED derived from the auto-consistent analysis of the stellar and dust emission. In this case, the SFH is described by an old and a young stellar population (represented in the cartoon). The attenuation of such populations in the optical bands is constrained by the energy emitted by dust at FIR wavelengths.

Giovannoli et al. (2011) have carried out a multi-wavelength analysis of 181 LIRGs

at $z \sim 0.7$ selected at 24 μm with 62 objects detected in MIPS 70 μm observed at the CDFS field. In order to derive galaxy properties, they have used the Code Investigating Galaxy Emission (CIGALE; Noll et al. 2009), fitting UV-to-FIR SEDs to models assuming an old and a young stellar population. For the MIPS-70 sub-sample they found SFRs ranging in $10 - 92$ $M_{\odot}$ yr^{-1}, $A(V)$ values in $0.5 - 2.1$ mag, and mass contributions from the young population to the total stellar mass lower than 10% for galaxies with $M_{*} > 10^{11} M_{\odot}$.

Buat et al. (2014) have selected 312 galaxies at 24 μm having multi-wavelength counterparts at $z > 1$ from the GOODS-South field. They find 92 and 54 sources with PACS 100 and 160 μm detections, respectively. They fitted and analyzed the data using CIGALE assuming several SFHs. Their results showed that the best-fit models are those with SFHs described with an old and a young population. From these models, they derived SFRs between 6 and 300 $M_{\odot}$ yr^{-1}. They concluded that regardless the SFH, the SFR determinations are robust when FIR data is available.

1.4 Aim and Objectives

The aim of this thesis is to address an auto-consistent analysis of the stellar and dust emission from IR-bright galaxies at intermediate redshift. In order to do that, we use a FIR-selected sample derived from a region of the sky with multi-wavelength observations the Subaru/XMM-Newton Deep Survey (SXDS) field. The FIR data of our galaxies includes both MIPS and at least 2 *Herschel* bands (from PACS and/or SPIRE). Therefore, we constrain the peak of the dust emission in an accurate manner. Combining this FIR information with UV-to-MIR photometry, we fit UV-to-FIR observed SEDs with self-consistent models in order to investigate detailedly the physical properties of IR-bright galaxies.

The objectives of this research are as follows:

- To derive reliable physical properties of the stellar populations of (U)LIRGS by breaking the age-dust degeneracy utilizing FIR data.
- To determine accurate values of the amount of attenuation of stellar light due to dust in these galaxies.
- To improve the stellar mass and SFR estimations of IR-bright galaxies.
- To investigate on the time spent by galaxies in the (U)LIRG phase.

- To estimate the amount of stellar mass that is added to a galaxy in such phase.
- To derive which stellar properties have more impact in the determination of stellar masses and SFRs of IR-bright galaxies.
- To evaluate how *a priori* assumptions in the modeling and different codes affect the results about the stellar population properties of (U)LIRGs.

Hence, we fit two-population models to the observed SED of IR-bright galaxies with and without FIR data. By doing this, we check the impact of the FIR information in breaking the age-dust degeneracy and the derivation of physical parameters, and we improve our determinations of the SFHs of galaxies, especially for (U)LIRGs.

1.5 Methodology and Chapter Overview

We use two codes that cope the auto-consistent modeling of the stellar and dust emission with energy balance techniques: CIGALE, and the Synthesizer code (Pérez-González et al. 2003, Pérez-González et al. 2008). By comparing the results obtained for the physical parameters of IR-bright galaxies from each code, we check the accuracy and the consistency in the determination of, e.g., the attenuation of UV/optical emission, the stellar mass values, and the SFRs. By determining the age of the young population and the burst mass fraction of the most significant models, we estimate lower limits for the lifetime and the mass added in the (U)LIRG phase. We analyze our SFH based on two stellar populations in order to determine which stellar properties are dominant when studying the $SFR - M_*$ relation.

With the intention of utilizing the aforementioned codes, we build FIR catalogs for the available observations at these wavelengths in order to determine an accurate value of the $L_{\rm TIR}$. We also compile and catalog the available UV-to-MIR data in order to find secure counterparts for the FIR detections and to obtain reliable and unambiguous fits to SPS models.

The organization of this document is as follows. In Chapter 2, we describe the FIR data reduction and how we construct and validate the reliability of FIR catalogs. In Chapter 3, we present the ancillary data compiled for this study, the construction of multi-wavelength catalogs, and the validation of the FIR-selected galaxy sample. In Chapter 4, we describe the SPS and dust modeling, and the main characteristics of the CIGALE and the Synthesizer code. In Chapter 5, we study the impact of FIR data in the modeling of the UV-to-FIR SED, compare fits and parameter values derived with

one and two population models and analyze the degenaracies in the solutions of such modeling. In Chapter 6, we present our results for the stellar properties of IR-bright galaxies derived from the modeling with the CIGALE and the Synthesizer code. We compare and discuss both sets of results. Finally, Chapter 7 presents the conclusions of this thesis.

Throughout this document, we use a cosmology with $H_o = 70$ km s^{-1} Mpc^{-1}, $\Omega_M = 0.3$ and $\Omega_\Lambda = 0.7$. All the magnitudes refer to the AB system.

Chapter 2

FIR Data Reduction and Cataloging

Given that one of the goals of this work is to describe and quantify the effects of the dust emission, when it is used to constrain the attenuation of the stellar populations of IR-bright galaxies, we need to determine the total infrared luminosity in the most accurate way. In order to fulfill this precise determination, we need to probe the dust emission around the FIR peak (where the dust radiates most of the energy it absorbs) with the largest number possible of MIR-FIR bands. This can be done by combining *Spitzer* and *Herschel* data, in particular, MIPS $24 + 70$ μm, and PACS and SPIRE bands. Considering that MIPS 70 μm observations are the shallowest from the ones mentioned above (see Section 2.1.1), we have chosen this band as selection basis in order to guarantee detections in both *Spitzer* MIPS bands, and therefore observational measurements before the FIR peak.

We describe in the next Sections the data adquistion and processing of the *Spitzer* MIPS and *Herschel* data.

2.1 *Spitzer* MIPS Data

The sample used in this study is based on the MIPS data of SXDS/UDS field, which was observed for the *Spitzer* Legacy Program for the UDS (SpUDS, Dunlop et al. 2007). The MIPS 24 and 70 μm imaging were taken using the scan map mode at the slow rate. This process required 3 scan legs for each Astronomical Observational Request (AOR). SpUDS comprised IRAC and MIPS observations, which were taken in 98 AORs in one epoch, February 2008. These observations covered an area of ~ 1 square degree with central coordinates at $\alpha = 02^{\rm h}17^{\rm m}35^{\rm s}$, $\delta = -04^{\circ}54'22''$.

2.1.1 The Catalog in the Selection Band: MIPS 70 μm

All the MIPS 70 μm Basic Calibrated Data (BCD; which are data derived from a single frame exposure in FITS format) from the program 40021 (PI, James S. Dunlop) were downloaded from the *Spitzer* Science Center (SSC) Archive. All these BCD were combined using the SSC MOsaicking and Point source EXtractor software (Makovoz and Khan 2005; MOPEX).

The MIPS 70 μm data present significant data artifacts due to the Gallium doping in Germanium photoconductive detector. The main artifacts are the stimulator-flash latents and the variations of the slow response as a function of time (see the MIPS Data Handbook[1]). The slow-response variations affect as dark horizontal stripes, and the stim latents are noticed as dark vertical stripes in the MIPS 70 μm mosaics (see, Fig. 2.1). Both artifacts need to be removed by filtering procedures.

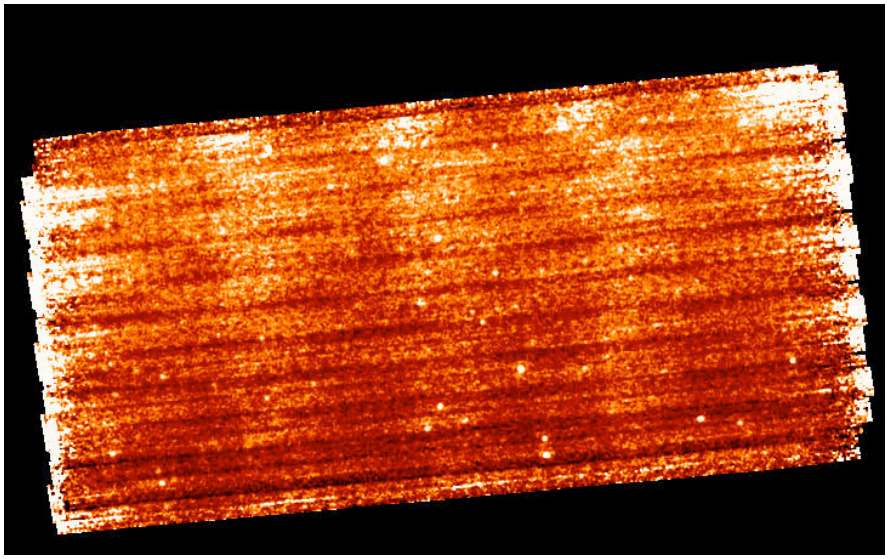

Figure 2.1 : Mosaic obtained from 4 AORs of unfiltered MIPS-70 BCDs. The in-scan dark horizontal stripes are due to fast/slow response variations of the detector. The bright vertical stripes are due to stimulator-flash latents.
Credits: Spitzer Science Center.

Then, the reduction process for the MIPS 70 μm data requires first removing slow-response variations by applying a high-pass temporal median filter per pixel (i.e., substract the median value per pixel of the adjacent BCDs as a function of time). Afterwards, the stim flash latents artifacts are removed by subtracting the median value of each column for every MIPS 70 μm BCD (see; the MIPS Data Handbook, and Frayer et al. 2006). Both filtering steps were done using $cleanup70.tcsh$ GeRT script, as it is

[1] MIPS Instrument Handbook: `http://irsa.ipac.caltech.edu/data/SPITZER/docs/mips/mipsinstrumenthandbook/1/`

explained in the SSC Germanium Reprocessing Tools (GeRT) documentation.

Once with the set of BCD free from artifacts, we can proceed to build the mosaic. The first step in the mosaicking process is to project the clean set of BCD onto a common image frame. This fiducial image frame defines the sky position, orientation and size of the mosaic. The BCD are distorted due to the MIPS optics (twist of the scanning mirror and distortion of the detector array). The distortions coefficients are included in the BCD headers, they are used for corrections in the projection process (see Fig 2.2). MOPEX gives the possibility to achieve this projection using linear, grid, and drizzle interpolation schemes. The value of an output interpolated pixel of the mosaic is equal to the weighted average of BCD input pixels overlapping such output pixel, the weights are the relative overlap areas (see upper panel of Fig 2.3). In the drizzle interpolation scheme, the input pixels are shrunk by a drizzle factor, the value of the shrunken pixels are equal to the input original pixels. These shrunken pixels are projected onto the fiducial image frame (see lower panel of Fig 2.3). Afterwards the BCD are projected, MOPEX flags pixels affected by cosmic rays and asteroids that were undetected in the first reduction step, using a multiframe temporal detection method. These flagged pixels are traced in order to create new masks which are used when the BCD are reprojected and mosaicked (see Fig. 2.4).

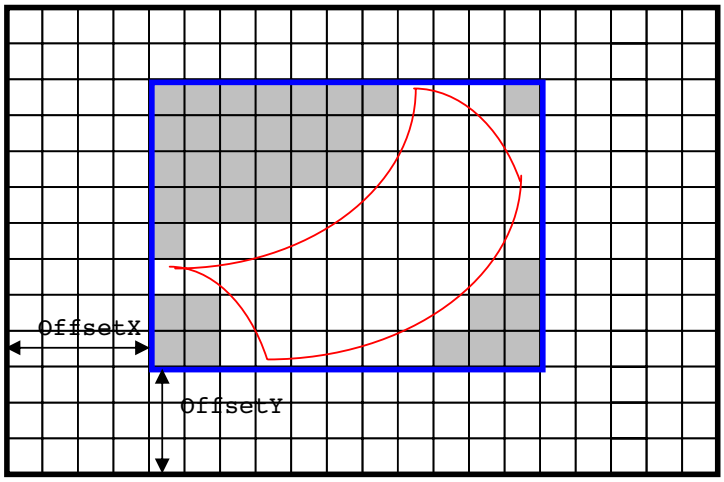

Figure 2.2 : The optical distorted input BCD images represented by the *red* region are projected onto the *black* reference common image frame. The minimum interpolated fiducial image frame is shown in *blue* containing all the input BCD images. The pixels with no overlap with the input BCD images are *shaded*.
Credits: Spitzer Science Center.

In our case for the SXDS/UDS field, a total of 51507 BCD units were projected using the drizzle interpolation technique, and they were mosaicked using an output square pixel size of $4.0''$.

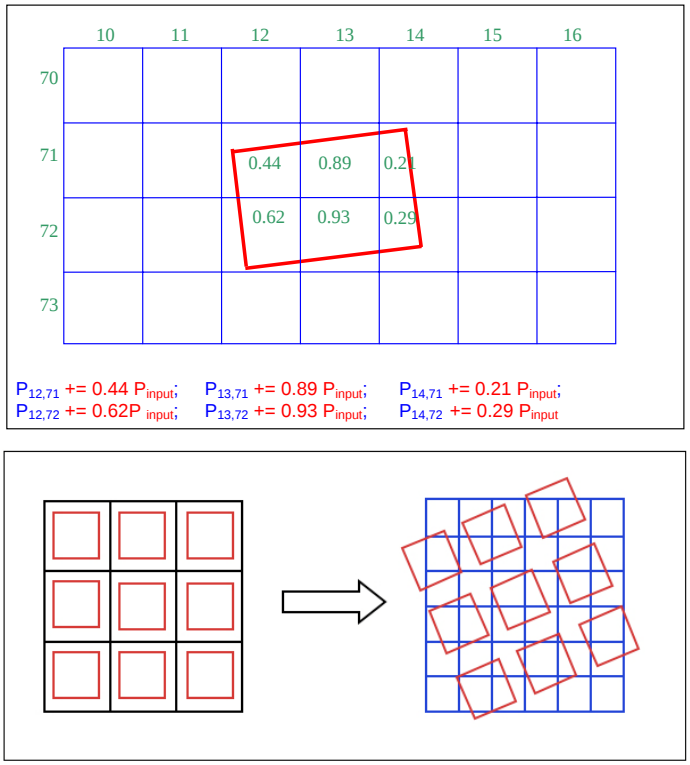

Figure 2.3 : *Upper panel:* Weighted average method for the output pixels of fixed size. *Lower panel*: Input pixels in black and drizzle pixels in red. The drizzle pixels are projected onto the fiducial image frame shown in blue.
Credits: Spitzer Science Center.

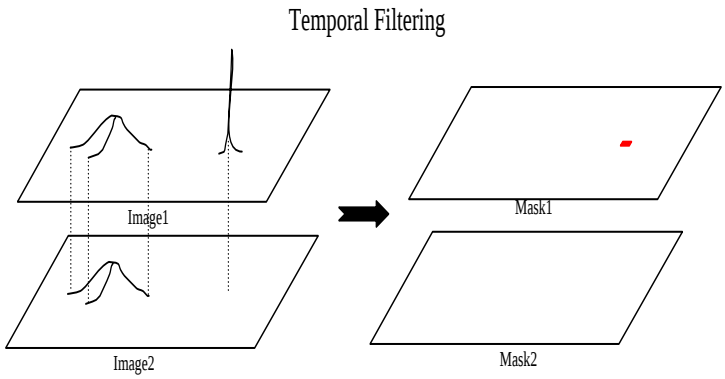

Figure 2.4 : Multiframe temporal detection cartoon showing two BCD from the same sky region. In the upper BCD a cosmic ray is detected and the corresponding pixel is masked.
Credits: Spitzer Science Center.

The presence of bright sources—Point Spread Function (PSF) having Full-Width at Half Maximum (FWHM) of $\sim 18''$—in the resulting mosaic produces a boost of the filtering effect. This boosting causes the subtraction of part of the source flux, which can be appreciated as negative side lobes surrounding the bright sources (see

Fig 2.5). We got rid of such problem following the procedure described in Frayer et al. (2009): (1) Making a first try mosaic after applying both aforementioned filtering steps, (2) identifying bright sources and doing a first attempt photometry (we take as bright sources each with flux $\geq$ 15 mJy), (3) masking bright sources in the original BCDs, (4) recalculating filtering corrections ignoring pixel containing bright sources in all the BCDs, and (5) doing the final co-addition of the re-filtered BCDs. The steps (1)-(4) were done using $cleanup70.tcsh$ GeRT script, as it is explained in the SSC Germanium Reprocessing Tools (GeRT) documentation. In Figure 2.6 is notorious a big improvement in the surroundings of bright sources, therefore preserving the flux. The final data co-addition was done as it is explained above with MOPEX.

In Figure 2.7, we show the final 70 μm mosaic. Additionally to this final mosaic, MOPEX can provide its associated coverage map, which indicates that our 70 μm mosaic has an average exposure time of ~ 1430 s per pixel.

The source detection and photometry for the MIPS 70 μm mosaic were carried out with a PSF technique plus aperture correction. We have detected 70 μm sources in two steps. In the former, we detected sources with SExtractor using as weighting image the coverage map. Subsequently, photometry was accomplished using *phot* and *allstar* tasks from the DAOPHOT package in the Image Reduction and Analysis Facility[2] (IRAF). In the second step, we have taken advantage of the noteworthy depth of the 24 μm SXDS/UDS mosaic ($S_{5\sigma}[24] \simeq 70$ μJy, see, Section 2.1.2, and upper panel of Fig. 2.8), using its World Coordinate System (WCS) position as priors for the locations of 70 μm sources.

In the former step, we detected sources in a first pass in the final MIPS 70 μm mosaic. We used SExtractor (`DETECT_MINAREA`$= 9$ and `THRESHOLD_TYPE RELATIVE` used as default) utilizing a `DETECTION_THRESHOLD`$= 1.7$, the weighting image for detections was the aforenamed coverage map. Then we built a empirical PSF (FWHM $\sim 18''$) with the bright isolated sources. Afterwards, we did the flux measurements for such first pass, and looked for possible sources in the residuals image, and then we did a second pass (using also `DETECTION_THRESHOLD`$= 1.7$). We extracted PSF photometry from all the objects of the two passes together. The PSF fitting method involves scaling the aforenamed empirical PSF to a circular aperture of $36''$ (9 pixels) in this case. The method provides the flux enclosed in this aperture, then an aperture correction is needed to consider the flux in the PSF wings outside of the chosen aperture. The sky estimation was performed first removing the large scale variation, and then measuring

[2]IRAF is distributed by the National Optical Astronomy Observatory, which is operated by the Association of Universities for Research in Astronomy (AURA), Inc., under cooperative agreement with the National Science Foundation

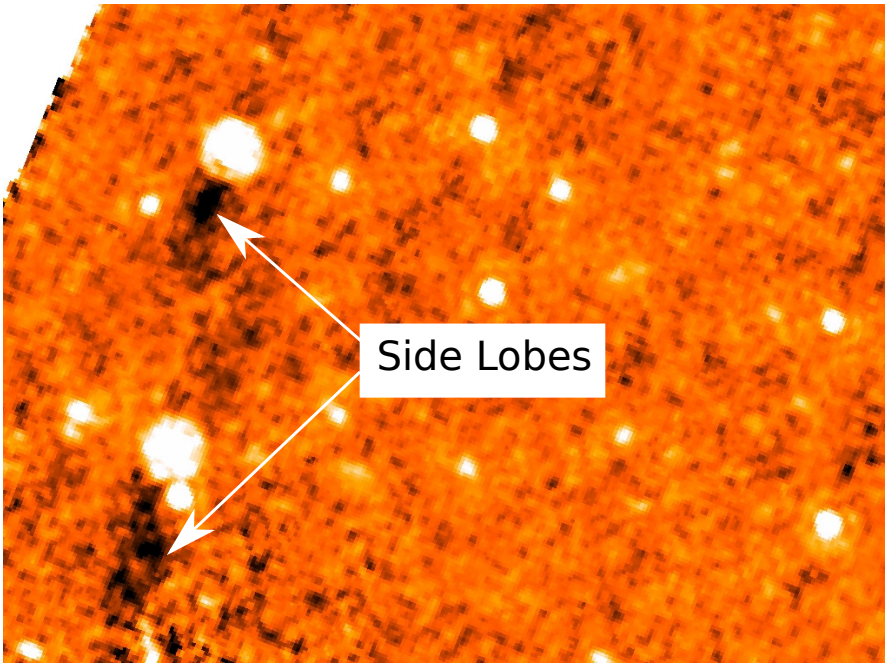

Figure 2.5 : A region of the MIPS 70 μm mosaic showing negative side lobes surrounding bright sources due to the boosting of the filtering effect.

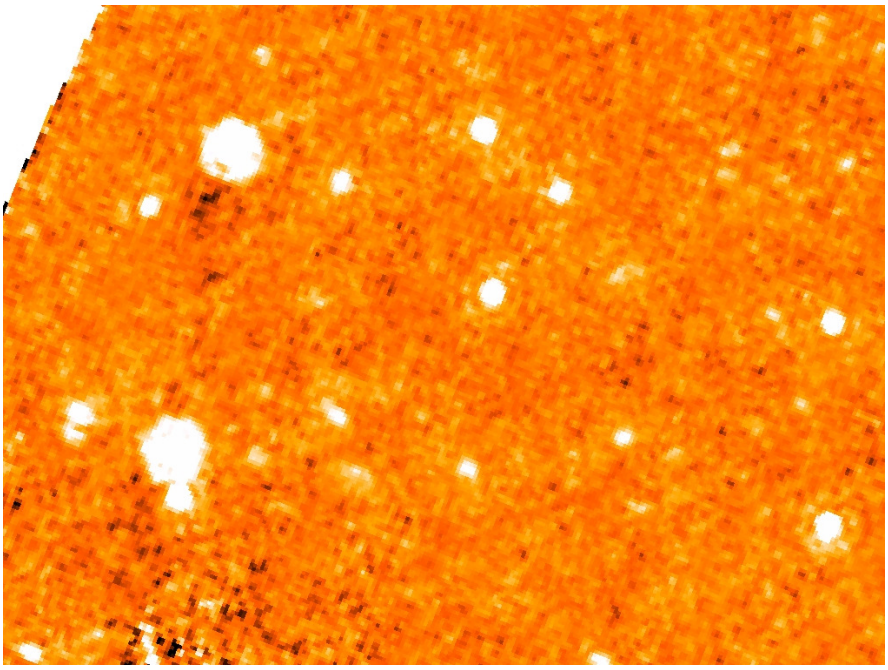

Figure 2.6 : A region of the MIPS 70 μm mosaic after masking bright sources and re-calculating filtering correction for the BCDs.

the background around each source using a background annulus of $28''$ measured from $80''$ to $108''$ from the central coordinates of the source, and we corrected to the total

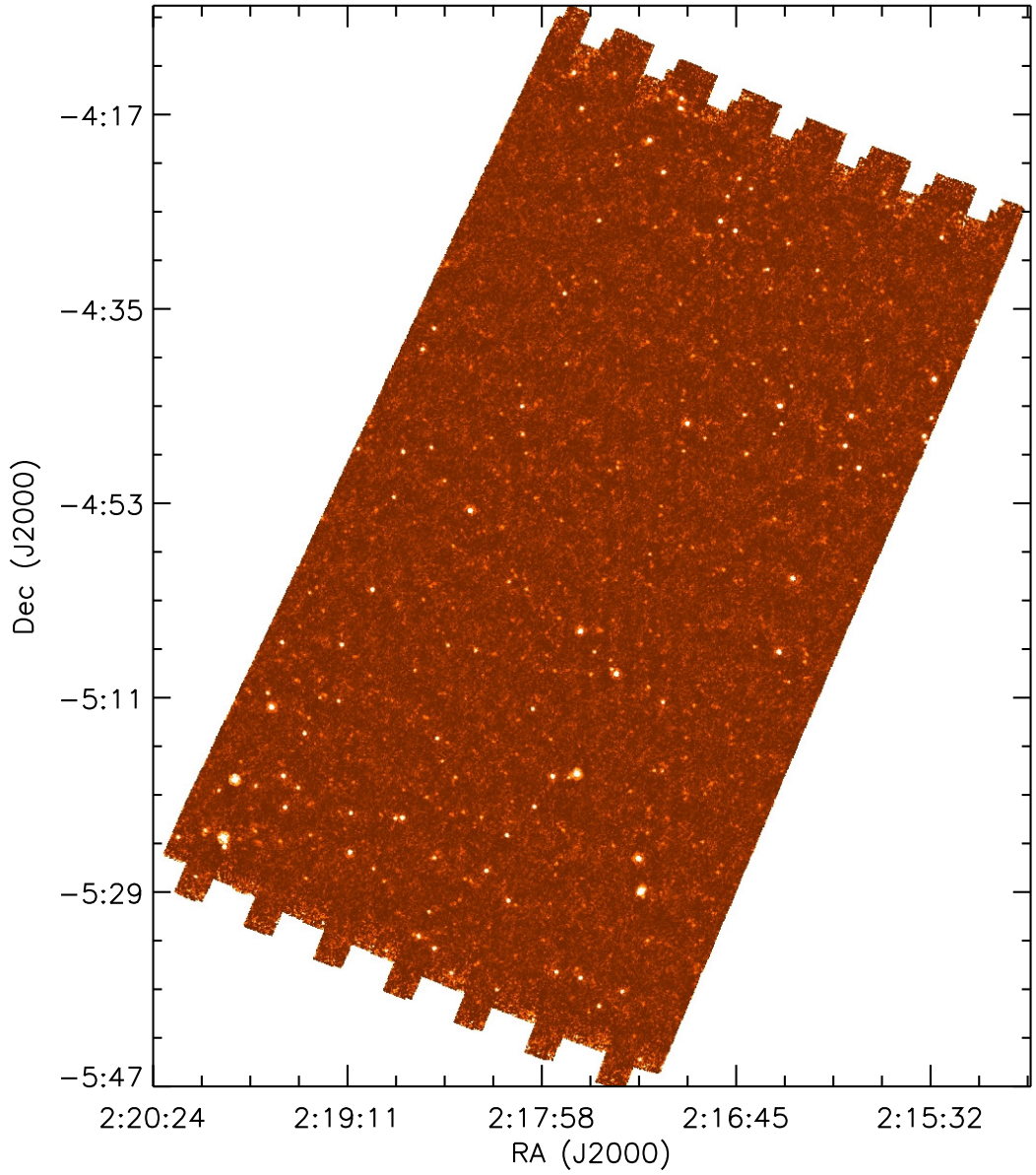

Figure 2.7 : MIPS 70 μm mosaic constructed with MOPEX for the SXDS/UDS field. The mosaic is aligned so that the North Celestial Pole is up.

flux using an aperture correction of 16%.

The errors of the MIPS 70 μm photometry were estimated from the sky uncertainty. The largest sky determination between *phot* and *allstar*, is compared with 3 different estimates, derived as explained in the appendix A of Pérez-González et al. (2008). First, measuring the average background in a sky box of $2'$ side surrounding each source, scaling this value with a factor $N^{1/2}$, where N are the number of pixels of the box. Second, measuring the average sky level on unconnected artificial circular apertures (of 9 pixel radii in this case), built with random sky pixels around each source. Third, the

flux measured on several circular apertures (of 9 pixel radii too) is fitted to a Gaussian function to obtain and rms sky fluctuation. The final error is set to largest value from the 5 estimations.

In the second step, we have employed a position prior method similar to which is described in Pérez-González et al. (2010). Fundamentally, the method combines high confidence direct detection positions with prior based positions. We cross-correlated the 70 μm catalog that we obtained in the first step with the 24 μm catalog (see Section 2.1.2) in a $3''$ search radius. We looked for differences in WCS for both catalogs, but we got that the WCS accuracy was $\sim 1/3$ of the 70 μm pixel size (i.e., $< 1.4''$), then an alignment between images was unnecessary (see Fig. 2.9). Hence, we located the 24 μm sources in the 70 μm image (see lower panel of Fig 2.8). The different PSF sizes of the 24 μm (FWHM $\sim 6''$) and the 70 μm (FWHM $\sim 18''$) bands indicated that we may have several 24 μm sources merged in one single 70 μm source in some cases (see blue open circles on lower panel of Fig. 2.8). Then, before measuring the photometry, we removed sources closer than three-quarters MIPS 70 μm FWHM ($13.5''$), retaining only the brightest source from each merged group (as it is indicated by the junction of blue lines on lower panel of Fig 2.8). The prior catalog was cut to a 5σ threshold in order to avoid spurious identifications in the MIPS 70 μm catalog. Nevertheless, the number of positions of sources with $\mathrm{S}[24] > 70$ μJy inside the 70 μm mosaic is ~ 20000. Then, we measured aperture photometry in a 3 pixel ($12''$) radius in the MIPS 70 μm image, and we only kept as reliable priors sources that were recentered in less than a 70 μm pixel and with magnitude error less than 0.11 mag (as indicated by green open circles in the lower panel of Fig. 2.8). Note that ~ 70 μJy at MIPS 24 μm implies a detection threshold of ~ 2.8 mJy at MIPS 70 μm for the reddest sources one could expect (according to the hottest dust temperature models of the CE01 templates, see Fig. 2.10). This is a quite comparison with the typical 5σ detection level in the MIPS 70 μm image (~ 9 mJy). We combined the purged list of prior sources with the 5σ direct detection in MIPS 70 μm list and applied the PSF fitting technique. An example of the final detections is shown as magenta open circles in Fig. 2.8.

The number of sources above the 5σ threshold in our final 70 μm catalog is 542. These 542 high-confidence objects are detected in an area of 1.15 deg^2 with homogeneous exposure time.

In order to determine the completeness levels, we carried out simulations. Basically, artificial sources were constructed using our empirical PSF, and they were inserted at positions into the 70 μm image considering the typical color $\mathrm{S}[70]/\mathrm{S}[24]$ for several 70 μm flux intervals (see Fig. 2.11). The number of sources inserted was $\sqrt{N}$, where

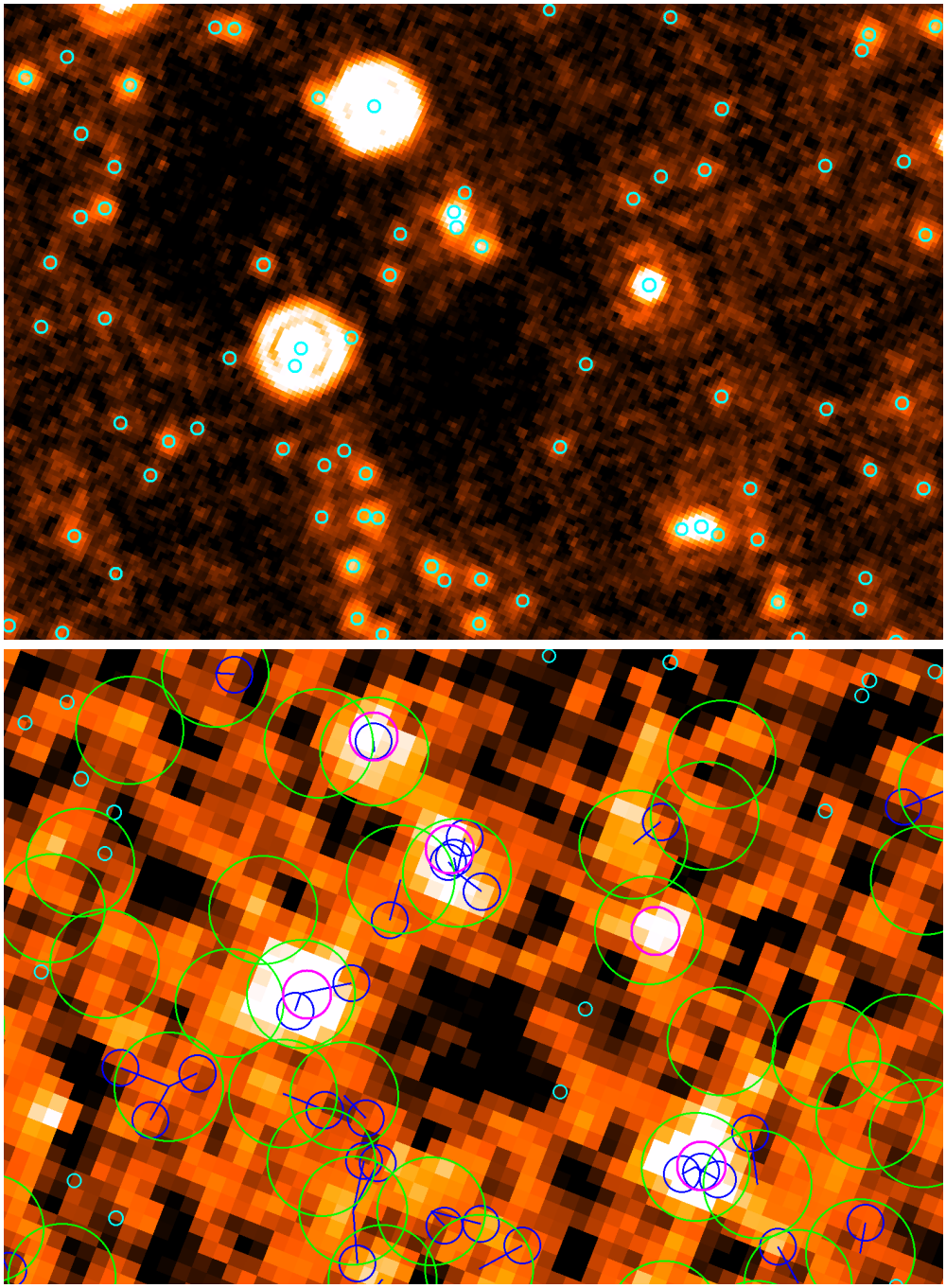

Figure 2.8 : *Upper panel:* A region of the MIPS-24 mosaic. The positions of sources with $S[24] > 70$ μJy obtained from the PSF-fitting cataloging method are shown as cyan open circles. *Lower panel:* A region with the same WCS of the upper panel, but observed with MIPS 70 μm. The locations of 24 μm sources above $S_{5\sigma}[24]$, i.e., the prior positions, are displayed in the 70 μm mosaic as small cyan open circles when they were rejected at 3 pixel aperture photometry, as medium open blue circles when they were merged in a location to try photometry at the 70 μm image, and as big open green circles in the positions where *phot*+*allstar* photometry was effectuated. The detections in our final MIPS 70 μm catalog are indicated as magenta open circles.

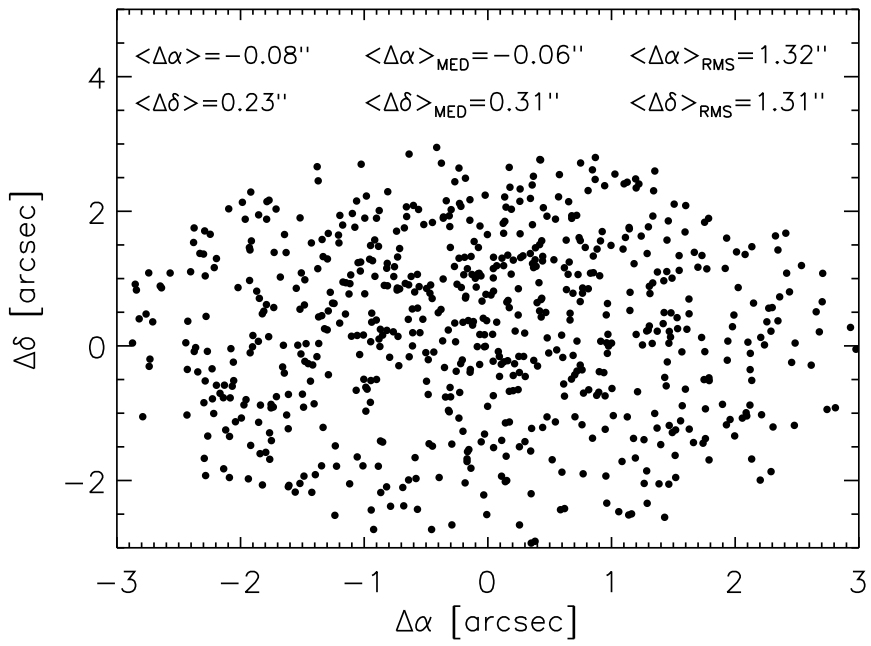

Figure 2.9 : Differences between right ascension and declination of the 70 μm sources with respect to the 24 μm objects. The random distribution of points indicates that there are not systematic differences in each set of WCS.

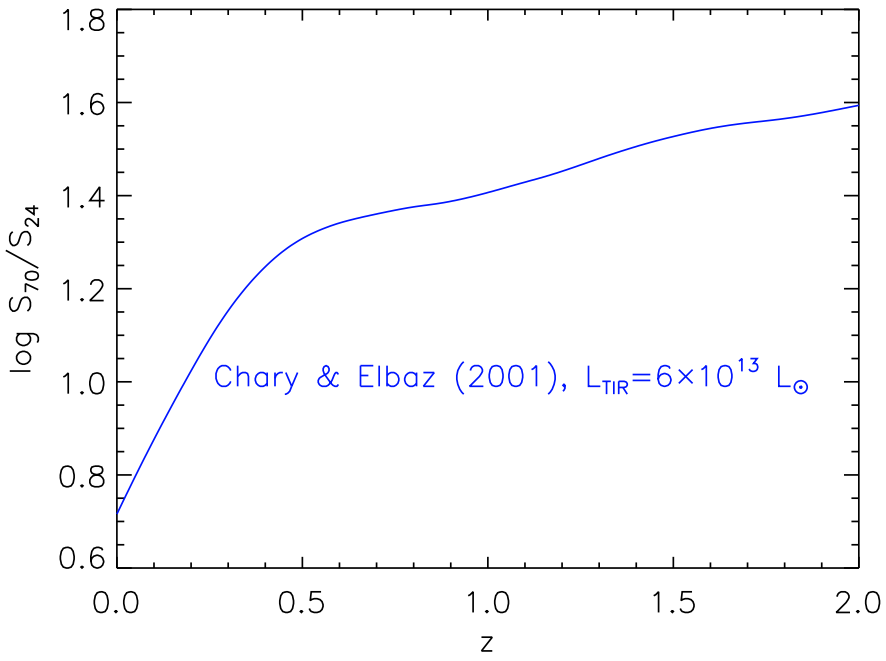

Figure 2.10 : Color $\log \mathrm{S}[70]/\mathrm{S}[24]$ as function of redshift. Assuming that MIPS 70 μm can detect objects a $z \sim 2$, $\mathrm{S}[24] = 70$ μJy corresponds to $\mathrm{S}[70] = 2.75$ mJy, for the most luminous models from the templates of Chary and Elbaz (2001).

N is the number of sources in each 70 μm flux interval, i.e., the statistical counting error, or 100 if $\sqrt{N} > 100$. A location of the 24 μm priors was chosen when the source at this position satisfied the 24μm flux limits (the 24μm flux was between the quartiles) of the color-flux diagram, and the $\mathrm{S}[24]_{5\sigma}$ threshold ($\sim$ 70 μJy) for each 70 μm flux interval. Then, these inserted sources were extracted using the same prior-based procedure followed for generating our 70 μm SXDS/UDS catalog. The completeness levels that we have obtained are shown in Fig. 2.12.

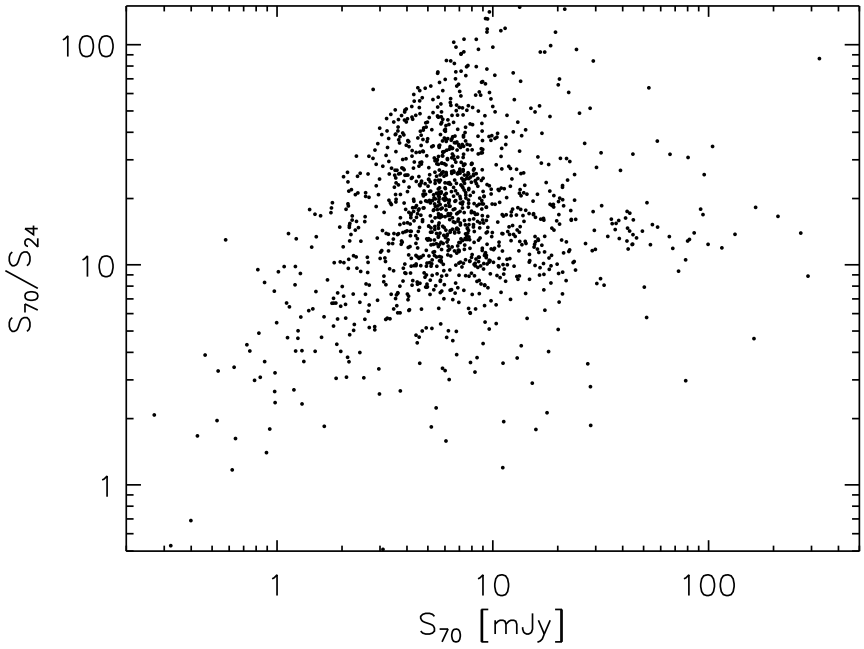

Figure 2.11 : S[70]/S[24] as function of 70 μm flux density of our final MIPS-70 catalog for SXDS/UDS field.

We also estimated from the same simulations the thresholds of flux density and signal-to-noise where the Eddington boosting (Eddington 1913) becomes relevant. We found that for $\mathrm{S}[70] \gtrsim 6$ mJy and $\mathrm{S/N} \gtrsim 4$ this flux boosting is $\lesssim 5\%$. Therefore, we have only used flux values above this threshold for fitting the completeness curves. Furthermore, the effect of this boosting is not significant for the sources included in our final catalog.

In order to compare with other 70 μm completeness estimations, we have also plotted in Fig. 2.12, the completeness data provided by Frayer et al. (2009) for the COSMOS field. Considering the curves of Fig. 2.12, we can stay that prior-based technique performs better than a blind detection for sky levels in $4 < \sigma < 7$.

We have counted the number of 70 μm sources in a set of flux bins for the SXDS/UDS

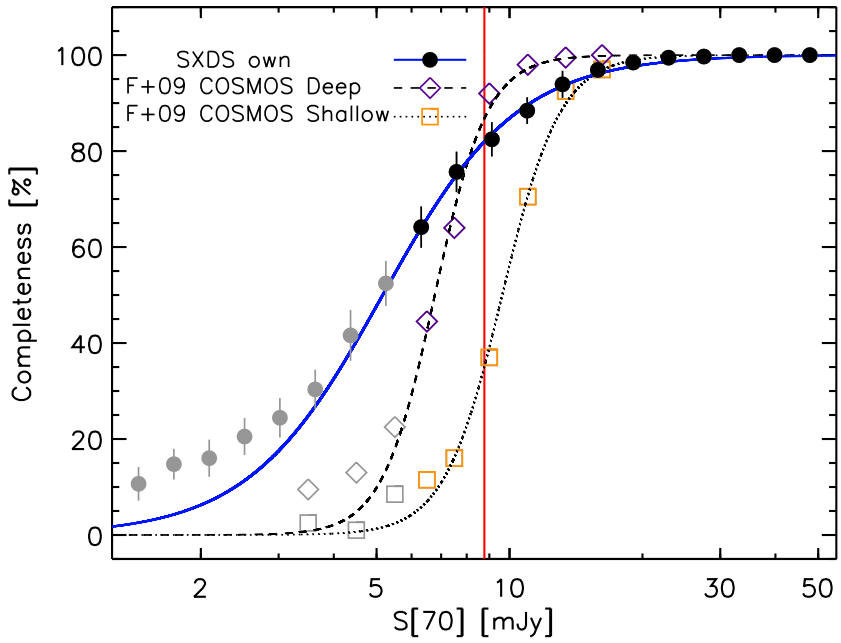

Figure 2.12 : The 70 μm completeness levels as a function of flux density determined by simulations using a prior-based PSF-fitting method for the SXDS/UDS field. The completeness estimations of Frayer et. al. 2009 (F+09, S-COSMOS) are shown for comparison. The red vertical line stands for $S[70]_{5\sigma} \sim 9$ mJy

Note : The grey symbols are not used for the fits.

field. In order to correct for incompleteness, we have divided for the completeness level corresponding to each flux bin in concordance with our completeness estimations (see Fig. 2.12). These differential number counts were normalized to the Euclidean slope, i.e., they are multiplied by $S[70]^{2.5}$, which is useful for visualizing a relatively flat distribution of galaxies. In Figure 2.13, we have plotted our derived differential number counts with their associated error bars which only take into account the statistical Poisson uncertainty. We also show in the aforenamed figure, the differential number counts at 70 μm derived in 3 earlier works (Frayer et al. 2006, and Frayer et al. 2009 using MIPS 70 μm; and Berta et al. 2011 utilizing PACS 70 μm).

Considering the uncertainties, our derived counts show a good agreement with these 3 other surveys (root-mean-square error $\sim 35\%$). At fluxes between $\sim 6 - 10$ mJy, our results are consistent with those derived by Frayer et al. (2006) for GOODS-N within $\sim 5\%$. We also observe the same turn on in the counts around $8 - 10$ mJy that Frayer et al. (2006, 2009) have pointed out. At fluxes between $\sim 10 - 20$ mJy, we noticed a break in the counts, but this break has also been presented in the MIPS 70 μm counts of Béthermin et al. (2010). At the brightest flux densities ($\sim 30 - 100$ mJy), our values are also compatible with the results of Frayer et al. (2009) within $\sim 20\%$.

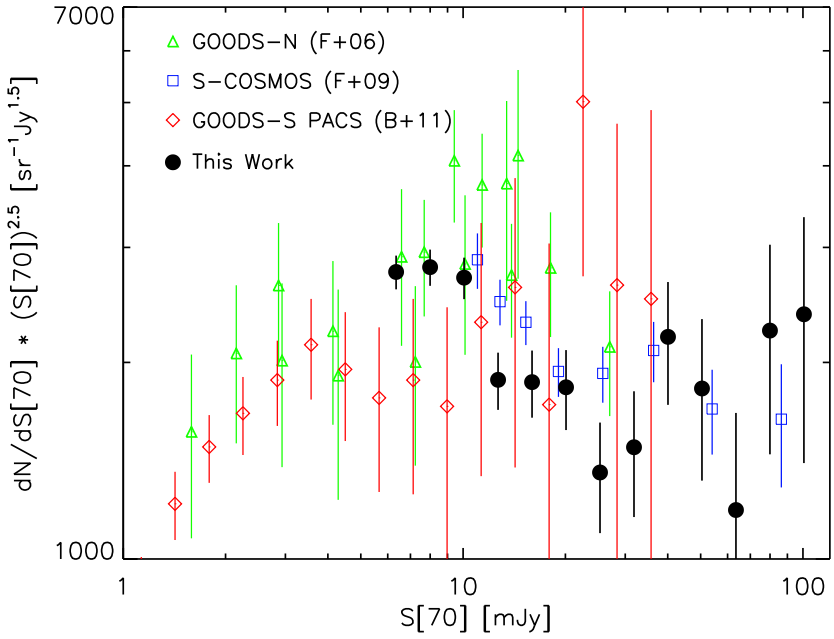

Figure 2.13 : Differential number counts at 70 μm for the SXDS/UDS field, normalized to the Euclidean slope (*black filled circles*). Several results from the literature are show for comparison; *open triangles:* Frayer et al. (2006; F+06) for GOODS-N, *open squares:* Frayer et al. (2009; F+09) for S-COSMOS, *open diamonds:* Bertal et al. (2011; B+11) for GOOD-S.

With regard to the PACS 70 μm counts of Berta et al. (2011) for GOOD-S, it is important to note that these estimations present the largest error bars. However, these authors have considered not only Poisson statistics, but also photometric error and calibration uncertainties in the estimations of such error bars. Our results agree with their values at fluxes ranging in $\sim 10-40$ mJy within $\sim 35\%$. Therefore, we can stay that our MIPS 70 μm differential counts for the SXDS/UDS field are constrained adequately.

The sample of 70 μm-selected galaxies with secure UV/optical-to-FIR counterparts will be described in the Chapter 3. But, as we mentioned at beginning of this Chapter, the MIPS 70 μm data are the shallowest from our MIPS and *Herschel* bands. The MIPS-24 and PACS channels are much deeper than the 70 μm band, as it is shown in the following Sections. Therefore for such channels, completeness estimations are unnecessary, because all the sources in these channels are bright. Regarding such 70 μm-selected sample with multi-wavelength photometry, the minimum 24 μm flux is 186 μJy (almost 3 times the $S_{5\sigma}[24]$ threshold $\sim$ 70 μJy, see Section 2.1.2), and the median flux is 636 μJy. For the PACS bands, such minima fluxes are 9.2 and 17.8 mJy (both above 2 times the 5σ detection limits of the catalogued regions, see Section 2.2.1), and the median fluxes are 28 and 44 mJy for the 100 and 160 μm channel, respectively. For the

SPIRE bands, I dare to use fluxes under the 5σ detections limits relying on our position prior based cataloging method and also on the extensive SPIRE cataloging tests based on simulations done by Wang et al. (2014) for the HerMES fields (including UDS; see Section 2.2.2.1). For the 250 μm channel, the minimum flux is 9.3 mJy ($\sim 3.5\sigma$, and it is the unique source under the 5σ detection threshold), the median flux is 47 mJy (almost 4 times larger than the 5σ detection limit, see Section 2.2). For the 350 μm band, the minimum flux is 12.0 mJy ($\sim 3.3\sigma$, and there are 4 objects under the 5σ detection threshold), the median flux is 35 mJy (almost 2 times larger than the 5σ detection limit, see also Section 2.2). For 500 μm channel, the minimum flux is 11.7 mJy ($\sim 3.3\sigma$) and the median flux is 16mJy ($\sim 4.4\sigma$ detection threshold, see Section 2.2). Then, the flux densities in this 500 μm channel are the less reliable, but we have used fluxes above 3σ noise level as other studies (e.g., Smith et al. 2012). We give further details about these debatable SPIRE sources in Section 2.2.2.1.

The full multi-wavelength photometry of the final 70 μm-selected sample is given in Table 3.6.

2.1.2 MIPS 24 μm Data

All the MIPS 24 μm Basic Calibrated Data also from the program 40021 (PI, James S. Dunlop) were downloaded from the SSC archive, and they were mosaicked using MOPEX too.

The reduction process for the MIPS 24 μm requires first removing artifacts from the whole BCD such as latents and jailbars (see the MIPS Instrument Handbook). The second step is to remove the background from each BCD. This background is estimated using a median filter, and then it is subtracted. Afterwards, bright sources are masked in the background-subtracted images in order they do not affect when creating the flat field. This flat field results from stacking the set of BCD and finding the median for each pixel in the stack. Finally, all BCD are divided by this flat field.

Once with the set of BCD free from artifacts, we proceeded to construct the mosaic. The mosaicking process was similar to that described above for the MIPS 70 μm data, projecting the set of MIPS-24 BCD in a common frame using the drizzle scheme, flagging bad pixels, and removing outliers. We have used an output square pixel size of $1.2''$ for our 24 μm mosaic which is show in Fig. 2.14. We also got the coverage map, which indicates that our 24 μm mosaic has an average exposure time of ~ 3300 s per pixel.

Photometry was also carried out with a PSF fitting method plus aperture correction, in a similar way as described in Pérez-González et al. (2005). The procedure is similar

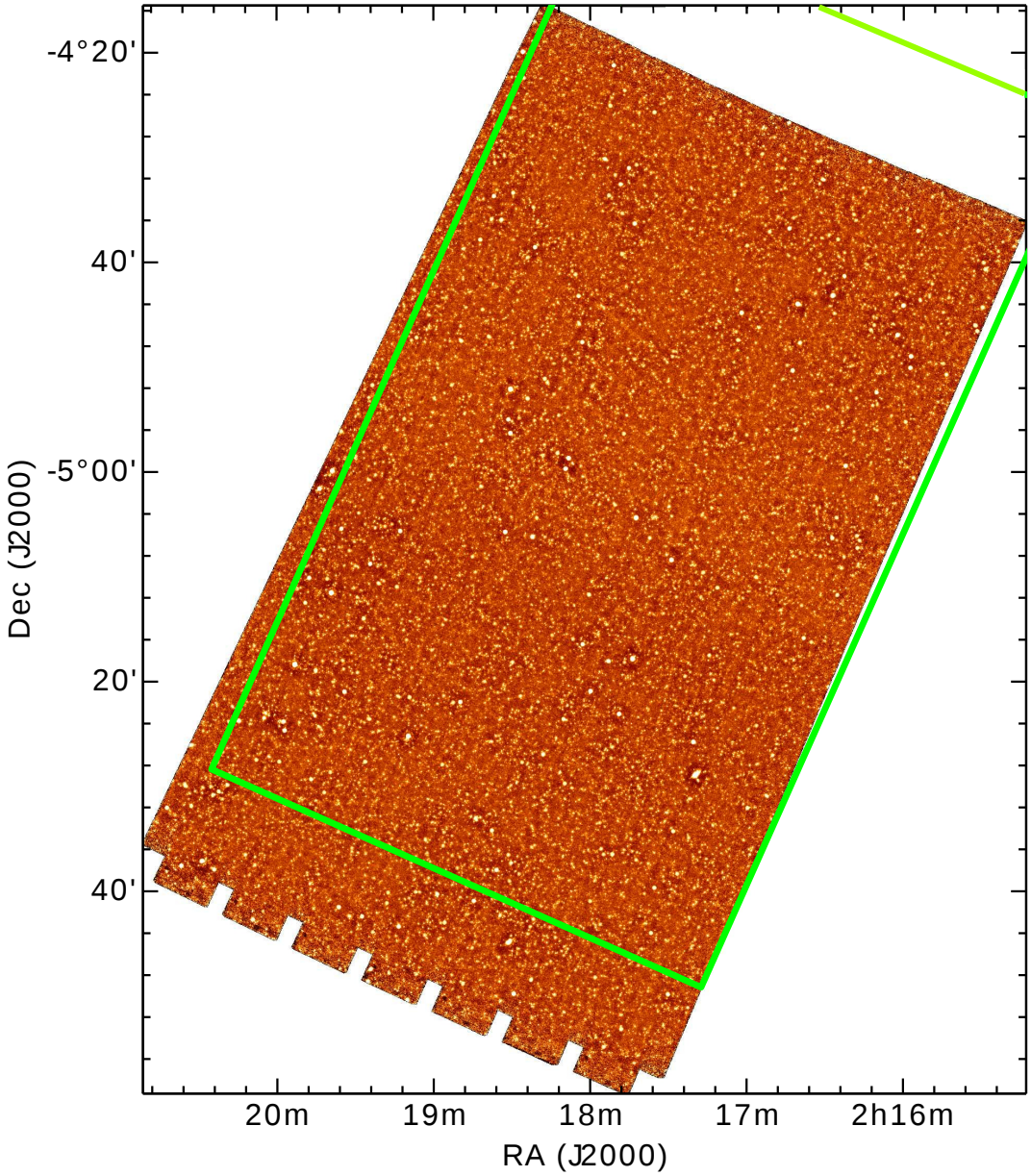

Figure 2.14 : MIPS 24 μm mosaic built with MOPEX for the SXDS/UDS field. The mosaic is aligned so that the North Celestial Pole is up. The green region shows the MIPS-70 mosaic footprint.

to the one described for the 70 μm image for the direct detection.

Considering the FWHM of the MIPS 24 μm PSF ($\sim 6''$), a lot of the sources are overlapped with other ones in our mosaic. The *allstar* task helps to deal with this crowdedness because it effectuates concurrent fits to multiple objects. Nevertheless, several passes were required to recover the faintest sources, which are commonly hidden by the brighter ones.

We proceeded as follows, we constructed an empirical PSF with the bright iso-

Table 2.1 : SExtractor detection thresholds for the several MIPS 24 μm passes

Pass Number	DETECTION_THRESHOLD	Source dens.	median flux
(1)	(2)	(3)	(4)
1	46.5	170.43	2.73 mJy
2	15.0	979.13	0.68 mJy
3	8.0	2554.78	0.33 mJy
4	3.0	10919.43	0.16 mJy
5	1.6	17868.70	70 μJy
6	3.0	299.13	98 μJy

Notes.— (1) Number of the pass in the detection of the MIPS-24 sources. (2) Sextractor detection threshold used in the in the original mosaic for the first pass and the residual images for subsequent passes. (3) Source density per square degree for each pass. (4) Median flux density for each pass.

lated sources in the mosaic. Then, we did the first pass to the mosaic with SExtractor (DETECT_MINAREA$= 9$ and THRESHOLD_TYPE RELATIVE used as default parameters) utilizing a DETECTION_THRESHOLD$= 46.5$, and proceeded to measure fluxes with *phot* and *allstar*. Afterwards, we looked for possible sources at the residual image. We tuned SExtractor for the best threshold to use in this image, and performed the next pass. The positions of the objects detected in the residual image were added to the initial list of sources, and another extraction on the original 24 μm mosaic was then executed. Six passes were performed, the detection threshold values, the surface densities and the median flux densities for each pass are indicated in Table 2.1. We extracted photometry using our empirical PSF of FWHM $\sim 6''$ (5 pixels) for all the sources from the six passes together in order to obtain an image with negligible residuals. A region with examples of the sources detected in the several passes is shown in Fig. 2.15.

The aforenamed empirical PSF was scaled within a fixed circular aperture of $12''$ (10 pixels) in this case. Accordingly to the MIPS Instrument Handbook, an aperture correction of 17% was required to correct to the total flux for an aperture radius of $12''$ and a background annulus of $8''$ measured from $34''$ to $42''$ from the source central coordinates. The sky estimation was accomplished in two phases, first removing the large scale variation which is caused by zodiacal light, and then measuring the background around each source.

The errors of the MIPS 24 μm photometry were estimated from the sky uncertainty in a similar way to the described for the MIPS-70 photometry.

Our final MIPS-24 catalog includes 25918 sources, 5σ about the sky level ($\mathrm{S}_{5\sigma}[24] =$

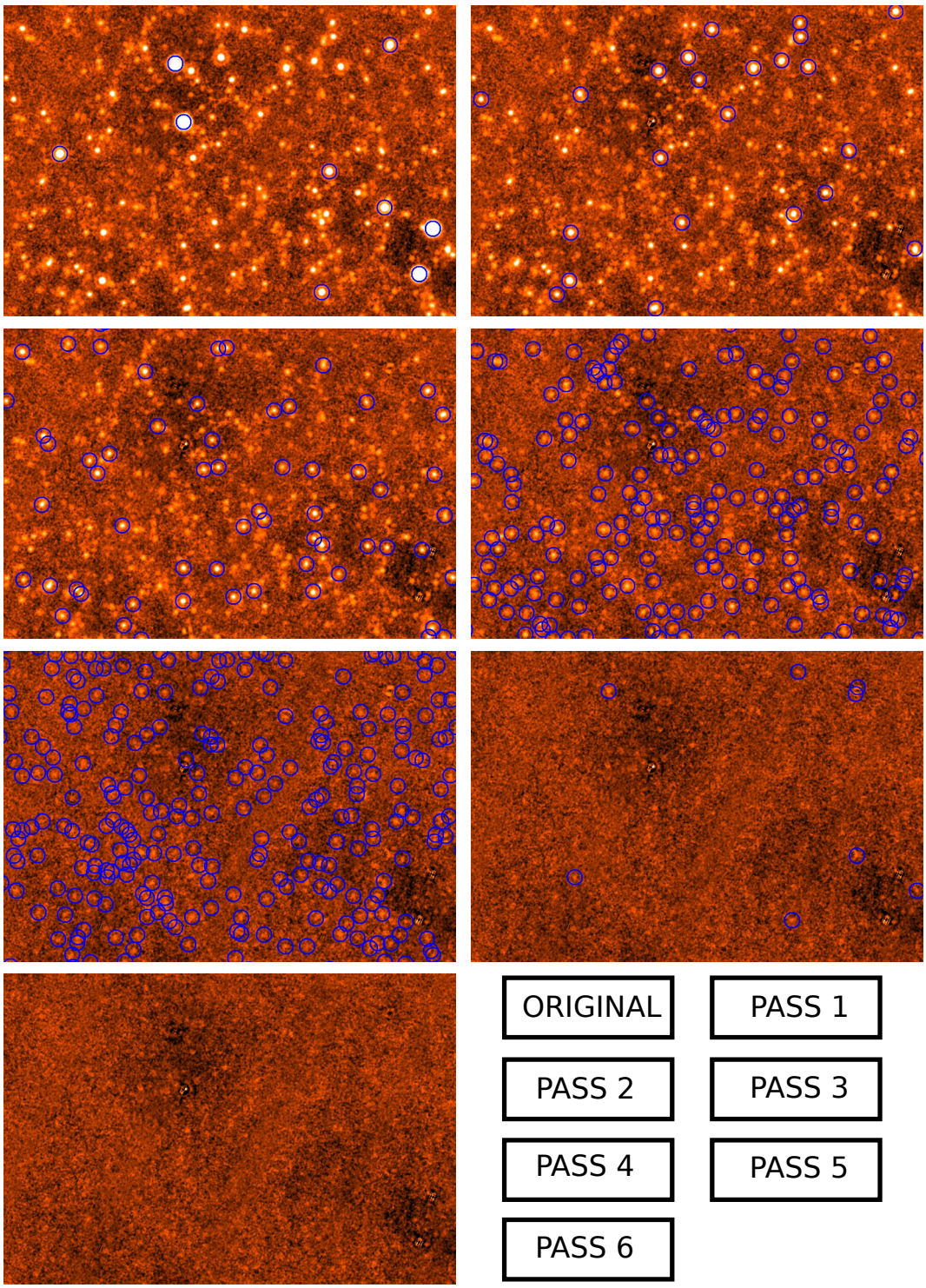

Figure 2.15 : *Upper left panel:* A region of the original MIPS 24 μm mosaic indicating the detections from the first pass. *Upper right panel:* A region of the residual image of the first pass showing the detections from the second pass. The other panels show the residual image of the n-th pass presenting the detections from the $n+1$ pass until $n = 5$. The disposition of the images is indicated in the bottom-right corner.

70 μJy), over a region of 1.15 deg^2 with homogeneous exposure time.

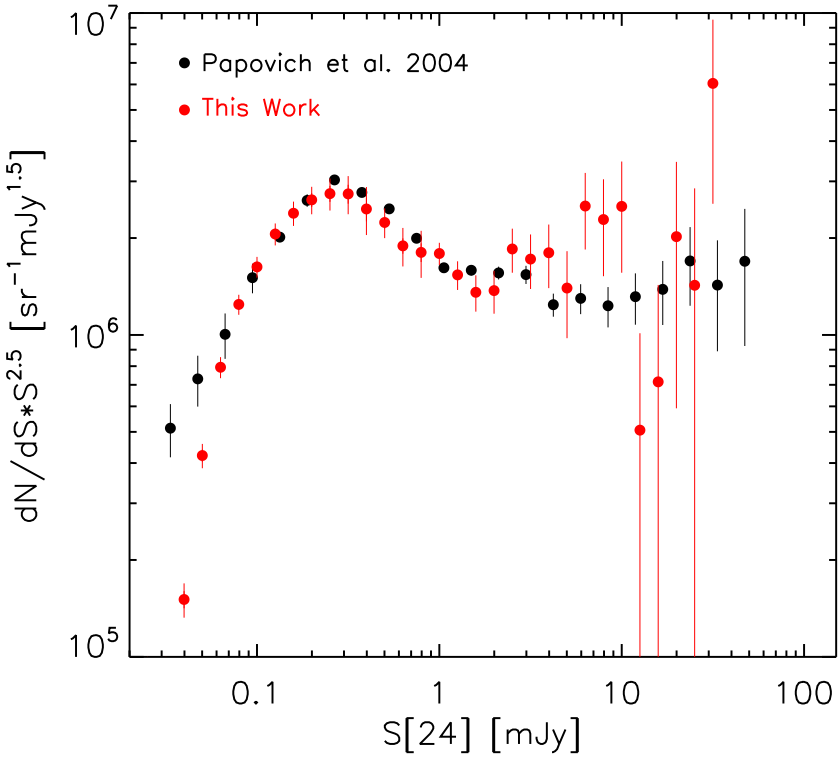

Figure 2.16 : 24 μm differential number counts derived from the SXDS/UDS field (fill red circles). The counts from Papovich et. al. (2004, fill black circles) are shown as a comparison basis. Our estimations are uncorrected from completeness, which is notorious for S[24] $<$ 70 μJy.

In order to check the robustness of our MIPS-24 catalog, we calculated the differential source number counts, which are shown in Fig. 2.16. These counts are also normalized to the euclidean slope to compare them with the counts determined by Papovich et al. (2004) derived from the several MIPS Guaranteed Time Observer (GTO) programs. Taking into account the uncertainties, our results present a good agreement with counts obtained from the GTO surveys. At fluxes between $\sim$ 70 μJy -5 mJy, our results and those of Papovich et al. (2004) present differences smaller than 10% in median. The differences at fluxes greater than $\sim$ 3 mJy are due to cosmic variance between the field we have surveyed and the fields pointed by the GTO programs. At fluxes lower than $\sim$ 70 μJy our cataloged objects underestimate the counts derived by Papovich et al. (2004). Nevertheless, we only use sources brighter than this 5σ level in our study.

2.2 *Herschel* Data

The FIR information used in this study includes PACS and SPIRE data of the UDS field, which was observed by *Herschel* as a part of the Key Program Guaranteed Time HerMES (Oliver et al. 2012; PI Seb Oliver, Proposal ID `KPGT_soliver_1`). The PACS 100 and 160 μm data were obtained in 12 AORs (the observation IDs are presented in Table 2.2), consuming 40.19 hours, and covering an area of ~ 0.9 deg^2. The SPIRE 250, 350 and 500 μm data were acquired in 7 AORs (the observation IDs are shown in Table 2.3), lasting 10.54 hours, and covering an area of ~ 2 deg^2.

We downloaded all public PACS data inside the UDS region from the *Herschel* Science Archive (HSA[3]), including targets with longer exposure time as: UDS-SCUBA (also for HerMES), and UDS-CANDELS (Proposal ID `OT2_mdickins_1`, PI Mark Dickinson); the observation IDs of both sets are indicated in Table 2.2. Regarding SPIRE, we downloaded also data from shallow observations taken using PACS/SPIRE parallel mode (for *XMM* VIDEO 1 in HerMES too), and data from deep observations also for UDS-CANDELS; the observation IDs of both sets are shown in Table 2.3.

We built the mosaics using the *Herschel* Interactive Processing Environment (HIPE) version 11. HIPE includes the common PACS photometer (Wieprecht et al. 2009) and SPIRE photometer (Dowell et al. 2010) pipelines, an some tailor-made methods for reducing data of both instruments. We show the footprints of the regions where we have cataloged PACS and SPIRE data over our 70 μm mosaic in Fig. 2.17.

2.2.1 PACS Data

The PACS photometer pipeline first processes chronological data frames from each AOR. This procedure is described in (Lutz et al. 2011), and it consists in: (1) finding operative blocks in the data; (2) flagging bad pixels, and saturated pixels; (3) converting detector signals from digital units to volts, and the chopper position from digital values to position angle; (4) finding pixels affected by glitches, and replacing their values using and interpolation method; and (5) applying recenter corrections based on MIPS 24 μm astrometry.

Afterwards the above procedure, we needed to treat with the $1/f$ noise component affecting each AOR timeline. The method we have used is recommended for cosmological surveys, it consists in using a high-pass filter for the detector timelines and then a direct projection into a common frame. We have used output pixel sizes of $1.2''$ and $2.4''$ for the PACS 100 and 160 μm mosaics, respectively. These maps are shown in

[3] `http://www.cosmos.esa.int/web/herschel/science-archive`

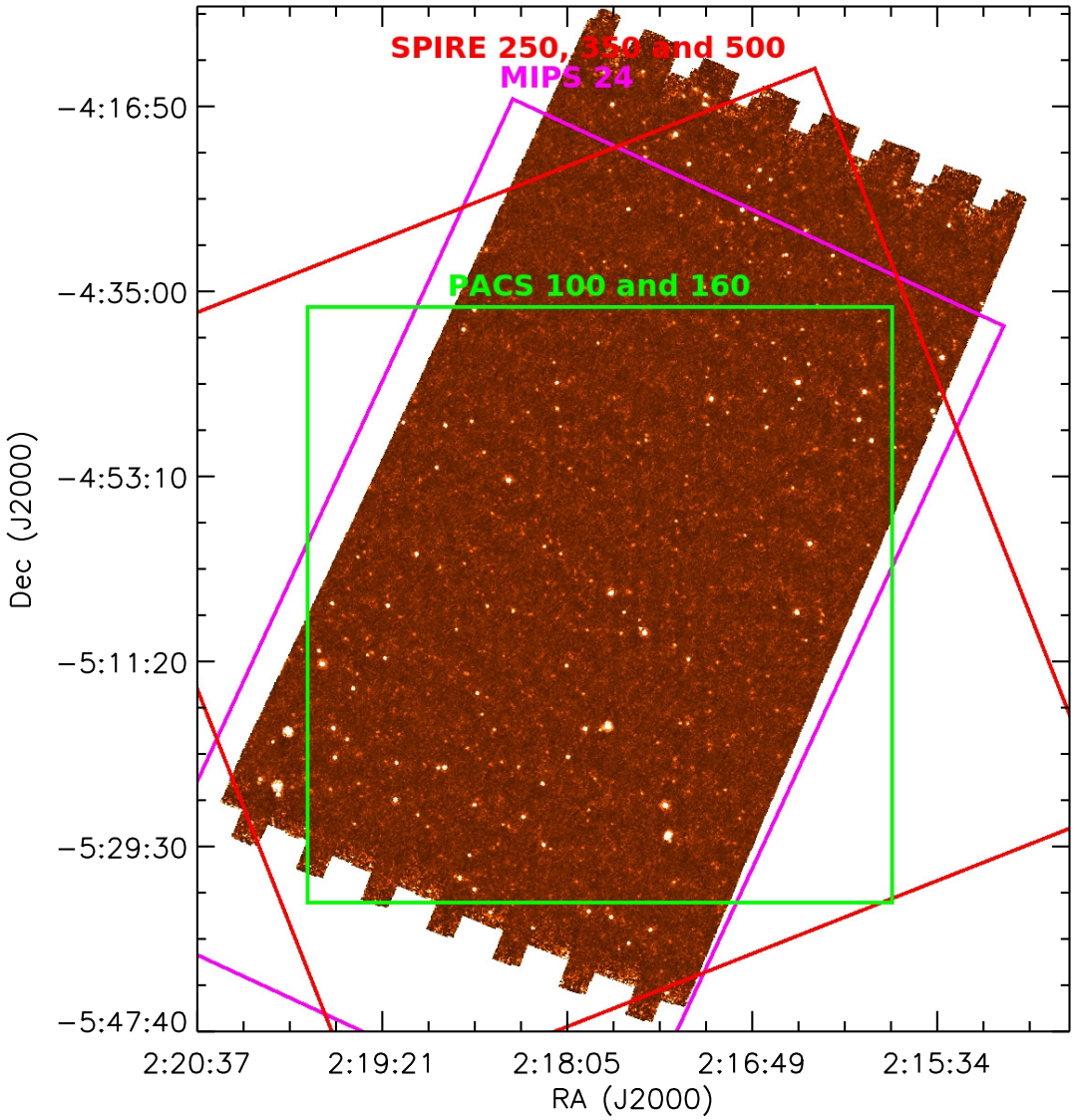

Figure 2.17 : Footprints of the MIPS-24, and the *Herschel* PACS and SPIRE regions of the SXDS/UDS field on top of our MIPS-70 mosaic. The region where we have cataloged data for PACS bands is delimited by a green box, and the one for the SPIRE channels is enclosed in a red box.

Figs. 2.18, and 2.19.

Source detection and photometry, for both PACS bands, were carried out based in 24 μm position prior method and PSF fitting as described above for the 70 μm catalog, and also in Pérez-González et al. (2010).

The first step was to align the PACS maps to the WCS of the MIPS 24 μm mosaic using the *ccmap* task from IRAF IMCOORDS. We obtained a WCS accuracy smaller than $0.9''$ and $1.3''$ between the MIPS 24 μm and PACS 100 and 160 μm, respectively

Table 2.2 : Observation IDs of the PACS data used for the mosaic of the UDS field.

Observation IDs		
UDS	UDS-SCUBA	UDS-CANDELS
(1)	(2)	(3)
1342214055	1342213952	1342247646
1342214056	1342213953	1342247647
1342214057	1342213954	1342247648
1342214058	1342213955	1342247649
1342214153	1342213956	1342247650
1342214154	1342213957	1342247675
1342214155	1342213958	1342247676
1342214156	1342213959	1342247677
1342214169	1342213960	1342247678
1342214205	1342213961	1342247679
1342214206	1342213962	1342247680
1342214207	1342213963	1342247698
	1342213964	1342247699
	1342214010	1342248021
	1342214011	1342248022
	1342214012	1342248023
	1342214013	1342248024
	1342214014	1342248095
	1342214015	1342248096
	1342214016	1342248097
	1342214017	1342248098
	1342214018	1342248099
	1342214019	1342248100
	1342214053	1342248290
	1342214054	1342248291
	1342214156	1342248724
		1342248725

Notes.— IDs of the three sets of observations utilized for constructing the PACS 100 and 160 μm mosaics. (1) Observation IDs for the UDS data (2) Observation IDs referring to the UDS-SCUBA data (3) Observation IDs for the UDS-CANDELS data

(see Fig. 2.20). Then, we combined positions obtained by direct detection from several passes in the respective map, with those of 24 μm sources inside each PACS mosaic (see upper panels of Figs. 2.21 and 2.22). We dealt with the different PSF sizes of MIPS 24 μm (FWHM $\sim 6''$) and PACS channels (FWHM $\sim 7'',\ 12''$ for green and red filters, respectively) by removing objects closer than $5''$ for the 100 μm band and closer than $7''$ for the 160 μm band of a given candidate (see blue open circles in lower panels of Figs. 2.21 and 2.22), keeping only a direct detection or the most luminous 24 μm source. Then, we measured aperture photometry in 4 pixel radius ($4.8''$), and 2 pixel

Table 2.3 : Observation IDs of the SPIRE data used for the mosaic of the SXDS/UDS field.

Observation IDs		
UDS	*XMM* VIDEO 1	UDS-CANDELS
(1)	(2)	(3)
1342201437	1342223217	1342247870
1342201486	1342223218	1342247871
1342201487	1342223265	1342247872
1342201488	1342223266	1342247873
1342201489		1342247874
1342201490		1342247875
1342201491		1342247876
		1342247877

Notes.— IDs of the three sets of observations used for building the SPIRE 250, 350 and 500 μm mosaics. (1) Observation IDs for the UDS data (2) Observation IDs referring to the *XMM* VIDEO 1 data (3) Observation IDs for the UDS-CANDELS data

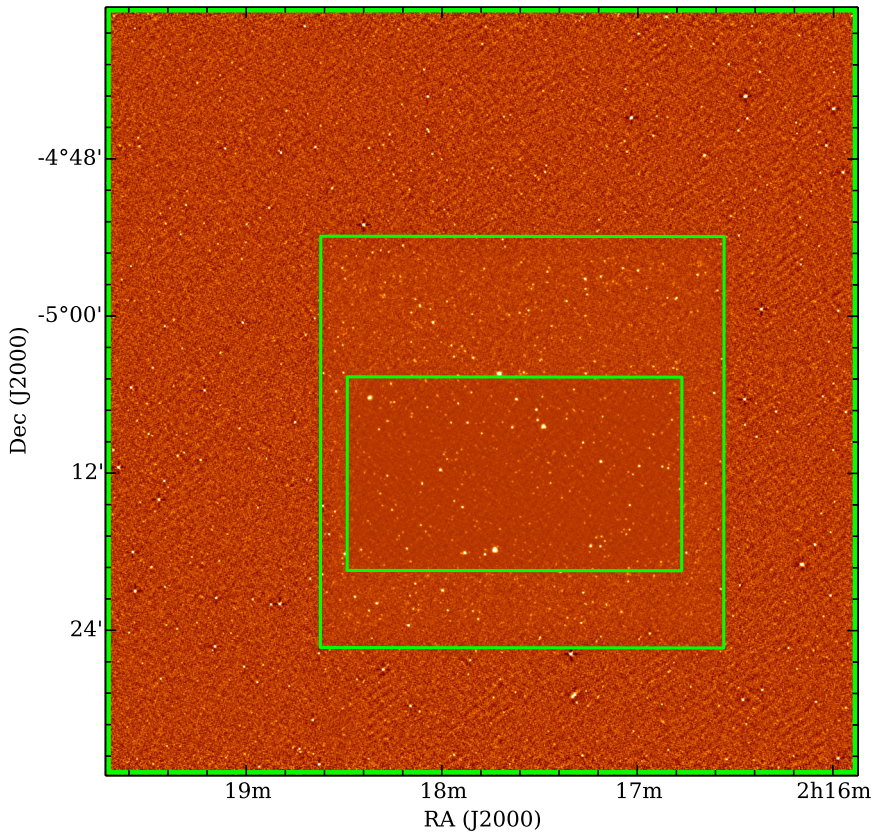

Figure 2.18 : PACS 100 μm mosaic built with HIPE for the UDS field. The mosaic is aligned so that the North Celestial Pole is up. The green rectangles delimit from the inner to the outer part the regions UDS-CANDELS, UDS-SCUBA, and UDS-NORMAL.

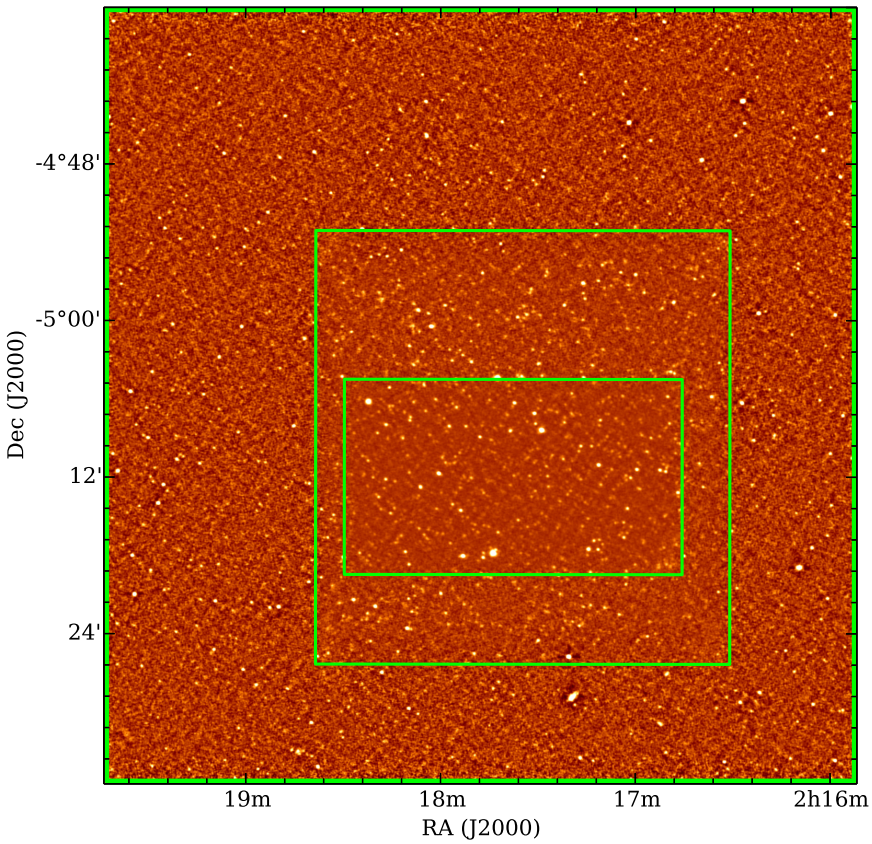

Figure 2.19 : PACS 160 μm mosaic constructed with HIPE for the UDS field. The mosaic is aligned so that the North Celestial Pole is up. The green rectangles delimit from the inner to the outer part the regions UDS-CANDELS, UDS-SCUBA, and UDS-NORMAL.

radius ($4.8''$), keeping only sources with measurements 5σ and 3σ above the sky level for the 100 μm, and 160 μm channels, respectively (see open green circles in in lower panels of Figs 2.21 and 2.22). We fitted empirical PSFs to the purged candidate list of each band, scaling the corresponding PSF with circular apertures of $5.0''$ and $7.2''$ for the 100 and 160 μm channels, respectively. Afterwards, we applied correction factors of 2.03 and 2.41 to the flux densities in the PACS green and red channels, correspondingly (Balog et al. 2014). These factors are necessary to account for the finite sizes of the PSFs and also for losses due to the high-pass filtering (Popesso et al. 2012).

The errors of the PACS 100 and 160 μm photometry were estimated from the sky uncertainty in a similar way to the described for the MIPS-70 photometry. But the average background was measured in a sky box of 1.5 and $2'$ for the 100 and 160 μm bands, respectively.

Taking into account that we have used PACS data with different exposure time, and that these regions with different coverage are appreciable in the sky level of the

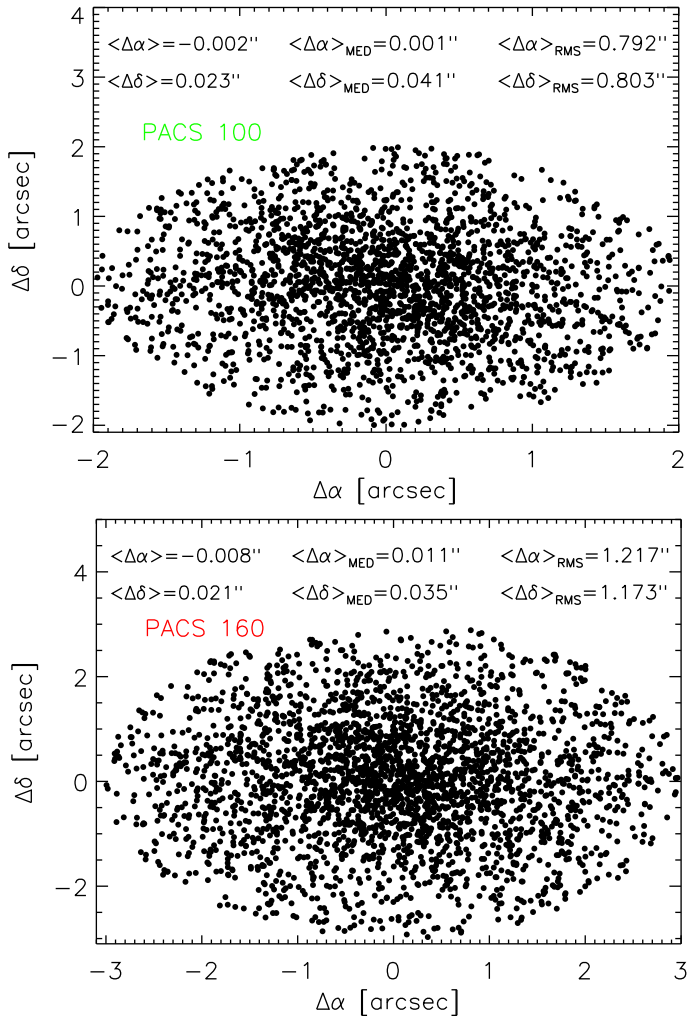

Figure 2.20 : *Upper panel:* Differences in the right ascension and declination of the 100 μm detections with respect to 24 μm sources. The random distributions of points shows that there are not systematic differences between each set of WCS. *Lower panel:* Similar plot to the upper panel but for the 160 μm band.

mosaics, we did catalogs for 3 different areas: UDS-CANDELS, UDS-SCUBA and UDS-NORMAL. These regions can be distinguished from the inner to the outer part, respectively, in Figs. 2.18 and 2.19.

Tables 2.4 and 2.5 summarize the main characteristic of the catalogs done for the 3 regions for each PACS band, including the 5σ detection level, and the number of sources above this 5σ threshold in the also mentioned area.

In order to check the robustness of our catalogs, we calculated The PACS 100 and 160 μm differential number counts for each of the 3 aforenamed UDS areas. We present these counts in Figs. 2.23 and 2.24. Our differential number counts are compared with the counts above the 80% completeness level of the works of Berta et al. (2011) and Magnelli et al. (2013). Taking into account the uncertainties, our PACS source counts

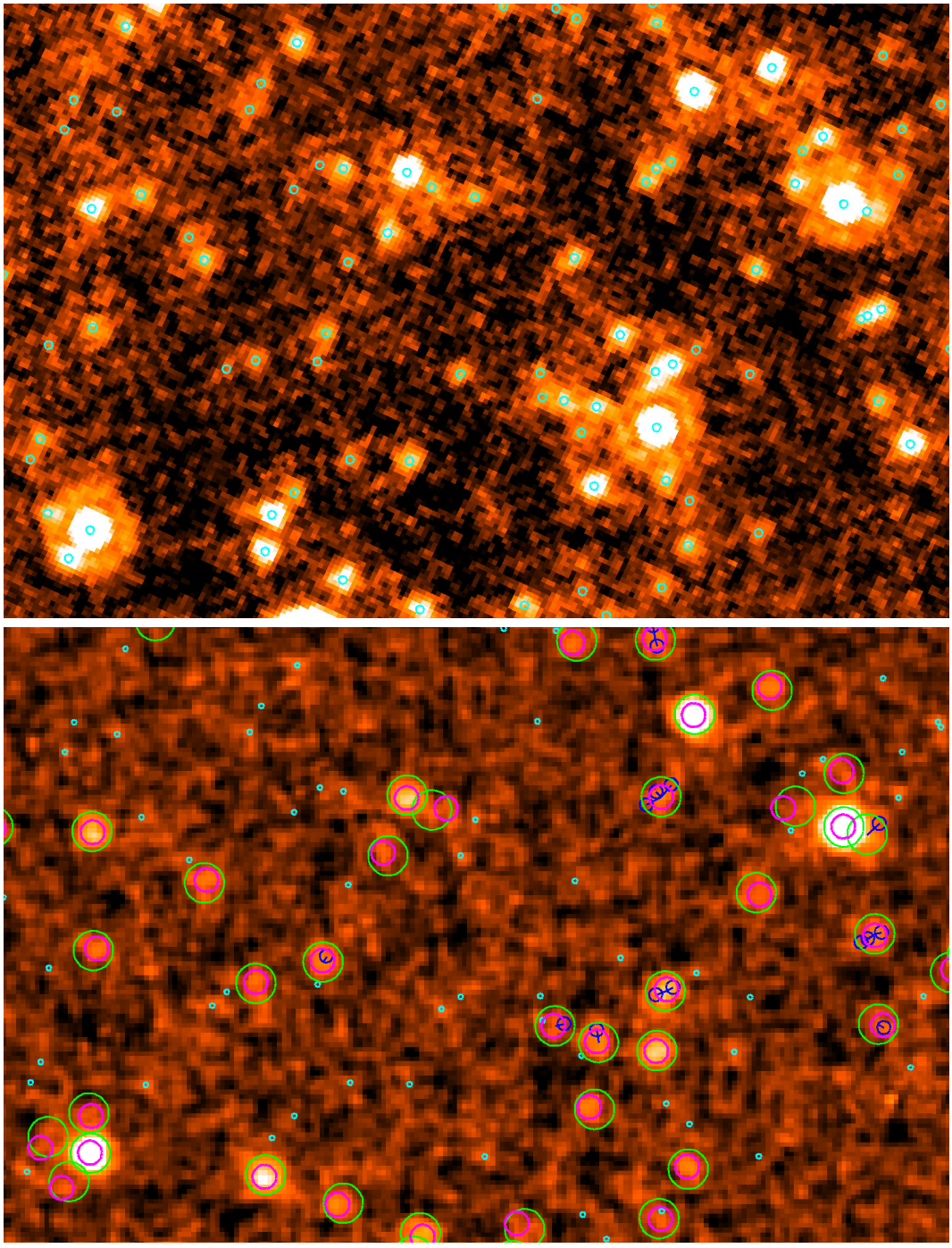

Figure 2.21 : *Upper panel:* A region of the MIPS-24 mosaic. The positions of the detection in our 24 μm catalog are shown with cyan open circles. *Lower panel:* A region with the same WCS of the upper panel, but observed with PACS 100 μm. The locations of 24 μm sources, i.e., the prior positions, are displayed as a small cyan open circles when they were rejected at 4 pixel aperture photometry, as medium blue circles when they were merged in a position to try photometry in the 100 μm mosaic, and as big open green circles in the positions where *phot+allstar* photometry was effectuated. The detections in our final PACS 100 μm catalog are indicated as magenta open circles.

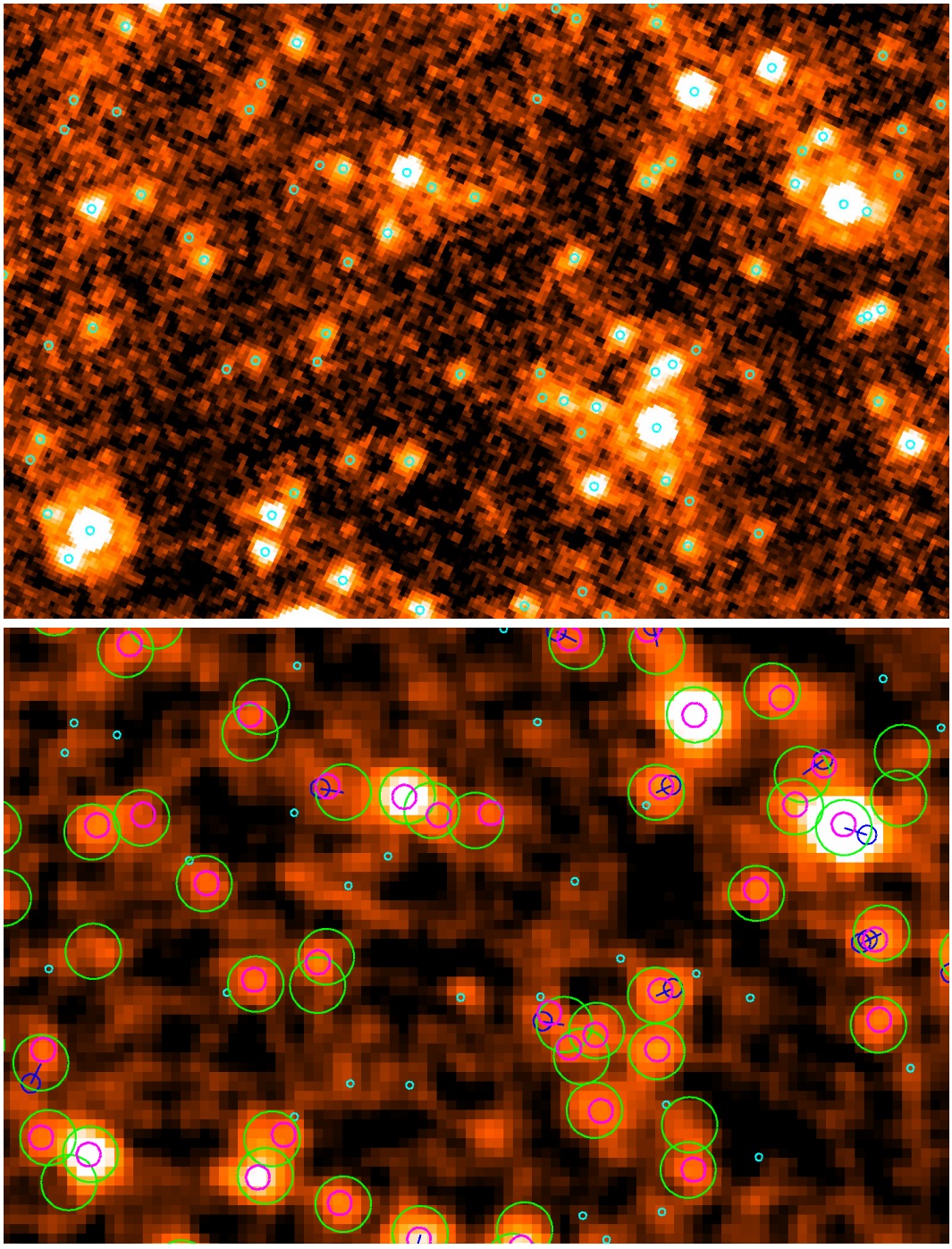

Figure 2.22 : *Upper panel*: Same region of the MIPS-24 mosaic of Fig. 2.21. The positions of the detection in our 24 μm catalog are shown with cyan open circles. *Lower panel:* A region with the same WCS of the upper panel, but observed with PACS 160 μm. The locations of 24 μm sources, i.e., the prior positions, are presented as a small cyan open circles when they were rejected at 2 pixel aperture photometry, as medium blue circles when they were merged in a position to try photometry in the 160 μm mosaic, and as big open green circles in the positions where *phot+allstar* photometry was effectuated. The detections in our final PACS 160 μm catalog are indicated as magenta open circles.

PACS 100 μm				
Region	Area	$t_{\rm exp}$	$S_{5\sigma}$	N
(1)	(2)	(3)	(4)	(5)
UDS-CANDELS	0.1	82.36	1.1	1505
UDS-SCUBA	0.2	40.19	2.4	941
UDS-NORMAL	0.6	25.93	4.1	1555

Table 2.4 : Properties of the PACS-100 catalogs of the different UDS regions

PACS 160 μm				
Region	Area	$t_{\rm exp}$	$S_{5\sigma}$	N
(1)	(2)	(3)	(4)	(5)
UDS-CANDELS	0.1	82.36	3.1	1198
UDS-SCUBA	0.2	40.19	5.8	1118
UDS-NORMAL	0.6	25.93	8.9	1842

Table 2.5 : Properties of the PACS-160 catalogs of the different UDS regions

Notes.— (1) Region of the catalog. (2) Area over the catalog was made. (3) Exposure time in hours of each target obtained from HSA. (4) flux density of the 5σ threshold in mJy. (5) Number of sources above the 5σ threshold in each region.

for the 3 UDS regions are in good agreement with the previous estimates for different fields over the flux ranges in common (an overall rms error of 30% and 25% for the 100 and 160 μm band, respectively). There are not enough sources in the brighter flux bins in order to determine adequate statistics for the small areas (UDS-CANDELS and UDS-SCUBA). This is indicated by the huge error bars in the results of the counts for these bright flux intervals.

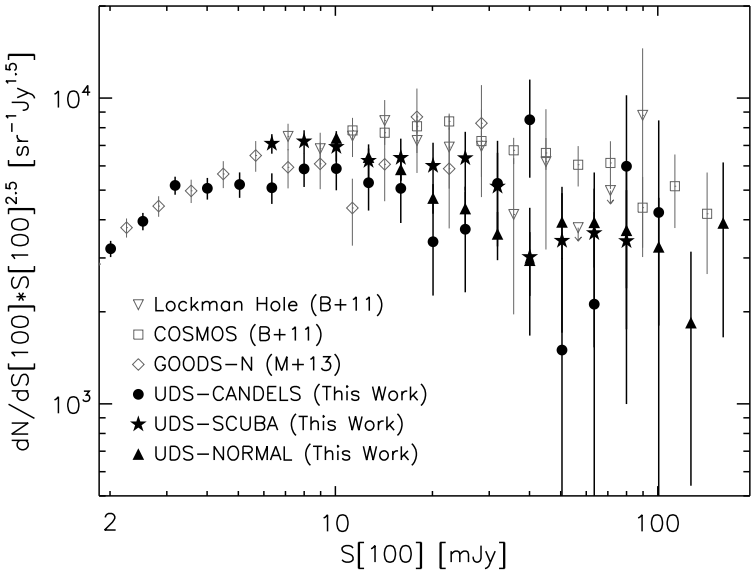

Figure 2.23 : PACS-100 differential number counts normalized to the Euclidean slope. *Filled circles, filled stars and filled triangles* show our source counts for UDS-CANDELS, UDS-SCUBA and UDS-NORMAL, respectively. The associated error bars for each of the 3 regions represent Poisson statistics. *Open triangles and open squares* stand for the estimations derived for the Lockman Hole and COSMOS (Berta et al. 2011; B+11). *Open diamonds* show the counts obtained for the GOODS-N survey (Magnelli et al. 2013; B+13)

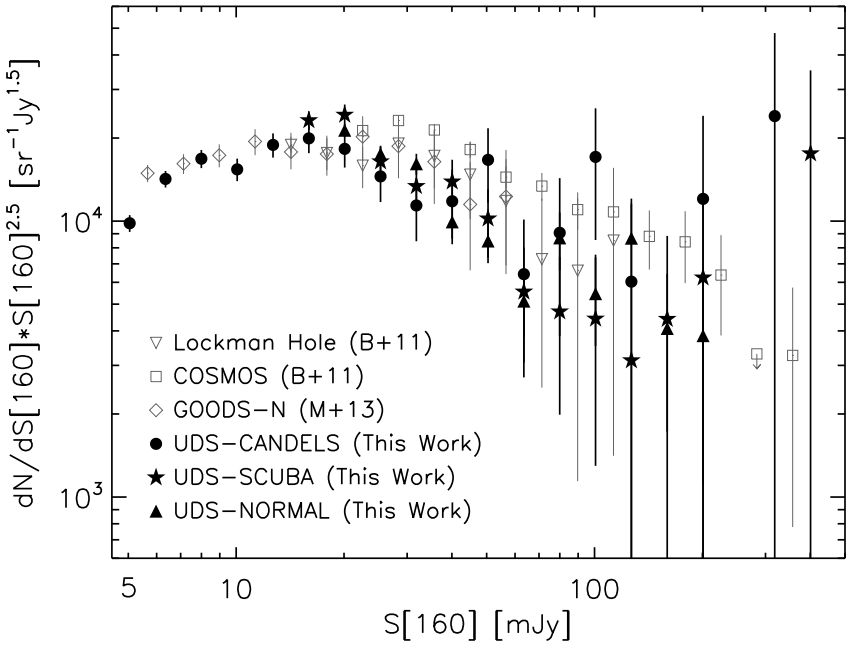

Figure 2.24 : PACS-160 differential number counts normalized to the Euclidean slope. *Filled circles, filled stars and filled triangles* present our source counts for UDS-CANDELS, UDS-SCUBA and UDS-NORMAL, respectively. The associated error bars for each of the 3 regions represent Poisson statistics. *Open triangles and open squares* show the estimations derived for the Lockman Hole and COSMOS (Berta et al. 2011; B+11). *Open diamonds* indicate the counts obtained for the GOODS-N survey (Magnelli et al. 2013; B+13)

2.2.2 SPIRE Data

The SPIRE photometer comprise the 250, 350 and 500 μm bolometer arrays observing at the same time. The observations of the SXDS/UDS field were done in scan map mode (see Table 2.3). This mode is designed to sample the voltage across each bolometer in the 3 arrays at 18.6 Hz for SPIRE-single observations. These chronological samples, which form a timeline, are processed for each bolometer in the 3 channels, using the SPIRE photometer pipeline.

The first step in the reduction process was to update the calibration context of all timelines, using the last calibration tree available at that epoch $spire\_cal\_11\_0$. We continued the aspects of the SPIRE photometer pipeline in the timelines of the 3 arrays, which basically are: (1) concatenating timelines, (2) correcting electrical cross-talk, (3) detecting and flagging jumps in the thermistor, (4) detecting and removing impulse-like glitches, (5) correcting for delays due to the electrical filter response, (6) converting from volts to flux density in each bolometer, (7) removing correlated noise due to temperature fluctuations, (8) correcting for the bolometers time response, (9)

adding pointing information to each timeline, and (10) correcting from on board time to international atomic time.

At this stage, the timelines of the full set of observations can be re-gridded onto sky to create the mosaics for each bolometer array. Hence, we built the mosaics using the common SPIRE map-making process (Roseboom et al. 2010, Smith et al. 2012) included in HIPE, the naive map-maker with the default pixels sizes of, 6, 10, and 14″ for the 250, 350, and 500 μm channels, respectively. The mosaics we have constructed for the SPIRE 250, 350 and 500 μm bands are presented in Fig. 2.25, 2.29, and 2.32, respectively. Although we downloaded the majority of the observed data over the SXDS/UDS field, we only made catalogs for the area covered by UDS ($\sim$ 2 deg^2, the HerMES target) because it presents an acceptable depth and uniformity. This area is indicated with a cyan box in the aforenamed figures.

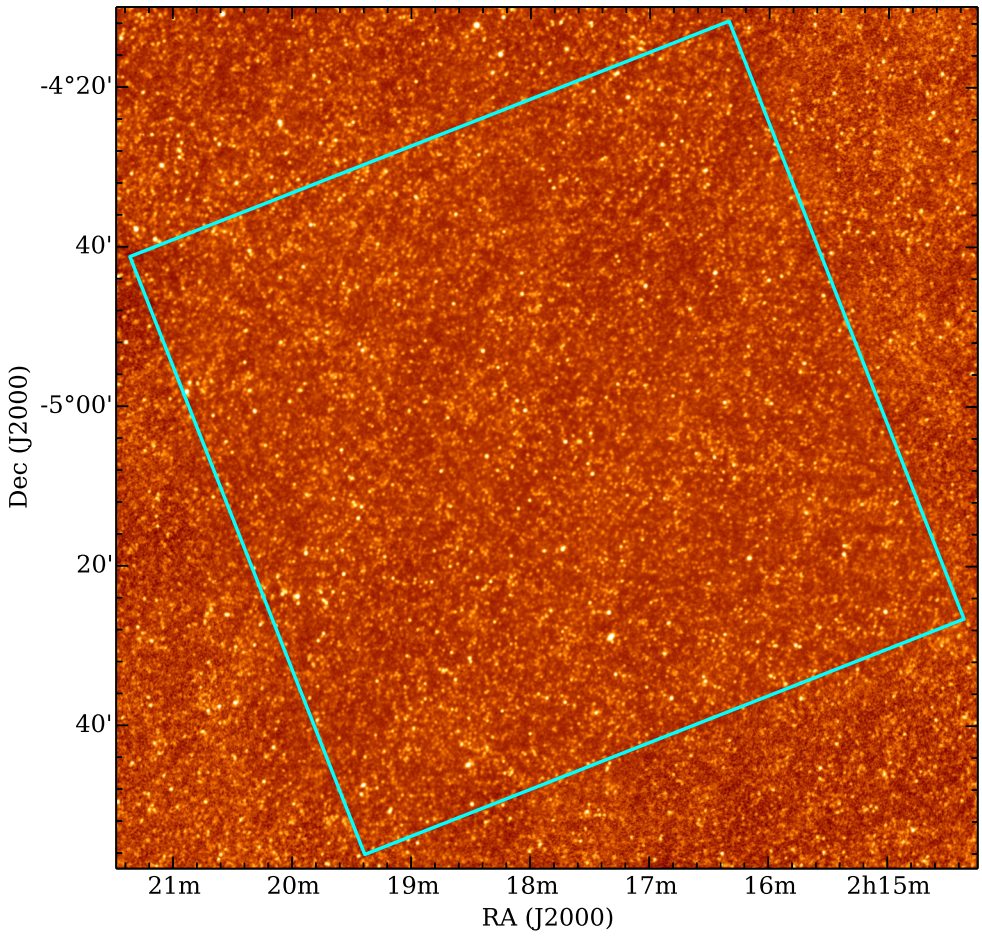

Figure 2.25 : SPIRE 250 μm mosaic constructed with the naive map-maker in HIPE for the SXDS/UDS field. The mosaic is aligned so that the North Celestial Pole is up. The cyan region indicates the area where the source catalog was made.

The alignment, source detection and photometry, for the three SPIRE channels, were also performed with the *ccmap* task, the position prior method and the PSF fitting technique, correspondingly.

We aligned the SPIRE 250 image to the WCS of the MIPS 24 μm mosaic, obtaining a WCS accuracy between the MIPS and SPIRE 250 maps inferior to $3''$ (see Fig. 2.26). Then, we used 24 μm positions as priors (see upper panel of Fig. 2.27) for the 250 μm band (PSF FWHM $\sim 18''$), removing sources closer than $12''$ of a given candidate (as show with blue open circles in the lower panel of Fig. 2.27), and keeping only the most luminous source in the channel between a direct detection and the 24 μm prior source. Then we measured aperture photometry in a small aperture of 2 pixel ($12''$) radius keeping only sources with flux density above the sky level (as indicated by open green circles in the lower panel of Fig. 2.27), to obtain a purged list of candidates.

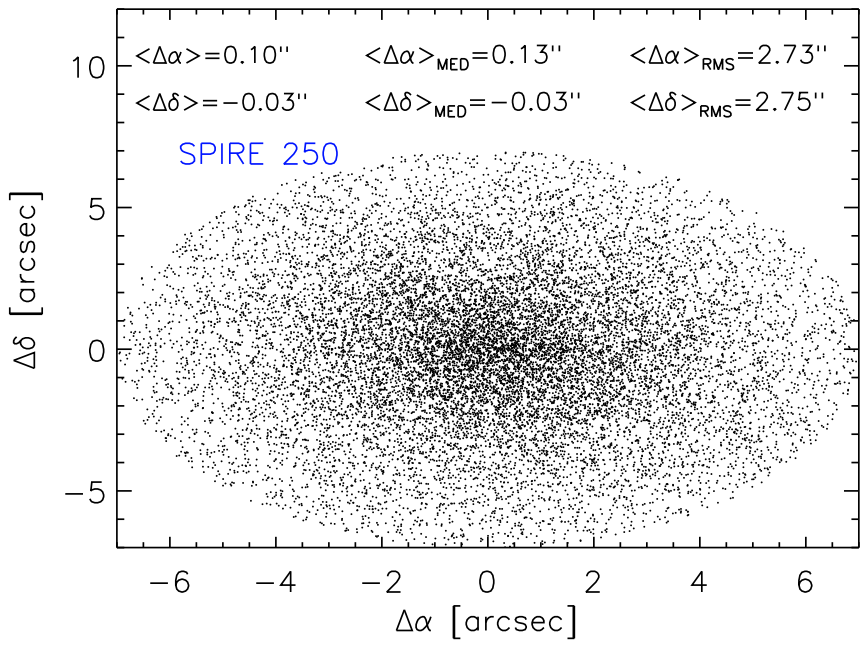

Figure 2.26 : Differences in right ascension and declination of the 250 μm detections with respect to the 24 μm sources. The random distribution of points show that there are not systematic differences between each set of WCS.

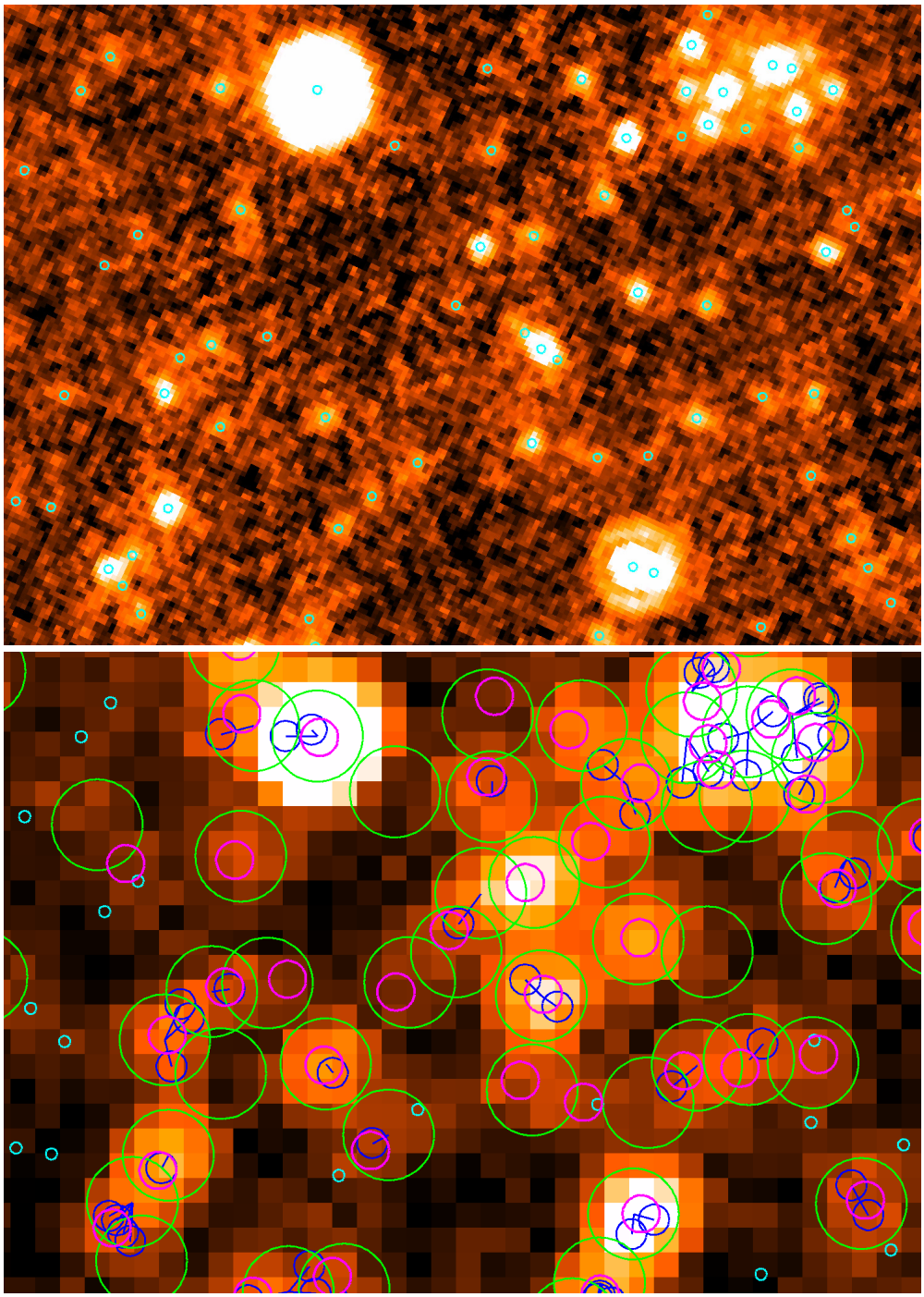

Figure 2.27 : *Upper panel:* A region of the MIPS-24 mosaic. The positions of the detection in our 24 μm catalog are shown with cyan open circles. *Lower panel:* A region with the same WCS of the upper panel, but observed with SPIRE 250 μm. The locations of 24 μm sources, i.e., the prior positions, are displayed as a small cyan open circles when they were rejected at 2 pixel aperture photometry, as medium blue circles when they were merged in a position to try photometry in the 250 μm mosaic, and as big open green circles in the positions where *phot+allstar* photometry was effectuated. The detections in our final SPIRE 250 μm catalog are indicated as magenta open circles.

The SPIRE 350 image was aligned to the WCS of the resulting SPIRE 250 mosaic from the above step. The WCS alignment between the SPIRE 350 and 250 maps has an rms smaller than $5''$ (see Fig. 2.28). In this case, we used as priors 250 μm source positions (see the upper panel of Fig. 2.30), considering the same removing distance of $12''$ (see the blue open circles in the lower panel of Fig.2.30) for a given a candidate in the 350 μm channel (PSF FWHM $\sim 25''$), but we gave preference to the prior positions compared with direct detections. Hence, our purged list of candidates included all the 250 μm objects separated in more than $12''$ (see the green open circles in the lower panel of Fig. 2.30).

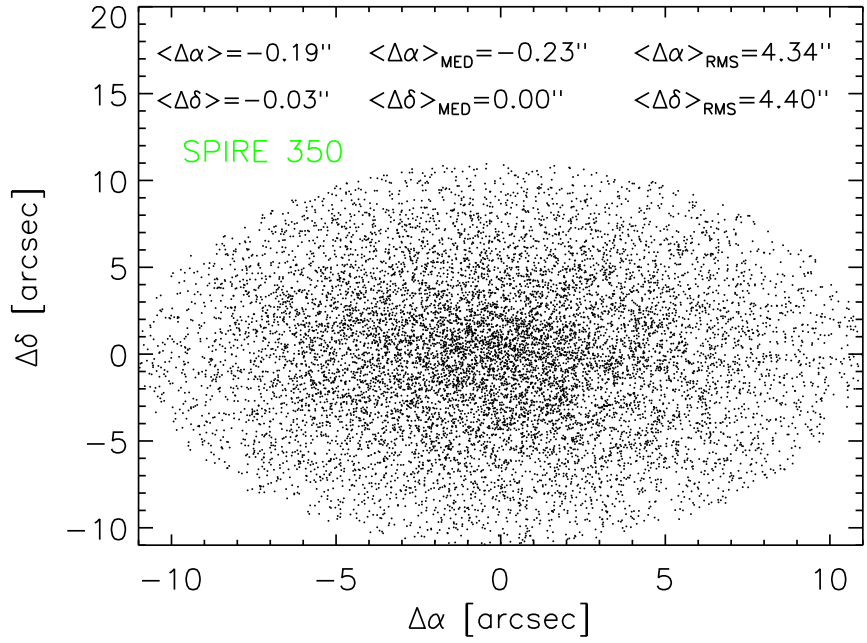

Figure 2.28 : Differences in right ascension and declination of the 350 μm detections with respect to the 250 μm objects. The random distribution of points show that there are not systematic differences between each set of WCS.

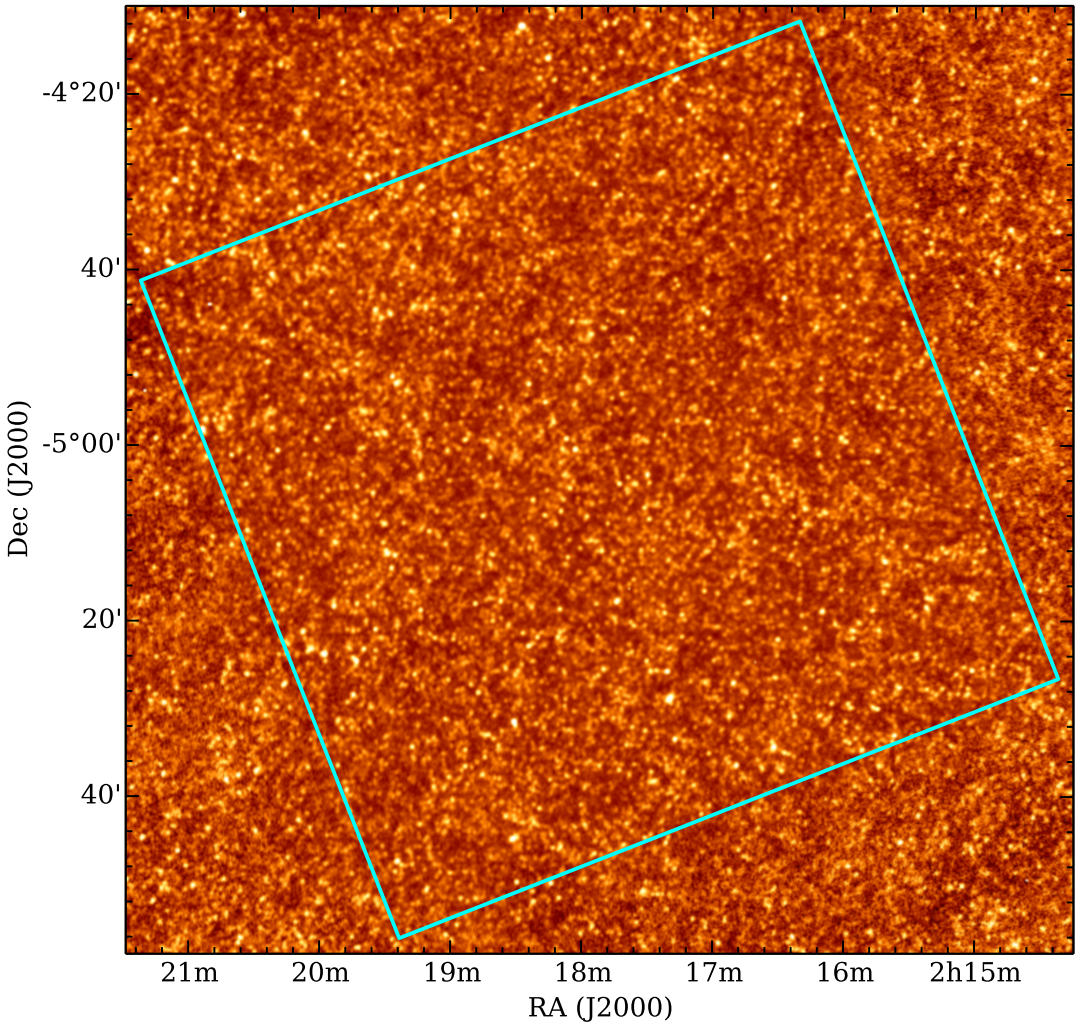

Figure 2.29 : SPIRE 350 μm mosaic built with the naive map-maker in HIPE for the SXDS/UDS field. The mosaic is aligned so that the North Celestial Pole is up. The cyan region indicates the area where the source catalog was made.

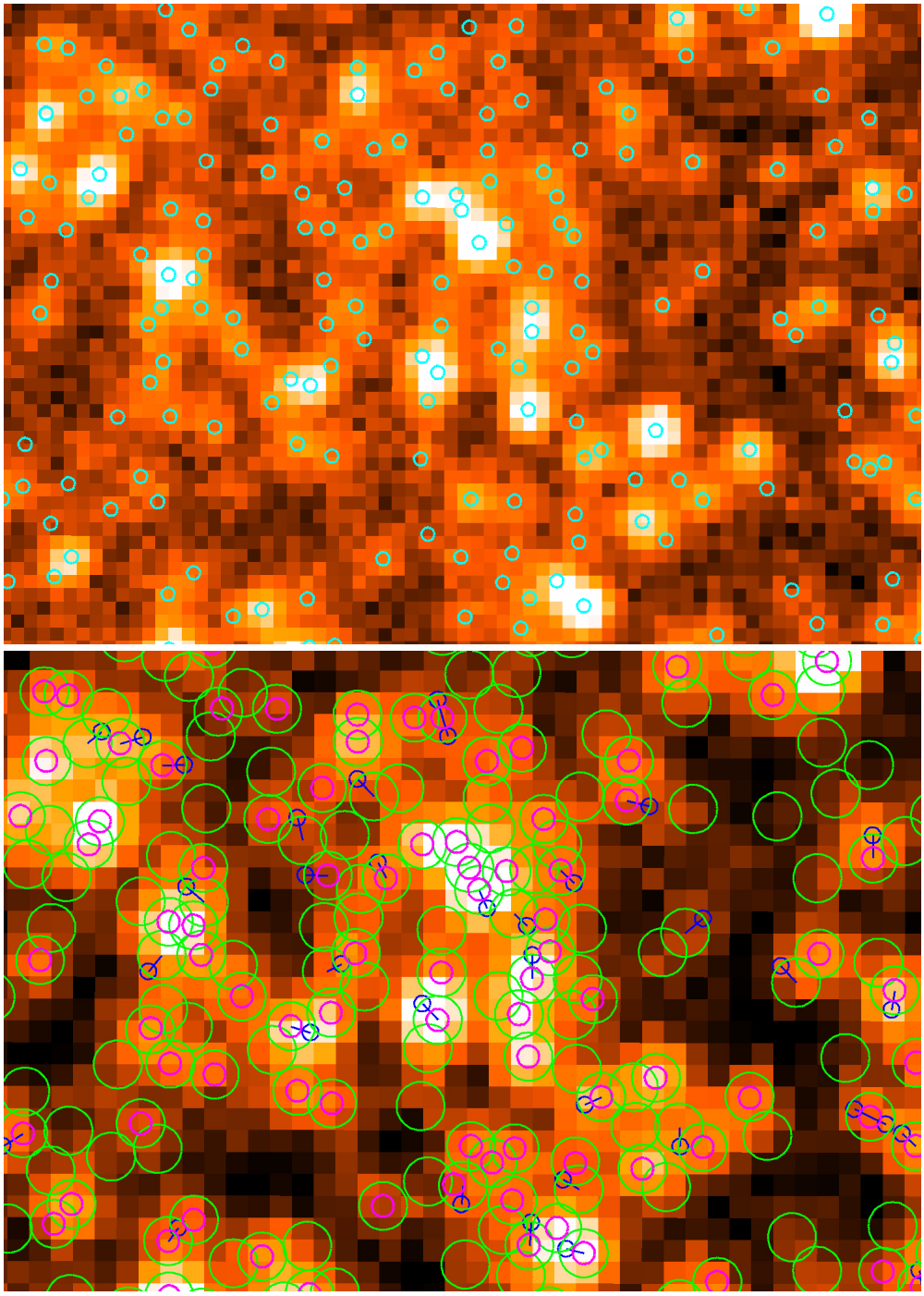

Figure 2.30 : *Upper panel:* A region of the SPIRE-250 mosaic. The positions of the detection in our 250 μm catalog are shown with cyan open circles. *Lower panel:* A region with the same WCS of the upper panel, but observed with SPIRE 350 μm. The locations of 250 μm sources, i.e., the prior positions, are presented as small blue open circles when they were merged in a position to try photometry in the 350 μm mosaic, and as big open green circles in the positions where *phot+allstar* photometry was effected. The detections in our final SPIRE 350 μm catalog are indicated as magenta open circles.

The SPIRE 500 image was aligned to the WCS of the SPIRE 350 mosaic, deriving a WCS accuracy inferior to $7''$ (see Fig. 2.31). Consequently for the 500 μm band (PSF FWHM $\sim 36''$), we used as priors the 350 μm object positions (shown as cyan open circles in the upper panel of Fig. 2.33), and removed sources closer than $17''$ from the combined list of priors and direct detections from the several passes (indicated with blue open circles in lower panel of Fig. 2.33), and we again gave preference to priors compared to direct detections. Considering that the 500 μm is in the part of the modified black body (used to represent the dust emission) where the FIR flux is decreasing, we also measured 2 pixel ($28''$) aperture photometry in this case. We only kept as candidates the sources with flux density above the sky level (represented by open green circles in the lower panel of Fig. 2.33).

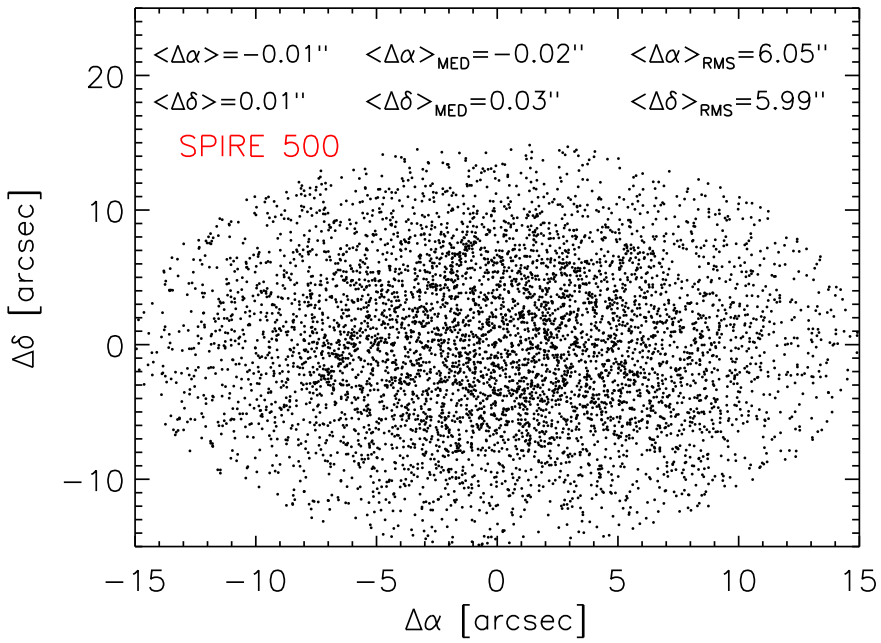

Figure 2.31 : Differences in right ascension and declination of the 500 μm detections with respect to the 350 μm objects. The random distribution of points indicate that there are not systematic differences between each set of WCS.

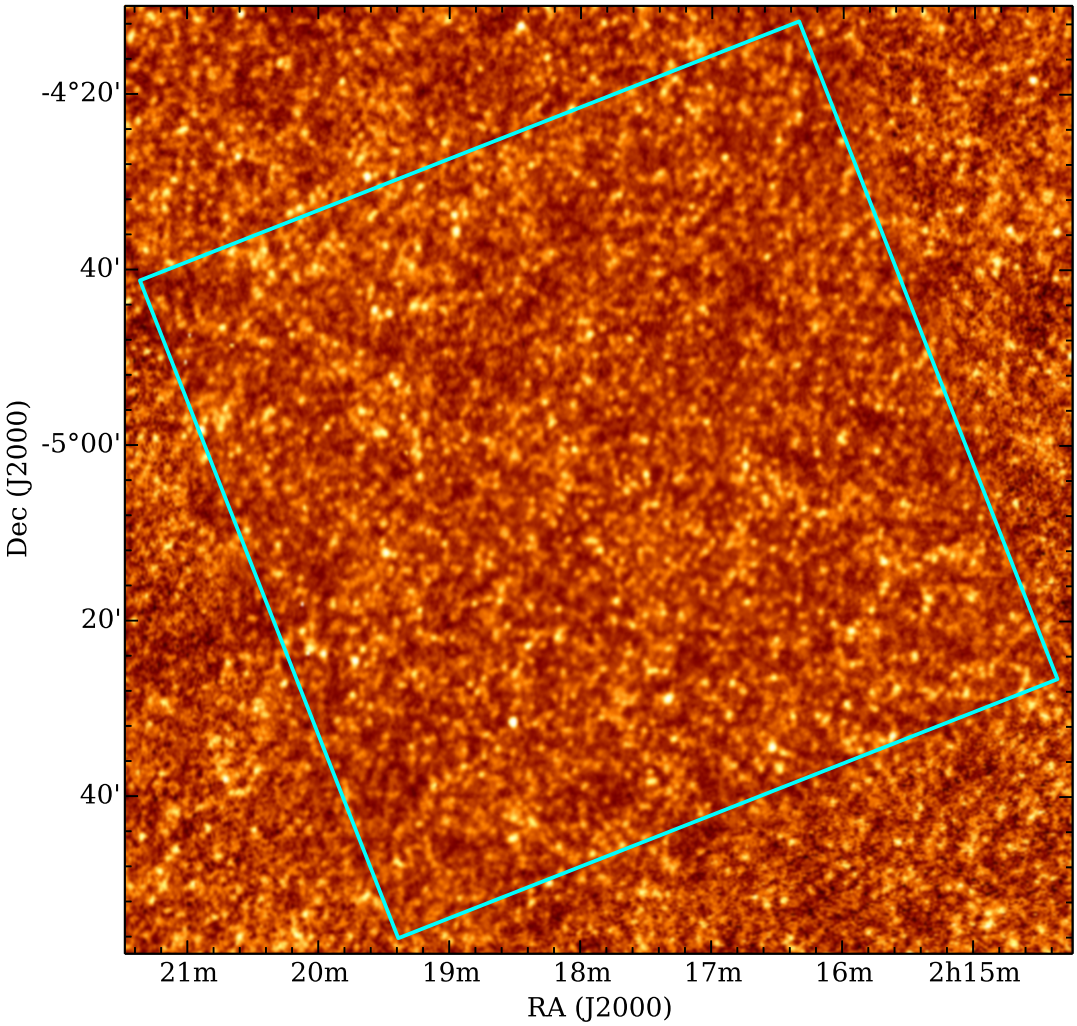

Figure 2.32 : SPIRE 500 μm mosaic constructed with the naive map-maker in HIPE for the SXDS/UDS field. The mosaic is aligned so that the North Celestial Pole is up. The cyan region indicates the area where the source catalog was made.

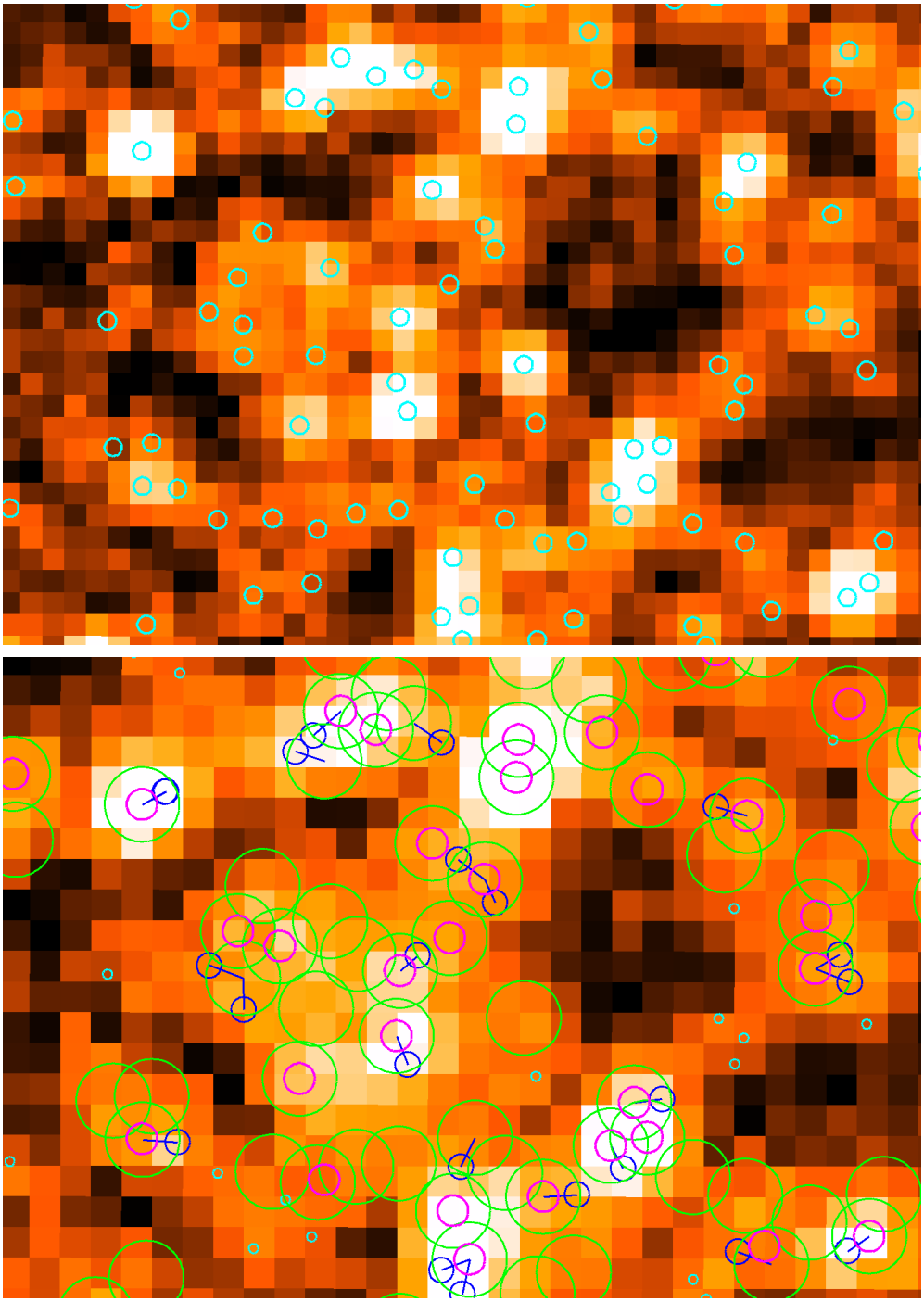

Figure 2.33 : *Upper panel:* A region of the SPIRE-350 mosaic. The positions of the detection in our 350 μm catalog are indicated with cyan open circles. *Lower panel:* A region with the same WCS of the upper panel, but observed with SPIRE 500 μm. The locations of 350 μm objects, i.e., the prior positions, are shown as a small cyan open circles when they were rejected at 2 pixel aperture photometry, as medium blue circles when they were merged in a position to try photometry in the 500 μm mosaic, and as big open green circles in the positions where *phot+allstar* photometry was effectuated. The detections in our final SPIRE 500 μm catalog are indicated as magenta open circles.

We constructed an empirical PSF using bright isolated sources for each SPIRE channel. We employed the PSF fitting technique over the purged list of candidates of the three bands, using circular apertures of radii 12, 20 and $28''$ for the 250, 350 and 500 μm channels, respectively. Then, we applied a calibration based on the beam sizes which were assumed Gaussians, and a correction factor ($\sim 10\%$) to consider the losses due to pixelation in the empirical PSFs. The errors of the SPIRE 250, 350, and 500 μm photometry were estimated from the sky uncertainty in a similar manner to the described for the MIPS-70 photometry. But the average background was measured in a sky box of 3, 4, and $6'$ for the 250, 350 and 500 μm channel, respectively.

It is important to note that we did not allow recenter in the *phot+allstar* tasks for the 350 and 500 μm bands. Therefore, the final detections in the 350 channel with 250 μm countepart, and in the 500 μm band with 350 and 250 μm associations are based on SPIRE-250 positions. Examples of the final detections in the 3 SPIRE channels are shown as magenta open circles in the lower panels of Figs. 2.27, 2.30, and 2.33 for the 250, 350 and 500 μm band, respectively.

Notwithstanding that we have used SPIRE data with different exposure time inside the UDS region (area ~ 2 deg^2), the background of our SPIRE maps appears uniform in this zone (see Fig. 2.25, 2.29 and, 2.32). Therefore, it is unnecessary to divide this region of the mosaics taking into account the different coverage. Hence, the SPIRE catalogs were done for each band in the whole observed UDS area.

Our final catalogs include 5479 sources ($S_{5\sigma}[250] = 13$ mJy) for SPIRE 250 μm, 1601 sources ($S_{5\sigma}[350] = 18$ mJy) for SPIRE 350 μm, and 553 sources ($S_{5\sigma}[500] = 18$ mJy) for SPIRE 500 μm detected in an area of ~ 2 deg^2. The 5σ noise levels estimated for the UDS fields are 11.2, 9.3 and 13.4 mJy for the SPIRE 250, 350 and 500 μm band, respectively (Oliver et al. 2012). In Figure 2.34, we present detections for the 3 SPIRE bands in a region with the same WCS.

In order to test the robustness and reliability of our UDS SPIRE catalogs, we calculated the 250, 350 and 500 μm differential number counts normalized to the Euclidean slope. These counts are shown in Figs. 2.35, 2.36 and 2.37. We compare our counts estimates with the measurements of the study of Oliver et al. (2012) for HerMES, which includes several fields with a total area of ~ 70 deg^2 (see the aforenamed paper for a full description), and the work Béthermin et al. (2012) for COSMOS and GOODS-N (also part of HerMES). Taking into account the uncertainties, our counts for the 3 SPIRE channels agree with these earlier works for the flux density range in common (an overall rms error of 10%, 15%, and 20% for the 250, 350 and 500 μm band, respectively).

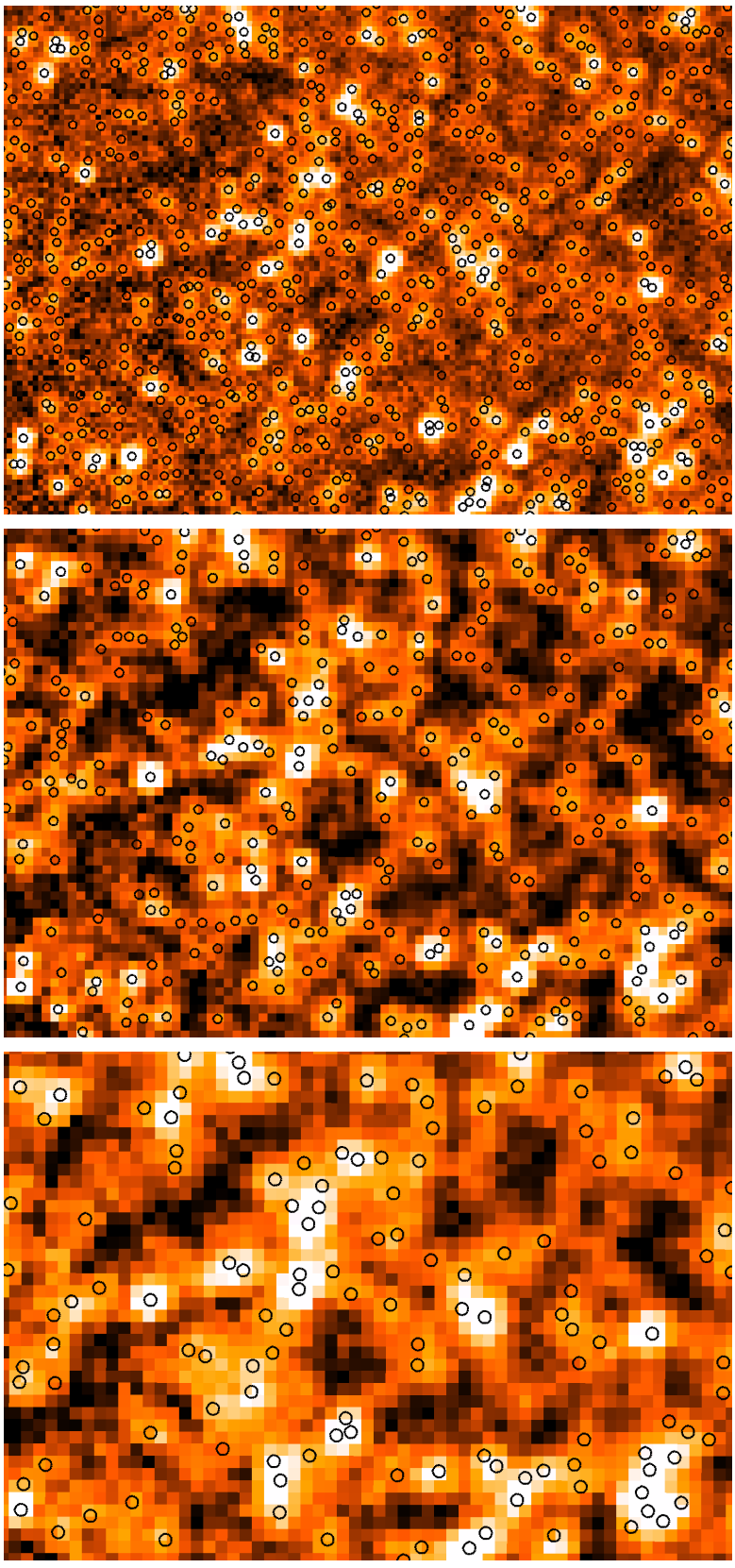

Figure 2.34 : Source detections in the 3 SPIRE channels are shown with black open circles in a sky zone with the same WCS. The upper panel shows the 250 μm band, the mid pannel presents the 350 μm channel, and the lower panel stands for the 500 μm band.

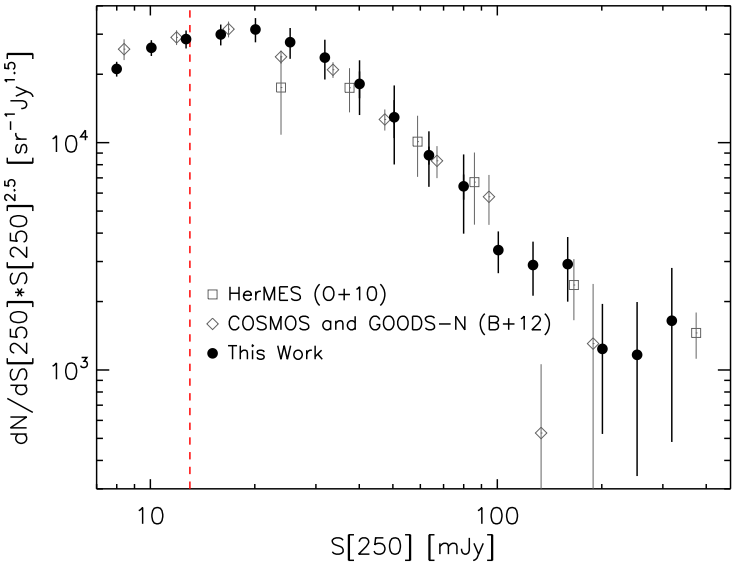

Figure 2.35 : SPIRE 250 differential number counts normalized to the Euclidean slope. *Filled circles* indicate our source counts for UDS. Their associated error bars stand for Poisson statistics. The vertical dashed red line indicates our 5σ detection threshold. *Open squares* are the estimations derived for HerMES (Oliver et al. 2010; O+10). *Open diamonds* show the counts obtained for COSMOS and GOODS-N (Béthermin et al. 2012; B+12). The error bars of both works include Poisson statistics and uncertainties in completeness corrections.

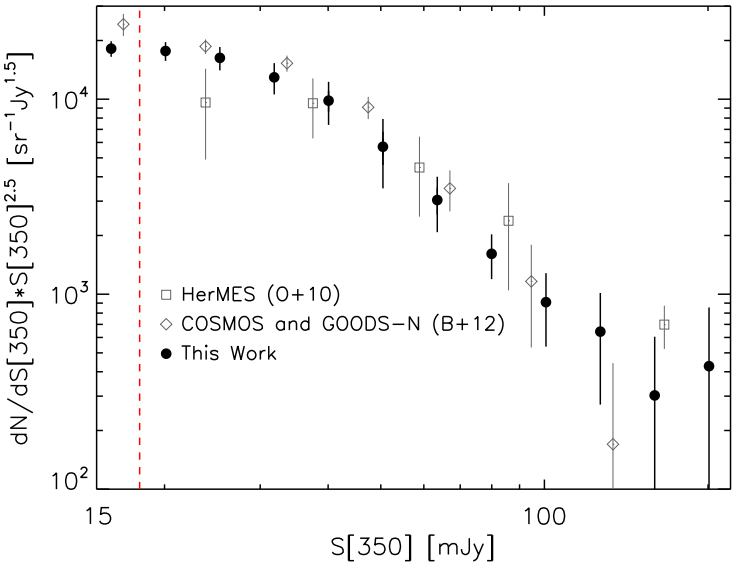

Figure 2.36 : SPIRE 350 differential number counts normalized to the Euclidean slope. *Filled circles* stand for our source counts for UDS. Their associated error bars show Poisson uncertainties. The vertical dashed red line indicates our 5σ detection threshold. *Open squares* are the estimations obtained for HerMES (Oliver et al. 2010; O+10). *Open diamonds* present the counts obtained for COSMOS and GOODS-N (Béthermin et al. 2012; B+12). The error bars of both works include Poisson statistics and uncertainties in completeness corrections.

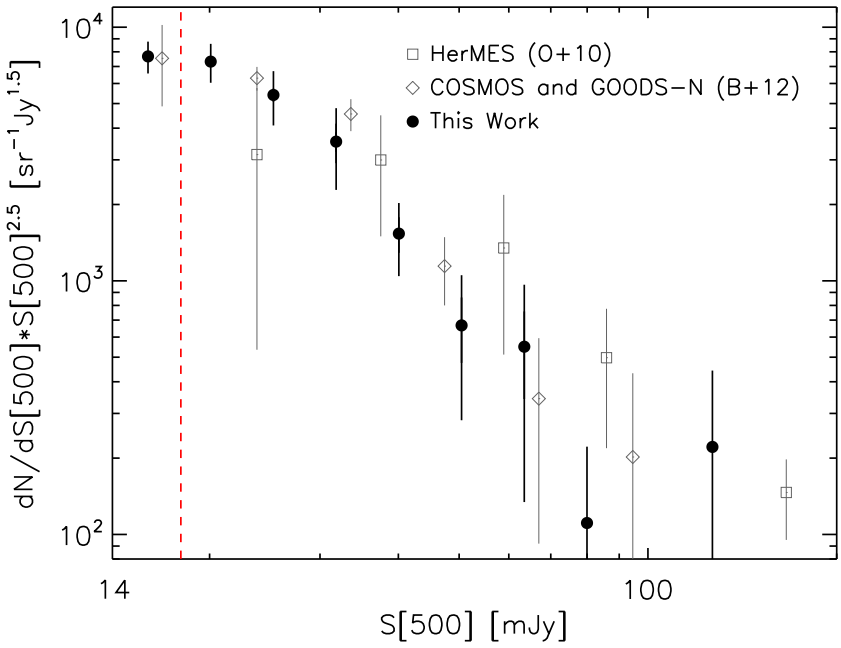

Figure 2.37 : SPIRE 500 differential number counts normalized to the Euclidean slope. *Filled circles* indicate our source counts for UDS. Their associated error bars stand for Poisson statistics. The vertical dashed red line indicates our 5σ detection threshold. *Open squares* are the estimations derived for HerMES (Oliver et al. 2010; O+10). *Open diamonds* show the counts obtained for COSMOS and GOODS-N (Béthermin et al. 2012; B+12). The error bars of both works include Poisson statistics and uncertainties in completeness corrections.

2.2.2.1 Debatable SPIRE detections

In this Section we discuss about the SPIRE sources that are below the 5σ detection thresholds (13, 18, and 18 mJy for the 250, 350, and 500 μm, respectively). The main problem of using objects with flux densities below the 5σ detection limit is that the different noise sources produce an overestimation of the object flux larger than the photometric error caused by the Gaussian approximation of the PSF (Wang et al. 2014). In other words, an object with an estimated flux density, S_e, and noise, σ_e, has a larger probability of being a fainter source on top of a noise peak than the contrary (Oliver et al. 2010). This is true for direct detections, but by using our prior-position based cataloging method, we are considering that such object has a clear detection on a band of noteworthy depth, the MIPS-24 band.

The faintest SPIRE-250 source from the final 70 μm sample showing a clear MIPS-24 detection ($\mathrm{S}[24] \sim 200$ μJy) is shown Fig. 2.38. Moreover, we also give in the same figure examples of the detections in the MIPS 70 μm and PACS 100 μm bands. Therefore, the probability of such 9.27 mJy SPIRE-250 source of being on top of a noise peak is small. We should mention that Wang et al. (2014) have made simulations injecting artificial sources in the HerMES images, and they have measured $\mathrm{S}_{\mathrm{out}} \sim 1.44 \times \mathrm{S}_{\mathrm{in}}$ at 10 mJy for SPIRE 250 μm using direct detections for the UDS. Such 44% error is almost twice our estimated uncertainty for this source, 23%.

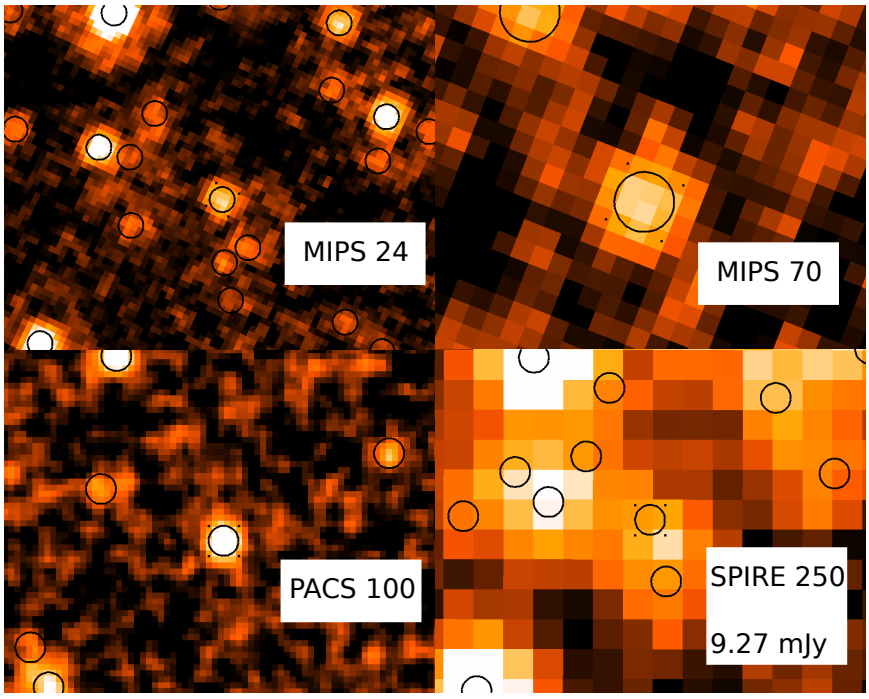

Figure 2.38 : Postage stamps from the MIPS, PACS 100, and SPIRE 250 μm bands of a source with $\mathrm{S}[250] = 9.27 \pm 2.13$ mJy.

For the 350 μm sources, the faintest one in the 70 μm-selected sample has flux, $\mathrm{S}[350] = 11.96$ mJy, showing an isolated clear detection in, e.g., MIPS 24, PACS 100, and SPIRE 250 μm bands (see Fig. 2.39). As mentioned above, we have used the SPIRE-250 positions to measure photometry at the 350 and 500 μm bands. In such case, the Wang et al. (2014) simulations resulted in $\mathrm{S_{out}} \sim 1.2 \times \mathrm{S_{in}}$ at 10 mJy for the UDS. This 20% uncertainty is smaller than our determined photometric uncertainty for this source 32%. Therefore, the possible flux boosting of this faint source is included in our determined photometric error, and the likelihood that our detection is due to a noise peak is really small.

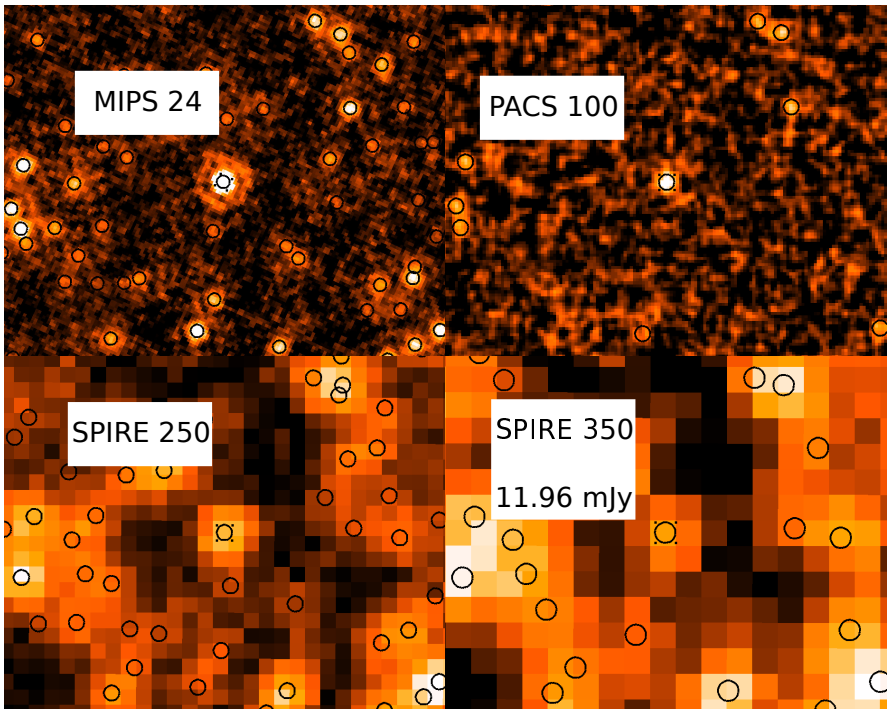

Figure 2.39 : Postage stamps from the MIPS 24, PACS 100, and SPIRE 250 and 350 μm channels of a an isolated FIR object with $\mathrm{S}[350] = 11.96 \pm 3.86$ mJy.

Other example of a faint 350 μm object is shown in Fig. 2.40. In this case, it has an estimated flux density of $S[350] = 13.54$ mJy and and associated photometric error of 2.68 mJy ($\sim$ 20%). We should note that the MIPS 24 μm counterpart has a bright companion, but it is clear that such companion is not detected in PACS and SPIRE bands.

Finally, for the 500 μm sources, the faintest one in the 70 μm-selected galaxies has a measurement of $S[500] = 11.74$ mJy. Wang et al. (2014) have determined for 500 μm sources based on 250 μm positions that $\mathrm{S_{out}} \sim 1.07 \times \mathrm{S_{in}}$ at 10 mJy for the UDS. For this faint source our estimated photometric uncertainty is 3.68 mJy, $\sim$ 26%, which

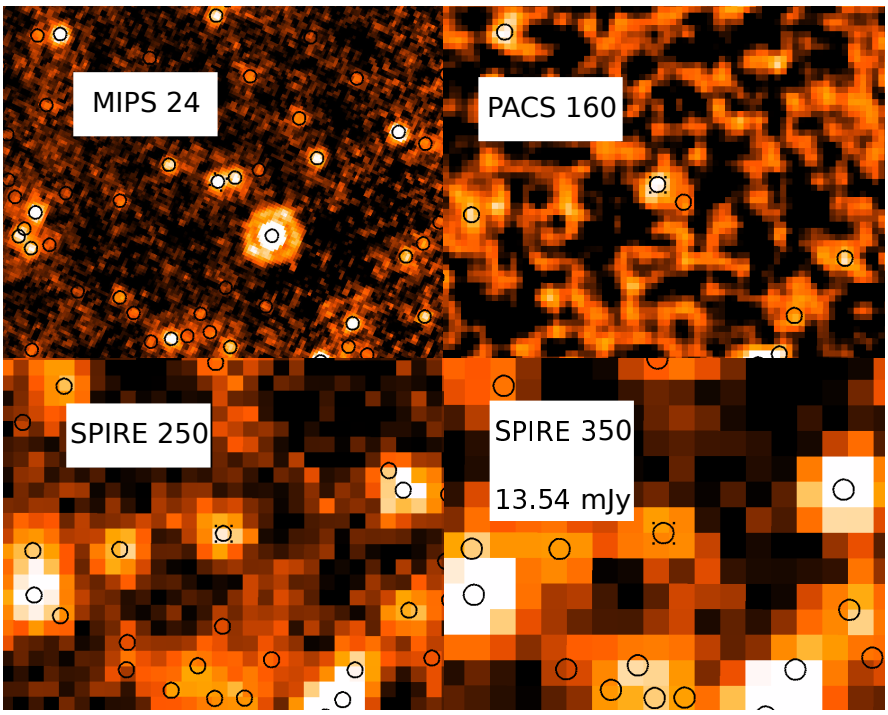

Figure 2.40 : Postage stamps from the MIPS 24, PACS 160, and SPIRE 250 and 350 μm bands of a source with $\mathrm{S}[350] = 13.54 \pm 2.68$ mJy.

is larger than the estimated flux boosting (7%). In Figure 2.41, we shown, e.g., clear detection in the MIPS, PACS 100, and SPIRE 250 and 350 μm bands. Therefore, the probability of this SPIRE-500 source of being on top of a noise fluctuation is minimal.

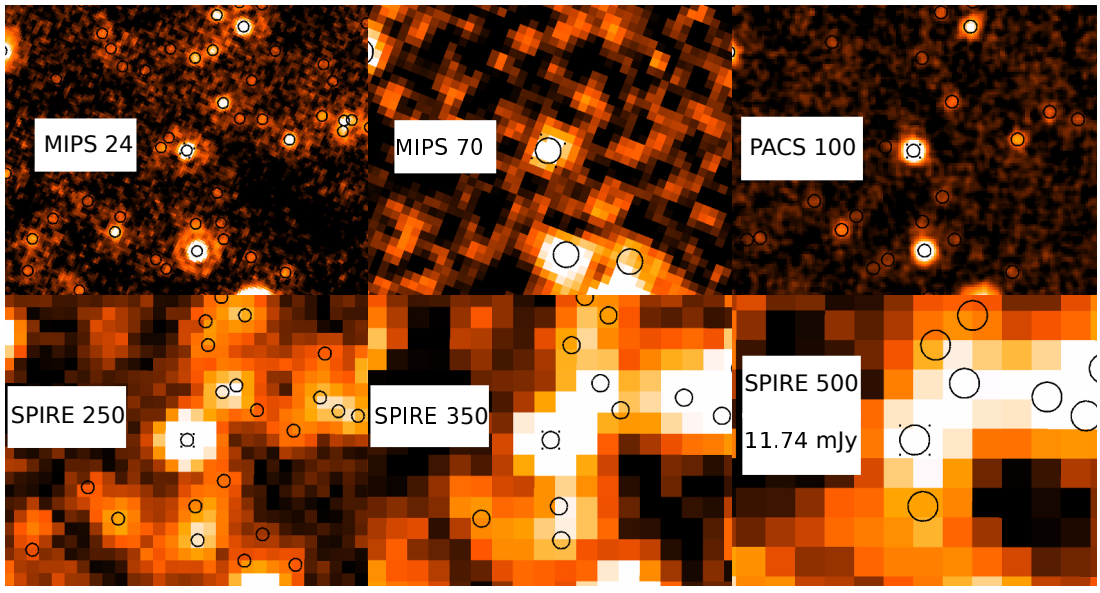

Figure 2.41 : Postage stamps from the MIPS, PACS 100, and the SPIRE 250, 350 and 500 μm bands of a source with $\mathrm{S}[500] = 11.74 \pm 3.68$ mJy.

In Figures 2.42 and 2.43, we present other two examples of faint SPIRE-500 objects. In this case the estimated flux densities are 12.86 and 15.84 mJy, and their associated uncertainties 3.73 (29%) and 3.08 mJy (20%), respectively. Both sources are detected in all the *Spitzer* and *Herschel* bands. Therefore, the likelihood of such detections of being caused by a spurious sources due to noise peaks is negligible.

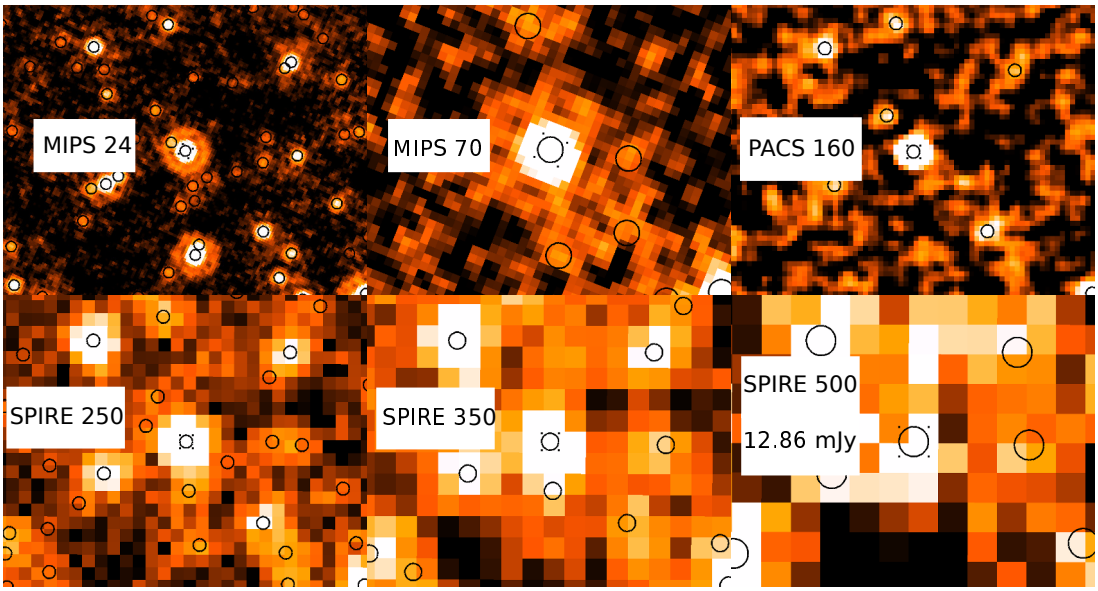

Figure 2.42 : Postage stamps from the MIPS, PACS 160, and the SPIRE 250, 350 and 500 μm bands of an object with $S[500] = 12.86 \pm 3.73$ mJy.

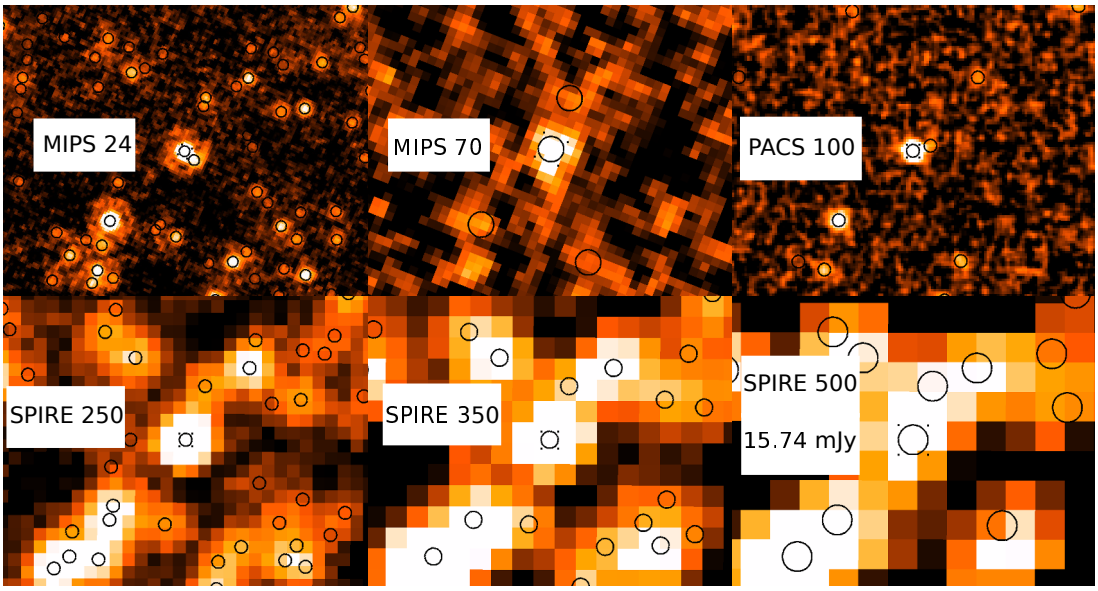

Figure 2.43 : Postage stamps from the MIPS, PACS 100, and the SPIRE 250, 350 and 500 μm bands of a source with $S[500] = 15.84 \pm 3.08$ mJy.

Considering the above mentioned facts, the less reliable source is the only SPIRE-250 object with flux density below the 5σ limit. Nevertheless, we have maintained SPIRE source above a 3σ noise threshold in order to have the largest possible number of measurements to constrain the dust emission parameterized with the $L_{\rm TIR}$. Such $L_{\rm TIR}$ values of our final MIPS-70 selected sample are described in the next Chapter.

Chapter 3

Sample Selection and Spectral Energy Distribution Construction

The main aim of this thesis is studying in detail the physical properties of the stellar populations of IR-bright galaxies using modeling techniques that treat the attenuation of the starlight and the dust emission in a self-consistent manner. In order to do that, we have focused on a region of the sky surveyed at the greater possible number of photometric bands. Among the several regions that fulfill that, we have chosen the Subaru/XMM-Newton Deep Survey (SXDS) centered at $\alpha = 02^{\rm h}18^{\rm m}00^{\rm s}$, $\delta = -05^{\circ}00'00''$, and covering an area of 1 deg^2 approximately. Figure 3.1 shows a three color optical image of SXDS field resulting from the combination of the B, R_c and i' filters, and footprints of UV-to-FIR surveys that also observed the SXDS/UDS field.

In order to acquire multi-wavelength data, the SXDS central coordinates were matched with that of the X-ray observations of XMM-Newton (Ueda et al. 2008). Subsequently, the SXDS was observed by ground and space-based telescopes, obtaining a wealth of data. The UV imaging from the Galaxy Evolution Explorer (GALEX; Martin et al. 2005) for the XMM-Newton Large Scale Structure Survey (XMMLSS) as a part of the Deep Imaging Survey (DIS). The optical broad-band imaging from Suprime-Cam (Miyazaki et al. 2002) as a part of the Subaru Telescope "Observatory Projects" (Furusawa et al. 2008). The near infrared broad-band imaging from UKIRT WFCAM (Casali et al. 2007) for the Ultra Deep Surver (UDS) included in the UKIRT Infrared Deep Sky Survey (UKIDSS; Lawrence et al. 2007). The mid infrared (MIR) photometric data from IRAC (Fazio et al. 2004), and MIPS (Rieke et al. 2004) on *Spitzer* as part of SpUDS (PI J. S. Dunlop), and the far infrared (FIR) data also from *Spitzer*/MIPS (for SpUDS too), PACS (Poglitsch et al. 2010), and SPIRE (Griffin et al. 2010) on *Herschel*

for the UDS as a part of HerMES (Oliver et al. 2012).

We have gathered such photometric data from UV to FIR wavelengths in order to assemble a sample of galaxies with comprehensive flux density measurements. Our intention is to work with galaxies having photometric measurements from UV/optical to FIR wavelengths in order to use the energy re-emmited by dust to constrain the attenuation of the stellar light. Therefore, we need sources with the largest possible number of flux measurements at the FIR in order to estimate an accurate total infrared luminosity ($L_{\rm TIR}$). Once with this sample, we can build UV-to-FIR SEDs and determine physical properties of these IR-bright galaxies. We give further details of all the data combined for this study in Section 3.2.

3.1 Sample Selection

Studying the dust emission of star-forming galaxies implies determining accurately the energy budget at MIR/FIR wavelengths. The FIR SEDs are explained mainly with two parameters: the $L_{\rm TIR}$ ($L(8-1000\ \mu{\rm m})$), and the dust temperature. Considering the parameter space of both quantities has allowed to characterize observational data at wavelengths greater than 8 μm with semi-empirical templates libraries (see, e.g., Chary and Elbaz 2001, Dale and Helou 2002, Rieke et al. 2009), and power-law/modified blackbody fitting methods (see, e.g., Blain et al. 2003, Casey 2012).

The sample of galaxies studied in this work was selected in a FIR band (MIPS 70 μm) with the goal of analyzing the dust emission. We have inclined for a selection in the MIPS 70 μm band in order to have sources with the best spectral coverage at MIR/FIR wavelengths: *Spitzer* MIPS $24+70$ μm, and *Herschel* PACS+SPIRE data. The MIPS 70 μm channel is preponderant in this selection because it is the shallowest band among the ones mentioned above. Using all this FIR information, we can estimate and restrict in an accurate manner the $L_{\rm TIR}$ for the galaxies in our sample. We have explained in detail the elaboration of MIR/FIR maps and catalogs in Chapter 2.

Selecting sources in the MIPS 70 μm band allows having a photometric point before the dust-emission peak ($\sim$100 μm at rest-frame wavelengths), and at the same time avoiding that this point is affected by the PAH emission (which would be the case for MIPS 24). At $z \lesssim 1.5$, the MIPS 70 μm detector is sensitive enough to get a significant population of galaxies (see, Elbaz et al. 2011), and at these redshifts its $\lambda_{\rm rf} \geq 28$ μm circumvents the PAH zone. Moreover, as indicated in Section 2.1.1, the beamsize of MIPS 70 μm observations (PSF FWHM $\sim 18''$) requires MIPS 24 μm data to help in the correct identification of multi-wavelength counterparts. Therefore, we first have concentrated our study in the regions of the SXDS/UDS field covered by both MIPS-70

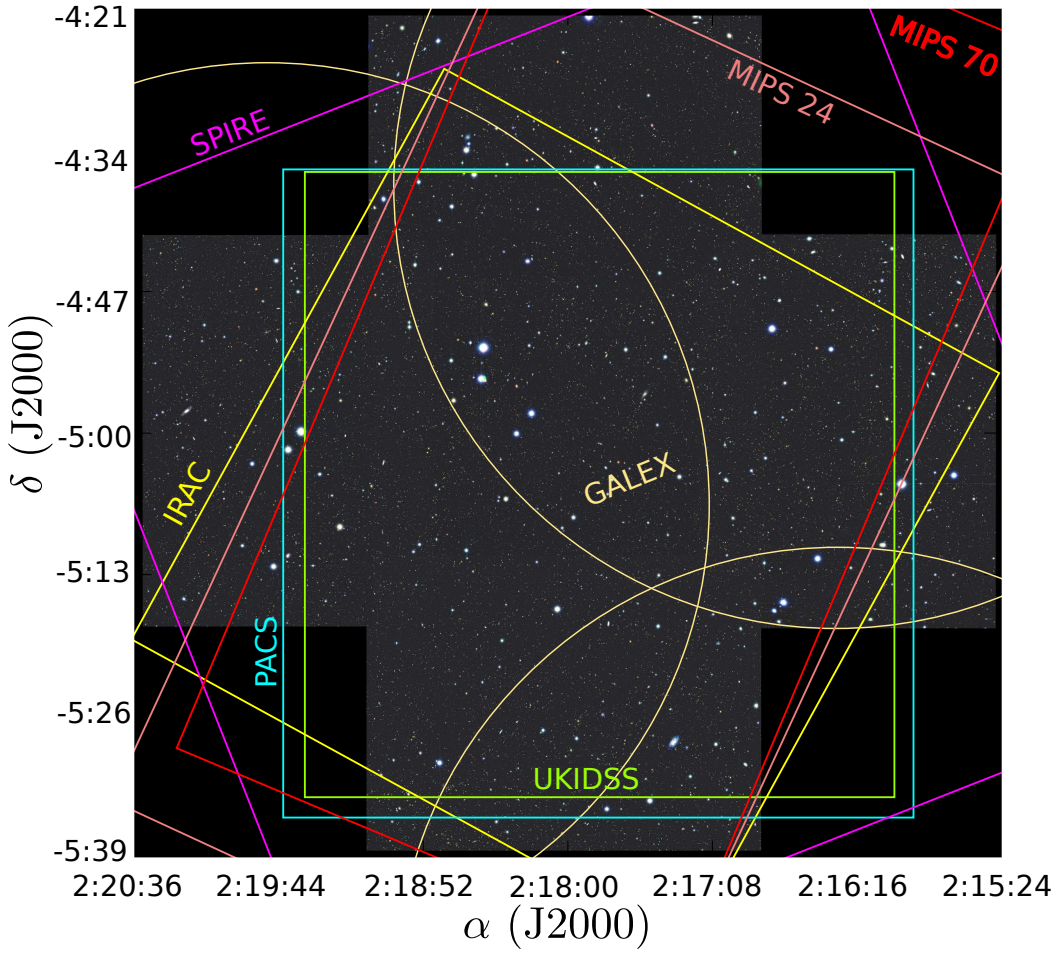

Figure 3.1 : Three color composite optical image of SXDS field obtained combining the B, R_c and i' filters of Suprime-Cam. *Credits:* `http://www.astr.tohoku.ac.jp/~akiyama/SXDS`
The footprints of several UV-to-FIR surveys which also pointed to the SXDS/UDS field are also shown: DIS-XMMLSS GALEX (FUV, NUV; pale-yellow circles) UKIDSS (JHK; green box), SpUDS IRAC (yellow box), SpUDS MIPS-24 (light coral box) and MIPS-70 (red box), UDS PACS (cyan box) and SPIRE (magenta box).

and MIPS-24 surveys (common area ~ 1 deg^2, see Fig. 3.2).

A MIPS 70 μm selection implies having SEDs of galaxies with dust temperature values encompassing the full dynamic range of dust heated by star formation (typically between $20 - 60$ K, Sanders and Mirabel 1996). This is due to the fact that the flux detection limit of MIPS-70 presents small variations within the mentioned dust temperature range. Such variations in observed flux densities are under a factor of 2 for wavelengths shorter than 250 μm, contrary to longer wavelengths in which the detec-

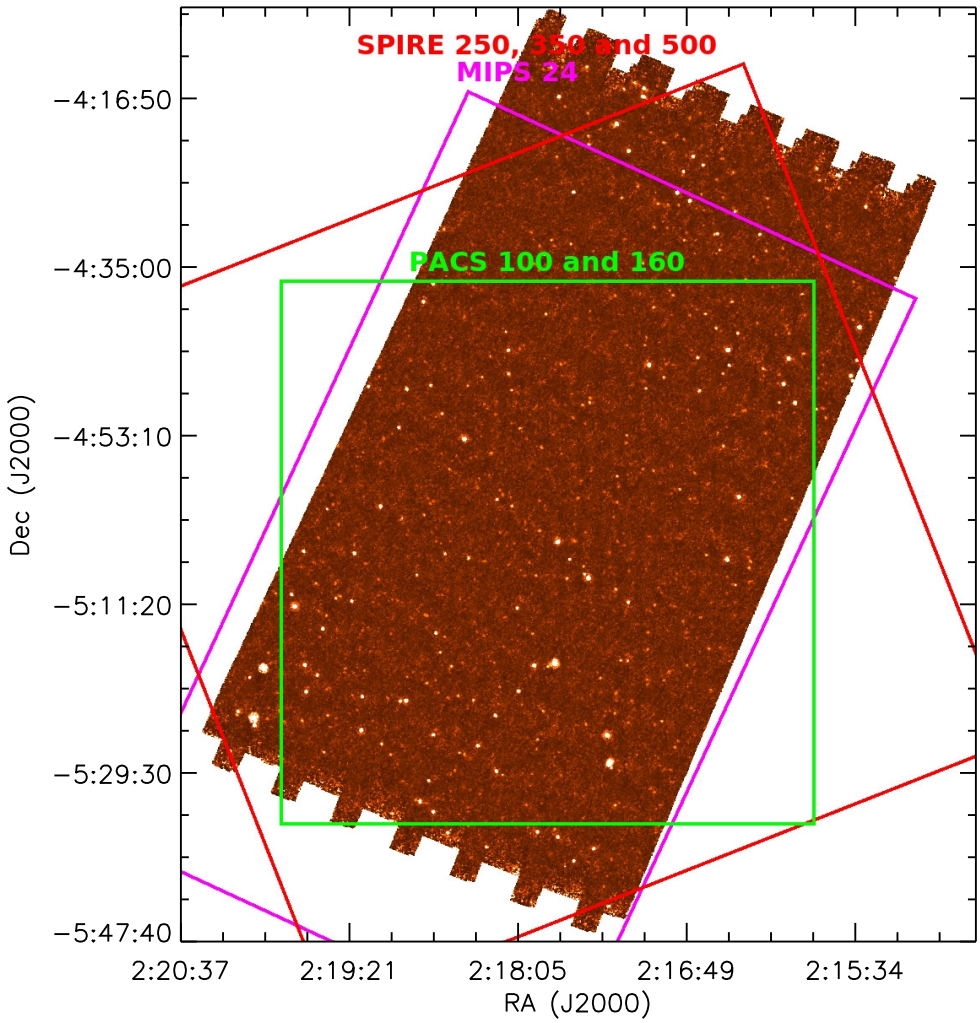

Figure 3.2 : Footprints of the MIPS-24, and the *Herschel* PACS and SPIRE regions of the SXDS/UDS field on top of our MIPS-70 mosaic built for the SXDS/UDS field. The overlapping area of the MIPS-70 and MIPS-24 surveys (~ 1 deg^2) is delimited by the mosaic and the magenta box.

tion limit decline is really pronounced with dust temperature increment (Casey et al. 2014).

As explained in Section 2.1.1, the MIPS 70 μm observations of the SXDS/UDS field were done for SpUDS, which also comprised IRAC data, taken in February 2008. We show a region of the SXDS/UDS field observed at 70, 24 and 3.6 μm in Fig. 3.3. This figure illustrates the source appearance and how the wide-beam of MIPS 70 μm limits the counterpart recognition at this wavelength. Then, it is crucial to count with 24 μm and IRAC observations in order to help with the multi-wavelength associations of each galaxy. Once we have *Spitzer* counterparts, we can proceed to find optical companions, and then we can estimate the redshift of each source by means of spectroscopic or

photometric techniques. A correct redshift estimation is critical to restrict the $L_{\rm TIR}$ of each source and to obtain reliable SED characteristics.

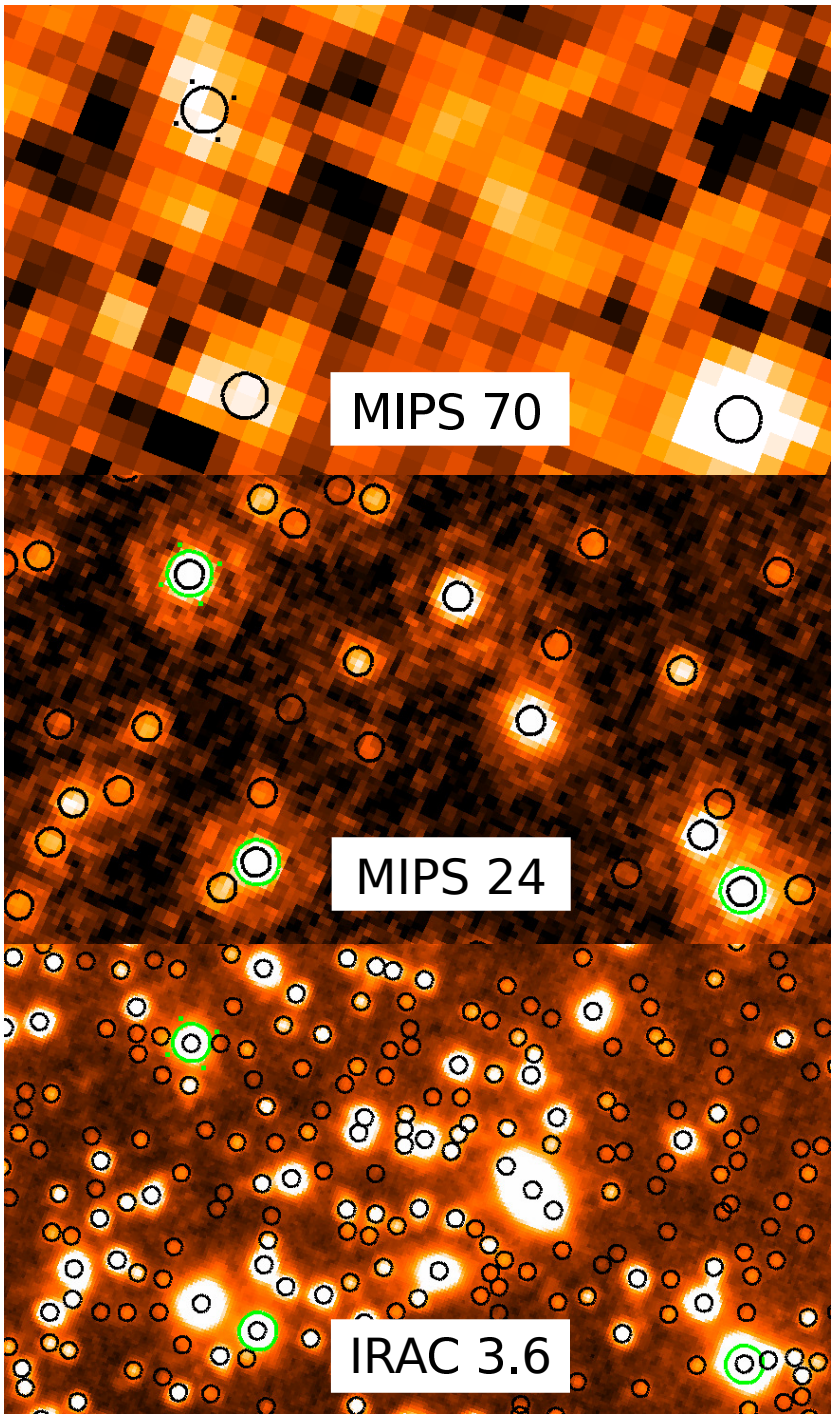

Figure 3.3 : A region of the SXDS/UDS field observed at 70 (upper panel), 24 (mid panel) and 3.6 μm (lower panel). The detections in each channel are presented with open black circles. The counterparts at 24 and 3.6 μm corresponding to 70 μm sources are indicated with open green circles in the mid and lower panels, respectively.

We have presented in Sections 2.1.1 and 2.1.2 the MIPS 70 and 24 μm catalogs. From the 542 sources at 70 μm with flux density above the 5σ threshold (777 objects above 4σ flux limit), only 456 (678) are located in the area in common with the MIPS-24 image (~ 1 deg^2). Such 456 (678) sources are our initial FIR selected sample. We will describe the ancillary data to study these MIPS-70 objects in the following Section.

3.2 Ancillary Data

In this Section, we describe the multi-wavelength sets in SXDS/UDS field compiled for this work in order to characterize our MIPS-70 selected sample. Table 3.1 summarizes the main characteristics of these collections including the wavelengths, magnitudes of the third quartile of the distribution of sources, magnitudes corresponding to the 5σ threshold above the sky level, FWHM of the PSFs, areas of the surveys, surface densities, and the source from which the information was obtained for each band. In the following we give further details about each data set.

3.2.1 Ultraviolet Data

The Galaxy Evolution Explorer (GALEX, Martin et al. 2005) carried out the first all-sky imaging in the UV part of the spectrum ($135 - 275$ nm). Among these imaging collections, GALEX carried out the Deep Imaging Survey (DIS). The DIS observing strategy was to dedicate 30000 seconds over an area of 80 deg^2. The SXDS field was observed as a part of the data for XMM-Newton Large Scale Structure Survey (XMMLSS), which was included in the GALEX DIS survey. XMMLSS observations were performed under both GALEX filters: FUV at 153 nm, and NUV at 231 nm. We downloaded the images and photometric catalogs for the area overlapping with SXDS (fields XMMLSS_04, XMMLSS_07 and XMMLSS_09; with a total area of ~ 3.2 deg^2). These images have a projected pixel scale of $1.5''$ and an average exposure time of ~ 24000 seconds in both channels.

For such photometric catalogs, we have adopted as limiting magnitude the third quartile of the magnitude distribution of the sample (hereafter the limiting magnitude for optical, near infrared and mid infrared data). These limiting magnitude are 24.8, and 24.4 for FUV and NUV filters, respectively. In Figure 3.4, we show these limiting magnitudes for both channels, and also the magnitudes for the 5σ thresholds (i.e., where signal-to-noise ratio is greater than 5, or the magnitude error is $\gtrsim 0.2$ mag).

Table 3.1 : Characteristics of the data compiled for the SXDS/UDS field

Band	$\lambda_{\rm eff}$	$m_{\rm Q_3}$	$m_{5\sigma}$	FWHM	Area	Surf. Dens.	Source
(1)	(2)	(3)	(4)	(5)	(6)	(7)	(8)
MIPS-70	72.5 μm	14.7 (5 mJy)	14.0 (9 mJy)	$18''$	1.2	0.13	Spitzer GTO
MIPS-24	23.8 μm	19.4 (63 μJy)	19.3 (70 μJy)	$6''$	1.2	6.00	Spitzer GTO
IRAC-3.6	3.56 μm	24.2	23.1	$2.1''$	1.0	36.65	Spitzer GTO
IRAC-4.5	4.50 μm	24.3	23.2	$2.1''$	1.0	35.14	Spitzer GTO
IRAC-5.8	5.74 μm	23.3	22.0	$2.3''$	1.0	25.92	Spitzer GTO
IRAC-8.0	7.93 μm	23.3	21.8	$2.3''$	1.0	23.91	Spitzer GTO
PACS-100[a]	102.4 μm	...	16.3 (1.1 mJy)	$7''$	0.1	4.18	Herschel OT2
		...	15.4 (2.4 mJy)		0.2	1.31	Herschel KPGT
		...	14.9 (4.1 mJy)		0.6	0.72	Herschel KPGT
PACS-160[a]	165.6 μm	...	15.2 (3.1 mJy)	$12''$	0.1	3.33	Herschel OT2
		...	14.5 (5.8 mJy)		0.2	1.55	Herschel KPGT
		...	14.0 (8.9 mJy)		0.6	0.85	Herschel KPGT
SPIRE-250	253.2 μm	14.7 (4.8 mJy)	13.6 (13 mJy)	$18''$	2.0	0.76	Herschel KPGT
SPIRE-350	355.9 μm	14.6 (5.5 mJy)	13.3 (18 mJy)	$26''$	2.0	0.22	Herschel KPGT
SPIRE-500	511.3 μm	14.6 (5.5 mJy)	13.3 (18 mJy)	$36''$	2.0	0.08	Herschel KPGT
FUV	153.9 nm	24.8	24.4	$5.5''$	3.2	2.00	Galex GTO
NUV	231.6 nm	24.4	24.2	$5.5''$	3.2	4.45	Galex GTO
B	441.9 nm	27.6	29.2	$0.9''$	1.2	135.26	Subaru/SuprimeCam
V	545.6 nm	27.3	28.9	$0.9''$	1.2	143.87	Subaru/SuprimeCam
R_c	651.8 nm	27.1	28.8	$0.8''$	1.2	130.21	Subaru/SuprimeCam
i'	766.9 nm	27.0	28.7	$0.9''$	1.2	137.32	Subaru/SuprimeCam
z'	906.8 nm	26.4	28.0	$0.9''$	1.2	108.86	Subaru/SuprimeCam
J	1.25 μm	24.2	25.4	$0.8''$	0.8	55.33	UKIRT/WFCAM
H	1.64 μm	23.0	24.1	$0.8''$	0.8	40.27	UKIRT/WFCAM
K	2.21 μm	22.9	24.1	$0.8''$	0.8	56.73	UKIRT/WFCAM

Notes.— (1) Name of the observing band. (2) Effective wavelength of the filter+detector. (3) magnitudes corresponding to the third quartile of the magnitude distribution (limiting magnitudes for the FUV to IRAC-8.0 bands). (4) magnitudes of a detection with SNR=5 (limiting manitudes for the MIPS 24 and PACS bands; for the MIPS-70 and SPIRE channels, see Sections 3.6 and 2.2.2.1). (5) median of the PSF FWHM in arcseconds. (6) Area covered by the surveys in deg^2. (7) source density per square arcminute up to the $m_{\rm Q_3}$ for FUV-to-8 μm bands and up to $m_{5\sigma}$ for the 24-to-500 μm channels. (8) Source from where the data were obtained.

[a] PACS limiting magnitudes for regions with different exposure time: UDS-CANDELS, UDS-SCUBA, and UDS-NORMAL, respectively (see Section 2.2.1 for details).

3.2.2 Optical Data

The ground-based optical imaging of the SXDS field was taken with SuprimeCam (Miyazaki et al. 2002) on the Subaru telescope at ManuaKea Hawaii, lasting a period of 3 years. The SuprimeCam has a $34' \times 27'$ field of view with a projected pixel scale of $0.202''$. Five continuous cross-shaped pointings with some overlapping, and circular

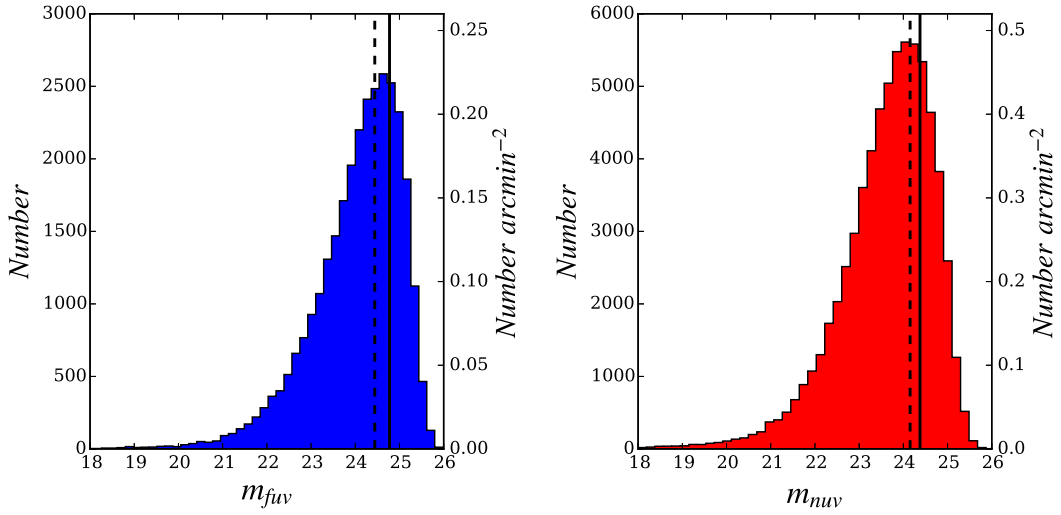

Figure 3.4 : Distribution of source magnitudes in GALEX filters. The *solid lines* shows the limiting magnitude defined as the third quartile of the distribution. The *dashed lines* stand for the 5σ-threshold magnitudes.

dithering were required to cover the SXDS field, reaching an area of $\sim$1.22 deg^2 (see Fig. 3.1). The Subaru imaging data used in our study comprised the broadband filters B, V, R_c, i', and z'. These observations got 160 hours from the Subaru Telescope "Observatory Projects" (see Furusawa et al. 2008 for more observational details).

Following the SXDS Data Release 1, we downloaded the five tile images for each one of the five filters from the Subaru official website[1]. Then, we performed source detection and photometry using SExtractor with typical methods (Bertin and Arnouts 1996). We did not apply filtering for detecting objects, and we took special care of the PHOT_AUTOPARAMS in order to check that we were using adequate apertures. Aftewards, we compared astrometry and photometry in the five tiles for each filter in order to discard repeated sources.

The limiting magnitudes of the five bands are shown in Table 3.1. We have also estimated the 5σ detection threshold magnitudes using the Sextractor photometric errors (see dashed lines in Fig. 3.5). Sextractor determines the photometric uncertainties using the pixel-by-pixel rms noise measurement. This technique tends to underestimate the true sky fluctuation due to signal correlation in neighboring pixels caused by astrometric reprojection of the tiles on a common grid (Gawiser et al. 2006). This fact indicates that the third quartile of the magnitude distribution is a better choice as limiting magnitude.

[1] `http://www.naoj.org/Science/SubaruProject/SXDS/`

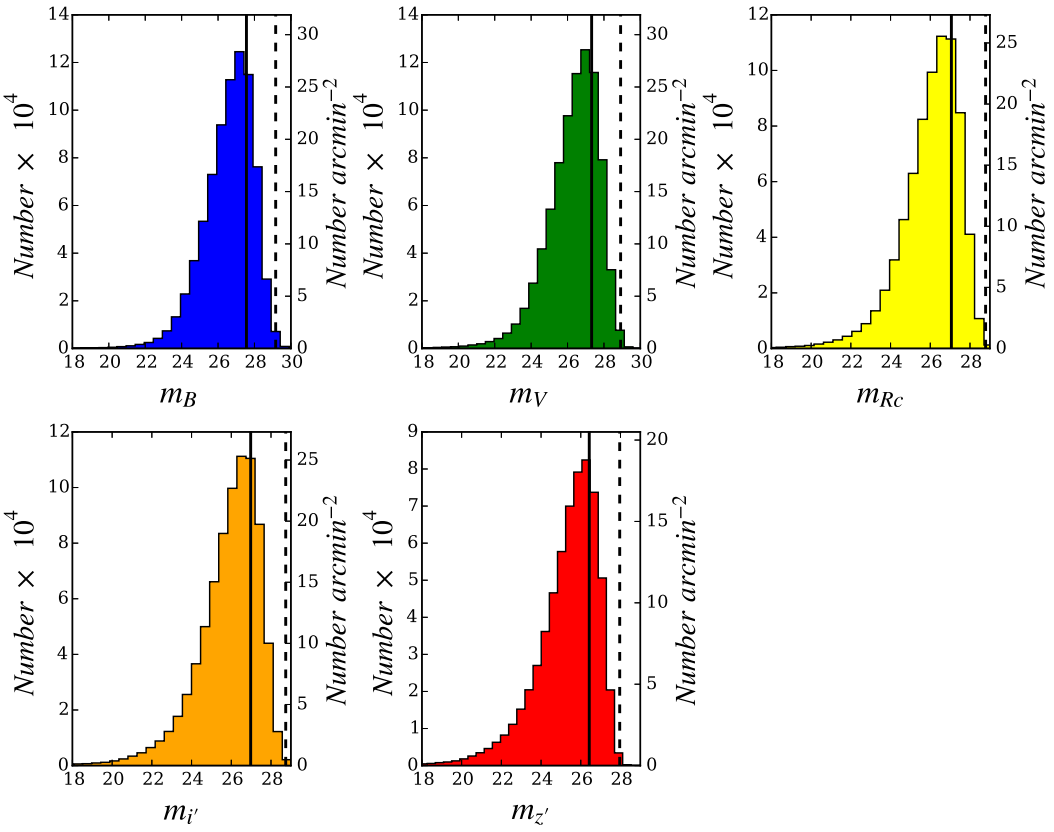

Figure 3.5 : Distribution of source magnitudes in SuprimeCam filters. The *dashed line* in each panel depicts the 5σ-threshold magnitude of each filter. The *solid line* in each panel stands for limiting magnitude of each channel.

3.2.3 Near Infrared Data

The SXDS field has also been observed with the United Kingdom Infrared Telescope Wide Field Camera (UKIRT WFCAM; Casali et al. 2007) for the Ultra Deep Survey (UDS; Almani et al. in prep.), which is the deepest constituent of the UKIRT Infrared Deep Sky Survey (UKIDSS; Lawrence et al. 2007). The UDS field has been observed since 2005, covering an area of 0.78 deg^2. WFCAM has a field of view of 0.207 deg^2 with a projected pixel scale of $0.134''$, its common observing procedure is made in four steps with some overlap. The area of the UDS has been covered using this nominal observing mode. The UDS data included in our study encompass imaging in the broadband filters, J, H, and K. We downloaded the four tiles of object and confidence images for these three filters from WFCAM science archive in its Data Release 8[2]. We carried out source extraction and photometry in each filter tile using SExtractor with standard procedures, and then compare astrometry and photometry in the four tiles for

[2] `http://surveys.roe.ac.uk/wsa/dr8plus_release.html`

each filter in order to drop repeated sources. The limiting magnitudes for the three filters are presented in Table 3.1. We have also determined the 5σ magnitudes using the Sextractor derived photometric uncertainties (see dashed lines in Fig. 3.6). The 5σ threshold magnitudes are again deeper than our assumed limiting magnitudes as can be observed in the magnitude distribution of each filter. This is due to the underestimation of the background around each source derived with Sextractor.

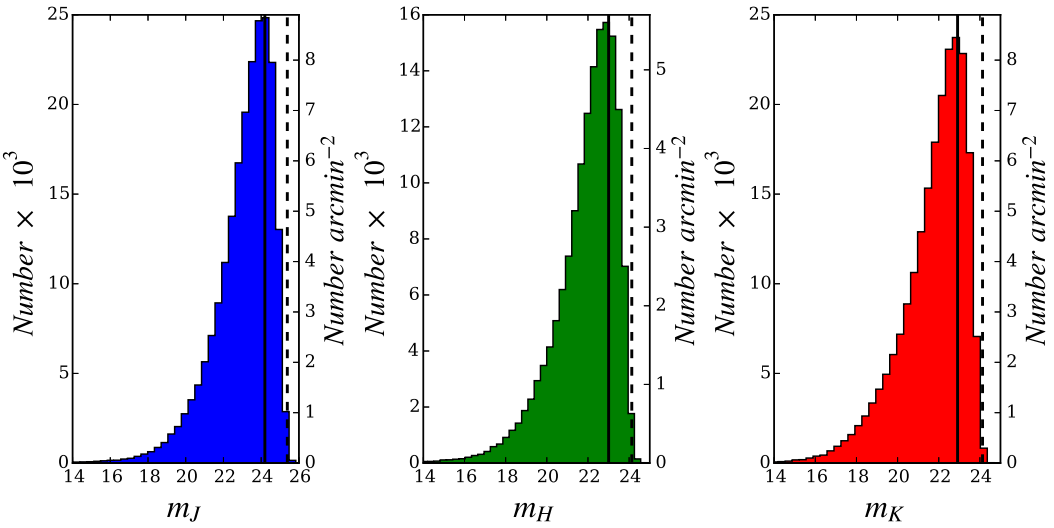

Figure 3.6 : Distribution of source magnitudes in WFCAM filters. The *solid line* in each panel represents the limiting magnitude of each filter. The *dashed line* in each panel shows the 5σ-threshold magnitude of each channel.

3.2.4 IRAC Data

The IRAC data used in this study come from the Spitzer Legacy Program for UDS (SpUDS; PI J. Dunlop). Observations were made in map mode for the four IRAC channels, 3.6, 4.5, 5.8 and 8.0 μm. They required 28 Astronomical Observational Requests (AORs) in one epoch, January 2008, covering an area $\sim$ 1 deg^2. The average exposure time per pixel is $\sim$ 1900 s for the channel 1 and 2, and $\sim$ 3200 s for channels 3 and 4. All the data were reduced with the general Spitzer pipeline which produce Basic Calibrated Data (BCD), and were mosaicked jointly using the technique of Huang et al. (2004). This technique comprises pointing honing, distortion correction, and mosaicking using a pixel scale half of the original (approximately 0.61$''$) with a drizzling strategy.

The source extraction and photometry was performed in a similar way as described in Appendix A from Pérez-González et al. (2008). Basically, we detected sources with SExtractor in the 3.6 μm and 4.5 μm separately. The 4.5 μm detections complement

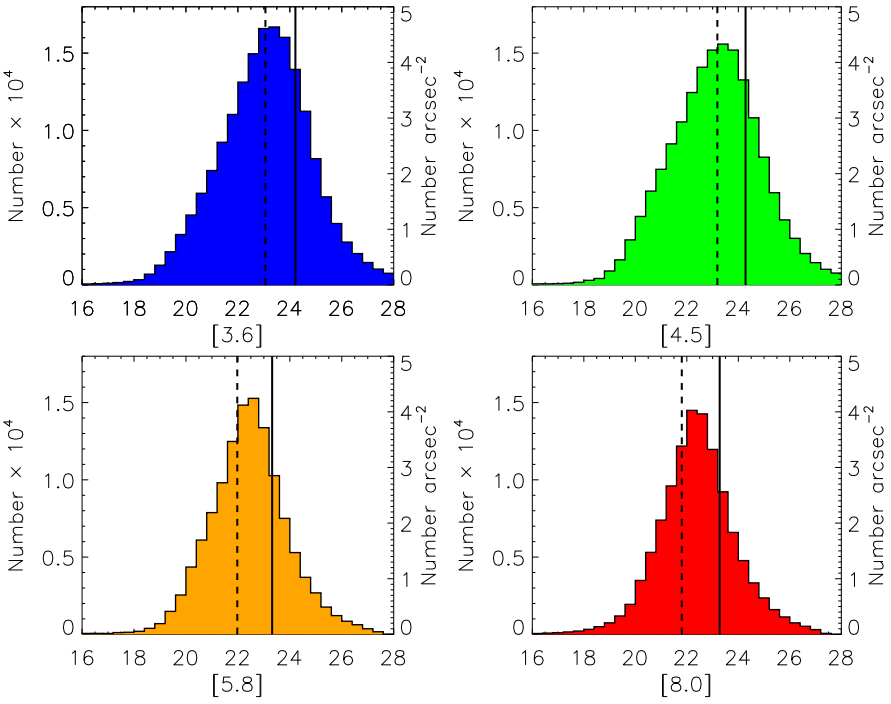

Figure 3.7 : Distribution of source magnitudes in IRAC filters. The *dashed line* in each panel indicates the 5σ threshold magnitude of each filter. The *solid line* in each panel stands for our adopted limiting magnitude of each channel.

and alleviate the SExtractor deblending problems due to the high crowdedness in 3.6 μm band. Then, we combined both list of sources by removing objects whose separation was smaller than $\sim 1''$. Aperture photometry was determined with SExtractor for each channel IRAC image, fixing the IRAC 3.6 + 4.5 positions in the four IRAC bands, and forcing measurements. We obtained the final integrated fluxes after applying aperture corrections based on empirical Point Spread Functions (PSFs). We measure the flux density enclosed in circular apertures of radius $2''$, and applied aperture corrections of 0.32 ± 0.03, 0.36 ± 0.03, 0.53 ± 0.02, and 0.65 ± 0.03 mag for channels 3.6, 4.5, 5.8 and 8.0 μm, respectively, where the corrections encompass the typical WCS alignment errors. The limiting magnitudes are indicated in Table 3.1. We have also estimated the 5σ threshold magnitudes (see dashed lines in Fig. 3.7). We disregarded the photometric error resulting for Sextractor measurements in this case. The IRAC photometric uncertainties were calculated considering contributions from the sky emission, the readout noise, the Poissonian photon counting, the uncertainties in the aperture corrections, and a 2% uncertainty from the zero-point absolute calibration (Reach et al. 2005). The technique we used to estimate the background fluctuations considers the signal correlation in adjacent pixels. This method is also utilized to derive the photo-

metric uncertainties in the matched aperture multi-wavelength catalog. It is similar to the technique we have applied to measure the photometric uncertainties in the FIR cataloging of Chapter 2, such method will be described in Section 3.3. In Figure 3.7, we notice that with this method the 5σ magnitudes are brighter than the ones derived with the third quartile of the magnitude distribution due to a more realistic estimation of the photometric errors. We keep our fiducial limiting magnitude for consistency with the other UV/optical bands.

3.2.5 MIPS Data

The MIPS data employed in this work were taken also for the Spitzer Legacy Program for UDS (SpUDS), these data have been described is Section 2.1. We remind the reader here briefly that the 24 and 70 μm imaging was taken using the scan map mode at the slow rate, requiring 3 scan legs for each AOR. SpUDS MIPS observations were taken in one epoch, February 2008, covering an area of approximately 1.2 deg^2.

The MIPS 24 μm data were combined using the SSC mosaicking software MOPEX (Version 18.3.1; Makovoz and Khan 2005). The final mosaic has an output square pixel of 1.2$''$, and an average exposure time of $\sim$ 3300 s per pixel. Traditionally, the photometric measurements in wavelengths longer than 10 μm are given in Janskys (Jy). We took as limiting flux the 5σ threshold above the sky level, which corresponds to $\sim$ 70 μJy ($\sim$19.3 mag). In this case, the limiting flux almost coincides with the third quartile of the source flux density distribution (19.4 mag; see Fig. 3.8).

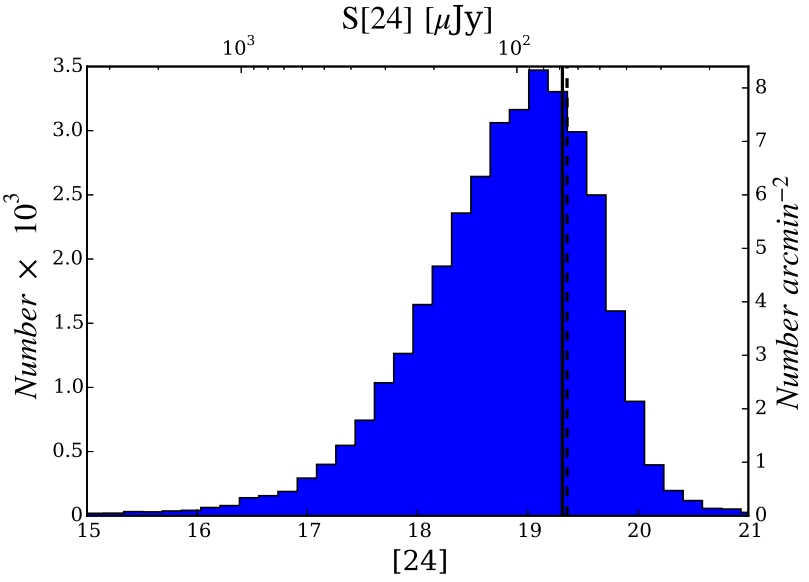

Figure 3.8 : Distribution of source magnitudes in MIPS 24 μm filter. *Dashed line*: the third quartile of the magnitude distribution. *Solid line*: magnitude corresponding to $S_{5\sigma}[24]$.

The MIPS 70 μm data were also mosaicked using MOPEX. The final 70 μm map has an output square pixel of 4″, and an average exposure time $\sim$ 1430 s per pixel. The flux corresponding to the 5σ threshold is $\sim$ 9mJy ($\sim$ 14.0 mag). This flux density threshold encompasses less than the bright half of the source distribution. In this case, the third quartile of the distribution corresponds to a low ($\sim 2.5\sigma$) threshold above the sky level (see Fig. 3.9).

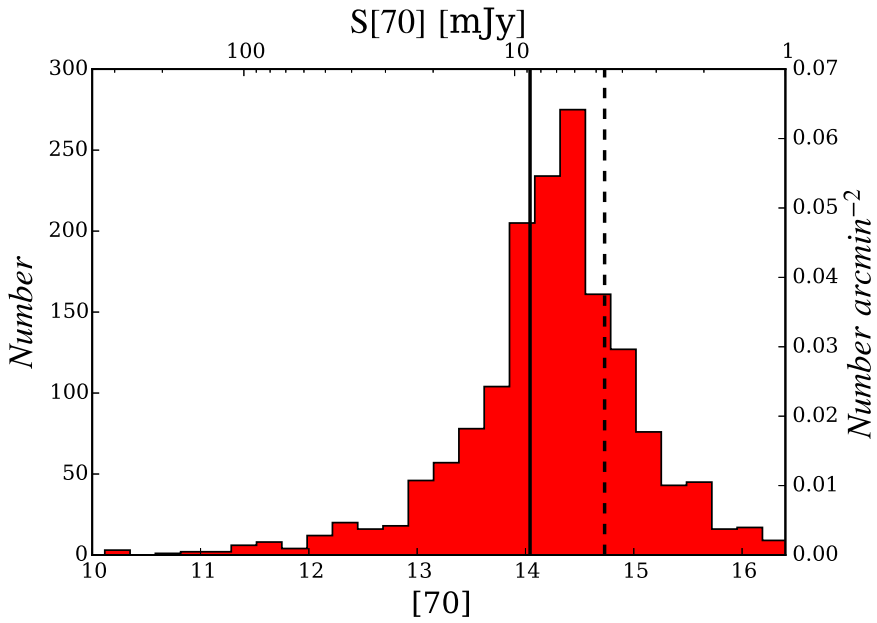

Figure 3.9 : Distribution of source magnitudes in MIPS 70 μm filter. *Dashed line*: the third quartile of the magnitude distribution. *Solid line*: magnitude corresponding to $S_{5\sigma}[70]$.

3.2.6 Herschel Data

The Herschel data used in this study encompass PACS and SPIRE imaging of the SXDS/UDS field, these data have already been presented in Section 2.2. We summarize here that this sky region was observed as a part of HerMES (Oliver et al. 2012). The PACS data were obtained in 12 AORs, lasting 40.19 hours, and covering an area of ~ 0.9 deg^2. The SPIRE data were acquired in 7 AORs, consuming 10.54 hours, and covering an area of ~ 2 deg^2.

We downloaded all public PACS data inside the UDS region from HSA, incorporating also 2 targets with longer exposure time. Hence, our UDS PACS data are composed of 3 regions with different exposure time comprehending an area of ~ 0.9 deg^2. These regions are: UDS-CANDELS (with an area of $\sim$ 0.1 deg^2), UDS-SCUBA (with an area of $\sim$ 0.2 deg^2), and UDS-NORMAL (with an area of $\sim$ 0.6 deg^2). We have

cataloged each region separately, the limiting fluxes (the 5σ threshold) for the PACS 100 μm band are 1.1, 2.4 and 4.1 mJy, and for the PACS 160 μm are 3.1, 5.8 and 8.9 mJy, corresponding to UDS-CANDELS, UDS-SCUBA and UDS-NORMAL, respectively. In Figure 3.10, we show the flux denisity distributions, and indicate the limiting fluxes of each region. We also show in this figure, the third quartile of the flux density distribution (dashed line in each panel), which is 3.1 and 7.9 mJy for the 100 and 160 μm channel, respectively. These values roughly agree with the 5σ threshold of our shallowest cataloged region, UDS-NORMAL (solid line in each panel).

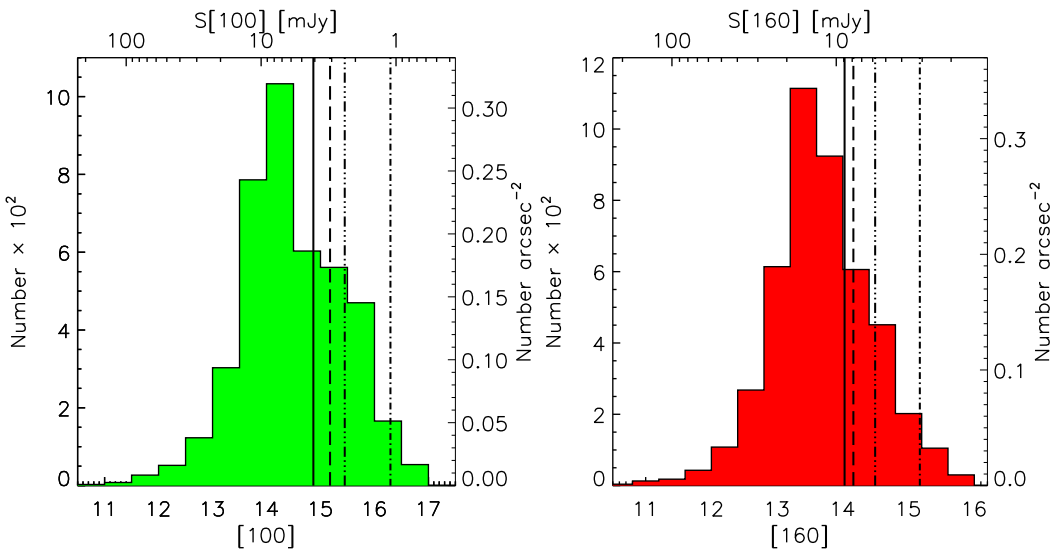

Figure 3.10 : Distribution of source magnitudes in PACS filters. The *dot-dashed, 3-dot-dashed* and *solid* lines show the magnitudes corresponding to the $\sim 5\sigma$ threshold above the sky level for the regions UDS-CANDELS, UDS-SCUBA, and UDS-NORMAL, respectively in both channels. The *dashed* lines show the third quartile of the magnitude (flux density) distributions.

We also downloaded all public SPIRE data for the UDS field from the HSA, including the targets from shallow observations *XMM* VIDEO 1 (in HerMES too) and UDS-CANDELS, a small region with larger exposure time. In this case, the cataloging process is unaffected by the different exposure time (see Section 2.2.2). The limiting fluxes (5σ threshold) for the SPIRE bands are 13, 18 and 18 mJy at 250, 350, and 500 μm, respectively. In Figure 3.11, we show these 5σ threshold fluxes (solid lines), and we also indicate the third quartile of the flux distribution (dashed lines) of each channel. Such third quartile corresponds roughly to confusion limit estimated for the UDS field (~ 5 mJy; Oliver et al. 2012).

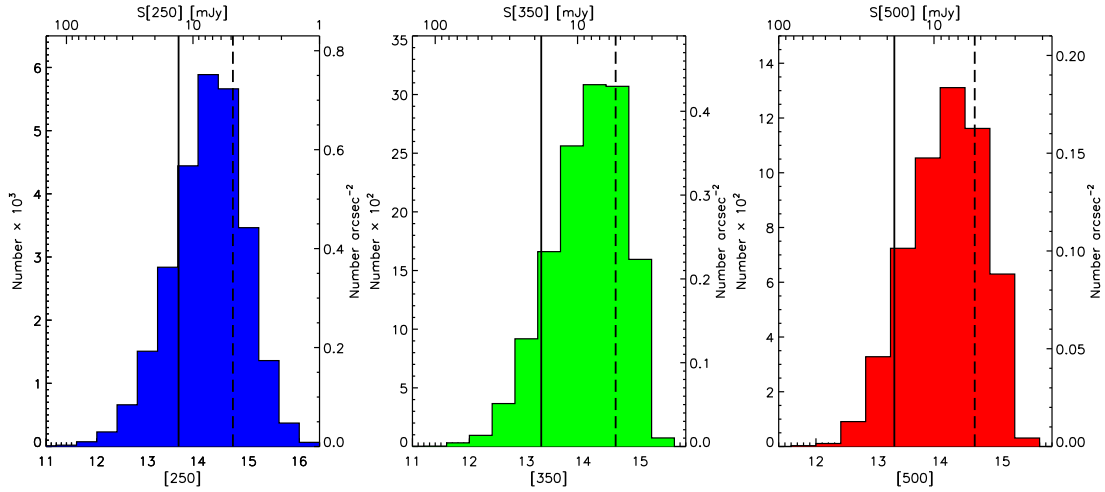

Figure 3.11 : Distribution of source magnitudes in SPIRE filters. The *dashed line* in each panel depicts the third quartile of the magnitude of each filter. The *solid line* indicates the magnitude corresponding to the 5σ threshold for each channel.

3.2.7 Redshift ancillary data

Various observational surveys have done a spectroscopic follow-up in the SXDS/UDS field. Frequently, the primary targets were X-ray emitters and radio sources observed exhaustively by several campaigns. Multi-object spectra were taken by Geach et al. (2007) using the Low Dispersion Survey Spectrograph (LDSS2) on the Magellan telescope. They were studying galaxies belonging to groups and clusters at $z \sim 0.5$, and harboring low-power radio sources. Spectra of galaxies of a cluster candidate at $z \sim 1.4$ were obtained by van Breukelen et al. (2007) using the DEep Imaging Multi-Object Spectrograph (DEIMOS) on the Keck 2 telescope. Faint Quasi-Stellar Objects at $1.57 < z < 3.29$ were followed by Smail et al. (2008) using the AAOmega spectrograph on the Anglo-Australian telescope. X-ray sources were also followed using the Faint Object CAmera and Spectrograph (FOCAS) on the SUBARU telescope by Akiyama et al. (in preparation), who also observed all the bright optical sources in the SXDS field with the 2-degree Field (2dF) spectrograph. An European Southern Observatory program (the UDSz, PI O. Almaini; see also, McLure et al. 2013, Bradshaw et al. 2013) has targeted ~ 3500 NIR-selected galaxies in the UDS field obtaining 1512 secure redshifts in the redshift range $0 < z < 4.8$. These spectra were acquired with the FOcal Reducer and low dispersion Spectograph 2 (FORS2) or VIsible Multi-Object Spectrograph (VIMOS), taking into account the magnitudes and colors of the sources.

3.3 Spectro-photometric Merged Catalogs

As we have mentioned in Section 3.1, a selection of galaxies in the MIPS-70 band requires 24 μm matches in order to locate relaible optical counterparts. Therefore, we have cut the *Spitzer* and *Herschel* catalogs for sky regions which include available Subaru data. The common sky region surveyed by *Spitzer*, *Herschel* and Subaru has an area of 0.88 deg^2. Having these cut catalogs, the first step to measure merged photometry was to match the coordinates of the MIPS 70 μm sources to the MIPS 24 μm filter and to R_c band. A $4''$ (the pixel size in the MIPS 70 μm mosaic), and a $6''$ search radii were used for the 24 μm and the R_c bands, respectively. The $4''$ radius establish that the possible MIPS-24 association will be located in the region covered by the central pixel of the MIPS-70 detection. The $6''$ radius, besides considering such central 70 μm source pixel, takes into account inherent differences in the astrometry between the Subaru R_c and the MIPS-70 images. Once with this purged list of 70 μm sources with 24 μm counterpart and an optical source in the proximity, we proceeded to generate a multi-wavelength catalog for our 70 μm selection using the Rainbow software package (see, Pérez-González et al. 2008, Barro et al. 2011a and references there in).

The Rainbow code commences by matching the coordinates of the sources from a master selection catalog (the 70 μm one in our case) to a referential optical band (R_c in our study). This reference helps to diminish the radius of the subsequent cross-correlations with the other photometric bands and the spectroscopic catalog. A $4''$ search radius was also used for the matching between the positions of the 70 μm-purged source list and the R_c band. Within this search radius, multiple identifications (i.e., multiple sources in the optical/NIR corresponding to the same 70 μm detection) were found for several sources. In such case, all optical sources within the search radius were kept as a possible counterpart for the 70 μm source.

Aperture-matched photometry was carried out cross-correlating the coordinates of the R_c identifications with each of the UV, optical, NIR, and IRAC catalogs using a search radius of $1.5''$. Employing the positions of such R_c identifications, it is possible to diminish the search radius to $0.8''$ in order to look for a secure match in the catalog of spectroscopic redshifts. The Rainbow code takes the Kron (1980) elliptical aperture best enclosing each one of these identifications, and translates it to the other optical/NIR bands. Before doing this translation, each image is re-aligned locally within a $4' \times 4'$ square to the reference one. This procedure allows an accurate positioning of the Kron aperture in all the bands. Such aperture should be large enough to enclose the PSF (two times the FWHM of the PSF or more) in all optical/NIR images.

In the case of IRAC bands, where the PSF is larger (FWHM $\sim$ $2''$), we adopted

the integrated magnitude measured in small apertures (applying aperture corrections) as explained in Section 3.2.4. When multiple identifications are found in the reference image, the IRAC photometry is remeasured following a deconvolution method similar to that used in Grazian et al. (2006) (see, Pérez-González et al. 2008, Barro et al. 2011a for a full description of this technique).

For the GALEX data, given that the PSF size is $6''-7''$ we have used the `mag_best` magnitude obtained with SExtractor.

Considering the comparatively large and different PSF sizes for the MIPS and *Herschel* bands, distinct search radius were used to cross-match the referential identifications with the MIR/FIR channels (see Table 3.2). For these bands, the integrated flux was assumed to be that determined from PSF fitting and aperture correction (using IRAF-DAOPHOT, see Sections 2.1 and 2.2 for a full description of the MIPS and *Herschel* cataloging methods). In the case of multiple identifications in the image used as reference, we have assigned to these referential sources only one counterpart in correspondence with each one of the MIPS and *Herschel* bands. Taking into account the different PSF sizes between the reference image and the FIR ones, an attempt of deconvolving a FIR detection based on the referential image would compel such FIR source to be deblended in various artificial counterparts.

Table 3.2 : Search radius for the MIR/FIR bands

Band	Search Radius [arcsec]
(1)	(2)
MIPS-24	2.5
MIPS-70	4.0
PACS-100	2.5
PACS-160	3.5
SPIRE-250	6.0
SPIRE-350	9.0
SPIRE-500	12.0

Notes.— (1) Name of the MIR/FIR band. (2) Search radius used from the referential sources to each MIR/FIR band.

The photometric uncertainties from the optical to IRAC images are estimated concurrently to the measurement of flux density in each of these bands. The Rainbow code uses 3 different methods for determining the photometric errors (see, Appendix A3 of Pérez-González et al. 2008). First, the average signal and background noise is measured in a circular ring of $5''$ width around each source. This noise is scaled with a

$N^{1/2}$ factor where N is the number of pixels in the Kron aperture. Second, the average sky signal is estimated on disconnected artificial apertures (of the same size of the Kron aperture) generated with random pure sky pixels around each source. Ultimately, the background noise is derived with the technique of Labbé et al. (2003). The flux measurements on various apertures (identical to the Kron one) are fitted to a Gaussian function producing an rms background fluctuation. The sky background value is settled as the resulting average of the 3 estimations, and the final photometric error is settled to the largest determination.

Thus, the Rainbow code obtains merged photometry from the UV to the FIR bands. Our initial MIPS-70 sample consists of 456 sources above the 5σ threshold (678 above the 4σ limit, hereafter the numbers in parentheses refer to 4σ 70 μm detections) located in the common area with the MIPS-24 image. From these 456 (678) objects only 349 (520) have a MIPS-24 counterpart in a search radius of $4''$. From the 349 5σ MIPS-70 sources a fraction of 7% —23 objects— have 2 MIPS-24 associations in the search radius, and a fraction of 1% —2 sources— have 3 24 μm counterparts in such radius. For the 520 4σ MIPS-70 detections the fractions are 8% (43 sources) and 1% (3 objects) with 2 and 3 24 μm matches, respectively. From these 349 (520) 70 μm sources with MIPS-24 associations, solely 298 (442) objects have also a Subaru R_c counterpart in a radius of $6''$. For such 298 (442) MIPS-70 sources the fractions of multiple 2 and 3 MIPS-24 matches are 7% —22 objects— (8% —34 objects—), and 1% —2 galaxies— ($< 1\%$ —2 galaxies—), correspondingly.

It is important to consider how many optical counterparts are associated to these 298 (442) reliable 70 μm sources for the multi-wavelength catalog. As we mentioned above, such master list including 298 (442) MIPS-70 objects was matched to the Subaru R_c reference band using a search radius of $4''$. This information is summarized in Tables 3.3 and 3.4 for the 5σ and 4σ flux density threshold case of the MIPS-70 sources, respectively. The fractions for both cases are similar. The fraction of 70 μm objects with 1–3 optical counterparts is $\sim 80\%$, and the fraction of sources with 5–9 optical associations is $\sim 10\%$. Hence, these 298 (442) MIPS-70 sources are associated to 703 (1077) optical objects, and the average number of optical counterparts for 70 μm detection is ~ 2.4.

In order to figure out which of these 703 (1077) optical sources are reliable counterparts of our MIPS-70 sources, we checked how many of such 703 (1077) optical objects has an associated 24 μm source in a search radius of $2.5''$. From these 703 (1077) optical galaxies only 400 (588) have a MIPS-24 counterpart in $2.5''$. The next check was to look for detections in the four IRAC bands of these 400 (588) optical sources with MIPS associations using a search radius of $1.5''$. For the 400 (588) optical

298 MIPS-70 sources (above 5σ threshold)		
No. R_c Assoc.	Frac. 70 μm obj.	No. 70 μm obj.
(1)	(2)	(3)
1	32%	95
2	31%	94
3	19%	58
4	9%	27
5	5%	15
6	1%	3
7	1%	4
8	$< 1\%$	1
9	$< 1\%$	1

Table 3.3 : Number of optical counterparts associated to the 5σ 70 μm sources

442 MIPS-70 sources (above 4σ threshold)		
No. R_c Assoc.	Frac. 70 μm obj.	No. 70 μm obj.
(1)	(2)	(3)
1	29%	127
2	31%	140
3	21%	92
4	10%	44
5	6%	26
6	1%	6
7	1%	5
8	$< 1\%$	1
9	$< 1\%$	1

Table 3.4 : Number of optical counterparts associated to the 4σ 70 μm sources

Notes.— (1) Number of Subaru R_c counterparts for a 70 μm source in a search radius of $4''$. (2) Fraction of 70 μm sources having the number of R_c counterparts of column (1). (3) Number of 70 μm objects having the number of R_c associations of column (1).

objects solely 397 (580) have flux measurements in the four IRAC channels. Hence, our optical reference galaxy sample is composed of 397 (580) with detections in the 5 SuprimeCam, 4 IRAC and 2 MIPS bands. These 397 (580) optical references are associated to 291 (426) MIPS-70 sources. Considering these 9-band identifications at wavelengths shorter than 24 μm the probability of a spurious association is low (less than 3%; see Pérez-González et al. 2005). We should notice also that using the optical-to-MIR associations, the average number of optical counterpart per 70 μm object has been diminished to ~ 1.4.

The following sample cut was related directly with the FIR detections, we seeked for the SuprimeCam-IRAC-MIPS sources having also at least one PACS and a 3σ SPIRE-250 detections in order to have at least 3 FIR measurements to determine the $L_{\rm TIR}$. From the 397 (580) SuprimeCam-IRAC-MIPS objects only 331 (453) sources have one PACS an a 3σ SPIRE-250 detection ($\sim 80\%$ of the SuprimeCam-IRAC-MIPS sample). We checked visually the SED of these 331 (453) objects to verify if the FIR detections (i.e., MIPS-70 and Herschel bands) present the characteristic modified blackbody shape of the FIR SED due to dust emission. Considering the different PSF sizes of the FIR bands, a non-physical jump in the FIR SED can appear if the MIPS-24 detection associated to the SuprimeCam-IRAC-MIPS source has a near 24 μm companion affecting the FIR counterparts. The effect of such companion can produce a deblending in one FIR band, but not in the others, due to a our prior-position based cataloging

method (see Chapter 2), or a flux boosting in one or more FIR bands. From the 331 (453) SuprimeCam-IRAC-MIPS objects with one PACS an a SPIRE-250 detections, 150 —$\sim$ 45%— (222 —$\sim$ 49%—) presented non-physical jumps in the FIR SED. Hence, we kept these 181 (231) robust optical sources with detections in 13 bands as possible counterparts for our MIPS-70 selected galaxies. Such 181 (231) optical references are associated to 153 (194) MIPS-70 objects (average number of optical counterparts ~ 1.2). From these 181 (231) only 147 (191) —a fraction of $\sim 80\%$— have been detected in the 3 WFCAM bands (J, H and K).

In order to assign secure optical associations to our MIPS-70 emitters, we need to estimate the photometric redshifts of these optical sources, this topic is addressed in Section 3.5. From these 181 (231) optical objects, reliable spectroscopic have been assigned to 81 (90) identifications ($\sim 40\%$ of our referential optical sample). However, before the determination of the photometric redshifts, we proceeded to identify how many objects from the 181 (231) are possibly hosting an AGN.

3.4 AGN identification

Given that the goal of this work is to study the properties of the stellar populations of dusty star-forming galaxies, we need to remove sources which can host an AGN from our referential optical sample. An AGN emits UV and X-ray photons which heat the dust that surrounds them. This hot dust is bright in MIR-FIR spectral range. Therefore, our MIPS-70 selected sample is prone to include AGN hosts. In order to remove these AGN candidates, we have applied the selection criteria of Donley et al. (2012) which is based in IRAC color-color diagrams. These criteria have been designed to avoid low- and high-redshift star-forming galaxies. They state that an AGN is selected when the following IRAC color-color cuts are satisfied (an example SED with several fractions on AGN contribution is shown in Fig. 3.12). Then, considering $\wedge$ as the logical "AND" operator, we have:

$$x = \log\left(\frac{f_{5.8\ \mu\mathrm{m}}}{f_{3.6\ \mu\mathrm{m}}}\right), \quad y = \log\left(\frac{f_{8.0\ \mu\mathrm{m}}}{f_{4.5\ \mu\mathrm{m}}}\right) \tag{3.1}$$

$$x \geq 0.08 \ \wedge \ y \geq 0.15$$

$$\wedge\, y \geq (1.21 \times x) - 0.27 \wedge y \leq (1.21 \times x) + 0.27 \tag{3.2}$$

$$\wedge f_{4.5\ \mu\mathrm{m}} > f_{3.6\ \mu\mathrm{m}} \wedge f_{5.8\ \mu\mathrm{m}} > f_{4.5\ \mu\mathrm{m}} \wedge f_{8.0\ \mu\mathrm{m}} > f_{5.8\ \mu\mathrm{m}}$$

We show in Figure 3.13, the IRAC colors of our initial sample that satisfy these criteria. Of the 181 (231) referential optical sources, $\sim 11\%$ —21 (26)— are selected

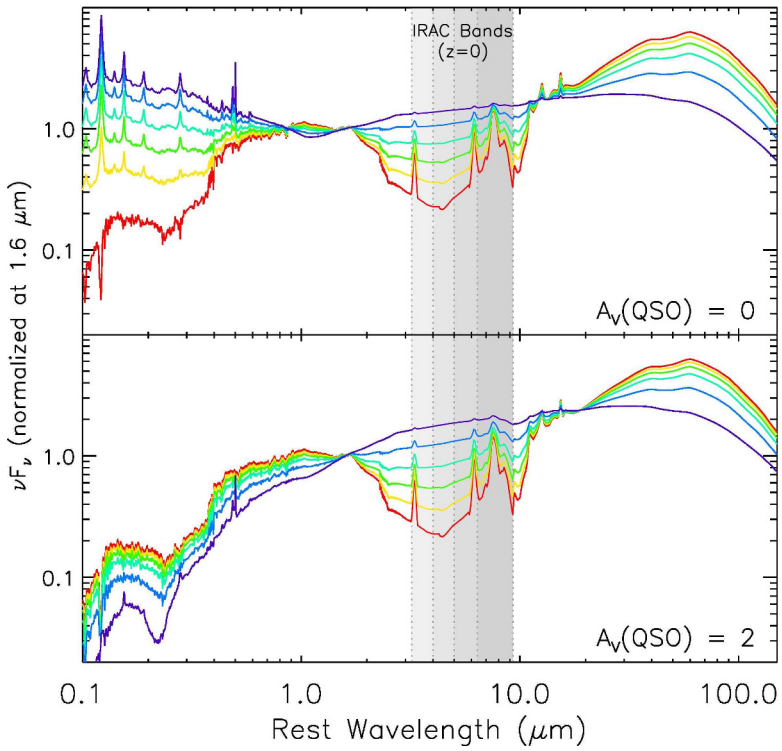

Figure 3.12 : Example SED scaled to present 1–10 μm AGN contributions of 0% (red solid line) to 95% (purple solid line). The SED is unattenuated in the upper panel, and it presents an attenuation of 2 mag in the V band in the lower panel. The bandwidths of the IRAC channels are indicated with grayscale strips.
Credits: Donley et al. (2012)

as AGN candidates. This fraction is slightly larger than the obtained from surveys including PACS 70 μm observations (a 7% is found in Gruppioni et al. 2013). Of these 21 (26) possible AGN hosts, 10 (11) have assigned a reliable spectroscopic redshift ($z_{\rm spec}$), an 8 of these 10 (11) objects have been classified as AGN spectroscopically.

3.5 Photometric Redshifts

We have computed photometric redshifts ($z_{\rm phot}$) using the code $EAZY$, which has been developed by Brammer et al. (2008), and Rainbow based wrappers. We have chosen this code because it is optimized for NIR-selected samples where many objects can be very faint in the observed optical bands. Given that our selection is based on MIPS 70 μm, our galaxies are dusty by nature which implies that their SEDs present high levels of attenuation in the optical spectral range. EAZY is also optimized for samples which present a biased subset of $z_{\rm spec}$ which may not represent the redshitfs of the general population. The code employs a set of templates fitted to synthetic photometry

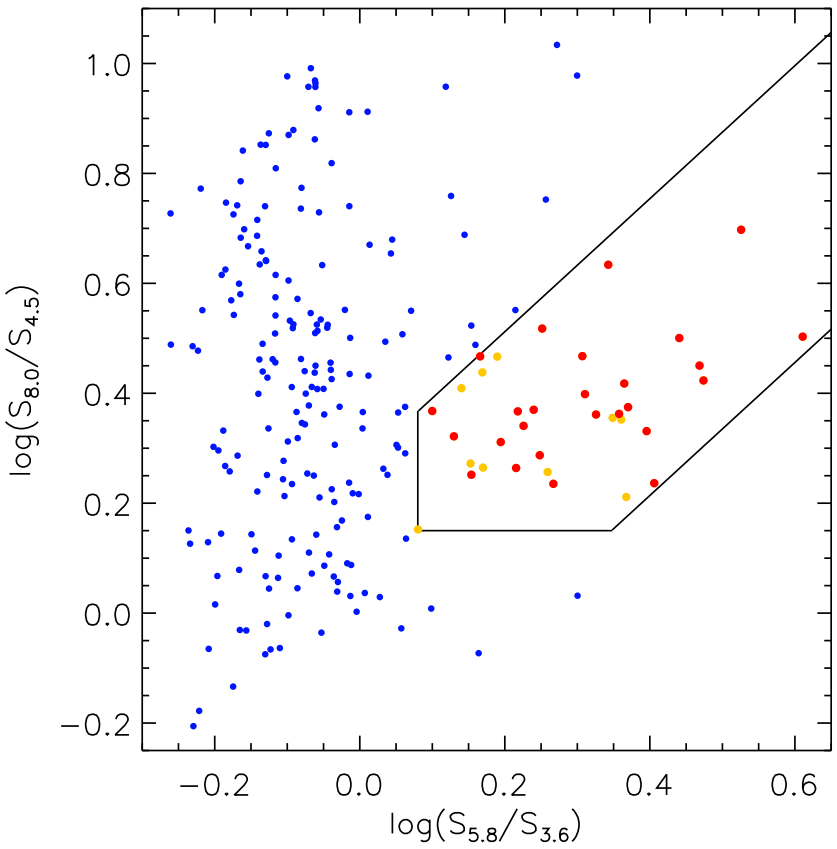

Figure 3.13 : AGN selection criteria of Donley et al. (2012) (*thick solid lines*). Our optical referential sample is plotted as *blue circles*. The objects that satisfy the AGN criteria are shown as *red circles*. Sources inside the area delimited by the thick solid lines but without a rising SED in the IRAC bands are excluded from the AGN selection (*orange circles*)

of mock galaxies derived from a semi-analitycal model implemented in the Millenium simulation (Springel et al. 2005, De Lucia and Blaizot 2007). The advantage of using this mock-galaxy sample is that it is complete at redshifts beyond the limits of the currently available spectroscopic surveys.

The $EAZY$ algorithm traverses through a grid of redshifts defined by the user, and at each redshift it estimates the best-fitting template spectrum using an akin χ^2 minimization method

$$\chi^2_{z,i} = \sum_{j=1}^{N_{\rm filt}} \frac{(T_{z,i,j} - F_j)^2}{(\delta F_j)^2}, \tag{3.3}$$

where $N_{\rm filt}$ is the number of filters, $T_{z,i,j}$ is the synthetic flux of the template i in the filter j for redshift z, and F_j is the observed flux in the filter j with an associated uncertainty δF_j. The code allows a linear combination of such synthetic templates, $T_z = \sum_{i=1}^{N_{\rm temp}} \alpha_i T_{z,i}$, which are taken from a user defined-list. $EAZY$ employs as default

option, an optimized set of 6 templates fitted to the photometry with PEGASE models (Fioc and Rocca-Volmerange 1997).

The code also makes use of a template error function that takes into account random and systematic differences between the observed photometry and the synthetic photometry at different wavelengths. Other characteristic of $EAZY$ is the use of a Bayesian prior on the redshift distribution (see, e.g., Benítez 2000). This prior helps to break possible degeneracies between multi-band colors and redshift.

We have kept all the sources with flux measurements in the the SuprimeCam, the WFCAM (if available), and the IRAC bands having counterparts in both MIPS channels and $z_{\rm spec}$ association as a training set for the the $z_{\rm phot}$ estimation. This is done considering that the photometry used in the $z_{\rm phot}$ fits come from optical to 4.5 μm wavelenghts. In other words, we use all the SuprimeCam-to-MIPS sources with counterpart in the spectroscopic catalog without effectuating a flux density cut in the 70 μm channel in such training set. The number of sources with associations in the above mentioned bands is 234.

In our $z_{\rm phot}$ estimation, we have used $EAZY$ with the default set of synthetic templates, the template error function, and the Bayesian prior. Several iterations were performed until obtaining the template error function that produces less scatter in the $z_{\rm spec} - z_{\rm phot}$ comparison.

In Figure 3.14, we present the comparison between $z_{\rm phot}$ and $z_{\rm spec}$ for the 234 optical sources with reliable spectroscopic redshift. We have adopted the normalized median absolute deviation ($\sigma_{\rm NMAD}$) of $\Delta z = z_{\rm phot} - z_{\rm spec}$ to quantify the photometric redshift accuracy:

$$\sigma_{\rm NMAD} = 1.48 \times {\rm median}\left(\left|\frac{\Delta z - {\rm median}(\Delta z)}{1 + z_{\rm spec}}\right|\right). \quad (3.4)$$

This quantity is equal to the standard deviation for a Gaussian distribution and it is less affected by the presence of outliers than the common accuracy estimator, the standard deviation divided by $(1 + z)$ (Ilbert et al. 2006).

The scatter of the whole spectroscopic sample is $\sigma_{\rm NMAD} = 0.026$, and the median of the common estimator results $|\Delta z|/(1 + z) = 0.018$. If we define η as the fraction of catastrophic outliers having $|\Delta z|/(1 + z) > 0.2$, expressing it as percentage, we get $\eta = 6\%$. Our $\sigma_{\rm NMAD}$ value is similar to that ($\sigma_{\rm NMAD} = 0.028$) estimated by Barro et al. (2011b) for a subsample of IRAC-selected objects which are detected in MIPS 70 μm. We have obtained a slightly higher η value (6% compared with 2%), but our catastrophic outliers with the largest dispersion are AGN candidates (their PLGs). These AGN hosts are 23 in our spectroscopic sample compared with 8 in theirs.

It is important to note that the majority of sources in our spectroscopic data are at

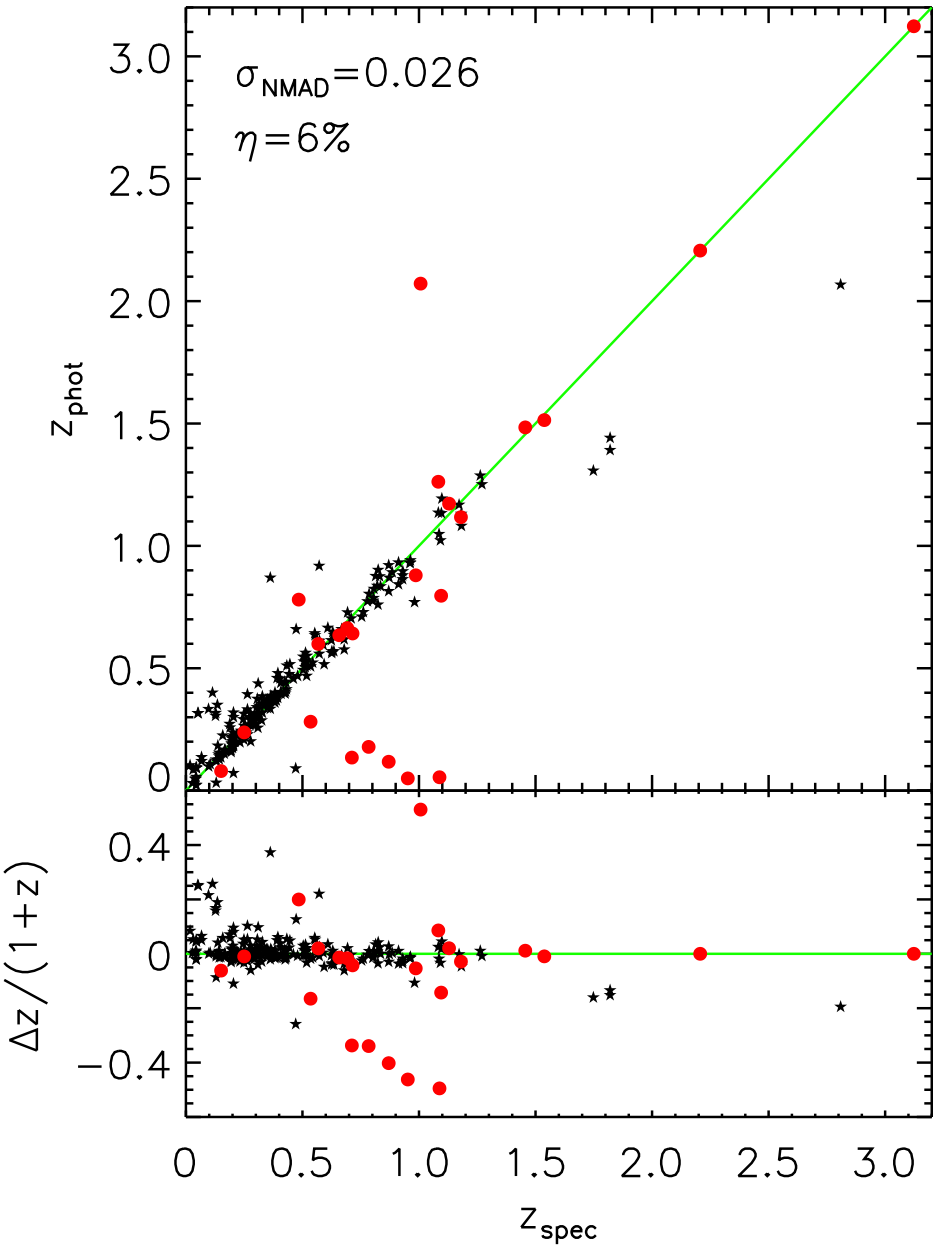

Figure 3.14 : *Upper panel:* Spectroscopic vs. photometric redshifts comparison. The filled black stars show the results for star-forming galaxies. The large filled red circles present the sources that satisfy the AGN criteria of Donley et al. (2012). *Lower panel:* scatter in $\Delta z/(1+z)$ as a function of redshift. The symbols have the same meaning as in the upper panel. It is notorious that the sources with larger scatter are objects selected as AGN.

$z < 1.3$ (223 objects, a fraction of $\sim 97\%$, see Fig. 3.15), this is expected considering the detection limits of MIPS-70 as a function of redshift, and that our sample is selected in this band. In Table 3.5, we present the quality of $z_{\rm phot}$ for spectroscopic redshift

interval. This quality is slightly worse for the last redshift interval ($z > 1.0$) than the median of the sample, which can be anticipated taking into account the few objects in the interval, and that these sources should be fainter in the optical-to-IRAC bands.

Table 3.5 : Photometric redshift accuracy for z-interval

Redshift	No.	$\sigma_{\rm NMAD}$	$\lvert\Delta z\rvert/(1+z)$	η
(1)	(2)	(3)	(4)	(5)
$0 < z < 0.5$	142	0.026	0.016	4%
$0.5 < z < 1.0$	68	0.033	0.020	7%
$z > 1.0$	24	0.043	0.027	8%

Notes.— (1) Spectroscopic redshift range. (2) Number of sources in redshift bin. (3) Median value of $|\Delta z|/(1+z)$. Percentage of catastrophic outliers ($|\Delta z|/(1+z) > 0.2$).

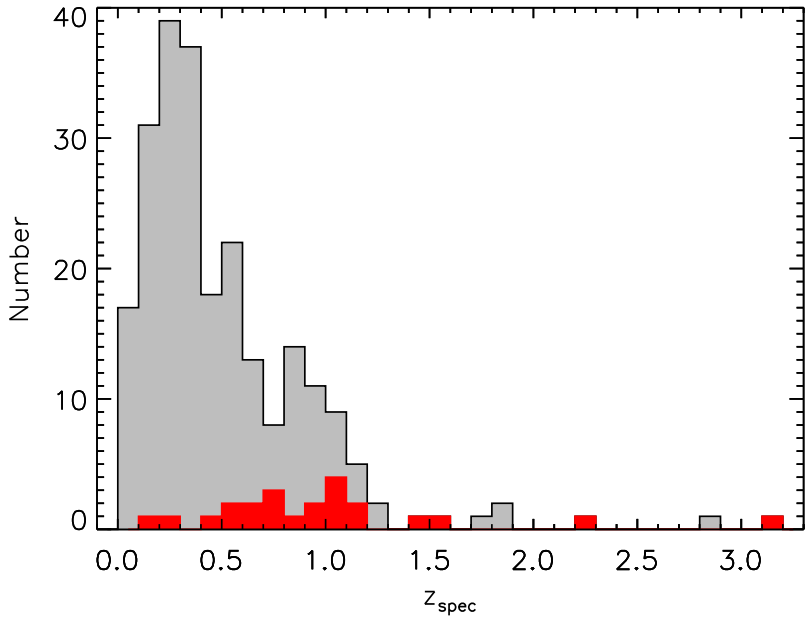

Figure 3.15 : Distributions of spectroscopic redshifts of the 234 galaxies (*gray filled histogram*), and of the $z_{\rm spec}$ of the sources that satisfy the AGN criteria of Donley et al. (2012) (*red filled histogram*).

In view of the fact that the results of above accuracy estimators ($\sigma_{\rm NMAD}$, η) are in good agreement with values found in the literature (see, e.g., Brammer et al. 2008, Barro et al. 2011b), we conclude that the SEDs derived from our multi-wavelength catalog are reliable to derive photometric redshifts. Using these $z_{\rm phot}$'s, we have estimated the $L_{\rm TIR}$ of our IR-bright galaxies.

3.6 Redshift Selection and Secure Counterpart Recognition

This study is based on a MIPS-70 selected sample, which should be proximate to a sample of dusty galaxies with high SFRs. We have already discussed that the beam sizes of the FIR bands make difficult to select a correct optical counterpart. To tackle this, we have selected high confidence 70 μm sources above the 5σ (4σ) flux threshold with 24 μm counterpart and a near source in the R_c band. Then, we have conducted multi-band identification and photometry gathering an initial sample of 397 (580) referential optical sources associated to 291 (426) MIPS-70 emmiters in an area of 0.88 deg^2. These optical objects are detected at least in the 5 SuprimeCam bands, the 4 IRAC channels, and the MIPS 24 and 70 μm filters. Then, we look for associations in the FIR, in particular, detections in at least one PACS band and above the 3σ threshold in SPIRE-250 channel. Only 331 (453) SuprimeCam-IRAC-MIPS objects have counterparts in the above mentioned Herschel bands. We have checked visually the SEDs of these 331 (453) in order to discard the objects with a non-physical jump in the FIR part of the SED. From such 331 (453) sources solely 181 (231) SuprimeCam-IRAC-MIPS sources present an acceptable FIR SED.

Considering our aim of studying star-forming galaxies, we proceeded to identify AGN candidates. Of the 181 (231) referential sources, 21 (26) were identified as AGN hosts and they were excluded from the sample. Then, we have centered on the redshift range where IR-bright galaxies become important in the SFR density of the Universe ($z \gtrsim 0.6$; see, e.g., Le Floc'h et al. 2005, Casey et al. 2012). Nevertheless, we should also consider the flux detection limits of MIPS-70 to impose an upper limit to the redshift range. Hence, we have selected sources with $z_{\rm spec}$ or $z_{\rm phot}$ in $0.6 \leq z \leq 1.5$. From the 160 (205) SuprimeCam-IRAC-MIPS sources (excluding obscured AGN) with at least one PACS and a SPIRE 250 detection only 27 (38) have redshift in $0.6 \leq z \leq 1.5$. This 27 (38) referential objects are associated to 25 (35) MIPS-70 emitters. Considering the moderate number of objects in our studied redshift range, hereafter, we have decided to work with the 38 referential sources associated to the 35 MIPS-70 objects above 4σ flux threshold.

We have checked visually the MIPS, IRAC, SuprimeCam, WFCAM, PACS and SPIRE images of these 38 sources. In order to assume an optical counterpart as secure, we have examined if the position of this optical source is centered in the location of its 24 μm counterpart, and if there is not a close optical neighbor (at different $z_{\rm spec}$ or $z_{\rm phot}$) possibly emitting at 24 μm. From such 38 reference sources, 19 optical detec-

tions presented positions displaced from the 24 μm counterpart locations (11 having a near companion at different $z_{\rm spec}$ or $z_{\rm phot}$, see Fig. 3.16; 4 presenting several optical neighbors impeding the identification of the correct counterpart; and 4 being spurious identifications noticed by their deficient UV-to-MIR SED).

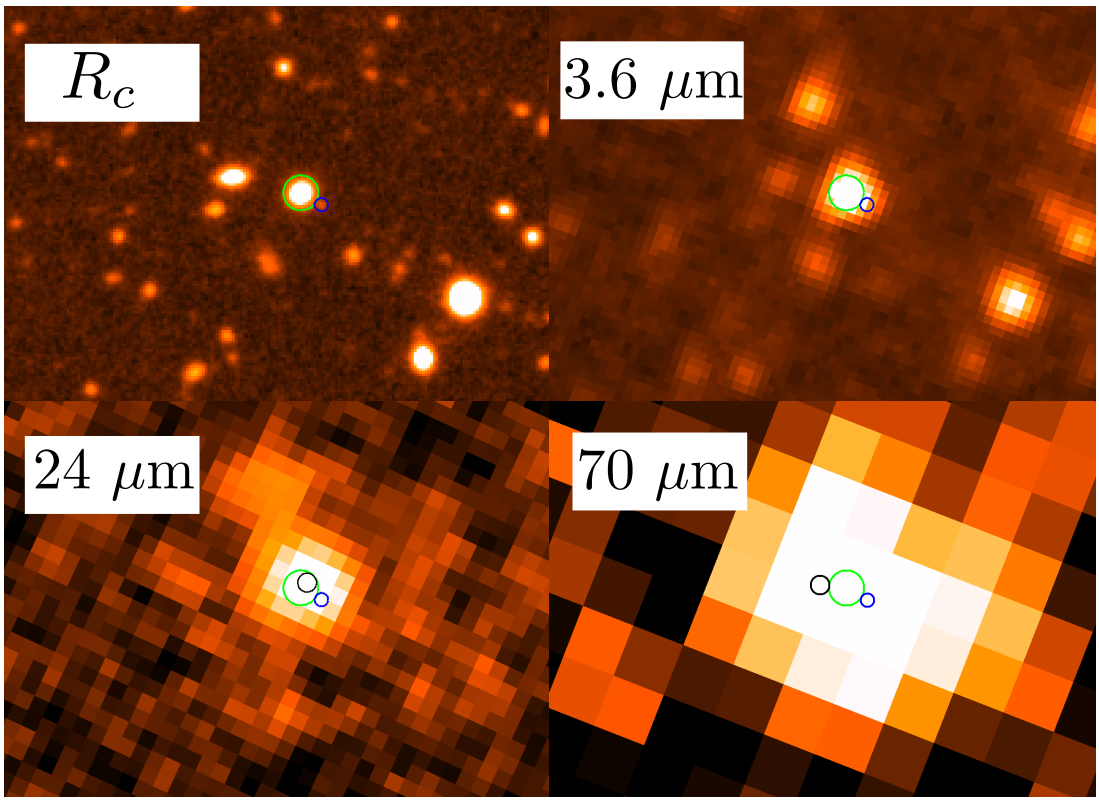

Figure 3.16 : Example of a source (small blue circle) with $z_{\rm phot} = 1.15$, rejected by having position displaced from the MIPS-24 counterpart position and a near R_c companion (large green circle) with $z_{\rm phot} = 0.46$. From left to right, from top to bottom, we show post-stamps for the R_c, 3.6, 24 and 70 μm bands showing that the most probable counterpart is indicated by the large green circle, which position matches better with the MIPS detections indicated with medium black circles.

We have arrived to a final sample composed by 19 galaxies with secure counterparts from optical to FIR wavelengths (see Fig. 3.17 for an example). The SED for these 19 sources is robust, with no contamination from nearby sources.

Of the 19 galaxies in the final sample; 95% are detected in the J, H and K filters; 5% and 10% in FUV and NUV bands; 95% and 89% in PACS 100 and 160 μm channels; and 100%, 74% and 37% in SPIRE 250, 350 and 500 μm filters, respectively (always satisfying the limiting magnitudes of Table 3.1).

The catalog with multi-band photometry for our final sample of MIPS-70 selected galaxies at $0.6 < z < 1.5$ in SXDS/UDS is presented in Table 3.6. The properties of the stellar populations of these 19 galaxies are studied detailedly in Chapters 5 and 6.

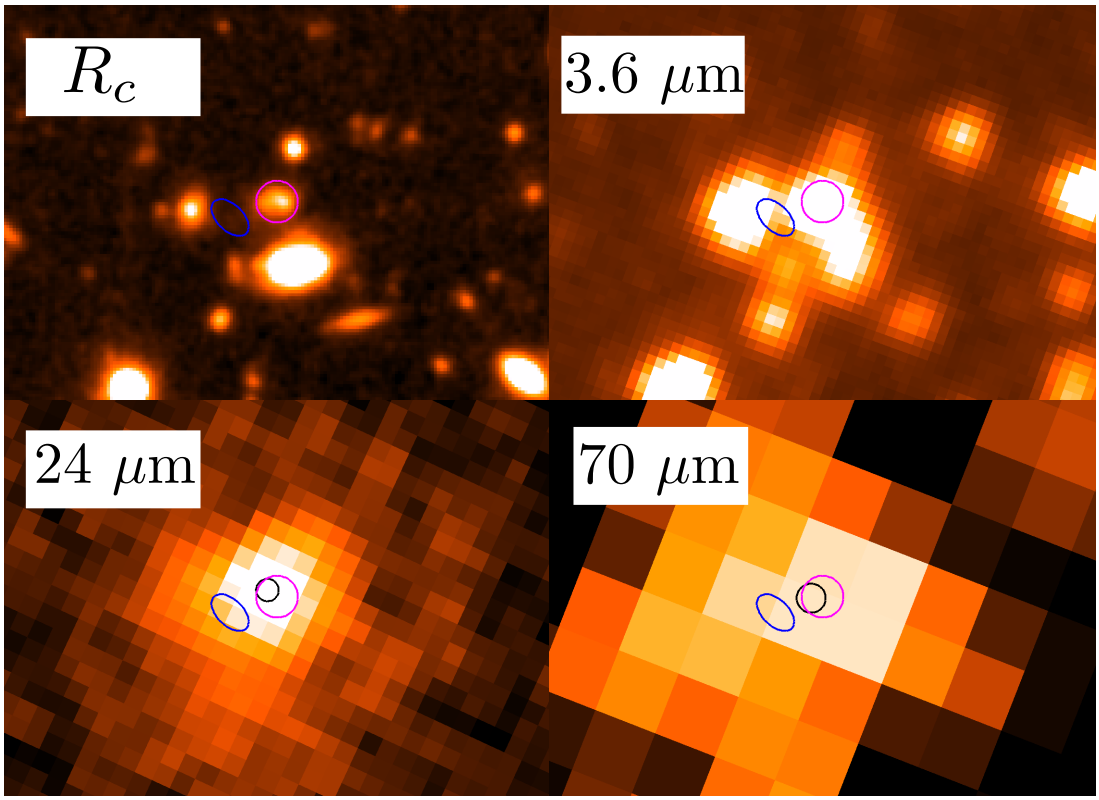

Figure 3.17 : Example of a source (large magenta circle) with $z_{\rm phot} = 1.14$, belonging to our final sample. The small blue circle represents a rejected spurious identification. From left to right, from top to bottom, we show post-stamps for the R_c, 3.6, 24 and 70 μm bands indicating that our selected galaxy has R_c position (large magenta circle) which center in agreement with the MIPS position centers indicated with medium black circles.

Table 3.6. MIPS 70 μm Sample (This Work). Multi-band Photometry

Galaxy	α	δ	z†	S_{70}	FUV	NUV	B	V	R_c	i'
				ΔS_{70}	ΔFUV	ΔNUV	ΔB	ΔV	ΔR_c	$\Delta i'$
				z'	J	H	K	[3.6]	[4.5]	[5.8]
				$\Delta z'$	ΔJ	ΔH	ΔK	Δ[3.6]	Δ[4.5]	Δ[5.8]
				[8.0]	S_{24}	S_{100}	S_{160}	S_{250}	S_{350}	S_{500}
				Δ[8.0]	ΔS_{24}	ΔS_{100}	ΔS_{160}	ΔS_{250}	ΔS_{350}	ΔS_{500}
(1)	(2)	(3)	(4)	(5)	(6)	(7)	(8)	(9)	(10)	(11)
				(12)	(13)	(14)	(15)	(16)	(17)	(18)
				(19)	(20)	(21)	(22)	(23)	(24)	(25)
				(26)	(27)	(28)	(29)	(30)	(31)	(32)
				(33)	(34)	(35)	(36)	(37)	(38)	(39)
				(40)	(41)	(42)	(43)	(44)	(45)	(46)
MIPS0000050_1	34.114364	−5.138740	0.97	10.76	···	···	25.01	24.22	23.68	22.68
				1.74	···	···	0.02	0.02	0.01	0.01
				22.13	21.29	20.93	20.30	19.87	19.98	20.16
				0.01	0.01	0.02	0.01	0.03	0.03	0.04
				19.82	0.56	27.77	30.58	30.99	13.67	···
				0.06	0.02	2.36	2.78	2.94	3.51	···
MIPS0000149_1	34.687484	−5.134991	0.67	22.21	···	···	24.57	23.30	22.12	21.39
				1.91	···	···	0.02	0.01	0.01	0.01
				20.92	20.13	19.48	18.94	18.77	19.07	18.86
				0.01	0.01	0.01	0.01	0.03	0.03	0.04
				18.90	0.92	29.98	78.81	82.11	47.00	15.04
				0.06	0.02	2.52	6.30	5.17	4.18	3.91
MIPS0000472_1	34.112593	−5.190671	1.03	7.74	···	···	24.73	24.33	23.90	23.17
				1.74	···	···	0.14	0.05	0.03	0.02
				22.57	21.51	20.99	20.36	19.76	19.97	20.01
				0.02	−0.02	−0.01	−0.01	0.03	0.03	0.04
				19.98	0.35	−···	19.03	19.54	13.54	···
				0.06	0.01	···	3.37	2.09	2.68	···
MIPS0000508_1	34.296925	−5.280626	0.72	8.15	···	···	26.16	25.25	24.12	23.38
				1.74	···	···	0.06	0.04	0.02	0.01
				23.00	22.19	21.61	20.93	20.48	20.70	20.56
				0.02	0.02	0.03	0.02	0.04	0.03	0.04
				20.56	0.32	16.91	25.81	16.04	···	···
				0.06	0.02	1.32	2.04	2.04	···	···
MIPS0000671_1	34.207175	−4.900883	0.67	7.48	22.88	21.32	20.85	20.58	20.16	19.99
				1.62	0.06	0.02	0.01	0.01	0.01	0.01
				20.01	19.79	19.56	19.48	19.70	19.94	19.73
				0.01	0.01	0.01	0.01	0.03	0.03	0.04
				19.72	0.54	9.20	···	13.11	···	···
				0.06	0.02	0.90	···	1.78	···	···

Table 3.6 (cont'd)

Galaxy	α	δ	z†	S_{70}	FUV	NUV	B	V	R_c	i'
				ΔS_{70}	ΔFUV	ΔNUV	ΔB	ΔV	ΔR_c	$\Delta i'$
				z'	J	H	K	[3.6]	[4.5]	[5.8]
				$\Delta z'$	ΔJ	ΔH	ΔK	Δ[3.6]	Δ[4.5]	Δ[5.8]
				[8.0]	S_{24}	S_{100}	S_{160}	S_{250}	S_{350}	S_{500}
				Δ[8.0]	ΔS_{24}	ΔS_{100}	ΔS_{160}	ΔS_{250}	ΔS_{350}	ΔS_{500}
(1)	(2)	(3)	(4)	(5)	(6)	(7)	(8)	(9)	(10)	(11)
				(12)	(13)	(14)	(15)	(16)	(17)	(18)
				(19)	(20)	(21)	(22)	(23)	(24)	(25)
				(26)	(27)	(28)	(29)	(30)	(31)	(32)
				(33)	(34)	(35)	(36)	(37)	(38)	(39)
				(40)	(41)	(42)	(43)	(44)	(45)	(46)
MIPS0000700_1	34.324584	−5.028091	0.8210†	10.69	···	···	23.69	22.86	22.19	21.27
				2.29	···	···	0.01	0.01	0.01	0.01
				20.78	20.10	19.75	19.28	19.16	19.45	19.33
				0.01	0.01	0.01	0.01	0.03	0.03	0.04
				19.17	1.00	15.78	24.50	21.09	11.96	···
				0.06	0.02	1.28	2.16	2.19	3.86	···
MIPS0000701_1	34.153409	−5.098265	0.8052†	19.15	···	···	22.17	21.71	21.28	20.72
				1.72	···	···	0.01	0.01	0.01	0.01
				20.51	19.98	19.76	19.39	19.17	19.48	19.29
				0.01	0.01	0.01	0.01	0.03	0.03	0.04
				19.27	1.05	39.83	56.86	50.49	29.30	···
				0.06	0.02	3.23	4.55	3.79	3.87	···
MIPS0000773	34.583684	−5.365429	0.80	21.05	···	···	24.96	23.77	22.87	21.83
				1.62	···	···	0.02	0.01	0.01	0.01
				21.34	20.48	19.92	19.33	18.82	19.15	19.13
				0.01	0.01	0.01	0.01	0.04	0.04	0.04
				19.31	0.92	51.03	92.98	79.66	45.14	15.74
				0.04	0.02	3.93	7.25	5.34	3.93	3.08
MIPS0000904_3	34.421511	−4.747594	1.16	12.26	···	···	25.98	25.15	24.51	23.45
				2.15	···	···	0.04	0.02	0.02	0.01
				22.73	21.90	21.33	20.56	19.47	19.21	19.09
				0.01	0.02	0.02	0.01	0.05	0.05	0.06
				18.53	0.50	28.55	51.40	62.23	45.55	19.90
				0.08	0.02	2.43	4.73	4.36	4.05	3.68
MIPS0000922_1	34.702728	−4.695410	0.8068†	7.96	···	···	24.13	23.30	22.66	21.94
				1.64	···	···	0.01	0.01	0.01	0.01
				21.50	20.54	20.13	19.54	19.14	19.45	19.27
				0.01	0.01	0.01	0.01	0.03	0.03	0.04
				19.54	0.87	14.15	26.05	27.90	14.47	···
				0.06	0.02	1.30	2.60	2.96	3.21	···

Table 3.6 (cont'd)

Galaxy	α	δ	z†	S_{70}	FUV	NUV	B	V	R_c	i'
				ΔS_{70}	ΔFUV	ΔNUV	ΔB	ΔV	ΔR_c	$\Delta i'$
				z'	J	H	K	[3.6]	[4.5]	[5.8]
				$\Delta z'$	ΔJ	ΔH	ΔK	Δ[3.6]	Δ[4.5]	Δ[5.8]
				[8.0]	S_{24}	S_{100}	S_{160}	S_{250}	S_{350}	S_{500}
				Δ[8.0]	ΔS_{24}	ΔS_{100}	ΔS_{160}	ΔS_{250}	ΔS_{350}	ΔS_{500}
(1)	(2)	(3)	(4)	(5)	(6)	(7)	(8)	(9)	(10)	(11)
				(12)	(13)	(14)	(15)	(16)	(17)	(18)
				(19)	(20)	(21)	(22)	(23)	(24)	(25)
				(26)	(27)	(28)	(29)	(30)	(31)	(32)
				(33)	(34)	(35)	(36)	(37)	(38)	(39)
				(40)	(41)	(42)	(43)	(44)	(45)	(46)
MIPS0001032_1	34.432285	−5.469208	1.14	9.34	···	···	24.69	24.05	23.66	22.89
				1.99	···	···	0.02	0.01	0.01	0.01
				22.39	21.75	21.38	20.67	19.79	19.83	20.20
				0.01	0.02	0.02	0.01	0.04	0.04	0.05
				19.91	0.59	13.28	···	47.21	33.09	···
				0.07	0.02	1.38	···	3.59	4.47	···
MIPS0001045_1	34.256062	−5.585097	0.80	9.15	···	···	24.16	23.10	22.37	21.39
				1.89	···	···	0.02	0.01	0.01	0.01
				20.85	···	···	···	18.68	19.11	19.12
				0.01	···	···	···	0.03	0.03	0.04
				19.44	0.83	18.59	44.07	53.56	38.70	18.02
				0.06	0.03	1.95	4.28	3.91	4.06	3.23
MIPS0001162_1	34.379796	−5.119139	1.2700†	18.15	···	···	23.26	22.86	22.49	22.02
				1.71	···	···	0.01	0.01	0.01	0.01
				21.30	20.60	20.07	19.59	19.06	18.90	19.09
				0.01	0.01	0.01	0.01	0.03	0.03	0.04
				18.83	0.64	48.06	84.76	71.85	45.14	11.74
				0.06	0.02	3.70	6.53	4.60	4.06	3.03
MIPS0001164_1	34.626990	−5.037358	1.12	12.58	···	···	25.17	24.53	24.19	23.56
				1.87	···	···	0.02	0.02	0.02	0.01
				23.03	22.43	22.03	21.39	20.63	20.81	21.15
				0.01	0.02	0.03	0.01	0.05	0.04	0.08
				20.97	0.22	19.37	17.77	9.27	···	···
				0.12	0.01	1.57	2.17	2.12	···	···
MIPS0001212	34.894621	−5.300254	0.71	66.27	···	···	24.30	23.35	22.37	21.66
				2.92	···	···	0.02	0.01	0.01	0.01
				21.31	20.73	20.25	19.71	19.30	19.62	19.39
				0.01	0.01	0.02	0.01	0.04	0.04	0.04
				18.86	2.09	90.70	105.05	65.59	34.56	12.86
				0.05	0.04	7.08	8.40	4.39	4.53	3.73

Table 3.6 (cont'd)

Galaxy	α	δ	z†	S_{70}	FUV	NUV	B	V	R_c	i'
				ΔS_{70}	ΔFUV	ΔNUV	ΔB	ΔV	ΔR_c	$\Delta i'$
				z'	J	H	K	[3.6]	[4.5]	[5.8]
				$\Delta z'$	ΔJ	ΔH	ΔK	Δ[3.6]	Δ[4.5]	Δ[5.8]
				[8.0]	S_{24}	S_{100}	S_{160}	S_{250}	S_{350}	S_{500}
				Δ[8.0]	ΔS_{24}	ΔS_{100}	ΔS_{160}	ΔS_{250}	ΔS_{350}	ΔS_{500}
(1)	(2)	(3)	(4)	(5)	(6)	(7)	(8)	(9)	(10)	(11)
				(12)	(13)	(14)	(15)	(16)	(17)	(18)
				(19)	(20)	(21)	(22)	(23)	(24)	(25)
				(26)	(27)	(28)	(29)	(30)	(31)	(32)
				(33)	(34)	(35)	(36)	(37)	(38)	(39)
				(40)	(41)	(42)	(43)	(44)	(45)	(46)
MIPS0001225	34.752794	−5.445827	0.8701†	25.22	···	···	23.68	23.09	22.62	21.74
				1.66	···	···	0.01	0.01	0.01	0.01
				21.36	20.83	20.49	20.07	19.51	19.69	19.84
				0.01	0.01	0.02	0.01	0.04	0.04	0.04
				19.52	0.52	43.85	73.21	59.16	36.25	···
				0.13	0.02	3.46	5.86	4.38	4.86	···
MIPS0001300_1	34.783759	−4.854334	0.95	7.44	···	···	25.85	25.08	24.31	23.28
				2.44	···	···	0.04	0.02	0.02	0.01
				22.71	21.80	21.27	20.73	20.08	20.23	20.36
				0.02	0.02	0.02	0.01	0.03	0.03	0.04
				20.39	0.19	13.09	22.48	17.59	···	···
				0.06	0.01	1.23	2.32	2.39	···	···
MIPS0001324_1	34.874495	−5.150121	0.72	16.34	···	24.10	23.24	22.53	21.84	21.27
				2.04	···	0.26	0.01	0.01	0.01	0.01
				20.96	20.24	19.63	18.95	18.50	18.78	18.58
				0.01	0.01	0.01	0.01	0.03	0.03	0.04
				18.68	1.44	32.63	59.45	51.86	37.47	28.01
				0.06	0.03	2.64	4.82	3.73	3.82	3.31
MIPS0001585_1	34.332061	−5.093650	0.92	12.15	···	···	24.69	23.83	23.26	22.38
				1.82	···	···	0.02	0.02	0.01	0.01
				21.88	20.83	20.60	20.04	19.61	19.81	19.72
				0.01	0.01	0.02	0.01	0.03	0.03	0.04
				19.55	0.94	22.11	29.31	20.16	···	···
				0.06	0.03	1.72	2.34	2.46	···	···

Note. — (1) Name of the galaxy. (2,3) Right ascension and declination (J2000) in degrees. (4) Photometric or spectroscopic redshift ($z_{\rm spec}$ indicated by a †). (5,27-32) flux densities in MIPS 70, 24; PACS 100, 160; SPIRE 250, 350, 500 in mJy. (6-11,19-25,33) Observed magnitude in FUV, NUV; B, V, R_c, i', z'; J, H, K; IRAC $3.6 - 8.0$ in the AB photometric system. (12,41-46) Associated uncertainties to MIPS 70, 24; PACS 100, 160; SPIRE 250, 350, 500 in mJy determined as described in Chapter 2. (13-18,26-32,40) Associated uncertainties to FUV, NUV; B, V, R_c, i', z'; J, H, K; IRAC $3.6 - 8.0$ as obtained from the aperture matched cataloging (see Section 3.3).
"···" indicate bands without detections or without reliable photometric measurements.

The redshift distribution of our final sample is shown in Fig. 3.18. There are 2 galaxies having $z_{\rm phot}$ in a different bin when compared with $z_{\rm spec}$. But the overall differences between both values are small, they are presented in Table 3.7. The normalized median absolute deviation calculated using only the galaxies which have $z_{\rm spec}$ of our final sample is $\sigma_{\rm NMAD} = 0.022$.

Therefore, our $z_{\rm phot}$ are accurate enough to be used for determining the $L_{\rm TIR}$ values, and to study the stellar population properties of the galaxies in our final sample.

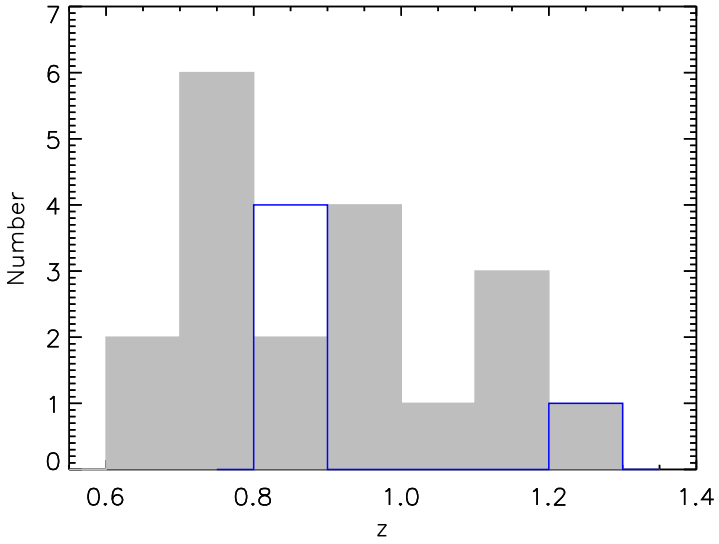

Figure 3.18 : Distributions of photometric redshifts of the final sample (*gray filled histogram*), and of the galaxies with spectroscopic redshift (*blue open histogram*).

Table 3.7 : Photometric redshift accuracy for the final sample.

Galaxy	$z_{\rm spec}$	$z_{\rm phot}$	$\lvert\Delta z\rvert/(1+z)$
(1)	(2)	(3)	(4)
MIPS0000700_1	0.8210	0.8400	0.010
MIPS0000701_1	0.8052	0.7900	0.008
MIPS0000922_1	0.8068	0.8200	0.007
MIPS0001162_1	1.2700	1.2500	0.009
MIPS0001225	0.8701	0.9200	0.027

Notes.— (1) Galaxy name. (2) Spectroscopic redshift. (3) Photometric redshift. (4) Scatter estimator ($|\Delta z|/(1+z)$) value.

At this point, it is important to notice that our multi-wavelength inventory has begun with the reduction and cataloging of raw FIR data derived from *Spitzer* and *Herschel*

observations of the SXDS field. Considering the depth of these FIR data, the condition of having detections in MIPS 24+70 and at least 2 *Herschel* bands, and also that we have centered our study in the redshift range $0.6 < z < 1.5$, we have finished with a reduced sample of objects. Nevertheless, a natural extension of this study is to enlarge the sample using public catalogs derived from several cosmological fields. Consequently, the representativeness of the galaxies that satisfy our selection process, and the significance of the stellar properties derived for these galaxies will be expanded.

3.7 Global Characteristics of Our Final Sample

In order to put in context our sample with a different sample presenting IR-bright galaxies, we have plotted in Fig. 3.19 the $L_{\rm TIR}$ of our objects compared with the $L_{\rm TIR}$ of galaxies having a $z_{\rm spec}$ located in the HDFN field. These HDFN sources have been queried from an IRAC-selected sample, we have used objects with counterparts in MIPS-24 band. The $L_{\rm TIR}$ value of each HDFN galaxy is the median value resulting from scaling its L_{24} luminosity using the templates of Chary and Elbaz (2001), Dale and Helou (2002), and Rieke et al. (2009) (hereafter, CE01, DH02, R+09, respectively). This query has been performed utilizing the public interface of Rainbow Cosmological Database (Pérez-González et al. 2008, Barro et al. 2011a).

Considering that the galaxies in our final sample present at least 3 detections at FIR wavelengths, our $L_{\rm TIR}$ values are obtained by fitting the observed flux densities at wavelengths larger equal 70 μm to the IR libraries of CE01, DH02, and R+09. This allows us to avoid the PAH absorptions and emissions reached by the 24 μm band in the redshift range that we are interested, $0.6 \leq z \leq 1.5$. We have selected as referential $L_{\rm TIR}$ (hereafter $L_{\rm TIR,ref}$), the value resulting from the best-fitting (that with the lowest χ^2) template from the aforementioned IR models.

Outwardly from Figure 3.19 our galaxies present large $L_{\rm TIR}$'s (SFRs), as it is expected due to their dusty nature and the selection that we have imposed. Our galaxies are 5 LIRGs and 14 ULIRGs (median $L_{\rm TIR} = 1.2{\times}10^{12}\ L_{\odot}$). Such intense IR luminosities will be used to constrain the dust attenuation suffered by their stellar populations as explained in the following Chapters.

We should also notice from the aforementioned figure, that our selection function is not recovering the whole (U)LIRG population at $0.6 < z < 1.5$. We are probably missing ULIRGs with a predominant cold dust component, and LIRGs with $\log L_{\rm TIR} \lesssim 11.5\ L_{\odot}$. These selection effects are mainly due to the detection limits of the MIPS-70 channel, but we should also take into account that we are excluding objects that present a non-physical jump in their FIR SED originated by the presence of a MIPS-24

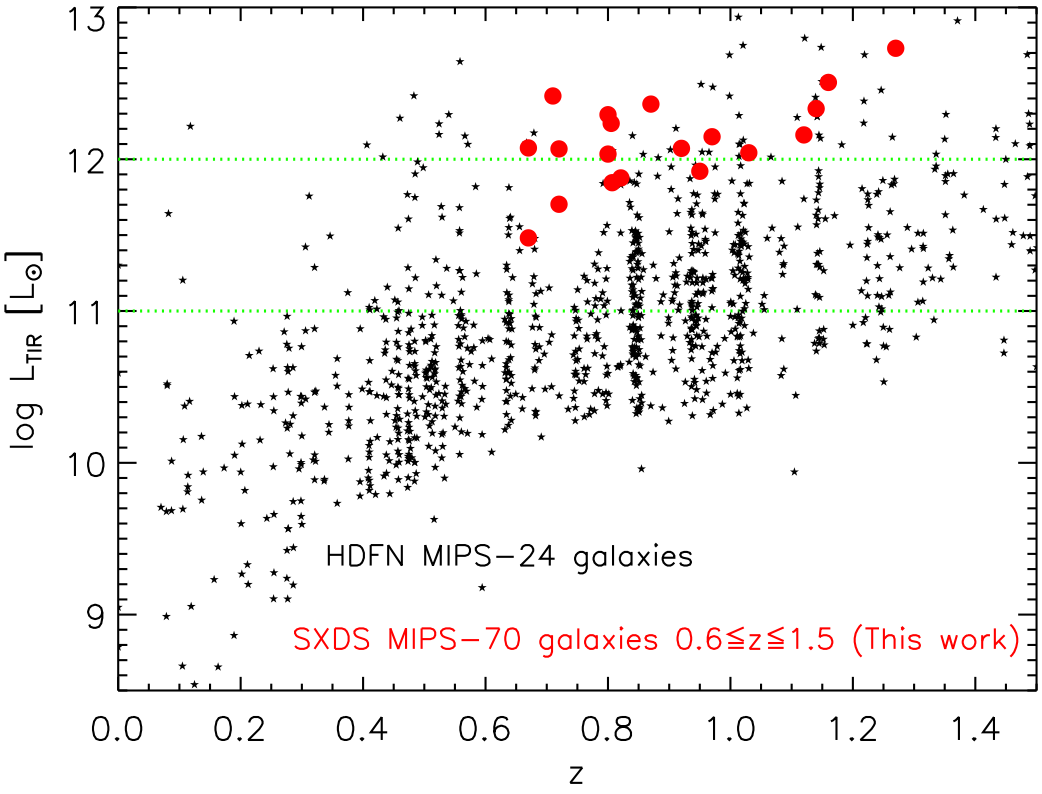

Figure 3.19 : Selection effect of $L_{\rm TIR}$ vs. z of our MIPS-70 emitters (*red circles*) compared to an IRAC sample with MIPS-24 detections (*black stars*) derived from the HDFN field. The division for LIRGs and ULIRGs are depicted with horizontal lines.

companion near to the 24 μm counterpart of our referential optical source. Therefore, we should consider these biases when placing our results about the stellar properties of these (U)LIRGs in the current paradigm of galaxy evolution (e.g. Hopkins et al. 2008).

We have also compared the stellar masses of the objects in our sample with those for the HDFN MIPS-24 detected galaxies in Fig. 3.20. The mass values of such HDFN galaxies are derived from a set of reference templates using one and two stellar population models (given in monochromatic luminosity per stellar mass; see Pérez-González et al. 2008 for a full explanation). The stellar mass is estimated scaling the best-fitting template to the observed photometry of each HDFN galaxy. The stellar masses of our objects are determined using such scale factor, but in our case we have only used 2 populations (described by an old and a young one) models (hereafter our fiducial stellar population models; the stellar modeling techniques are described in the next Chapter).

We can notice from the aforenamed figure that our galaxies have stellar masses spanning the mass range ($\sim$ 10^{10} – 10^{11} $M_\odot$) where most of the HDFN sources are located. Hence, our objects present typical galaxy stellar mass values, their median

value is $5 \times 10^{10}\ M_{\odot}$ (that of the Milky Way).

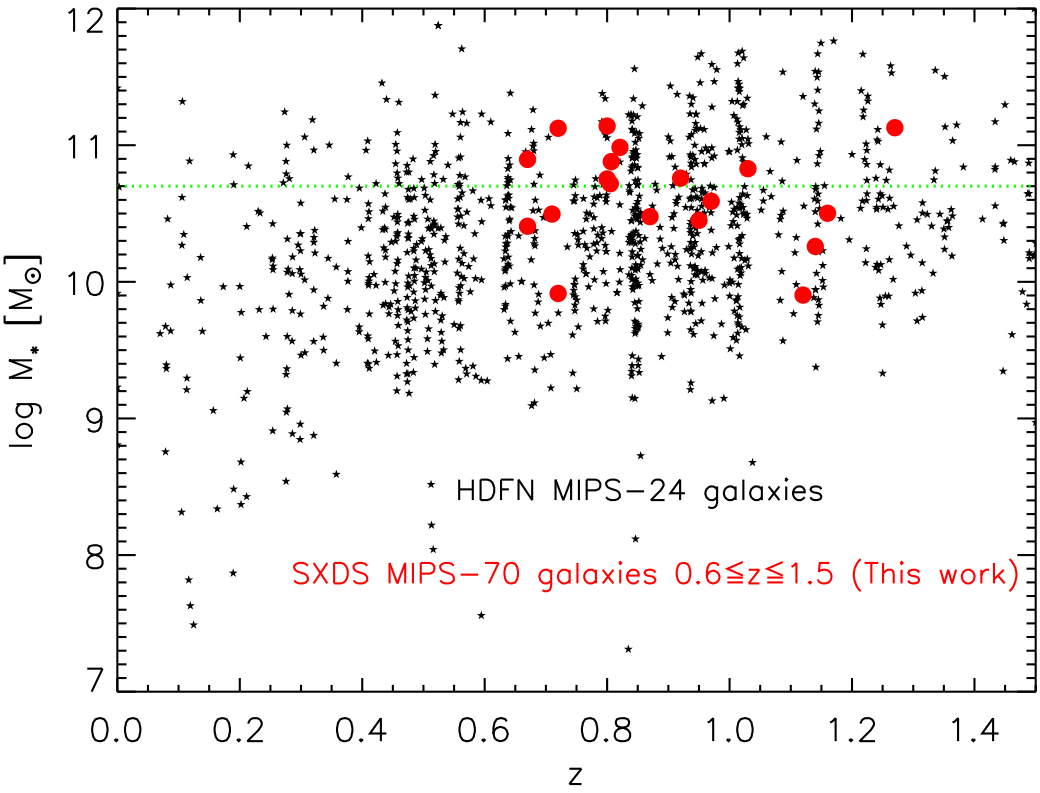

Figure 3.20 : Stellar mass versus redshift for our MIPS-70 galaxies (*red circles*) compared with an IRAC sample with MIPS-24 counterparts (*black stars*) obtained from the HDFN field. The stellar mass of the Milky Way is marked with the horizontal line.

Chapter 4

Self-consistent Stellar Population and Dust Emission Modeling

One of the goals of this work is the characterization of the stellar population properties of our sample of IR-bright objects. Considering each galaxy in our sample as an ensemble of stars, gas and dust, we know that all radiation from UV to FIR emerges from stars directly or absorbed and re-emitted by the ISM. We have to take into account ruling out objects hosting an AGN, which can heat the ISM producing MIR-FIR emission. The properties of the stars in a galaxy are commonly resumed in two main parameters: the SFR, and the stellar mass.

Several works in the literature claim that there must be a correlation between star formation rate and stellar mass (see, e.g., Brinchmann et al. 2004; Rodighiero et al. 2011). In order to test the existence of this correlation, we need accurate estimations of stellar masses and SFRs.

The main technique used for SFR determination relies on semi-empirical calibrations. The SFR is estimated by trying to isolate the emission of recently formed stars in concordance with the available observational data, and then applying a conversion factor to transform the observable into a SFR (see, e.g., Kennicutt 1998). This transformation requires several assumptions, the main one is to suppose that the SFR remains constant for a given timescale. However, special attention is required for setting this timescale, because it needs to be in agreement with the nature of the objects under study (Calzetti 2013).

Other technique used for SFR and stellar mass estimation is based on the modeling of the stellar emission of a galaxy assuming a specific SFH and an extinction law to account for the starlight attenuation due to dust absorption. By fitting the observed flux densities that shape the SEDs to a set of models, we can derive galaxy properties such

as the aforementioned stellar mass and SFR. We focus in these modeling techniques throughout this Chapter.

We have employed SPS models taking into account the attenuation effects of dust with a given extinction law, and the re-emission properties of dust in the IR wavelength range. Therefore, we have fitted models in a self-consistent way to the observed flux densities from UV to FIR. We use two codes which manage an energy balance approach: the Code Investigating GALaxy Emission (CIGALE[1], Noll et al. 2009), and the code described in Pérez-González et al. (2008) (the Synthesizer code, see also Pérez-González et al. 2003, 2013). We describe the modeling and fitting techniques of the CIGALE and Synthesizer codes in sections 4.2.1 and 4.2.2 respectively.

4.1 Modeling Ingredients

The first step in the modeling process is to assume a SFH. The most commonly functions adopted for SFHs include: single stellar population with exponentially decreasing SFR (see, e.g., Ilbert et al. 2013, Muzzin et al. 2013), single stellar population with exponentially increasing SFR (see, e.g., Pforr et al. 2012, Reddy et al. 2012), two stellar populations characterized by a recent stellar population on top of an old stellar population built with an exponentially declining star formation rate (with both stellar populations linked by their mass fraction, see, e.g., Borch et al. 2006, Pérez-González et al. 2008).

Given the active star-forming nature of our sources, and therefore their significant FIR emission, it is more adequate to use two stellar populations to model their SFHs (Lee et al. 2009, Melnick and De Propris 2013, Michałowski et al. 2014, Buat et al. 2014). We have assumed two exponentially decreasing SFRs to reproduce two different stellar populations (an old and a young one). The old population is characterized by a timescale $\tau_{\rm old}$, an age $t_{\rm old}$, a metallicity $Z_{\rm old}$, and its light is attenuated by an amount outlined by the parameter $A(V)_{\rm old}$. The young population is assumed to be generated by a recent burst of star formation, also declining exponentially, overlapped with the old population. The young population is described by a timescale $\tau_{\rm you}$, an age $t_{\rm you}$, a metallicity $Z_{\rm you}$, and its emission is attenuated by the quantity $A(V)_{\rm you}$. We can express the star formation rate as a combination of both populations:

$$SFR(t) = \alpha_{\rm old} \cdot e^{-\frac{t}{\tau_{\rm old}}} \cdot H[t] + \alpha_{\rm you} \cdot e^{-\frac{[t-(t_{\rm old}-t_{\rm you})]}{\tau_{\rm you}}} \cdot H[t-(t_{\rm old}-t_{\rm you})], \quad (4.1)$$

where $\alpha_{\rm old}$ denotes the SFR at the onset of the old population, $\alpha_{\rm you}$ is the value of the SFR at the beginning of the second star formation burst, and H is the heaviside step

[1]CIGALE web site: `http://cigale.oamp.fr/`

function. The old and young stellar populations are linked by the burst intensity, which is defined as the ratio of the young stellar population mass over the total stellar mass of the galaxy. Therefore, the burst intensity b is always encompassed between 0 and 1. The values of $\alpha_{\rm old}$ and $\alpha_{\rm you}$ depend on b (i.e., the stellar mass of the old and the young population, see Fig. 4.1).

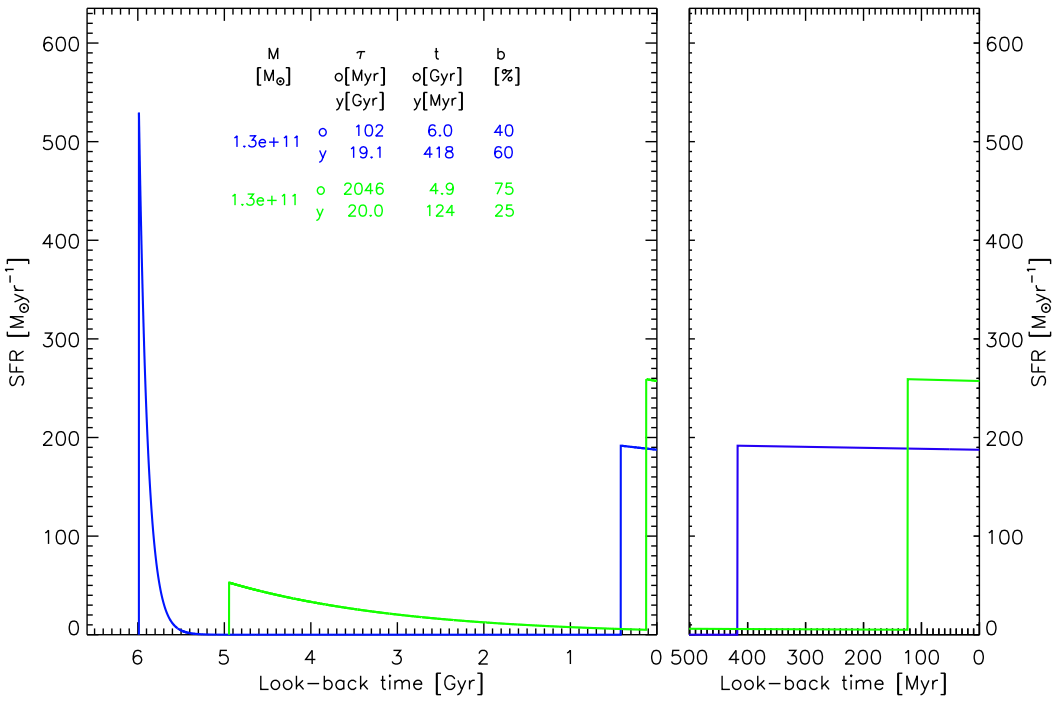

Figure 4.1 : *Left panel:* Two examples of the SFH defined by Eq. 4.1, with different values of $t_{\rm old}, \tau_{\rm old}, t_{\rm you}, \tau_{\rm old}$ and b (as indicated in the legends) for a galaxy having stellar mass, $M_* = 1.3 \times 10^{11}\ M_\odot$. *Right panel:* An expansion of the look-back time axis in order to appreciate better the SFH of the young population.

In order to account for the effects of dust on the UV/optical light coming from such stellar populations, it is necessary to measure the total emission scattered and absorbed in and out of our line of sight by such dust, and to consider the geometrical star-dust distribution. It is a common practice to assume that dust is found between us and the stellar populations of the galaxy. This foreground dust screen approximation should consider the thickness of the dust layer. Hence, the light we observe from the stellar population can be represented as:

$$I(\lambda)_{\rm obs} = I_{\rm SP}(\lambda) \cdot e^{-a_\lambda \Delta\tau}, \tag{4.2}$$

where $\Delta\tau$ stands for the thickness of the screen. Calzetti et al. (1994, 2000) derived an empirical law for starbust galaxies assuming a_λ a polynomial function of $1/\lambda$, and Charlot and Fall (2000) used a power law, $a_\lambda \propto \lambda^{-0.7}$, to represent such attenuation.

Throughout our study, we will use the Calzetti et al. (2000) attenuation law, which is plotted in Fig. 4.2 for an amount of extinction in the V band of 3 magnitudes, and a total-to-selective extinction ratio, $R_V \simeq 4.1$.

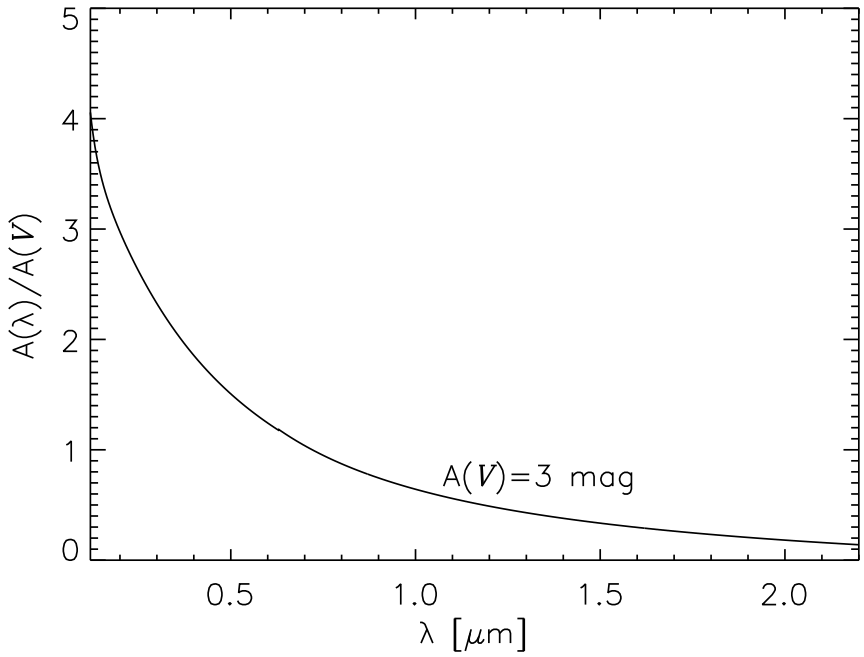

Figure 4.2 : Calzetti et al. (2000) empirical extinction law as a function of wavelength.

The emission of dust grains of different size and temperature governs the SED of star-forming galaxies at wavelengths $\gtrsim 8$ μm. Hence, there are several models which combine dust distributions of different grain sizes and their emission properties with stellar population models in order to predict the IR emission of such dust grains. Silva et al. (1998) created the GRASIL code to model the emission of galaxies considering the dust absorption, and stellar and dust emission from UV-to-FIR wavelengths by means of radiative-transfer techniques. In order to do so, they consider SPS models, gas fractions in the interstellar medium and the molecular clouds, a distribution of dust grain sizes, and dust-stars geometry. Chary and Elbaz (2001) utilized GRASIL and the work of Silva et al. (1998) to build a template set of IR SEDs for galaxies out to $z \sim 1$, with the purpose of quantifying the contribution of the different populations of galaxies to the CIB. Chary and Elbaz (2001) constructed 4 IR SEDs with GRASIL to fit the observed FIR photometry of 4 near galaxies of increasing IR luminosity: M51, M82, NGC6090 and Arp 220. They substituted the MIR part of the spectra of such 4 SEDs with observed spectra obtained with ISOCAM. Then, they interpolated among the 4 SEDs to span several IR luminosity values.

Using a different approach, Dale et al. (2001) generated IR SEDs from several dust

emission curves, assuming that the dust grain masses follow a power-law over different radiation field intensities. PAHs, large and small grains are considered and compared to observed data from IRAS, ISOCAM, and ISOPHOT of 69 near IR-bright galaxies. Dale and Helou (2002) improved the Dale et al. (2001) model premises about radiation field intensity and dust emissivity, and extended the model calibration at wavelengths larger than 120 μm.

Other set of templates frequently used to fit IR SEDs is that of Rieke et al. (2009). These authors utilized comprehensive *Spitzer* observations of eleven near (U)LIRGs to build a template library in the wavelength range 0.4 μm – 30 cm and spanning luminosities 5×10^9–10^{13} $L_\odot$. They used *Spitzer*-IRS and ISO spectra to model the part of the templates at rest-frame wavelengths $\lesssim 35$ μm, matching the 0.4–5 μm range with attenuated stellar models. The FIR part of the SED is modeled with a modified black body fitted with dust temperatures ranging 38–64 K and emissivity index $0.7 < \beta < 1$.

As mentioned in Section 3.7, we have computed the $L_{\rm TIR}$ of our sources from the best-fitting template of the 3 aforementioned libraries. We show in Figure 4.3 an example SED with FIR observed data fitted with a template of each of these 3 sets.

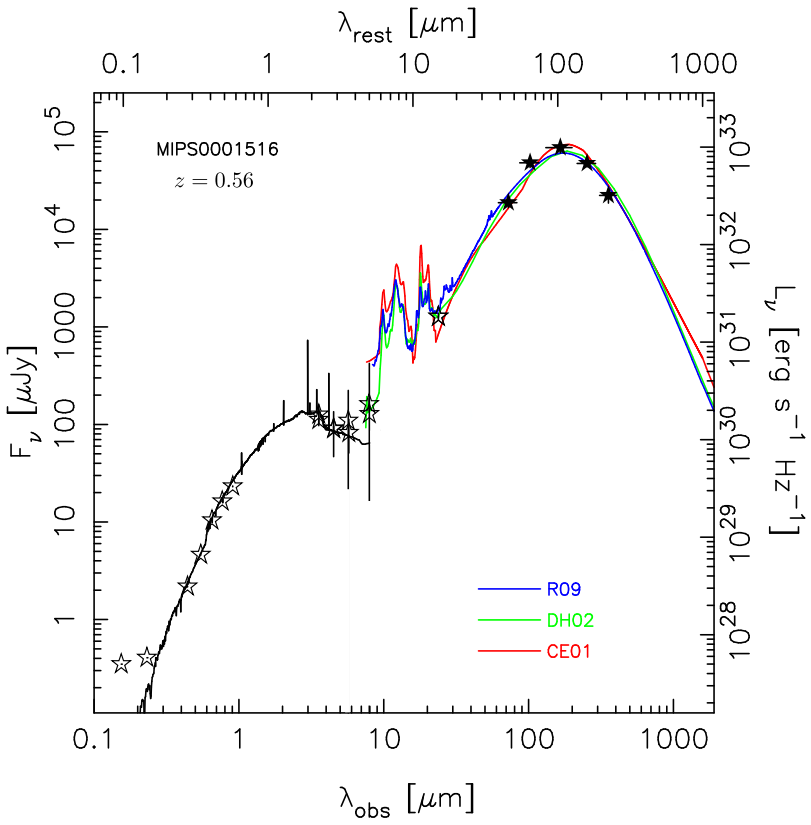

Figure 4.3 : An example SED showing the FIR data fitted by a template of the libraries of Chary and Elbaz (2001) (CE01; red line), Dale and Helou (2002) (DH02; green line), and Rieke et al. (2009) (R09; blue line). Only the filled stars are used in the fit.

In order to characterize the stellar population parameters of our galaxy sample, we should derive the nine parameters defining the properties of the old and the young stellar populations from the fit of the SED of each galaxy: $\tau_{\rm old}$, $t_{\rm old}$, $Z_{\rm old}$, $A(V)_{\rm old}$, $\tau_{\rm you}$, $t_{\rm you}$, $Z_{\rm you}$, $A(V)_{\rm you}$, and b. In our study, the amount of the extinction in V band of both populations is constrained, balancing this absorbed energy with the energy re-emitted by dust at FIR wavelengths. This is what we call the FIR prior.

We describe in Section 4.2.1 the assumptions adopted and the range explored for these nine parameters in the space of solutions probed by CIGALE, and its fitting strategy. The ranges of the parameters investigated by the Synthesizer code, and its fitting procedure are detailed in Section 4.2.2. We compare in Chapter 6 the parameter values obtained with both codes, and we identify the parameters which are more relevant from the two population modeling. We also pay attention to the parameters for which the codes get robust results, and to the parameters which can not be correctly constrained in the SFHs of our IR-selected galaxy sample.

4.2 Self-consistent Modeling of Stars and Dust

4.2.1 The Code Investigating GALaxy Emission (CIGALE)

The CIGALE is a code which simultaneously fits the stellar and dust emission implemented in a set of models to the observed flux densities that constitute the SED of a galaxy. Afterwards, the code derives the galaxy properties using a Bayesian-like analysis. The CIGALE was assembled from an algorithm first outlined in Burgarella et al. (2005) but the building blocks of the code and the fitting and analysis strategies were formally described in Noll et al. (2009).

Basically, the CIGALE constructs SPS models using Maraston (2005) or PEGASE (Fioc and Rocca-Volmerange 1997) libraries. The effects of dust are considered by attenuating the stellar spectra using the synthetic curves of Calzetti et al. (1994, 2000) and re-emitting the absorbed energy in the MIR-FIR wavelengths. This dust re-radiation is characterized by means of the semi-empirical templates of Dale and Helou (2002). The energy balance argument is implemented linking the aforementioned templates to the attenuated stellar spectra through $L_{\rm TIR}$, which represents the stellar luminosity absorbed by the dust and re-radiated in the MIR-FIR spectral range (see Noll et al. 2009 for a detailed description).

4.2.1.1 Generating Stellar Population Models with CIGALE

We have used the Maraston (2005) models because they are the default preferred option in the CIGALE implementation. Noll et al. (2009) argue that Maraston (2005) models treat the thermally pulsating asymptotic giant branch stars in a more feasible way than PEGASE models. Their argument is based on the work of Maraston et al. (2006) and Salimbeni et al. (2009) (see also MacArthur et al. 2010). However, other studies question the relevance of the asymptotic giant branch in the modelling (see, e.g., Marigo and Girardi 2007; Davidzon et al. 2013). Nevertheless, all the works found in the literature that use the CIGALE have adopted the Maraston (2005) models (see, e.g., Giovannoli et al. 2011, Boquien et al. 2012, Buat et al. 2014).

We have assumed a SFH for the CIGALE models according to Equation (4.1) and a Salpeter (1955) Initial Mass Function. Even though the CIGALE allows to use stellar populations models of different metallicity Z, we have fixed the metallicity to the solar value following the aforementioned studies in the literature which have used the CIGALE, and considering that it is infesiable to break the age-metallicity degeneracy with broadband data (O'connell 1986).

We are characterizing the stellar populations of a sample of IR-bright galaxies with redshift between 0.6 and 1.5. Given the large number of possible models ($\sim 8 \times 10^6$) which can be explored in the above redshift range and hard-disc storage limitation, we have divided the sample in four redshift bins: $0.6 < z \leq 0.8$, $0.8 < z \leq 1.0$, $1.0 < z \leq 1.2$, and $1.2 < z \leq 1.5$. We have run the CIGALE in each redshift bin. The ages explored for the old stellar population in each redshift bin and the full set of values of the other parameters investigated are listed in Table 4.1. Following the work of Giovannoli et al. (2011), we have fixed the the e-folding time for the young stellar population to $\tau_{\rm you} = 20$ Gyr in the four redshift bins. This is equivalent to consider a constant burst of star formation during the age of the young stellar population, $t_{\rm you}$, which is considered from 0.001 to 1 Gyr. The connection between the young and the old stellar population is given by the mass fraction of the young population with respect to the total stellar mass (the burst intensity b) which is explored in the range 0 to 1.

Once the stellar population models are generated, the next step is to attenuate them by means of the Calzetti et al. (2000) law. The CIGALE gives the possibility of varying the slope of this Calzetti law and adding a UV bump. We have decided to employ a pure Calzetti law without a bump because it is the option in common with the possible attenuation laws implemented in the Synthesizer code. The CIGALE allows considering that the old stellar population is less affected by the dust attenuation than the young population. The attenuation in the V band is first estimated for the young population, with

the quantity $A(V)_{\rm you}$. The effect of dust in the old population is parameterized with a reduction factor relative to the attenuation in the young one, $f_{\rm att}$. We have explored $A(V)_{\rm you}$ in the range 0.15 to 4.2 mag, and $f_{\rm att}$ in the range 0 to 1.

Table 4.1 : Input parameters of the CIGALE and their explored range

Parameter	Symbol	Range
Metallicities	Z	0.02
e-folding times of the old stellar population in Gyr	$\tau_{\rm old}$	0.1, 1, 3, 10
ages of the old stellar population in Gyr	$t_{\rm old}$	3, 5, 7 for $0.6 < z \leq 0.8$
		2, 4, 6 for $0.8 < z \leq 1.0$
		1, 3, 5 for $1.0 < z \leq 1.2$
		2, 4, 5 for $1.2 < z \leq 1.5$
e-folding times of the young stellar population in Gyr	$\tau_{\rm you}$	20
Ages of the young stellar population in Gyr	$t_{\rm you}$	0.001, 0.01, 0.025, 0.05,
		0.075, 0.1, 0.2, 0.3, 0.4,
		0.5, 0.6, 0.7, 0.8, 0.9, 1
Mass fraction of young population or burst intensity	b	0, 0.001, 0.005, 0.01,
		0.05, 0.06, 0.07, 0.08,
		0.09, 0.1, 0.2, 0.3, 0.4
		0.5, 0.6, 0.7, 0.8, 0.999
V-band attenuation for the young population in mag	$A(V)_{\rm you}$	0.15, 0.30, 0.45, 0.6,
		0.75, 0.9, 1.05, 1.2,
		1.35, 1.5, 1.65, 1.8,
		1.95, 2.1, 2.25, 2.4,
		2.55, 2.7, 2.85, 3.0,
		3.15, 3.3, 3.45, 3.6,
		3.75, 3.9, 4.05, 4.2
Reduction factor of $A(V)_{\rm you}$ for the old population	$f_{\rm att}$	0, 0.25, 0.5, 0.75, 1

4.2.1.2 The CIGALE Fitting Procedure

The CIGALE tries to fit the set of UV-FIR models generated previously to the observed flux densities of each galaxy in all the available bands. Hence, the full set of models are displaced according to the redshift of each object, and the redshifted spectra are convolved with the response curve of the filters before the fitting. These redshifted and convolved models are also corrected for an attenuation due to intergalactic medium by

means of the Meiksin (2006) procedure. The full resulting set of models are compared with the observed galaxy photometry under a set of k bands, using a χ^2 minimization process as follows:

$$\chi^2(M_{gal}) = \sum_{i=1}^{k} \frac{(M_{gal}\ f_{mod,i} - f_{obs,i})^2}{\sigma^2_{obs,i}}, \tag{4.3}$$

where $f_{mod,i}$ is the modeled flux density per solar mass and $f_{obs,i}$ is the observed flux density under the band i respectively, and M_{gal} (the galaxy mass) is a free parameter given in solar masses. The photometric errors in each filter are considered by $\sigma_{obs,i}$. All available data points with observed wavelength shorter than 550 μm are included in our fits, except MIPS 24 μm data. As it is explained in Section 3.7, the observed flux at 24 μm could reach the part of the SED including PAHs for some redshifts, affecting the proper estimation of $L_{\rm TIR}$.

The derived χ^2 of the models are compared in order to find out which model provides the minimum χ^2 from the whole model grid to the observed photometry of each galaxy. Furthermore, computing χ^2 of each model enables to build probability distribution functions, and to infer galaxy properties from these distributions. Hence, the main idea is to find out the most probable model (that with the minimum χ^2), or using Bayesian terminology, the probability of the data D provided by the model M. Therefore, we can compute this probability as: P(D|M) $\propto e^{-\chi^2/2}$ (see Kauffmann et al. 2003, Walcher et al. 2008). In order to estimate the parameters for a particular galaxy, the probabilities for all models are calculated and summed (integrated) over all parameters, excluding the parameter to be determined, which produces a probability distribution function. The average and width of the distribution give us a robust estimation of the parameter and its associated error.

Noll et al. (2009) followed a different approach for estimating the parameter value and its error based on integrated probabilities. They integrate the probability distribution function to infer the likelihood of a model as follows:

$$p(\chi^2, n) = \int_{\chi^2}^{\infty} \frac{x^{(n/2)-1}\ e^{-x/2}}{2^{n/2}\ \Gamma(n/2)}\ {\rm d}x, \tag{4.4}$$

where Γ denotes the Gamma function and $n = k - 1$ are the degrees of freedom corresponding to the k filters used.

For deriving the expected values of each parameter, it is necessary to link the likelihood $p(\chi^2, x)$ for the m generated models to the probability distribution function $P(x)$. In order to achieve this, a fixed number l of equally-sized bins are defined for each parameter. The bins span from the lowest to the highest parameter value in the set of

models. The characteristic probability P_i of each bin i is estimated finding the sum of the probabilities $p_j(\chi^2, n)$ of the j models located inside the bin i. The coefficient a_{ji} is equal to 1 if a model j is included in the bin i, otherwise $a_{ji} = 0$. Writing this procedure in a Bayesian approach:

$$P_i(x) = \sum_{j=1,\ldots,m} [a_{ji}\, p_j(\chi^2, n)]. \tag{4.5}$$

Using the $P_i(x) = P_i$ as weights for each bin, the expected value of each parameter is given by the following Equation:

$$\langle x \rangle = \frac{\sum_{i=1}^{l} P_i\, x_i}{\sum_{i=1}^{l} P_i}, \tag{4.6}$$

where x_i is the parameter value of the best fitting model of each bin. The standard deviation from the expected value of each parameter is estimated as

$$\sigma_x = \sqrt{\frac{\sum_{i=1}^{l} (x_i - \langle x \rangle)^2\, P_i}{\sum_{i=1}^{l} P_i}}. \tag{4.7}$$

The above described procedure is called "the sum method" by Noll et al. (2009). We use this method to constrain the value of the parameters listed in Table 4.1. Once these basic parameters are constrained, we can describe the SFHs of our galaxy sample, which are represented by the proposed Equation 4.1. Besides the basic parameters, the CIGALE provides the scaling factor M_{gal} and additional supplementary output parameters as the mass weighted age and the SFRs averaged over different periods of time (see the CIGALE README file for a full description of the output parameters[2]).

We comment on the CIGALE estimates of the SFH parameters in Chapter 6, where we compare these estimates with those obtained with the Synthesizer code.

4.2.2 The Synthesizer code

The Synthesizer code generates SPS models using customary libraries (see, e.g., Fioc and Rocca-Volmerange 1997; Bruzual and Charlot 2003; Maraston 2005), considering the effects of dust by a given extinction law (e.g., Charlot and Fall 2000, Calzetti et al. 2000). The observed flux densities are compared to the models in order to derive galaxy properties. Uncertainties in the derived parameters and degeneracies in the solutions are analyzed using a Monte Carlo algorithm. The energy balance argument is taken into account providing a $L_{\rm TIR}$ estimated previously (our $L_{\rm TIR,ref}$ computed from

[2]README file of the CIGALE available at: `http://cigale.oamp.fr/readme-CIGALE.pdf`

the best-fitting—that with the lowest χ^2—template from the 3 IR dust-emission models explained in Section 4.1), to constrain the amount of energy absorbed by the dust from the UV-optical starlight. Such $L_{\rm TIR,ref}$ could be varied between a certain level previously defined, during the fitting process of the Synthesizer code.

4.2.2.1 Producing Stellar Population Models with the Synthesizer code

In order to fairly compare the fitting results of the Synthesizer and CIGALE codes, we have assumed the same parametrization for the SFH (Eq. 4.1) and the same library of SPS models (Maraston 2005; the default library in CIGALE Fortran 2013/11/18) in both codes.

Therefore, we have an evolved stellar population (decaying exponentially) characterized by a timescale $\tau_{\rm old}$, an age $t_{\rm old}$, a metallicity $Z_{\rm old}$, and attenuated by an amount given by $A(V)_{\rm old}$. Overlapped on to this evolved population, we have a recent burst of star formation, also declining exponentially, described by a timescale $\tau_{\rm you}$, an age $t_{\rm you}$, a metallicity $Z_{\rm you}$, an attenuation $A(V)_{\rm you}$, and the burst strength b.

We produced Maraston (2005) stellar population models, assuming a Salpeter (1955) stellar mass function with $0.1 < M < 100\ M_{\odot}$, and allowing the models to be attenuated by the law of Calzetti et al. (2000). Hence, all the a priori parameters assumed for the Synthesizer code are equal to those assumed for the CIGALE.

Our two stellar population models required nine parameters to be fitted: (1) $\tau_{\rm old}$, (2) $t_{\rm old}$, (3) $A(V)_{\rm old}$, (4) $Z_{\rm old}$, (5) $\tau_{\rm you}$, (6) $t_{\rm you}$, (7) $A(V)_{\rm you}$, (8) $Z_{\rm you}$, and (9) b. We have fixed $Z_{\rm old}$ and $Z_{\rm you}$ to the solar value, and $\tau_{\rm you}$ only takes the values of 16 and 20 Gyr in order to be consistent with the assumptions that we adopted for the CIGALE code.

Although the Synthesizer code is more flexible than the CIGALE in requirements of computing time and hard-disc space, we have decided to divide the sample in the same redshift bins and to explore the same range of input parameters that we have used in the CIGALE. The full set of these input parameters is listed in Table 4.2.

4.2.2.2 The Synthesizer Fitting Procedure

The Synthesizer code shifts the SPS models generated previously to the redshift of each galaxy and then these redshifted models are convolved with the transmission curves of a set of n filters. After this, the synthetic flux densities of the resulting models are compared with the observed photometric data from the sample of IR-bright objects by means of a reduced χ^2 estimator. The expression of this estimator is:

$$\chi^2 = \sum_{i=1}^{n} \frac{(F_{obs,i} - K \cdot F_{mod,i})^2}{\sigma^2_{obs,i}}, \tag{4.8}$$

Table 4.2 : Input parameters of the Synthesizer code and their explored range

Parameter	Symbol	Range
Metallicities	Z	0.02
e-folding times of the old stellar population in Gyr	$\tau_{\rm old}$	from 0.1 to 10 using logarithmic intervals of 0.5 dex
Ages of the old stellar population in Gyr	$t_{\rm old}$	3, 4, 5, 6, 7 for $0.6 < z \leq 0.8$ 2, 3, 4, 5, 6 for $0.8 < z \leq 1.0$ 1, 1.5, 2, 3, 4, 5 for $1.0 < z \leq 1.2$ 2, 3, 4, 5 for $1.2 < z \leq 1.5$
V-band attenuation for the old population in mag	$A(V)_{\rm old}$	from 0 to 1.5 in increments of 0.1
e-folding times of the young stellar population in Gyr	$\tau_{\rm you}$	16, 20
Ages of the young stellar population in Myr	$t_{\rm you}$	1, 1.5, 2, 2.5, 3, 3.5, 4, 4.5, 5, 5.5, 6, 6.5, 7, 7.5, 8, 8.5, 9, 9.5, 10, 15, 20, 25, 30, 35, 40, 45, 50, 55, 60, 65, 70, 75, 80, 85, 90, 95, 100, 200, 300, 400, 500, 600, 700, 800, 900, 1000
Burst intensity	b	from 0.1 to 0.6 in increments of 0.05
V-band attenuation for the young population in mag	$A(V)_{\rm you}$	from 0 to 4.2 in increments of 0.1

where $F_{obs,i}$ is the observed flux density and $F_{mod,i}$ is the modeled flux density per solar mass under the filter i, respectively, and $\sigma_{obs,i}$ are the photometric uncertainties associated to each filter. A normalization factor K is required to scale the input models to the observed photometry and determine galaxy properties such as the stellar mass, and the star formation rate. We have included in the fitting process all the available data points for rest-frame wavelengths shorter than 4 μm, because the integrated emission in this wavelength regime should be dominated by stars for the galaxies in our sample. Hence, the Synthesizer fitting procedure is similar to the CIGALE one.

The energy balance approach is implemented in the Synthesizer code by fitting our determined $L_{\rm TIR,ref}$ to the stellar energy absorbed by the dust from the UV-optical spectral range. Therefore, this dust-absorbed energy is not a free parameter, it is constrained according to the MIR-FIR energy re-radiated by the dust, i.e., the FIR prior.

Given the large range of values to be investigated for the nine parameters of the two population in these models, and hence the large number of feasible solutions, the time required to explore the complete space of solutions for each object (located at different z) becomes prohibitive. Therefore, the Synthesizer code has in its implementation a minimization strategy based in a genetic algorithm (Charbonneau 1995), which allows to avoid assessing the minimization function at all points in the solution space (see the Appendix B of Pérez-González et al. 2008 for a full description).

In order to examine the uncertainties in the derived parameters and consider the probable degeneracies in the solutions, The Synthesizer code performs Monte Carlo simulations for each galaxy. The technique consists in varying randomly each observed flux density within a Gaussian distribution of width equal to its corresponding photometric error, and repeat the fit again with all feasible models. We executed the Synthesizer code 3000 times and then inspected the set of solutions. This inspection included the identification of clusters of solutions by means of a k-means method. A statistical significance was assigned to each cluster, defined as the fraction of the 3000 distinct solutions, which belonged to the cluster. Hence, we grouped solutions which provide similar results and calculated the median value and scatter of each group in the multi-dimensional space formed by the nine fitted parameters.

Finally, we have considered the most significant cluster as the best solution. The median value and scatter obtained in the logarithmic space of these nine parameters are compared with the parameters derived using CIGALE in Chapter 6.

In the following Chapter we investigate how the stellar parameters vary for different possible solutions which fit the observed photometry of the galaxies in our sample. In order to do so, we analyze the different clusters obtained from the Monte Carlo simulations with the Synthesizer code.

We also compare the goodness of fit, and study the differences in the stellar mass and SFR values between models with two populations (2P) with and without FIR data to evaluate the utility of using the FIR constraint. We also check if it is possible to simplify the 2P models to one stellar population (1P) models using the FIR prior.

Chapter 5

Robustness of the Analysis of the Stellar and Dust Emission: the FIR prior

Following the main objective of this work, we have characterized the stellar and dust attenuation properties of a sample of IR-bright galaxies at intermediate redshift. This goal has been fulfilled fitting a wealth of multi-wavelength data, which encompass the UV to FIR spectral range, to a set of galaxy 2P synthesis models. We assume as reference such 2P models, considering the dusty nature (i.e., star-forming nature) of our objects, and the recent work in the literature showing that a multi-component SFH is a good choice for dusty star-forming galaxies (see, e.g., Dunlop 2011, Michałowski et al. 2014, Casey et al. 2014). Hence, we assume as fiducial 2P models using the FIR constraint derived with the Synthesizer code and the Maraston (2005) library. We compare the physical parameters derived with these fiducial models to the parameters obtained with 2P models without using the FIR information. This is done in order to check the impact of using the FIR prior in the resulting physical parameters. We also study if it is possible to simplify our fiducial models to 1P models with the FIR constraint by comparing the goodness of the fits determined for each set of models.

It is important to mention that the trustworthiness and accuracy of the resulting physical properties will depend on the photometric uncertainties, and the degeneracies between such properties given the wavelength coverage and the quality of the available photometry.

Among the well-known degeneracies we have the age-metallicity, the age-dust and the age-burst strength. Considering that we have fixed the metallicity to the solar value in our study (see Sections 4.2.1.1 and 4.2.2.1), the age-metallicity degeneracy is not

discernible in our work. Given that our selection is based on FIR data, our objects are dusty galaxies which host young stellar populations disposed to suffer the age-dust and age-burst strength degeneracies. We will investigate on the effects of these two degeneracies. Consequently, we want to evaluate how the a priori assumptions in the modeling affect the results about the stellar population properties of IR-bright galaxies as stellar mass, SFR, attenuations and ages. In other words, we want to answer the following questions:

1. What is the usefulness of the FIR prior on the determination of the physical parameters of our objects?

2. How do these physical parameters change when using 2P models with FIR data instead of 2P models without FIR information?

3. Is it possible to simplify our fiducial 2P models with FIR prior (i.e., to use 1P models with FIR constraint)?

4. What happen to these stellar parameters when using 1P models with FIR data?

We will work in these questions throughout this Chapter.

5.1 Two Population models with and without the FIR prior

In this section we compare the solutions determined from 2P models using the FIR prior with the solutions obtained from 2P models without using the FIR constraint. Both sets of solutions are derived using the Synthesizer code with SPS models of Maraston (2005). Our goal is to test the value of employing the FIR information to constrain the attenuation of the stellar emission, and to quantify the impact of this constraint in the estimation of the physical parameters of IR-bright galaxies. To do so, we have performed Monte Carlo simulations and we have characterized the clusters of solutions identified in each set of models for each galaxy in our sample. The Monte Carlo simulations technique was described in Section 4.2.2.2, but we remember the reader that it consists in varying randomly each observed flux density within a Gaussian distribution of width equal to its corresponding photometric error, and repeat the fit again with all feasible models. We have used 3000 test particles and then inspected the set of solutions identifying the clustering pattern with a k-means method. A statistical significance was assigned to each cluster, defined as the fraction of the 3000 distinct solutions, which belonged to the cluster.

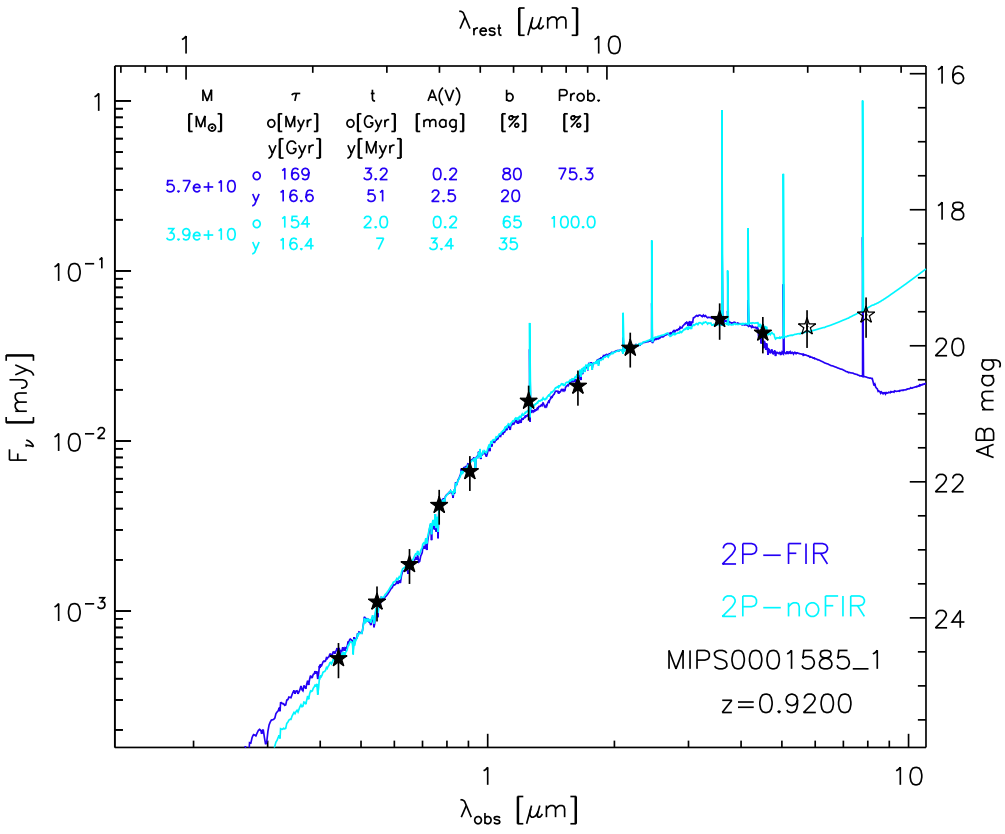

Figure 5.1 : An example of the resulting fit to the UV-to-MIR SED for our IR-bright galaxies at $0.6 \leq z \leq 1.5$. The results of the fitting process for the most significant cluster identified with the Synthesizer code are plotted. The *blue line* stands for the spectrum where the FIR prior is used, the *cyan line* shows the spectrum resulting without the FIR constraint. The parameter values obtained from each modeling case are also shown (M_*, τ, t, $A(V)$, b, Prob.). Photometric data points include the uncertainties (multiplied by 2.5 for visualization), only the *filled black stars* are used in the fit.

In Table 5.1, we present the values of the stellar parameters derived from the analysis of the set of solutions from the Monte Carlo simulations for the 2P models with and without the FIR constraint. We have chosen the plane $(\tau_{\rm you}, t_{\rm you})$ as the most appropriate to identify the clusters in both 2P cases. Such choice was based on a visual inspection of the distributions of the solution data points on different bidimensional spaces of the parameters of the old and the young population. Hence, the median values of the parameters of the old population of each different cluster are projections corresponding to the model selected in the space $(\tau_{\rm you}, t_{\rm you})$ for such cluster identified for each object. We assume as best solution the most significant cluster for each object in both modeling cases.

In Figure 5.1, we show an example SED resulting from the fitting of 2P models with and without FIR data. The amount of attenuation in the V band is ~ 1 mag larger for the

modeling case where the FIR information is omitted compared to the that when using the FIR prior. This large $A(V)_{\rm you} = 3.4$ mag is accompanied with a short age for the young population $t_{\rm you} = 7$ Myr, which evidences the age-dust degeneracy. For the 2P modeling case without the FIR prior, the results point to an overestimation of $A(V)_{\rm you}$, and an underestimation of $t_{\rm you}$ compared to the 2P models with the FIR constraint.

5.1.1 Goodness of the Fits and Cluster Analysis of 2P Models

Following the aim of appraising the modeling of the stellar populations for both 2P cases, it is interesting to discuss the goodness of the fits of the selected models derived from the analysis with the Synthesizer code. To do so, we evaluate the goodness of fit of the UV-to-MIR spectral range (see Fig. 5.1). We have used a $\chi^2_{\rm UV/MIR}$ estimator defined as:

$$\chi^2_{\rm UV/MIR} = \frac{1}{N-1}\sum_{i=1}^{N}\frac{(m_{obs,i}-m_{mod,i})^2}{\sigma^2_{obs,i}}, \tag{5.1}$$

where $m_{obs,i}$ is the observed magnitude under each band, $m_{mod,i}$ is the magnitude resulting from the convolution of each filter response curve and the modeled spectrum of the Synthesizer code, and $\sigma_{obs,i}$ is the photometric uncertainty associated to each band. We have added in quadrature a constant uncertainty of 0.1 mag to the background noise estimation for each filter. This constant uncertainty takes into account differences in the zero point absolute calibration between the UV-to-MIR bands (see, e.g., Yagi et al. 2013), and uncertainties due to aperture choices and aperture corrections. The quantity N is the number of available data points from FUV to MIR. The largest wavelength considered in this case is 4.5 μm.

We have plotted in Fig. 5.2 the $\chi^2_{\rm UV/MIR}$ distributions for the 2P models with and without FIR constraint. The distribution of the 2P models without FIR information concentrates in slightly lower $\chi^2_{\rm UV/MIR}$ values compared with the one with the FIR prior. This is expected considering that the $A(V)$ values when the FIR data is omitted are less restricted, i.e., there is no energy balance between the dust emission and the stellar light obscuration. Therefore, the amount of attenuation can reach larger or smaller values than in the case constrained by the FIR prior. We have also estimated the median, and the 16 and 84-percentile values for the two cases, obtaining $1.4^{+0.9}_{-0.5}$ for the 2P one without FIR data, and $1.7^{+1.4}_{-0.7}$ for the one with the FIR constraint. The distribution of the FIR prior case presents 1 galaxy in the high $\chi^2_{\rm UV/MIR}$ values tail. Even though the median of 2P case omitting the FIR information is a little shorter than the FIR-constrained one, they are close enough to be considered analogous. Therefore the goodness of the fits are similar for each 2P modeling case.

Table 5.1. Stellar Population Synthesis Results from the Synthesizer code for Galaxies at $0.6 \leq z \leq 1.5$

Galaxy	z†	FIR	$\log M$ $[M_\odot]$	Pop.	τ old [Myr] you [Gyr]	Age old [Gyr] you [Myr]	$A(V)$ [mag]	Z $[Z_\odot]$	b [%]	Prob. [%]
(1)	(2)	(3)	(4)	(5)	(6)	(7)	(8)	(9)	(10)	(11)
MIPS0000050_1	0.97	yes	$10.6^{+0.1}_{-0.1}$	old	219^{+47}_{-69}	$2.3^{+1.0}_{-0.4}$	$0.09^{+0.19}_{-0.09}$	1.0		100.0
				you	$18.1^{+3.3}_{-3.0}$	11^{+4}_{-2}	$2.71^{+0.14}_{-0.12}$	1.0	12^{+5}_{-2}	
		no	$10.6^{+0.1}_{-0.1}$	old	220^{+44}_{-40}	$2.0^{+0.3}_{-0.2}$	$0.00^{+0.05}_{-0.00}$	1.0		43.5
				you	$17.0^{+3.5}_{-2.4}$	87^{+16}_{-18}	$2.50^{+0.05}_{-0.05}$	1.0	38^{+3}_{-5}	
			$10.6^{+0.1}_{-0.1}$	old	191^{+63}_{-72}	$2.2^{+0.9}_{-0.3}$	$0.01^{+0.06}_{-0.01}$	1.0		40.6
				you	$16.9^{+3.5}_{-2.3}$	201^{+27}_{-23}	$2.40^{+0.05}_{-0.05}$	1.0	56^{+4}_{-2}	
			$10.5^{+0.1}_{-0.1}$	old	247^{+30}_{-33}	$2.0^{+0.3}_{-0.2}$	$0.04^{+0.13}_{-0.04}$	1.0		15.9
				you	$16.5^{+3.1}_{-2.1}$	7^{+1}_{-1}	$3.45^{+0.08}_{-0.09}$	1.0	40^{+5}_{-5}	
MIPS0000149_1	0.67	yes	$10.9^{+0.1}_{-0.1}$	old	129^{+128}_{-34}	$3.2^{+0.8}_{-0.5}$	$0.02^{+0.08}_{-0.02}$	1.0		65.3
				you	$17.4^{+3.6}_{-2.7}$	206^{+49}_{-25}	$3.21^{+0.08}_{-0.08}$	1.0	52^{+4}_{-3}	
			$10.8^{+0.1}_{-0.1}$	old	200^{+62}_{-94}	$3.1^{+0.7}_{-0.4}$	$0.04^{+0.08}_{-0.04}$	1.0		34.7
				you	$17.3^{+3.7}_{-2.5}$	87^{+17}_{-14}	$3.37^{+0.06}_{-0.08}$	1.0	35^{+2}_{-4}	
		no	$10.8^{+0.1}_{-0.1}$	old	199^{+62}_{-93}	$3.1^{+0.7}_{-0.4}$	$0.03^{+0.08}_{-0.03}$	1.0		57.0
				you	$17.1^{+3.5}_{-2.4}$	86^{+17}_{-16}	$3.38^{+0.07}_{-0.08}$	1.0	35^{+2}_{-5}	
			$10.9^{+0.1}_{-0.1}$	old	137^{+118}_{-40}	$3.2^{+0.8}_{-0.5}$	$0.00^{+0.06}_{-0.00}$	1.0		43.0
				you	$16.7^{+3.3}_{-2.3}$	204^{+31}_{-24}	$3.22^{+0.08}_{-0.07}$	1.0	54^{+2}_{-4}	
MIPS0000472_1	1.03	yes	$10.8^{+0.1}_{-0.1}$	old	119^{+121}_{-24}	$3.7^{+0.8}_{-0.8}$	$0.91^{+0.22}_{-0.18}$	1.0		100.0
				you	$18.9^{+2.8}_{-3.0}$	39^{+16}_{-12}	$2.48^{+0.07}_{-0.08}$	1.0	15^{+5}_{-5}	
		no	$10.7^{+0.1}_{-0.1}$	old	138^{+111}_{-42}	$4.0^{+1.0}_{-1.0}$	$0.95^{+0.36}_{-0.21}$	1.0		100.0
				you	$17.6^{+3.3}_{-2.6}$	9^{+1}_{-1}	$3.14^{+0.10}_{-0.12}$	1.0	22^{+8}_{-7}	
MIPS0000508_1	0.72	yes	$9.9^{+0.1}_{-0.1}$	old	210^{+58}_{-106}	$3.1^{+0.9}_{-0.4}$	$0.02^{+0.10}_{-0.02}$	1.0		100.0
				you	$18.9^{+3.0}_{-3.1}$	16^{+4}_{-2}	$3.16^{+0.12}_{-0.11}$	1.0	25^{+5}_{-5}	
		no	$9.9^{+0.1}_{-0.1}$	old	222^{+47}_{-115}	$3.0^{+0.4}_{-0.3}$	$0.00^{+0.05}_{-0.00}$	1.0		87.0
				you	$19.3^{+2.7}_{-2.7}$	10^{+1}_{-1}	$3.61^{+0.09}_{-0.08}$	1.0	35^{+5}_{-5}	
			$9.9^{+0.1}_{-0.1}$	old	218^{+48}_{-116}	$3.0^{+0.5}_{-0.4}$	$0.00^{+0.05}_{-0.00}$	1.0		13.0
				you	$19.7^{+2.6}_{-2.6}$	22^{+9}_{-5}	$3.34^{+0.08}_{-0.09}$	1.0	32^{+9}_{-6}	
MIPS0000671_1	0.67	yes	$10.4^{+0.1}_{-0.1}$	old	131^{+122}_{-35}	$5.1^{+1.1}_{-1.0}$	$0.01^{+0.07}_{-0.01}$	1.0		79.0
				you	$15.9^{+1.9}_{-1.7}$	200^{+24}_{-22}	$0.50^{+0.05}_{-0.05}$	1.0	60^{+1}_{-4}	
			$10.4^{+0.1}_{-0.1}$	old	104^{+24}_{-14}	$3.7^{+2.4}_{-0.9}$	$0.01^{+0.07}_{-0.01}$	1.0		21.0
				you	$15.8^{+2.0}_{-1.6}$	99^{+13}_{-11}	$0.53^{+0.08}_{-0.07}$	1.0	40^{+20}_{-5}	
		no	$10.4^{+0.1}_{-0.1}$	old	195^{+38}_{-77}	$5.1^{+0.8}_{-0.6}$	$0.01^{+0.06}_{-0.01}$	1.0		100.0
				you	$15.9^{+2.0}_{-1.8}$	201^{+28}_{-23}	$0.50^{+0.05}_{-0.05}$	1.0	60^{+1}_{-1}	

Table 5.1 (cont'd)

Galaxy	z†	FIR	$\log M$ [$M_\odot$]	Pop.	τ old [Myr] you [Gyr]	Age old [Gyr] you [Myr]	$A(V)$ [mag]	Z [$Z_\odot$]	b [%]	Prob. [%]
(1)	(2)	(3)	(4)	(5)	(6)	(7)	(8)	(9)	(10)	(11)
MIPS0000700_1	0.8210†	yes	$11.0^{+0.1}_{-0.1}$	old	198^{+60}_{-71}	$2.9^{+0.4}_{-0.5}$	$0.00^{+0.06}_{-0.00}$	1.0		67.7
				you	$17.4^{+3.4}_{-2.7}$	94^{+13}_{-15}	$2.10^{+0.05}_{-0.06}$	1.0	15^{+1}_{-1}	
			$11.0^{+0.1}_{-0.1}$	old	159^{+99}_{-50}	$2.9^{+0.7}_{-0.8}$	$0.04^{+0.08}_{-0.04}$	1.0		32.3
				you	$17.5^{+3.4}_{-2.6}$	235^{+84}_{-48}	$1.99^{+0.06}_{-0.07}$	1.0	27^{+8}_{-3}	
		no	$10.9^{+0.1}_{-0.1}$	old	136^{+28}_{-20}	$2.3^{+0.9}_{-0.4}$	$0.10^{+0.05}_{-0.05}$	1.0		100.0
				you	$18.0^{+3.2}_{-3.0}$	6^{+1}_{-1}	$2.94^{+0.08}_{-0.07}$	1.0	10^{+1}_{-1}	
MIPS0000701_1	0.8052†	yes	$10.7^{+0.1}_{-0.1}$	old	235^{+40}_{-96}	$2.1^{+0.8}_{-0.3}$	$0.02^{+0.07}_{-0.02}$	1.0		80.7
				you	$18.7^{+3.0}_{-3.1}$	10^{+2}_{-1}	$1.68^{+0.07}_{-0.08}$	1.0	11^{+2}_{-1}	
			$10.4^{+0.1}_{-0.1}$	old	218^{+51}_{-110}	$3.9^{+0.9}_{-1.0}$	$0.01^{+0.07}_{-0.01}$	1.0		19.3
				you	$16.0^{+2.3}_{-1.9}$	44^{+12}_{-11}	$1.60^{+0.05}_{-0.06}$	1.0	60^{+1}_{-3}	
		no	$10.6^{+0.1}_{-0.1}$	old	250^{+32}_{-28}	$2.0^{+0.3}_{-0.2}$	$0.01^{+0.07}_{-0.01}$	1.0		100.0
				you	$16.6^{+3.3}_{-2.0}$	6^{+1}_{-1}	$2.40^{+0.05}_{-0.05}$	1.0	40^{+1}_{-5}	
MIPS0000773	0.80	yes	$10.8^{+0.1}_{-0.1}$	old	208^{+51}_{-65}	$2.0^{+0.2}_{-0.2}$	$0.01^{+0.07}_{-0.01}$	1.0		100.0
				you	$18.2^{+3.3}_{-3.1}$	53^{+20}_{-17}	$3.51^{+0.10}_{-0.09}$	1.0	40^{+6}_{-9}	
		no	$10.8^{+0.1}_{-0.1}$	old	189^{+67}_{-54}	$2.0^{+0.3}_{-0.2}$	$0.06^{+0.09}_{-0.06}$	1.0		70.0
				you	$17.9^{+3.4}_{-3.1}$	56^{+27}_{-20}	$3.34^{+0.12}_{-0.08}$	1.0	30^{+8}_{-9}	
			$10.7^{+0.1}_{-0.1}$	old	201^{+57}_{-60}	$2.0^{+0.2}_{-0.2}$	$0.12^{+0.08}_{-0.09}$	1.0		30.0
				you	$16.8^{+3.3}_{-2.1}$	9^{+1}_{-1}	$3.80^{+0.21}_{-0.18}$	1.0	20^{+5}_{-5}	
MIPS0000904_3	1.16	yes	$10.5^{+0.1}_{-0.1}$	old	149^{+24}_{-30}	$1.0^{+0.1}_{-0.1}$	$0.01^{+0.07}_{-0.01}$	1.0		100.0
				you	$18.3^{+3.2}_{-3.2}$	17^{+7}_{-3}	$3.87^{+0.25}_{-0.27}$	1.0	51^{+5}_{-4}	
		no	$10.7^{+0.1}_{-0.1}$	old	112^{+23}_{-18}	$1.0^{+0.1}_{-0.1}$	$0.66^{+0.13}_{-0.14}$	1.0		100.0
				you	$17.9^{+3.3}_{-2.8}$	2^{+1}_{-1}	$4.11^{+0.09}_{-0.10}$	1.0	51^{+5}_{-5}	
MIPS0000922_1	0.8068†	yes	$10.9^{+0.1}_{-0.1}$	old	202^{+61}_{-103}	$2.9^{+1.5}_{-0.9}$	$1.46^{+0.07}_{-0.13}$	1.0		72.7
				you	$17.5^{+3.4}_{-2.8}$	396^{+76}_{-75}	$2.20^{+0.08}_{-0.08}$	1.0	59^{+2}_{-8}	
			$10.9^{+0.1}_{-0.1}$	old	232^{+40}_{-83}	$2.0^{+0.2}_{-0.2}$	$1.09^{+0.11}_{-0.13}$	1.0		15.6
				you	$19.3^{+3.1}_{-2.6}$	81^{+21}_{-22}	$2.31^{+0.07}_{-0.06}$	1.0	20^{+2}_{-5}	
			$10.9^{+0.1}_{-0.1}$	old	232^{+42}_{-115}	$2.0^{+0.2}_{-0.2}$	$1.47^{+0.06}_{-0.09}$	1.0		11.7
				you	$19.2^{+2.6}_{-3.2}$	201^{+38}_{-22}	$2.29^{+0.06}_{-0.07}$	1.0	40^{+10}_{-9}	
		no	$10.5^{+0.1}_{-0.1}$	old	175^{+51}_{-42}	$2.0^{+0.2}_{-0.2}$	$0.17^{+0.11}_{-0.10}$	1.0		100.0
				you	$16.3^{+2.6}_{-2.0}$	8^{+1}_{-1}	$3.18^{+0.10}_{-0.10}$	1.0	35^{+5}_{-5}	
MIPS0001032_1	1.14	yes	$10.3^{+0.1}_{-0.1}$	old	127^{+35}_{-26}	$1.0^{+0.1}_{-0.1}$	$0.01^{+0.07}_{-0.01}$	1.0		100.0
				you	$19.1^{+2.9}_{-3.2}$	22^{+5}_{-6}	$2.52^{+0.08}_{-0.06}$	1.0	60^{+2}_{-9}	
		no	$10.7^{+0.1}_{-0.1}$	old	151^{+100}_{-45}	$1.0^{+0.1}_{-0.1}$	$1.47^{+0.07}_{-0.12}$	1.0		100.0
				you	$17.8^{+3.4}_{-2.8}$	3^{+1}_{-1}	$3.23^{+0.10}_{-0.08}$	1.0	34^{+6}_{-5}	

Table 5.1 (cont'd)

Galaxy	z†	FIR	$\log M$ $[M_\odot]$	Pop.	τ old [Myr] you [Gyr]	Age old [Gyr] you [Myr]	$A(V)$ [mag]	Z $[Z_\odot]$	b [%]	Prob. [%]
(1)	(2)	(3)	(4)	(5)	(6)	(7)	(8)	(9)	(10)	(11)
MIPS0001045_1	0.80	yes	$11.1^{+0.1}_{-0.1}$	old	166^{+59}_{-26}	$3.1^{+0.6}_{-0.4}$	$0.30^{+0.12}_{-0.10}$	1.0		81.6
				you	$18.8^{+2.9}_{-3.2}$	81^{+16}_{-15}	$2.60^{+0.07}_{-0.08}$	1.0	15^{+1}_{-4}	
			$11.2^{+0.1}_{-0.1}$	old	162^{+40}_{-28}	$3.2^{+1.0}_{-0.5}$	$0.26^{+0.10}_{-0.17}$	1.0		18.4
				you	$18.9^{+3.0}_{-3.7}$	211^{+83}_{-30}	$2.51^{+0.09}_{-0.09}$	1.0	26^{+5}_{-2}	
		no	$10.9^{+0.1}_{-0.1}$	old	190^{+54}_{-58}	$2.0^{+0.3}_{-0.2}$	$0.03^{+0.09}_{-0.03}$	1.0		51.5
				you	$18.0^{+3.3}_{-2.9}$	54^{+23}_{-20}	$2.82^{+0.07}_{-0.06}$	1.0	21^{+6}_{-6}	
			$10.9^{+0.1}_{-0.1}$	old	224^{+45}_{-62}	$2.0^{+0.3}_{-0.2}$	$0.18^{+0.32}_{-0.15}$	1.0		48.5
				you	$17.6^{+3.4}_{-2.8}$	8^{+1}_{-2}	$3.39^{+0.15}_{-0.19}$	1.0	15^{+5}_{-5}	
MIPS0001162_1	1.2700†	yes	$11.1^{+0.1}_{-0.2}$	old	236^{+37}_{-81}	$2.2^{+0.9}_{-0.4}$	$0.10^{+0.19}_{-0.10}$	1.0		94.3
				you	$17.5^{+3.4}_{-2.7}$	11^{+5}_{-2}	$2.20^{+0.09}_{-0.09}$	1.0	15^{+13}_{-4}	
			$10.9^{+0.1}_{-0.1}$	old	227^{+42}_{-73}	$3.2^{+0.8}_{-0.6}$	$0.01^{+0.09}_{-0.01}$	1.0		5.7
				you	$16.6^{+2.0}_{-2.0}$	43^{+10}_{-6}	$2.11^{+0.05}_{-0.05}$	1.0	60^{+2}_{-5}	
		no	$11.0^{+0.1}_{-0.1}$	old	251^{+30}_{-29}	$2.0^{+0.3}_{-0.2}$	$0.00^{+0.05}_{-0.00}$	1.0		67.4
				you	$18.0^{+3.4}_{-2.8}$	78^{+15}_{-15}	$2.00^{+0.05}_{-0.05}$	1.0	52^{+6}_{-8}	
			$10.9^{+0.1}_{-0.1}$	old	248^{+34}_{-30}	$2.0^{+0.3}_{-0.2}$	$0.03^{+0.09}_{-0.03}$	1.0		32.6
				you	$18.8^{+2.8}_{-3.1}$	9^{+1}_{-1}	$2.68^{+0.07}_{-0.17}$	1.0	56^{+5}_{-25}	
MIPS0001164_1	1.12	yes	$9.9^{+0.1}_{-0.1}$	old	129^{+38}_{-24}	$1.0^{+0.1}_{-0.1}$	$0.06^{+0.26}_{-0.06}$	1.0		100.0
				you	$18.2^{+3.3}_{-3.1}$	10^{+1}_{-1}	$2.60^{+0.06}_{-0.07}$	1.0	56^{+5}_{-10}	
		no	$10.3^{+0.1}_{-0.1}$	old	181^{+68}_{-47}	$1.0^{+0.2}_{-0.1}$	$1.44^{+0.08}_{-0.14}$	1.0		93.5
				you	$17.0^{+3.4}_{-2.3}$	4^{+1}_{-1}	$3.00^{+0.10}_{-0.13}$	1.0	30^{+6}_{-6}	
			$9.9^{+0.1}_{-0.1}$	old	116^{+27}_{-23}	$1.0^{+0.1}_{-0.1}$	$0.04^{+0.09}_{-0.04}$	1.0		6.5
				you	$19.3^{+2.6}_{-2.9}$	11^{+12}_{-1}	$2.58^{+0.06}_{-0.27}$	1.0	60^{+1}_{-1}	
MIPS0001212	0.71	yes	$10.5^{+0.1}_{-0.1}$	old	245^{+32}_{-41}	$3.0^{+0.4}_{-0.3}$	$0.00^{+0.06}_{-0.00}$	1.0		87.4
				you	$19.5^{+2.5}_{-2.8}$	9^{+1}_{-1}	$3.22^{+0.09}_{-0.09}$	1.0	22^{+4}_{-2}	
			$10.7^{+0.1}_{-0.1}$	old	247^{+35}_{-28}	$3.0^{+0.3}_{-0.4}$	$0.30^{+0.08}_{-0.09}$	1.0		12.6
				you	$16.3^{+3.2}_{-1.8}$	2^{+1}_{-1}	$3.21^{+0.07}_{-0.06}$	1.0	11^{+1}_{-1}	
		no	$10.5^{+0.1}_{-0.1}$	old	104^{+97}_{-14}	$3.0^{+0.4}_{-0.3}$	$0.00^{+0.05}_{-0.00}$	1.0		90.2
				you	$17.6^{+3.3}_{-2.7}$	44^{+18}_{-13}	$2.79^{+0.06}_{-0.07}$	1.0	33^{+11}_{-8}	
			$10.5^{+0.1}_{-0.1}$	old	104^{+74}_{-12}	$3.0^{+0.5}_{-0.4}$	$0.00^{+0.04}_{-0.00}$	1.0		9.8
				you	$18.4^{+3.3}_{-3.0}$	10^{+2}_{-1}	$3.15^{+0.12}_{-0.16}$	1.0	21^{+5}_{-5}	

Table 5.1 (cont'd)

Galaxy	z†	FIR	$\log M$ [$M_\odot$]	Pop.	τ old [Myr] you [Gyr]	Age old [Gyr] you [Myr]	$A(V)$ [mag]	Z [$Z_\odot$]	b [%]	Prob. [%]
(1)	(2)	(3)	(4)	(5)	(6)	(7)	(8)	(9)	(10)	(11)
MIPS0001225	0.8701†	yes	$10.5^{+0.1}_{-0.1}$	old	243^{+34}_{-38}	$2.0^{+0.3}_{-0.2}$	$0.03^{+0.12}_{-0.03}$	1.0		59.8
				you	$19.4^{+2.6}_{-3.0}$	10^{+1}_{-1}	$2.52^{+0.09}_{-0.08}$	1.0	25^{+2}_{-5}	
			$10.7^{+0.1}_{-0.1}$	old	247^{+32}_{-36}	$2.0^{+0.3}_{-0.2}$	$0.20^{+0.11}_{-0.10}$	1.0		40.2
				you	$17.5^{+3.4}_{-2.5}$	2^{+1}_{-1}	$2.51^{+0.08}_{-0.08}$	1.0	10^{+1}_{-1}	
		no	$10.6^{+0.1}_{-0.1}$	old	252^{+30}_{-27}	$2.0^{+0.2}_{-0.2}$	$0.28^{+0.09}_{-0.10}$	1.0		95.9
				you	$18.1^{+3.3}_{-3.0}$	4^{+1}_{-1}	$3.08^{+0.06}_{-0.09}$	1.0	31^{+5}_{-10}	
			$10.5^{+0.1}_{-0.1}$	old	249^{+34}_{-23}	$2.0^{+0.2}_{-0.2}$	$0.00^{+0.06}_{-0.00}$	1.0		4.1
				you	$19.9^{+1.9}_{-3.0}$	27^{+16}_{-11}	$2.11^{+0.13}_{-0.06}$	1.0	17^{+9}_{-2}	
MIPS0001300_1	0.95	yes	$10.4^{+0.1}_{-0.1}$	old	231^{+40}_{-42}	$2.0^{+0.3}_{-0.2}$	$0.51^{+0.13}_{-0.24}$	1.0		100.0
				you	$19.0^{+2.8}_{-2.9}$	71^{+21}_{-20}	$3.03^{+0.12}_{-0.08}$	1.0	46^{+10}_{-10}	
		no	$10.4^{+0.1}_{-0.1}$	old	235^{+38}_{-39}	$2.0^{+0.2}_{-0.2}$	$0.05^{+0.10}_{-0.05}$	1.0		76.6
				you	$17.6^{+3.3}_{-2.8}$	63^{+24}_{-21}	$3.05^{+0.09}_{-0.08}$	1.0	45^{+7}_{-10}	
			$10.3^{+0.1}_{-0.1}$	old	244^{+36}_{-35}	$2.0^{+0.3}_{-0.2}$	$0.07^{+0.11}_{-0.07}$	1.0		23.4
				you	$17.9^{+3.2}_{-2.9}$	9^{+1}_{-1}	$3.55^{+0.16}_{-0.13}$	1.0	26^{+9}_{-4}	
MIPS0001324_1	0.72	yes	$11.1^{+0.1}_{-0.1}$	old	102^{+16}_{-12}	$6.0^{+0.7}_{-0.7}$	$1.48^{+0.06}_{-0.08}$	1.0		85.2
				you	$19.1^{+2.9}_{-3.0}$	418^{+75}_{-55}	$2.37^{+0.08}_{-0.11}$	1.0	60^{+1}_{-4}	
			$11.3^{+0.1}_{-0.1}$	old	115^{+130}_{-21}	$4.9^{+1.3}_{-1.9}$	$1.50^{+0.05}_{-0.06}$	1.0		14.8
				you	$19.9^{+2.2}_{-2.1}$	74^{+15}_{-16}	$2.37^{+0.06}_{-0.08}$	1.0	10^{+1}_{-1}	
		no	$10.4^{+0.1}_{-0.1}$	old	238^{+36}_{-89}	$3.0^{+0.5}_{-0.4}$	$0.04^{+0.09}_{-0.04}$	1.0		100.0
				you	$19.7^{+2.5}_{-2.4}$	15^{+2}_{-2}	$2.80^{+0.05}_{-0.06}$	1.0	56^{+4}_{-2}	
MIPS0001585_1	0.92	yes	$10.8^{+0.1}_{-0.1}$	old	169^{+51}_{-36}	$3.2^{+1.0}_{-0.6}$	$0.17^{+0.09}_{-0.11}$	1.0		75.3
				you	$16.6^{+3.3}_{-2.0}$	51^{+17}_{-15}	$2.50^{+0.06}_{-0.05}$	1.0	20^{+5}_{-6}	
			$10.8^{+0.1}_{-0.1}$	old	167^{+38}_{-24}	$3.0^{+0.7}_{-0.4}$	$0.19^{+0.06}_{-0.09}$	1.0		24.7
				you	$19.4^{+2.8}_{-2.9}$	20^{+3}_{-4}	$2.60^{+0.06}_{-0.07}$	1.0	11^{+1}_{-1}	
		no	$10.6^{+0.1}_{-0.1}$	old	154^{+28}_{-34}	$2.0^{+0.3}_{-0.2}$	$0.18^{+0.09}_{-0.08}$	1.0		100.0
				you	$16.4^{+2.9}_{-2.0}$	7^{+1}_{-1}	$3.39^{+0.06}_{-0.07}$	1.0	35^{+4}_{-4}	

Note. — Results for the two stellar population modeling of the SEDs of our sample of IR-bright galaxies. The different clusters identified for each galaxy are shown. The use of the FIR prior is specified. Median and 1σ error values are shown for each parameter derived with the Synthesizer code. (1) Name of the galaxy. (2) Photometric or spectroscopic redshift ($z_{\rm spec}$ indicated by a †). (3) Use of the FIR prior. (4) Stellar mass (in solar units) and its uncertainty derived from the logarithmic space. (5) Parameter values for the old or the young population. (6) e-folding time and its uncertainty (old population in Myr and young population in Gyr). (7) Age and its uncertainty (old population in Gyr and young population in Myr). (8) Extinction in the V-band and its uncertainty in mag. (9) Metallicity value (fixed to the solar value) in solar units. (10) Burst intensity fraction and its uncertainty in percentage. (11) Statistical significance of this solution (in %).

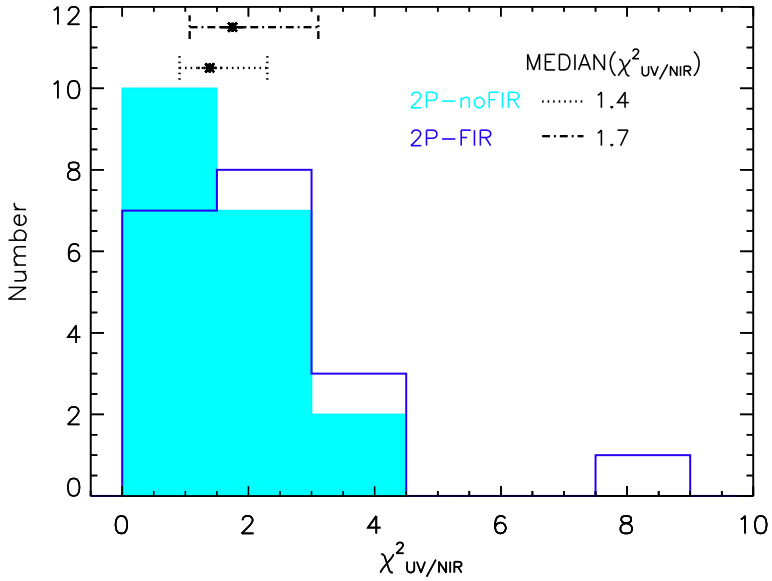

Figure 5.2 : Distributions of $\chi^2_{\rm UV/MIR}$ values obtained evaluating the UV-to-MIR spectral range for both 2P models. *Filled cyan:* Results from the 2P models without FIR information. *Open blue:* Results from 2P models using the FIR prior. The median values and the 16 and 84-percentile of the distributions are indicated.

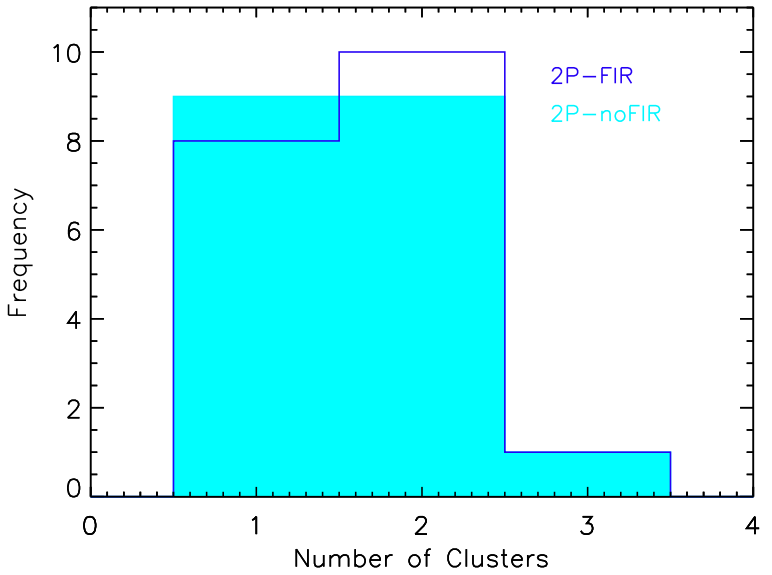

Figure 5.3 : Distribution of the number of clusters of solutions identified for each object using 2P models with *(open blue histogram)* and without *(filled cyan histogram)* the FIR prior for our sample of IR-bright galaxies.

In Figure 5.3, we show the distributions of the number of clusters identified for the

2P models with and without the FIR prior. Typically, $1-2$ clusters were identified for both cases, and there is one galaxy with 3 clusters recognized in both sets too. The distributions for both cases are similar, which suggests that the values of $t_{\rm you}$ are dominant in the identification of the clusters, given that $t_{\rm you}/\tau_{\rm you} \ll 1$, for both sets of models.

In Figure 5.4, we present the distributions of significance level for the 2P models with and without the FIR photometry. We have estimated the median values and the 16 and 84-percentile for both cases, obtaining $87^{+13}_{-14}\%$ when using the FIR constraint, and $96^{+4}_{-29}\%$ without consider the FIR data. Therefore, the median values are compatible, but the distribution of 2P models without the FIR prior shows a tail towards solution with significance level less than 50%. This tail suggests that FIR constraint aids to select a cluster of solutions when galaxies present the age-dust degeneracy.

Regarding the case using the FIR prior, for those galaxies with 2 and 3 clusters of solutions, the dominant solution has a median significance of 79%, with the lowest value being 60%. Respecting the case of omitting the FIR data, those galaxies with more than one cluster have a median significance of 74%, with 3 models obtaining 40–60%. Obviously, in the galaxies with only one cluster identified, the significance is 100%.

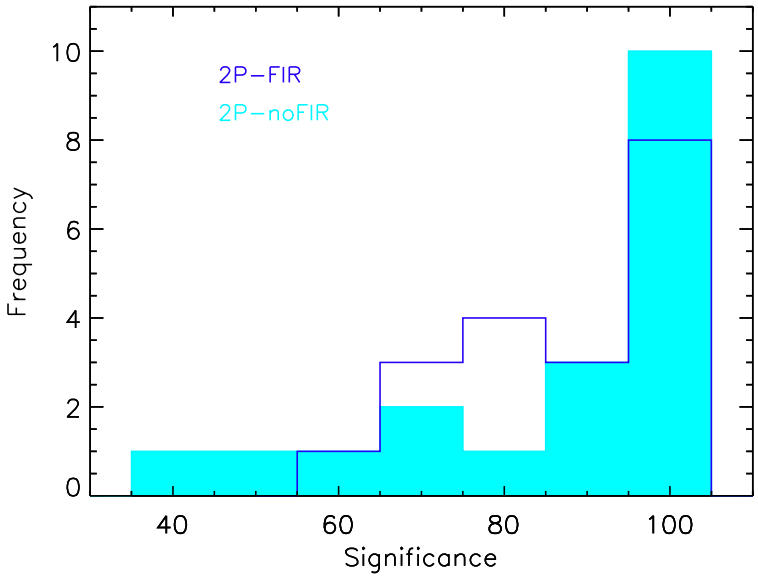

Figure 5.4 : Distribution of significance level of the clusters of solutions identified for each object using 2P models with *(blue open)* and without *(cyan filled)* the FIR prior for our sample of IR-bright galaxies.

We now show two examples of the results of the Monte Carlo simulation runs for the

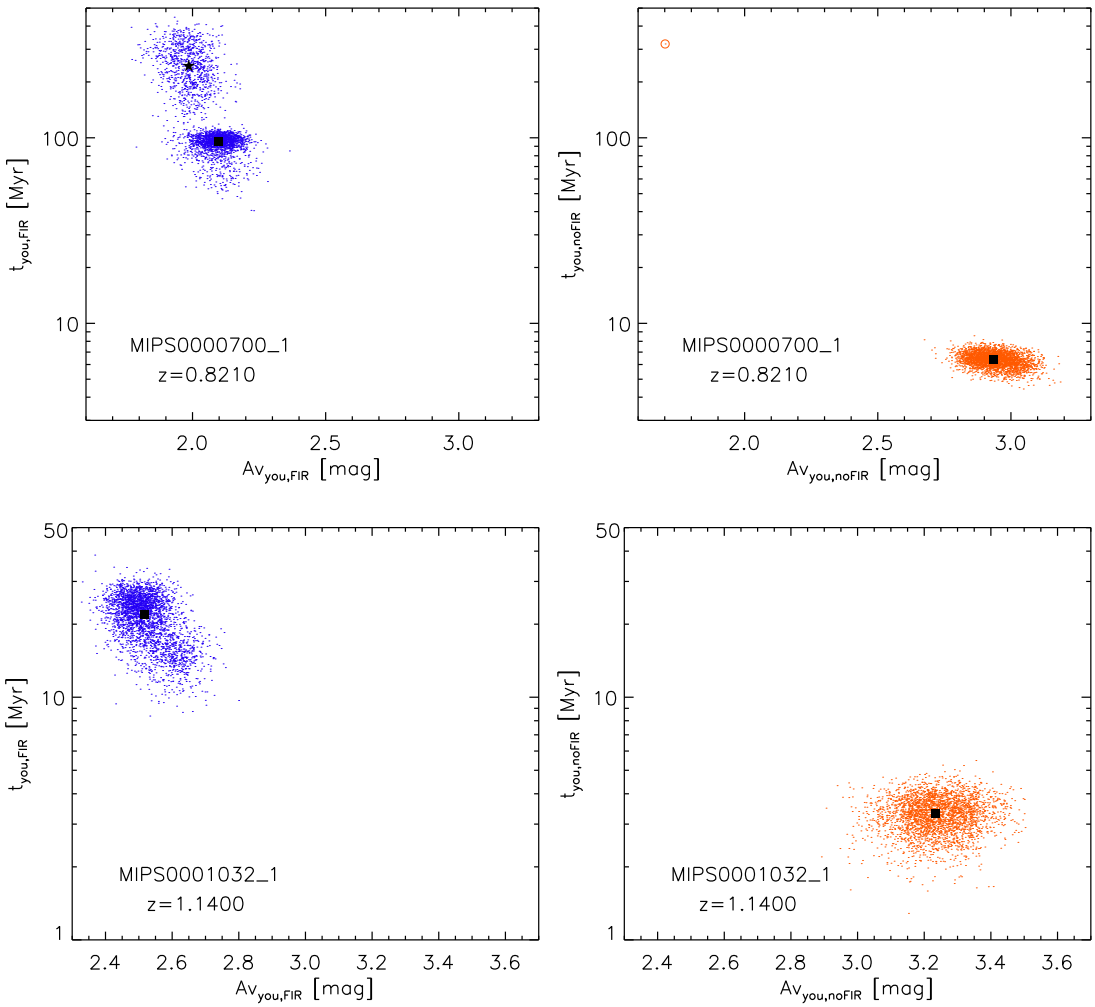

Figure 5.5 : Two examples (one per row) of the plane attenuation-age of the young population from the results of the Monte Carlo simulations for 2P models with *(left panels)* and without *(right panels)* the FIR prior of our sample of IR-bright galaxies. Each dot represents a solution from the 3000 iterations shown in each panel. The median solution for the most significant cluster is marked with a *filled black square* in each panel. When several clusters are identified the secondary solutions are marked with a *filled black star*. The open orange circle is displayed for denoting that there is a solution with $A(V)_{\rm you} \simeq 1.6$ mag and $t_{\rm you} \simeq 200$ Myr in the top right panel.

2P models with and without the FIR prior in Fig. 5.5. With regard to MIPS0000700_1, we observe for the FIR prior case that the attenuation values are in $1.70 < A(V)_{\rm you,FIR} < 2.30$ mag, and that there are two clusters differentiated mostly in the young age, the significant one with $t_{\rm you,FIR} \simeq 100$ Myr and $A(V)_{\rm you,FIR} \simeq 2.1$ mag, and a secondary one where $t_{\rm you,FIR} \simeq 230$ Myr and $A(V)_{\rm you,FIR} \simeq 2.0$ mag. When the FIR data are missing, we notice that the attenuation values are in $1.90 < A(V)_{\rm you,noFIR} < 3.30$ mag, and that the young ages concentrate mainly in $4 < t_{\rm you,noFIR} < 9$ Myr, with only one cluster

identified where $A(V)_{\rm you,noFIR} \simeq 2.9$ mag and $t_{\rm you,noFIR} \simeq 6$ Myr. Hence, we have and overestimation of the attenuation of ~ 0.9 mag, and an underestimation of the young population age in a factor larger than 10, if the FIR information is absent.

With respect to MIPS0001032_1, both modeling cases result with a cluster, but with different values of attenuation and age. The median value pairs are $A(V)_{\rm you,FIR} \simeq 2.5$ mag, with $t_{\rm you,FIR} \simeq 23$ Myr when using the FIR prior, and $A(V)_{\rm you,noFIR} \simeq 3.2$ mag, with $t_{\rm you,noFIR} \simeq 3$ Myr when excluding the FIR photometry. Then, the difference in attenuation is ~ 0.7 mag, and the age is smaller in a factor near to 8 without the FIR constraint.

Both examples evidence clearly that the attenuation and the age are degenerated for both 2P cases. The colors of the young stellar spectra are beguiled to a younger and more attenuated population, if the FIR prior is unavailable. Therefore, we can stay that the presence of FIR data certainly aids in breaking the age-dust degeneracy.

5.1.2 Comparison of Stellar Masses from both 2P Models

Now we turn to compare the stellar masses derived with the 2P models with and without the FIR prior generated using the Synthesizer code. In Figure 5.6, we present the stellar mass values determined with both set of models and their ratios.

The stellar masses estimated when the FIR information is available are in $7.9 \times 10^9 < M_{*,\rm 2P-FIR}/M_\odot < 1.4 \times 10^{11}$, with median, and the 16 and 84-percentile of $5.2^{+4.4}_{-2.7} \times 10^{10} M_\odot$, and a median uncertainty of 0.06 dex. The stellar masses obtained when the FIR data are omitted range in $7.6 \times 10^9 < M_{*,\rm 2P-noFIR}/M_\odot < 1.1 \times 10^{11}$, with median value, and the 16 and 84-percentile of $3.8^{+2.8}_{-1.3} \times 10^{10} M_\odot$, and a median uncertainty of 0.06 dex. For 8 galaxies (42% of the sample) the stellar masses determined with the FIR prior are larger than those derived without the FIR constraint.

In the lower panel of Fig. 5.6, we show the ratio between the stellar masses derived with the models when the FIR photometry is omitted and our fiducial set of models. On median, stellar masses estimated with the 2P-FIR models are 10% larger than those obtained with 2P-noFIR models. The ratio values are in $0.2 \leq M_{*,\rm 2P-noFIR}/M_{*,\rm 2P-FIR} < 2.7$, considering their propagated uncertainties, 47% of the objects have obtained a similar stellar mass values from the solutions of each case.

Attending to this lower panel, we observe 2 galaxies with ratio values greater than 2, and 2 objects with $M_{*,\rm 2P-noFIR}/M_{*,\rm 2P-FIR} < 0.5$. When comparing both sets of models, we notice that the solutions for these objects exhibit a significant change in the attenuation of the old population (see Fig. 5.7). With respect to the galaxies with ratio above 2, the attenuation values are $A(V)_{\rm old,FIR} \simeq 0$, and $A(V)_{\rm old,noFIR} \simeq 1.5$ mag. The

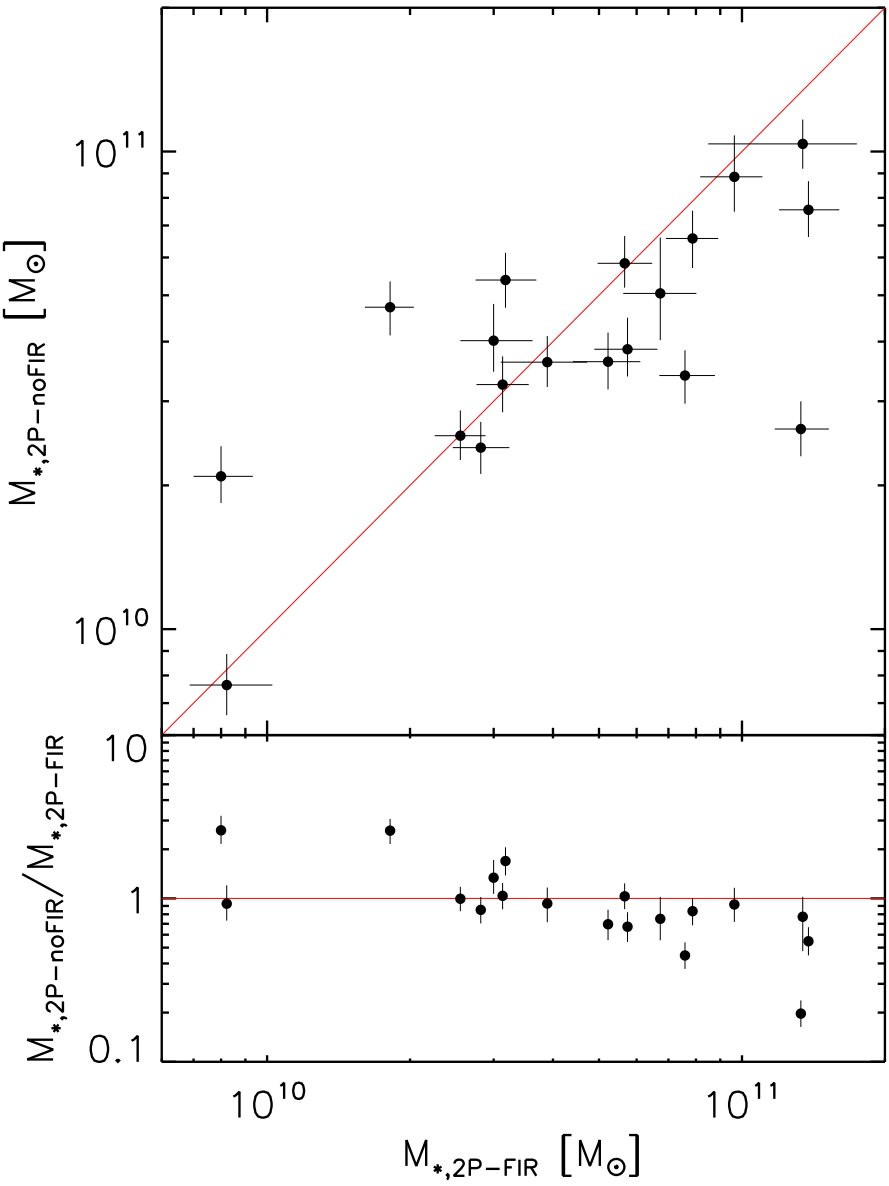

Figure 5.6 : *Upper panel:* Comparison between the stellar masses (M_*) derived with the 2P models using the FIR prior on x-axis, and those derived from the 2P models without the FIR constraint on y-axis, both estimated with the Synthesizer code. The filled circles with error bars show the median values and the 1σ uncertainties. *Lower panel:* Ratio of the stellar masses derived with both set of models. The error bars show the propagated uncertainties.

attenuation values for the case omitting the FIR information result on higher values of intrinsic luminosity, and consequently higher stellar masses are estimated for this case.

Regarding the objects with ratio below 0.5, the attenuation values are $A(V)_{\rm old,FIR} \simeq 1.5$, and $A(V)_{\rm old,noFIR} \simeq 0$. In addition to the higher attenuations for these models using the FIR prior, their associated young ages are $\simeq 400$ Myr, such timescale is large

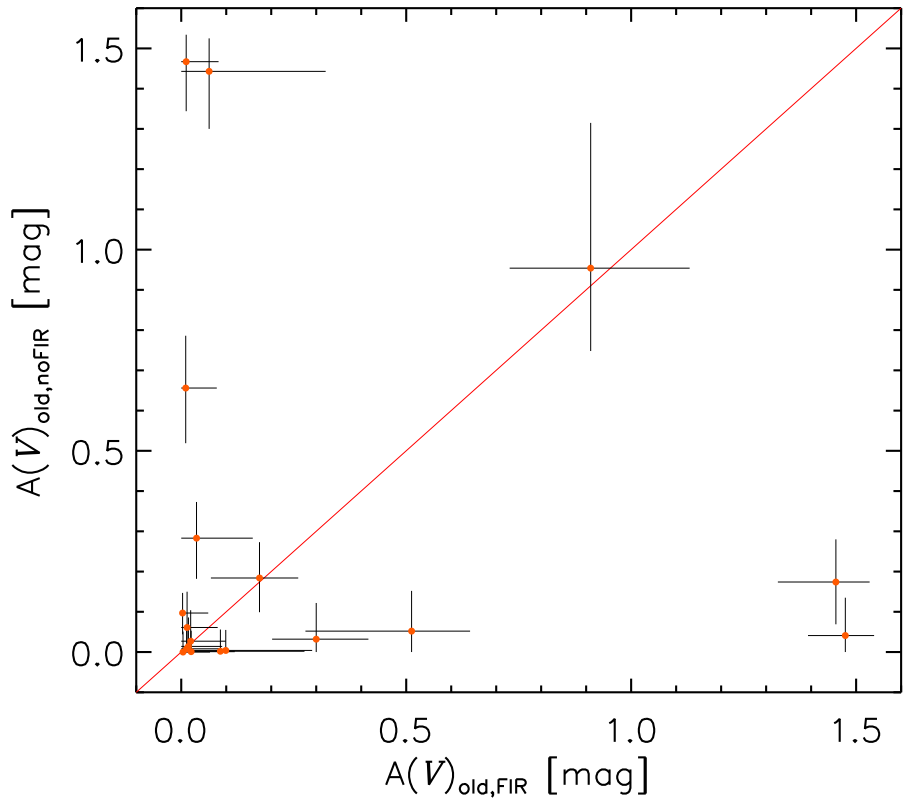

Figure 5.7 : Comparison between the attenuations of the old population of the 2P models using the FIR prior, $A(V)_{\rm you,FIR}$, on x-axis, and the attenuations of the 2P models without the FIR prior, $A(V)_{\rm you,noFIR}$, on y-axis, both derived with the Synthesizer code. The filled circles with error bars show the median values and the 1σ uncertainties.

enough to form stars which contribute with a considerable flux to the longer wavelength optical and NIR bands. The combination of these two effects produce stellar mass values which are higher for this modeling case.

Having estimated the stellar masses, we move to compare the mass weighted ages determined with and without the FIR constraint that we show in Fig. 5.8. The mass weighted age is defined as:

$$t_M = \frac{\int_0^{t_{\rm old}} t \cdot SFR(t)\ {\rm d}t}{\int_0^{t_{\rm old}} SFR(t)\ {\rm d}t}, \tag{5.2}$$

The values estimated using the solutions with FIR information are in $0.3 < t_{M,\rm FIR} < 3.2$ Gyr, with a median value, and the 16 and 84-percentile of $1.6^{+0.8}_{-0.6}$ Gyr. The results derived omitting the FIR data are in $0.4 < t_{M,\rm noFIR} < 2.9$ Gyr, with a median value, and the 16 and 84-percentile of $1.2^{+0.7}_{-0.3}$ Gyr. Hence, the two sets of models inspect

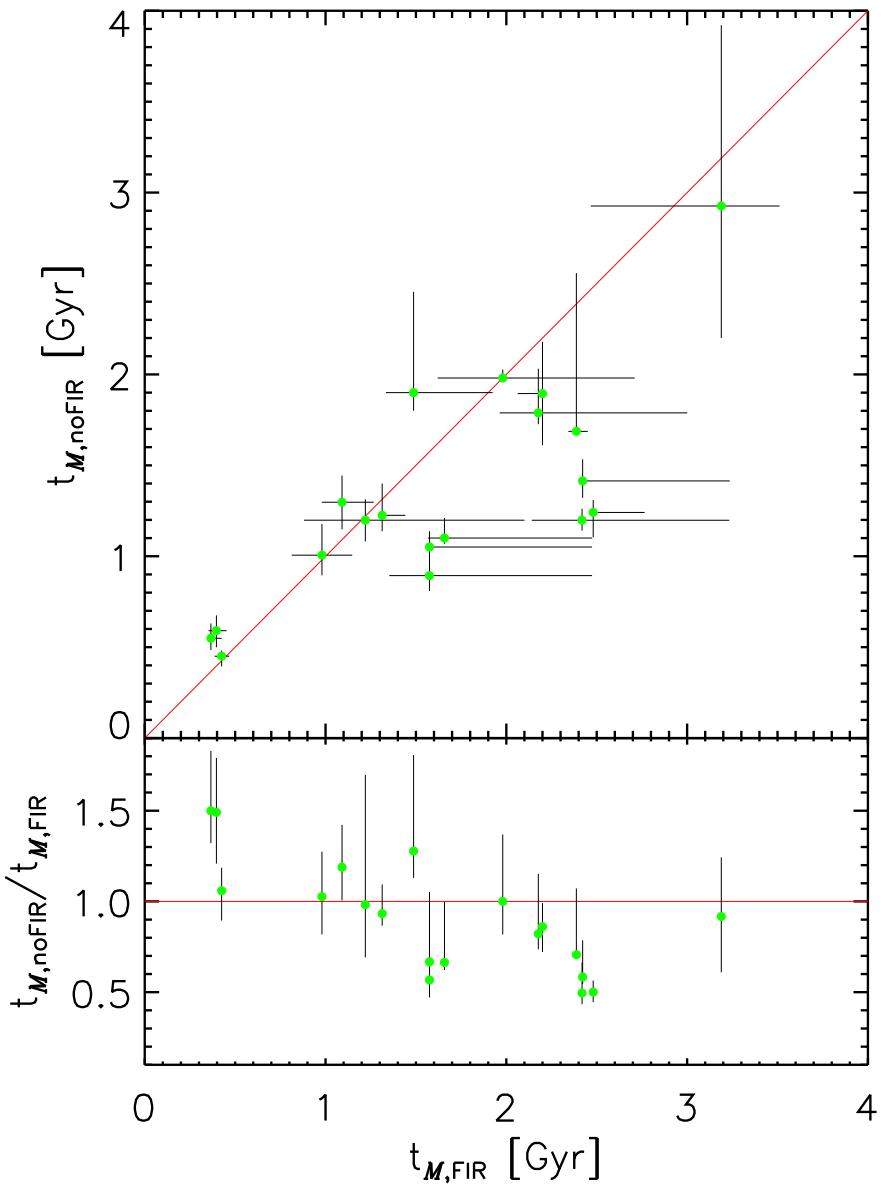

Figure 5.8 : *Upper panel:* Comparison between the mass weighted ages (t_M) derived with 2P models using the FIR prior on x-axis, and those derived with 2P without the FIR constraint on y-axis, both estimated with the Synthesizer code. The filled circles with error bars show the median values and the 1σ uncertainties. *Lower panel:* Ratio of the mass weighted ages derived with both sets of models. The error bars show the propagated uncertainties.

comparable mass weighted age values.

The mass weighted age indicates the average age of the stellar populations which form a galaxy. Considering that the young ages for the case without the FIR prior are typically shorter than their respective values when using the FIR constraint, the moderate shift observed in the median for this modeling case is expected.

In the lower panel of Fig. 5.8, we show the ratio between the mass weighted ages derived from both sets of models, and their respective propagated uncertainties. The ratio values are in $0.4 < t_{M,\mathrm{noFIR}}/t_{M,\mathrm{FIR}} < 1.6$. Taking into account the propagated uncertainties, 47% of our galaxies have obtained a compatible value of mass weighted age from the results of each modeling case. Notwithstanding, considering that the precision in the determination of the mass values, a factor $2-3$ (see, e.g., Pérez-González et al. 2008), we appraise that the mass weighted age values from each set of models are in close agreement.

There are 2 galaxies with ratio ~ 1.5, but these sources present a mass ratio greater than 2. There are also 2 objects with ratio ~ 0.5, one of this objects has a mass ratio ~ 0.2, and the other shows a significant change in the age of the old population. Therefore, the differences in mass weighted age values between each case are originated mainly in variations on the results for the total stellar mass and the age of the old population.

5.1.3 Comparison of the SFRs from both 2P models and SFRs from observables

We compare now the SFR values based on SED fitting derived with the Synthesizer code (for the 2P models with and without the FIR prior) with SFR values based on a few observables, the FIR and UV emission ($SFR_{\mathrm{UV+IR}}$). In Figure 5.9, we have plotted such comparisons.

The $SFR_{\mathrm{UV+IR}}$ is determined from a linear combination of the unobscured UV luminosity, and the re-emitted FIR emission of recently formed stars. We use the recipe of Bell et al. (2005), which takes into account the unextinguished escaping photons in the UV, and the calibration for the total infrared luminosity of Kennicutt (1998). This calibration for a Salpeter (1955) initial mass function results in:

$$SFR_{\mathrm{UV+IR}}(M_{\odot}/\mathrm{yr}) = 1.8 \times 10^{-10}[3.3L(0.28) + L(\mathrm{TIR})]/L_{\odot}, \qquad (5.3)$$

where $L(0.28) = \nu L_{\nu}(0.28)$ is the monochromatic luminosity at 0.28 μm, and $L(\mathrm{TIR})$ is the integrated luminosity from 8 to 1000 μm. The $L(0.28)$ values are obtained by interpolating in the best-fitting synthetic template obtained from a trained set of the Rainbow Cosmological Surveys Database (see, e.g., Pérez-González et al. 2008; Barro et al. 2011a), and the $L(\mathrm{TIR})$ values are our $L_{\mathrm{TIR,ref}}$.

We have estimated the contribution of the unobscured UV luminosity to $SFR_{\mathrm{UV+IR}}$ for our sample and it is less than 5% on average. Considering the minimal contribution of the UV spectral part to our values of $SFR_{\mathrm{UV+IR}}$, the main source of uncertainty in these SFR estimations is originated by our $L_{\mathrm{TIR,ref}}$ calculations. When converting these

$\sigma_{L_{\rm TIR}}$ values (defined in Eq. 5.4) to uncertainties of $SFR_{\rm UV+IR}$ we obtain values lower than 0.05 dex, such $SFR_{\rm UV+IR}$ errors are shown in both panels of Fig. 5.9.

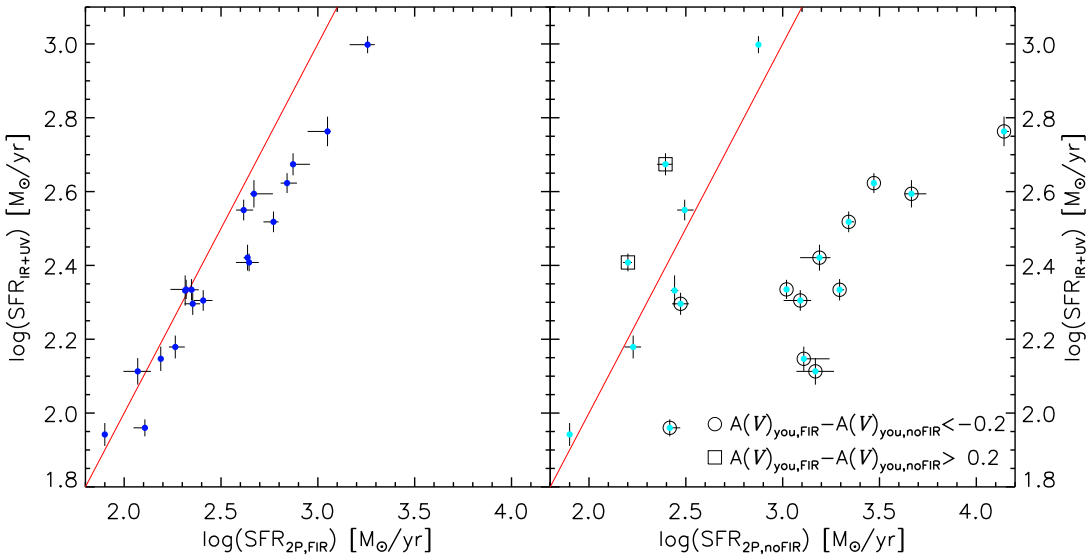

Figure 5.9 : *Left panel:* Comparison between the SFRs derived with 2P-FIR models and those derived with the observed FIR and UV (filled blue circles). *Right panel:* Comparison between the SFRs obtained with 2P-noFIR models and those determined with the observed FIR and UV (filled cyan circles). The filled symbols with error bars show the median values and the 1σ uncertainties derived from the logarithmic space. The open symbols denote objects with differences in the $A(V)_{\rm you}$ values as indicated in the legends.

The $SFR_{\rm UV+IR}$ values are in $1.94 < \log(SFR_{\rm UV+IR}) < 3.00$ dex with a median associated error of 0.03 dex, the median value and the 16 and 84-percentile are $2.33^{+0.29}_{-0.18}$ dex. The SFRs based on SED-fitting determined when using the FIR data are in $1.89 < \log(SFR_{\rm 2P,FIR}) < 3.26$ dex with a median uncertainty of 0.04 dex, the median, and the 16 and 84-percentile are $2.41^{+0.43}_{-0.22}$ dex. Outwardly from Fig. 5.9, it is clear that the $SFR_{\rm 2P,FIR}$ values are more similar to the $SFR_{\rm UV+IR}$ results than the $SFR_{\rm 2P,noFIR}$ values. The median difference between the $SFR_{\rm 2P,FIR}$ and $SFR_{\rm UV+IR}$ results is ~ 0.09 dex. There is a positive offset (~ 0.2 dex) for high $SFR_{\rm 2P,FIR}$ values compared with the $SFR_{\rm UV+IR}$ results. We will discuss about this offset in Chapter 6.

The SED-fit SFRs derived omitting the FIR data are in $1.89 < \log(SFR_{\rm 2P,noFIR}) < 4.15$ dex, with a median error of 0.04 dex, the median value, and the 16 and 84-percentile are $3.34^{+0.32}_{-0.63}$ dex. Considering that the SFRs of each set of models have changed when its respective values differ in 0.3 dex or more, for a considerable fraction, 58% of all galaxies, the SFRs derived without the FIR information are larger than those estimated considering the FIR constraint. On the other hand, for a small fraction, 16% of all sources, The SFRs determined with the FIR prior are larger that those ob-

tained without the FIR information. The median difference between the models without FIR data and our fiducial models is $\Delta(\log(SFR_{\rm 2P,noFIR}) - \log(SFR_{\rm 2P,FIR})) = 0.55$ dex, but differences for individual objects can reach values larger than 1 dex.

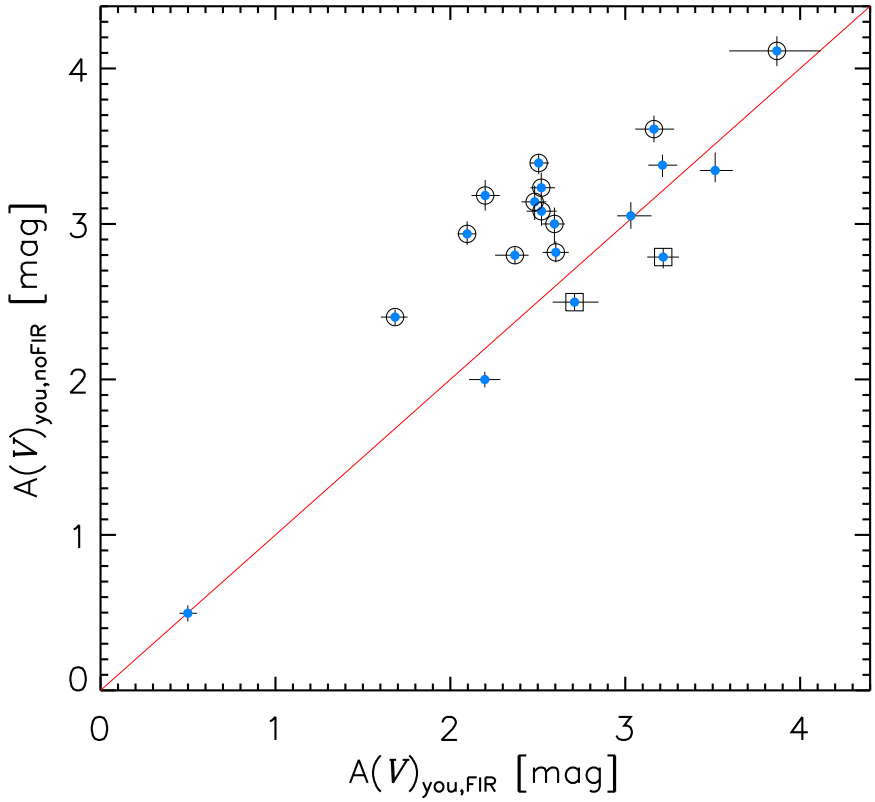

Figure 5.10 : Comparison between the attenuations of the young population of the 2P models using the FIR prior, $A(V)_{\rm you,FIR}$, on x-axis, and the attenuations of the 2P models without the FIR prior, $A(V)_{\rm you,noFIR}$, on y-axis, both derived with the Synthesizer code. The filled circles with error bars show the median values and the 1σ uncertainties. The *open circles* denote objects where $A(V)_{\rm you,FIR} - A(V)_{\rm you,noFIR} < -0.2$ mag, and the *open squares* indicate galaxies where $A(V)_{\rm you,FIR} - A(V)_{\rm you,noFIR} > 0.2$ mag.

To study the cause of the difference of SED-fit SFR values between the 2P cases, we show in Fig. 5.10 the scatter plot of the results of the attenuation in the V band for the young population determined from the 2P models with and without the usage of the FIR photometry. The solutions estimated using the FIR prior are in $0.49 < A(V)_{\rm you,FIR} < 3.87$ mag, with a median uncertainty of 0.08 mag, the median value, and the 16 and 84-percentile are $2.52^{+0.69}_{-0.32}$ mag. The results derived without employing the FIR data are in $0.49 < A(V)_{\rm you,noFIR} < 4.12$ mag, with a median error of 0.07 mag, the median value, and the 16 and 84-percentile are $3.05^{+0.33}_{-0.55}$ mag. Considering that the young attenuation has changed when the values of each case differ in more

than 0.2 mag, a significant fraction, 63% of all galaxies, presents higher $A(V)_{\rm you,noFIR}$ when FIR constraint is omitted. A small fraction, 10% of all galaxies, shows lower $A(V)_{\rm you,noFIR}$ without using the FIR constraint (both fractions are marked in Fig 5.10).

Examining all the galaxies as a whole, the median difference is $\Delta(A(V)_{\rm you,noFIR} - A(V)_{\rm you,FIR}) = 0.4$ mag, but individual objects can reach differences of 0.7 mag. This fact evidences that the absence of FIR photometry results mostly in a overestimation of the attenuation values of the young population when 2P models are considered.

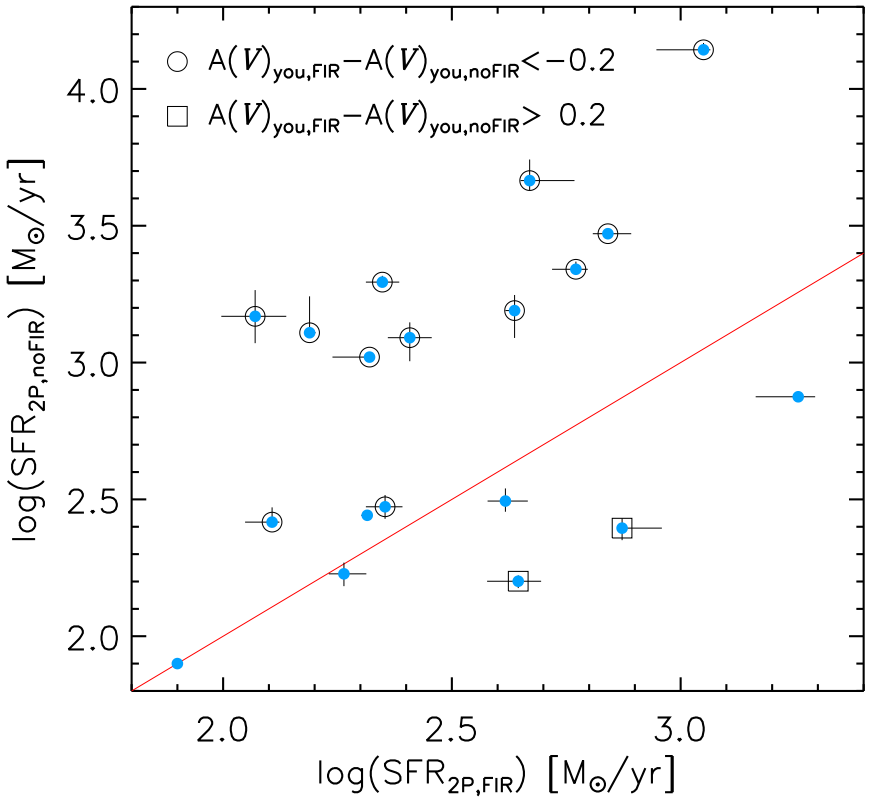

Figure 5.11 : Comparison between the SFRs derived with the FIR prior on x-axis, and those derived when the FIR information is omitted on y-axis. The filled circles with error bars show the median values and the 1σ uncertainties derived from the logarithmic space.

In order to evince the impact of the age-dust degeneracy in the SFR estimations, we have marked in the right panel of Fig. 5.9, and in Fig. 5.11 the galaxies with $A(V)_{\rm you,FIR} - A(V)_{\rm you,noFIR} < -0.2$ mag. All these objects, except one galaxy present $\Delta(\log(SFR_{\rm 2P,noFIR}) - \log(SFR_{\rm 2P,FIR})) > 0.3$ dex. In Figure 5.11, the galaxy satisfying the above attenuation difference, but with 2P-SED-fit SFR difference of ~ 0.12 dex is MIPS0001045_1. This galaxy has $A(V)_{\rm you,FIR} - A(V)_{\rm you,noFIR} = -0.22$ mag, which is near to the threshold we have chosen. In addition, this object presents a significant change in the old age, which results in a variation of the burst intensity between each

modeling case. Nevertheless, we should mention that the aim of choosing a threshold of attenuation variation is not to explain how the SFR or other physical property changes between each modeling case for all our sample. Our purpose is to exemplify how the age-dust degeneracy misleads the parameter determination for the SFH of IR-bright galaxies, and to show that the FIR prior helps to break such degeneracy.

Concerning the objects with $A(V)_{\rm you,FIR} - A(V)_{\rm you,noFIR} > 0.2$ mag in the aforenamed figure, they also show a variation of greater than 0.3 dex in the SED-fit SFR values determined with the FIR information. There is an object presenting a variation in SFR from SED-fitting larger than 0.3 dex which is unmarked. This galaxy, MIPS0001162_1, has $A(V)_{\rm you,FIR} - A(V)_{\rm you,noFIR} = 0.2$ mag, which is in the limit of the our selected threshold.

5.1.4 Final Remarks on Age-Dust Degeneracy and 2P models

To close this Section, we refer to the age of the young population, showing in Fig. 5.12 the comparison between the values for the 2P models with and without the FIR information. The solutions obtained for the FIR prior case are in $8 < t_{\rm you,FIR} < 419$ Myr, with a median value, and the 16 and 84-percentile of 39^{+161}_{-29} Myr. The results determined when omitting the FIR data are in $1 < t_{\rm you,noFIR} < 202$ Myr with a median value, and the 16 and 84-percentile of 10^{+67}_{-6} Myr.

We have indicated in the aforenamed figure, the galaxies where the young attenuations have changed. Distinctly, the objects presenting larger attenuations have shorter young ages in both modeling cases, which is a manifest evidence of the age-dust degeneracy. The difference in the young ages of each set of models for these sources is larger than a factor ~ 1.5. There are some galaxies showing differences in the young age that are unmarked. This is not surprising because the presence of FIR information helps to break the age-dust degeneracy, but the young age is also degenerated with the burst intensity. In other words, an increase in b is associated to an increase in $t_{\rm you}$, and a decrease in b is also connected to a decrease in $t_{\rm you}$. We will return to the age-burst strength degeneracy in Chapter 6.

With regard to the age of the old population, the values obtained from both 2P cases are almost similar for all the objects. Only for a small fraction, 21% of all galaxies, the old age has changed significantly between each modeling case. Therefore, the addition of FIR data has a minor impact in the determination of the ages of the old population. This is expected because the FIR photometry traces the dust content of the galaxies which is related with recent star formation events.

Buat et al. (2014) studied a sample of $z > 1$ galaxies using 2P models and the FIR

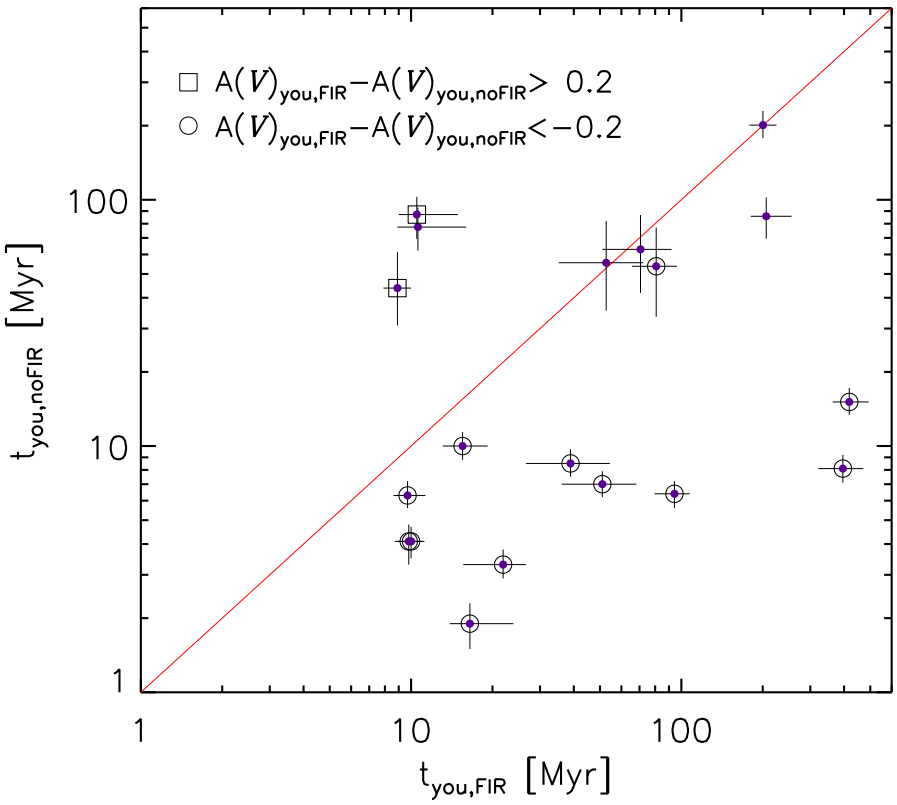

Figure 5.12 : Comparison between the ages of the young population of the 2P models using the FIR prior, $t_{\rm you,FIR}$, on x-axis, and the ages of the 2P models without the FIR prior, $t_{\rm you,noFIR}$, on y-axis, both derived with the Synthesizer code. The filled circles with error bars show the median values and the 1σ uncertainties.

prior, and they found compatible tendencies in the ages of both populations with and without the addition of FIR information. Hence, our findings are similar to their results for the old stellar population, but not for the young population case. We have noticed a significant change in the young ages for more than a half of the objects in our sample when the FIR data are omitted.

5.2 Solutions with two and one population models using the FIR prior

In this section we compare the solutions derived from our fiducial 2P models with the solutions obtained from 1P models ($SFR(t) = \alpha \cdot e^{-t/\tau}$), using the Synthesizer code and the Maraston (2005) library for both sets. The attenuation in the V band of both cases is constrained with the FIR prior. Our goal is to test the importance of using two populations in the estimations of the physical parameters of IR-bright galaxies. To do

so, we have compared the goodness of the fits, and the results for the stellar properties of each set of models.

5.2.1 Goodness of the Fits of 2P and 1P Models

The goodness of fit is evaluated for the UV/MIR and the FIR part of the spectrum of each galaxy, separately. For the UV/MIR spectral range we use the estimator defined in the Eq. 5.1. Considering that the energy balance argument in the Synthesizer code is implemented linking $L_{\rm TIR}$ with the attenuated stellar spectrum, the obvious choice for assessing the goodness of fit in the FIR spectral range is to perform $L_{\rm TIR}$ comparisons. Hence, we evaluate the goodness of fit comparing respectively, the $L_{\rm TIR,2P}$ fitted for the output spectrum of the 2P models and the $L_{\rm TIR,1P}$ resulting from fitting process of the 1P models with our referential $L_{\rm TIR,ref}$ using an akin $\chi^2_{L_{TIR}}$ estimator, which is expressed as:

$$\chi^2_{L_{\rm TIR}} = \frac{(\log L_{\rm TIR,ref} - \log L_{\rm TIR,mod})^2}{\sigma^2_{L_{\rm TIR}}}, \tag{5.4}$$

where $L_{\rm TIR,mod}$ references $L_{\rm TIR,2P}$ or $L_{\rm TIR,1P}$, and $\sigma_{L_{\rm TIR}}$ is the uncertainty in the $L_{\rm TIR,ref}$ determination expressed in dex. This uncertainty is the result of adding in quadrature the dispersion between the $L_{\rm TIR}$ estimations resulting from the infrared libraries used in Section 3.7 (CE01, DH02, and R+09), and a constant value of 0.022 dex (equivalent to 5% of the $L_{\rm TIR}$ of each galaxy). This constant value is used to consider uncertainties in the absolute calibration and the confusion noise of the MIPS, PACS and SPIRE instruments.

We have plotted in Fig. 5.13 the $\chi^2_{\rm UV/MIR}$ distributions for the 2P and 1P models. The distribution of the 2P case concentrates in lower $\chi^2_{\rm UV/MIR}$ values compared with the distribution of the 1P case. We have estimated the median, and the 16 and 84-percentile values for the 2P and the 1P models, obtaining $1.7^{+1.4}_{-0.6}$ for the 2P case, and $3.4^{+3.0}_{-1.3}$ for the 1P case. Hence, the $\chi^2_{\rm UV/MIR}$ values of the 1P models are more spread to larger values than the 2P ones. When comparing the median values, we observe that the 1P median is almost 1σ away from the 2P one. Therefore, we conclude that the 2P models perform better than the 1P ones in the FUV-to-MIR spectral range.

We have also plotted the $\chi^2_{L_{\rm TIR}}$ distributions for both cases (see Fig. 5.14), these distributions are alike, but with the 1P one having 2 more objects in the lowest bin of $\chi^2_{L_{\rm TIR}}$ values. The median, and the 16 and 84-percentile are $0.8^{+5.7}_{-0.7}$ and $1.4^{+1.8}_{-1.3}$ for the 1P models and the 2P models, respectively. The distribution of the 2P case presents 1 galaxy in the high $\chi^2_{L_{\rm TIR}}$ values tail. Although the 1P median is a little shorter than the 2P one, they are close enough to be considered similar. Furthermore, the 1σ values of

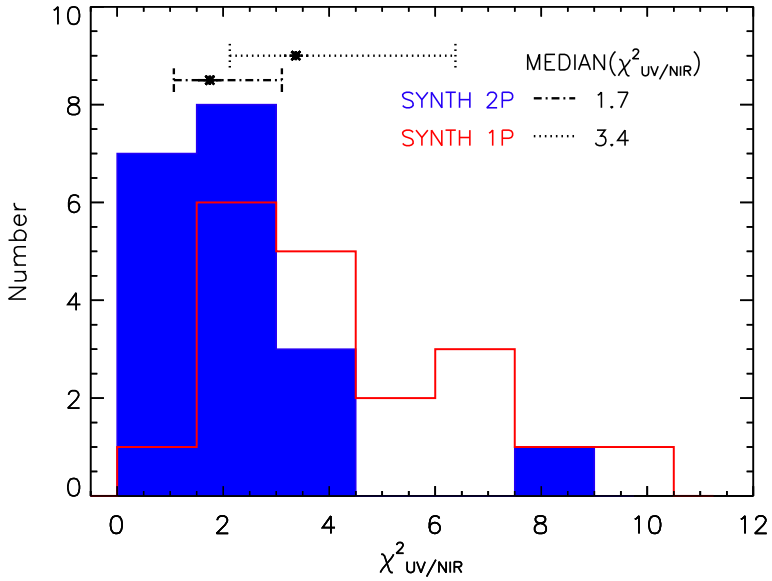

Figure 5.13 : Distributions of $\chi^2_{\rm UV/MIR}$ values obtained evaluating the UV-to-MIR spectral range for the 2P and 1P models derived with the Synthesizer code. *Filled blue:* Results for the 2P models. *Open red:* Results for the 1P models. The median values, and the 16 and 84-percentile of the distributions are indicated.

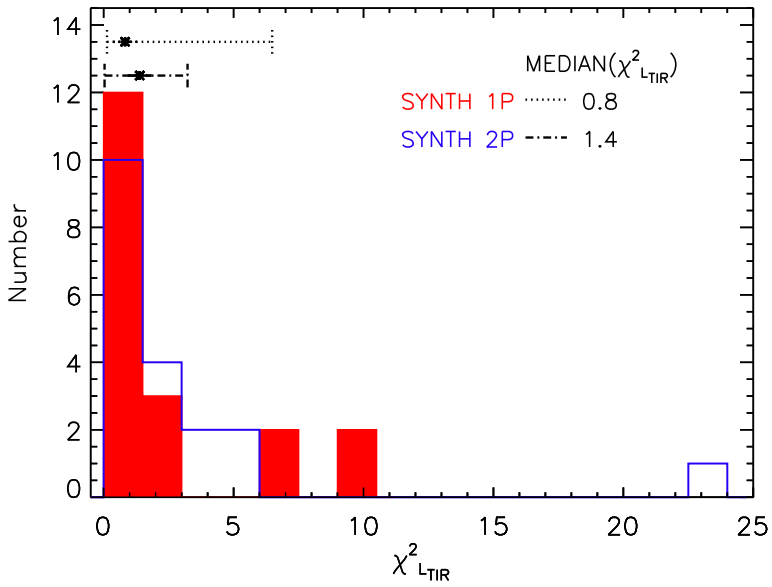

Figure 5.14 : Distributions of $\chi^2_{L_{\rm TIR}}$ values obtained from comparisons with the observed $L_{\rm TIR,ref}$ for the 2P and 1P models derived with the Synthesizer code. *Filled red:* Results for the 1P models. *Open blue:* Results for the 2P models. The median values, and the 16 and 84-percentile of the distributions are shown.

the 2P case are included in the 1P ones, indicating a comparable performance of the 1P and 2P models in the FIR spectral range.

We now compare the goodness of the fits of the 2P and 1P models of our galaxy sample as a whole. With respect to the UV-to-MIR spectral range (see Fig 5.15), more than a half, 58% of all galaxies, is better fitted using the 2P models. A non negligible fraction, 37% of all galaxies, is obtaining similar values of χ^2 for the 2P and 1P models. There is one galaxy (5% of the total) fitted with the 1P models which has lower χ^2 value than the result obtained 2P models. Nevertheless, the 2P spectrum for this source has and absorption line which is concurrent with the i' band wavelength. This fact is biasing the χ^2 estimation towards the 1P model (see Appendix A).

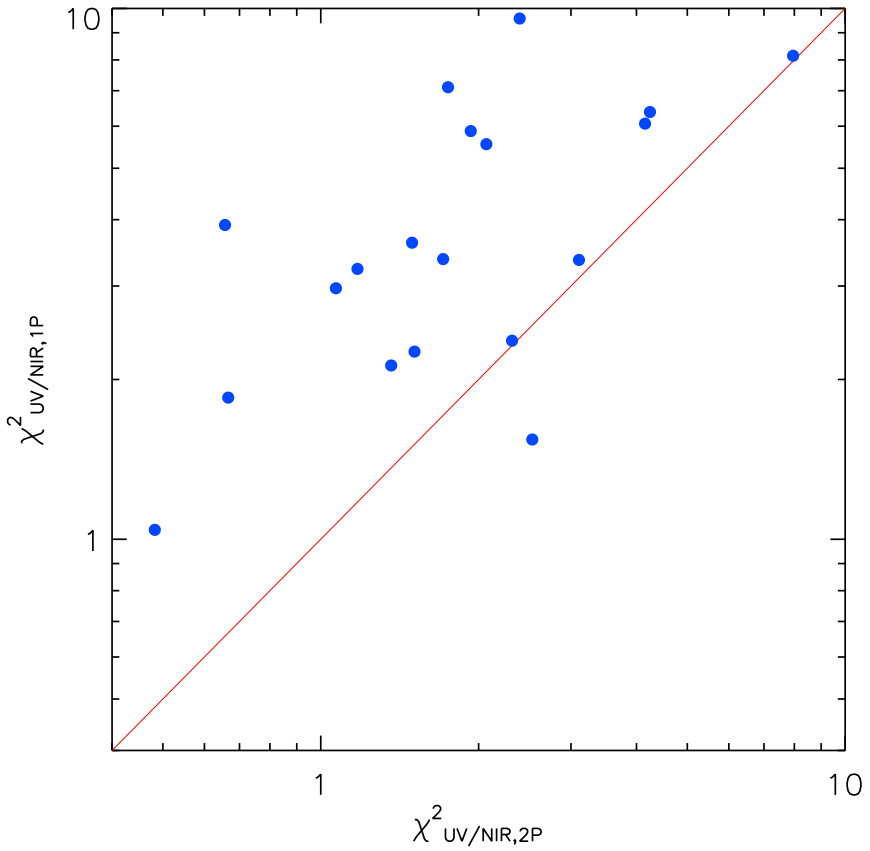

Figure 5.15 : Scatter plot of $\chi^2_{\rm UV/MIR}$ values obtained evaluating the UV-to-MIR spectral range for the 2P and 1P models derived with the Synthesizer code.

With respect to the FIR spectral range, we find that an equal fraction (37%) is better fitted by each set of models. A fraction of 26% presents similar $\chi^2_{L_{\rm TIR}}$ values for both cases. Nevertheless, we should remember that using the FIR prior involves constraining the amount of attenuation in the V band of the 2P and 1P models with the dust re-emitted energy derived from the $L_{\rm TIR,ref}$. Hence, the possible solutions for both sets of

models are those which satisfy the energy balance between $A(V)$ and $L_{\rm TIR,ref} \pm \sigma_{L_{\rm TIR}}$. Therefore, the similar results for each set of models are expected.

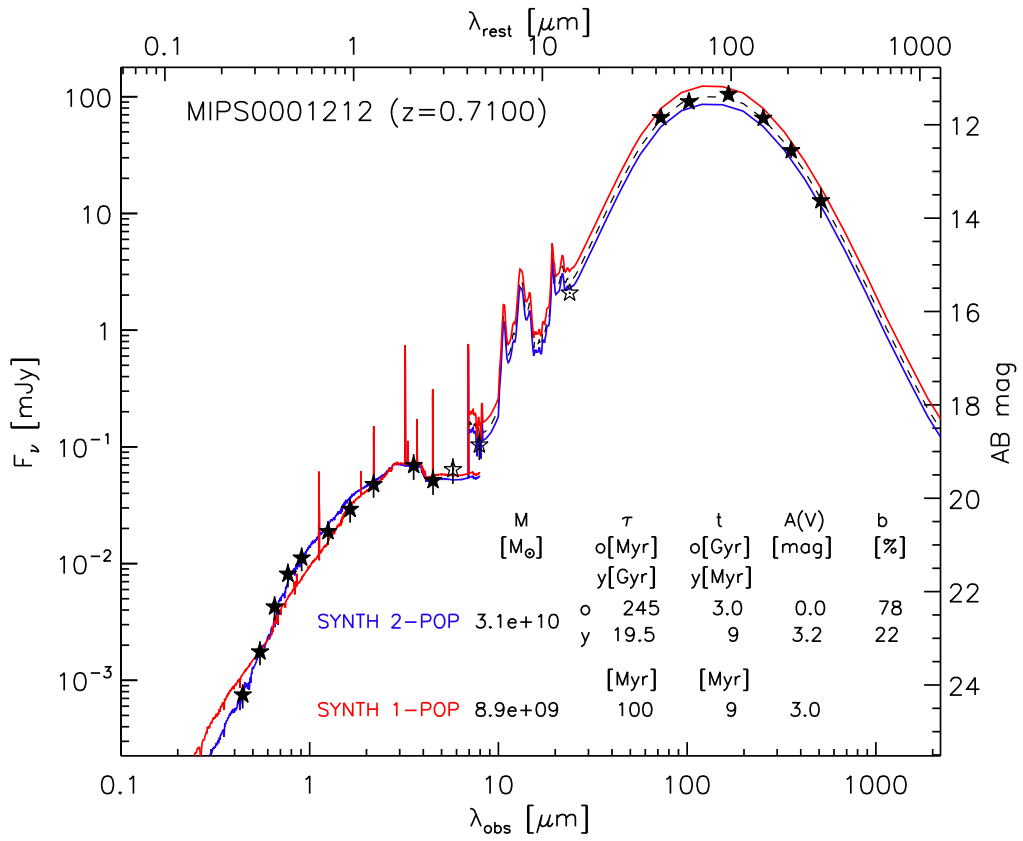

Figure 5.16 : An example of the resulting fit to the whole UV-to-FIR SED for our IR-bright galaxies with the Syntesizer code. *Solid blue line:* Result of the fitting process obtained with 2P models. *Solid red line:* Fit derived using 1P models. The parameter values of the solutions are also shown (M_*, τ, t, $A(V)$, b) for the 2P and 1P models, respectively. *Dashed black line:* Fit to the FIR photometry ($\lambda_{\rm obs} \geq 70$ μm). Photometric data points include the uncertainties (multiplied by 2.5 from UV to IRAC bands for visualization), only the *filled black stars* are used in the fit.

In Figures 5.16 and 5.17, we show two examples of the obtained SED fits using 2P and 1P models with the FIR prior, the SEDs of all galaxies are plotted in Appendix A. For the first galaxy, MIPS0001212 ($z = 0.71$), the resulting spectrum for the 1P model presents an excess of flux density in the blue wavelengths when compared with the observed photometry, which suggests the need of a larger value of $A(V)_{\rm 1P,FIR}$ for a good fit. This spectrum also evidences a deficit of flux in the i', z' and J bands, this is due to the fact that the age of the 1P models is 9 Myr. This short age is not enough to have a considerable number of red stars, which contribute mainly with stellar mass. Therefore, the need of and old population is evident. We should mention that $t_{\rm you} = 9$

Myr too, for the 2P case, but $b = 22\%$ which indicates that most of the stellar mass comes from the old population.

In the case of MIPS0001300_1 ($z = 0.95$), we observe a good fit for the 1P and 2P models. The 1P model also presents an excess of flux density in the blue part of the spectrum, but the constraint of using the FIR prior rejects reaching higher $A(V)_{1P}$ values.

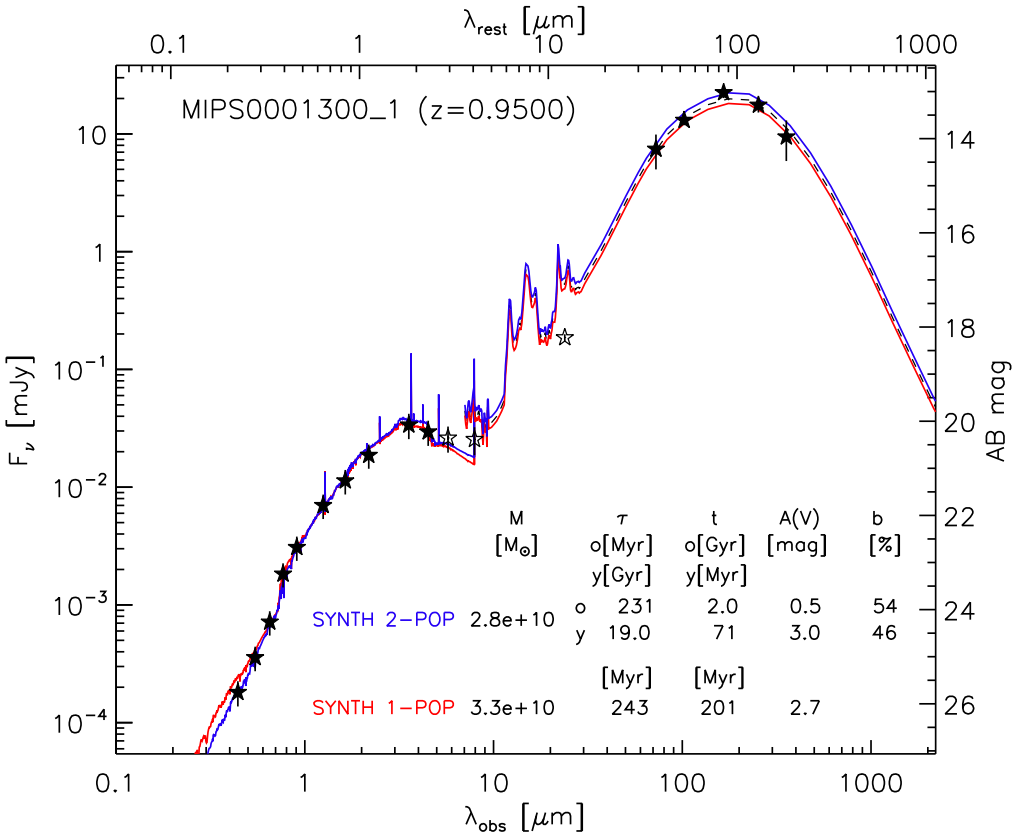

Figure 5.17 : An example of the resulting fit to the whole UV-to-FIR SED for our IR-bright galaxies with the Syntesizer code. *Solid blue line:* Result of the fitting process derived with 2P models. *Solid red line:* Fit obtained using 1P models. The parameter values of the solutions are also shown (M_*, τ, t, $A(V)$, b) for the 2P and 1P models, respectively. *Dashed black line:* Fit to the FIR photometry ($\lambda_{\rm obs} \geq 70$ μm). Photometric data points include the uncertainties (multiplied by 2.5 from UV to IRAC bands for visualization), only the *filled black stars* are used in the fit.

5.2.2 Stellar Masses and SFR estimations with 2P and 1P models

Here we compare the stellar masses and SFRs estimated using the 2P and 1P models using the FIR prior, with both sets of models derived employing the Synthesizer code. The stellar mass and the SFR estimations present a high dependency on the adopted SPS

model and SFH (see, e.g., Lee et al. 2009, Pforr et al. 2012). Given that we have used the Maraston (2005) models, the differences in our stellar mass and SFR determinations originate mainly in the assumed SFHs.

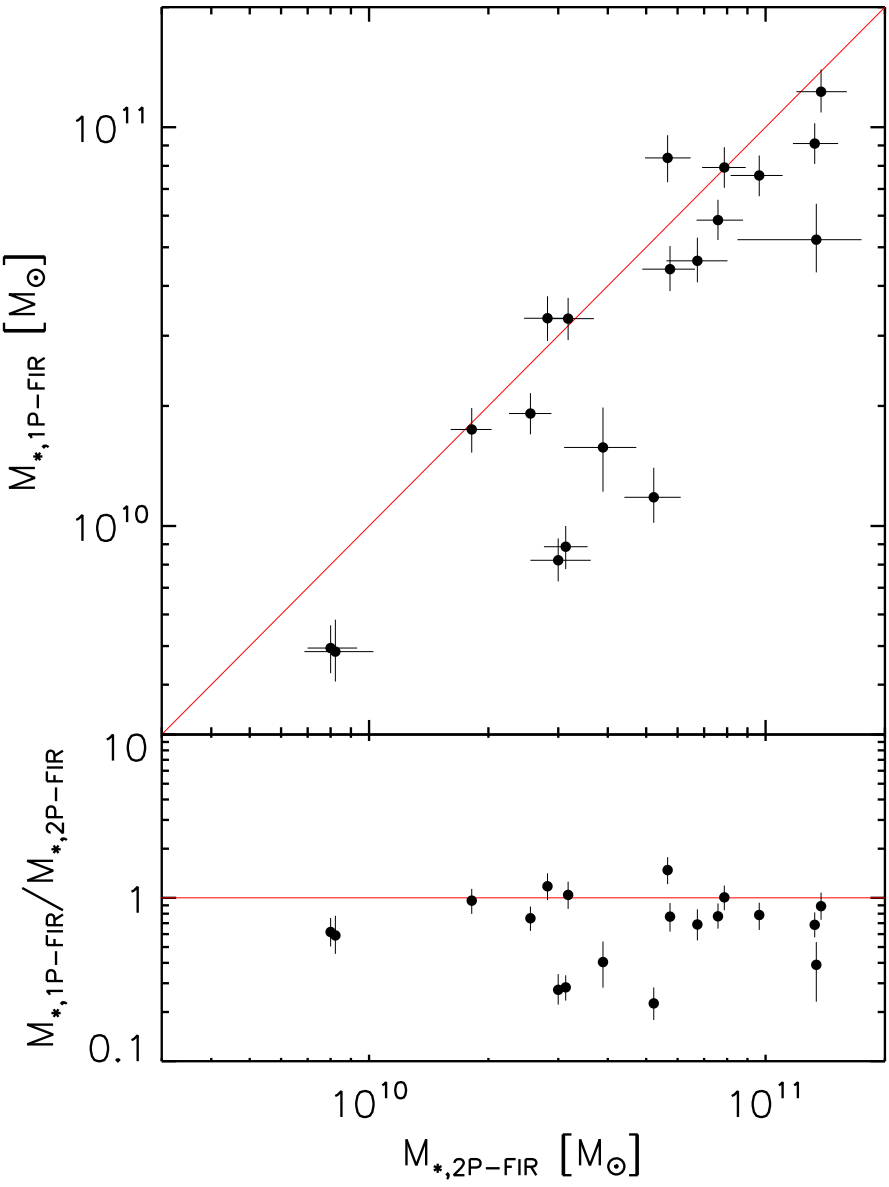

Figure 5.18 : *Upper panel:* Comparison between the stellar masses (M_*) derived with the 2P models using the FIR prior on x-axis, and those derived with the 1P models using the FIR constraint on y-axis. The filled circles with error bars show the median values and the 1σ uncertainties. *Lower panel:* Ratio of the stellar masses derived with both set of models. The error bars show the propagated uncertainties.

In Figure 5.18, we show the comparison of the stellar masses derived with the 1P and the 2P models using the FIR prior and their ratios. The stellar mass values obtained with the 2P models are in $7.9 \times 10^9 < M_{*,\mathrm{2P-FIR}}/M_\odot < 1.4 \times 10^{11}$, with median, and

the 16 and 84-percentile of $5.2^{+4.4}_{-2.7} \times 10^{10} M_{\odot}$, and a median uncertainty of 0.06 dex. The stellar masses determined with the 1P models are in $4.8 \times 10^{9} < M_{*,\mathrm{1P-FIR}}/M_{\odot} < 1.3 \times 10^{11}$, with median value, and the 16 and 84-percentile of $3.3^{+4.6}_{-2.4} \times 10^{10} M_{\odot}$, and an average uncertainty of 0.05 dex. For 14 galaxies (74% of the sample) the stellar masses estimated with the 2P models are larger than those derived with the 1P models. The median difference found between our referential modeling and the 1P case is $\Delta(\log(M_{*,\mathrm{2P-FIR}}) - \log(M_{*,\mathrm{1P-FIR}})) = 0.13$ dex. In other words, the stellar masses derived with the 2P models are $\sim 35\%$ larger than those obtained with the 1P models.

In the lower panel of Fig. 5.18, we show the ratio between the 1P and the 2P models derived stellar masses. The ratio values are in $0.2 < M_{*,\mathrm{1P-FIR}}/M_{*,\mathrm{2P-FIR}} < 1.5$, considering their propagated uncertainties, 26% of the objects have obtained a similar stellar mass values from the solutions of each set of models. Notwithstanding, the typical precision expected from estimations derived with SPS models is factor of $\sim 2-3$ (see, e.g., Pérez-González et al. 2008, Pforr et al. 2012, Michałowski et al. 2014), and 83% of our objects fulfill this condition. Attending to the lower panel of Fig. 5.18, we observe 5 galaxies separated from the main group which have ratio values lower than 0.5. These 5 objects are: MIPS0000050_1, MIPS0000701_1, MIPS0001162_1, MIPS0001212, and MIPS0001225 (see Appendix A). Referring to the 1P case, the median solutions for these 5 objects present age values shorter than 100 Myr. For 4 of these 5 sources an excess of flux density in the blue wavelengths is observed, and the fitted spectra of the 5 objects exhibit a deficit of flux density in the longer wavelength optical and NIR bands when compared with the observed photometry.

We should mention that when using a single population to fit the SEDs of star forming galaxies, such population should be young in order to match the UV-observed photometry. If a single burst is assumed in a nearly constant SFH, the ongoing SFR is settled by the current UV emission, and the timescale of continuous star formation of the galaxy is established by the longer wavelength optical and NIR flux (Dunlop 2011). Therefore, ages shorter than 100 Myr may not contribute with enough optical-NIR flux to match the observed photometry in these bands.

If we omit these low ratio objects, the average ratio is 0.87 ± 0.24. Hence, a good agreement is found between the masses of 2P and 1P models, with the 2P models obtaining a 10% higher stellar mass than the 1P models. Nevertheless, Dunlop (2011) studied the properties of dusty star forming galaxies at high redshift, and he suggested that 2P models can lead to higher stellar mass determinations than 1P models, which is compatible with our findings.

Consequently, the main problems affecting the goodness of the fits of the 1P models are an understimation of attenuation and the short ages for the population (< 100 Myr)

which yield to a dearth of stellar mass. The former is caused by using the FIR prior to constrain $A(V)_{1P}$, larger values of attenuation are not allowed because they will need a larger quantities of re-emitted energy by the dust compared with the values that are observed. The latter is originated in assembling the different stellar populations into only one young population, which provides high luminosity, but not enough stellar mass. The ages of the 1P models are also restricted by the FIR prior because and old population should not be suffering attenuation levels larger than 2 mag. Therefore, the FIR prior is useful to show that 1P models are not always well-suited to fit the UV-to-FIR SEDs and to derive physical parameters of (U)LIRGs.

We now move to compare the SED-fit SFRs derived from the 2P and 1P models with and without the FIR prior with SFR values based on the observed FIR and UV data. In Figure 5.19, we show such comparisons.

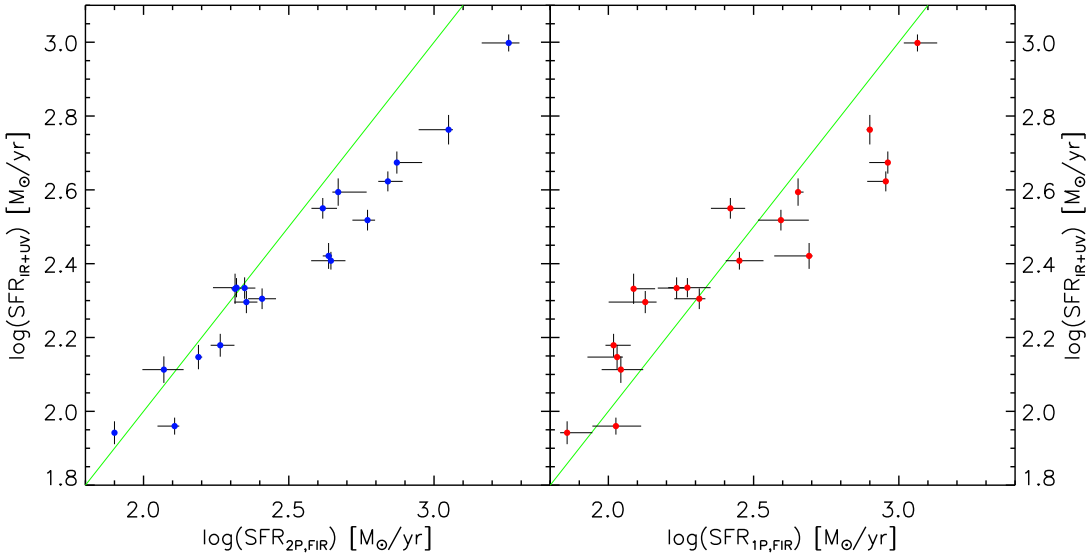

Figure 5.19 : *Left panel:* Comparison between the SFRs derived with 2P models using the FIR prior and those derived with the observed FIR and UV (filled blue circles). *Right panel:* Comparison between the SFRs obtained with 1P models using the FIR constraint and those determined with the observed FIR and UV (filled cyan circles). The filled symbols with error bars show the median values and the 1σ uncertainties derived from the logarithmic space.

The values for $SFR_{\rm UV+IR}$ and $SFR_{\rm 2P,FIR}$ have been described in Section 5.1.3. The SED-fit SFR obtained with the 1P models are in $1.85 < \log(SFR_{1P}) < 3.06$, with median value, and the 16 and 84-percentile of $2.31^{+0.59}_{-0.28}$, and a median uncertainty of 0.06 dex. Seemingly from Figure 5.19, the SED-fit SFRs derived from 1P models appear having a larger scatter than the SFRs from the 2P models compared with the $SFR_{\rm UV+IR}$ values. We have estimated the rms values for both SFR differences result-

ing, $\Delta(\log(SFR_{\rm 1P,FIR}) - \log(SFR_{\rm UV+IR}))_{\rm rms} = 0.16$ dex, and $\Delta(\log(SFR_{\rm 2P,FIR}) - \log(SFR_{\rm UV+IR}))_{\rm rms} = 0.11$ dex. Hence, the SED-fit SFRs from the 2P models are more similar than the ones from 1P models compared with the $SFR_{\rm UV+IR}$ values.

As we mentioned in the beginning of Chapter 4, the SFRs from the observables are derived from simple models assuming constant star formation for a timescale. The Kennicutt (1998) calibration was derived from the stellar population synthesis models of Leitherer and Heckman (1995) with constant star formation in a timescale of ~ 100 Myr. A significant fraction, 47% of our sources, have obtained $t_{\rm you,FIR} < 30$ Myr (see Fig. 5.12 and Table 5.1). Hence, maybe the Kennicutt (1998) calibration is not appropriated for all our objects. We return to this topic on Chapter 6.

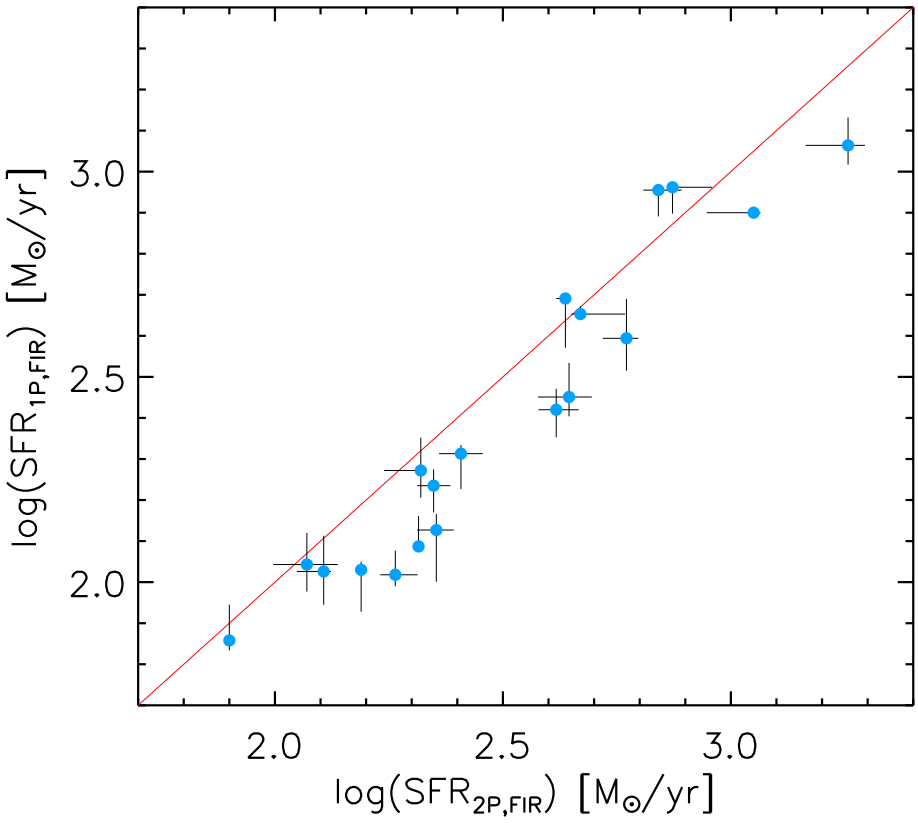

Figure 5.20 : Comparison between the SED-fit SFRs derived with the 2P models x-axis, and those derived with the 1P models on y-axis, using the FIR prior in both cases. The filled circles with error bars show the median values and the 1σ uncertainties derived from the logarithmic space.

Now we compare the $SFR_{\rm 2P,FIR}$ values with the $SFR_{\rm 1P,FIR}$ results in Fig. 5.20. For a considerable fraction, 68% of all galaxies, the SFRs derived with the 2P models are larger than those estimated with the 1P models. The median difference found between our fiducial model and 1P case is $\Delta(\log(SFR_{\rm 2P,FIR}) - \log(SFR_{\rm 1P,FIR})) = 0.10$

dex. Attending to Fig. 5.20, we observe that various sources present a shift of ~ 0.2 dex to higher SFR values for the 2P models. Interestingly, these objects show $t/\tau > 0.8$ for the 1P case or mass ratios less than 0.4 (see Fig 5.18). Therefore, this suggest that these galaxies present a SFH which is far from a constant one or a mass deficit in the 1P models.

Buat et al. (2014) studied a sample of $z > 1$ galaxies using the FIR prior, and they found a modest offset (~ 0.04 dex) to higher SFR values for the 2P models compared with the 1P models, this offset is smaller than the one (~ 0.1 dex) found in our results.

5.2.3 Final remarks on the 2P and 1P modeling differences

To finish this Section, we check the effect of the FIR prior in the attenuation values derived for the 2P and 1P models. To do so, we compare the $A(V)_{\rm 1P,FIR}$ values determined for the 1P case with the $A(V)_{\rm you,FIR}$ values derived for the 2P case in Fig. 5.21. We observe a positive offset in $A(V)_{\rm you,FIR}$ for various objects, $\Delta(A(V)_{\rm you,FIR} - A(V)_{\rm 1P,FIR}) \simeq 0.2$ mag. This is expected considering that there are two bursts in the 2P models which implies to divide the intrinsic luminosity (mass), and that the values for $A(V)_{\rm old,FIR}$ are typically low (see Appendix A).

We should mention that we are comparing $A(V)_{\rm you,FIR}$ with attenuations derived from models of a single more luminous burst, which results from assembling several stellar populations with different ages and attenuation levels into one single population. Therefore, the dust absorbed energy is manifested mainly in the young population which provides only a fraction of the total stellar mass. From the 9 objects presenting the aforenamed 0.2 mag offset, 8 are not fitted correctly with 1P models, presenting an excess of flux in the blue part of the spectrum. This suggests that one population is not enough to satisfy the requirements of luminosity and mass for the UV-to-NIR observed photometry of our IR-bright galaxies.

Hence, we can stay that the SEDs of our IR-bright galaxies are better fitted using 2P models. The young population can tackle the obscured UV emission which is re-emitted by the dust in the FIR bands, whereas the old population provides the optical/NIR emission which is necessary to match the observed photometry in these bands. Conversely, the 1P models try to emulate the observed UV-to-NIR fluxes with only one population which typically results on unappropriated SED fits, and low stellar mass and SFR values.

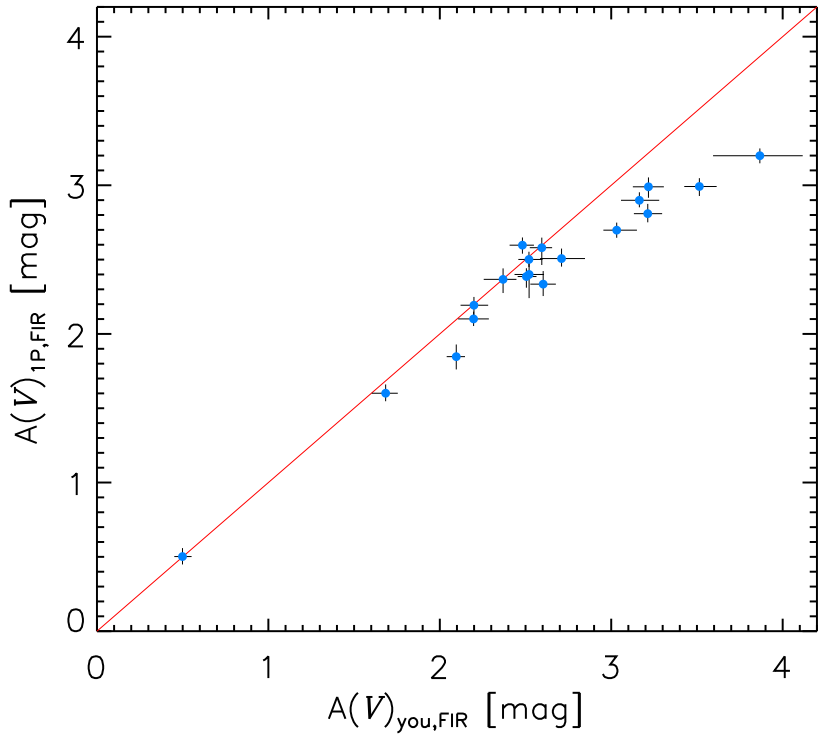

Figure 5.21 : Comparison between the attenuations of the young population of the 2P models, $A(V)_{\rm you,FIR}$, on x-axis, and the attenuations of the 1P models, $A(V)_{\rm 1P,FIR}$, on y-axis, both derived with the Synthesizer code using the FIR prior. The filled circles with error bars show the median values and the 1σ uncertainties.

5.3 Summary

In this Chapter we have studied how the a priori assumptions in the modeling influence the determination of the physical parameters of IR-bright galaxies. To do that, we have compared the results obtained for such parameters from 2P models with and without using the FIR prior, and 1P models with the FIR constraint, finding the following:

- The FIR prior helps to break the age-dust degeneracy by constraining the attenuation of the young population in the 2P modeling case. This constraint yields to a more robust determination of the SFRs, and young stellar population ages.

- Concerning the 2P models, the lack of FIR photometry results mainly in an overestimation of the attenuation of the young population. A slight excess ($\sim$ 0.2 mag) in such attenuation can produce a considerable underestimation (of a factor $\sim$ 6 in median) of the young population age. These two facts results on increasing the uncertainty of the SFH, and this uncertainty affects the determination of the SED-fit SFRs, which can be overestimated in more than order of magnitude

when compared with $SFR_{\rm UV+IR}$ values.

- When using the FIR prior, the 2P models fit better the UV-to-MIR observed SED than the 1P models. Such 1P models with larger $\chi^2_{\rm UV/MIR}$ values present an excess and a deficit of flux density in the blue and NIR part of their fitted spectrum, respectively. Such excess is due to an underestimation ($\gtrsim 0.2$ mag) of $A(V)_{\rm 1P,FIR}$ compared with $A(V)_{\rm you,FIR}$, and such deficit is originated in the determination of short stellar population ages ($\lesssim 100$ Myr).

- Stellar masses derived with 2P-FIR models are in median 35% larger than those obtained with 1P-FIR models. But, 1P-FIR models with larger $\chi^2_{\rm UV/MIR}$ values can reach stellar masses smaller in a factor of 2 than those derived with 2P-FIR models. SED-fit SFRs derived with 1P-FIR models present a larger scatter (~ 0.16 dex) than those derived with 2P-FIR models (~ 0.11 dex) when compared with $SFR_{\rm UV+IR}$ values. SED-fit SFRs determined with 1P-FIR models can be 0.2 dex smaller than those derived with 2P-FIR models. This is caused by an SFH which is far from constant ($t/\tau > 0.8$) or a dearth of mass in the 1P-FIR models.

Chapter 6

The Properties of the Stellar Populations in $0.6 < z < 1.5$ (U)LIRGs

In Chapter 5 we have studied how *a priori* assumptions in the modeling affect the results about the stellar population properties of IR-bright galaxies using the Synthesizer code. We have concluded that 2P models using the FIR prior are the best suited to determine robust physical properties of (U)LIRGs. In this Chapter, we move to discuss how the usage of different codes influences the results for such stellar population properties. In order to do so, we compare the solutions obtained for these physical properties derived from two codes that manage a self-consistent modeling of the UV-to-FIR SED of galaxies: the CIGALE and the Synthesizer codes.

We use 2P-FIR models for both codes exploring the parameter values described in Sections 4.2.1 and 4.2.2 for the CIGALE and the Synthesizer code, respectively.

6.1 Comparing Physical Properties Derived with CIGALE and Synthesizer Codes

In this section, we compare the characterization of the stellar populations of a sample of star-forming galaxies derived by the CIGALE and Synthesizer codes, which manage energy balance techniques to connect the dust absorbed and re-emitted energy. We have fitted seven parameters which describe an assumed SFH (Equation 4.1) with the aforementioned codes. By comparing the parameter values obtained with the codes for the two population models, we can identify which parameters are dominant and if they are properly constrained or not.

We have also searched for a correlation between the values of each parameter expected by the Synthesizer and CIGALE codes using Monte Carlo simulations and a Bayesian analysis, respectively.

6.1.1 SED-fitting Results and Goodness of the Fits

In Table 6.1 we present the parameter values of the SPS models derived from the analysis of the plausible solutions with the Synthesizer and CIGALE codes for our sample of IR-bright star-forming galaxies. We show in the upper panels of Fig. 6.1, the complete UV-to-FIR SEDs for two galaxies in the sample. We also provide the results of the median solution of the most significant cluster derived from the Monte Carlo simulation analysis with the Synthesizer code, and the average parameter values estimated with the CIGALE from the Bayesian analysis of its full set of models. We present in the lower panels of Fig. 6.1, the SFHs obtained with the parameters described in Table 6.1 for the Synthesizer and CIGALE codes. The SEDs and the SFHs of all galaxies are plotted in Appendix B.

Following the aim of assess the modeling of the stellar populations of our sample taking into account the constraint of the attenuation of such populations with the dust reradiated FIR emission, it is interesting to discuss the goodness of the fits of the selected models derived from the analysis with the Synthesizer and CIGALE codes. To do so, we appraise the goodness of fit of the UV/MIR and FIR part of the spectrum of each galaxy (see Fig. 6.1), separately. For the UV/MIR spectral range we use the $\chi^2_{\rm UV/MIR}$ estimator defined in Eq 5.1. For the Synthesizer code the largest wavelength considered in this case is 4.5 μm, and the largest wavelength evaluated for the CIGALE is 8 μm, both in observed-frame. The results of $\chi^2_{\rm UV/MIR}$ for all the galaxies in our sample are shown in Table 6.2. We notice from the aforementioned table that a considerable fraction, 63% of all galaxies, is better fitted by the Synthesizer code.

Considering that the direct observable $L_{\rm TIR}$ is commonly transformed into a SFR, and that the energy balance argument in the CIGALE and Synthesizer codes is implemented connecting $L_{\rm TIR}$ with the attenuated stellar spectrum, we also evaluate the goodness of fit comparing respectively, the $L_{\rm TIR,CIG}$ from the output spectrum of the CIGALE and the $L_{\rm TIR,SYN}$ which is used in the fitting process of the Synthesizer code with our referential $L_{\rm TIR,ref}$ using the $\chi^2_{L_{\rm TIR}}$ defined in Eq.5.4. The results of $\chi^2_{L_{\rm TIR}}$ for all the objects in our sample are also shown in Table 6.2.

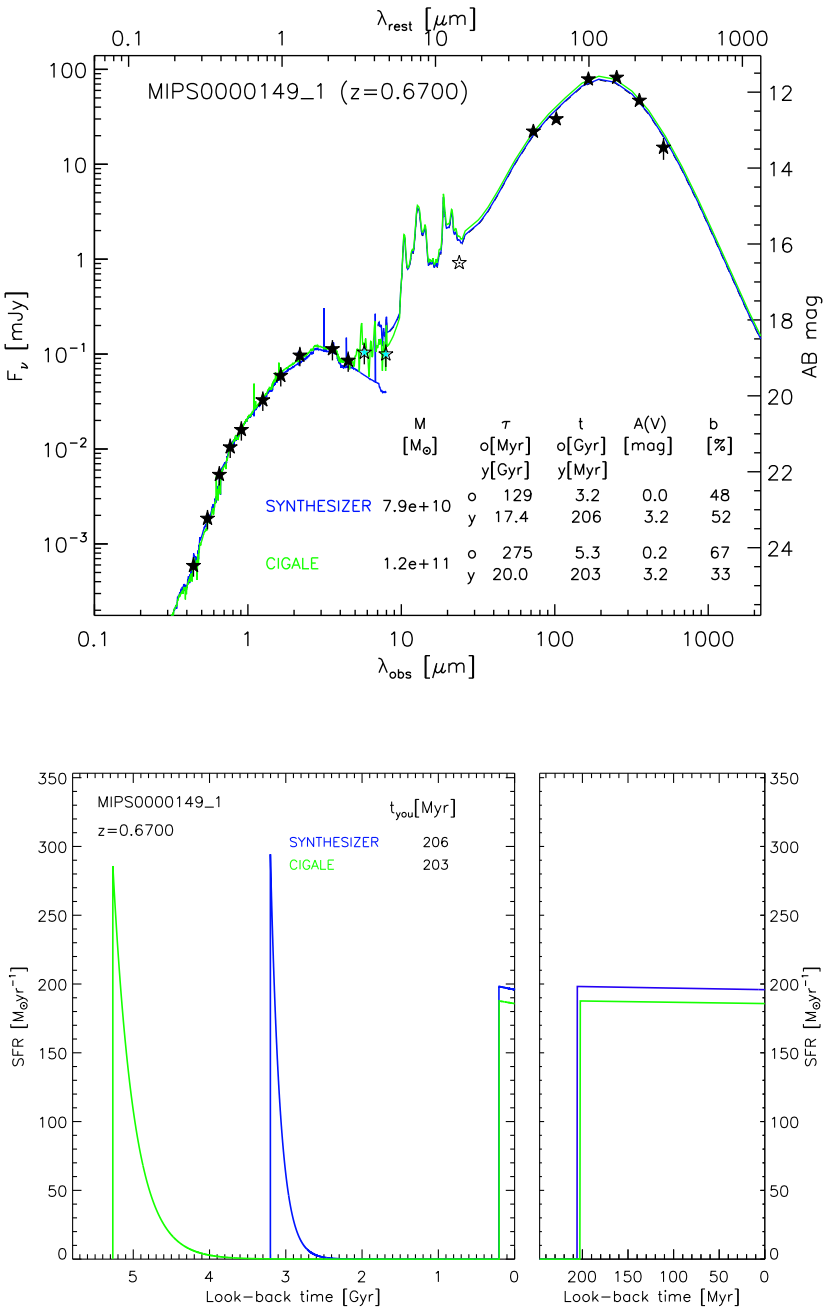

Figure 6.1 : *Upper panel:* An example of the resulting fit to the whole UV-to-FIR SED for our IR-bright galaxies at $0.6 \leq z \leq 1.5$. *Solid blue line:* Result of the fitting process obtained with the Synthesizer code. *Solid green line:* Fit obtained with the Bayesian analysis of the CIGALE. The parameter values of the solutions are also shown (M_*, τ, t, $A(V)$, b) for the Synthesizer and the CIGALE codes, respectively. *Dashed black line:* Fit to the FIR photometry ($\lambda_{obs} \geq 70$ μm). Photometric data points include the uncertainties (multiplied by 2.5 from UV to IRAC bands for visualization), only the *filled black stars* are used in the Synthesizer fit, while the *filled black and cyan stars* are used in the CIGALE fit. *Lower panel:* The SFHs of the galaxy shown in the upper panel. The same color code lines, and the same parameter values are used for building the SFHs of the Synthesizer and CIGALE codes, as it is indicated in the upper panel. The ages of the young population in Myr are also shown for the Synthesizer and CIGALE codes, respectively. An expansion of the look-back time axis is shown to visualize better the SFH of the young population.

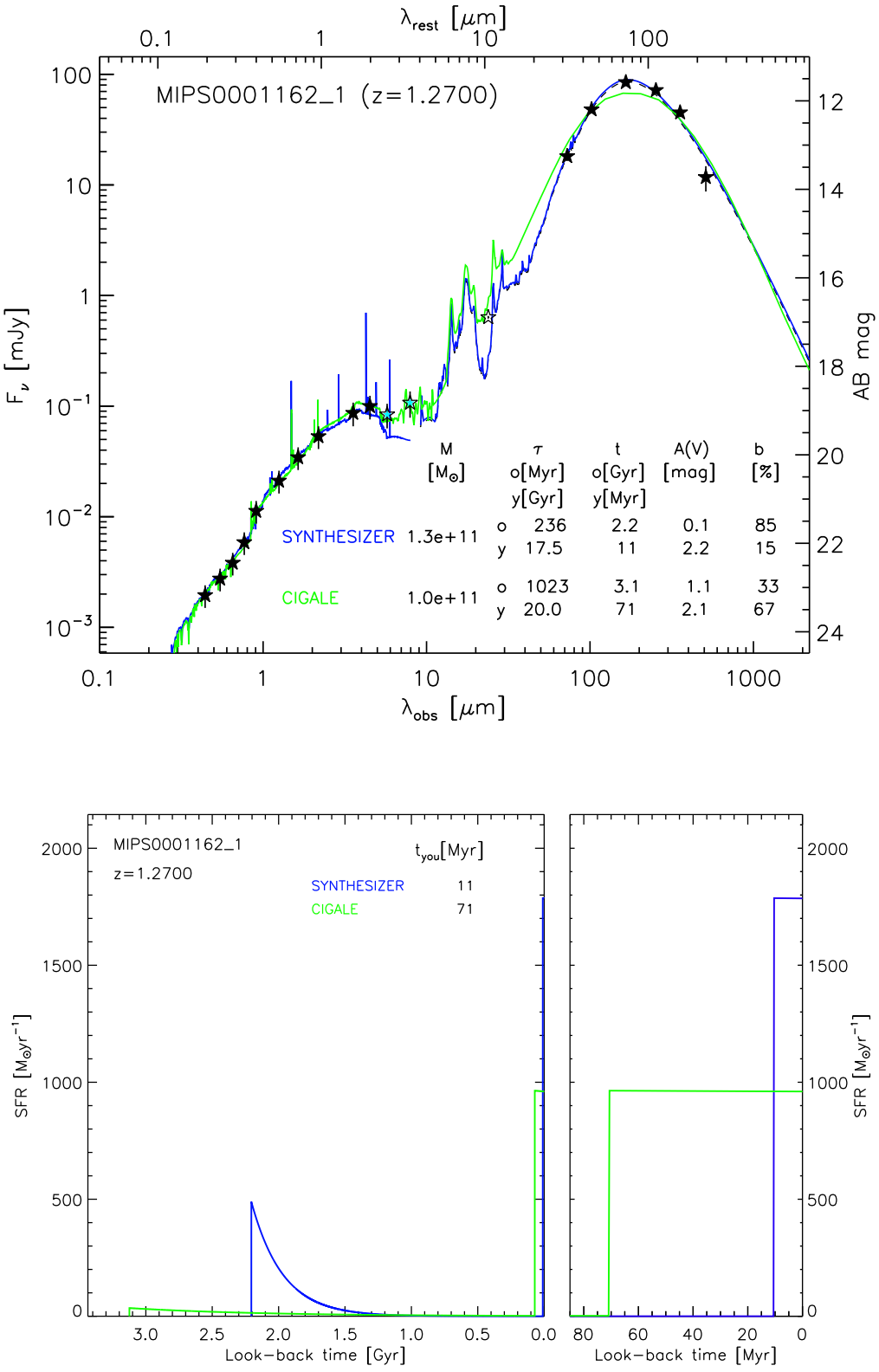

Figure 6.1 : cont'd

Table 6.1. Stellar Population Synthesis Results for Star Forming Galaxies at $0.6 \leq z \leq 1.5$ derived with the CIGALE and Synthesizer Codes

Galaxy	z†	Code	log M $[M_\odot]$	Pop.	τ old [Myr] you [Gyr]	Age old [Gyr] you [Myr]	$A(V)$ [mag]	Z $[Z_\odot]$	b [%]
(1)	(2)	(3)	(4)	(5)	(6)	(7)	(8)	(9)	(10)
MIPS0000050_1	0.9700	Synthesizer	$10.6^{+0.1}_{-0.1}$	old	219^{+47}_{-69}	$2.3^{+1.0}_{-0.4}$	$0.09^{+0.19}_{-0.09}$	1.0	
				you	$18.1^{+3.3}_{-3.0}$	11^{+4}_{-2}	$2.71^{+0.14}_{-0.12}$	1.0	12^{+5}_{-2}
		CIGALE	10.6 ± 0.1	old	337^{+1219}_{-264}	3.2 ± 1.0	$0.66^{+0.85}_{-0.66}$	1.0	
				you	20.0	97^{+112}_{-52}	2.65 ± 0.28	1.0	56 ± 29
MIPS0000149_1	0.67	Synthesizer	$10.9^{+0.1}_{-0.1}$	old	129^{+128}_{-34}	$3.2^{+0.8}_{-0.5}$	$0.02^{+0.08}_{-0.02}$	1.0	
				you	$17.4^{+3.6}_{-2.7}$	206^{+49}_{-25}	$3.21^{+0.08}_{-0.08}$	1.0	52^{+4}_{-3}
		CIGALE	11.1 ± 0.1	old	275^{+588}_{-187}	5.3 ± 1.5	$0.25^{+0.37}_{-0.25}$	1.0	
				you	20.0	203^{+235}_{-109}	3.21 ± 0.32	1.0	33 ± 19
MIPS0000472_1	1.03	Synthesizer	$10.8^{+0.1}_{-0.1}$	old	119^{+121}_{-24}	$3.7^{+0.8}_{-0.8}$	$0.91^{+0.22}_{-0.18}$	1.0	
				you	$18.9^{+2.8}_{-3.0}$	39^{+16}_{-12}	$2.48^{+0.07}_{-0.08}$	1.0	15^{+5}_{-5}
		CIGALE	10.8 ± 0.2	old	1372^{+6076}_{-1119}	3.8 ± 1.4	$1.54^{+0.85}_{-0.85}$	1.0	
				you	20.0	120^{+167}_{-70}	2.59 ± 0.47	1.0	39 ± 30
MIPS0000508_1	0.72	Synthesizer	$9.9^{+0.1}_{-0.1}$	old	210^{+58}_{-106}	$3.1^{+0.9}_{-0.4}$	$0.02^{+0.10}_{-0.02}$	1.0	
				you	$18.9^{+3.0}_{-3.1}$	16^{+4}_{-2}	$3.16^{+0.12}_{-0.11}$	1.0	25^{+5}_{-5}
		CIGALE	10.0 ± 0.1	old	757^{+3162}_{-610}	5.2 ± 1.6	$1.22^{+1.10}_{-1.10}$	1.0	
				you	20.0	82^{+56}_{-33}	3.12 ± 0.20	1.0	61 ± 26
MIPS0000671_1	0.67	Synthesizer	$10.4^{+0.1}_{-0.1}$	old	131^{+122}_{-35}	$5.1^{+1.1}_{-1.0}$	$0.01^{+0.07}_{-0.01}$	1.0	
				you	$15.9^{+1.9}_{-1.7}$	200^{+24}_{-22}	$0.50^{+0.05}_{-0.05}$	1.0	60^{+1}_{-4}
		CIGALE	10.5 ± 0.1	old	1042^{+4792}_{-856}	5.2 ± 1.6	$0.23^{+0.17}_{-0.17}$	1.0	
				you	20.0	241^{+111}_{-76}	0.47 ± 0.05	1.0	56 ± 25
MIPS0000700_1	0.8210†	Synthesizer	$11.0^{+0.1}_{-0.1}$	old	198^{+60}_{-71}	$2.9^{+0.4}_{-0.5}$	$0.00^{+0.06}_{-0.00}$	1.0	
				you	$17.4^{+3.4}_{-2.7}$	94^{+13}_{-15}	$2.10^{+0.05}_{-0.06}$	1.0	15^{+1}_{-1}
		CIGALE	11.1 ± 0.1	old	432^{+876}_{-289}	4.2 ± 1.2	$0.06^{+0.16}_{-0.06}$	1.0	
				you	20.0	138^{+164}_{-75}	1.80 ± 0.77	1.0	14 ± 11
MIPS0000701_1	0.8052†	Synthesizer	$10.7^{+0.1}_{-0.1}$	old	235^{+40}_{-96}	$2.1^{+0.8}_{-0.3}$	$0.02^{+0.07}_{-0.02}$	1.0	
				you	$18.7^{+3.0}_{-3.1}$	10^{+2}_{-1}	$1.68^{+0.07}_{-0.08}$	1.0	11^{+2}_{-1}
		CIGALE	10.5 ± 0.2	old	1343^{+6039}_{-1099}	4.1 ± 1.6	$0.77^{+0.60}_{-0.60}$	1.0	
				you	20.0	69^{+46}_{-28}	1.63 ± 0.29	1.0	59 ± 26
MIPS0000773	0.80	Synthesizer	$10.8^{+0.1}_{-0.1}$	old	208^{+51}_{-65}	$2.0^{+0.2}_{-0.2}$	$0.01^{+0.07}_{-0.01}$	1.0	
				you	$18.2^{+3.3}_{-3.1}$	53^{+20}_{-17}	$3.51^{+0.10}_{-0.09}$	1.0	40^{+6}_{-9}
		CIGALE	11.0 ± 0.1	old	195^{+358}_{-126}	4.2 ± 1.8	$0.08^{+0.25}_{-0.08}$	1.0	
				you	20.0	74^{+100}_{-42}	3.32 ± 0.26	1.0	28 ± 20
MIPS0000904_3	1.16	Synthesizer	$10.5^{+0.1}_{-0.1}$	old	149^{+24}_{-30}	$1.0^{+0.1}_{-0.1}$	$0.01^{+0.07}_{-0.01}$	1.0	
				you	$18.3^{+3.2}_{-3.2}$	17^{+7}_{-3}	$3.87^{+0.25}_{-0.27}$	1.0	51^{+5}_{-4}
		CIGALE	10.6 ± 0.1	old	109^{+59}_{-38}	2.1 ± 1.5	$0.06^{+0.22}_{-0.06}$	1.0	
				you	20.0	35^{+18}_{-12}	3.37 ± 0.18	1.0	54 ± 16

Table 6.1 (cont'd)

Galaxy	z†	Code	log M [$M_\odot$]	Pop.	τ old [Myr] you [Gyr]	Age old [Gyr] you [Myr]	$A(V)$ [mag]	Z [$Z_\odot$]	b [%]
(1)	(2)	(3)	(4)	(5)	(6)	(7)	(8)	(9)	(10)
MIPS0000922_1	0.8068†	Synthesizer	$10.9^{+0.1}_{-0.1}$	old	202^{+61}_{-103}	$2.9^{+1.5}_{-0.9}$	$1.46^{+0.07}_{-0.13}$	1.0	
				you	$17.5^{+3.4}_{-2.8}$	396^{+76}_{-75}	$2.20^{+0.08}_{-0.08}$	1.0	59^{+2}_{-8}
		CIGALE	11.0 ± 0.1	old	1494^{+6255}_{-1206}	4.7 ± 1.4	$1.31^{+0.69}_{-0.69}$	1.0	
				you	20.0	302^{+397}_{-171}	2.10 ± 0.46	1.0	42 ± 30
MIPS0001032_1	1.14	Synthesizer	$10.3^{+0.1}_{-0.1}$	old	127^{+35}_{-26}	$1.0^{+0.1}_{-0.1}$	$0.01^{+0.07}_{-0.01}$	1.0	
				you	$19.1^{+2.9}_{-3.2}$	22^{+5}_{-6}	$2.52^{+0.08}_{-0.06}$	1.0	60^{+2}_{-9}
		CIGALE	10.5 ± 0.1	old	1065^{+4974}_{-877}	3.2 ± 1.6	$1.43^{+0.78}_{-0.78}$	1.0	
				you	20.0	59^{+33}_{-21}	2.35 ± 0.09	1.0	66 ± 24
MIPS0001045_1	0.80	Synthesizer	$11.1^{+0.1}_{-0.1}$	old	166^{+59}_{-26}	$3.1^{+0.6}_{-0.4}$	$0.30^{+0.12}_{-0.10}$	1.0	
				you	$18.8^{+2.9}_{-3.2}$	81^{+16}_{-15}	$2.60^{+0.07}_{-0.08}$	1.0	15^{+1}_{-4}
		CIGALE	11.2 ± 0.1	old	263^{+557}_{-179}	4.6 ± 1.5	$0.36^{+0.34}_{-0.34}$	1.0	
				you	20.0	252^{+520}_{-170}	2.46 ± 0.23	1.0	26 ± 18
MIPS0001162_1	1.2700†	Synthesizer	$11.1^{+0.1}_{-0.2}$	old	236^{+37}_{-81}	$2.2^{+0.9}_{-0.4}$	$0.10^{+0.19}_{-0.10}$	1.0	
				you	$17.5^{+3.4}_{-2.7}$	11^{+5}_{-2}	$2.20^{+0.09}_{-0.09}$	1.0	15^{+13}_{-4}
		CIGALE	11.0 ± 0.1	old	1023^{+4735}_{-841}	3.1 ± 1.0	$1.12^{+0.73}_{-0.73}$	1.0	
				you	20.0	71^{+39}_{-25}	2.15 ± 0.10	1.0	67 ± 24
MIPS0001164_1	1.12	Synthesizer	$9.9^{+0.1}_{-0.1}$	old	129^{+38}_{-24}	$1.0^{+0.1}_{-0.1}$	$0.06^{+0.26}_{-0.06}$	1.0	
				you	$18.2^{+3.3}_{-3.1}$	10^{+1}_{-1}	$2.60^{+0.06}_{-0.07}$	1.0	56^{+5}_{-10}
		CIGALE	10.1 ± 0.2	old	1059^{+4909}_{-871}	3.3 ± 1.6	$1.25^{+0.79}_{-0.79}$	1.0	
				you	20.0	24^{+28}_{-13}	2.35 ± 0.13	1.0	59 ± 30
MIPS0001212	0.71	Synthesizer	$10.5^{+0.1}_{-0.1}$	old	245^{+32}_{-41}	$3.0^{+0.4}_{-0.3}$	$0.00^{+0.06}_{-0.00}$	1.0	
				you	$19.5^{+2.5}_{-2.8}$	9^{+1}_{-1}	$3.22^{+0.09}_{-0.09}$	1.0	22^{+4}_{-2}
		CIGALE	10.7 ± 0.1	old	324^{+708}_{-222}	5.5 ± 1.4	$0.03^{+0.16}_{-0.03}$	1.0	
				you	20.0	10^{+1}_{-1}	3.18 ± 0.22	1.0	11 ± 5
MIPS0001225	0.8701†	Synthesizer	$10.5^{+0.1}_{-0.1}$	old	243^{+34}_{-38}	$2.0^{+0.3}_{-0.2}$	$0.03^{+0.12}_{-0.03}$	1.0	
				you	$19.4^{+2.6}_{-3.0}$	10^{+1}_{-1}	$2.52^{+0.09}_{-0.08}$	1.0	25^{+2}_{-5}
		CIGALE	10.6 ± 0.2	old	1459^{+5962}_{-1172}	4.1 ± 1.7	$0.80^{+0.76}_{-0.76}$	1.0	
				you	20.0	16^{+27}_{-10}	2.57 ± 0.47	1.0	35 ± 35
MIPS0001300_1	0.9500	Synthesizer	$10.4^{+0.1}_{-0.1}$	old	231^{+40}_{-42}	$2.0^{+0.3}_{-0.2}$	$0.51^{+0.13}_{-0.24}$	1.0	
				you	$19.0^{+2.8}_{-2.9}$	71^{+21}_{-20}	$3.03^{+0.12}_{-0.08}$	1.0	46^{+10}_{-10}
		CIGALE	10.6 ± 0.1	old	425^{+1798}_{-344}	3.2 ± 1.0	$1.08^{+0.98}_{-0.98}$	1.0	
				you	20.0	169^{+171}_{-85}	2.83 ± 0.18	1.0	61 ± 27
MIPS0001324_1	0.7200	Synthesizer	$11.1^{+0.1}_{-0.1}$	old	102^{+16}_{-12}	$6.0^{+0.7}_{-0.7}$	$1.48^{+0.06}_{-0.08}$	1.0	
				you	$19.1^{+2.9}_{-3.0}$	418^{+75}_{-55}	$2.37^{+0.08}_{-0.11}$	1.0	60^{+1}_{-4}
		CIGALE	11.1 ± 0.2	old	2046^{+8294}_{-1641}	4.9 ± 1.6	$1.53^{+0.97}_{-0.97}$	1.0	
				you	20.0	124^{+170}_{-72}	2.23 ± 0.66	1.0	25 ± 25

Table 6.1 (cont'd)

Galaxy	z†	Code	log M $[M_\odot]$	Pop.	τ old [Myr] you [Gyr]	Age old [Gyr] you [Myr]	$A(V)$ [mag]	Z $[Z_\odot]$	b [%]
(1)	(2)	(3)	(4)	(5)	(6)	(7)	(8)	(9)	(10)
MIPS0001585_1	0.9200	Synthesizer	$10.8^{+0.1}_{-0.1}$	old	169^{+51}_{-36}	$3.2^{+1.0}_{-0.6}$	$0.17^{+0.09}_{-0.11}$	1.0	
				you	$16.6^{+3.3}_{-2.0}$	51^{+17}_{-15}	$2.50^{+0.06}_{-0.05}$	1.0	20^{+5}_{-6}
		CIGALE	10.8 ± 0.1	old	339^{+1105}_{-260}	4.3 ± 1.5	$0.54^{+0.74}_{-0.54}$	1.0	
				you	20.0	137^{+176}_{-77}	2.49 ± 0.25	1.0	49 ± 30

Note. — Results for the two stellar population modeling of the SEDs of our sample of IR-bright galaxies. Median and 1σ error values are shown for each parameter derived with the Synthesizer code. The expected and standard deviation (or upper and lower limits when changing from logarithmic space to linear space) values are quoted for each parameter estimated with the CIGALE. (1) Name of the galaxy. (2) Photometric or spectroscopic redshift ($z_{\rm spec}$ indicated by a †). (3) Code used to derive the parameters. (4) Stellar mass (in solar units) and its uncertainty derived from the logarithmic space. (5) Parameter values for the old or the young population. (6) e-folding time and its uncertainty (old population in Myr and young population in Gyr). (7) Age and its uncertainty (old population in Gyr and young population in Myr). (8) Extinction in the V-band and its uncertainty in mag. (9) Metallicity value (fixed to the solar value) in solar units. (10) Burst intensity fraction and its uncertainty in percentage.

As a second test, we have plotted in Fig. 6.2 the $\chi^2_{\rm UV/MIR}$ distributions for the Synthesizer and CIGALE codes. The distribution of the Synthesizer code concentrates in lower $\chi^2_{\rm UV/MIR}$ values compared with the CIGALE one. We have also estimated the median, and the 16 and 84-percentile values for the two codes, obtaining $1.7^{+1.4}_{-0.6}$ for the Synthesizer code, and $4.0^{+3.0}_{-2.4}$ for the CIGALE. Hence, the $\chi^2_{\rm UV/MIR}$ values of the CIGALE are more spread to larger values than the Synthesizer ones. When comparing the median values, we observe that the CIGALE median is almost 1σ away from the Synthesizer one. Therefore, we conclude that the Synthesizer code performs better than the CIGALE in the FUV-to-MIR spectral range.

When inspecting the FIR spectral range, we find that a slightly larger fraction, 52% of all galaxies, is better fitted by the CIGALE. We have also plotted the $\chi^2_{L_{\rm TIR}}$ distributions for both codes (see Fig. 6.3), these distributions are alike, but with the CIGALE one having 2 more objects in the lowest bin of $\chi^2_{L_{\rm TIR}}$ values. The median, and the 16 and 84-percentile are $0.9^{+3.2}_{-0.8}$ and $1.4^{+1.8}_{-1.3}$ for the CIGALE and the Synthesizer code, respectively. The distribution of the Synthesizer code presents 1 galaxy in the high $\chi^2_{L_{\rm TIR}}$ values tail. Even though the CIGALE median is a little shorter than the Synthesizer one, they are close enough to be considered analogous. Furthermore, the 1σ values of the Synthesizer code are included in the CIGALE ones, pointing to a comparable performance of each code in the FIR spectral range.

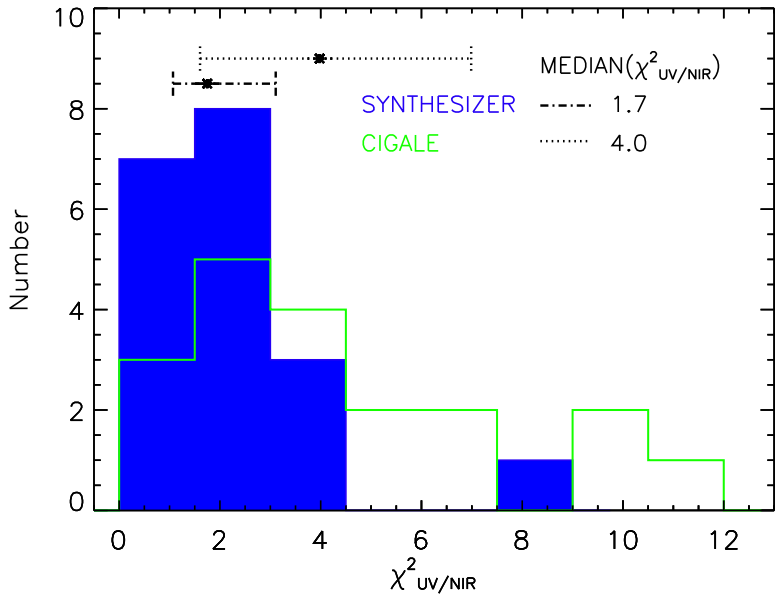

Figure 6.2 : Distributions of $\chi^2_{\rm UV/MIR}$ values obtained evaluating the UV-to-MIR spectral range for the Synthesizer and CIGALE codes. *Fill blue:* Results from the Synthesizer code. *Open green:* Results from the CIGALE. The median values, and the 16 and 84-percentile of the distributions are indicated.

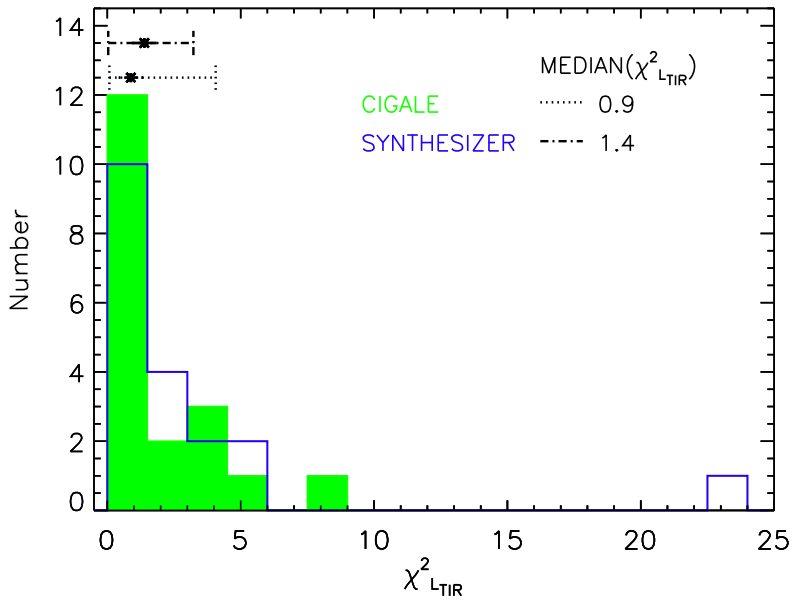

Figure 6.3 : Distributions of $\chi^2_{\rm L_{TIR}}$ values obtained from comparisons with the observed $L_{\rm TIR,ref}$ for the Synthesizer and CIGALE codes. *Fill green:* Results for the CIGALE. *Open blue:* Results for the Synthesizer code. The median values, and the 16 and 84-percentile of the distributions are shown.

Table 6.2 : Goodness of Fit Results for Star Forming Galaxies at $0.6 \leq z \leq 1.5$

Galaxy	Code	$\chi^2_{UV,MIR}$	$\chi^2_{L_{TIR}}$
(1)	(2)	(3)	(4)
MIPS0000050_1	Synthesizer	1.7	3.1
	CIGALE	4.0	< 0.1
MIPS0000149_1	Synthesizer	1.7	< 0.1
	CIGALE	1.6	0.9
MIPS0000472_1	Synthesizer	0.5	3.2
	CIGALE	1.0	8.3
MIPS0000508_1	Synthesizer	2.1	2.2
	CIGALE	4.5	< 0.1
MIPS0000671_1	Synthesizer	4.2	0.6
	CIGALE	1.3	0.2
MIPS0000700_1	Synthesizer	1.1	< 0.1
	CIGALE	2.7	1.3
MIPS0000701_1	Synthesizer	1.5	1.4
	CIGALE	6.1	0.1
MIPS0000773	Synthesizer	0.7	1.3
	CIGALE	4.5	5.8
MIPS0000904_3	Synthesizer	4.2	3.0
	CIGALE	4.6	4.0
MIPS0000922_1	Synthesizer	2.3	0.7
	CIGALE	9.4	0.3
MIPS0001032_1	Synthesizer	3.1	< 0.1
	CIGALE	4.2	1.1
MIPS0001045_1	Synthesizer	1.2	5.1
	CIGALE	10.8	0.1
MIPS0001162_1	Synthesizer	0.7	0.7
	CIGALE	0.7	0.7
MIPS0001164_1	Synthesizer	1.5	< 0.1
	CIGALE	2.8	4.4
MIPS0001212	Synthesizer	2.4	4.8
	CIGALE	3.7	0.1
MIPS0001225	Synthesizer	1.9	1.3
	CIGALE	9.4	0.6
MIPS0001300_1	Synthesizer	2.5	2.7
	CIGALE	2.4	2.1
MIPS0001324_1	Synthesizer	8.0	22.5
	CIGALE	7.0	1.6
MIPS0001585_1	Synthesizer	1.4	1.9
	CIGALE	1.7	4.1

Note.— Results for the goodness of fit to the SEDs of our sample of IR-bright galaxies. (1) Name of the galaxy. (2) Code being evaluated. (3) Goodness of fit of the FUV-to-NIR spectral range (as explained in the text). (4) Goodness of fit of the FIR spectral range (as explained in the text).

We now move to describe the parameters of the SFHs obtained from the SED-fitting results. Outwardly from the lower panels of Fig. 6.1, we perceive that these SFHs are characterized by a extremely recent burst, overlapped to an evolved stellar population. The ages of this old population differ in $\sim 1-2$ Gyr between the CIGALE and Synthesizer results for most of the objects in our sample. Attending to these differences, we have estimated the mass weighted age with the results of the Synthesizer code, which represents the average age of the mix of the two stellar populations. The CIGALE also provides this value as an output parameter. The mass weighted age is a secondary parameter, in the sense that it is derived from the main parameters: M_*, $\tau_{\rm old}$, $t_{\rm old}$, $\tau_{\rm you}$, $t_{\rm you}$, and b. In Section 6.1.4, we present the comparison of the mass weighted ages obtained from the Synthesizer and the CIGALE codes.

In Sections 6.1.2 and 6.1.3, we compare separately each parameter of the young and the old population obtained as a median solution from the Monte Carlo simulations of the Synthesizer code with its respective analog derived as the expected value from the Bayesian analysis with the CIGALE. By considering both sets of results, we can account for the real uncertainties and systematic errors in the derived parameters related to each code and its analysis methodology.

6.1.2 Properties of the Young Population

In this Section, we compare the parameters fitted to the young population of our sample of IR-bright galaxies with the Synthesizer code and the CIGALE. As we have fixed the value of Z in both codes and $\tau_{\rm you}$ is also unvaried in the CIGALE, we can only look for a possible correlation for three parameters: the age $t_{\rm you}$, the attenuation $A(V)_{\rm you}$, and the burst intensity b.

In Figure 6.4, we show the comparison of the age of the young stellar population estimated with both codes, and their ratio. The median values of the solutions for the young population age derived with the Synthesizer code are in $8 < t_{\rm you,SYNT} < 419$ Myr, with a median value, and the 16 and 84-percentile of 39^{+161}_{-29} Myr. The respective expected values estimated from the CIGALE are in $9 < t_{\rm you,CIGA} < 302$ Myr, with the median value, and the 16 and 84-percentile of 97^{+106}_{-62} Myr. Hence, both sets of solutions spam similar age values, but with the Synthesizer code getting age values near 400 Myr for 2 galaxies which have burst intensity $\sim 60\%$. The Synthesizer code also inclines for shorter age values in median (see left part of Fig. 6.4), 47% of the ages estimated by the Synthesizer code are shorter than 39 Myr, while only 21% of the ages derived with the CIGALE fulfill this condition. In order to quantify the level of correlation

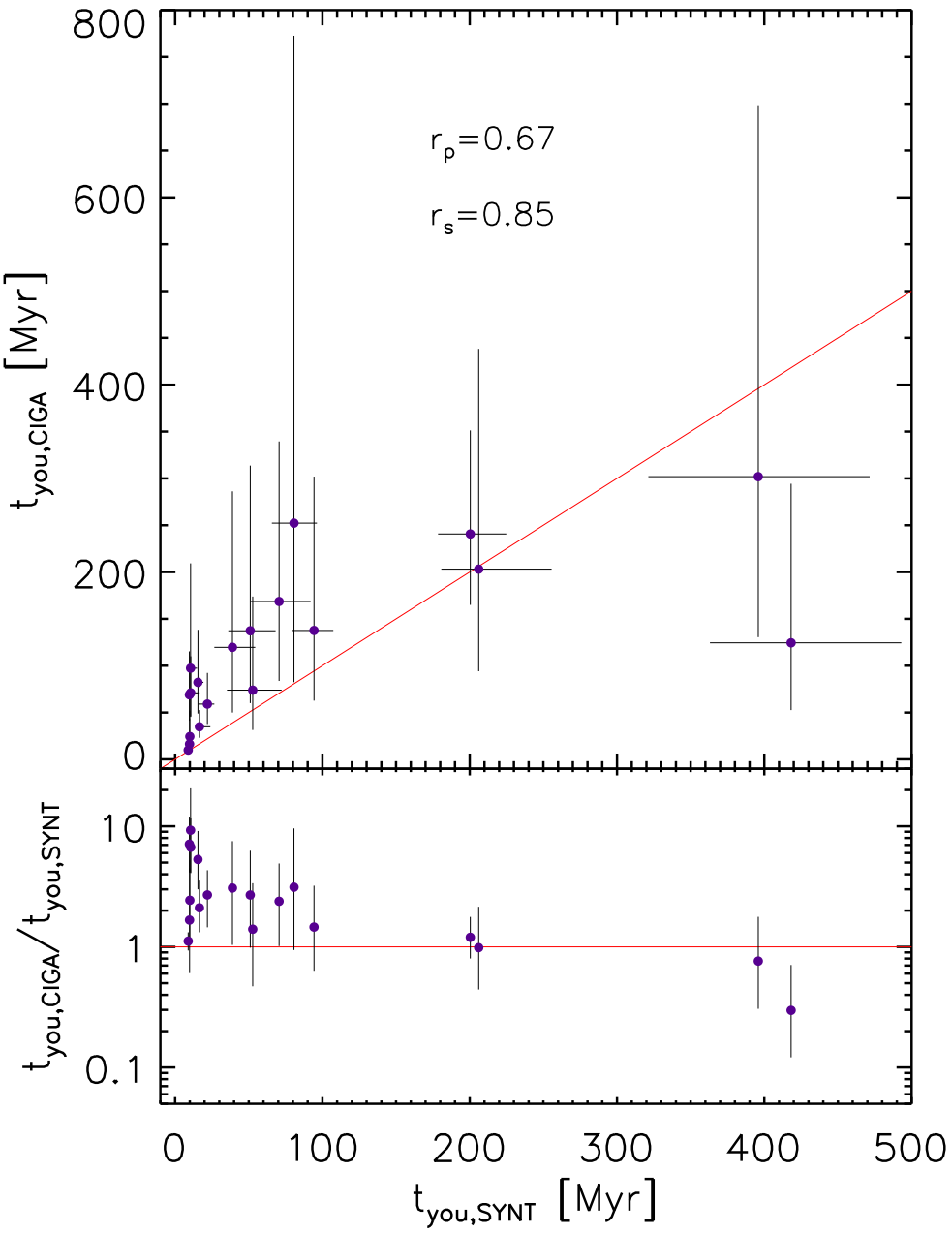

Figure 6.4 : *Upper panel:* Comparison between the ages of the young stellar population ($t_{\rm you}$) derived by the Synthesizer code on x-axis, and those derived by the CIGALE on y-axis. The filled circles with error bars show the median values and their 1σ uncertainties estimated with the Synthesizer code, and the expected values and the standard deviations estimated with the CIGALE as it is explained in Sections 4.2.2.2, and 4.2.1.2. The Pearson and Spearman correlation coefficients are also shown. *Lower panel:* Ratio of the ages derived with both codes. The error bars show the propagated uncertainties.

between the young age values obtained from both codes, we have estimated the linear Pearson Correlation coefficient, which is moderately high: $r_p = 0.67$. An assumption in the computation of this coefficient is that the variables have a Gaussian distribution,

which could be unfulfilled in our case. Therefore, we have also estimated the Spearman correlation coefficient with no assumption used in its computation. We have gotten $r_s = 0.85$, with and associated probability of no correlation of $p_s = 4.7 \times 10^{-6}$.

In the lower panel of Fig. 6.4, we show the ratios between the ages of the young population derived with the CIGALE and the Synthesizer codes and their respective propagated uncertainties. The ratio values are in $0.3 < t_{\rm you,CIGA}/t_{\rm you,SYNT} < 9.3$, taking into account the propagated uncertainties, 47% of the galaxies have obtained a similar age value for the young population from the results of each code. It can also be noticed from Fig. 6.4, that 79% of all galaxies have obtained $t_{\rm you,SYNT} < 100$ Myr from the Synthesizer code results, while only 53% of the young populations ages derived with the CIGALE are shorter than such age value. Regarding the objects with young population age shorter than 100 Myr from the Synthesizer code, we observe that their median young population age ratio is 2.7, i.e., that these objects have in median an age of the young population that is less than a half of the young population age derived with the CIGALE.

Considering the above results, we can state that there is a significant correlation between the ages of the young population estimated with the Synthesizer and the CIGALE codes for our galaxy sample. Consequently, we can appraise that the age of the young population has been adequately constrained for our galaxies, with the Synthesizer code tending to fit shorter young ages than the CIGALE for a significant part of the sample.

We have also looked for possible correlations between $t_{\rm you}$ and other physical properties of our galaxy sample. We have found a correlation between $L_{\rm TIR}$ and $t_{\rm you}$, which is shown in figure 6.5. We have used the $L_{\rm TIR,ref}$ values because they are obtained fitting only the FIR data and choosing the best-fitting template obtained from the whole set of IR models of the three libraries (CE01, DH02, and R+09) that we have considered. There is a trend of increasing the age for the young stellar population when decreasing the total infrared luminosity. The correlation is observed for the young ages derived with both codes. A similar result is found in Lemaux et al. (2014) measuring the A/K ratio (i.e., the ratio between the contribution of early type stars and late type stars), the equivalent width of Hδ, and the strength of continuum break at 4000Å in a composite spectra of a sample of $0.5 < z < 2$ Herschel detected galaxies in the Canada-France-Hawaii Telescope Legacy Survey (see their Sections 4.4.1, and 4.4.2). They explain this effect by distinguishing the LIRG and ULIRG population, mentioning that LIRGs are experiencing rejuvenated starbursts while ULIRGs could be suffering an initial violent starbust or a strong rejuvenating event.

It is important to note that although our determined SFH for the young stellar popu-

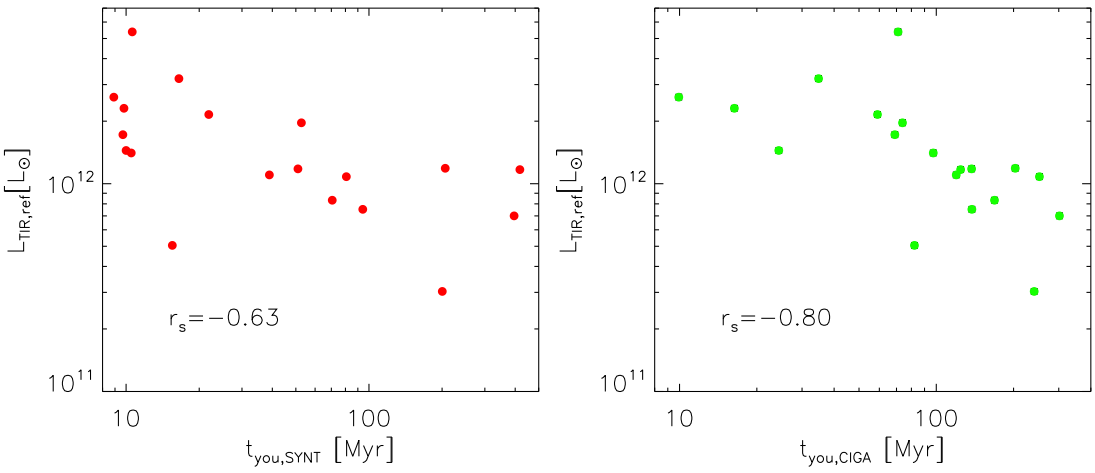

Figure 6.5 : *Left panel:* $t_{\rm you}$ vs. $L_{\rm TIR,ref}$ correlation for our sample of star-forming galaxies for the age young values derived with the Synthesizer code. *Right panel:* The same in the left panel, but for the age young values of the CIGALE. We show the Spearman correlation coefficient in each panel. There is a trend of higher $L_{\rm TIR}$ values with shorter ages for the young population.

lation is practically constant (see lower panels of Fig. 6.1 and Appendix B), considering the $t_{\rm you}$ – $L_{\rm TIR,ref}$ correlation we can state that we are observing our objects at a different evolutionary moment of the (U)LIRG phase. From this fact, and taking into account our assumed SFH ($SFR(t) \sim e^{-t/\tau}$), we can derive a timescale (i.e., when the $L_{\rm TIR}$ or SFR decreases a factor e) of $\sim 100 - 150$ Myr for this SFH. From these timescale, it is inferred that, on average, we are observing galaxies at half of their lifetime in the (U)LIRG phase (which is what could be expected). Therefore, our estimation of the duration of the (U)LIRG phase is $\sim 200 - 300$ Myr which is in agreement with the values inferred for the lifetime of starbust phase of sub-millimeter (sub-mm) galaxies $\sim 100 - 300$ Myr (Swinbank et al. 2006, Hickox et al. 2012).

In Figure 6.6, we compare the attenuations in the V band determined with the Synthesizer and CIGALE codes for the young stellar population. The median values of the solutions estimated with the Synthesizer code are in $0.49 < A(V)_{\rm you,SYNT} < 3.87$ mag, with a median value, and the 16 and 84-percentile of $2.52^{+0.69}_{-0.32}$ mag. The expected values derived with the CIGALE are in $0.46 < A(V)_{\rm you,CIGA} < 3.37$ mag, with a median value, and the 16 and 84-percentile of $2.49^{+0.69}_{-0.39}$ mag. Then, both codes provide similar ranges of $A(V)_{\rm you}$ values, as could be expected taking into account the energy balance approach used in both codes. The Synthesizer code constrains the amount of attenuation of the stellar populations $A(V)$ with the dust re-emitted energy derived from an independently computed $L_{\rm TIR}$, and the CIGALE scales the IR templates according to the energy absorbed by the dust derived from the attenuated stellar populations models.

There is a clear correlation between the $A(V)_{\rm you}$ values estimated with both codes in Fig. 6.6. Nevertheless, we have estimated the Pearson correlation coefficient, which resulted $r_p = 0.98$, and the Spearman correlation coefficient, which is $r_s = 0.95$ with a probability $p_s = 7.8 \times 10^{-10}$ of getting this result as a mere coincidence.

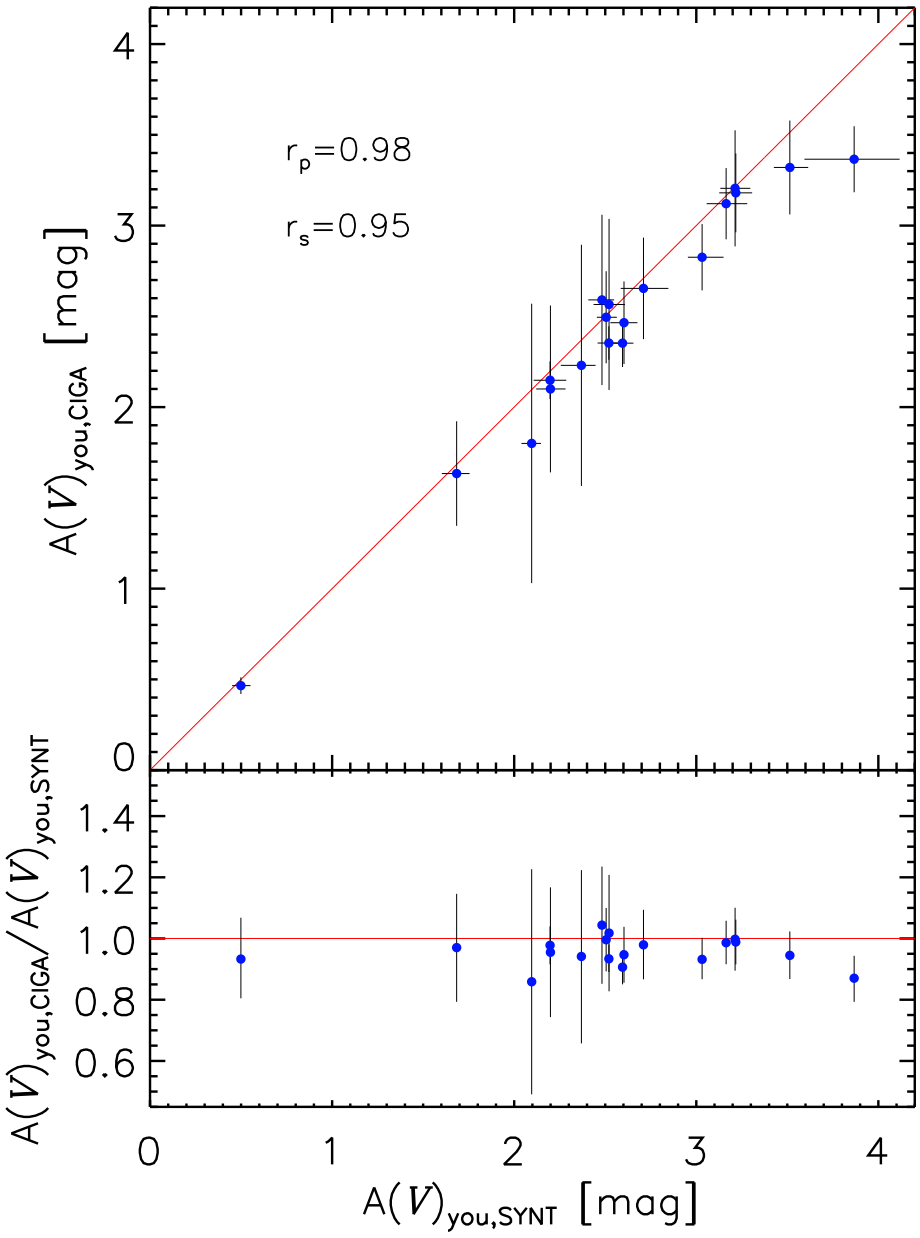

Figure 6.6 : *Upper panel:* Comparison between the attenuations of the young stellar population, $A(V)_{\rm you}$, derived by the Synthesizer code on x-axis, and those derived by the CIGALE on y-axis. The filled circles with error bars show the median values and their 1σ uncertainties estimated with the Synthesizer code, and the expected values and the standard deviations estimated with the CIGALE. *Lower panel:* Ratio of the attenuations of the young population derived with both codes. The error bars show the propagated uncertainties.

In the lower panel of Fig. 6.6 we show the ratios between the CIGALE and the Synthesizer codes obtained attenuations for the young population with their respective propagated uncertainties. The ratio values are in $0.8 < A(V)_{\rm you,CIGA}/A(V)_{\rm you,SYNT} < 1.1$, considering the propagated uncertainties, 84% of the galaxies have gotten a similar value of attenuation for the young population from the results of each code.

The majority of our objects (89%) presents $A(V)_{\rm you} > 2$ mag, which is not surprising given our sample selection based on the 70 μm emission that could be biased towards recent merger events (see Pope et al. 2013). There is a galaxy with low $A(V)_{\rm you} \sim 0.5$ mag, this object has photometric data in both GALEX bands, and it is the object with the lowest $L_{\rm TIR}$. We have not found any study in the literature exploring $A(V)_{\rm you}$ attenuation values higher than ~ 2 mag with our assumed SFH (Eq. 4.1), except Pérez-González et al. (2008). This attenuation range has not been investigated using the CIGALE either (Giovannoli et al. 2011, Buat et al. 2014).

We have compared our results with those obtained by Rowlands et al. (2014), who studied the physical properties of a rest-frame 250 μm selected sample of dusty massive galaxies from $0 < z < 5.3$. They used a tuned version of the MAGPHYS code (da Cunha et al. 2008), which estimates the dust attenuation using the Charlot and Fall (2000) model. This model accounts for the different attenuation suffered by young and old stars considering that young stars are born in dense molecular clouds, and hence their light is more attenuated than the one from old stars. The model parameterizes the attenuation in the young population emission by means of the optical depth of dust in the birth clouds, $\hat{\tau}_{\lambda}^{\rm BC}$. Transforming the $\hat{\tau}_{V}^{\rm BC}$ reported in Rowlands et al. (2014) to $A(V)_{\rm you}$ for their objects in our redshift range, we obtained that their objects have $2.40 < A(V)_{\rm you} < 8.80$, which are even higher than our values. Therefore, the attenuation values derived for the young population in our galaxy sample are within the standard range of values for dusty galaxies at these redshifts.

In Figure 6.7 we present the comparison of the intensity of the recent burst (expressed in percentage) which gives rise to the young stellar population estimated with the two codes. The median values of the solutions derived with the Synthesizer code range in $10 < b_{\rm SYNT} < 60\%$, with a median value, and 16 and 84-percentile of $25^{+34}_{-9}\%$. The expected values determined with the CIGALE are in $10 < b_{\rm CIGA} < 67\%$, with a median value, and the 16 and 84-percentile of $49^{+11}_{-23}\%$. Hence, the two sets of solutions inspect comparable burst intensity values. There is not a visible correlation in Fig. 6.7, but the uncertainties of the burst intensity values derived with the CIGALE are huge, with 2 galaxies having uncertainties of the same order that the obtained values.

Following Giovannoli et al. (2011), we explored a range in burst intensity from 0

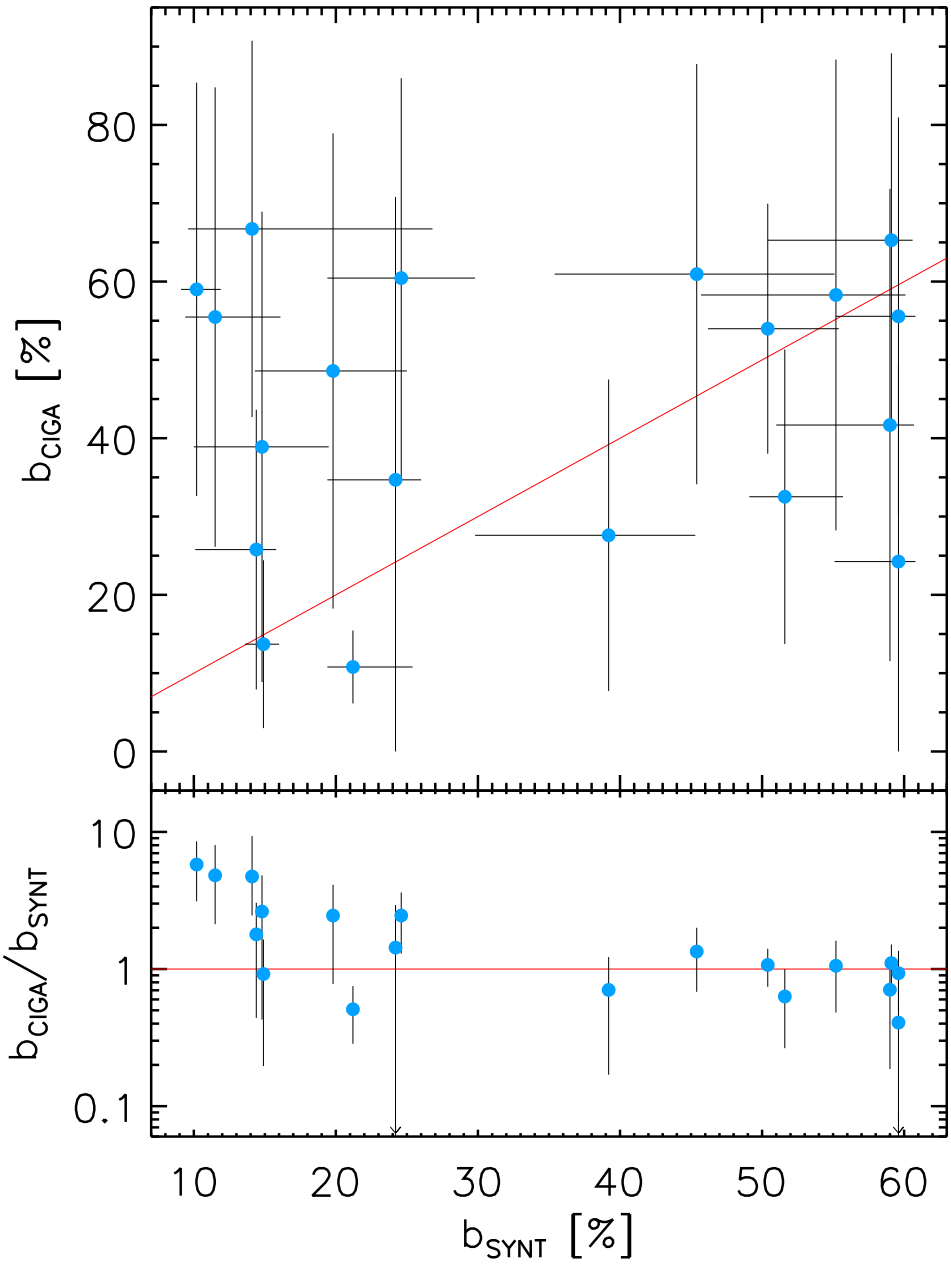

Figure 6.7 : *Upper panel:* Comparison between the burst intensities b of the young stellar population derived by the Synthesizer code on x-axis, and those derived by the CIGALE on y-axis. The filled circles with error bars show the average values and the 1σ uncertainties estimated with the Synthesizer code, and the expected values and the standard deviations estimated with the CIGALE. *Lower panel:* Ratio of the burst intensity derived with both codes. The error bars show the propagated uncertainties. The downward arrows indicate that error bars could reach a ratio of zero.

to 99.9% (but investigating more burst intensity values) using the CIGALE (see table 4.1). They built a mock catalog in their study, adding an error of 10% to the flux in each of their bands. They estimated a Pearson correlation coefficient between the mock and

the real catalog with 70 μm detections which resulted $r_p = 0.54$, hence the correlation is moderately significant. They also found some galaxies having uncertainties of the same order of the burst intensity values in the real sample.

In our study, we also left b as free as possible. The recent work of Buat et al. (2014) using also CIGALE only explored burst intensities until 50% (their $f_{\rm ySP}$), which is compatible with most of our objects (12 from the Synthesizer code analysis, and 10 from the CIGALE analysis). Anyway, we should consider that 14 of our objects are ULIRGs, and these objects should be suffering vigorous starbursts (see, e.g., Rowlands et al. 2014, Lemaux et al. 2014). Therefore, the range of b studied in our work is adequate.

In the lower panel of Fig. 6.7 we show the ratio between the burst intensities derived with the CIGALE and the Synthesizer codes and their respective propagated uncertainties. The ratio values are in $0.4 < b_{\rm CIGA}/b_{\rm SYNT} < 5.8$, taking into account the propagated uncertainties, 63% of our objects have obtained a compatible value of burst intensity of the young population from the results of each code. It should be noticed that 2 galaxies have huge uncertainties in the ratio value, suggesting that their ratio may reach a value of 0.

Hence, our IR-bright galaxy sample presents young populations forming stars in approximately constant manner. Their ages are shorter than ~ 400 Myr, with median values of ~ 40 and ~ 100 Myr for the Synthesizer code and the CIGALE respectively. The attenuations in the V band of these young bursts are larger than ~ 2 mag for most of the objects, with median value of ~ 2.5 mag for both codes. The burst intensities can form $\sim 10 - 60\%$ of the total stellar mass, with median value of $\sim 25\%$ for the Synthesizer code, and $\sim 50\%$ for the CIGALE.

6.1.3 Properties of the Old Population

Here we compare the parameters obtained for the old stellar population with the Synthesizer and CIGALE codes. The parameters that we have analyzed for the old population are the exponential decay factor $(\tau_{\rm old})$, the age $(t_{\rm old})$, and the attenuation $(A(V)_{\rm old})$.

In Figure 6.8, we compare the e-folding time $\tau_{\rm old}$ determined with the Synthesizer and CIGALE codes for the old stellar population. The median values of the solutions estimated with the Synthesizer code are in $101 < \tau_{\rm old,SYNT} < 245$ Myr, with a median value, and the 16 and 84-percentile of 198^{+37}_{-69} Myr. The expected values derived with the CIGALE are in $108 < \tau_{\rm old,CIGA} < 2047$ Myr, with a median value, and the 16 and 84-percentile of 757^{+615}_{-481} Myr. Although the values of $\tau_{\rm old}$ derived with each code are

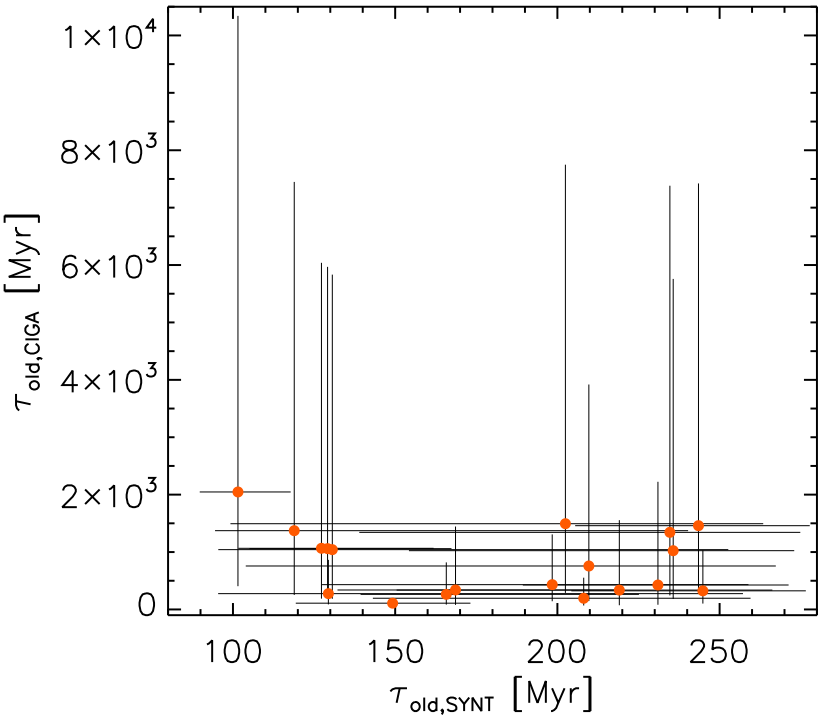

Figure 6.8 : Comparison between the exponential decay factors of the old stellar population ($\tau_{\rm old}$) derived by the Synthesizer code on x-axis, and those derived by the CIGALE on y-axis. The filled circles with error bars show the median values and the 1σ uncertainties estimated with the Synthesizer code, and the expected values and the standard deviations derived with the CIGALE.

similar for half of the galaxies (with differences between a factor of 2), the CIGALE finds much higher values of $\tau_{\rm old}$ in some objects than the Synthesizer code. This effect could be caused by the few discrete values examined in the CIGALE (0.1, 1, 3, and 10 Gyr) in order to keep reasonable numbers of computing time and hard-disc storage. We have used in our study a similar set of $\tau_{\rm old,CIGA}$ values to the ones explored in several works consulted in the literature using the CIGALE (see, e.g., Noll et al. 2009, Giovannoli et al. 2011, Buat et al. 2011). In such studies, it has been found that the $\tau_{\rm old}$ values are unsatisfactorily estimated, and almost unconstrained.

Just attending to Fig. 6.8, it is obvious that there is no correlation between the values of $\tau_{\rm old}$ estimated with the CIGALE and the Synthesizer code. The $\tau_{\rm old}$ values determined with the CIGALE group near to $\sim 250 - 400$, and $\sim 1000 - 1500$ Myr, whereas the huge upper errors suggest that some models with $\tau_{\rm old} = 10$ Gyr have been used in the Bayesian analysis.

Looking at the results of the Synthesizer code we can notice that their confidence intervals are also large. We have explored with the Synthesizer code $\tau_{\rm old}$ values from

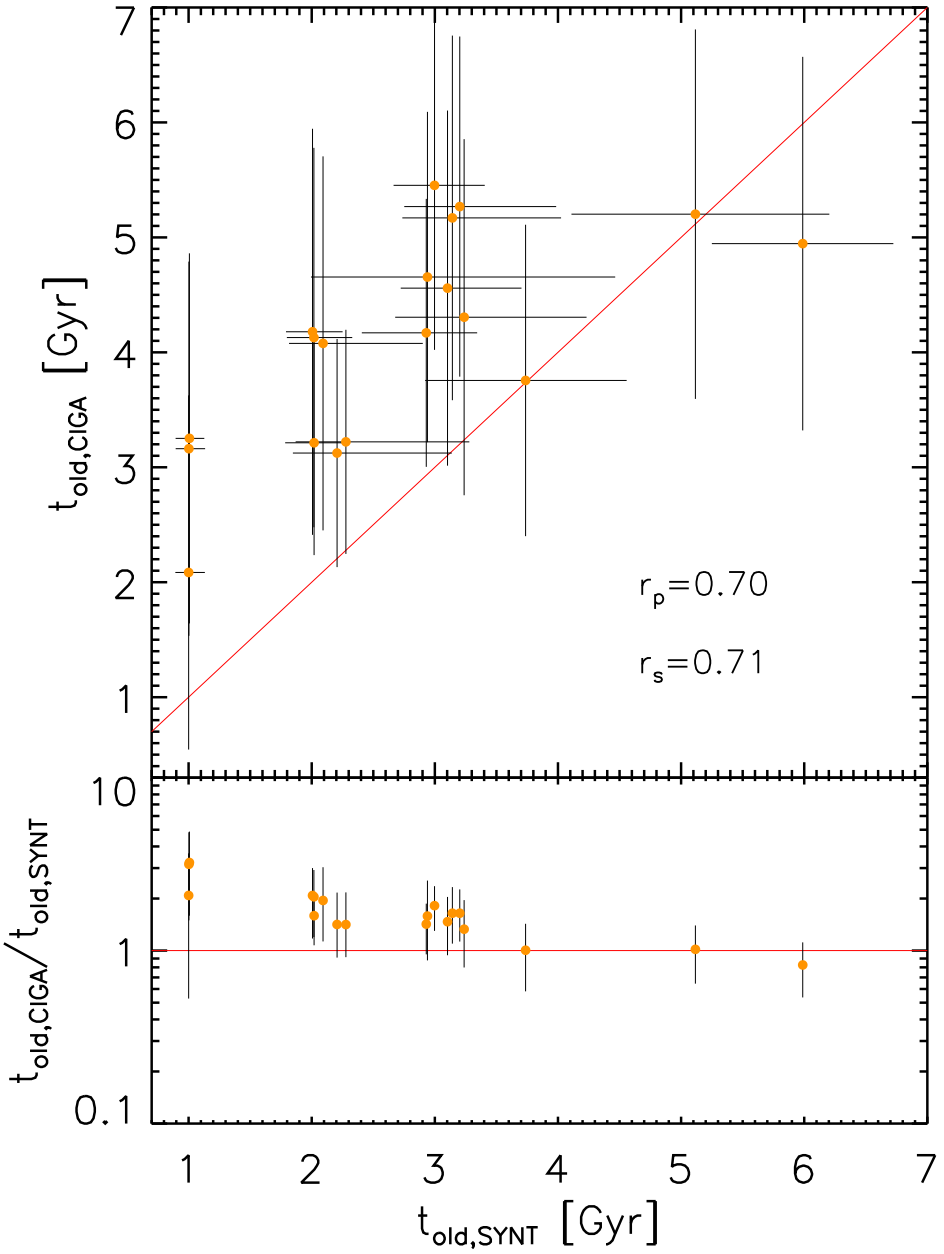

Figure 6.9 : *Upper panel:* Comparison between the ages of the old stellar population ($t_{\rm old}$) derived by the Synthesizer code on x-axis, and those derived by the CIGALE on y-axis. The filled circles with error bars show the median values and the 1σ uncertainties estimated with the Synthesizer code, and the expected values and the standard deviations obtained with the CIGALE. *Lower panel:* Ratio of the ages derived with both codes. The error bars show the propagated uncertainties.

100 Myr to 10 Gyr using a logarithmic interval of 0.5 dex, so the trend seen in $\tau_{\rm old}$ of obtaining values less than 1 Gyr is not caused by a discretization effect in the range of possible values considered. Furthermore, the large uncertainties in the results of

the Synthesizer code support the fact that the range of feasible $\tau_{\rm old}$ values is considerable, and that this parameter is not sufficiently constrained. It is important to note that $\tau_{\rm old}$ was sampled adequately with the Synthesizer code, so the scarce sampling in the CIGALE is not biasing our findings.

In Figure 6.9, we show the comparison of the ages of the old stellar population estimated with both codes. The median values of the solutions estimated with the Synthesizer code are in $1.0 \leq t_{\rm old,SYNT} < 6.0$ Gyr, with a median value, and the 16 and 84-percentile of $2.9^{+0.3}_{-0.9}$ Gyr. The expected values estimated with the CIGALE are in $2.0 < t_{\rm old,CIGA} \leq 5.5$ Gyr, with a median value, and the 16 and 84-percentile of $4.2^{+1.0}_{-1.0}$ Gyr. It is not surprising that CIGALE results are in a shorter interval, because we only explore three age values in each redshift bin with this code (see table 4.1). The most plausible models in each redshift bin have taken the central values of each age interval, but models with the other two ages have also gotten a small probability in the Bayesian analysis, which is indicated with the associated uncertainties to the preferred values from the CIGALE results.

As it is explained in Section 4.2.2, we have divided the sample in the same redshift bins that we used in the CIGALE for the study with the Synthesizer code. We have also included in the input parameters of the Synthesizer code the old ages used in the CIGALE for each redshift bin, but with a better sampling (see Table 4.2). Therefore we have done a fair comparison between the ages of the old population for the two codes.

Anyway, both sets of solutions spam compatible age values, but with the Synthesizer code old ages grouping near ~ 2, and ~ 3 Gyr. The Synthesizer code also inclines for shorter old age values, it has obtained ages shorter than 3.5 Gyr for 84% of the objects, while only 32% of the old ages derived with the CIGALE fulfill this condition. We have estimated the Pearson correlation coefficient between both sets of old ages, which results: $r_p = 0.70$. We have also estimated the Spearman correlation coefficient obtaining $r_s = 0.71$ with an associated probability of no significance of $p_s = 7.4{\times}10^{-4}$.

In the lower panel of Fig. 6.9, we show the ratios between the old ages obtained with the CIGALE and the Synthesizer codes with their respective propagated uncertainties. The ratio values are in $0.8 < t_{\rm old,CIGA}/t_{\rm old,SYNT} < 3.3$, considering the propagated uncertainties, 53% of the galaxies have gotten a compatible age value for the old population from the results of each code, what can be an expected result taking into account that we have divided the sample in the same redshift bins, and that we have explored similar old age values in each redshift bin. It is important to note that the old ages shorter than 3.5 Gyr obtained with the Synthesizer code have a median old age ratio of 1.6, i.e. these galaxies have in median and old age that is almost a half of the old age

derived with the CIGALE.

Considering the above findings, we can state that there is a moderate correlation between the ages of the old population derived with the CIGALE and the Synthesizer codes for our galaxy sample. Accordingly, we can deem that the age of the old population has been reasonably constrained for our objects, with the Synthesizer code tending to obtain shorter old ages for a significant part of the sample.

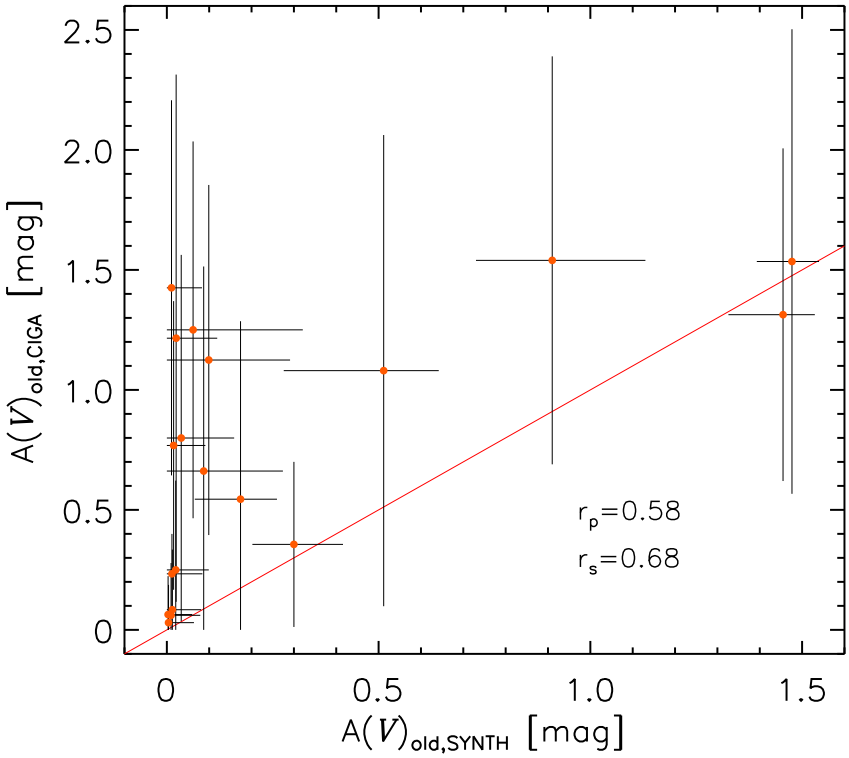

Figure 6.10 : Comparison between the attenuations of the old stellar population $A(V)_{\rm old}$ derived by the Synthesizer code on x-axis, and those derived by the CIGALE on y-axis. The filled circles with error bars show the median values and the 1σ uncertainties estimated with the Synthesizer code, and the results and propagated uncertainties estimated with the $f_{\rm att}$ and $A(V)_{\rm you}$ values derived using the CIGALE.

In Figure 6.10, we compare the amounts of attenuation estimated with the Synthesizer and CIGALE codes for the old stellar population. We should notice that the CIGALE does not offer $A(V)_{\rm old}$ as an output parameter, it quantifies the attenuation of the old population using a reduction factor relative to the young one $f_{\rm att}$, as it is explained in section 4.2.1. We have estimated the attenuation in the old population for the CIGALE as $A(V)_{\rm old,CIGA} = f_{\rm att} \cdot A(V)_{\rm you,CIGA}$, propagating its uncertainty using the $f_{\rm att}$ and $A(V)_{\rm you,CIGA}$ associated errors. The values derived with the CIGALE results are in $0.02 < A(V)_{\rm old,CIGA} < 1.54$ mag, with a median value, and the 16 and

84-percentile of $0.77^{+0.54}_{-0.69}$ mag.

The Synthesizer code allows to explore different unconnected values for the extinction in the V band of the young and old stellar populations. The median values derived with the Synthesizer code for the attenuation of the old population are in $0 < A(V)_{\rm old,SYNT} < 1.48$ mag, with median, and the 16 and 84-percentile of $0.03^{+0.48}_{-0.02}$ mag.

Although the results of both codes survey comparable $A(V)_{\rm old}$ intervals, the CIGALE results present 8 objects (42% of the sample) with $A(V)_{\rm old,CIGA} > 1.00$ mag, such attenuation values seem too large for old populations with ages $\sim 3-5$ Gyr. The Synthesizer code results only exhibit 2 galaxies (10% of the sample) with $A(V)_{\rm old,SYNT} > 1.00$ mag. We should also notice that the results of the Synthesizer code present 13 galaxies (68% of the sample) with $A(V)_{\rm old,SYNT} < 0.10$ mag, whereas only 4 objects (21% of the sample) fulfill this condition from the CIGALE results.

Although the main aspects of $A(V)_{\rm old}$ are outlined in the paragraphs above, we have also estimated the Pearson correlation coefficient, which resulted $r_p = 0.58$, and the Spearman correlation coefficient, which is $r_s = 0.68$, with an associated probability of getting this result as coincidence of $p_s = 1.4 \times 10^{-4}$.

Considering the above results, we can state that the attenuation of the old population is moderately constrained for our galaxies, with the CIGALE code tending to fit higher extinction values than the Synthesizer code for a significant part of the sample.

Hence, our IR-bright galaxy sample presents old populations with ages larger than 1 Gyr ($\sim 3-4$ Gyr in median), with e-folding times of ~ 200 Myr from the Synthesizer code results, and ~ 800 Myr from the CIGALE results. Such e-folding time differences are compensated with the CIGALE obtaining less intense initial bursts (see lower panels of Fig. B.1). The old populations are nearly unattenuated from the Synthesizer code results, and they present an attenuation of ~ 0.8 mag (in median) from the CIGALE results.

6.1.4 Stellar Masses and Star Formation Rates

The model templates of the CIGALE and the Synthesizer codes are depicted in flux density and luminosity per unit of stellar mass at all wavelengths, respectively. Hence, the CIGALE (the Synthesizer code) derives the stellar mass of each galaxy by scaling the selected template to the observed monochromatic flux densities (luminosities). Therefore, the stellar mass of each galaxy is estimated averaging the scale factor of each band using as weight its respective photometric error. This method is more robust

against photometric and template uncertainties in a single band, and the effects caused by assuming a particular SFH.

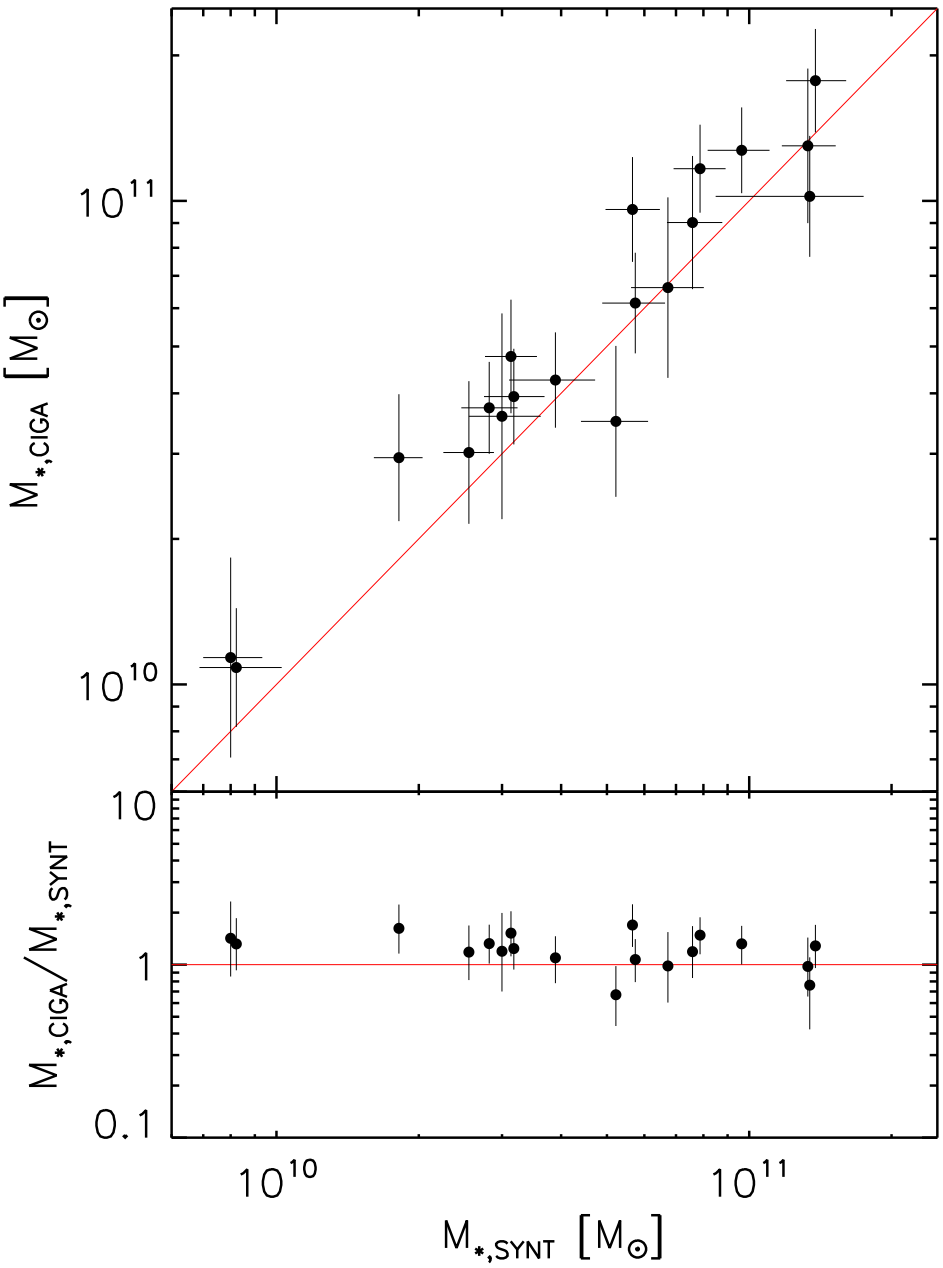

Figure 6.11 : *Upper panel:* Comparison between the stellar masses (M_*) derived by the Synthesizer code on x-axis, and those derived by the CIGALE on y-axis. The filled circles with error bars show the median values and the 1σ uncertainties estimated with the Synthesizer code, and the expected values stand and the standard deviations derived with the CIGALE. *Lower panel:* Ratio of the stellar masses derived with both codes. The error bars show the propagated uncertainties.

In Figure 6.11, we show the comparison of the stellar masses derived with the

CIGALE and Synthesizer codes and their ratios. The stellar mass values obtained with the Synthesizer code are in $7.9 \times 10^9 < M_{*,\mathrm{SYNT}}/M_\odot < 1.4 \times 10^{11}$, with median, and the 16 and 84-percentile of $5.2^{+4.4}_{-2.7} \times 10^{10} M_\odot$, and a median uncertainty of 0.06 dex. The stellar masses determined with the CIGALE are in $1.0 \times 10^{10} < M_{*,\mathrm{CIGA}}/M_\odot < 1.8 \times 10^{11}$, with median value, and the 16 and 84-percentile of $4.8^{+6.9}_{-1.8} \times 10^{10} M_\odot$, and a median uncertainty of 0.12 dex. For 15 galaxies (79% of the sample) the stellar masses estimated with the CIGALE are larger than those derived with the Synthesizer code. On average, stellar masses estimated with the CIGALE are 20% larger than those obtained with the Synthesizer code.

In the lower panel of Fig. 6.11, we show the ratio between the CIGALE and the Synthesizer code derived stellar masses. The ratio values are in $0.6 < M_{*,\mathrm{CIGA}}/M_{*,\mathrm{SYNT}} < 1.7$, considering their propagated uncertainties, 63% of the objects have obtained a similar stellar mass value from the solutions of each code. Therefore, the derived stellar masses from both codes present smaller differences than the typical precision expected from estimations derived with SPS models, a factor of $\sim 2 - 3$ (see, e.g., Pérez-González et al. 2008, Pforr et al. 2012, Michałowski et al. 2014).

Having estimated the stellar masses, we move to the comparison of the mass weighted ages determined with both codes that we show in Fig. 6.12. The median values estimated using the solutions from the Synthesizer code are in $0.3 < t_{M,\mathrm{SYNT}} < 3.2$ Gyr, with a median value, and the 16 and 84-percentile of $1.6^{+0.8}_{-0.6}$ Gyr. The expected values derived from the CIGALE are in $0.4 < t_{M,\mathrm{CIGA}} < 4.2$ Gyr, with a median value, and the 16 and 84-percentile of $1.2^{+1.6}_{-0.5}$ Gyr. Hence the two sets of solutions inspect comparable mass weighted age values. As we have mentioned before, the mass weighted age represents the average age of the stellar populations which form a galaxy. In our adopted SFH, these stellar populations are outlined in an old and a young population. We have shown in Section 6.1.2, the parameters of the young population present acceptable correlations and are constrained adequately, except the burst intensity. We have also pointed out in Section 6.1.3 that the parameters of the old population are correlated and constrained moderately, except the e-folding time. Therefore, it is expected to observe a modest correlation in figure 6.12. We have estimated the Pearson correlation coefficient, which resulted $r_p = 0.46$, and the Spearman correlation coefficient, which is $r_s = 0.56$ with a probability of no correlation of $p_s = 1.3 \times 10^{-2}$.

In the lower panel of Fig. 6.12, we show the ratio between the mass weighted ages derived with the CIGALE and the Synthesizer codes, and their respective propagated uncertainties. The ratio values are in $0.2 < t_{M,\mathrm{CIGA}}/t_{M,\mathrm{SYNT}} < 2.2$. Taking into account the propagated uncertainties, 84% of our galaxies have obtained a compatible value of mass weighted age from the results of each code, but we should notice that

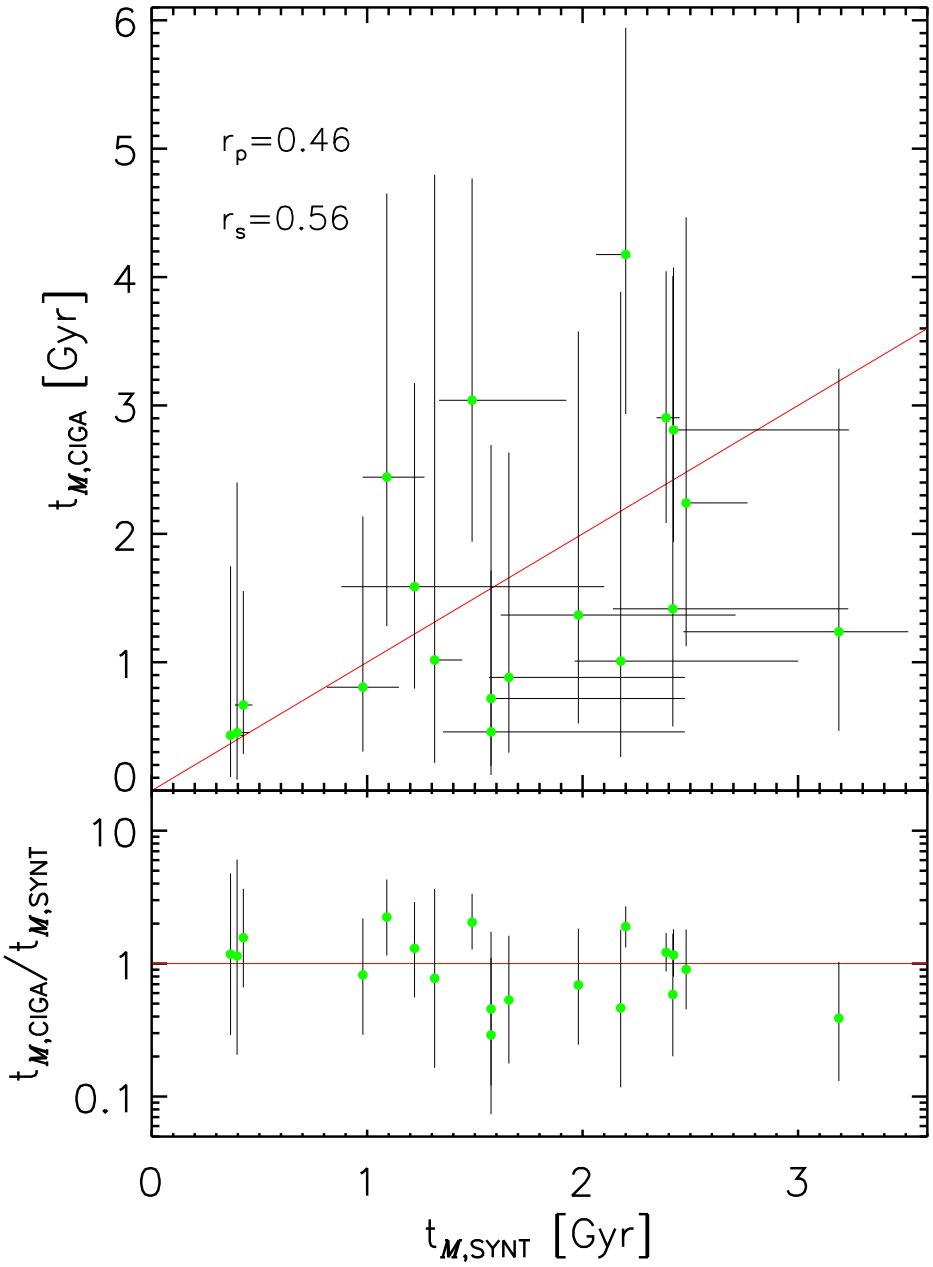

Figure 6.12 : *Upper panel:* Comparison between the mass weighted ages (t_M) derived by the Synthesizer code on x-axis, and those derived by CIGALE on y-axis. The filled circles with error bars show the median values and the 1σ uncertainties estimated with the Synthesizer code, and the expected values and the standard deviations derived with the CIGALE. *Lower panel:* Ratio of the mass weighted ages derived with both codes. The error bars show the propagated uncertainties.

each code also has derived huge uncertainties associated to its obtained values of mass weighted age.

Considering the findings of Sections 6.1.2 and 6.1.3, and the good agreement in

the results of the stellar mass values from both codes, we suggest that the cause of the difference in the mass weighted age values between both codes should be the distinct burst intensity values of the young population.

We now turn to the estimation of star formation rates, we should remind that the strength of our sample is its FIR selection (all our objects are detected in both *Spitzer*-MIPS bands, and at least two *Herschel* bands) because the FIR emission is a powerful indicator of recent star formation. This selection was done with the aim of characterizing the stellar populations of IR-bright objects by fitting their observed UV-to-FIR flux densities with self-consistent stellar population models.

Considering the FIR prior ($L_{\rm TIR}$) as an input to constrain the parameters which results of the stellar population modeling, Buat et al. (2014) have studied a sample of $z > 1$ galaxies with several objects detected in MIPS 24 μm and PACS bands using the CIGALE. They have concluded that the best fits are obtained with a SFH characterized by two populations. They have also shown that their SED-derived SFR estimations are robust if measurements that sample the dust continuum emission are considered in the fitting process.

In the upper panels of Fig. 6.13, we compare the SFRs estimated from UV-to-FIR SED modeling ($SFR_{\rm SED}$) using the Synthesizer and the CIGALE codes with the SFRs based on a linear combination of the unobscured UV luminosity, and the re-emitted FIR emission of recently formed stars ($SFR_{\rm UV+IR}$). For the latter, we use the recipe of Bell et al. (2005), which takes into account the unattenuated escaping photons in the UV and the calibration for $L_{\rm TIR}$ of Kennicutt (1998), assuming a Salpeter (1955) initial mass function (see Eq. 5.3, and Section 5.1.3).

The values of $SFR_{\rm SED}$ obtained from the results of the Synthesizer and CIGALE codes are presented in Table 6.3. The uncertainties in $SFR_{\rm SED}$ are the 16 and the 84-percentile derived from the results of Monte Carlo simulations with the Synthesizer code, and the standard deviations obtained from the Bayesian analysis with the CIGALE (see also the upper panels of Fig 6.13).

We compare the instantaneous SFR median values derived with the Synthesizer code, $SFR_{\rm SED,SYNTH}$, with the $SFR_{\rm UV+IR}$ values in the upper left panel of Fig. 6.13. We observe a positive offset ($\sim 0.2 - 0.3$ dex) in the values of $SFR_{\rm SED,SYNTH}$ for 42% of the objects in our sample. In the upper right panel of Fig. 6.13, we also compare the current SFR expected values obtained with the CIGALE, $SFR_{\rm SED,CIGA}$, with the SFR_{UV+IR} values. We also notice 2 objects with a positive offset ($\sim$ 0.1 dex, but one is within its standard deviation), and 1 object with a negative offset ($\sim$ 0.1 dex, also within its standard deviation) for $SFR_{\rm SED,CIGA}$ results. It is important to note that

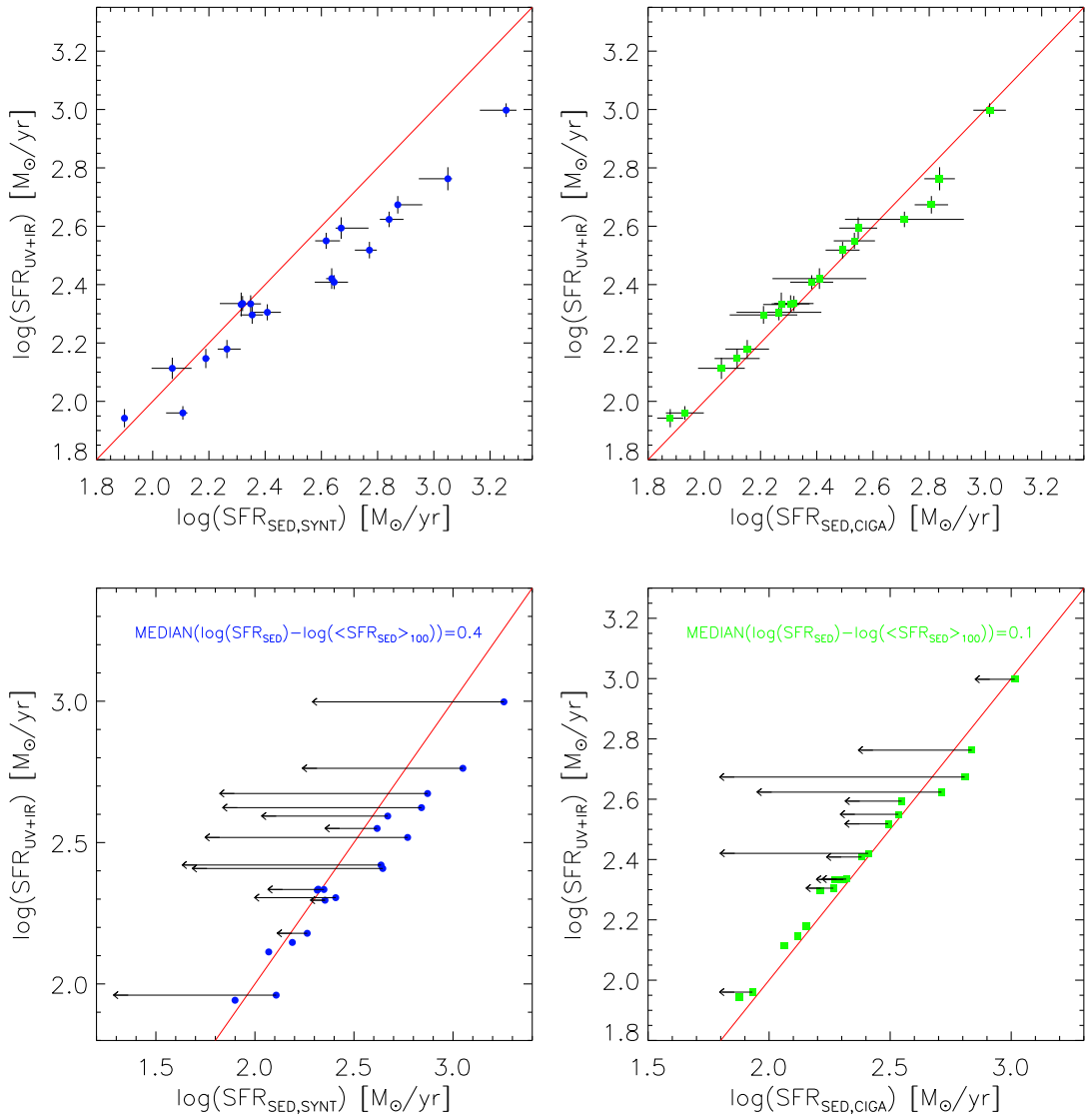

Figure 6.13 : *Upper left panel:* $SFR_{\rm SED,SYNT}$ vs. $SFR_{\rm UV+IR}$. The median values of current SFR estimated with the Synthesizer code and their 1σ uncertainties are shown in x-axis. The SFR values from Eq. 5.3 and their uncertainties are plotted on y-axis. *Upper right panel:* $SFR_{\rm SED,CIGA}$ vs. SFR_{UV+IR}. On x-axis, we show the expected values of current SFR and their standard deviation derived with the CIGALE. Y-axis is equal to the one on upper left panel. *Lower left panel:* $SFR_{\rm SED,SYNT}$ vs. $SFR_{\rm UV+IR}$ with the arrows depicting the objects where $SFR_{\rm SED,SYNT}$ changes when averaging in a timescale of 100 Myr. The median difference is also shown. *Lower right panel:* Same as lower left panel but for the CIGALE results.

$SFR_{SED,SYNTH}$ values are larger than $SFR_{SED,CIGA}$ results in ~ 0.1 dex on average, but the difference between individual objects can reach ~ 0.3 dex.

In the lower panels of Fig. 6.13, we show the galaxies where $SFR_{\rm SED}$ changes when averaging over a timescale of 100 Myr. This $\langle SFR_{\rm SED}\rangle_{100}$ is provided as a sec-

ondary parameter from the Bayesian analysis of the CIGALE, and we have also estimated it with the results of the Synthesizer code. Attending to the lower left panel of Fig. 6.13, we observe that 74% of our galaxies have diminished their $SFR_{\rm SED,SYNT}$ when averaging over 100 Myr. We consider a valid movement when the displacement is greater than the average uncertainty of the instantaneous $SFR_{\rm SED}$ (the x-axis error bars of the upper left panel of Fig. 6.13, 0.04 dex for the Synthesizer code results). The median displacement of the whole sample is 0.4 dex. Looking to the lower right panel of Fig. 6.13, we also notice that 68% of our objects have decreased their $SFR_{\rm SED,CIGA}$ when considering the average over 100 Myr (the average uncertainty of $SFR_{\rm SED,CIGA}$ is 0.09 dex), with a median displacement for all objects of 0.1 dex.

Considering the above findings, we can state that the SFRs determined using FIR and UV photometry by means of SED fitting or observational calibrations are not similar to SFRs averaged over a timescale of 100 Myr (see also, e.g. Buat et al. 2014).

Now we move to investigate the origin of the moderate offset of $\sim 0.2 - 0.3$ dex between $SFR_{\rm SED,SYNTH}$ and $SFR_{\rm UV+IR}$. In order to do so, we have looked for a characteristic distinguishing such offset objects. We have found that the galaxies with $t_{\rm you,SYNT} < 20$ Myr are the ones presenting the offset (see left panel of Fig. 6.14), which is in agreement with the finding of Section 6.1.2 showing that the direct observable $L_{\rm TIR,ref}$ correlates with $t_{\rm you}$ with the most IR luminous objects having the shorter ages for the young population (see Fig. 6.5). We have also marked in the left panel of Fig. 6.14 the objects with $t_{\rm you,CIGA} < 20$ Myr. These objects also present an offset of ~ 0.1 dex between $SFR_{\rm SED,CIGA}$ and $SFR_{\rm UV+IR}$.

In a recent review, Calzetti (2013) has presented SFR calibrations assuming different timescales of constant star formation. A timescale of 10 Myr is better suited for our galaxies with short young population ages than the one ($\sim$ 100 Myr) of Kennicutt (1998) . Calzetti calibrations are derived assuming a Kroupa (2001) initial mass function. In order to convert the 10 Myr calibration to one based on a Salpeter (1955) initial mass function, we multiply it by 1.6. Hence, expressing the calibration in solar luminosity units, we have:

$$SFR_{\rm UV+IR}(M_\odot/{\rm yr}) = 2.3 \times 10^{-10}[3.3L(0.28) + L({\rm TIR})]/{\rm L}_\odot, \qquad (6.1)$$

We show in the right panel of Fig. 6.14 the $SFR_{\rm UV+IR}$ corrected values, after applying Eq. (6.1) to galaxies which have obtained $t_{\rm you} < 20$ Myr from the Synthesizer code and the CIGALE results. A better agreement is observed in SFRs estimated with the IR+UV calibrations and those derived from the SED-fitting, but there is still a small offset in $SFR_{\rm SED}$ for those objects with $t_{\rm you} < 20$ Myr from the Synthesizer code

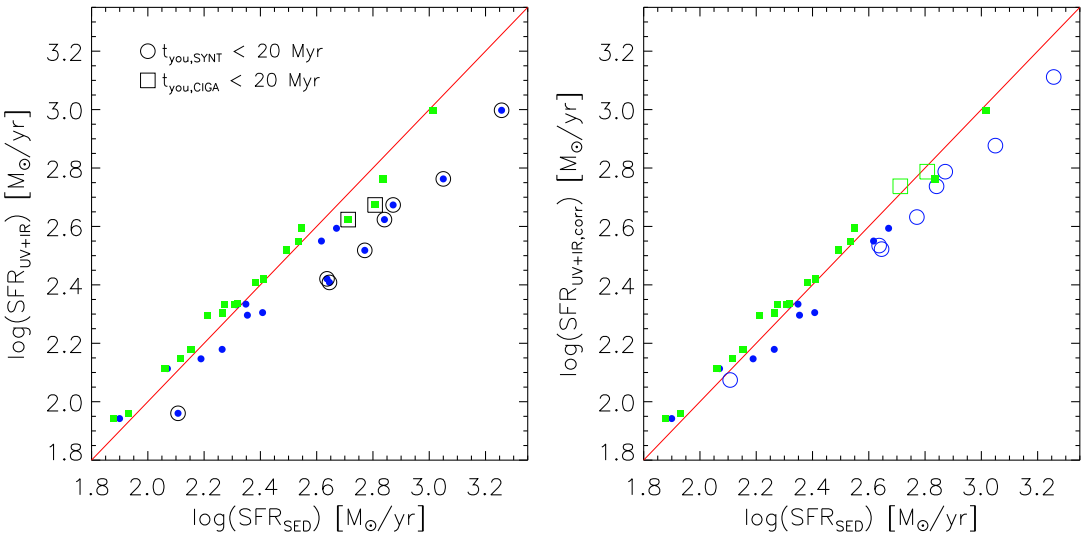

Figure 6.14 : *Left panel:* SFR_{SED} vs. SFR_{UV+IR}. The *filled blue circles* stand for the median values derived with the Synthesizer code. The *filled green squares* show the expected values derived with the CIGALE. Objects with $t_{\rm you} < 20$ Myr are also displayed. *Right Panel:* The *filled symbols* represent the same as in the left panel. The *open symbols* show the corrected $SFR_{\rm UV+IR}$ values after applying the empirical calibration described by Eq. (6.1) to objects with $t_{\rm you} < 20$ Myr.

results. Therefore, SFRs estimated for IR-bright galaxies at intermediate redshifts with the standard calibration of Kennicutt (1998) should be considered lower limits, if the age of young population is unknown.

Buat et al. (2014) have found a similar result when comparing $SFR_{\rm UV+IR}$ estimated with the calibration of Iglesias-Páramo et al. (2006) for a Kroupa (2001) initial mass function with $SFR_{\rm SED}$ derived with the CIGALE. They attribute this effect to the young populations with ages shorter than 100 Myr, which have not reached a steady production of UV radiation heating the dust grains.

Having estimated the stellar masses and the SFRs, we show the scatter plot between such properties for our sample in Fig. 6.15. Several works have been devoted to the study of the $SFR-M_*$ relation (see, e.g., Elbaz et al. 2007; Daddi et al. 2007). In those efforts, it has been found that such relationship follow a tight correlation for normal star forming galaxies, forming the so-called main sequence, with some outliers named starbusts. This relation is also presumed to evolve with redshift (see, e.g., Noeske et al. 2007; Wuyts et al. 2011).

Given that our objects are at $0.6 < z < 1.3$, we have also plotted in Fig. 6.15 the $SFR - M_*$ relation of Elbaz et al. (2007) at $z \sim 1$, and a comparison galaxy sample of the Cosmic Assemble Near-infrared Deep Legacy Survey (CANDELS) from the COSMOS, GOODS-N, UDS and EGS fields (see, Koekemoer et al. 2011; Galametz et al.

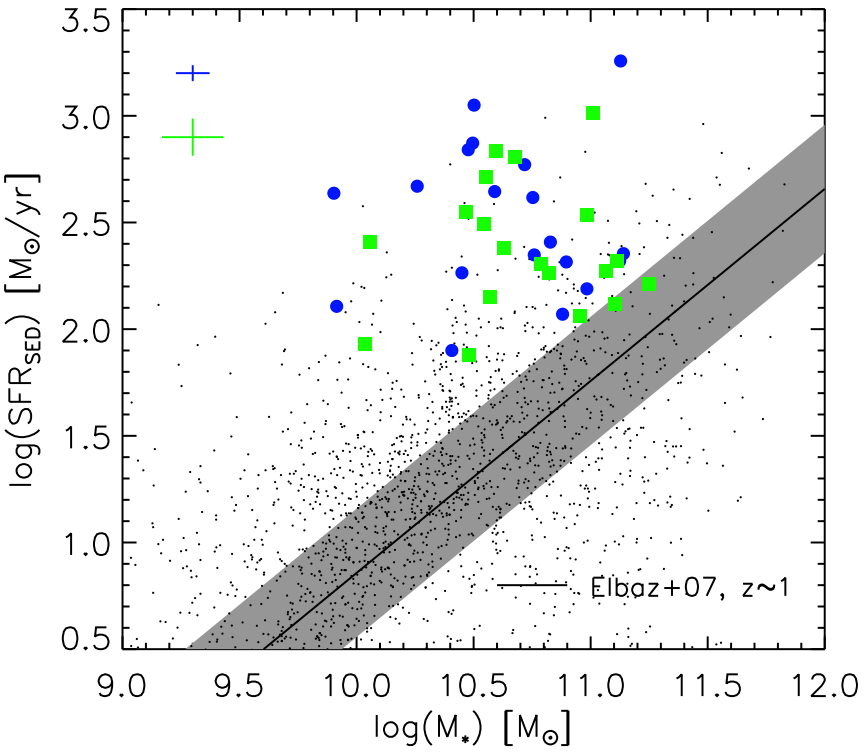

Figure 6.15 : M_* vs. $SFR_{\rm SED}$. The *filled blue circles* show the median values estimated with the Synthesizer code. The *filled green squares* show the expected values obtained with the CIGALE. The average uncertainties of the whole sample are also displayed for each code. The *black solid line* stands for the relationship presented in Elbaz et al. (2007) with its 68% confidence level marked with the *gray shaded area*. The black dots show galaxies from CANDELS at $0.6 < z < 1.3$ as explained in the text.

2013). The photometric redshifts, the stellar masses and the SFRs of the comparison sample are not published yet, but they are available through the public interface of the Rainbow Cosmological Surveys Database (see, Pérez-González et al. 2008; Barro et al. 2011a).

Attending to Figure 6.15, we observe that only 21% of the objects from the results of the Synthesizer code, and 26% of the objects from the results of the CIGALE would be in the main sequence taking into account the uncertainties in the parameters and in the Elbaz et al. (2007) relation. Therefore, most of the objects in our sample have a starbust nature which means that they are forming stars actively. When looking to the comparison sample, we notice that more than a half of the objects are located in the main sequence, but there are also a considerable quantity of galaxies out of the sequence. The latter could be originated because we have selected CANDELS objects with FIR data in order to fairly compare with our galaxies. It is also important to consider that there are some CANDELS sources having similar masses and SFRs that

the objects in our sample, indicating the presence of starbusts of similar kind in several cosmological fields.

Our galaxies lie $\sim$ 1 dex above the main sequence in median as derived from the results of both codes. We also notice that there is not a clear dependence of SFR on stellar mass. This lack of correlation between M_* and SFR has also been found in the recent works of Lee et al. (2013) and Lemaux et al. (2014) devoted to *Herschel*-selected galaxies in the COSMOS and CFHTLS-D1 fields, respectively. We return to this topic in Section 6.2.

Other important parameter used frequently to characterize the properties of galaxies is the specific star formation rate ($sSFR = SFR/M_*$). Given the correlation of having higher SFRs when going to larger masses (the main sequence), the sSFR measures the efficiency of a galaxy in forming stars independently of its mass. In the left panel of Fig. 6.16, we compare the sSFRs derived with the Synthesizer with those derived with the CIGALE. We present the sSFR values and their propagated uncertainties for the results of both codes in Table 6.3. We observe that $sSFR_{\rm SYNT}$ values are higher than $sSFR_{\rm CIGA}$ results in $\sim$ 0.2 dex on average, but the difference in individual objects can reach $\sim$ 0.4 dex. Taking into account the uncertainties, 42% of the galaxies in our sample present similar sSFR values from the results of each code.

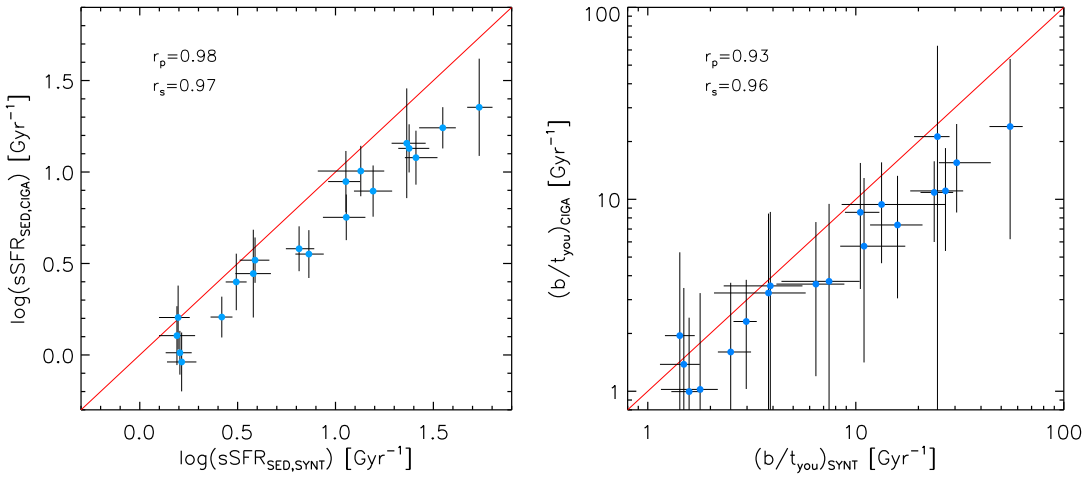

Figure 6.16 : *Left panel:* Comparison between the $sSFRs$ derived by the Synthesizer code on x-axis, and those derived by CIGALE on y-axis. The filled circles with error bars show the median values and their 1σ uncertainties estimated with the Synthesizer code, and the expected values and the standard deviations derived with the CIGALE. *Right panel:* Comparison between $b/t_{\rm you}$ ratios estimated with the Synthesizer code on x-axis, and such ratios derived with the CIGALE on y-axis. The filled circles with error bars show the ratio of the median values and their propagated uncertainties estimated with the Synthesizer code, and the ratio of the expected values and their propagated uncertainties derived with the CIGALE.

Table 6.3 : Star Formation Rates for Our Galaxies at $0.6 \leq z \leq 1.5$

Galaxy	Code	$\log(SFR_{\rm SED})$ $[M_\odot/\rm yr]$	$\log(sSFR_{\rm SED})$ $[\rm Gyr^{-1}]$	$\log(b/t_{\rm you})$ $[\rm Gyr^{-1}]$
(1)	(2)	(3)	(4)	(5)
MIPS0000050_1	Synthesizer	$2.65^{+0.05}_{-0.07}$	$1.05^{+0.10}_{-0.12}$	$1.04^{+0.20}_{-0.11}$
	CIGALE	2.38 ± 0.08	0.75 ± 0.12	$0.76^{+0.36}_{-0.61}$
MIPS0000149_1	Synthesizer	$2.31^{+0.01}_{-0.01}$	$0.42^{+0.05}_{-0.06}$	$0.40^{+0.10}_{-0.06}$
	CIGALE	2.27 ± 0.06	0.21 ± 0.11	$0.20^{+0.36}_{-0.67}$
MIPS0000472_1	Synthesizer	$2.41^{+0.05}_{-0.05}$	$0.58^{+0.09}_{-0.09}$	$0.58^{+0.18}_{-0.26}$
	CIGALE	2.27 ± 0.15	0.44 ± 0.24	$0.51^{+0.41}_{-1.48}$
MIPS0000508_1	Synthesizer	$2.11^{+0.02}_{-0.06}$	$1.19^{+0.10}_{-0.10}$	$1.20^{+0.12}_{-0.13}$
	CIGALE	1.93 ± 0.07	0.90 ± 0.14	$0.87^{+0.26}_{-0.38}$
MIPS0000671_1	Synthesizer	$1.90^{+0.00}_{-0.00}$	$0.49^{+0.05}_{-0.05}$	$0.47^{+0.05}_{-0.06}$
	CIGALE	1.88 ± 0.05	0.40 ± 0.15	$0.36^{+0.22}_{-0.35}$
MIPS0000700_1	Synthesizer	$2.19^{+0.01}_{-0.01}$	$0.21^{+0.06}_{-0.07}$	$0.20^{+0.06}_{-0.09}$
	CIGALE	2.12 ± 0.08	0.01 ± 0.12	$0.00^{+0.39}_{-1.33}$
MIPS0000701_1	Synthesizer	$2.77^{+0.03}_{-0.05}$	$1.05^{+0.07}_{-0.09}$	$1.02^{+0.09}_{-0.07}$
	CIGALE	2.49 ± 0.06	0.95 ± 0.17	$0.93^{+0.26}_{-0.40}$
MIPS0000773	Synthesizer	$2.62^{+0.05}_{-0.04}$	$0.86^{+0.08}_{-0.07}$	$0.87^{+0.15}_{-0.23}$
	CIGALE	2.53 ± 0.07	0.55 ± 0.13	$0.57^{+0.40}_{-1.11}$
MIPS0000904_3	Synthesizer	$3.05^{+0.02}_{-0.10}$	$1.55^{+0.07}_{-0.12}$	$1.48^{+0.16}_{-0.09}$
	CIGALE	2.84 ± 0.05	1.24 ± 0.11	$1.19^{+0.20}_{-0.26}$
MIPS0000922_1	Synthesizer	$2.07^{+0.07}_{-0.07}$	$0.19^{+0.09}_{-0.09}$	$0.17^{+0.08}_{-0.11}$
	CIGALE	2.06 ± 0.08	0.11 ± 0.16	$0.14^{+0.40}_{-1.09}$
MIPS0001032_1	Synthesizer	$2.67^{+0.10}_{-0.02}$	$1.41^{+0.11}_{-0.06}$	$1.43^{+0.08}_{-0.17}$
	CIGALE	2.55 ± 0.07	1.08 ± 0.15	$1.04^{+0.22}_{-0.31}$
MIPS0001045_1	Synthesizer	$2.35^{+0.04}_{-0.04}$	$0.21^{+0.08}_{-0.07}$	$0.25^{+0.09}_{-0.19}$
	CIGALE	2.21 ± 0.12	-0.04 ± 0.16	$0.01^{+0.50}_{-1.47}$
MIPS0001162_1	Synthesizer	$3.26^{+0.04}_{-0.09}$	$1.13^{+0.12}_{-0.22}$	$1.12^{+0.31}_{-0.19}$
	CIGALE	3.01 ± 0.06	1.01 ± 0.14	$0.97^{+0.22}_{-0.31}$
MIPS0001164_1	Synthesizer	$2.64^{+0.01}_{-0.02}$	$1.73^{+0.07}_{-0.06}$	$1.74^{+0.06}_{-0.10}$
	CIGALE	2.41 ± 0.17	1.35 ± 0.27	$1.38^{+0.35}_{-0.59}$
MIPS0001212	Synthesizer	$2.87^{+0.09}_{-0.01}$	$1.38^{+0.10}_{-0.06}$	$1.38^{+0.09}_{-0.07}$
	CIGALE	2.81 ± 0.06	1.13 ± 0.13	$1.04^{+0.16}_{-0.26}$
MIPS0001225	Synthesizer	$2.84^{+0.05}_{-0.03}$	$1.36^{+0.10}_{-0.08}$	$1.39^{+0.06}_{-0.11}$
	CIGALE	2.71 ± 0.21	1.16 ± 0.30	$1.33^{+0.47}_{-1.33}$
MIPS0001300_1	Synthesizer	$2.26^{+0.05}_{-0.03}$	$0.81^{+0.08}_{-0.07}$	$0.81^{+0.14}_{-0.19}$
	CIGALE	2.15 ± 0.08	0.58 ± 0.12	$0.56^{+0.32}_{-0.48}$
MIPS0001324_1	Synthesizer	$2.32^{+0.01}_{-0.08}$	$0.20^{+0.06}_{-0.10}$	$0.15^{+0.07}_{-0.07}$
	CIGALE	2.32 ± 0.07	0.20 ± 0.17	$0.29^{+0.43}_{-0.29}$
MIPS0001585_1	Synthesizer	$2.35^{+0.04}_{-0.04}$	$0.59^{+0.07}_{-0.08}$	$0.59^{+0.15}_{-0.22}$
	CIGALE	2.31 ± 0.07	0.52 ± 0.12	$0.55^{+0.39}_{-0.80}$

Note.— Results for the SFRs, sSFRs and $b/t_{\rm you}$ obtained from SED-fitting of our sample of IR-bright galaxies. (1) Name of the galaxy. (2) Code being evaluated. (3) Star formation rate and its uncertainty (in $M_\odot/\rm yr$) derived from the logarithmic space. (4) Specific star formation rate and its uncertainty (in $\rm Gyr^{-1}$) obtained from the logarithmic space. (5) ratio of burst intensity per age of the young population and its uncertainty (in $\rm Gyr^{-1}$) expressed in the logarithmic space.

Now we return to our assumed SFH (Eq. 4.1) in order to link some of the findings of this Chapter. The instantaneous SFR (our $SFR_{\rm SED}$) observed for each galaxy is dominated by the contribution of the young population (see lower panels Fig. 6.1). Hence, we can approximate $SFR_{\rm SED} \simeq SFR_{\rm SED,you}$, with $SFR_{\rm SED,you}$ being compatible with a constant SFR (see Section 6.1.2), this constant SFR can be expressed as the ratio of stellar mass of the young population divided by the young age. Writing these facts in form of a equation, we have:

$$SFR_{\rm SED} \simeq SFR_{\rm SED,you} \simeq \frac{M_{*,\rm you}}{t_{\rm you}} = \frac{M_* \cdot b}{t_{\rm you}}, \tag{6.2}$$

where M_* is the total stellar mass, and b is the burst intensity. This expression can be rewritten as:

$$sSFR_{\rm SED} = \frac{SFR_{\rm SED}}{M_*} \simeq \frac{b}{t_{\rm you}}. \tag{6.3}$$

In the right panel of Fig. 6.16, we compare the $b/t_{\rm you}$ ratio values obtained from the Synthesizer code with those results derived with the CIGALE. The $b/t_{\rm you}$ ratio values and their propagated uncertainties are presented in Table 6.3. It is clear that the values of sSFR and $b/t_{\rm you}$ are really similar attending to Fig. 6.16 and Table 6.3. Nonetheless, we have applied a Kolmogorov-Smirnov test in order to corroborate if the sSFR and $b/t_{\rm you}$ values from each code are derived from the same distribution. The result is $P_{\rm K-S} = 0.99$ for both codes. In other words, the sSFR and $b/t_{\rm you}$ values determined with each code are drawn from the same distribution with a 99% of significance.

These findings corroborate what is expressed in Eq. (6.3): the instantaneous sSFR is well approximated with the $b/t_{\rm you}$ ratio for the galaxies in our sample and our assumed SFH. Notwithstanding the clear visible correlation in both panels of Fig. 6.16, we have estimated the Pearson correlation coefficient for the sSFR comparison which results, $r_p = 0.98$, and also for the $b/t_{\rm you}$ comparison obtaining $r_p = 0.93$. We have also computed the Spearman correlation coefficient for both comparisons, which is for the sSFR, $r_s = 0.97$ with a probability of no correlation of $p_s = 1.7 \times 10^{-11}$. The value obtained for the $b/t_{\rm you}$ is $r_s = 0.96$, with a probability $p_s = 4.0 \times 10^{-11}$ of getting this result as mere coincidence. We should notice that the uncertainties in the $b/t_{\rm you}$ values are huge for the CIGALE results, this is originated from the propagation of the large uncertainties in $b_{\rm CIGA}$ and $t_{\rm you,CIGA}$.

Considering the above findings, we can state that both codes present compatible sSFRs. Therefore, the parameters fitted for the young stellar population $(A(V)_{\rm you}, t_{\rm you}, b)$ are dominant and properly constrained for our assumed SFH and the nature of the galax-

ies in our sample. The $A(V)_{\rm you}$ values are driven by the FIR prior, the $L_{\rm TIR}$, and the b and $t_{\rm you}$ values are directly related with the $sFR_{\rm SED}$ values. Such parameters, b and $t_{\rm you}$, are degenerated, i.e., a high value of b connected to a large value of $t_{\rm you}$ is difficult to be disentangled of a short b value associated to a small value of $t_{\rm you}$. We should notice that the Synthesizer code present moderately higher SFRs and sSFRs than the CIGALE. We suggest that the shorter values of $t_{you,\rm SYNT}$ cause these offsets, given that the CIGALE derives slightly higher stellar masses and higher young population ages in average than the Synthesizer code.

6.2 Comparison of the physical properties of our (U)LIRGs with other samples of IR-bright galaxies

In this Section we estimate two fundamental properties of (U)LIRGs: the dust temperature ($T_{\rm d}$) and the dust mass ($M_{\rm d}$). We obtain such estimations in order to compare the values derived for these properties of our (U)LIRGs with those of the sample of SCUBA-2 sub-millimeter galaxies observed in the COSMOS field by Casey et al. (2013). We also compare the SFRs (which is equivalent to compare $L_{\rm TIR}$ in dusty star-forming galaxies) of our (U)LIRG sample with those of SCUBA-2 galaxy sample.

We also compare the stellar masses and SFRs of our sample with those of the PACS and the SPIRE selected samples of Lo Faro et al. (2013) and Lemaux et al. (2014) derived from the GOODS-S and the CFHTLS-D1 fields, respectively. We place these stellar mass and SFR values in the $SFR-M_*$ plane, and discuss about these properties of our objects in comparison with those of the Lemaux et al., and Lo Faro et al. samples.

6.2.1 Comparing physical properties of (U)LIRGs at $0.6 < z < 1.5$ with those of SCUBA-2 sub-mm galaxies

In order to obtain the $T_{\rm d}$ and $M_{\rm d}$ we use the mid-infrared (MIR) powerlaw plus gray-body SED-fitting method of Casey (2012). This method fits a powerlaw characterized by a mid-infrared index α, the $L_{\rm TIR}$, the $T_{\rm d}$ and the emissivity index β, depending on the available FIR-to-mm available data points. Following Casey et al. (2013), we fix $\beta = 1.5$. In Casey work is manifested that when ≥ 4 MIR-FIR data points are available, it is possible to constrain α, $L_{\rm TIR}$, and $T_{\rm d}$ (obtained as $\propto 1/\lambda_{\rm peak}$ by means of the Wien displacement law, where $\lambda_{\rm peak}$ is the rest-frame SED peak wavelength). First, we use all the 24 to 500 μm accessible photometry of our sample to constrain these 3 parameters, getting α_o values from 1.8 to 3.0. Then in order to do a fair comparison with

our $L_{\rm TIR,ref}$ (derived from the ≥ 70 μm FIR data points and the IR libraries described in Chapter 4), we fix α to 2.0 for $1.8 \leq \alpha_o < 2.25$, and to 2.5 for $2.25 < \alpha_o < 3.0$, and do not use the MIPS-24 data point in the powerlaw+graybody fit. The results for the $L_{\rm TIR}$ comparison are shown in Fig. 6.17, where $L_{\rm TIR,CA12}$ represents the $L_{\rm TIR}$ derived from the powerlaw+graybody method.

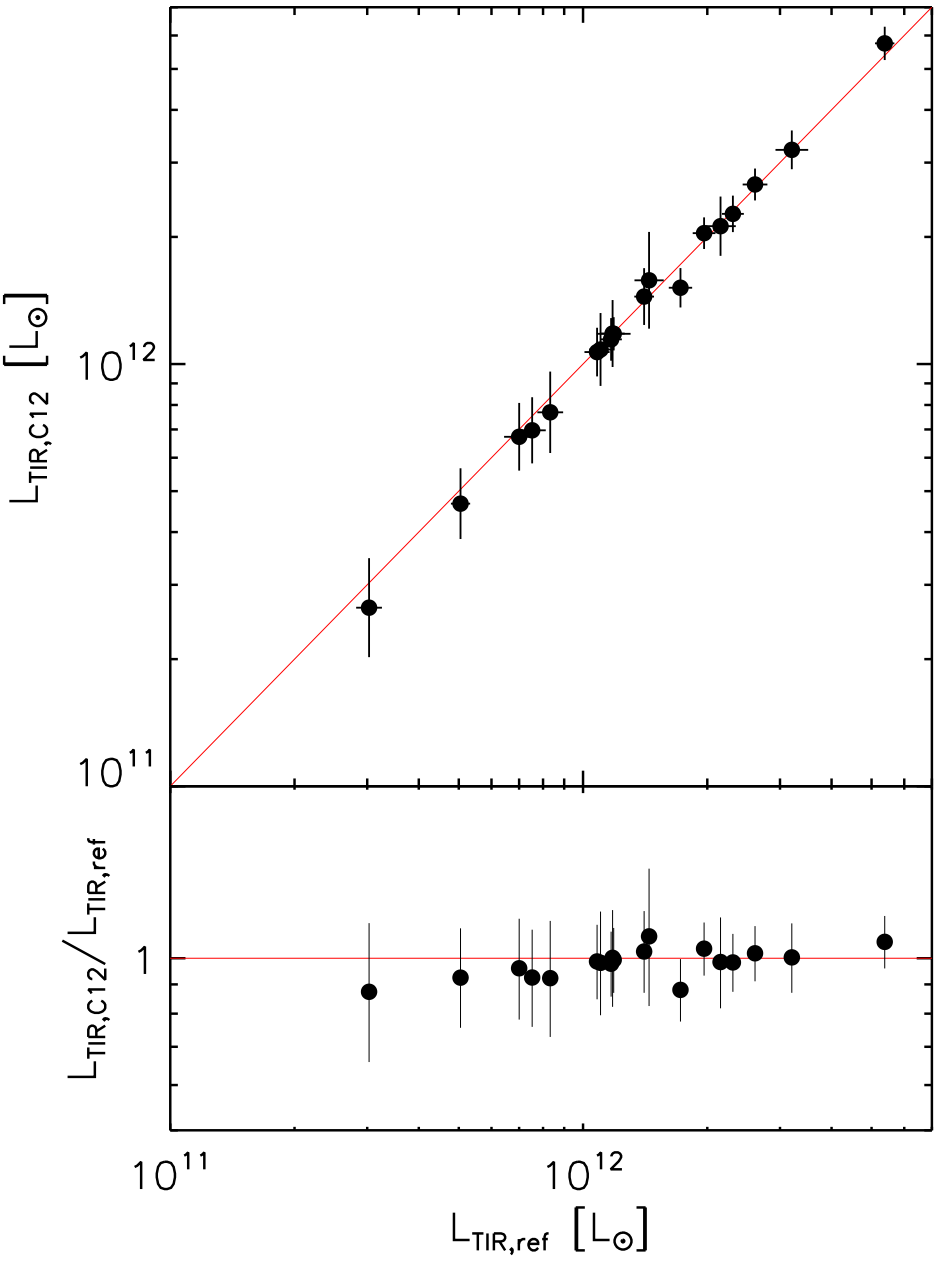

Figure 6.17 : *Upper panel:* Comparison between the $L_{\rm TIR}$ values derived by the best-fitting template among the IR models of CE01, DH02 and R+09 on x-axis, and those derived by powerlaw+graybody method on y-axis. *Lower panel:* Ratio of the $L_{\rm TIR}$ values derived with each technique. The error bars show the propagated uncertainties.

Outwardly from the aforementioned figure, we observe the the results derived from each method are compatible. The differences between the values obtained by each technique are $\lesssim 13\%$.

Once with comparable $L_{\rm TIR}$ determinations, we proceed to show the $L_{\rm TIR}$ as a function of redshift for the SCUBA-2 sub-mm galaxy sample and our (U)LIRG sample in Fig. 6.18.

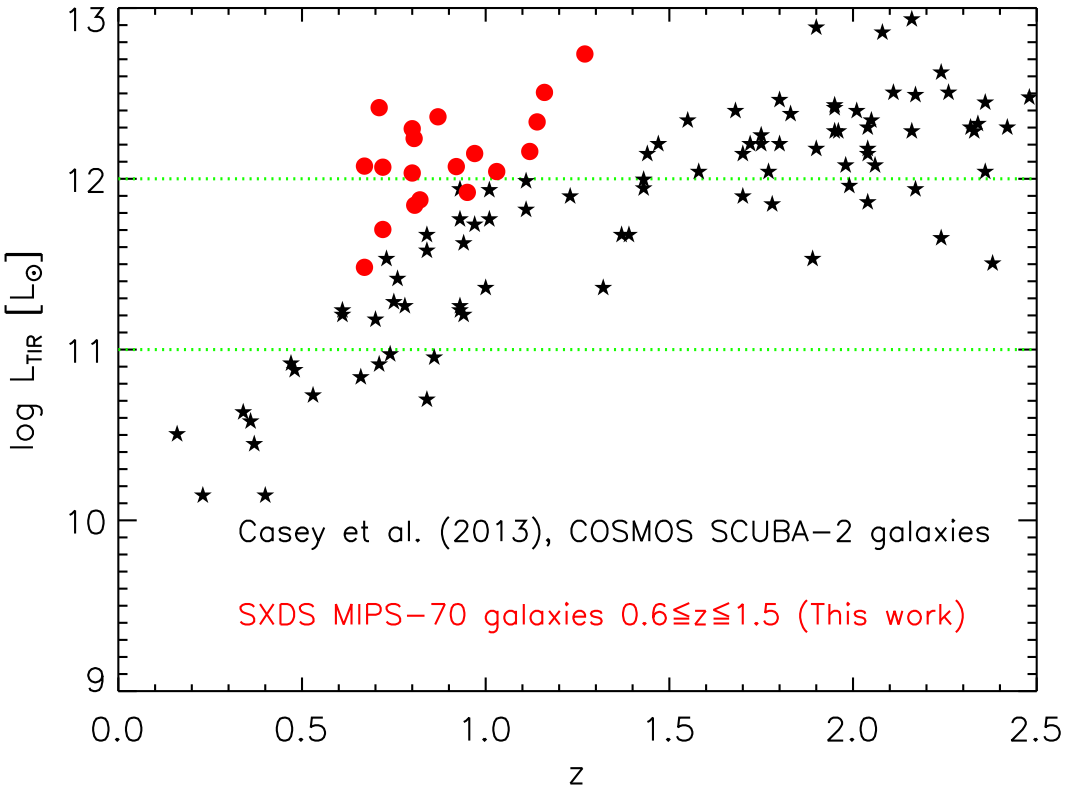

Figure 6.18 : Selection effect of $L_{\rm TIR}$ vs. z of our MIPS-70 emitters (*red circles*) compared to that of the SCUBA-2 sub-mm galaxies of Casey et al.(2013; *black stars*) derived from the COSMOS field. The division for LIRGs and ULIRGs are depicted with horizontal lines.

We observe in the aforenamed figure that the $L_{\rm TIR}$ values of our (U)LIRGs at $0.6 \leq z \leq 1.5$ are compatible with those of the SCUBA-2 sub-mm galaxy sample at $z \sim 2$.

Casey et al. (2013) derive $SFR_{\rm IR}$ via the Kennicutt (1998) calibration, and obtained an average value of SFR ~ 200 M$_\odot$yr^{-1}. We have shown in Section 6.1.4 that our SED-fit derived SFR values are, on median, slightly higher than the $SFR_{\rm IR}$ values, but those values are comparable. The median SED-derived SFR of our (U)LIRG sample is ~ 230 M$_\odot$yr^{-1}. We show the SFRs as a function of redshift of our sample and the Casey et al. (2013) sample in Fig. 6.19.

Considering the findings of Figures 6.18 and 6.19, we can stay that SFRs of our

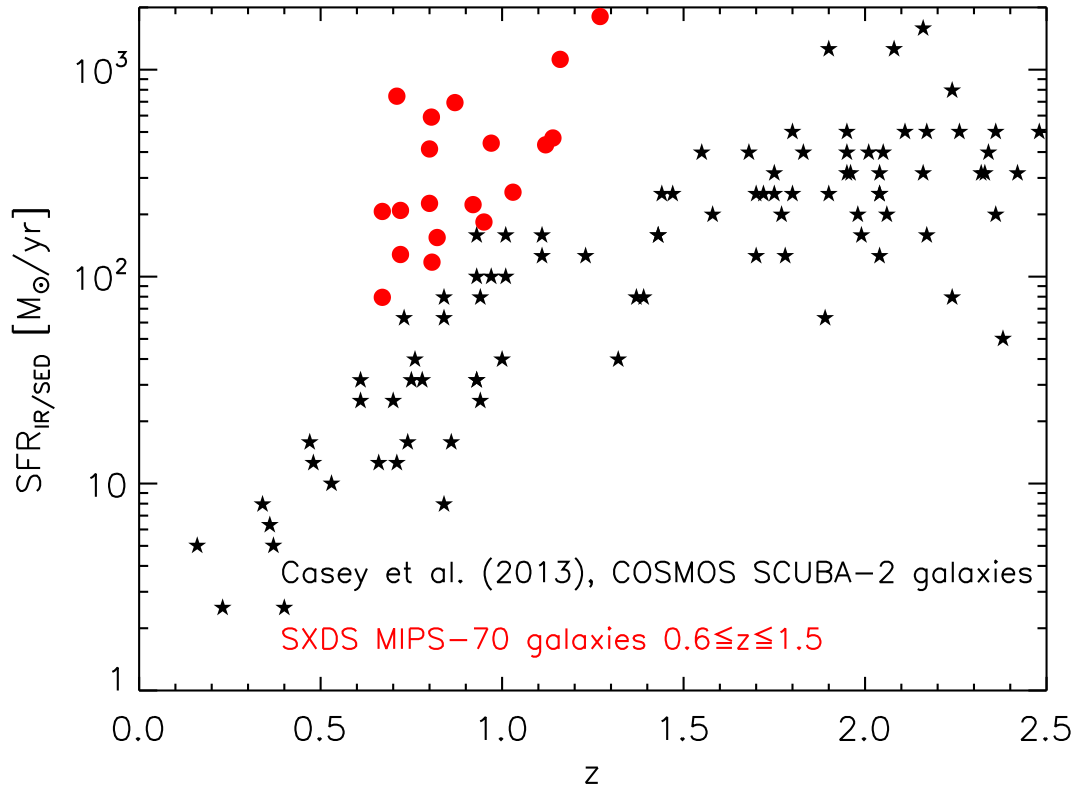

Figure 6.19 : Comparison of SED-derived SFRs of our (U)LIRG sample (*red circles*) with the $SFR_{\rm IR}$ values of SCUBA-2 galaxies of Casey et al.(2013; *black stars*) as a function of redshift.

ULIRGs are compatible with those of SCUBA-2 sub-mm galaxies $\sim$ 200 M$_\odot$yr^{-1}, which is the typical value of of high mass ($> 10^{10}$ $M_\odot$) normal galaxies at $z \sim 2$ (Casey et al. 2013).

Now we move to compare the dust temperature values derived from the power-law+graybody method ($T_{\rm d,C12}$) with those obtained from the best-fitting template of the considered IR libraries ($T_{\rm d,ref}$) for our sample of (U)LIRGs. Both set of values are $\propto 1/\lambda_{\rm peak}$, where $\lambda_{\rm peak}$ is the rest-frame SED peak wavelength of the power pow-erlaw+graybody technique and best-fitting template, respectively. The comparison of $T_{\rm d,C12}$ and $T_{\rm d,ref}$ are show in Fig. 6.20.

An evident fact from the aforementioned figure is that the dust temperatures of the IR templates are quantized (see, e.g. Casey 2012 for a full discussion). This is noticeable in the left part of Fig. 6.20, where 6 galaxies get the same value of $T_{\rm d,ref}$ ($\sim$ 25 K). We should also consider that the our (U)LIRG population probably hosts dust grains of different sizes and temperatures, and that a powerlaw may not represent the diversity of PAHs. Nevertheless, the differences of the dust temperature values

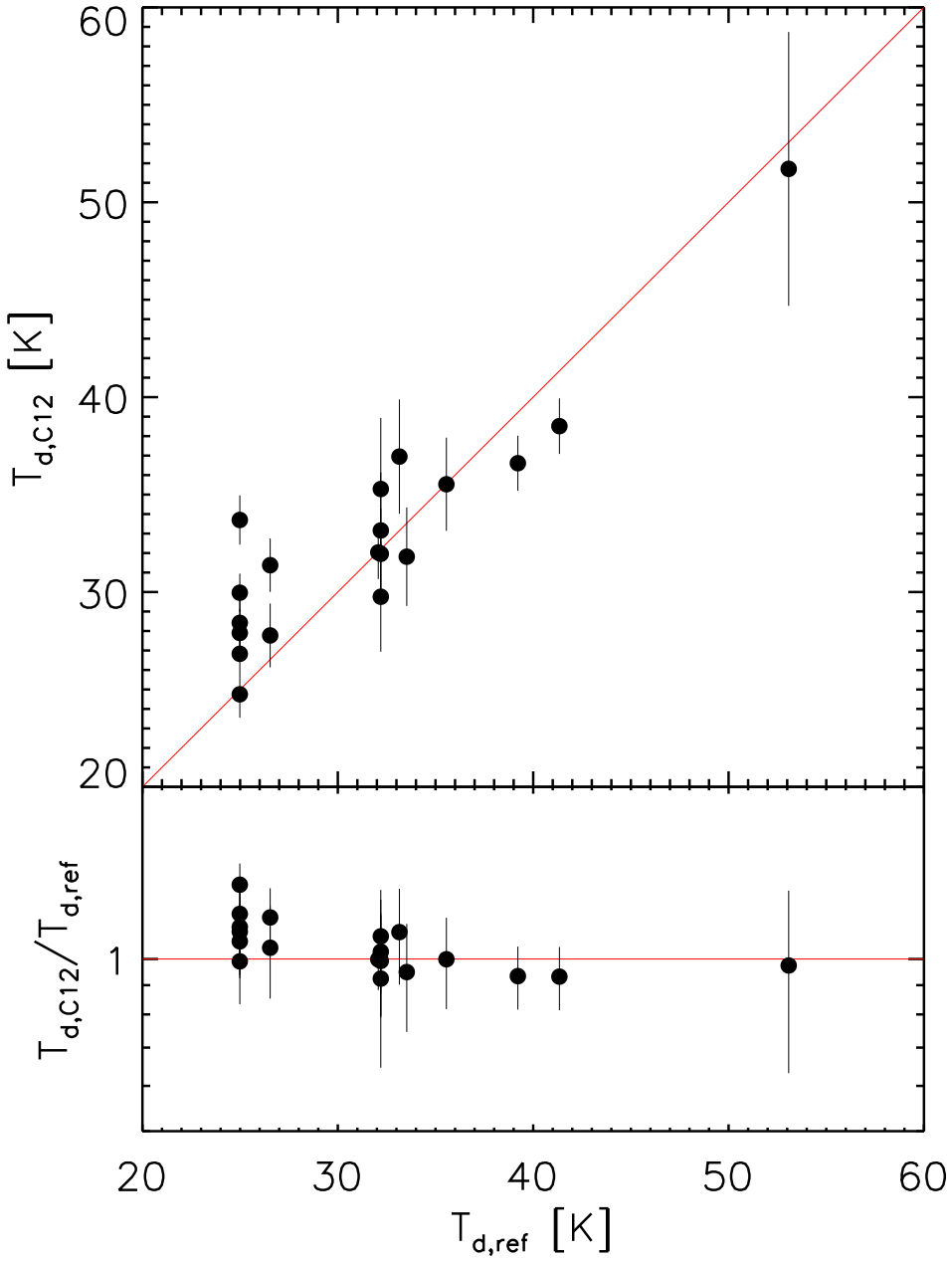

Figure 6.20 : *Upper panel:* Comparison between the $T_{\rm d,ref}$ values derived by the best-fitting template among the IR models of CE01, DH02 and R+09 on x-axis, and those derived by powerlaw+graybody method on y-axis. *Lower panel:* Ratio of the $T_{\rm d}$ values derived with each technique. The error bars show the propagated uncertainties.

obtained from each methods are smaller than $\sim 40\%$. Both sets of $T_{\rm d}$ values range from ~ 25 to ~ 53 K. Given that we are interested on contrast the dust temperature results of our sample of (U)LIRGs with those derived for the SCUBA-2 sub-mm galaxies. We use the $T_{\rm d,C12}$ in the following comparisons.

In Figure 6.21, we show the $L_{\rm TIR}$ values as a function of dust temperature, $T_{\rm d}$, for our sample of (U)LIRGs and the SCUBA-2 selected galaxies. Half of our (U)LIRGs are located at lower $L_{\rm TIR}$ values, but all of them present $T_{\rm d}$ values within the larger range of dust temperatures of the SCUBA-2 sample. However, this also shows that our (U)LIRGs present hot dust grains that produce a shift in $\lambda_{\rm peak}$ to shorter wavelengths. Although this differences are due to the selection function of each sample, we are observing that half of our sample is inaccessible to sub-mm detectors. For example, 4 of our 5 LIRGs cannot be detected by SCUBA-2, due to their warmer dust temperatures, which also true for 4 of our 14 ULIRGs. This is expected because sub-mm samples are biased to colder dust temperatures.

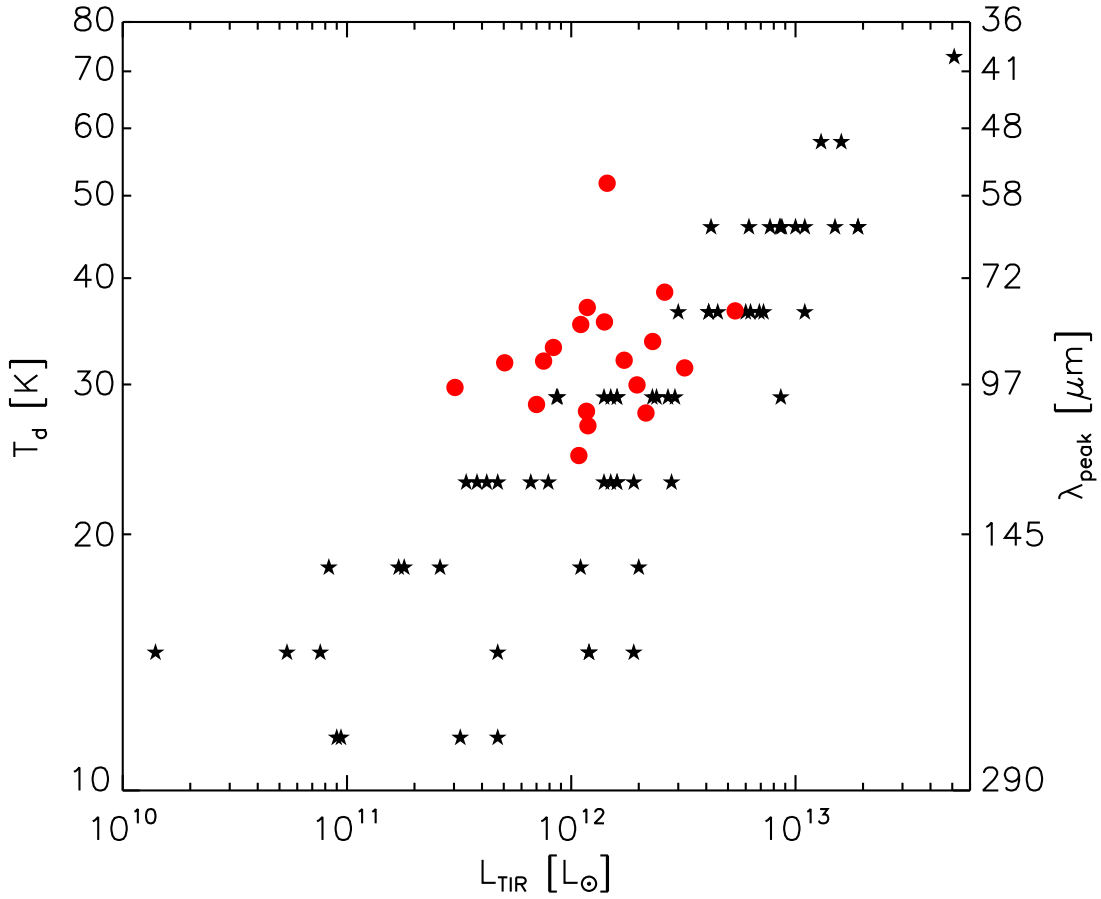

Figure 6.21 : Infrared luminosity against fitted SED dust temperature of our MIPS-70 emitters (*red circles*) compared to that of the SCUBA-2 sub-mm galaxies of Casey et al.(2013; *black stars*) obtained from the COSMOS field.

Notwithstanding, half of our (U)LIRG sample overlaps in $L_{\rm TIR}$ and $T_{\rm d}$ values with the results determined for SCUBA-2 selected galaxies. This fact strengthens our finding of similar average SFR of our (U)LIRG sample at $z \sim 1$ and sub-mm galaxies at

$z \sim 2$, and corroborates that hot-dust ULIRGs are uncommon objects which constitute an intermediate redshift extension of high-z sub-mm galaxies (Casey et al. 2009).

A distinct approach to IR-bright galaxies is considering their dust mass instead of their $L_{\rm TIR}$. Dust mass indicates the disponible material to form new stars. Therefore, dust mass can be considered a stellar mass tracer. In Figure 6.22, we show the dust-mass estimations for our (U)LIRG sample and those for the SCUBA-2 sub-mm galaxies.

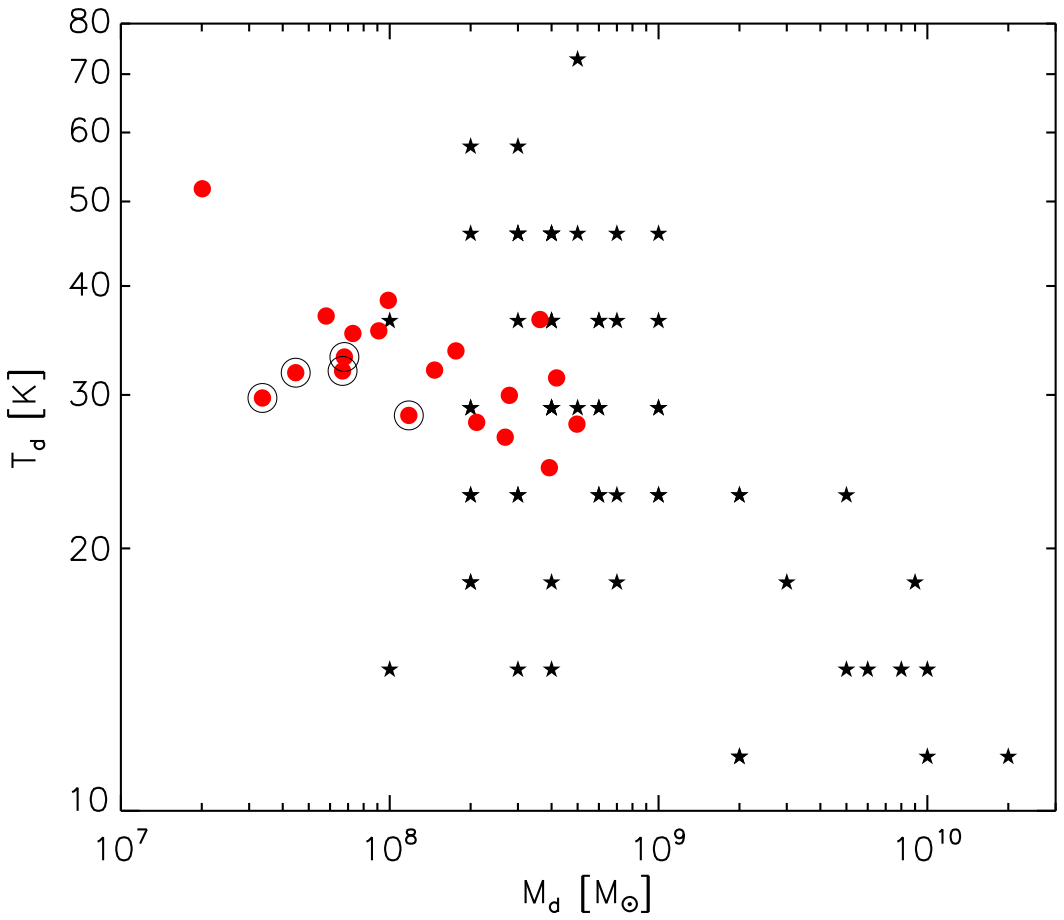

Figure 6.22 : Dust mass against dust temperature of our MIPS-70 emitters (*red circles*) compared to that of the SCUBA-2 sub-mm galaxies of Casey et al.(2013; *black stars*) derived from the COSMOS field. Our MIPS-70 LIRGs are indicated with *open black circles*.

SCUBA-2 objects present typically larger dust masses than our ULIRGs. However, more than a half of our sample has $T_{\rm d}$ and $M_{\rm d}$ values overlapping with those of the SCUBA-2 galaxies. There is a weak correlation between $M_{\rm d}$ and $T_{\rm d}$ in our (U)LIRGs ($r_s = -0.5$, $p_s = 2.9 \times 10^{-2}$). Taking into account this, we can state that dust mass diminishes when dust temperature increases due to the recent born stars. In other words, new stars increase the radiation field intensity heating the surrounding dust. If we exclude the 5 LIRGs of our sample, such $M_{\rm d} - T_{\rm d}$ correlation is more significant ($r_s =$

-0.7, $p_s = 2.9 \times 10^{-3}$), which suggest that LIRGs and ULIRGs at $z \sim 1$ present a different evolutionary path. These findings also evidence that hot-dust ULIRGs at intermediate redshift probably represent an evolved stage of high-z sub-mm galaxies.

6.2.2 Stellar mass and SFR comparisons of (U)LIRGs at $0.6 < z < 1.5$ with other *Herschel*-selected galaxies

In this Section we focus on comparisons of stellar masses and SFRs of our (U)LIRG sample with the *Herschel*-selected samples of Lo Faro et al. (2013) and Lemaux et al. (2014) derived from the GOODS-S and the CFHTLS-D1 fields, respectively. We have collected the galaxies of these samples located at the same redshifts of the (U)LIRGs of our sample, $0.6 < z < 1.5$. Hence, we use the Lo Faro et al. LIRGs at $z \sim 1$ and the SPIRE-250 detected objects of Lemaux et al. within the aforenamed redshift interval. This is done in order to fairly compare such samples with our (U)LIRGs.

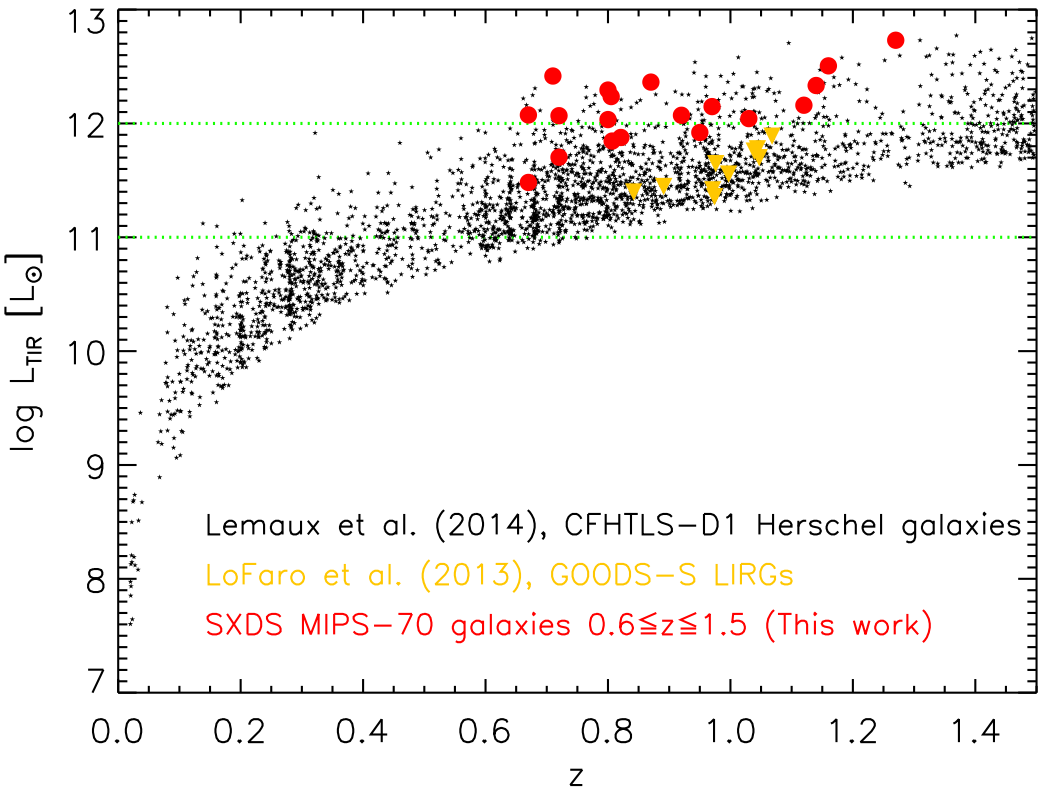

Figure 6.23 : Selection effect of $L_{\rm TIR}$ vs. z of our MIPS-70 emitters (*red circles*) compared to that of SPIRE-250 selected galaxies of Lemaux et al.(2014; *black stars*) derived from CFHTLS-D1 field, and the *Herschel*-selected LIRGs of Lo Faro et al. (2013; *orange inverted triangles*) obtained from the GOOD-S field. The division for LIRGs and ULIRGs are depicted with horizontal lines.

In Figure 6.23, we show the $L_{\rm TIR}$ values as a function of redshift of the 3 samples. The $L_{\rm TIR}$ values of our (U)LIRGs are our $L_{\rm TIR,ref}$ (see Section 4.1), the $L_{\rm TIR}$ for the Lemaux et al. and Lo Faro et al. sample are obtained using the IR templates of Dale and Helou (2002), and GRASIL (Silva et al. 1998), respectively.

Outwardly from the aforementioned figure, we observe what we have already mentioned in Section 3.7, the galaxies in our sample present extreme infrared luminosities, even for a SPIRE-250 selected sample. This is noticed by the location of our objects in the upper part of the $L_{\rm TIR} - z$ plane where the density of SPIRE-250 selected sources is lower, which manifests the selection effect of our sample imposed by the detection limits of the MIPS 70 channel. We should also notice that our sample of (U)LIRGs is missing the galaxies with cold dust temperature, which is in agreement with our finding in Section 6.2.1, our sample is biased to hot-dust (U)LIRGs. The Lo Faro et al. LIRGs occupy the same space in the $L_{\rm TIR} - z$ plane that the average population of the SPIRE-250 selected sample of Lemaux et al.

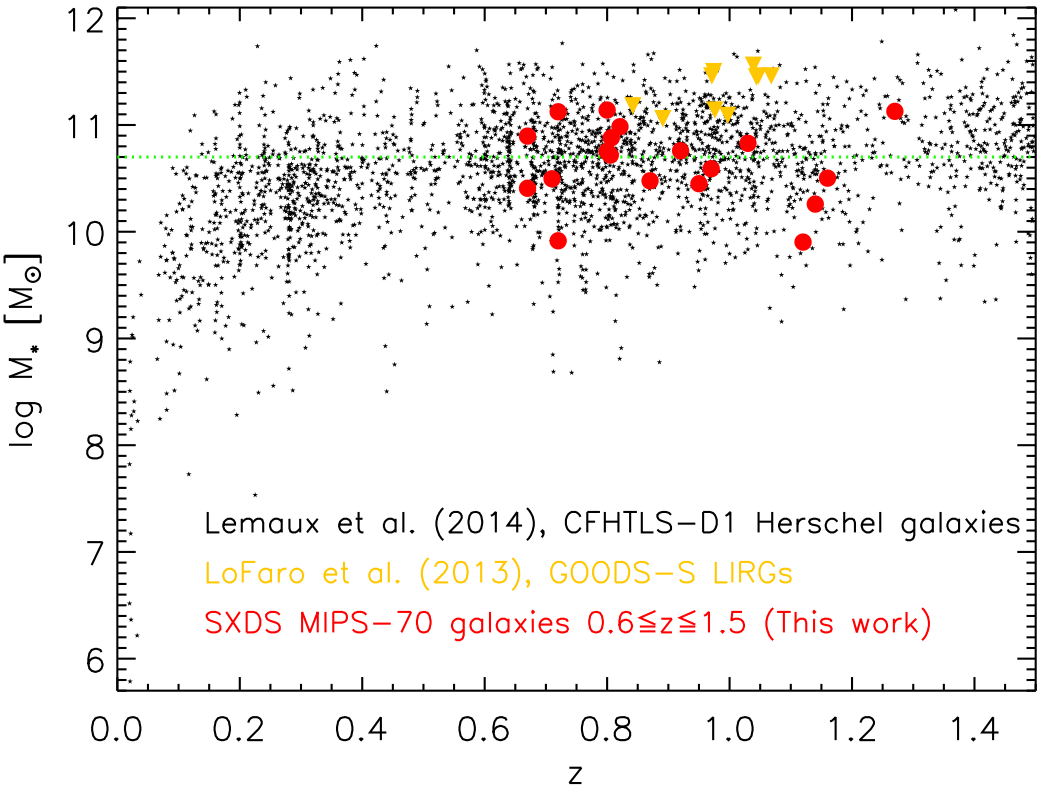

Figure 6.24 : Stellar mass versus redshift for our MIPS-70 galaxies (*red circles*) compared with the SPIRE-250 selected sample of Lemaux et al. (2014; *black stars*) obtained from CFHTLS-D1 field, and the *Herschel*-selected LIRGs of Lo Faro et al. (2013; *orange inverted triangles*) derived from the GOOD-S field. The stellar mass of the Milky Way is marked with the horizontal line.

Now we move to place the stellar mass estimations for the 3 samples as a function of redshift that we show in Fig. 6.24. The stellar masses of our sample of (U)LIRGs are derived using the Synthesizer code assuming a Salpeter (1955) IMF, and a two stellar population SFH (see Section 4.1). The stellar mass values of the Lemaux et al. sample are obtained using the Le Phare code (Ilbert et al. 2006), a SFH depicted by one population, and a Chabrier (2003) IMF. The stellar masses from Lo Faro et al. are determined using GRASIL, and one-population SFH (sometimes including a burst) and also a Chabrier IMF. In order to account for the differences in IMF we add 0.24 dex to the stellar mass values of Lemaux et al. and Lo Faro et al. samples.

We notice from the aforenamed figure that the stellar masses of our (U)LIRGs range in the typical values of those of the SPIRE-250 selected galaxies of Lemaux et al. However, the stellar masses of the LIRGs of Lo Faro et al. occupy the space of the high-mass values where the density of objects is lower. Lo Faro et al. compare the GRASIL stellar mass determinations with those obtained with the HYPERZ code (Bolzonella et al. 2000). They find that the HYPERZ stellar masses are underestimated due to an underestimation of $A(V)$. Nevertheless, we have found $A(V)_{\rm you}$ as high as the GRASIL estimations (~ 4 mag), and we do not obtain those high stellar masses.

A natural extension after comparing infrared luminosities and stellar masses is to situate the galaxies of the 3 samples in the $SFR - M_*$ plane. In Figure 6.25 we show the $SFR - M_*$ relation for the 3 samples. The SFRs for our sample of (U)LIRGs are obtained from SED-fitting using our fiducial SFH (two stellar populations with their $A(V)$ constrained by the FIR prior; see Sections 5.1 and 6.1.4). The SFRs for the Lemaux et al. sample are determined using the Kennicutt (1998) calibration. The SFRs for the LIRGs of Lo Faro et al. are derived also from SED-fitting using GRASIL. It is evident from the aforementioned figure that the Lemaux. et al sample does not present a clear dependence of SFR on stellar mass. This is also true for our sample of (U)LIRGs, and other recent studies of *Herschel*-selected galaxies over areas $\gtrsim 0.8$ deg^2 where is possible to find objects with extreme infrared luminosities (see, e.g, Lee et al. 2013). In Figure 6.25, we show with a blue solid line the so-called main sequence (a typical assumption that SFRs depend on stellar mass values) determined by Elbaz et al. (2007) for $z \sim 1$ galaxies. It is clear that more than a half of the SPIRE-250 selected galaxies of Lemaux et al. are above such main sequence, which is also true for all the objects of our sample (see Section 6.1.4 for a full discussion). All the Lo Faro et al. LIRGs lie below the main sequence. Besides the high stellar masses found with GRASIL for such LIRGs, Lo Faro et al. also state that SFR determined using the Kennicutt calibration overestimate the SFRs compared with the SED-derived SFRs determined with GRASIL. Such overestimation is not found in the SED-fitting SFRs

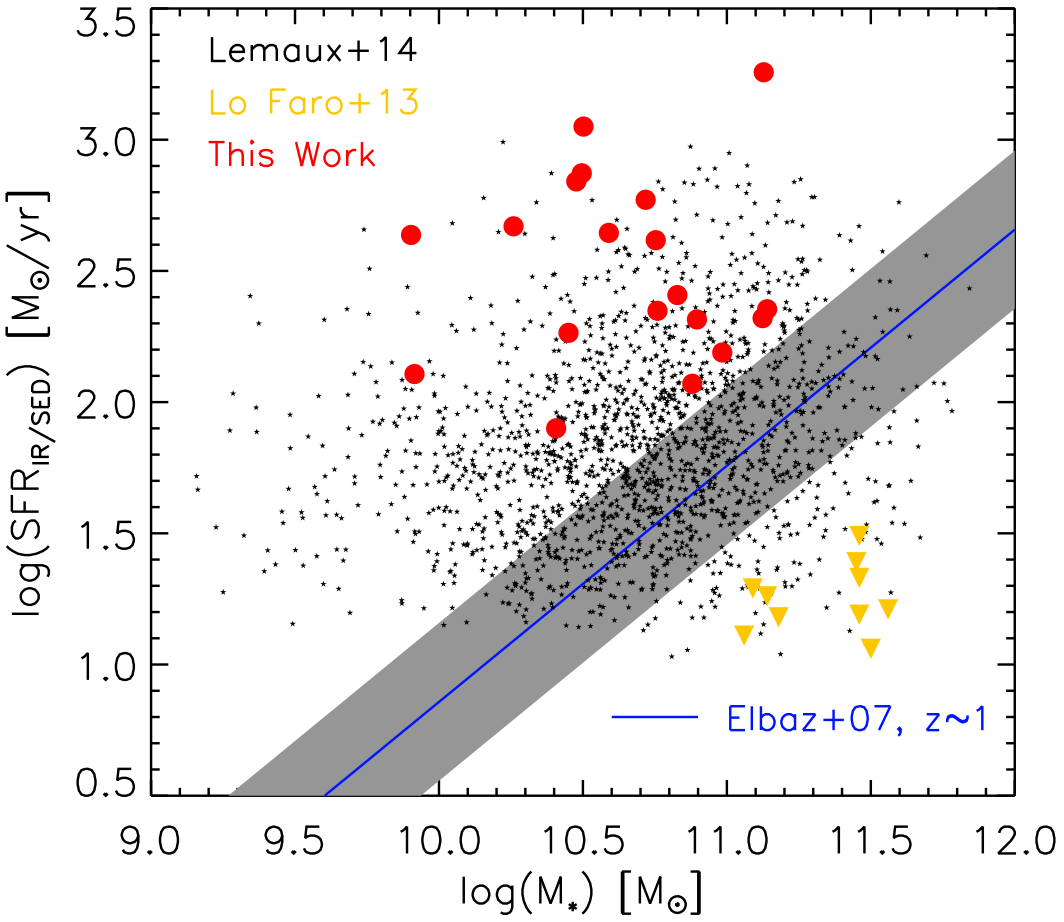

Figure 6.25 : M_* vs. $SFR_{\rm IR/SED}$. The *filled red circles* show the SED-derived SFR values estimated with the Synthesizer code of our sample of (U)LIRGs. The *black stars* show the $SFR_{\rm IR}$ values from the Lemaux et al. (2014) sample. The *orange inverted triangles* depict SED-fitting SFR values obtained with GRASIL of the LIRGs of Lo Faro et al. (2013). The stellar mass values of the 3 samples are derived as explained in the text. The *blue solid line* stands for the relationship presented in Elbaz et al. (2007) with its 68% confidence level marked with the *gray shaded area*.

of this study and other recent works using also a self-consistent analysis of the stellar and dust emission (see, e.g., Utomo et al. 2014, Buat et al. 2014). Notwithstanding, the LIRGs of Lo Faro et al. occupy a space also covered by the sample of Lemaux et al., and therefore this LIRG can be experiencing a more evolved state in the sub-mm–ULIRG paradigm of galaxy evolution.

Chapter 7

Conclusions

In the work presented in this thesis, we have studied detailedly the physical properties of the stellar populations of IR-bright galaxies by analyzing the UV-to-FIR observed SED from a FIR-selected sample of 19 galaxies (5 LIRGs and 14 ULIRGs) at $0.6 < z < 1.5$, with secure multi-wavelength counterparts. The sample has been based on *Spitzer*/MIPS (the sources selected at 70 μm but all with 24 μm data), and *Herschel* detections from the Subaru/XMM-Newton Deep Survey field. Using 3 (or more) FIR bands, we have constrained accurately the $L_{\rm TIR}$ of all galaxies in the sample. Combining these FIR data with UV-to-MIR photometry, we have fitted models considering the stellar and dust emission with energy balance techniques. We have assumed as fiducial the Maraston (2005) models, the Salpeter (1955) IMF, and a SFH depicted by young stellar population forming stars in a roughly constant manner on top of and evolved population each parameterized with an exponentially decaying-τ form. We have fixed the metallicity to the solar value for both populations. We have contrasted fits with and without FIR data. When using FIR data, their associated $L_{\rm TIR}$ value is used to constrain the amount of attenuation of stellar light. This constraint is called "the FIR prior". We have assessed if the FIR prior is useful to overcome the age-dust degeneracy, yielding to a reliable determination of the stellar population properties of (U)LIRGs. We have also compared fits obtained with our fiducial two population models including FIR data with those resulting from one population models using the FIR constraint. We have done that to check if is possible to simplify our assumed SFH. We have derived parameter values for stellar masses, SFRs, attenuations, ages, decaying factors, and burst intensities (i.e., fractions of the total stellar mass in the young population) using two codes with auto-consistent modeling capabilities, the Synthesizer and the CIGALE. We use a χ^2-like estimator to compare the goodness of the fits of each code for UV-to-MIR and FIR wavelengths, separately. The fitting strategies of both codes incorporate procedures

to estimate uncertainties in the derived parameters and to consider degeneracies in the solutions. By comparing the parameter values derived with each code, we have assessed which physical properties obtain consistent results and which parameters are dominant on the model solutions. This work has yielded the following results:

1. The $L_{\rm TIR}$ of our sample ranges from 3.0×10^{11} to 5.4×10^{12} $L_{\odot}$, with 5 LIRGs (median $L_{\rm TIR} = 7.0 \times 10^{11}$ $L_{\odot}$), and 14 ULIRGs (median $L_{\rm TIR} = 1.6 \times 10^{12}$ $L_{\odot}$).

Regarding the usage of the FIR data and the comparisons of SFHs with one and two stellar populations, we have deduced that:

2. Excluding the FIR data in two population models results mainly in an overestimation of the attenuation of the young population with a median value of 0.4 mag. This overestimation translates in a underestimation of the young population ages of a factor ~ 6 in median. This evidences the efficacy of the FIR prior in breaking the age-dust degeneracy, providing reliable attenuation and age values for the young population, and improving the determinations of the SFHs of (U)LIRGs. Therefore, two population models with FIR data are the most suited to reproduce the stellar properties of the IR-bright galaxies of our sample.

3. For models using FIR information, one population models present inferior goodness of the fit compared with two population models. One population models exhibit an underestimation of the amount of attenuation and a deficit of stellar mass, which translates in an underestimation of SFRs. When using one population, it should be young to match the UV/optical observed photometry, but simultaneously it should last enough time to form enough red stars contributing with stellar mass. Both conditions are hardly satisfied with one population models, which evidences the need of two populations for a robust modeling of the stellar spectrum of our IR-bright galaxies.

By comparing the parameter values derived with the CIGALE and Synthesizer codes, our results point out:

4. Regarding the goodness of the fits, we find that the distribution of $\chi^2_{\rm UV/MIR}$ from the Synthesizer code concentrates in lower values (median $1.7^{+1.4}_{-0.6}$) compared with the CIGALE one (median $4.0^{+3.0}_{-2.4}$), and that 63% of all galaxies are better fitted by the Synthesizer code, which shows that the Synthesizer code performs better in the UV-to-MIR spectral range. For the FIR wavelengths, the distributions of $\chi^2_{L_{\rm TIR}}$ from each code are compatible, with medians $0.9^{+3.2}_{-0.8}$ and $1.4^{+1.8}_{-1.3}$

for the CIGALE and the Synthesizer code, respectively, which indicates a similar performance of each code in the FIR spectral range.

5. Concerning the SFH, we observe that the young population dominates the recent star formation and that the contribution of the old population is mostly to the stellar mass. Specifically for the young population, we find that:

   (a) The attenuation values of the young population, $A(V)_{\rm you}$, determined with both codes are in compatible ranges $\sim 0.5 - 3.5$ mag, The median value is ~ 2.5, with most of the galaxies (89%) presenting $A(V)_{\rm you} > 2$ mag. The median difference between codes is smaller than 0.1 mag. Both set of values are clearly correlated with Spearman coefficient and probability of no significance of $r_s = 0.95$ and 7.8×10^{-10}, respectively. This shows that the energy-balance technique of the two different codes produce consistent results, indicating that the $A(V)_{\rm you}$ values are properly constrained by the FIR prior.

   (b) The ages of the young population, $t_{\rm you}$, are shorter than ~ 400 Myr, with median values ~ 40 and ~ 100 Myr for the Synthesizer code and the CIGALE, respectively. There is a correlation between the set of $t_{\rm you}$ values of each code, with Spearman coefficient and probability of no significance of $r_s = 0.85$ and 4.7×10^{-6}, respectively. These results show that the age of the young population has been adequately constrained.

   A significant fraction, 79% of all galaxies have $t_{\rm you} < 100$ Myr as derived from the Synthesizer code results, which is also true for 53% of the sources as derived from the solutions of the CIGALE. Considering the young population ages as lower limits of the time a galaxy spent in the (U)LIRG phase, such fractions agree with the estimates of the starburst lifetime of sub-millimeter galaxies $\sim 100 - 300$ Myr (Hickox et al. 2012, Swinbank et al. 2006). So, on average, we are observing galaxies at half of their lifetime in that (U)LIRG phase (which is what could be expected).

   We have found a correlation between $L_{\rm TIR}$ and $t_{\rm you}$ for both codes, the age of the young population increases as the total infrared luminosity decreases. This correlation is also found in the studies of Lemaux et al. (2014) deriving ages of the young population from spectroscopic data of *Herschel*-selected galaxies.

   (c) The burst intensities, b, i.e., the fraction of the total stellar mass due to the young population are in $\sim 10 - 60\%$, with median values of $\sim 25\%$ and

$\sim 50\%$ for the Synthesizer code and the CIGALE, respectively. These high burst intensities are also found in Lemaux et al. (2014) for ULIRGs.

The determination of the properties for the old population are affected by large uncertainties, linked to degenerations and the fact that the new stars typically outshine the old population through most of the SED. Nonetheless, both codes derived ages of the old population larger than 1 Gyr, with median values $\sim 3-4$ Gyr. The e-folding time values have medians of 200 and 800 Myr as derived from the Synthesizer code and the CIGALE, respectively. These e-folding time differences are compensated with the CIGALE obtaining less intense initial bursts. The old populations are nearly unattenuated ($A(V)_{\rm old,SYNT} < 0.1$ mag in median) as derived from the Synthesizer code results, and they present an attenuation in the V band of 0.8 mag in median as determined from the solutions of the CIGALE.

6. Regarding the stellar masses, both codes yield similar results in the range $\sim 1 \times 10^{10} - 2 \times 10^{11}$ $M_{\odot}$, with median values $5.2^{+4.4}_{-2.7} \times 10^{10} M_{\odot}$ and $4.8^{+6.9}_{-1.8} \times 10^{10} M_{\odot}$ as derived from the Synthesizer and the CIGALE results, respectively. The stellar mass values from both codes are similar, which is expected considering that they have used the same SFH, IMF, and Maraston (2005) models. These stellar mass values are compatible with previous estimations derived for $z > 1$ sub-mm galaxies, and distant red galaxies (Wardlow et al. 2011, Bussmann et al. 2012, Rowlands et al. 2014).

7. The instantaneous SFRs derived from SED fitting range in $\sim 70 - 2000$ $M_{\odot}$ yr^{-1} for the Synthesizer code, and $\sim 70 - 1000$ $M_{\odot}$ yr^{-1} for the CIGALE. The instantaneous SED-derived SFRs from the CIGALE are in good agreement with the classical tracer $SFR_{\rm UV+IR}$ obtained assuming constant SFR over a timescale of 100 Myr. Conversely, the current SFRs derived with the Synthesizer code are $\sim 20\%$ higher than both estimations in median. Furthermore, when the ages of young population are shorter than 20 Myr, SED-fitting derived SFRs are $\sim 60\%$ and $\sim 30\%$ higher for the Synthesizer code and the CIGALE, respectively, compared to those obtained with such classical tracer. A better agreement is found for the SFRs of these young bursts when compared with a $SFR_{\rm UV+IR}$ calibration assuming constant SFR over a timescale of 10 Myr. Therefore, SFRs estimated with the standard calibration of Kennicutt (1998) for (U)LIRGs should be considered lower limits, if the age of young population is unknown.

   The median SED-derived SFR of our sample is ~ 230 $M_{\odot}$yr^{-1}, which is similar to that obtained for SCUBA-2 galaxies (Casey et al. 2013). Assuming the median

SFR of our sample and a lifetime for the starburst phase of 100 Myr, suggest that the stellar mass added during such phase reach $\sim 2 \times 10^{10}\ M_{\odot}$. This stellar mass value corresponds to a fraction of $\sim 40\%$ of the median stellar mass derived for our sample with each code.

8. Concerning the $SFR-M_{*}$ relation (main sequence) as derived from the solutions of both codes, our sources lie ~ 1 dex above the main sequence with no clear dependence of SFR on stellar mass. This result agrees with other recent studies based on FIR selected samples (Lee et al. 2013, Lemaux et al. 2014).

9. The sSFR of our sample range in $\sim 1 - 54$ Gyr^{-1} for the results from the Synthesizer code, and in $\sim 1 - 23$ Gyr^{-1} from the solutions of the CIGALE, with the Synthesizer code obtaining sSFR a factor ~ 1.6 larger than the CIGALE. The median sSFR are ~ 7.3, and ~ 3.8 Gyr^{-1} for the Synthesizer code and the CIGALE, respectively. These median values are significantly higher than the median sSFR of a 'normal' galaxy at $z \sim 1$ ($\sim 0.4 - 0.5$ Gyr^{-1}; Elbaz et al. 2011). This result confirms that the objects in our sample present extreme starbursts.

10. Our galaxies show a current SFRs dominated by the contribution of the young population. Such young populations form stars in a roughly constant manner, which allows the approximation, $sSFR \simeq b/t_{\rm you}$. This result indicates that the energy balance technique of each code results in the conservation of the sSFR. The FIR prior constrains mainly the attenuation of the young population. This attenuation leads to determine a proper age for the young population, which such age related with a suitable burst intensity. This result also shows that there are degeneracies between the burst strength and the age the young stellar populations, i.e., a massive burst of star formation with relatively larger age (e.g., $b = 50\%,\ t_{\rm you} = 140$ Myr) has a similar emission than a less massive burst with shorter age (e.g., $b = 20\%,\ t_{\rm you} = 50$ Myr).

With the advent of new FIR missions as SPICA, the number of (U)LIRGs at $0.6 < z < 1.5$ will be incremented enormously. Using this wealth of IR-bright galaxies we will increase the statistics in the study of this kind of (U)LIRGs, and therefore we will improve the significance of our findings.

Appendix A

UV-to-FIR SEDs for 2P and 1P models

We plot in Fig. A.1, the complete UV-to-FIR SEDs derived from the fits of 2-POP and 1-POP models using the Synthesizer for our sample of IR-bright galaxies. We also provide the results of the median solutions of the most significant clusters derived from the Monte Carlo simulation analysis for the 2-POP and 1-POP models, respectively.

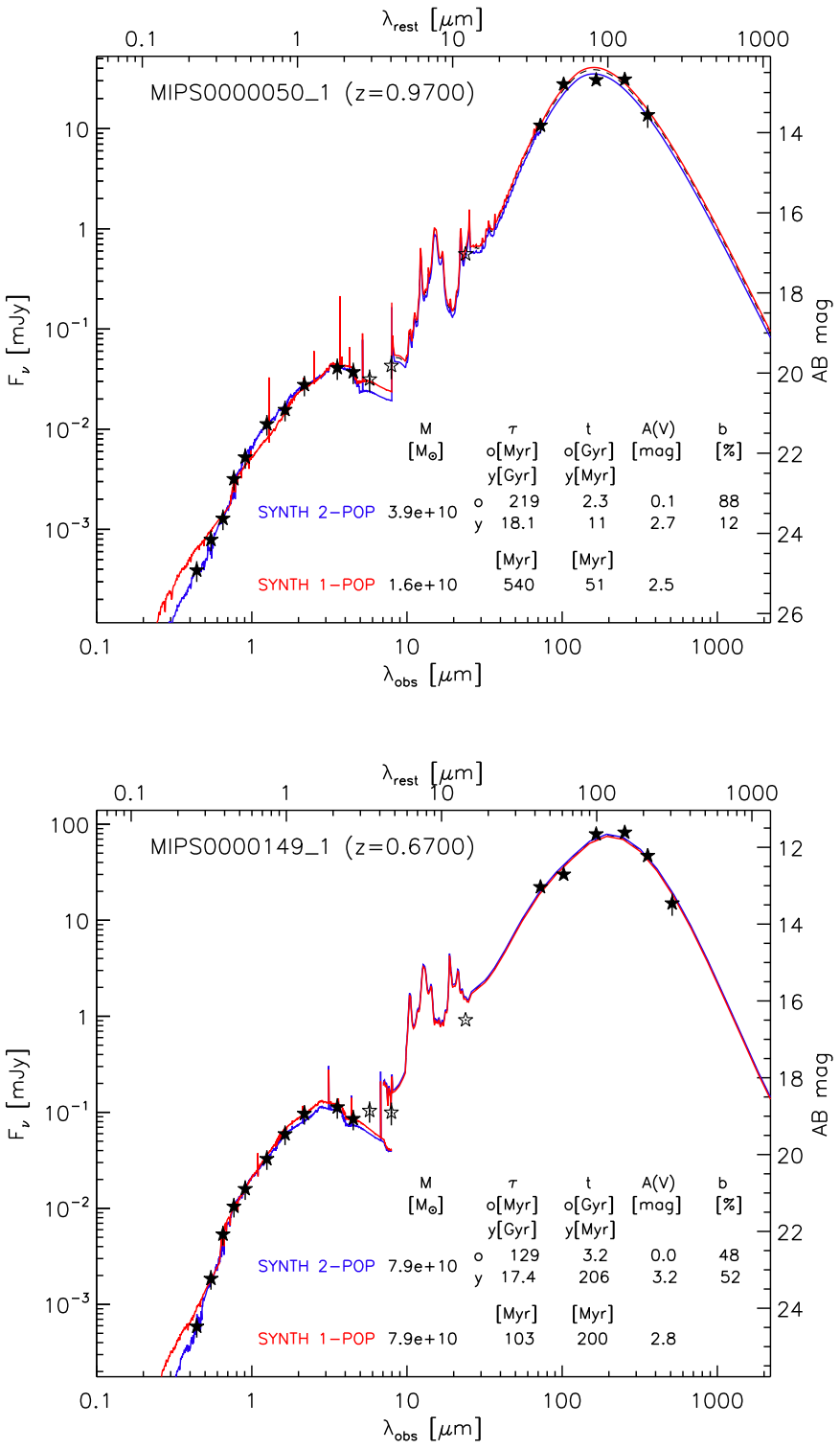

Figure A.1 : Two examples of the resulting fit to the whole UV-to-FIR SED for our IR-bright galaxies with the Syntesizer code. *Solid blue line:* Result of the fitting process obtained with 2-POP models. *Solid red line:* Fit derived using 1-POP models. The parameter values of the solutions are also shown (M_*, τ, t, $A(V)$, b) for the 2-POP and 1-POP models, respectively. *Dashed black line:* Fit to the FIR photometry ($\lambda_{obs} \geq 70$ μm). Photometric data points include the uncertainties (multiplied by 2.5 from UV to IRAC bands for visualization), only the *filled black stars* are used in the fit.

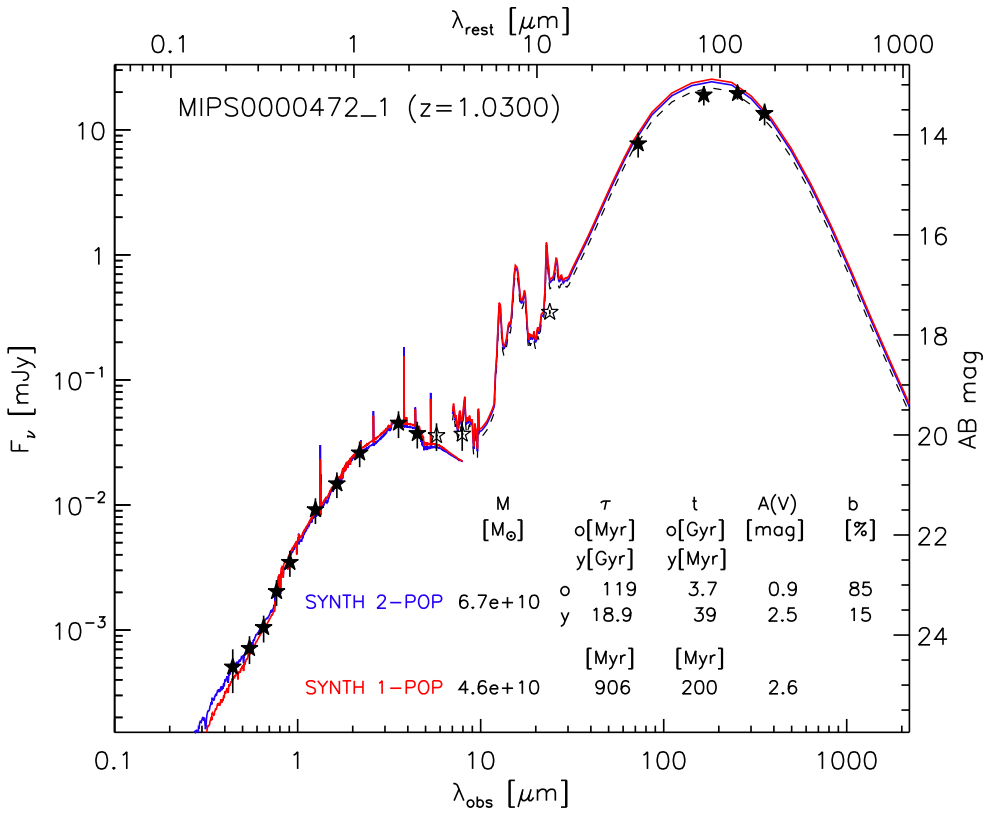

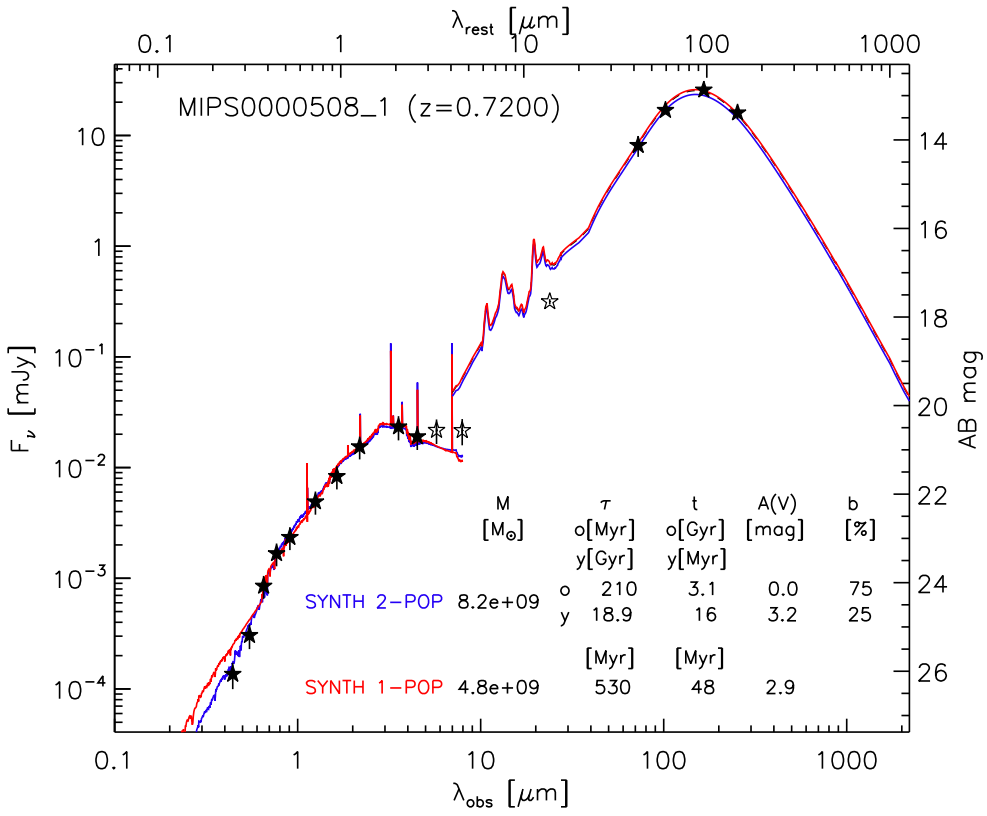

Figure A.1 : cont'd

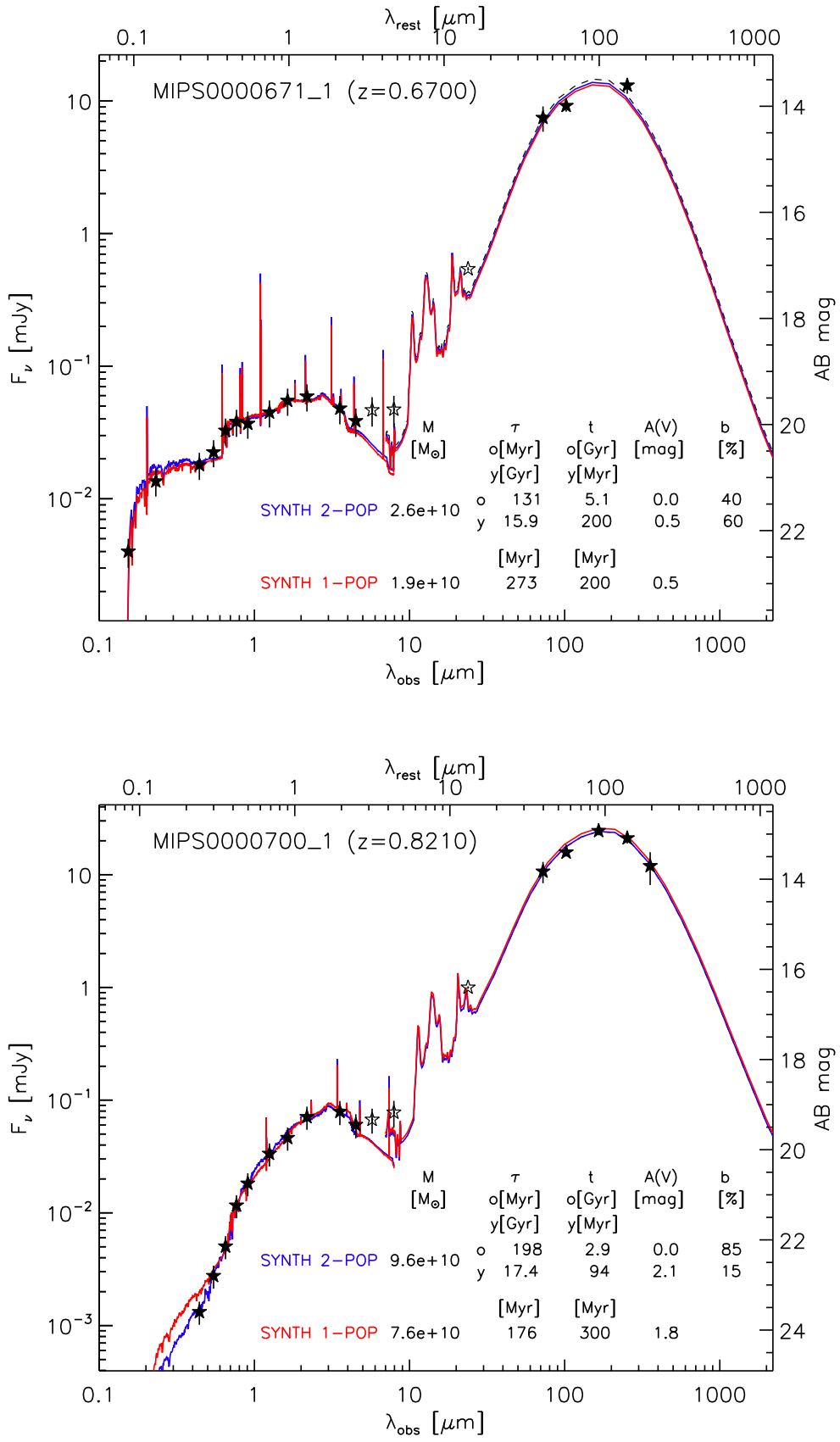

Figure A.1 : cont'd

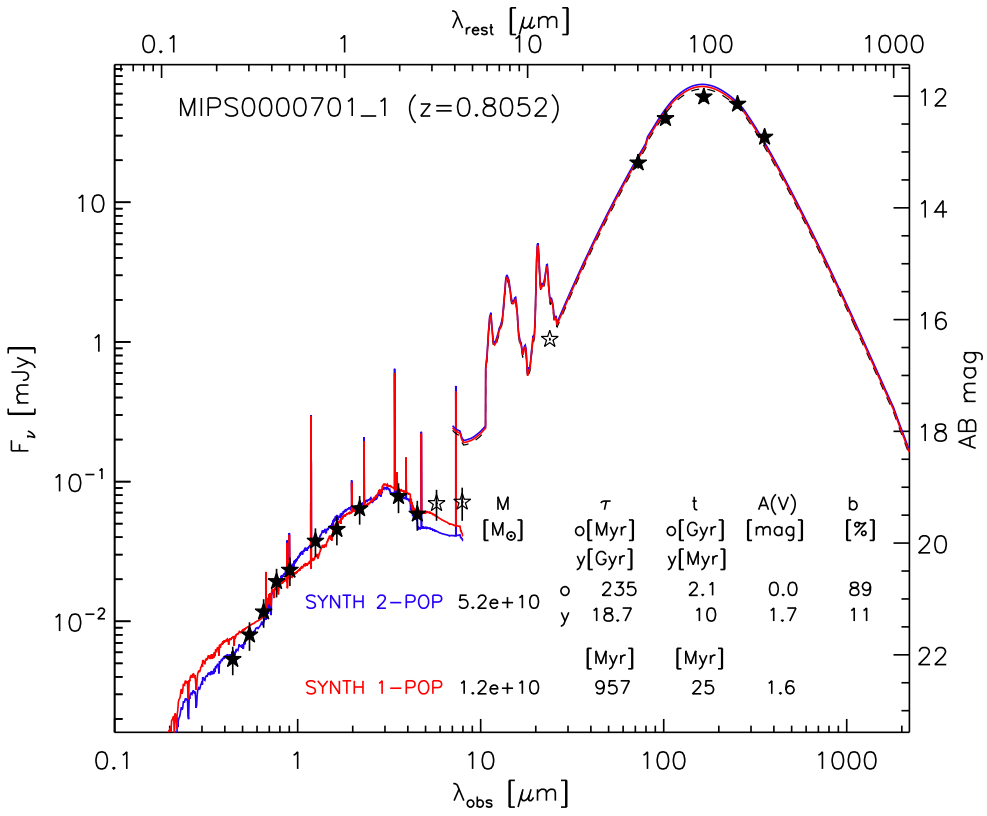

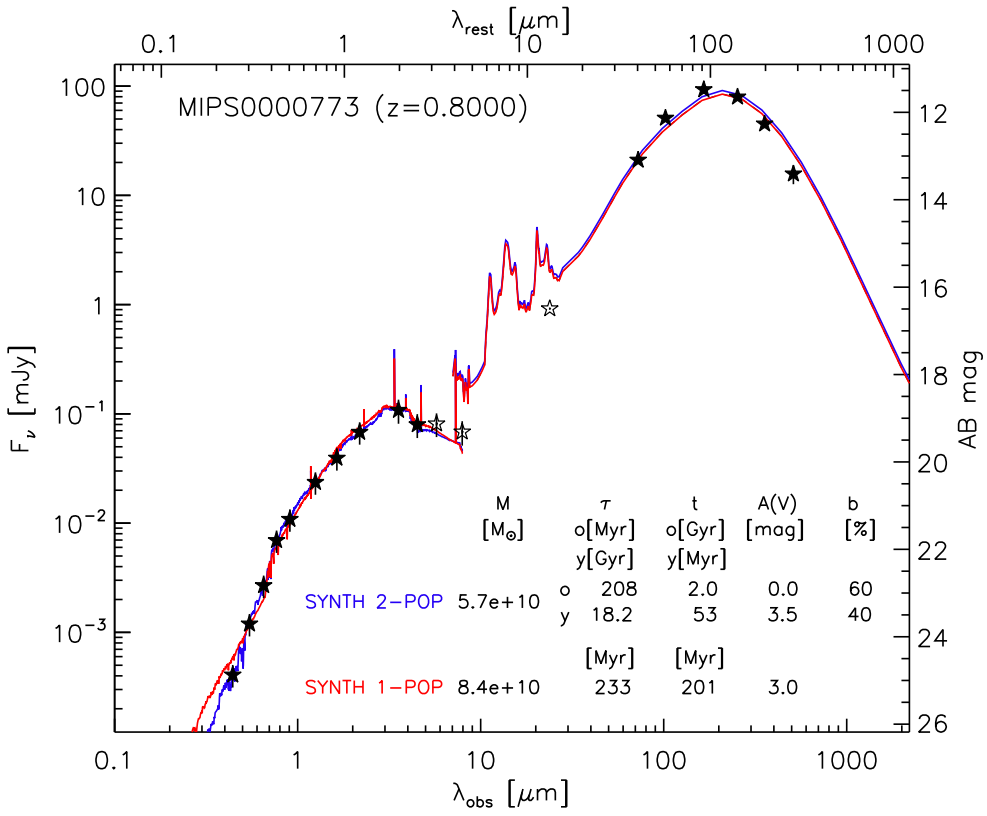

Figure A.1 : cont'd

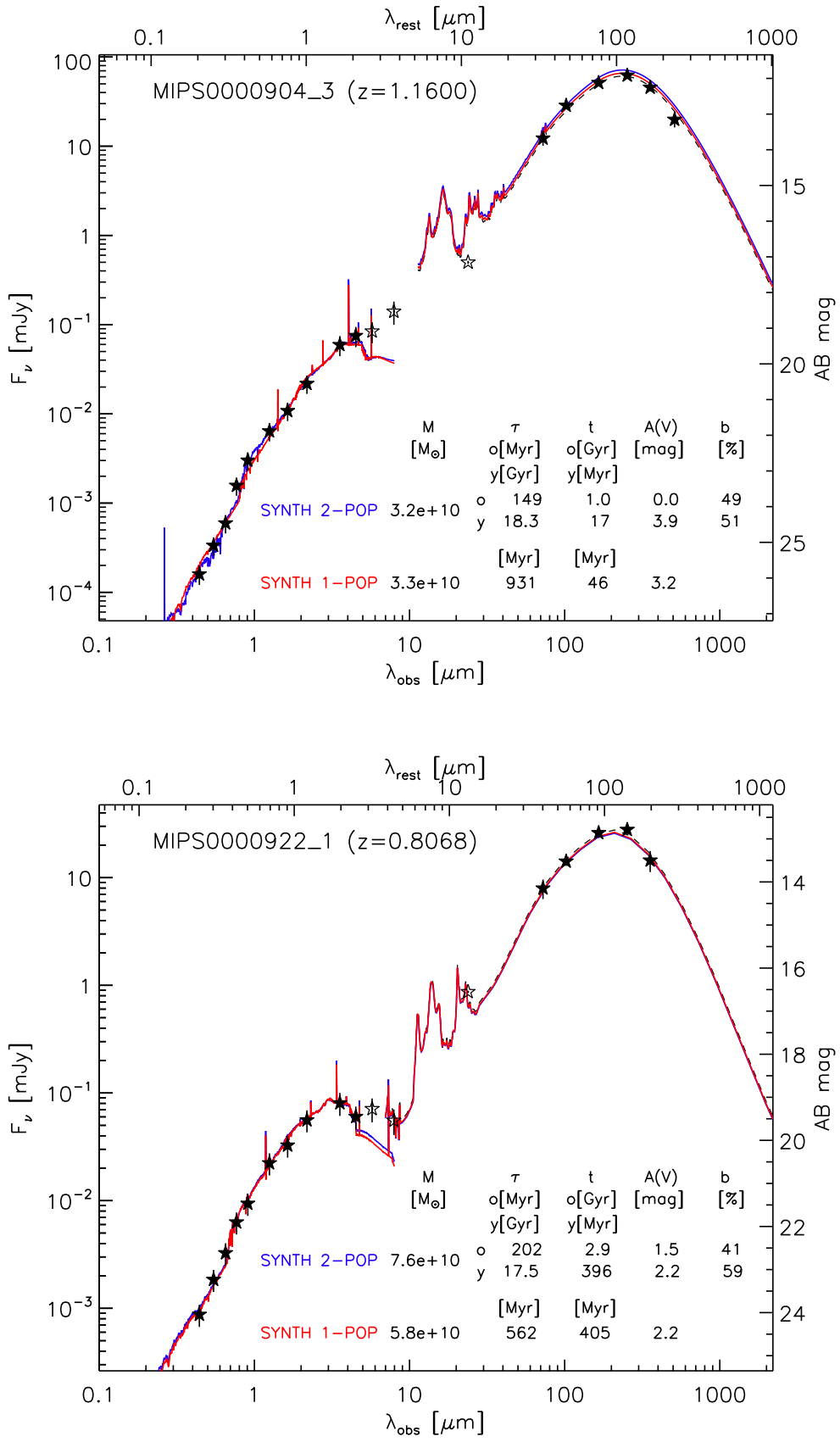

Figure A.1 : cont'd

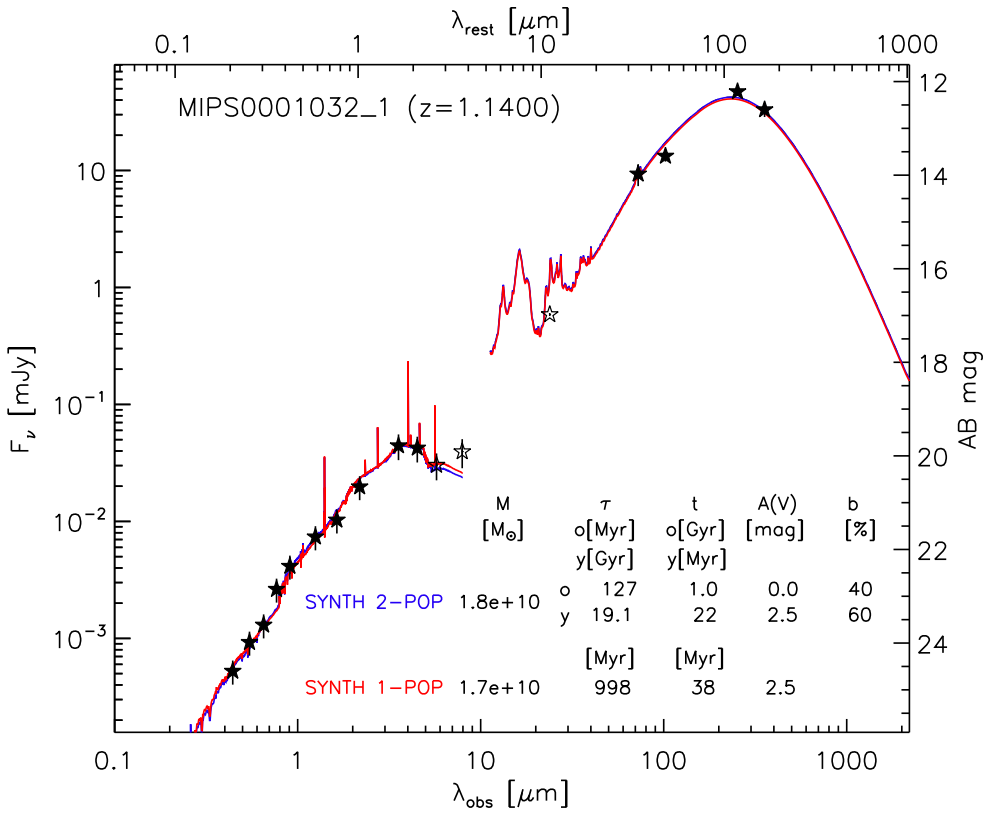

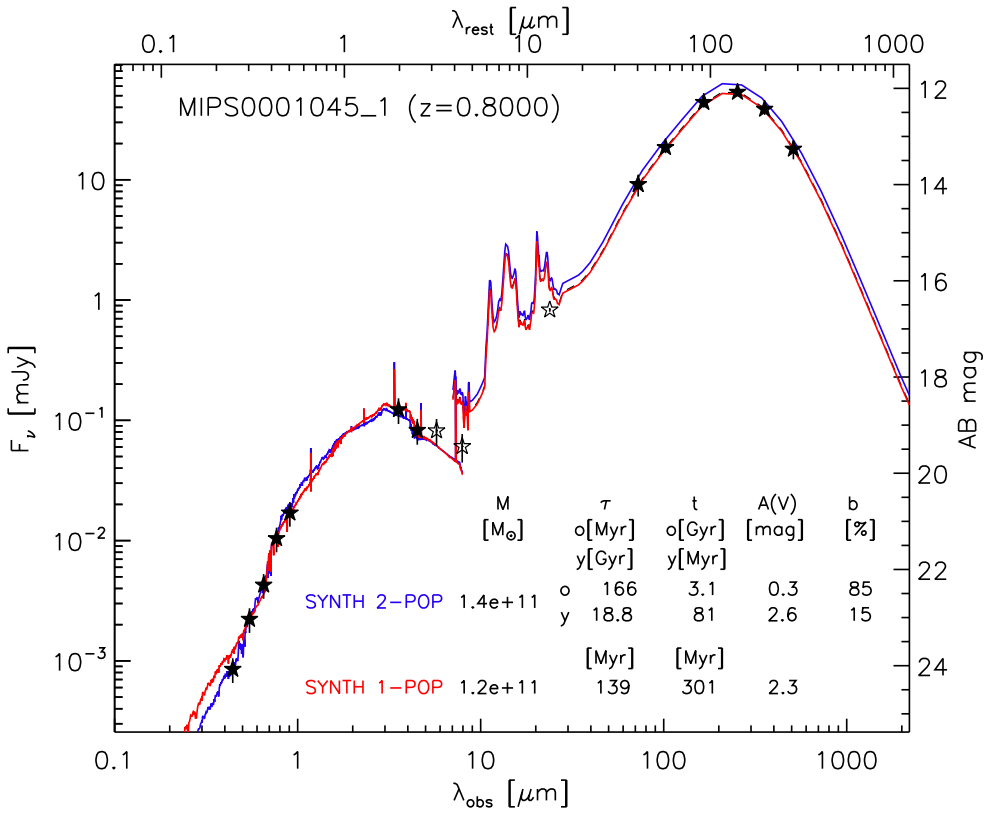

Figure A.1 : cont'd

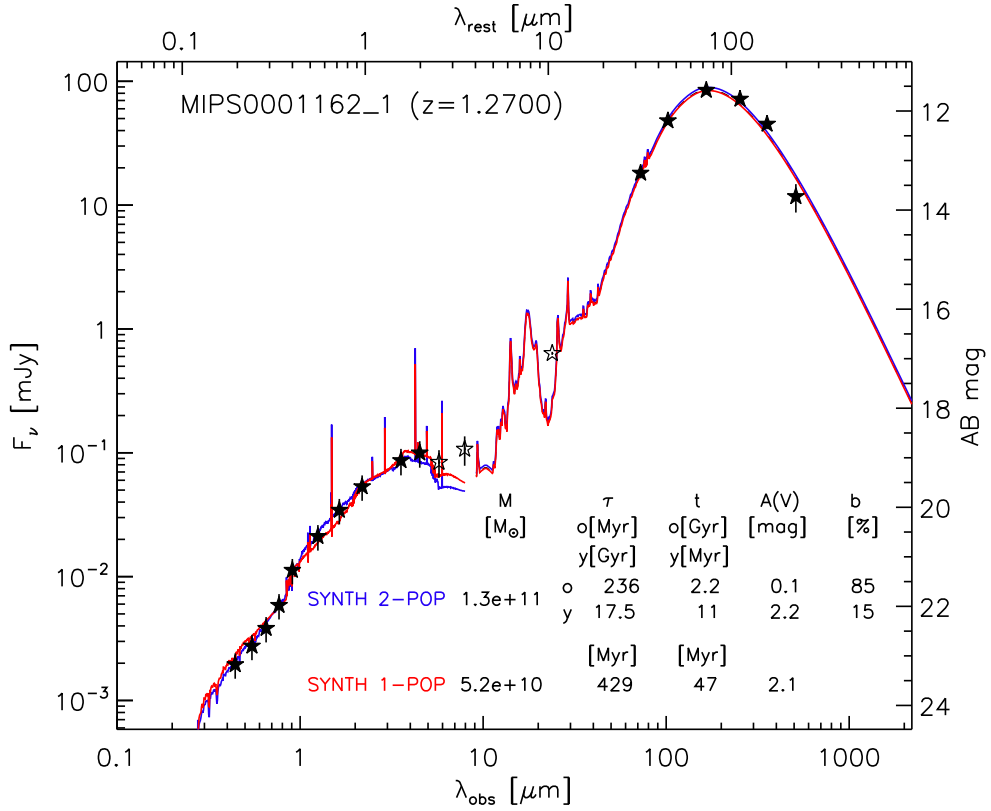

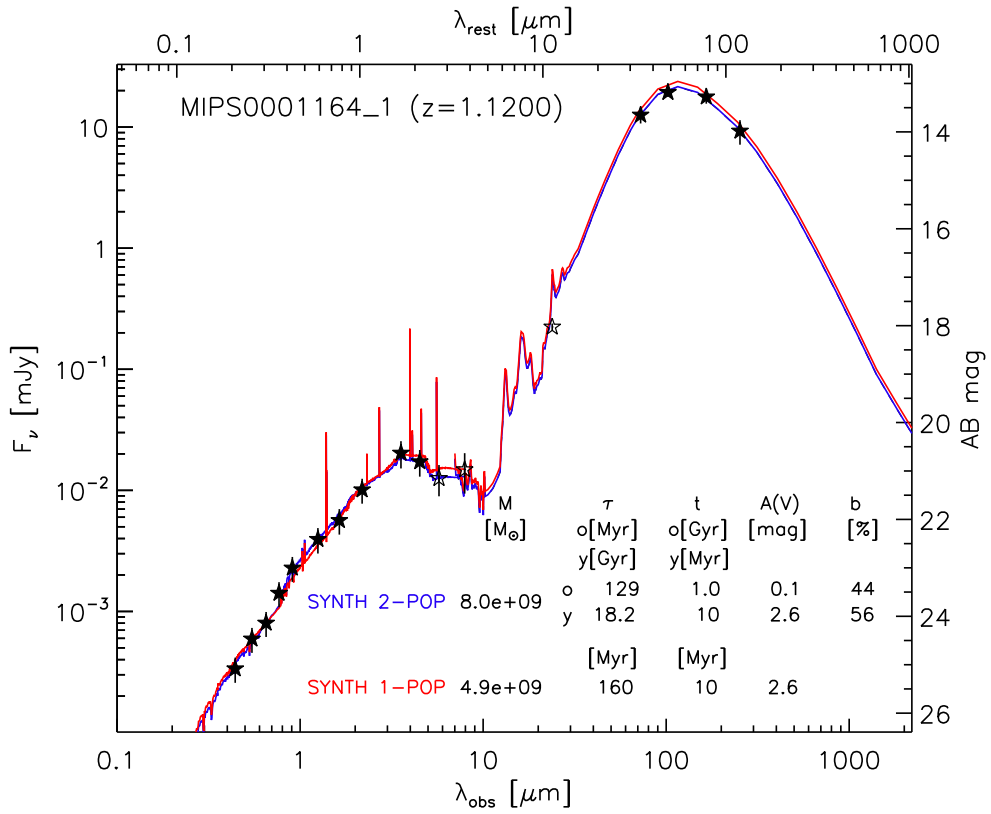

Figure A.1 : cont'd

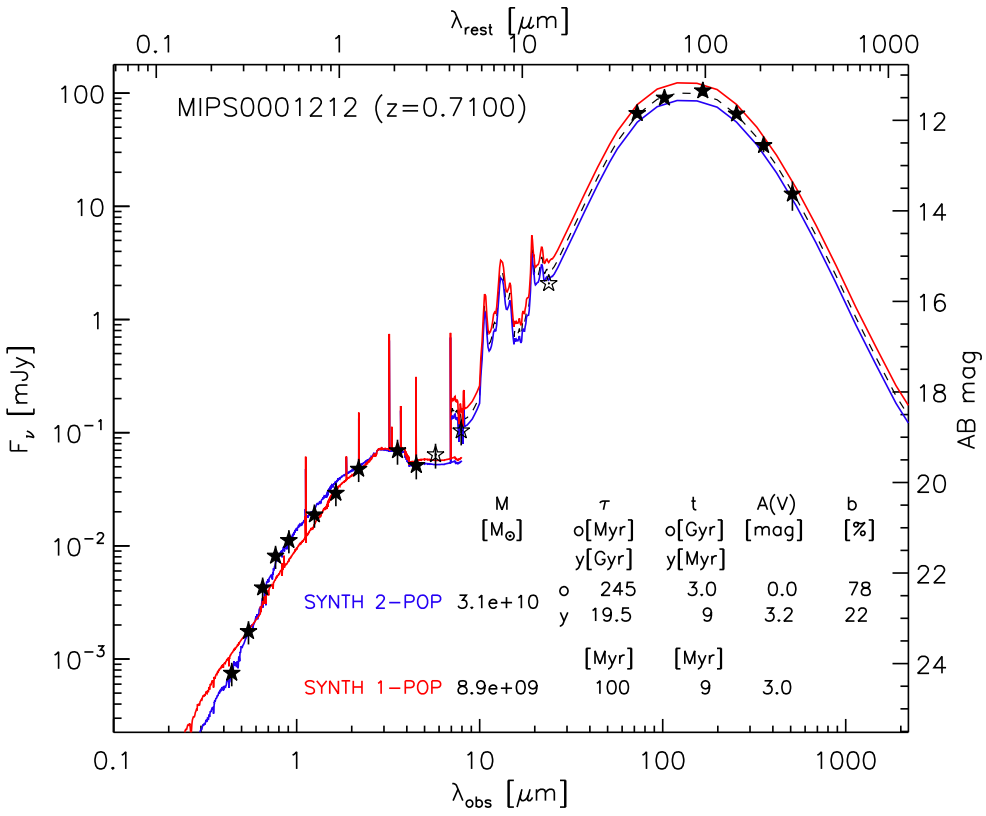

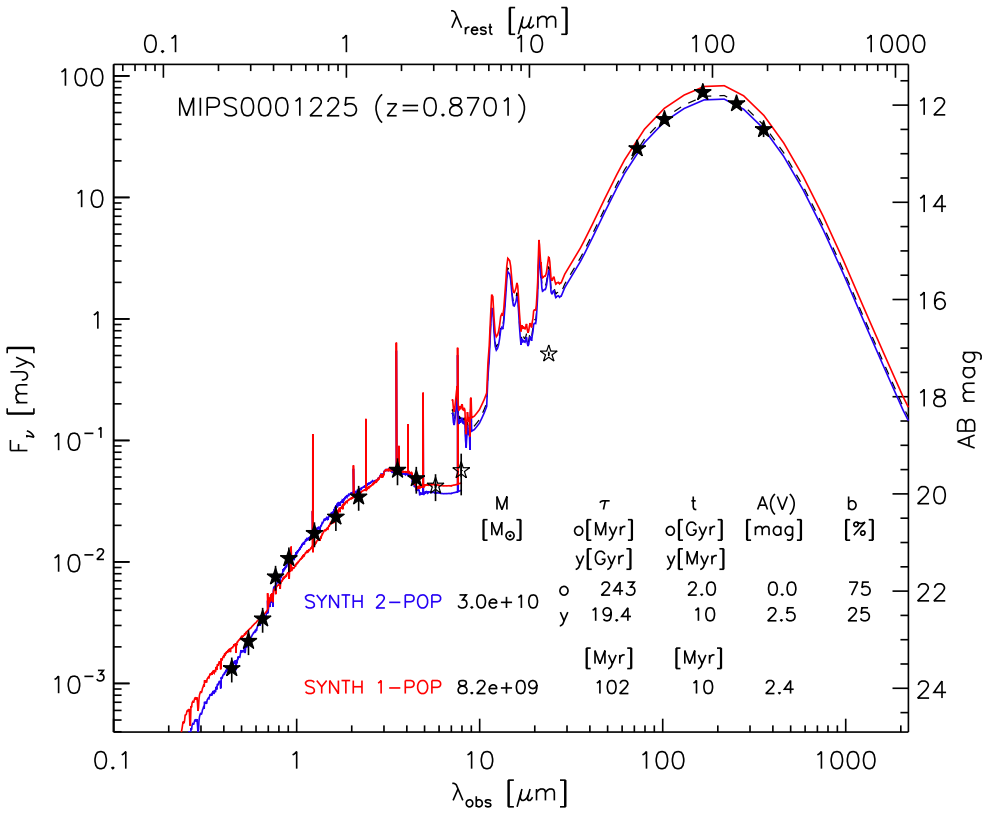

Figure A.1 : cont'd

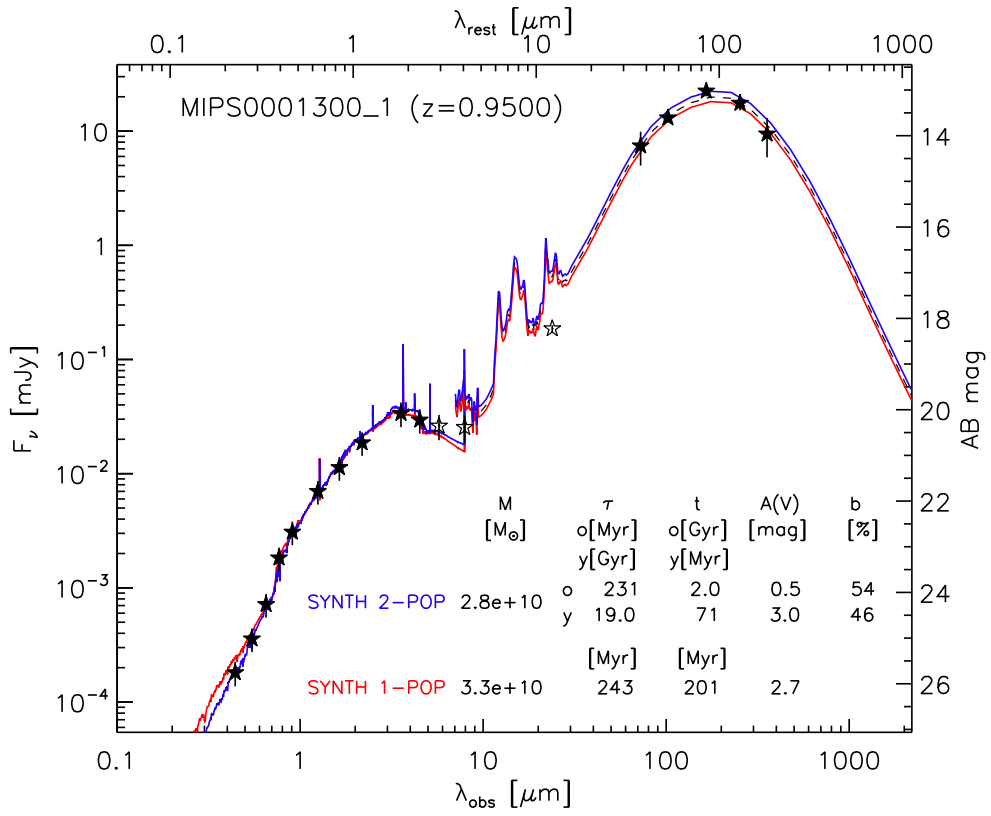

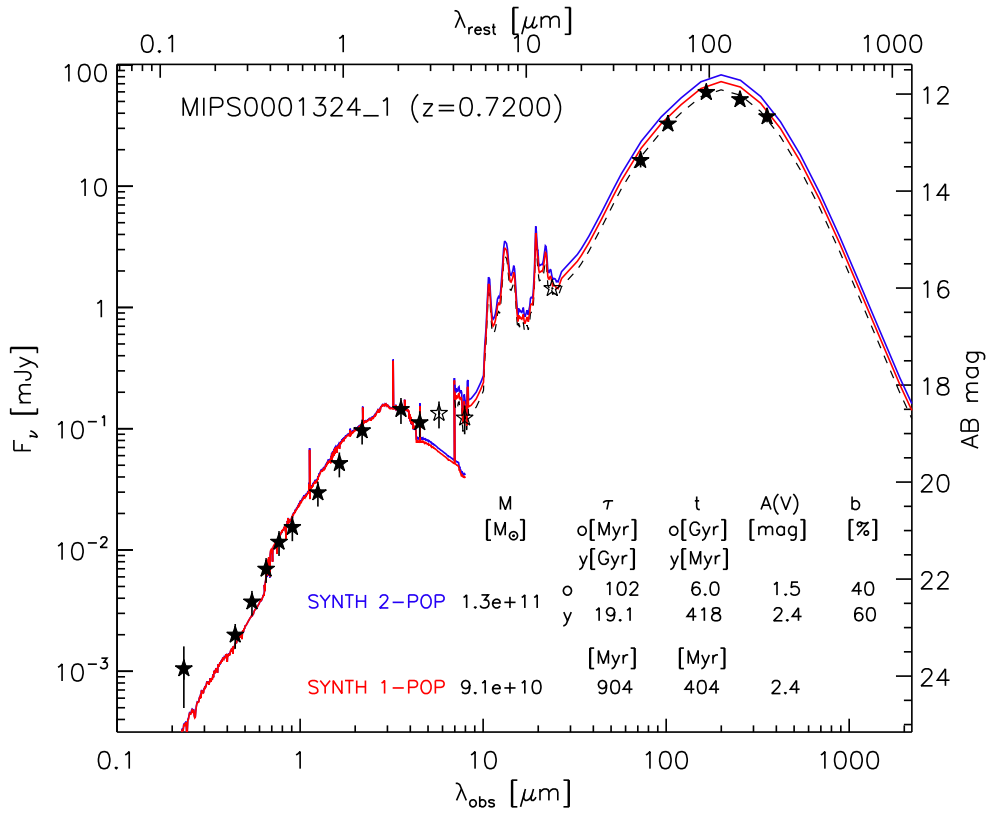

Figure A.1 : cont'd

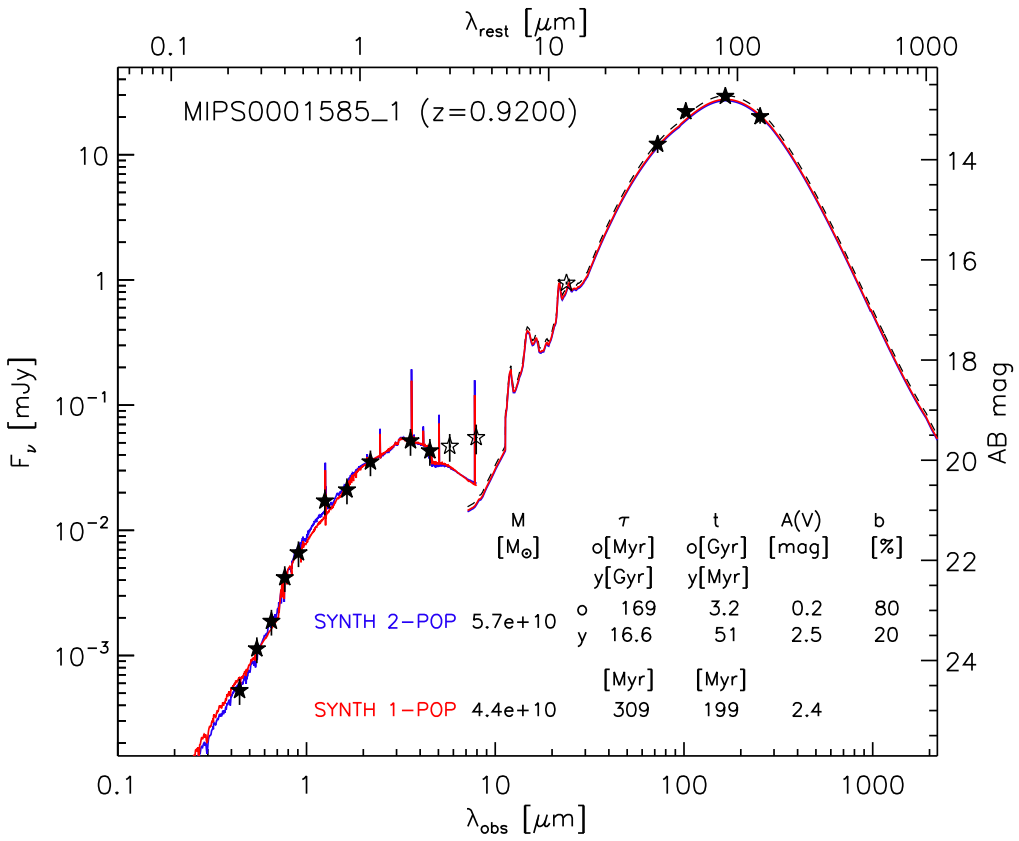

Figure A.1 cont'd : An example of the resulting fit to the whole UV-to-FIR SED for our IR-bright galaxies with the Syntesizer code. *Solid blue line:* Result of the fitting process obtained with 2-POP models. *Solid red line:* Fit derived using 1-POP models. The parameter values of the solutions are also shown (M_*, τ, t, $A(V)$, b) for the 2-POP and 1-POP models, respectively. *Dashed black line:* Fit to the FIR photometry ($\lambda_{obs} \geq 70$ μm). Photometric data points include the uncertainties (multiplied by 2.5 from UV to IRAC bands for visualization), only the *filled black stars* are used in the fit.

Appendix B

SEDs and SFHs derived with the CIGALE and Synthesizer Codes

We present in the upper panels of Fig. B.1, the complete UV-to-FIR SEDs for our sample of IR-bright galaxies. We also provide the results of the median solution of the most significant cluster derived from the Monte Carlo simulation analysis with the Synthesizer code, and the average parameter values estimated with the CIGALE from the Bayesian analysis of its full set of models. We present in the lower panels of Fig. B.1, the SFHs obtained with the parameters described in Table 6.1 for the Synthesizer and CIGALE codes, as explained in Chapter 6.

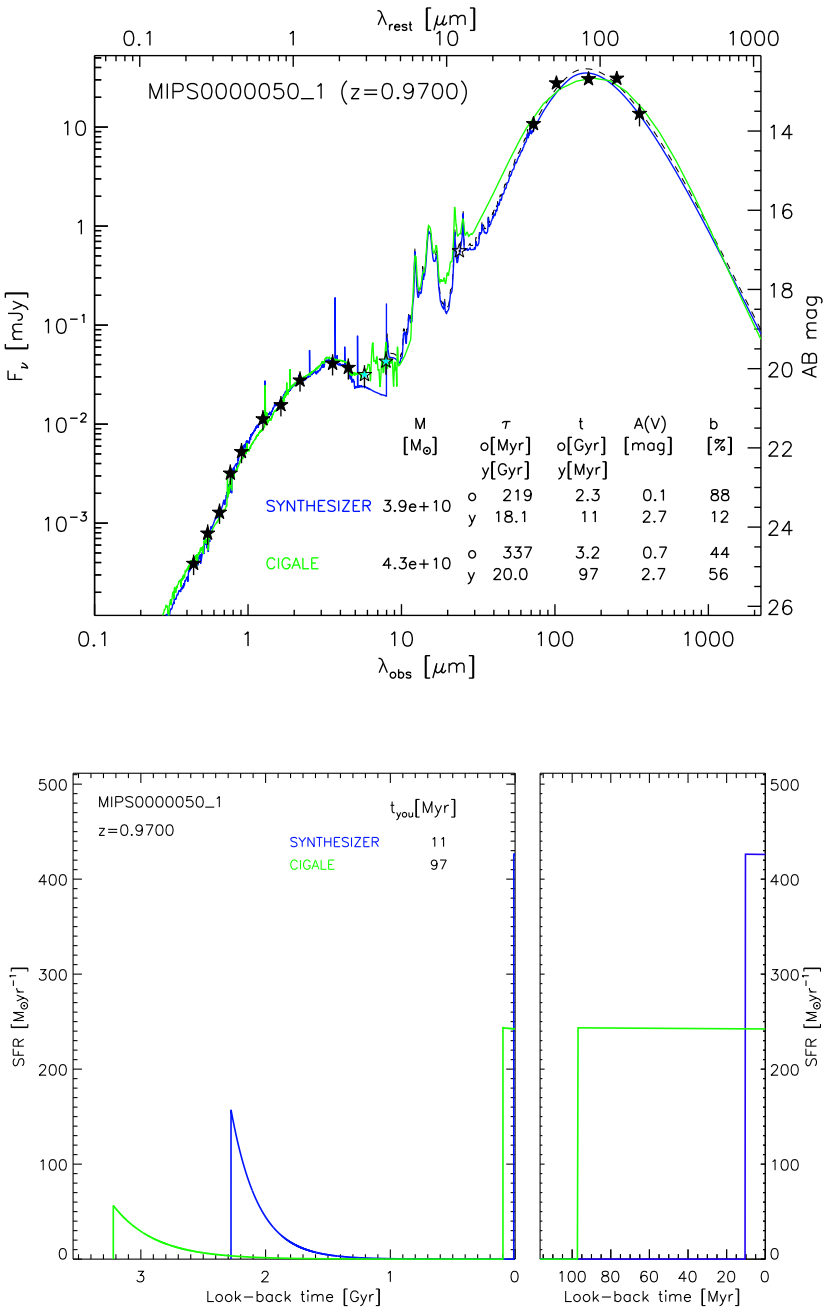

Figure B.1 : *Upper panel:* An example of the resulting fit to the whole UV-to-FIR SED for our IR-bright galaxies at $0.6 \leq z \leq 1.5$. *Solid blue line:* Result of the fitting process obtained with the Synthesizer code. *Solid green line:* Fit obtained with the Bayesian analysis of the CIGALE. The parameter values of the solutions are also shown (M_*, τ, t, $A(V)$, b) for the Synthesizer and the CIGALE codes, respectively. *Dashed black line:* Fit to the FIR photometry ($\lambda_{obs} \geq 70$ μm). Photometric data points include the uncertainties (multiplied by 2.5 from UV to IRAC bands for visualization), only the *filled black stars* are used in the Synthesizer fit, while the *filled black and cyan stars* are used in the CIGALE fit. *Lower panel:* The SFHs of the galaxy shown in the upper panel. Same color code lines, and the same parameter values are used for building the SFHs of the Synthesizer and CIGALE codes, as it is indicated in the upper panel. The ages of the young population in Myr are also shown for the Synthesizer and CIGALE codes, respectively. An expansion of the look-back time axis is shown to visualize better the SFH of the young population.

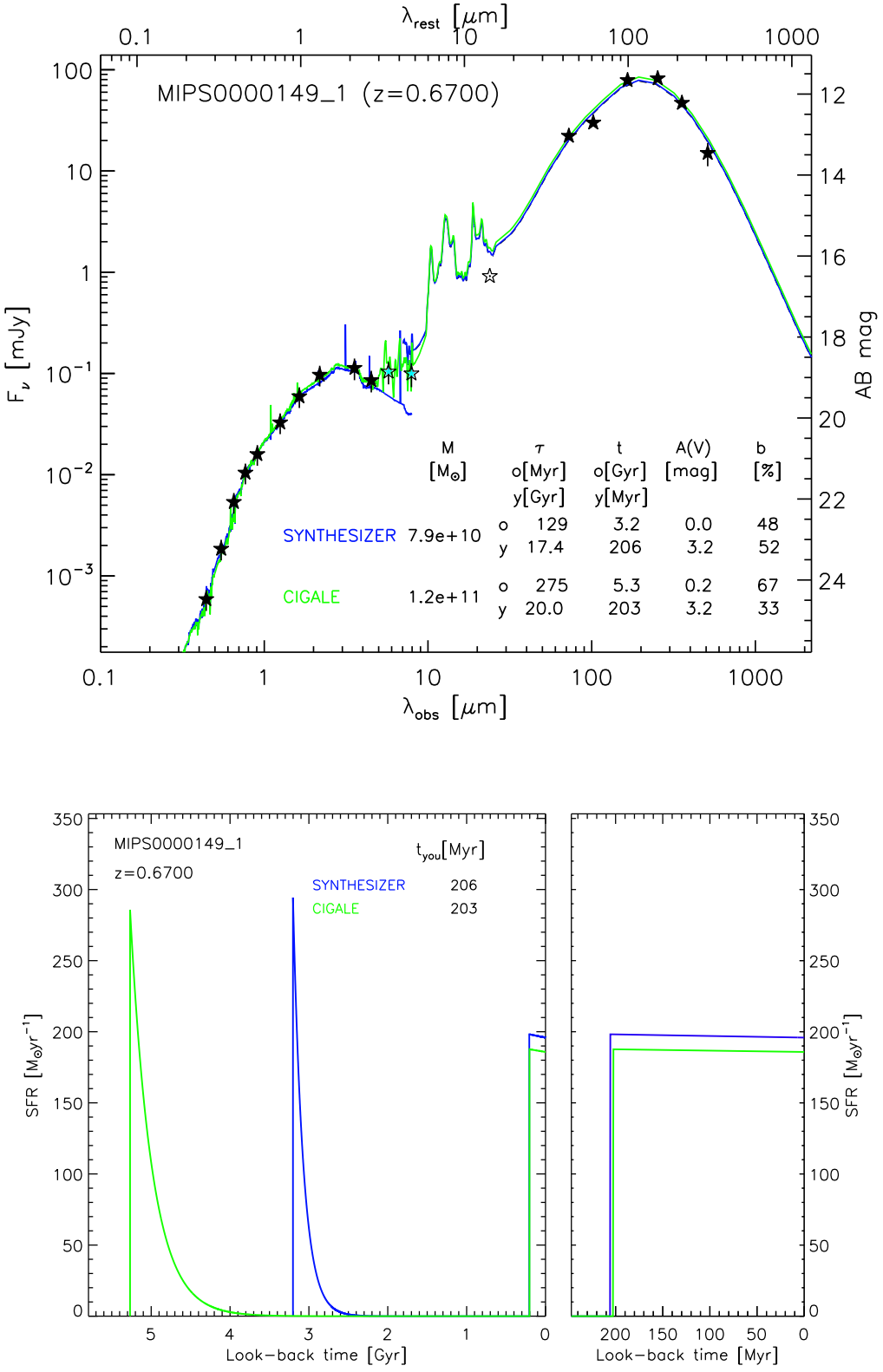

Figure B.1 : cont'd

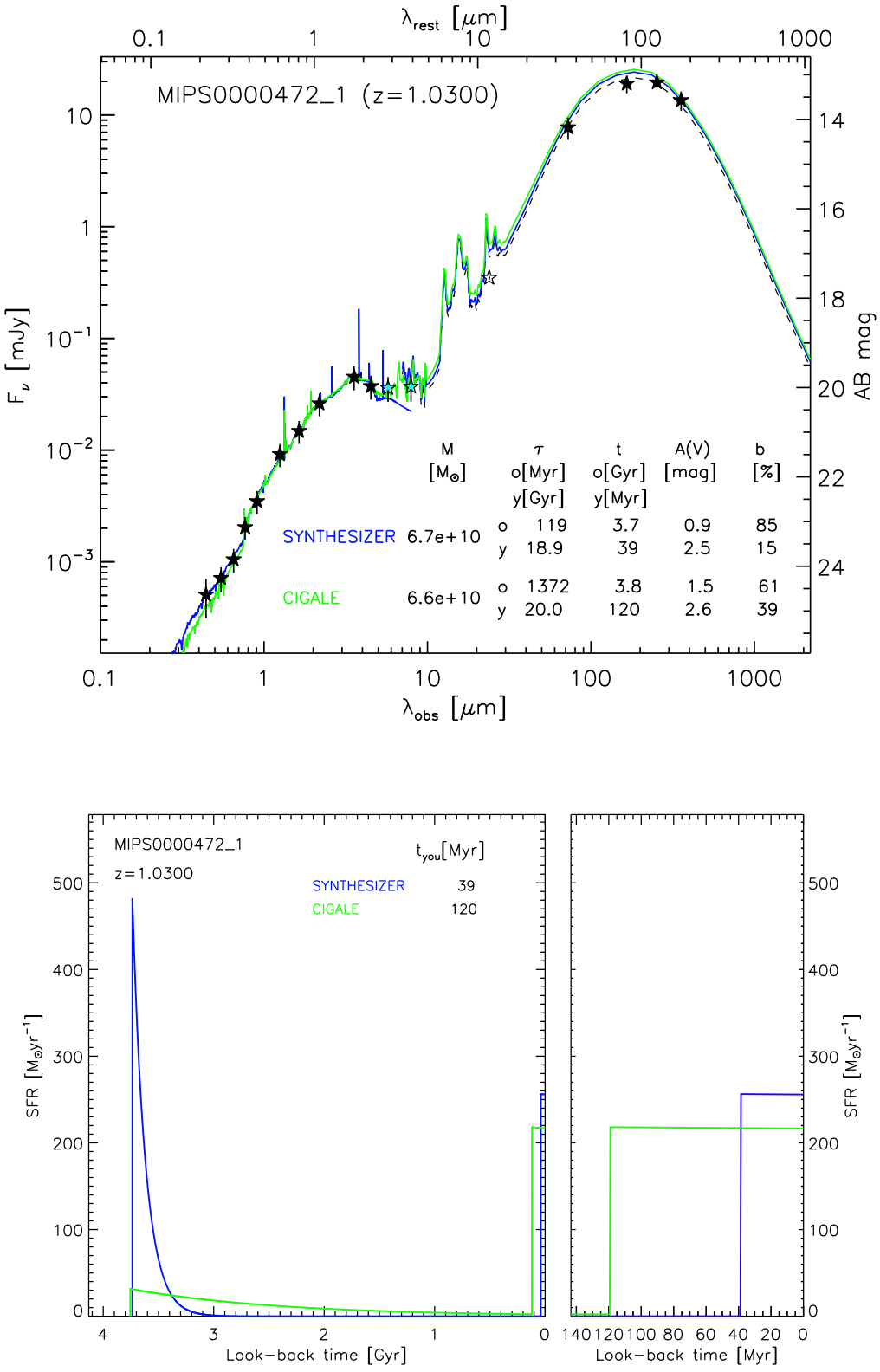

Figure B.1 : cont'd

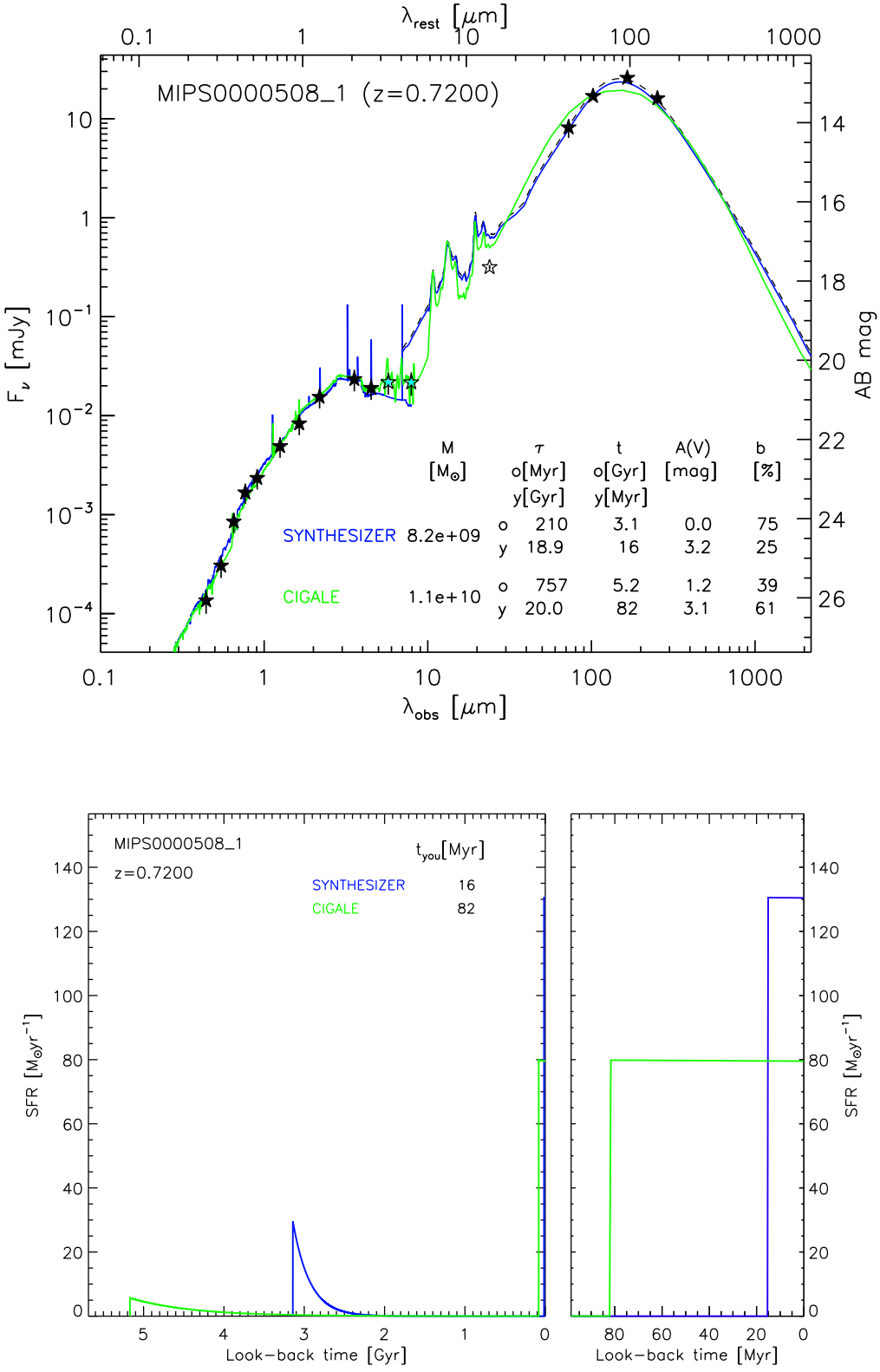

Figure B.1 : cont'd

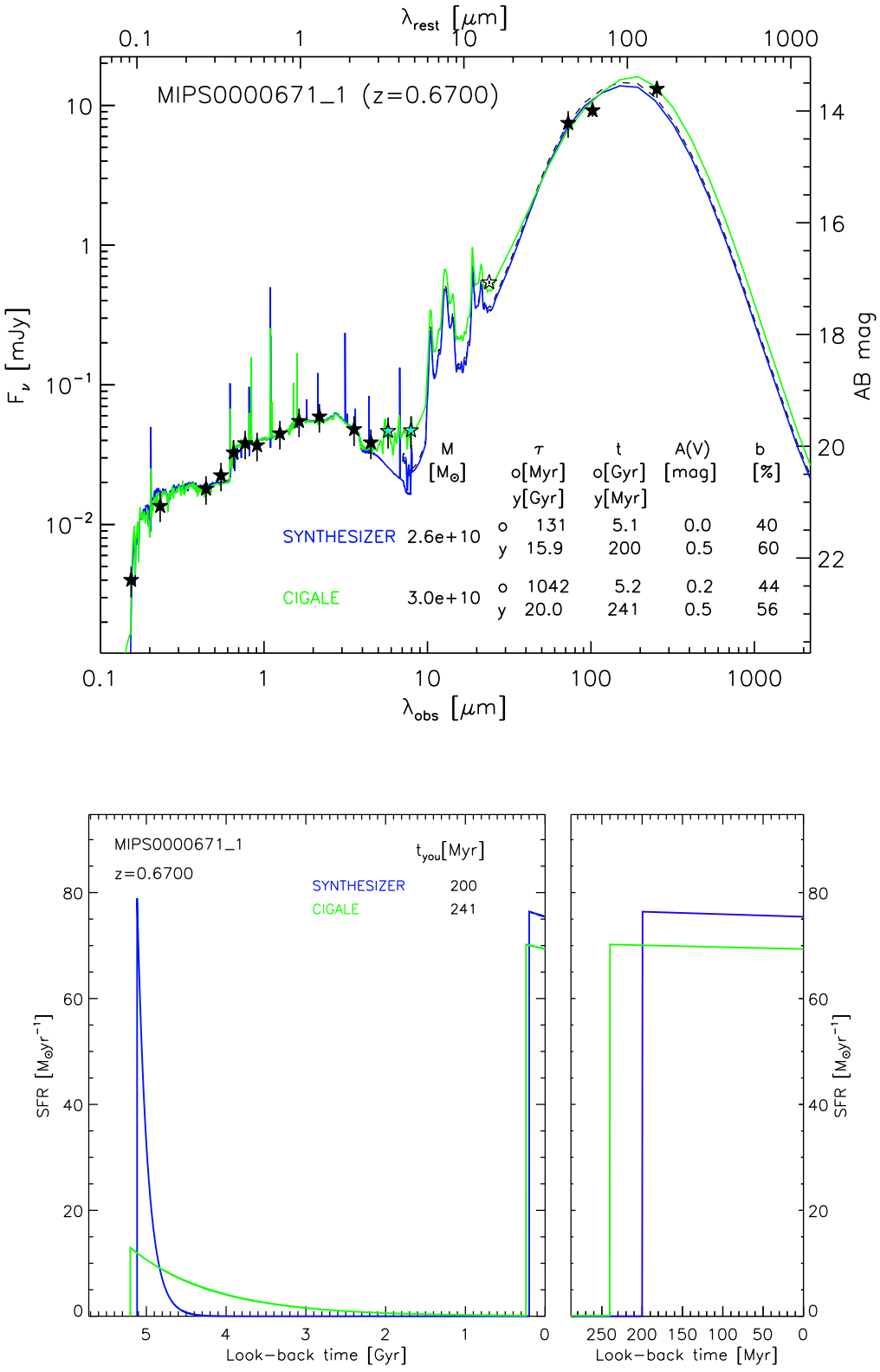

Figure B.1 : cont'd

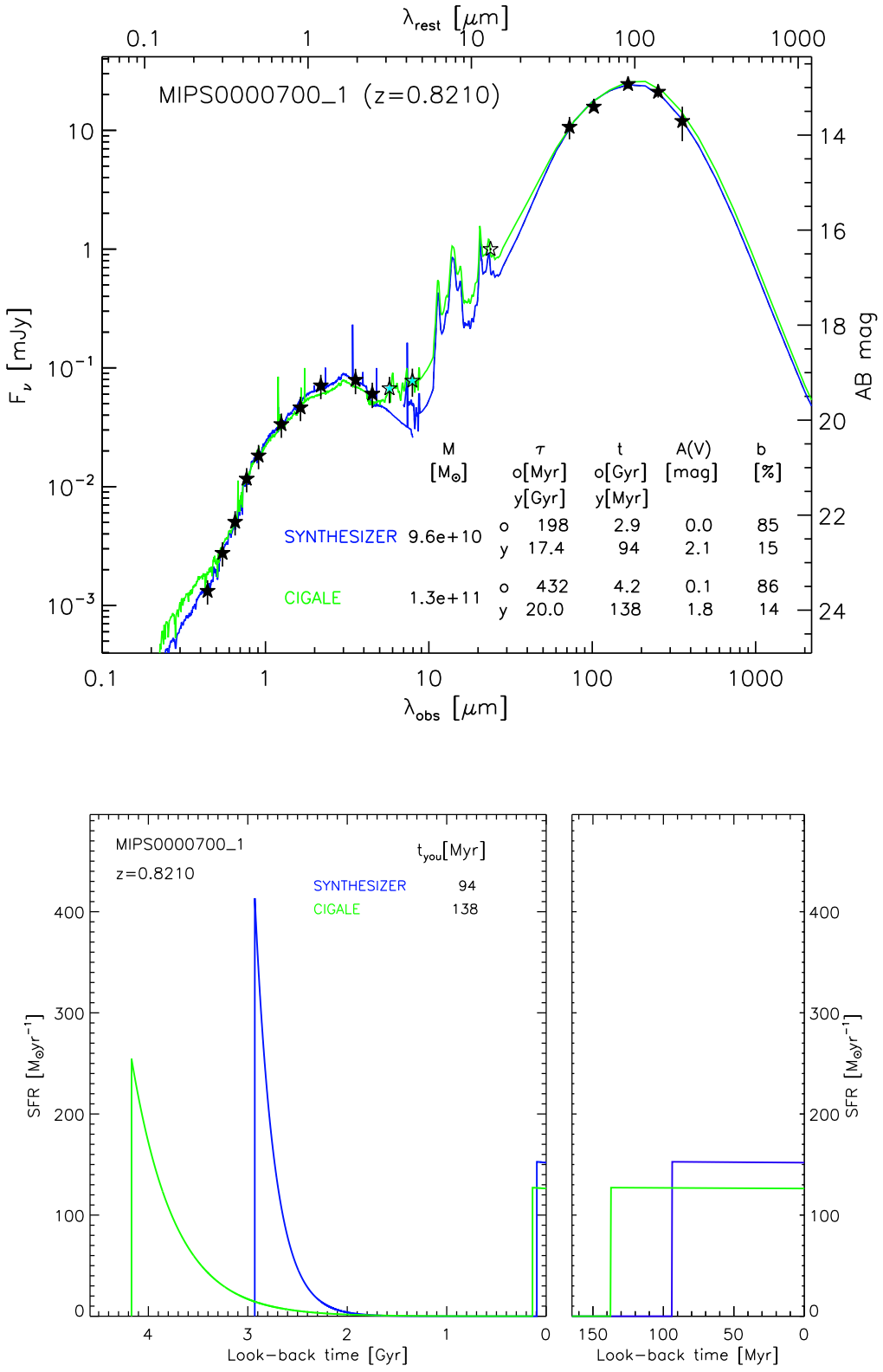

Figure B.1 : cont'd

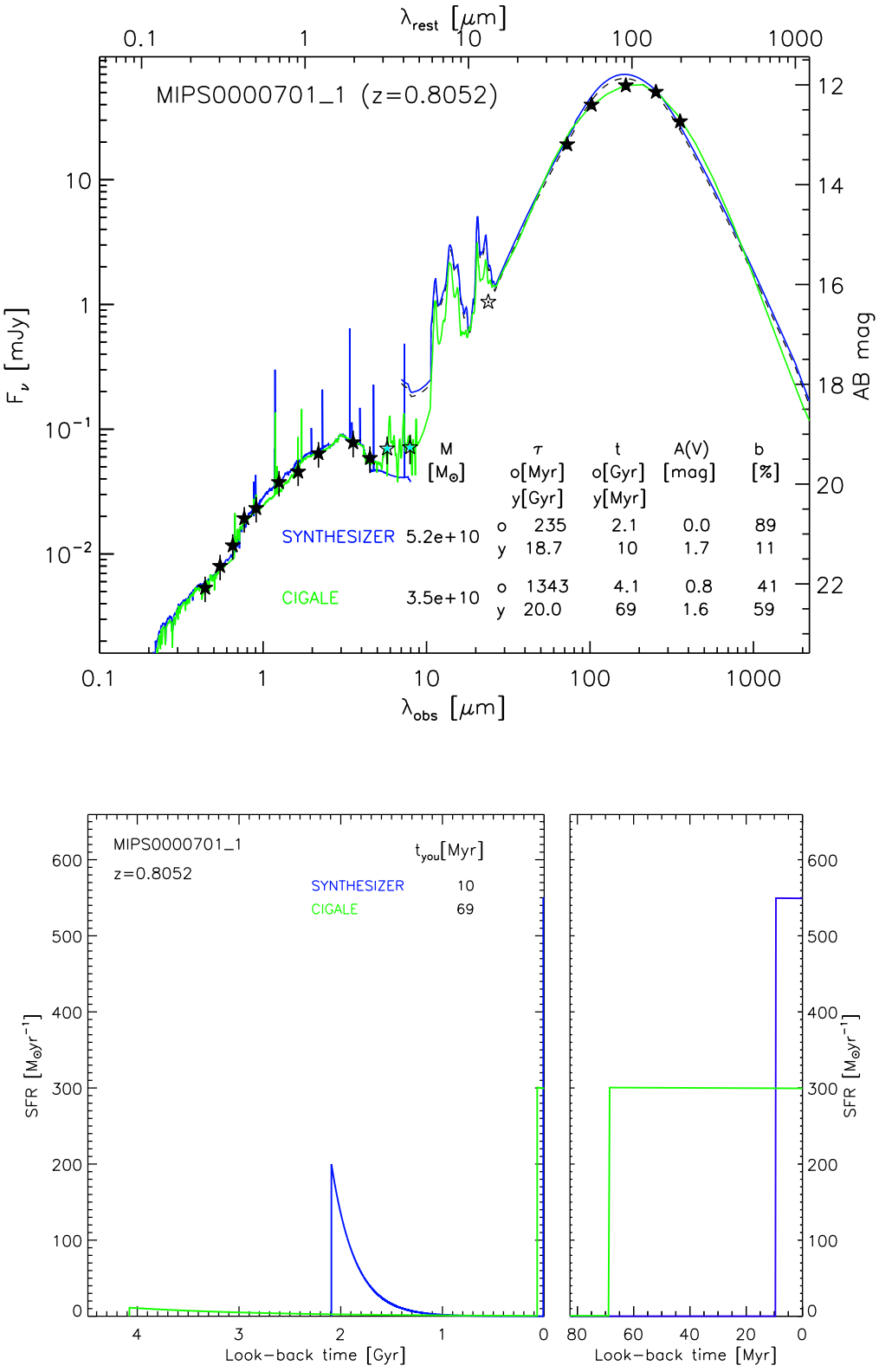

Figure B.1 : cont'd

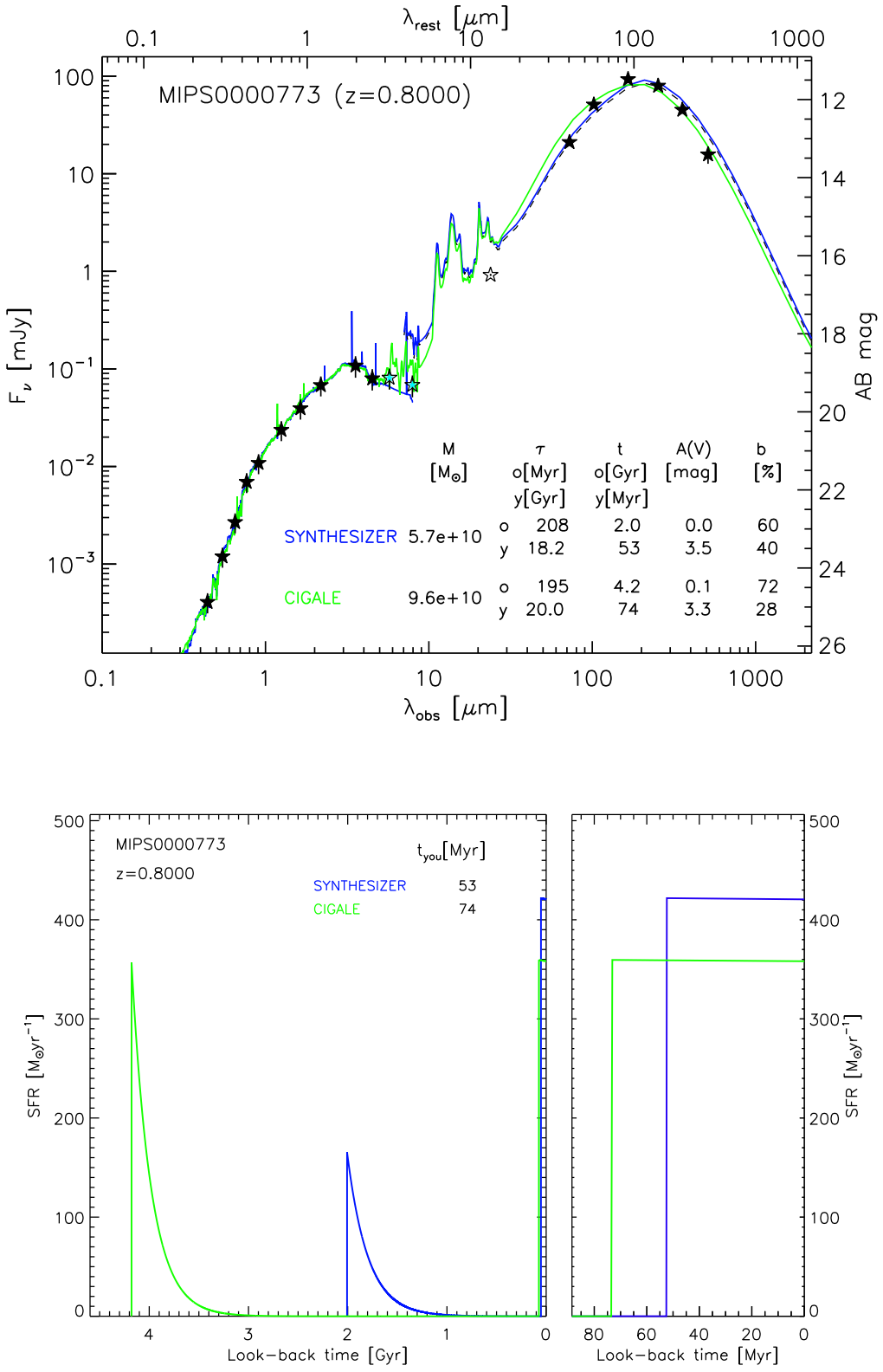

Figure B.1 : cont'd

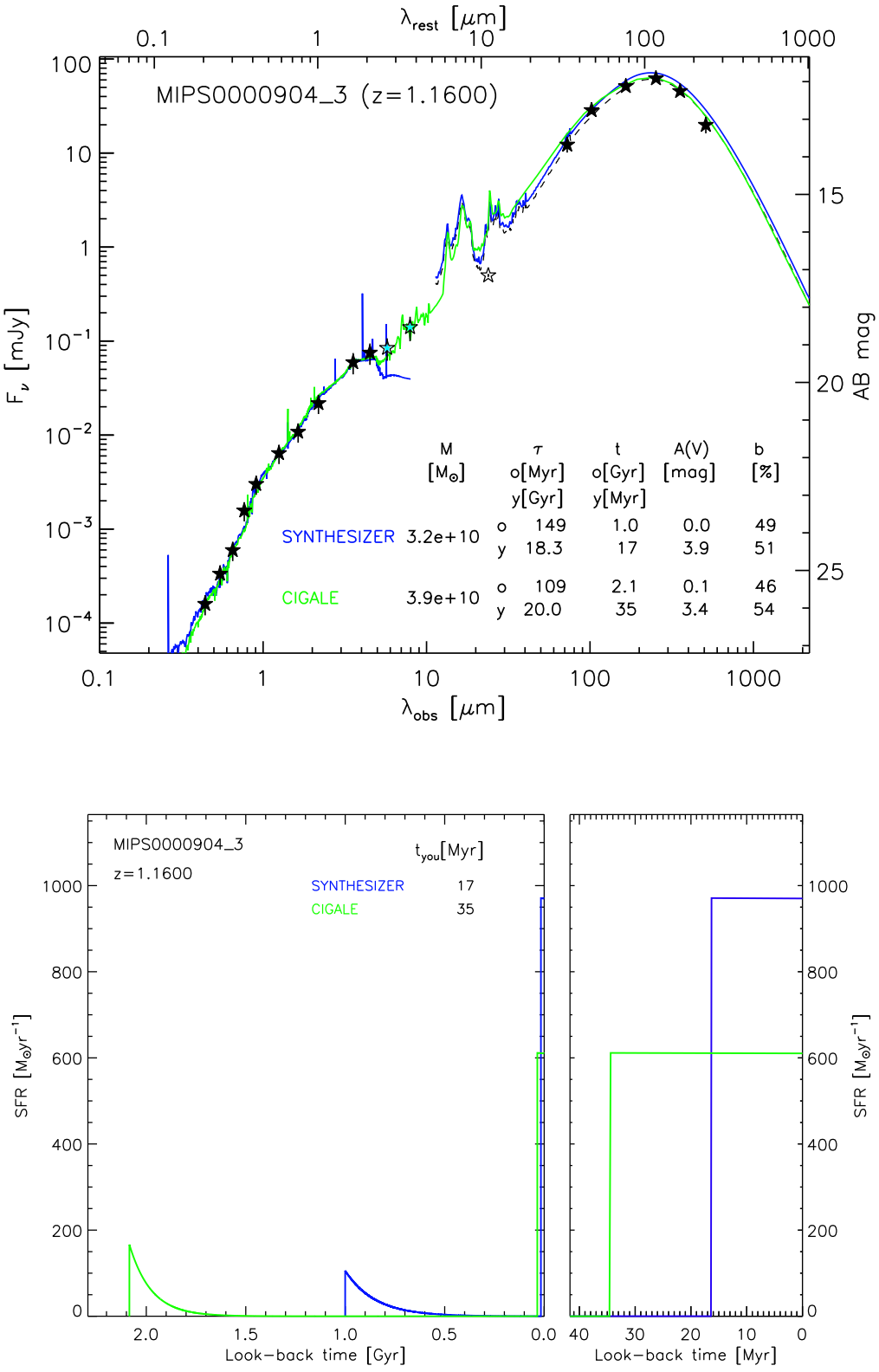

Figure B.1 : cont'd

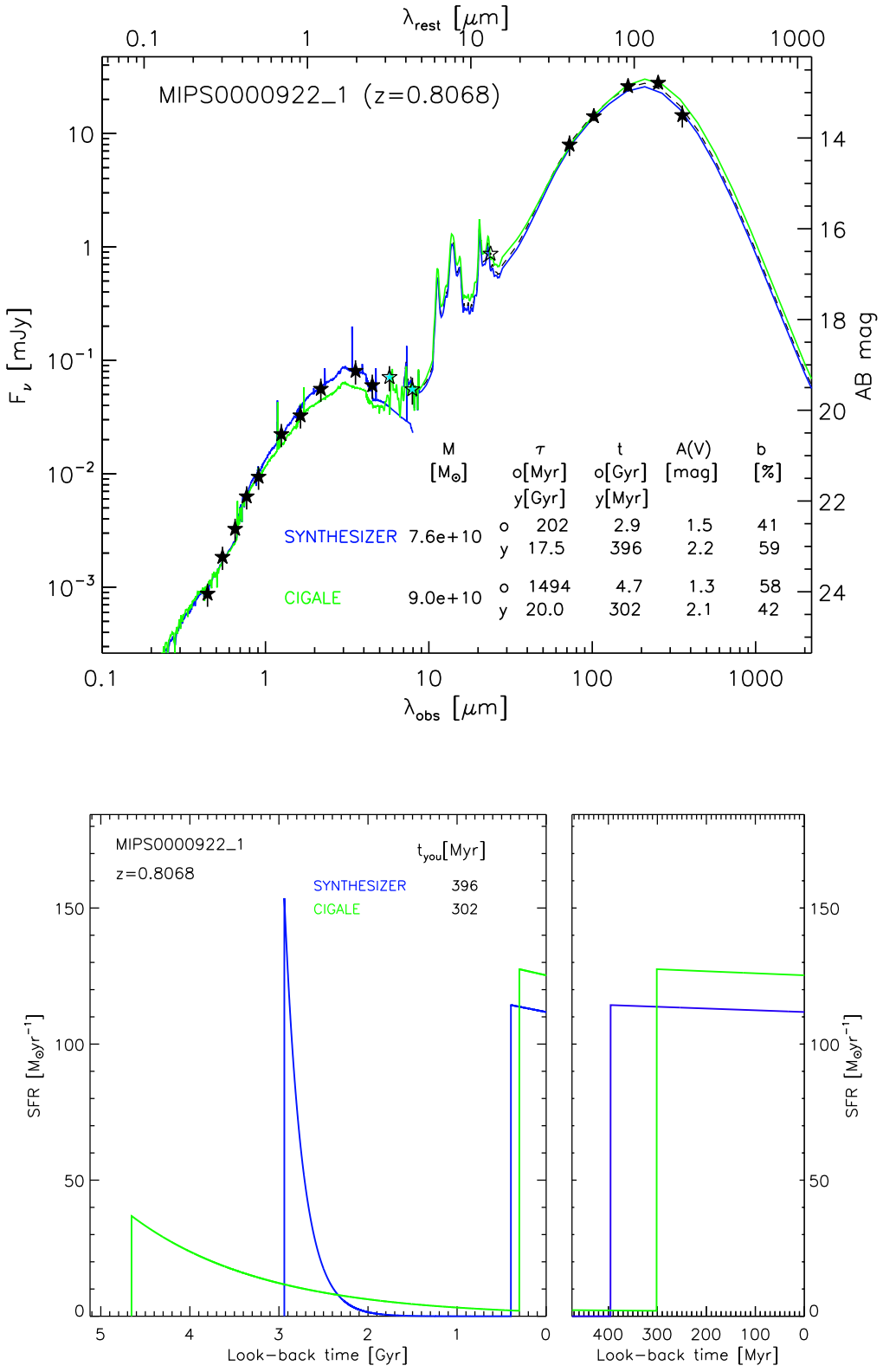

Figure B.1 : cont'd

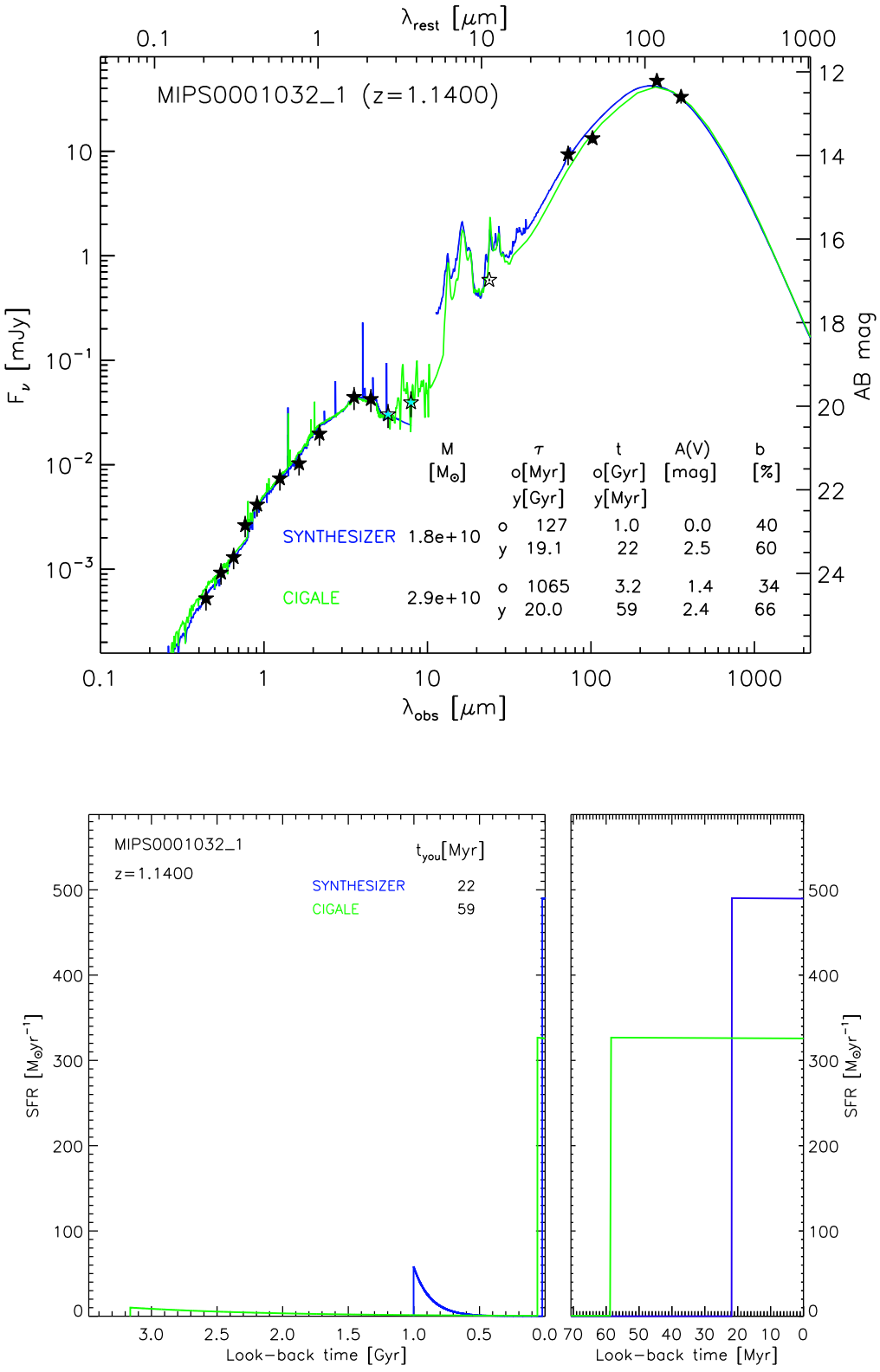

Figure B.1 : cont'd

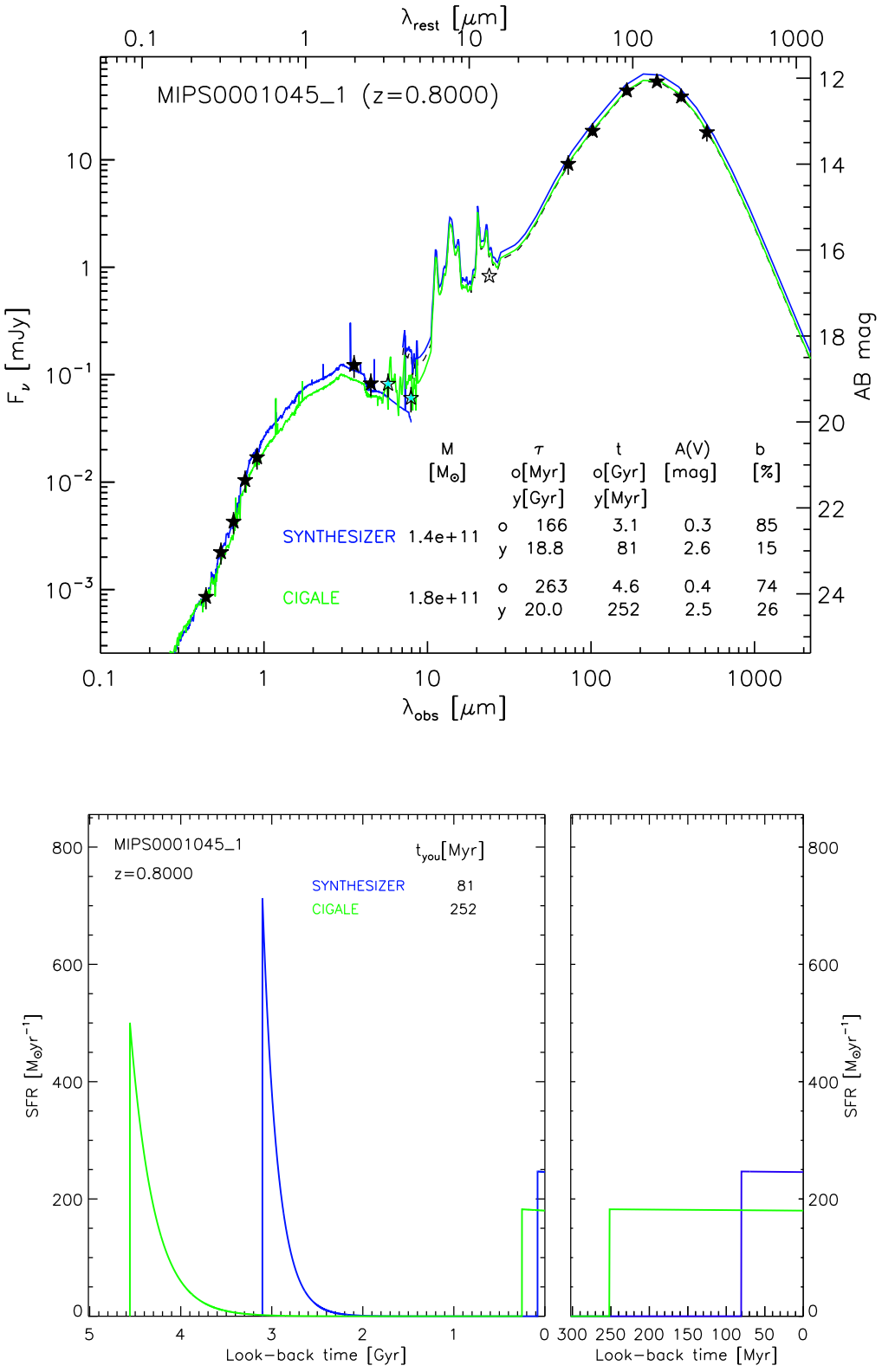

Figure B.1 : cont'd

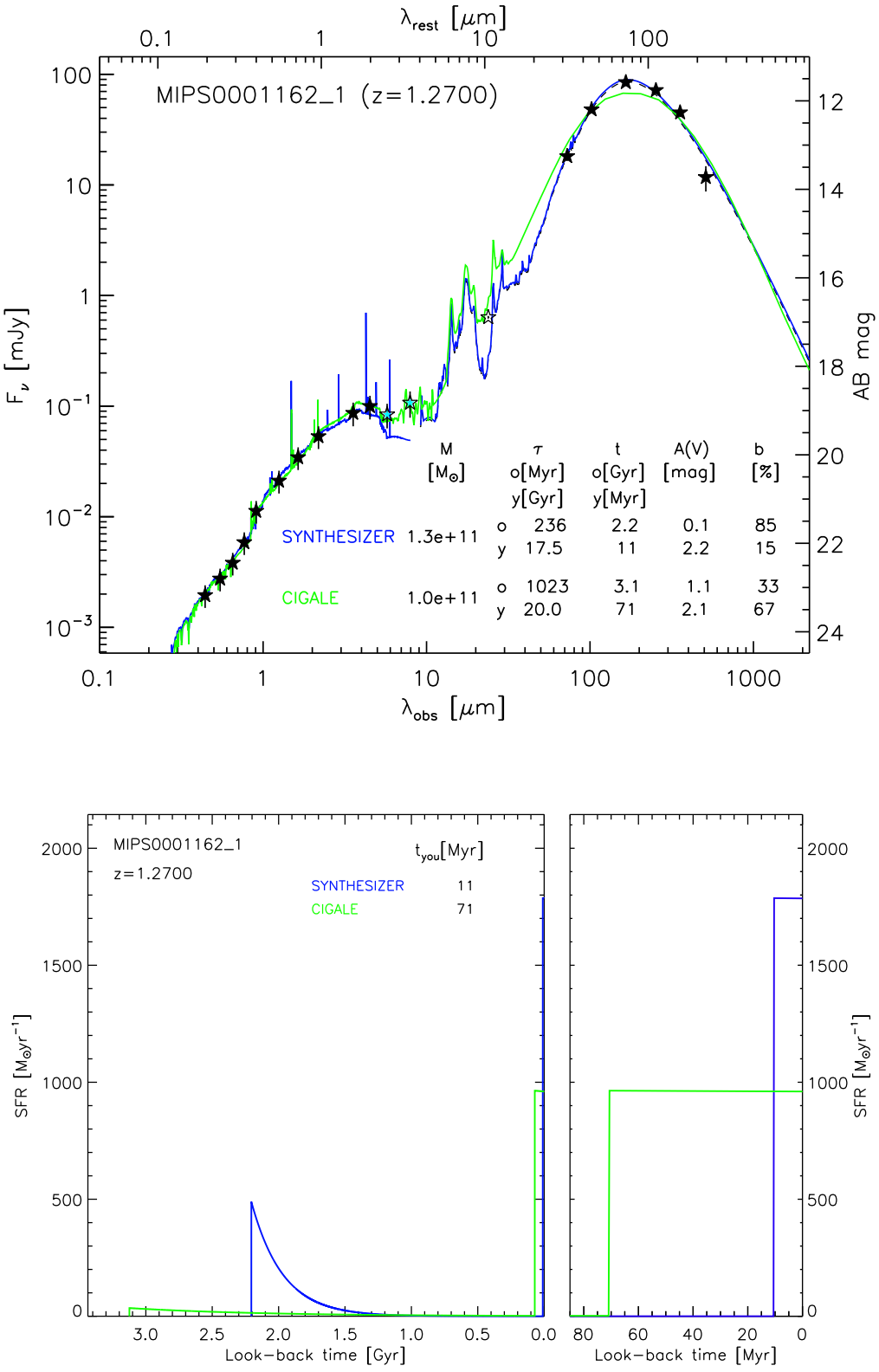

Figure B.1 : cont'd

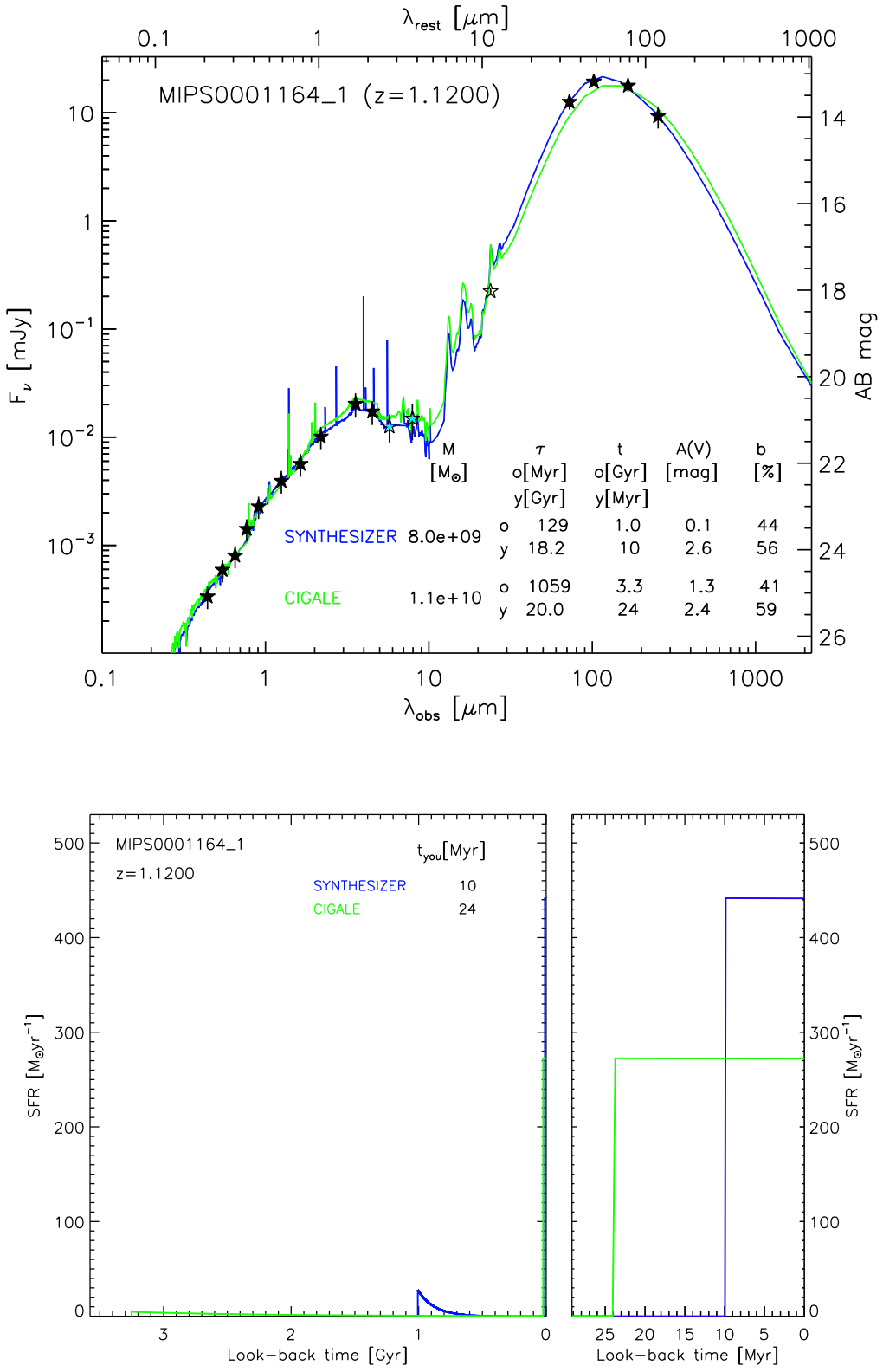

Figure B.1 : cont'd

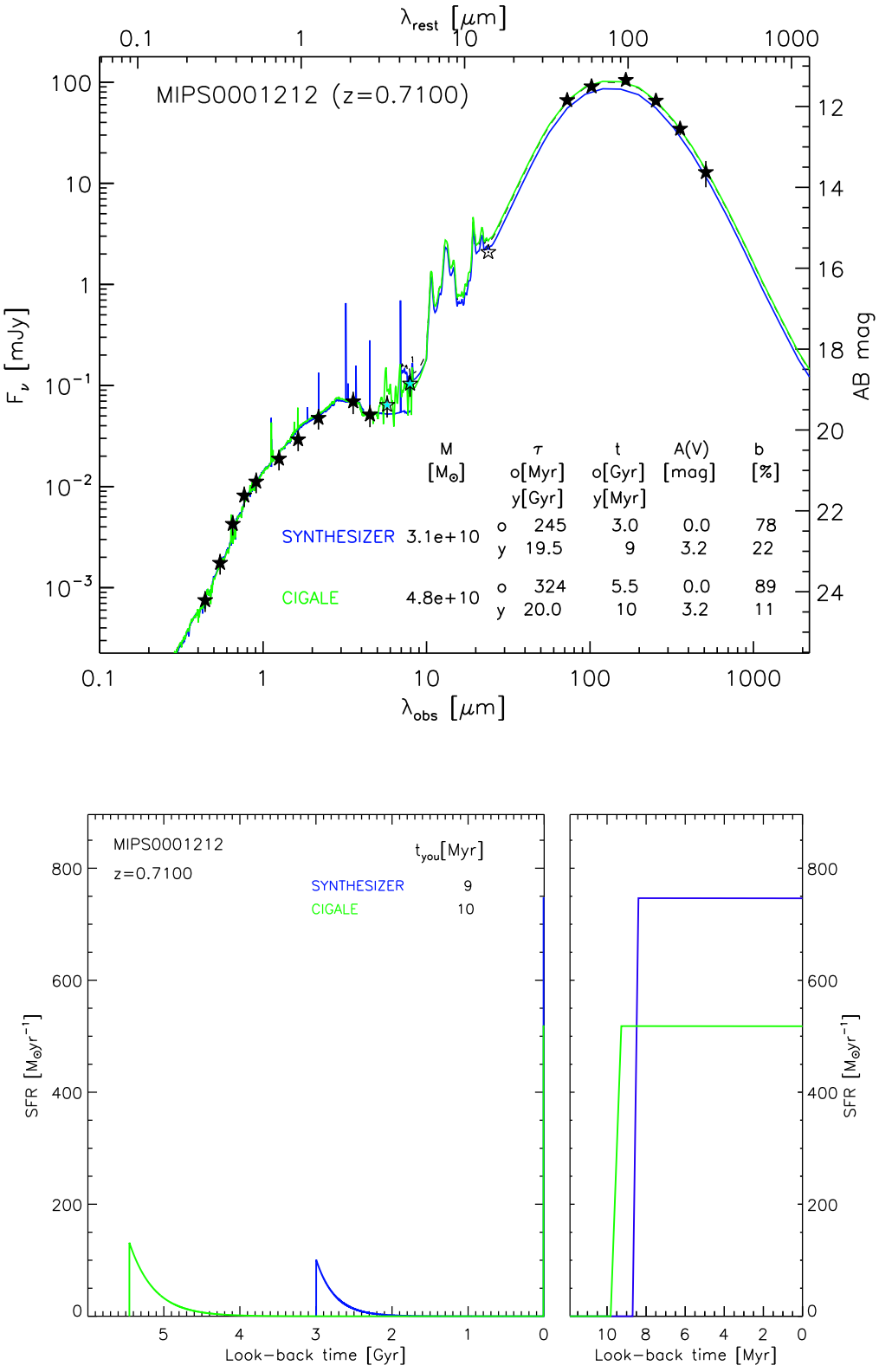

Figure B.1 : cont'd

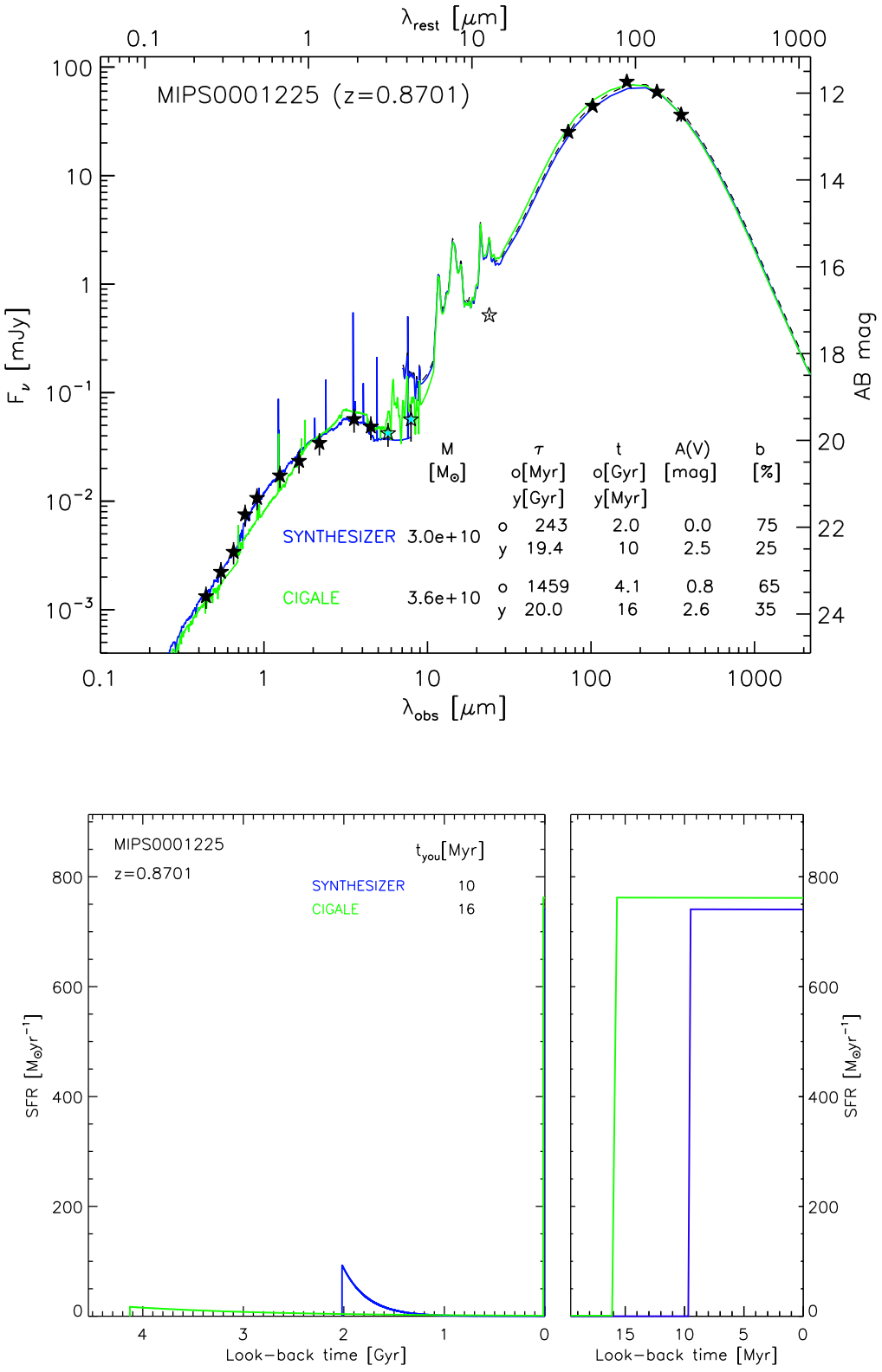

Figure B.1 : cont'd

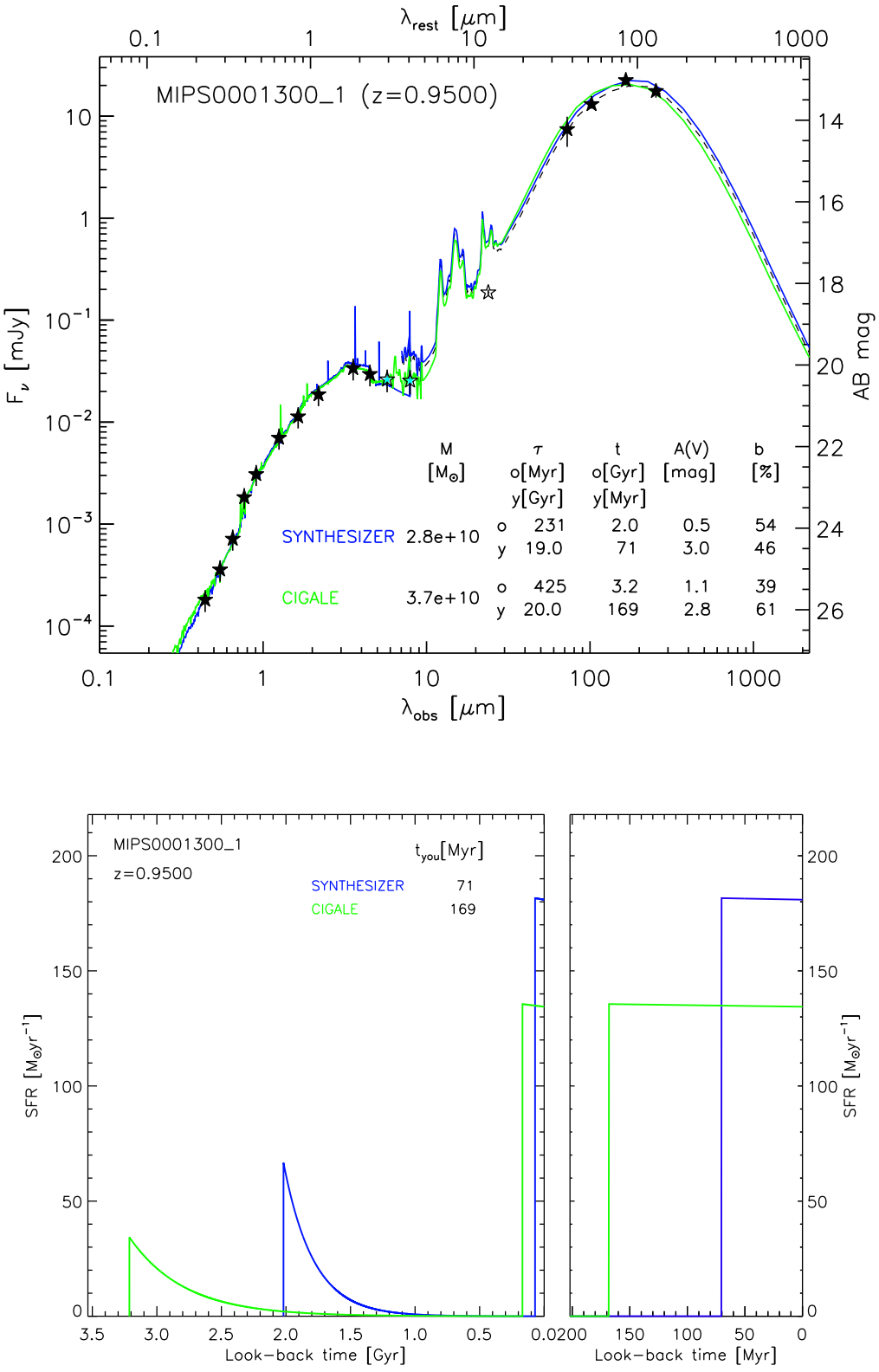

Figure B.1 : cont'd

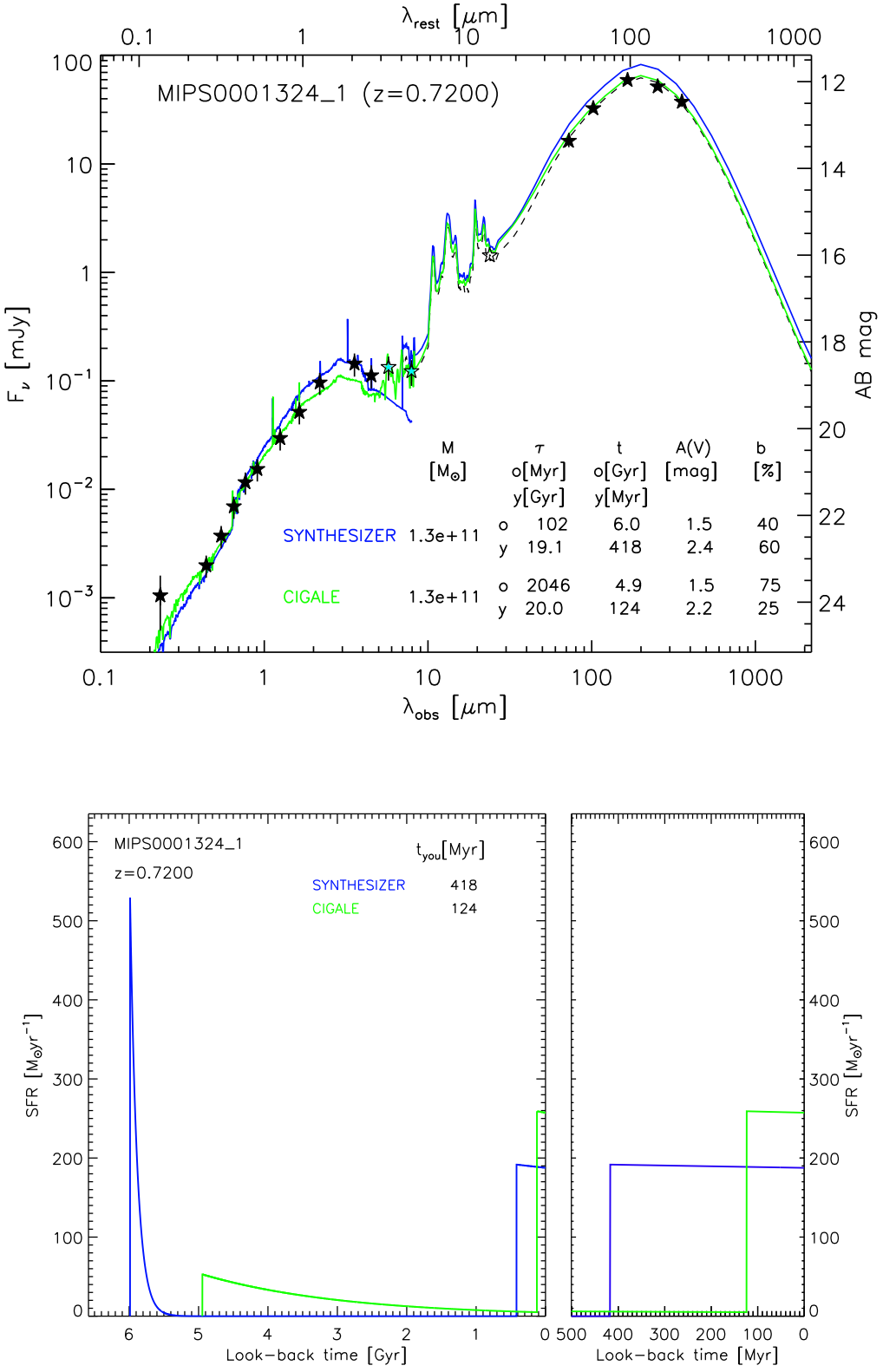

Figure B.1 : cont'd

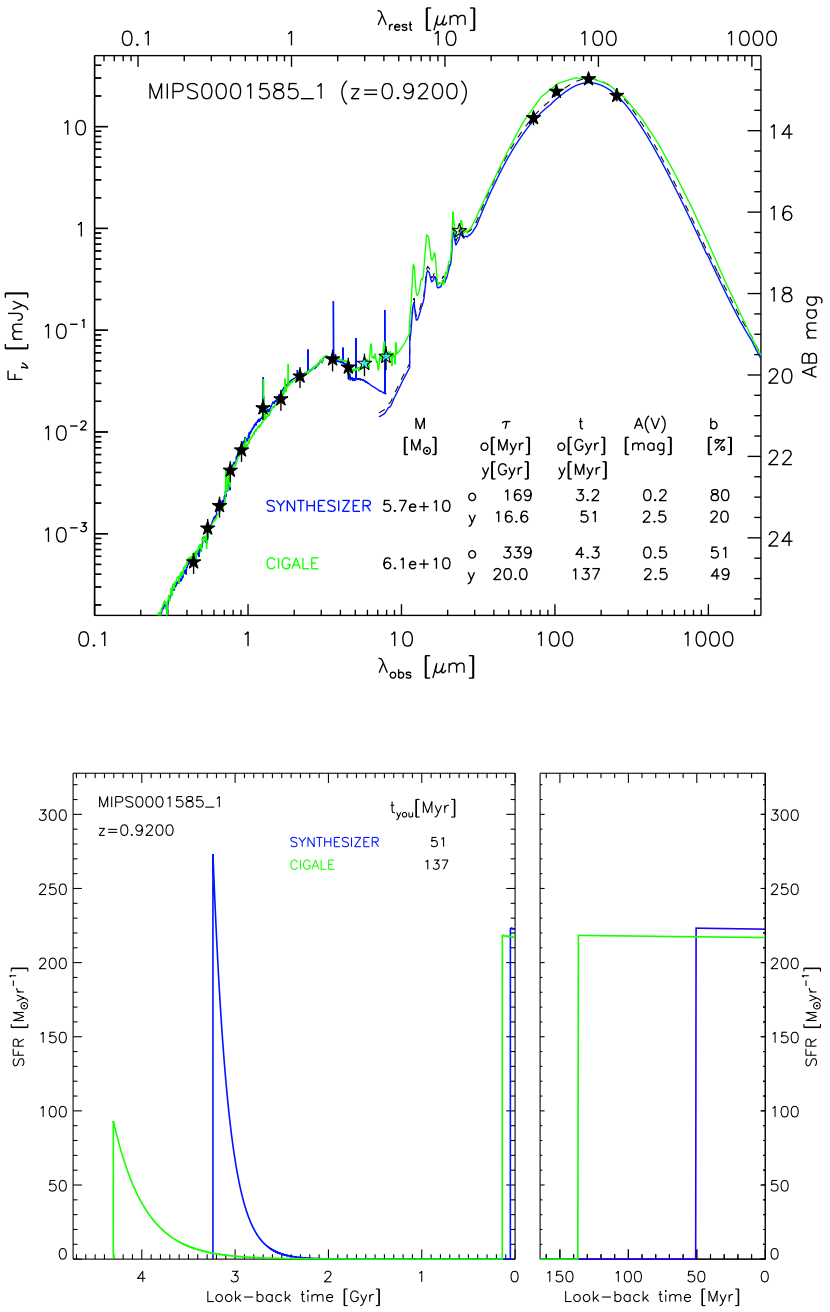

Figure B.1 cont'd : *Upper panel:* An example of the resulting fit to the whole UV-to-FIR SED for our IR-bright galaxies at $0.6 \leq z \leq 1.5$. *Solid blue line:* Result of the fitting process obtained with the Synthesizer code. *Solid green line:* Fit obtained with the Bayesian analysis of the CIGALE. The parameter values of the solutions are also shown (M_*, τ, t, $A(V)$, b) for the Synthesizer and the CIGALE codes, respectively. *Dashed black line:* Fit to the FIR photometry ($\lambda_{obs} \geq 70$ μm). Photometric data points include the uncertainties (multiplied by 2.5 from UV to IRAC bands for visualization), only the *filled black stars* are used in the Synthesizer fit, while the *filled black and cyan stars* are used in the CIGALE fit. *Lower panel:* The SFHs of the galaxy shown in the upper panel. Same color code lines, and the same parameter values are used for building the SFHs of the Synthesizer and CIGALE codes, as it is indicated in the upper panel. The ages of the young population in Myr are also shown for the Synthesizer and CIGALE codes, respectively. An expansion of the look-back time axis is shown to visualize better the SFH of the young population.

List of Figures

List of Tables

Bibliography

Armus, L., Heckman, T., and Miley, G.: 1987, *AJ* **94**, 831

Armus, L., Mazzarella, J. M., Evans, A. S., Surace, J. A., Sanders, D. B., Iwasawa, K., Frayer, D. T., Howell, J. H., Chan, B., Petric, A., Vavilkin, T., Kim, D. C., Haan, S., Inami, H., Murphy, E. J., Appleton, P. N., Barnes, J. E., Bothun, G., Bridge, C. R., Charmandaris, V., Jensen, J. B., Kewley, L. J., Lord, S., Madore, B. F., Marshall, J. A., Melbourne, J. E., Rich, J., Satyapal, S., Schulz, B., Spoon, H. W. W., Sturm, E., U, V., Veilleux, S., and Xu, K.: 2009, *PASP* **121**, 559

Balog, Z., Müller, T., Nielbock, M., Altieri, B., Klaas, U., Blommaert, J., Linz, H., Lutz, D., Moór, A., Billot, N., Sauvage, M., and Okumura, K.: 2014, *Experimental Astronomy* **37**, 129

Barro, G., Pérez-González, P. G., Gallego, J., Ashby, M. L. N., Kajisawa, M., Miyazaki, S., Villar, V., Yamada, T., and Zamorano, J.: 2011a, *ApJS* **193**, 13

Barro, G., Pérez-González, P. G., Gallego, J., Ashby, M. L. N., Kajisawa, M., Miyazaki, S., Villar, V., Yamada, T., and Zamorano, J.: 2011b, *ApJS* **193**, 30

Barvainis, R., Tacconi, L., Antonucci, R., Alloin, D., and Coleman, P.: 1994, *Nature* **371**, 586

Bell, E. F., Papovich, C., Wolf, C., Le Floc'h, E., Caldwell, J. A. R., Barden, M., Egami, E., McIntosh, D. H., Meisenheimer, K., Pérez-González, P. G., Rieke, G. H., Rieke, M. J., Rigby, J. R., and Rix, H.-W.: 2005, *ApJ* **625**, 23

Benítez, N.: 2000, *ApJ* **536**, 571

Berta, S., Magnelli, B., Nordon, R., Lutz, D., Wuyts, S., Altieri, B., Andreani, P., Aussel, H., Castañeda, H., Cepa, J., Cimatti, A., Daddi, E., Elbaz, D., Förster Schreiber, N. M., Genzel, R., Le Floc'h, E., Maiolino, R., Pérez-Fournon, I., Poglitsch, A., Popesso, P., Pozzi, F., Riguccini, L., Rodighiero, G., Sanchez-Portal, M., Sturm, E., Tacconi, L. J., and Valtchanov, I.: 2011, *A&A* **532**, A49

Bertelli, G., Bressan, A., Chiosi, C., Fagotto, F., and Nasi, E.: 1994, *A&AS* **106**, 275

Bertin, E. and Arnouts, S.: 1996, *A&AS* **117**, 393

Béthermin, M., Dole, H., Beelen, A., and Aussel, H.: 2010, *A&A* **512**, A78

Béthermin, M., Le Floc'h, E., Ilbert, O., Conley, A., Lagache, G., Amblard, A., Arumugam, V., Aussel, H., Berta, S., Bock, J., Boselli, A., Buat, V., Casey, C. M., Castro-Rodríguez, N., Cava, A., Clements, D. L., Cooray, A., Dowell, C. D., Eales, S., Farrah, D., Franceschini, A., Glenn, J., Griffin, M., Hatziminaoglou, E., Heinis, S., Ibar, E., Ivison, R. J., Kartaltepe, J. S., Levenson, L., Magdis, G., Marchetti, L., Marsden, G., Nguyen, H. T., O'Halloran, B., Oliver, S. J., Omont, A., Page, M. J., Panuzzo, P., Papageorgiou, A., Pearson, C. P., Pérez-Fournon, I., Pohlen, M., Rigopoulou, D., Roseboom, I. G., Rowan-Robinson, M., Salvato, M., Schulz, B., Scott, D., Seymour, N., Shupe, D. L., Smith, A. J., Symeonidis, M., Trichas, M., Tugwell, K. E., Vaccari, M., Valtchanov, I., Vieira, J. D., Viero, M., Wang, L., Xu, C. K., and Zemcov, M.: 2012, *A&A* **542**, A58

Blain, A. W., Barnard, V. E., and Chapman, S. C.: 2003, *MNRAS* **338**, 733

Bolzonella, M., Miralles, J.-M., and Pelló, R.: 2000, *A&A* **363**, 476

Boquien, M., Buat, V., Boselli, A., Baes, M., Bendo, G. J., Ciesla, L., Cooray, A., Cortese, L., Eales, S., Gavazzi, G., Gomez, H. L., Lebouteiller, V., Pappalardo, C., Pohlen, M., Smith, M. W. L., and Spinoglio, L.: 2012, *A&A* **539**, A145

Borch, A., Meisenheimer, K., Bell, E. F., Rix, H.-W., Wolf, C., Dye, S., Kleinheinrich, M., Kovacs, Z., and Wisotzki, L.: 2006, *A&A* **453**, 869

Bouwens, R. J., Illingworth, G. D., Oesch, P. A., Franx, M., Labbé, I., Trenti, M., van Dokkum, P., Carollo, C. M., González, V., Smit, R., and Magee, D.: 2012a, *ApJ* **754**, 83

Bouwens, R. J., Illingworth, G. D., Oesch, P. A., Trenti, M., Labbé, I., Franx, M., Stiavelli, M., Carollo, C. M., van Dokkum, P., and Magee, D.: 2012b, *ApJ* **752**, L5

Bradshaw, E. J., Almaini, O., Hartley, W. G., Smith, K. T., Conselice, C. J., Dunlop, J. S., Simpson, C., Chuter, R. W., Cirasuolo, M., Foucaud, S., McLure, R. J., Mortlock, A., and Pearce, H.: 2013, *MNRAS* **433**, 194

Brammer, G. B., van Dokkum, P. G., and Coppi, P.: 2008, *ApJ* **686**, 1503

Brand, K., Dey, A., Weedman, D., Desai, V., Le Floc'h, E., Jannuzi, B. T., Soifer, B. T., Brown, M. J. I., Eisenhardt, P., Gorjian, V., Papovich, C., Smith, H. A., Willner, S. P., and Cool, R. J.: 2006, *ApJ* **644**, 143

Brinchmann, J., Charlot, S., White, S. D. M., Tremonti, C., Kauffmann, G., Heckman, T., and Brinkmann, J.: 2004, *MNRAS* **351**, 1151

Bruzual, A. G. and Charlot, S.: 1993, *ApJ* **405**, 538

Bruzual, G. and Charlot, S.: 2003, *MNRAS* **344**, 1000

Buat, V., Giovannoli, E., Heinis, S., Charmandaris, V., Coia, D., Daddi, E., Dickinson, M., Elbaz, D., Hwang, H. S., Morrison, G., Dasyra, K., Aussel, H., Altieri, B., Dannerbauer, H., Kartaltepe, J., Leiton, R., Magdis, G., Magnelli, B., and Popesso, P.: 2011, *A&A* **533**, A93

Buat, V., Heinis, S., Boquien, M., Burgarella, D., Charmandaris, V., Boissier, S., Boselli, A., Le Borgne, D., and Morrison, G.: 2014, *A&A* **561**, A39

Burgarella, D., Buat, V., and Iglesias-Páramo, J.: 2005, *MNRAS* **360**, 1413

Bussmann, R. S., Dey, A., Armus, L., Brown, M. J. I., Desai, V., Gonzalez, A. H., Jannuzi, B. T., Melbourne, J., and Soifer, B. T.: 2012, *ApJ* **744**, 150

Calzetti, D.: 2013, *Star Formation Rate Indicators*, p. 419

Calzetti, D., Armus, L., Bohlin, R. C., Kinney, A. L., Koornneef, J., and Storchi-Bergmann, T.: 2000, *ApJ* **533**, 682

Calzetti, D., Kinney, A. L., and Storchi-Bergmann, T.: 1994, *ApJ* **429**, 582

Caputi, K. I., Lagache, G., Yan, L., Dole, H., Bavouzet, N., Le Floc'h, E., Choi, P. I., Helou, G., and Reddy, N.: 2007, *ApJ* **660**, 97

Casali, M., Adamson, A., Alves de Oliveira, C., Almaini, O., Burch, K., Chuter, T., Elliot, J., Folger, M., Foucaud, S., Hambly, N., Hastie, M., Henry, D., Hirst, P., Irwin, M., Ives, D., Lawrence, A., Laidlaw, K., Lee, D., Lewis, J., Lunney, D., McLay, S., Montgomery, D., Pickup, A., Read, M., Rees, N., Robson, I., Sekiguchi, K., Vick, A., Warren, S., and Woodward, B.: 2007, *A&A* **467**, 777

Casey, C. M.: 2012, *MNRAS* **425**, 3094

Casey, C. M., Berta, S., Béthermin, M., Bock, J., Bridge, C., Budynkiewicz, J., Burgarella, D., Chapin, E., Chapman, S. C., Clements, D. L., Conley, A., Conselice, C. J., Cooray, A., Farrah, D., Hatziminaoglou, E., Ivison, R. J., le Floc'h, E., Lutz, D., Magdis, G., Magnelli, B., Oliver, S. J., Page, M. J., Pozzi, F., Rigopoulou, D., Riguccini, L., Roseboom, I. G., Sanders, D. B., Scott, D., Seymour, N., Valtchanov, I., Vieira, J. D., Viero, M., and Wardlow, J.: 2012, *ApJ* **761**, 140

Casey, C. M., Chapman, S. C., Beswick, R. J., Biggs, A. D., Blain, A. W., Hainline, L. J., Ivison, R. J., Muxlow, T. W. B., and Smail, I.: 2009, *MNRAS* **399**, 121

Casey, C. M., Chen, C.-C., Cowie, L. L., Barger, A. J., Capak, P., Ilbert, O., Koss, M., Lee, N., Le Floc'h, E., Sanders, D. B., and Williams, J. P.: 2013, *MNRAS* **436**, 1919

Casey, C. M., Narayanan, D., and Cooray, A.: 2014, *Phys. Rep.* **541**, 45

Cesarsky, D., Lequeux, J., Abergel, A., Perault, M., Palazzi, E., Madden, S., and Tran, D.: 1996, *A&A* **315**, L305

Chabrier, G.: 2001, *ApJ* **554**, 1274

Chabrier, G.: 2003, *PASP* **115**, 763

Charbonneau, P.: 1995, *ApJS* **101**, 309

Charlot, S. and Fall, S. M.: 2000, *ApJ* **539**, 718

Chary, R. and Elbaz, D.: 2001, *ApJ* **556**, 562

Conroy, C.: 2013, *ARA&A* **51**, 393

Cucciati, O., Tresse, L., Ilbert, O., Le Fèvre, O., Garilli, B., Le Brun, V., Cassata, P., Franzetti, P., Maccagni, D., Scodeggio, M., Zucca, E., Zamorani, G., Bardelli, S., Bolzonella, M., Bielby, R. M., McCracken, H. J., Zanichelli, A., and Vergani, D.: 2012, *A&A* **539**, A31

da Cunha, E., Charlot, S., and Elbaz, D.: 2008, *MNRAS* **388**, 1595

Daddi, E., Dickinson, M., Morrison, G., Chary, R., Cimatti, A., Elbaz, D., Frayer, D., Renzini, A., Pope, A., Alexander, D. M., Bauer, F. E., Giavalisco, M., Huynh, M., Kurk, J., and Mignoli, M.: 2007, *ApJ* **670**, 156

Dale, D. A. and Helou, G.: 2002, *ApJ* **576**, 159

Dale, D. A., Helou, G., Contursi, A., Silbermann, N. A., and Kolhatkar, S.: 2001, *ApJ* **549**, 215

Davidzon, I., Bolzonella, M., Coupon, J., Ilbert, O., Arnouts, S., de la Torre, S., Fritz, A., De Lucia, G., Iovino, A., Granett, B. R., Zamorani, G., Guzzo, L., Abbas, U., Adami, C., Bel, J., Bottini, D., Branchini, E., Cappi, A., Cucciati, O., Franzetti, P., Fumana, M., Garilli, B., Krywult, J., Le Brun, V., Le Fèvre, O., Maccagni, D., Małek, K., Marulli, F., McCracken, H. J., Paioro, L., Peacock, J. A., Polletta, M., Pollo, A., Schlagenhaufer, H., Scodeggio, M., Tasca, L. A. M., Tojeiro, R., Vergani, D., Zanichelli, A., Burden, A., Di Porto, C., Marchetti, A., Marinoni, C., Mellier, Y., Moscardini, L., Moutard, T., Nichol, R. C., Percival, W. J., Phleps, S., and Wolk, M.: 2013, *A&A* **558**, A23

De Lucia, G. and Blaizot, J.: 2007, *MNRAS* **375**, 2

Donley, J. L., Koekemoer, A. M., Brusa, M., Capak, P., Cardamone, C. N., Civano, F., Ilbert, O., Impey, C. D., Kartaltepe, J. S., Miyaji, T., Salvato, M., Sanders, D. B., Trump, J. R., and Zamorani, G.: 2012, *ApJ* **748**, 142

Dowell, C. D., Pohlen, M., Pearson, C., Griffin, M., Lim, T., Bendo, G. J., Benielli, D., Bock, J. J., Chanial, P., Clements, D. L., Conversi, L., Ferlet, M., Fulton, T., Gastaud, R., Glenn, J., Grundy, T., Guest, S., King, K. J., Leeks, S. J., Levenson, L., Lu, N., Morris, H., Nguyen, H., O'Halloran, B., Oliver, S., Panuzzo, P., Papageorgiou, A., Polehampton, E., Rigopoulou, D., Roussel, H., Schneider, N., Schulz, B., Schwartz, A., Shupe, D. L., Sibthorpe, B., Sidher, S., Smith, A. J., Swinyard, B. M., Trichas, M., Valtchanov, I., Woodcraft, A. L., Xu, C. K., and Zhang, L.: 2010, in *Society of Photo-Optical Instrumentation Engineers (SPIE) Conference Series*, Vol. 7731 of *Society of Photo-Optical Instrumentation Engineers (SPIE) Conference Series*, p. 36

Dunlop, J., Akiyama, M., Alexander, D., Almaini, O., Borys, C., Bouwens, R., Bremer, M., Cimatti, A., Cirasuolo, M., Clewley, L., Conselice, C., Coppin, K., Dalton, G., Damen, M., Dunne, L., Dye, S., Eales, S., Edge, A., Egami, E., Fall, M., Farrah, D., Ferguson, H., Finoguenov, A., Foucaud, S., Franx, M., Furusawa, H., Huang, J., Ibar, E., Illingworth, G., Ivison, R., Jarvis, M., Labbe, I., Lawrence, A., Maddox, S., McLure, R., Mortier, A., Oliver, S., Ouchi, M., Page, M., Papovich, C., Quadri, R., Rawlings, S., Rieke, G., Schiminovich, D., Sekiguchi, K., Serjeant, S., Simpson, C., Smail, I., Stanway, E., Taylor, A., Watson, M., Williams, R., Yamada, T., van Breukelen, C., and van Dokkum, P.: 2007, *A Spitzer Public Legacy survey of the UKIDSS Ultra Deep Survey*, Spitzer Proposal

Dunlop, J. S.: 2011, in W. Wang, J. Lu, Z. Luo, Z. Yang, H. Hua, and Z. Chen (eds.), *Galaxy Evolution: Infrared to Millimeter Wavelength Perspective*, Vol. 446 of *Astronomical Society of the Pacific Conference Series*, p. 209

Eales, S., Dunne, L., Clements, D., Cooray, A., de Zotti, G., Dye, S., Ivison, R., Jarvis, M., Lagache, G., Maddox, S., Negrello, M., Serjeant, S., Thompson, M. A., van Kampen, E., Amblard, A., Andreani, P., Baes, M., Beelen, A., Bendo, G. J., Benford, D., Bertoldi, F., Bock, J., Bonfield, D., Boselli, A., Bridge, C., Buat, V., Burgarella, D., Carlberg, R., Cava, A., Chanial, P., Charlot, S., Christopher, N., Coles, P., Cortese, L., Dariush, A., da Cunha, E., Dalton, G., Danese, L., Dannerbauer, H., Driver, S., Dunlop, J., Fan, L., Farrah, D., Frayer, D., Frenk, C., Geach, J., Gardner, J., Gomez, H., González-Nuevo, J., González-Solares, E., Griffin, M., Hardcastle, M., Hatziminaoglou, E., Herranz, D., Hughes, D., Ibar, E., Jeong, W.-S., Lacey, C., Lapi, A., Lawrence, A., Lee, M., Leeuw, L., Liske, J., López-Caniego, M., Müller, T., Nandra, K., Panuzzo, P., Papageorgiou, A., Patanchon, G., Peacock, J., Pearson, C., Phillipps, S., Pohlen, M., Popescu, C., Rawlings, S., Rigby, E., Rigopoulou, M., Robotham, A., Rodighiero, G., Sansom, A., Schulz, B., Scott, D., Smith, D. J. B., Sibthorpe, B., Smail, I., Stevens, J., Sutherland, W., Takeuchi, T., Tedds, J., Temi, P., Tuffs, R., Trichas, M., Vaccari, M., Valtchanov, I., van der Werf, P., Verma, A., Vieria, J., Vlahakis, C., and White, G. J.: 2010, *PASP* **122**, 499

Eddington, A. S.: 1913, *MNRAS* **73**, 359

Elbaz, D., Cesarsky, C. J., Chanial, P., Aussel, H., Franceschini, A., Fadda, D., and Chary, R. R.: 2002, *A&A* **384**, 848

Elbaz, D., Daddi, E., Le Borgne, D., Dickinson, M., Alexander, D. M., Chary, R.-R., Starck, J.-L., Brandt, W. N., Kitzbichler, M., MacDonald, E., Nonino, M., Popesso, P., Stern, D., and Vanzella, E.: 2007, *A&A* **468**, 33

Elbaz, D., Dickinson, M., Hwang, H. S., Díaz-Santos, T., Magdis, G., Magnelli, B., Le Borgne, D., Galliano, F., Pannella, M., Chanial, P., Armus, L., Charmandaris, V., Daddi, E., Aussel, H., Popesso, P., Kartaltepe, J., Altieri, B., Valtchanov, I., Coia, D., Dannerbauer, H., Dasyra, K., Leiton, R., Mazzarella, J., Alexander, D. M., Buat, V., Burgarella, D., Chary, R.-R., Gilli, R., Ivison, R. J., Juneau, S., Le Floc'h, E., Lutz, D., Morrison, G. E., Mullaney, J. R., Murphy, E., Pope, A., Scott, D., Brodwin, M., Calzetti, D., Cesarsky, C., Charlot, S., Dole, H., Eisenhardt, P., Ferguson, H. C., Förster Schreiber, N., Frayer, D., Giavalisco, M., Huynh, M., Koekemoer, A. M.,

Papovich, C., Reddy, N., Surace, C., Teplitz, H., Yun, M. S., and Wilson, G.: 2011, *A&A* **533**, A119

Farrah, D., Rowan-Robinson, M., Oliver, S., Serjeant, S., Borne, K., Lawrence, A., Lucas, R. A., Bushouse, H., and Colina, L.: 2001, *MNRAS* **326**, 1333

Fazio, G. G., Hora, J. L., Allen, L. E., Ashby, M. L. N., Barmby, P., Deutsch, L. K., Huang, J.-S., Kleiner, S., Marengo, M., Megeath, S. T., Melnick, G. J., Pahre, M. A., Patten, B. M., Polizotti, J., Smith, H. A., Taylor, R. S., Wang, Z., Willner, S. P., Hoffmann, W. F., Pipher, J. L., Forrest, W. J., McMurty, C. W., McCreight, C. R., McKelvey, M. E., McMurray, R. E., Koch, D. G., Moseley, S. H., Arendt, R. G., Mentzell, J. E., Marx, C. T., Losch, P., Mayman, P., Eichhorn, W., Krebs, D., Jhabvala, M., Gezari, D. Y., Fixsen, D. J., Flores, J., Shakoorzadeh, K., Jungo, R., Hakun, C., Workman, L., Karpati, G., Kichak, R., Whitley, R., Mann, S., Tollestrup, E. V., Eisenhardt, P., Stern, D., Gorjian, V., Bhattacharya, B., Carey, S., Nelson, B. O., Glaccum, W. J., Lacy, M., Lowrance, P. J., Laine, S., Reach, W. T., Stauffer, J. A., Surace, J. A., Wilson, G., Wright, E. L., Hoffman, A., Domingo, G., and Cohen, M.: 2004, *ApJS* **154**, 10

Fioc, M. and Rocca-Volmerange, B.: 1997, *A&A* **326**, 950

Frayer, D. T., Fadda, D., Yan, L., Marleau, F. R., Choi, P. I., Helou, G., Soifer, B. T., Appleton, P. N., Armus, L., Beck, R., Dole, H., Engelbracht, C. W., Fang, F., Gordon, K. D., Heinrichsen, I., Henderson, D., Hesselroth, T., Im, M., Kelly, D. M., Lacy, M., Laine, S., Latter, W. B., Mahoney, W., Makovoz, D., Masci, F. J., Morrison, J. E., Moshir, M., Noriega-Crespo, A., Padgett, D. L., Pesenson, M., Shupe, D. L., Squires, G. K., Storrie-Lombardi, L. J., Surace, J. A., Teplitz, H. I., and Wilson, G.: 2006, *AJ* **131**, 250

Frayer, D. T., Sanders, D. B., Surace, J. A., Aussel, H., Salvato, M., Le Floc'h, E., Huynh, M. T., Scoville, N. Z., Afonso-Luis, A., Bhattacharya, B., Capak, P., Fadda, D., Fu, H., Helou, G., Ilbert, O., Kartaltepe, J. S., Koekemoer, A. M., Lee, N., Murphy, E., Sargent, M. T., Schinnerer, E., Sheth, K., Shopbell, P. L., Shupe, D. L., and Yan, L.: 2009, *AJ* **138**, 1261

Furusawa, H., Kosugi, G., Akiyama, M., Takata, T., Sekiguchi, K., Tanaka, I., Iwata, I., Kajisawa, M., Yasuda, N., Doi, M., Ouchi, M., Simpson, C., Shimasaku, K., Yamada, T., Furusawa, J., Morokuma, T., Ishida, C. M., Aoki, K., Fuse, T., Imanishi, M., Iye, M., Karoji, H., Kobayashi, N., Kodama, T., Komiyama, Y., Maeda, Y., Miyazaki,

S., Mizumoto, Y., Nakata, F., Noumaru, J., Ogasawara, R., Okamura, S., Saito, T., Sasaki, T., Ueda, Y., and Yoshida, M.: 2008, *ApJS* **176**, 1

Galametz, A., Grazian, A., Fontana, A., Ferguson, H. C., Ashby, M. L. N., Barro, G., Castellano, M., Dahlen, T., Donley, J. L., Faber, S. M., Grogin, N., Guo, Y., Huang, K.-H., Kocevski, D. D., Koekemoer, A. M., Lee, K.-S., McGrath, E. J., Peth, M., Willner, S. P., Almaini, O., Cooper, M., Cooray, A., Conselice, C. J., Dickinson, M., Dunlop, J. S., Fazio, G. G., Foucaud, S., Gardner, J. P., Giavalisco, M., Hathi, N. P., Hartley, W. G., Koo, D. C., Lai, K., de Mello, D. F., McLure, R. J., Lucas, R. A., Paris, D., Pentericci, L., Santini, P., Simpson, C., Sommariva, V., Targett, T., Weiner, B. J., Wuyts, S., and the CANDELS Team: 2013, *ApJS* **206**, 10

Gawiser, E., van Dokkum, P. G., Herrera, D., Maza, J., Castander, F. J., Infante, L., Lira, P., Quadri, R., Toner, R., Treister, E., Urry, C. M., Altmann, M., Assef, R., Christlein, D., Coppi, P. S., Durán, M. F., Franx, M., Galaz, G., Huerta, L., Liu, C., López, S., Méndez, R., Moore, D. C., Rubio, M., Ruiz, M. T., Toft, S., and Yi, S. K.: 2006, *ApJS* **162**, 1

Geach, J. E., Simpson, C., Rawlings, S., Read, A. M., and Watson, M.: 2007, *MNRAS* **381**, 1369

Gil de Paz, A. and Madore, B. F.: 2002, *AJ* **123**, 1864

Giovannoli, E., Buat, V., Noll, S., Burgarella, D., and Magnelli, B.: 2011, *A&A* **525**, A150

Gordon, K. D., Calzetti, D., and Witt, A. N.: 1997, *ApJ* **487**, 625

Grazian, A., Fontana, A., de Santis, C., Nonino, M., Salimbeni, S., Giallongo, E., Cristiani, S., Gallozzi, S., and Vanzella, E.: 2006, *A&A* **449**, 951

Griffin, M. J., Abergel, A., Abreu, A., Ade, P. A. R., André, P., Augueres, J.-L., Babbedge, T., Bae, Y., Baillie, T., Baluteau, J.-P., Barlow, M. J., Bendo, G., Benielli, D., Bock, J. J., Bonhomme, P., Brisbin, D., Brockley-Blatt, C., Caldwell, M., Cara, C., Castro-Rodriguez, N., Cerulli, R., Chanial, P., Chen, S., Clark, E., Clements, D. L., Clerc, L., Coker, J., Communal, D., Conversi, L., Cox, P., Crumb, D., Cunningham, C., Daly, F., Davis, G. R., de Antoni, P., Delderfield, J., Devin, N., di Giorgio, A., Didschuns, I., Dohlen, K., Donati, M., Dowell, A., Dowell, C. D., Duband, L., Dumaye, L., Emery, R. J., Ferlet, M., Ferrand, D., Fontignie, J., Fox, M., Franceschini, A., Frerking, M., Fulton, T., Garcia, J., Gastaud, R., Gear, W. K., Glenn, J., Goizel, A., Griffin, D. K., Grundy, T., Guest, S., Guillemet, L., Hargrave, P. C., Harwit, M.,

Hastings, P., Hatziminaoglou, E., Herman, M., Hinde, B., Hristov, V., Huang, M., Imhof, P., Isaak, K. J., Israelsson, U., Ivison, R. J., Jennings, D., Kiernan, B., King, K. J., Lange, A. E., Latter, W., Laurent, G., Laurent, P., Leeks, S. J., Lellouch, E., Levenson, L., Li, B., Li, J., Lilienthal, J., Lim, T., Liu, S. J., Lu, N., Madden, S., Mainetti, G., Marliani, P., McKay, D., Mercier, K., Molinari, S., Morris, H., Moseley, H., Mulder, J., Mur, M., Naylor, D. A., Nguyen, H., O'Halloran, B., Oliver, S., Olofsson, G., Olofsson, H.-G., Orfei, R., Page, M. J., Pain, I., Panuzzo, P., Papageorgiou, A., Parks, G., Parr-Burman, P., Pearce, A., Pearson, C., Pérez-Fournon, I., Pinsard, F., Pisano, G., Podosek, J., Pohlen, M., Polehampton, E. T., Pouliquen, D., Rigopoulou, D., Rizzo, D., Roseboom, I. G., Roussel, H., Rowan-Robinson, M., Rownd, B., Saraceno, P., Sauvage, M., Savage, R., Savini, G., Sawyer, E., Scharmberg, C., Schmitt, D., Schneider, N., Schulz, B., Schwartz, A., Shafer, R., Shupe, D. L., Sibthorpe, B., Sidher, S., Smith, A., Smith, A. J., Smith, D., Spencer, L., Stobie, B., Sudiwala, R., Sukhatme, K., Surace, C., Stevens, J. A., Swinyard, B. M., Trichas, M., Tourette, T., Triou, H., Tseng, S., Tucker, C., Turner, A., Vaccari, M., Valtchanov, I., Vigroux, L., Virique, E., Voellmer, G., Walker, H., Ward, R., Waskett, T., Weilert, M., Wesson, R., White, G. J., Whitehouse, N., Wilson, C. D., Winter, B., Woodcraft, A. L., Wright, G. S., Xu, C. K., Zavagno, A., Zemcov, M., Zhang, L., and Zonca, E.: 2010, *A&A* **518**, L3

Groves, B., Dopita, M. A., Sutherland, R. S., Kewley, L. J., Fischera, J., Leitherer, C., Brandl, B., and van Breugel, W.: 2008, *ApJS* **176**, 438

Gruppioni, C., Pozzi, F., Rodighiero, G., Delvecchio, I., Berta, S., Pozzetti, L., Zamorani, G., Andreani, P., Cimatti, A., Ilbert, O., Le Floc'h, E., Lutz, D., Magnelli, B., Marchetti, L., Monaco, P., Nordon, R., Oliver, S., Popesso, P., Riguccini, L., Roseboom, I., Rosario, D. J., Sargent, M., Vaccari, M., Altieri, B., Aussel, H., Bongiovanni, A., Cepa, J., Daddi, E., Domínguez-Sánchez, H., Elbaz, D., Förster Schreiber, N., Genzel, R., Iribarrem, A., Magliocchetti, M., Maiolino, R., Poglitsch, A., Pérez García, A., Sanchez-Portal, M., Sturm, E., Tacconi, L., Valtchanov, I., Amblard, A., Arumugam, V., Bethermin, M., Bock, J., Boselli, A., Buat, V., Burgarella, D., Castro-Rodríguez, N., Cava, A., Chanial, P., Clements, D. L., Conley, A., Cooray, A., Dowell, C. D., Dwek, E., Eales, S., Franceschini, A., Glenn, J., Griffin, M., Hatziminaoglou, E., Ibar, E., Isaak, K., Ivison, R. J., Lagache, G., Levenson, L., Lu, N., Madden, S., Maffei, B., Mainetti, G., Nguyen, H. T., O'Halloran, B., Page, M. J., Panuzzo, P., Papageorgiou, A., Pearson, C. P., Pérez-Fournon, I., Pohlen, M., Rigopoulou, D., Rowan-Robinson, M., Schulz, B., Scott, D., Seymour, N., Shupe, D. L., Smith, A. J., Stevens, J. A., Symeonidis, M., Trichas, M., Tugwell, K. E., Vigroux, L., Wang, L.,

Wright, G., Xu, C. K., Zemcov, M., Bardelli, S., Carollo, M., Contini, T., Le Févre, O., Lilly, S., Mainieri, V., Renzini, A., Scodeggio, M., and Zucca, E.: 2013, *MNRAS* **432**, 23

Hickox, R. C., Wardlow, J. L., Smail, I., Myers, A. D., Alexander, D. M., Swinbank, A. M., Danielson, A. L. R., Stott, J. P., Chapman, S. C., Coppin, K. E. K., Dunlop, J. S., Gawiser, E., Lutz, D., van der Werf, P., and Weiß, A.: 2012, *MNRAS* **421**, 284

Hopkins, A. M. and Beacom, J. F.: 2006, *ApJ* **651**, 142

Hopkins, P. F., Hernquist, L., Cox, T. J., and Kereš, D.: 2008, *ApJS* **175**, 356

Huang, J.-S., Barmby, P., Fazio, G. G., Willner, S. P., Wilson, G., Rigopoulou, D., Alonso-Herrero, A., Dole, H., Egami, E., Le Floc'h, E., Papovich, C., Pérez-González, P. G., Rigby, J., Engelbracht, C. W., Gordon, K., Hines, D., Rieke, M., Rieke, G. H., Meisenheimer, K., and Miyazaki, S.: 2004, *ApJS* **154**, 44

Hung, C.-L., Sanders, D. B., Casey, C. M., Lee, N., Barnes, J. E., Capak, P., Kartaltepe, J. S., Koss, M., Larson, K. L., Le Floc'h, E., Lockhart, K., Man, A. W. S., Mann, A. W., Riguccini, L., Scoville, N., and Symeonidis, M.: 2013, *ApJ* **778**, 129

Iglesias-Páramo, J., Buat, V., Takeuchi, T. T., Xu, K., Boissier, S., Boselli, A., Burgarella, D., Madore, B. F., Gil de Paz, A., Bianchi, L., Barlow, T. A., Byun, Y.-I., Donas, J., Forster, K., Friedman, P. G., Heckman, T. M., Jelinski, P. N., Lee, Y.-W., Malina, R. F., Martin, D. C., Milliard, B., Morrissey, P. F., Neff, S. G., Rich, R. M., Schiminovich, D., Seibert, M., Siegmund, O. H. W., Small, T., Szalay, A. S., Welsh, B. Y., and Wyder, T. K.: 2006, *ApJS* **164**, 38

Ilbert, O., Arnouts, S., McCracken, H. J., Bolzonella, M., Bertin, E., Le Fèvre, O., Mellier, Y., Zamorani, G., Pellò, R., Iovino, A., Tresse, L., Le Brun, V., Bottini, D., Garilli, B., Maccagni, D., Picat, J. P., Scaramella, R., Scodeggio, M., Vettolani, G., Zanichelli, A., Adami, C., Bardelli, S., Cappi, A., Charlot, S., Ciliegi, P., Contini, T., Cucciati, O., Foucaud, S., Franzetti, P., Gavignaud, I., Guzzo, L., Marano, B., Marinoni, C., Mazure, A., Meneux, B., Merighi, R., Paltani, S., Pollo, A., Pozzetti, L., Radovich, M., Zucca, E., Bondi, M., Bongiorno, A., Busarello, G., de La Torre, S., Gregorini, L., Lamareille, F., Mathez, G., Merluzzi, P., Ripepi, V., Rizzo, D., and Vergani, D.: 2006, *A&A* **457**, 841

Ilbert, O., McCracken, H. J., Le Fèvre, O., Capak, P., Dunlop, J., Karim, A., Renzini, M. A., Caputi, K., Boissier, S., Arnouts, S., Aussel, H., Comparat, J., Guo, Q., Hudelot, P., Kartaltepe, J., Kneib, J. P., Krogager, J. K., Le Floc'h, E., Lilly, S., Mellier,

Y., Milvang-Jensen, B., Moutard, T., Onodera, M., Richard, J., Salvato, M., Sanders, D. B., Scoville, N., Silverman, J. D., Taniguchi, Y., Tasca, L., Thomas, R., Toft, S., Tresse, L., Vergani, D., Wolk, M., and Zirm, A.: 2013, *A&A* **556**, A55

Kartaltepe, J. S., Dickinson, M., Alexander, D. M., Bell, E. F., Dahlen, T., Elbaz, D., Faber, S. M., Lotz, J., McIntosh, D. H., Wiklind, T., Altieri, B., Aussel, H., Bethermin, M., Bournaud, F., Charmandaris, V., Conselice, C. J., Cooray, A., Dannerbauer, H., Davé, R., Dunlop, J., Dekel, A., Ferguson, H. C., Grogin, N. A., Hwang, H. S., Ivison, R., Kocevski, D., Koekemoer, A., Koo, D. C., Lai, K., Leiton, R., Lucas, R. A., Lutz, D., Magdis, G., Magnelli, B., Morrison, G., Mozena, M., Mullaney, J., Newman, J. A., Pope, A., Popesso, P., van der Wel, A., Weiner, B., and Wuyts, S.: 2012, *ApJ* **757**, 23

Kartaltepe, J. S., Sanders, D. B., Le Floc'h, E., Frayer, D. T., Aussel, H., Arnouts, S., Ilbert, O., Salvato, M., Scoville, N. Z., Surace, J., Yan, L., Capak, P., Caputi, K., Carollo, C. M., Cassata, P., Civano, F., Hasinger, G., Koekemoer, A. M., Le Fèvre, O., Lilly, S., Liu, C. T., McCracken, H. J., Schinnerer, E., Smolčić, V., Taniguchi, Y., Thompson, D. J., Trump, J., Baldassare, V. F., and Fiorenza, S. L.: 2010, *ApJ* **721**, 98

Kartaltepe, J. S., Sanders, D. B., Scoville, N. Z., Calzetti, D., Capak, P., Koekemoer, A., Mobasher, B., Murayama, T., Salvato, M., Sasaki, S. S., and Taniguchi, Y.: 2007, *ApJS* **172**, 320

Kauffmann, G., Heckman, T. M., White, S. D. M., Charlot, S., Tremonti, C., Brinchmann, J., Bruzual, G., Peng, E. W., Seibert, M., Bernardi, M., Blanton, M., Brinkmann, J., Castander, F., Csábai, I., Fukugita, M., Ivezic, Z., Munn, J. A., Nichol, R. C., Padmanabhan, N., Thakar, A. R., Weinberg, D. H., and York, D.: 2003, *MNRAS* **341**, 33

Kennicutt, Jr., R. C.: 1998, *ARA&A* **36**, 189

Kessler, M. F., Steinz, J. A., Anderegg, M. E., Clavel, J., Drechsel, G., Estaria, P., Faelker, J., Riedinger, J. R., Robson, A., Taylor, B. G., and Ximénez de Ferrán, S.: 1996, *A&A* **315**, L27

Kim, D.-C., Evans, A. S., Vavilkin, T., Armus, L., Mazzarella, J. M., Sheth, K., Surace, J. A., Haan, S., Howell, J. H., Díaz-Santos, T., Petric, A., Iwasawa, K., Privon, G. C., and Sanders, D. B.: 2013, *ApJ* **768**, 102

Kleinmann, D. E. and Low, F. J.: 1970, *ApJ* **159**, L165

Koekemoer, A. M., Faber, S. M., Ferguson, H. C., Grogin, N. A., Kocevski, D. D., Koo, D. C., Lai, K., Lotz, J. M., Lucas, R. A., McGrath, E. J., Ogaz, S., Rajan, A., Riess, A. G., Rodney, S. A., Strolger, L., Casertano, S., Castellano, M., Dahlen, T., Dickinson, M., Dolch, T., Fontana, A., Giavalisco, M., Grazian, A., Guo, Y., Hathi, N. P., Huang, K.-H., van der Wel, A., Yan, H.-J., Acquaviva, V., Alexander, D. M., Almaini, O., Ashby, M. L. N., Barden, M., Bell, E. F., Bournaud, F., Brown, T. M., Caputi, K. I., Cassata, P., Challis, P. J., Chary, R.-R., Cheung, E., Cirasuolo, M., Conselice, C. J., Roshan Cooray, A., Croton, D. J., Daddi, E., Davé, R., de Mello, D. F., de Ravel, L., Dekel, A., Donley, J. L., Dunlop, J. S., Dutton, A. A., Elbaz, D., Fazio, G. G., Filippenko, A. V., Finkelstein, S. L., Frazer, C., Gardner, J. P., Garnavich, P. M., Gawiser, E., Gruetzbauch, R., Hartley, W. G., Häussler, B., Herrington, J., Hopkins, P. F., Huang, J.-S., Jha, S. W., Johnson, A., Kartaltepe, J. S., Khostovan, A. A., Kirshner, R. P., Lani, C., Lee, K.-S., Li, W., Madau, P., McCarthy, P. J., McIntosh, D. H., McLure, R. J., McPartland, C., Mobasher, B., Moreira, H., Mortlock, A., Moustakas, L. A., Mozena, M., Nandra, K., Newman, J. A., Nielsen, J. L., Niemi, S., Noeske, K. G., Papovich, C. J., Pentericci, L., Pope, A., Primack, J. R., Ravindranath, S., Reddy, N. A., Renzini, A., Rix, H.-W., Robaina, A. R., Rosario, D. J., Rosati, P., Salimbeni, S., Scarlata, C., Siana, B., Simard, L., Smidt, J., Snyder, D., Somerville, R. S., Spinrad, H., Straughn, A. N., Telford, O., Teplitz, H. I., Trump, J. R., Vargas, C., Villforth, C., Wagner, C. R., Wandro, P., Wechsler, R. H., Weiner, B. J., Wiklind, T., Wild, V., Wilson, G., Wuyts, S., and Yun, M. S.: 2011, *ApJS* **197**, 36

Kron, R. G.: 1980, *ApJS* **43**, 305

Kroupa, P.: 2001, *MNRAS* **322**, 231

Kurucz, R. L.: 1992, in B. Barbuy and A. Renzini (eds.), *The Stellar Populations of Galaxies*, Vol. 149 of *IAU Symposium*, p. 225

Labbé, I., Franx, M., Rudnick, G., Schreiber, N. M. F., Rix, H.-W., Moorwood, A., van Dokkum, P. G., van der Werf, P., Röttgering, H., van Starkenburg, L., van der Wel, A., Kuijken, K., and Daddi, E.: 2003, *AJ* **125**, 1107

Larson, R. B. and Tinsley, B. M.: 1978, *ApJ* **219**, 46

Lawrence, A., Warren, S. J., Almaini, O., Edge, A. C., Hambly, N. C., Jameson, R. F., Lucas, P., Casali, M., Adamson, A., Dye, S., Emerson, J. P., Foucaud, S., Hewett, P., Hirst, P., Hodgkin, S. T., Irwin, M. J., Lodieu, N., McMahon, R. G., Simpson, C., Smail, I., Mortlock, D., and Folger, M.: 2007, *MNRAS* **379**, 1599

Le Floc'h, E., Papovich, C., Dole, H., Bell, E. F., Lagache, G., Rieke, G. H., Egami, E., Pérez-González, P. G., Alonso-Herrero, A., Rieke, M. J., Blaylock, M., Engelbracht, C. W., Gordon, K. D., Hines, D. C., Misselt, K. A., Morrison, J. E., and Mould, J.: 2005, *ApJ* **632**, 169

Le Floc'h, E., Pérez-González, P. G., Rieke, G. H., Papovich, C., Huang, J.-S., Barmby, P., Dole, H., Egami, E., Alonso-Herrero, A., Wilson, G., Miyazaki, S., Rigby, J. R., Bei, L., Blaylock, M., Engelbracht, C. W., Fazio, G. G., Frayer, D. T., Gordon, K. D., Hines, D. C., Misselt, K. A., Morrison, J. E., Muzerolle, J., Rieke, M. J., Rigopoulou, D., Su, K. Y. L., Willner, S. P., and Young, E. T.: 2004, *ApJS* **154**, 170

Lee, N., Sanders, D. B., Casey, C. M., Scoville, N. Z., Hung, C.-L., Le Floc'h, E., Ilbert, O., Aussel, H., Capak, P., Kartaltepe, J. S., Roseboom, I., Salvato, M., Aravena, M., Berta, S., Bock, J., Oliver, S. J., Riguccini, L., and Symeonidis, M.: 2013, *ApJ* **778**, 131

Lee, S.-K., Idzi, R., Ferguson, H. C., Somerville, R. S., Wiklind, T., and Giavalisco, M.: 2009, *ApJS* **184**, 100

Leitherer, C. and Heckman, T. M.: 1995, *ApJS* **96**, 9

Lejeune, T. and Schaerer, D.: 2001, *A&A* **366**, 538

Lemaux, B. C., Le Floc'h, E., Le Fèvre, O., Ilbert, O., Tresse, L., Lubin, L. M., Zamorani, G., Gal, R. R., Ciliegi, P., Cassata, P., Kocevski, D. D., McGrath, E. J., Bardelli, S., Zucca, E., and Squires, G. K.: 2014, *A&A* **572**, A90

Lemke, D., Ábrahám, P., Haas, M., Héraudeau, P., Hotzel, S., Kiss, C., Klaas, U., Krause, O., Leinert, C., Meisenheimer, K., Stickel, M., Tóth, L. V., Juvela, M., Mattila, K., Chini, R., Müller, S. A. H., Linden-Vørnle, M. J. D., and Nørgaard-Nielsen, H. U.: 2001, in M. Harwit and M. G. Hauser (eds.), *The Extragalactic Infrared Background and its Cosmological Implications*, Vol. 204 of *IAU Symposium*, p. 247

Lo Faro, B., Franceschini, A., Vaccari, M., Silva, L., Rodighiero, G., Berta, S., Bock, J., Burgarella, D., Buat, V., Cava, A., Clements, D. L., Cooray, A., Farrah, D., Feltre, A., González Solares, E. A., Hurley, P., Lutz, D., Magdis, G., Magnelli, B., Marchetti, L., Oliver, S. J., Page, M. J., Popesso, P., Pozzi, F., Rigopoulou, D., Rowan-Robinson, M., Roseboom, I. G., Scott, D., Smith, A. J., Symeonidis, M., Wang, L., and Wuyts, S.: 2013, *ApJ* **762**, 108

Lonsdale, C. J., Farrah, D., and Smith, H. E.: 2006, *Ultraluminous Infrared Galaxies*, p. 285

Lonsdale, C. J., Smith, H. E., Rowan-Robinson, M., Surace, J., Shupe, D., Xu, C., Oliver, S., Padgett, D., Fang, F., Conrow, T., Franceschini, A., Gautier, N., Griffin, M., Hacking, P., Masci, F., Morrison, G., O'Linger, J., Owen, F., Pérez-Fournon, I., Pierre, M., Puetter, R., Stacey, G., Castro, S., Polletta, M. d. C., Farrah, D., Jarrett, T., Frayer, D., Siana, B., Babbedge, T., Dye, S., Fox, M., Gonzalez-Solares, E., Salaman, M., Berta, S., Condon, J. J., Dole, H., and Serjeant, S.: 2003, *PASP* **115**, 897

Low, J. and Kleinmann, D. E.: 1968, *AJ* **73**, 868

Lutz, D., Poglitsch, A., Altieri, B., Andreani, P., Aussel, H., Berta, S., Bongiovanni, A., Brisbin, D., Cava, A., Cepa, J., Cimatti, A., Daddi, E., Dominguez-Sanchez, H., Elbaz, D., Förster Schreiber, N. M., Genzel, R., Grazian, A., Gruppioni, C., Harwit, M., Le Floc'h, E., Magdis, G., Magnelli, B., Maiolino, R., Nordon, R., Pérez García, A. M., Popesso, P., Pozzi, F., Riguccini, L., Rodighiero, G., Saintonge, A., Sanchez Portal, M., Santini, P., Shao, L., Sturm, E., Tacconi, L. J., Valtchanov, I., Wetzstein, M., and Wieprecht, E.: 2011, *Astron Astrophys.,* **532**, A90

MacArthur, L. A., McDonald, M., Courteau, S., and Jesús González, J.: 2010, *ApJ* **718**, 768

Madau, P. and Dickinson, M.: 2014, *ARA&A* **52**, 415

Madau, P., Ferguson, H. C., Dickinson, M. E., Giavalisco, M., Steidel, C. C., and Fruchter, A.: 1996, *MNRAS* **283**, 1388

Magnelli, B., Elbaz, D., Chary, R. R., Dickinson, M., Le Borgne, D., Frayer, D. T., and Willmer, C. N. A.: 2011, *A&A* **528**, A35

Magnelli, B., Popesso, P., Berta, S., Pozzi, F., Elbaz, D., Lutz, D., Dickinson, M., Altieri, B., Andreani, P., Aussel, H., Béthermin, M., Bongiovanni, A., Cepa, J., Charmandaris, V., Chary, R.-R., Cimatti, A., Daddi, E., Förster Schreiber, N. M., Genzel, R., Gruppioni, C., Harwit, M., Hwang, H. S., Ivison, R. J., Magdis, G., Maiolino, R., Murphy, E., Nordon, R., Pannella, M., Pérez García, A., Poglitsch, A., Rosario, D., Sanchez-Portal, M., Santini, P., Scott, D., Sturm, E., Tacconi, L. J., and Valtchanov, I.: 2013, *A&A* **553**, A132

Makovoz, D. and Khan, I.: 2005, *ASPC Series,* 347, 81.

Maraston, C.: 2005, *MNRAS* **362**, 799

Maraston, C., Daddi, E., Renzini, A., Cimatti, A., Dickinson, M., Papovich, C., Pasquali, A., and Pirzkal, N.: 2006, *ApJ* **652**, 85

Marigo, P. and Girardi, L.: 2007, *A&A* **469**, 239

Marigo, P., Girardi, L., Bressan, A., Groenewegen, M. A. T., Silva, L., and Granato, G. L.: 2008, *A&A* **482**, 883

Martin, D. C., Fanson, J., Schiminovich, D., Morrissey, P., Friedman, P. G., Barlow, T. A., Conrow, T., Grange, R., Jelinsky, P. N., Milliard, B., Siegmund, O. H. W., Bianchi, L., Byun, Y.-I., Donas, J., Forster, K., Heckman, T. M., Lee, Y.-W., Madore, B. F., Malina, R. F., Neff, S. G., Rich, R. M., Small, T., Surber, F., Szalay, A. S., Welsh, B., and Wyder, T. K.: 2005, *ApJ* **619**, L1

Martins, L. P., González Delgado, R. M., Leitherer, C., Cerviño, M., and Hauschildt, P.: 2005, *MNRAS* **358**, 49

McLure, R. J., Pearce, H. J., Dunlop, J. S., Cirasuolo, M., Curtis-Lake, E., Bruce, V. A., Caputi, K. I., Almaini, O., Bonfield, D. G., Bradshaw, E. J., Buitrago, F., Chuter, R., Foucaud, S., Hartley, W. G., and Jarvis, M. J.: 2013, *MNRAS* **428**, 1088

Meiksin, A.: 2006, *MNRAS* **365**, 807

Melnick, J. and De Propris, R.: 2013, *MNRAS* **431**, 2034

Melnick, J. and Mirabel, I. F.: 1990, *A&A* **231**, L19

Michałowski, M. J., Hayward, C. C., Dunlop, J. S., Bruce, V. A., Cirasuolo, M., Cullen, F., and Hernquist, L.: 2014, *A&A* **571**, A75

Miyazaki, S., Komiyama, Y., Sekiguchi, M., Okamura, S., Doi, M., Furusawa, H., Hamabe, M., Imi, K., Kimura, M., Nakata, F., Okada, N., Ouchi, M., Shimasaku, K., Yagi, M., and Yasuda, N.: 2002, *PASJ* **54**, 833

Murphy, E. J., Chary, R.-R., Dickinson, M., Pope, A., Frayer, D. T., and Lin, L.: 2011, *ApJ* **732**, 126

Muzzin, A., Marchesini, D., Stefanon, M., Franx, M., McCracken, H. J., Milvang-Jensen, B., Dunlop, J. S., Fynbo, J. P. U., Brammer, G., Labbé, I., and van Dokkum, P. G.: 2013, *ApJ* **777**, 18

Neugebauer, G., Habing, H. J., van Duinen, R., Aumann, H. H., Baud, B., Beichman, C. A., Beintema, D. A., Boggess, N., Clegg, P. E., de Jong, T., Emerson, J. P., Gautier, T. N., Gillett, F. C., Harris, S., Hauser, M. G., Houck, J. R., Jennings, R. E., Low, F. J., Marsden, P. L., Miley, G., Olnon, F. M., Pottasch, S. R., Raimond, E., Rowan-Robinson, M., Soifer, B. T., Walker, R. G., Wesselius, P. R., and Young, E.: 1984, *ApJ* **278**, L1

Noeske, K. G., Faber, S. M., Weiner, B. J., Koo, D. C., Primack, J. R., Dekel, A., Papovich, C., Conselice, C. J., Le Floc'h, E., Rieke, G. H., Coil, A. L., Lotz, J. M., Somerville, R. S., and Bundy, K.: 2007, *ApJ* **660**, L47

Noll, S., Burgarella, D., Giovannoli, E., Buat, V., Marcillac, D., and Muñoz-Mateos, J. C.: 2009, *A&A* **507**, 1793

O'connell, R. W.: 1986, *Stellar Populations*, p. 167

Oliver, S., Rowan-Robinson, M., Alexander, D. M., Almaini, O., Balcells, M., Baker, A. C., Barcons, X., Barden, M., Bellas-Velidis, I., Cabrera-Guerra, F., Carballo, R., Cesarsky, C. J., Ciliegi, P., Clements, D. L., Crockett, H., Danese, L., Dapergolas, A., Drolias, B., Eaton, N., Efstathiou, A., Egami, E., Elbaz, D., Fadda, D., Fox, M., Franceschini, A., Genzel, R., Goldschmidt, P., Graham, M., Gonzalez-Serrano, J. I., Gonzalez-Solares, E. A., Granato, G. L., Gruppioni, C., Herbstmeier, U., Héraudeau, P., Joshi, M., Kontizas, E., Kontizas, M., Kotilainen, J. K., Kunze, D., La Franca, F., Lari, C., Lawrence, A., Lemke, D., Linden-Vørnle, M. J. D., Mann, R. G., Márquez, I., Masegosa, J., Mattila, K., McMahon, R. G., Miley, G., Missoulis, V., Mobasher, B., Morel, T., Nørgaard-Nielsen, H., Omont, A., Papadopoulos, P., Perez-Fournon, I., Puget, J.-L., Rigopoulou, D., Rocca-Volmerange, B., Serjeant, S., Silva, L., Sumner, T., Surace, C., Vaisanen, P., van der Werf, P. P., Verma, A., Vigroux, L., Villar-Martin, M., and Willott, C. J.: 2000, *MNRAS* **316**, 749

Oliver, S. J., Bock, J., Altieri, B., Amblard, A., Arumugam, V., Aussel, H., Babbedge, T., Beelen, A., Béthermin, M., Blain, A., Boselli, A., Bridge, C., Brisbin, D., Buat, V., Burgarella, D., Castro-Rodríguez, N., Cava, A., Chanial, P., Cirasuolo, M., Clements, D. L., Conley, A., Conversi, L., Cooray, A., Dowell, C. D., Dubois, E. N., Dwek, E., Dye, S., Eales, S., Elbaz, D., Farrah, D., Feltre, A., Ferrero, P., Fiolet, N., Fox, M., Franceschini, A., Gear, W., Giovannoli, E., Glenn, J., Gong, Y., González Solares, E. A., Griffin, M., Halpern, M., Harwit, M., Hatziminaoglou, E., Heinis, S., Hurley, P., Hwang, H. S., Hyde, A., Ibar, E., Ilbert, O., Isaak, K., Ivison, R. J., Lagache, G., Le Floc'h, E., Levenson, L., Faro, B. L., Lu, N., Madden, S., Maffei, B., Magdis,

G., Mainetti, G., Marchetti, L., Marsden, G., Marshall, J., Mortier, A. M. J., Nguyen, H. T., O'Halloran, B., Omont, A., Page, M. J., Panuzzo, P., Papageorgiou, A., Patel, H., Pearson, C. P., Pérez-Fournon, I., Pohlen, M., Rawlings, J. I., Raymond, G., Rigopoulou, D., Riguccini, L., Rizzo, D., Rodighiero, G., Roseboom, I. G., Rowan-Robinson, M., Sánchez Portal, M., Schulz, B., Scott, D., Seymour, N., Shupe, D. L., Smith, A. J., Stevens, J. A., Symeonidis, M., Trichas, M., Tugwell, K. E., Vaccari, M., Valtchanov, I., Vieira, J. D., Viero, M., Vigroux, L., Wang, L., Ward, R., Wardlow, J., Wright, G., Xu, C. K., and Zemcov, M.: 2012, *MNRAS* **424**, 1614

Oliver, S. J., Wang, L., Smith, A. J., Altieri, B., Amblard, A., Arumugam, V., Auld, R., Aussel, H., Babbedge, T., Blain, A., Bock, J., Boselli, A., Buat, V., Burgarella, D., Castro-Rodríguez, N., Cava, A., Chanial, P., Clements, D. L., Conley, A., Conversi, L., Cooray, A., Dowell, C. D., Dwek, E., Eales, S., Elbaz, D., Fox, M., Franceschini, A., Gear, W., Glenn, J., Griffin, M., Halpern, M., Hatziminaoglou, E., Ibar, E., Isaak, K., Ivison, R. J., Lagache, G., Levenson, L., Lu, N., Madden, S., Maffei, B., Mainetti, G., Marchetti, L., Mitchell-Wynne, K., Mortier, A. M. J., Nguyen, H. T., O'Halloran, B., Omont, A., Page, M. J., Panuzzo, P., Papageorgiou, A., Pearson, C. P., Pérez-Fournon, I., Pohlen, M., Rawlings, J. I., Raymond, G., Rigopoulou, D., Rizzo, D., Roseboom, I. G., Rowan-Robinson, M., Sánchez Portal, M., Savage, R., Schulz, B., Scott, D., Seymour, N., Shupe, D. L., Stevens, J. A., Symeonidis, M., Trichas, M., Tugwell, K. E., Vaccari, M., Valiante, E., Valtchanov, I., Vieira, J. D., Vigroux, L., Ward, R., Wright, G., Xu, C. K., and Zemcov, M.: 2010, *A&A* **518**, L21

Papovich, C., Dole, H., Egami, E., Le Floc'h, E., Pérez-González, P. G., Alonso-Herrero, A., Bai, L., Beichman, C. A., Blaylock, M., Engelbracht, C. W., Gordon, K. D., Hines, D. C., Misselt, K. A., Morrison, J. E., Mould, J., Muzerolle, J., Neugebauer, G., Richards, P. L., Rieke, G. H., Rieke, M. J., Rigby, J. R., Su, K. Y. L., and Young, E. T.: 2004, *ApJS* **154**, 70

Partridge, R. B. and Peebles, P. J. E.: 1967, *ApJ* **148**, 377

Pérez-González, P. G., Cava, A., Barro, G., Villar, V., Cardiel, N., Ferreras, I., Rodríguez-Espinosa, J. M., Alonso-Herrero, A., Balcells, M., Cenarro, J., Cepa, J., Charlot, S., Cimatti, A., Conselice, C. J., Daddi, E., Donley, J., Elbaz, D., Espino, N., Gallego, J., Gobat, R., González-Martín, O., Guzmán, R., Hernán-Caballero, A., Muñoz-Tuñón, C., Renzini, A., Rodríguez-Zaurín, J., Tresse, L., Trujillo, I., and Zamorano, J.: 2013, *ApJ* **762**, 46

Pérez-González, P. G., Egami, E., Rex, M., Rawle, T. D., Kneib, J.-P., Richard, J., Johansson, D., Altieri, B., Blain, A. W., Bock, J. J., Boone, F., Bridge, C. R., Chung, S. M., Clément, B., Clowe, D., Combes, F., Cuby, J.-G., Dessauges-Zavadsky, M., Dowell, C. D., Espino-Briones, N., Fadda, D., Fiedler, A. K., Gonzalez, A., Horellou, C., Ilbert, O., Ivison, R. J., Jauzac, M., Lutz, D., Pelló, R., Pereira, M. J., Rieke, G. H., Rodighiero, G., Schaerer, D., Smith, G. P., Valtchanov, I., Walth, G. L., van der Werf, P., Werner, M. W., and Zemcov, M.: 2010, *A&A* **518**, L15

Pérez-González, P. G., Gil de Paz, A., Zamorano, J., Gallego, J., Alonso-Herrero, A., and Aragón-Salamanca, A.: 2003, *MNRAS* **338**, 508

Pérez-González, P. G., Rieke, G. H., Egami, E., Alonso-Herrero, A., Dole, H., Papovich, C., Blaylock, M., Jones, J., Rieke, M., Rigby, J., Barmby, P., Fazio, G. G., Huang, J., and Martin, C.: 2005, *ApJ* **630**, 82

Pérez-González, P. G., Rieke, G. H., Villar, V., Barro, G., Blaylock, M., Egami, E., Gallego, J., Gil de Paz, A., Pascual, S., Zamorano, J., and Donley, J. L.: 2008, *ApJ* **675**, 234

Pforr, J., Maraston, C., and Tonini, C.: 2012, *MNRAS* **422**, 3285

Pickles, A. J.: 1998, *PASP* **110**, 863

Pietrinferni, A., Cassisi, S., Salaris, M., and Castelli, F.: 2004, *ApJ* **612**, 168

Pilbratt, G. L., Riedinger, J. R., Passvogel, T., Crone, G., Doyle, D., Gageur, U., Heras, A. M., Jewell, C., Metcalfe, L., Ott, S., and Schmidt, M.: 2010, *A&A* **518**, L1

Piovan, L., Tantalo, R., and Chiosi, C.: 2006, *MNRAS* **366**, 923

Poglitsch, A., Waelkens, C., Geis, N., Feuchtgruber, H., Vandenbussche, B., Rodriguez, L., Krause, O., Renotte, E., van Hoof, C., Saraceno, P., Cepa, J., Kerschbaum, F., Agnèse, P., Ali, B., Altieri, B., Andreani, P., Augueres, J.-L., Balog, Z., Barl, L., Bauer, O. H., Belbachir, N., Benedettini, M., Billot, N., Boulade, O., Bischof, H., Blommaert, J., Callut, E., Cara, C., Cerulli, R., Cesarsky, D., Contursi, A., Creten, Y., De Meester, W., Doublier, V., Doumayrou, E., Duband, L., Exter, K., Genzel, R., Gillis, J.-M., Grözinger, U., Henning, T., Herreros, J., Huygen, R., Inguscio, M., Jakob, G., Jamar, C., Jean, C., de Jong, J., Katterloher, R., Kiss, C., Klaas, U., Lemke, D., Lutz, D., Madden, S., Marquet, B., Martignac, J., Mazy, A., Merken, P., Montfort, F., Morbidelli, L., Müller, T., Nielbock, M., Okumura, K., Orfei, R., Ottensamer, R., Pezzuto, S., Popesso, P., Putzeys, J., Regibo, S., Reveret, V., Royer, P., Sauvage, M.,

Schreiber, J., Stegmaier, J., Schmitt, D., Schubert, J., Sturm, E., Thiel, M., Tofani, G., Vavrek, R., Wetzstein, M., Wieprecht, E., and Wiezorrek, E.: 2010, *A&A* **518**, L2

Pope, A., Wagg, J., Frayer, D., Armus, L., Chary, R.-R., Daddi, E., Desai, V., Dickinson, M. E., Elbaz, D., Gabor, J., and Kirkpatrick, A.: 2013, *ApJ* **772**, 92

Popescu, C. C., Tuffs, R. J., Dopita, M. A., Fischera, J., Kylafis, N. D., and Madore, B. F.: 2011, *A&A* **527**, A109

Popesso, P., Magnelli, B., Buttiglione, S., Lutz, D., Poglitsch, A., Berta, S., Nordon, R., Altieri, B., Aussel, H., Billot, N., Gastaud, R., Ali, B., Balog, Z., Cava, A., Feuchtgruber, H., Gonzalez Garcia, B., Geis, N., Kiss, C., Klaas, U., Linz, H., Liu, X. C., Moor, A., Morin, B., Muller, T., Nielbock, M., Okumura, K., Osterhage, S., Ottensamer, R., Paladini, R., Pezzuto, S., Dublier Pritchard, V., Regibo, S., Rodighiero, G., Royer, P., Sauvage, M., Sturm, E., Wetzstein, M., Wieprecht, E., and Wiezorrek, E.: 2012, *ArXiv e-prints* 1211.4257.

Puget, J.-L., Abergel, A., Bernard, J.-P., Boulanger, F., Burton, W. B., Desert, F.-X., and Hartmann, D.: 1996, *A&A* **308**, L5

Puget, J. L., Lagache, G., Clements, D. L., Reach, W. T., Aussel, H., Bouchet, F. R., Cesarsky, C., Désert, F. X., Dole, H., Elbaz, D., Franceschini, A., Guiderdoni, B., and Moorwood, A. F. M.: 1999, *A&A* **345**, 29

Reach, W. T., Megeath, S. T., Cohen, M., Hora, J., Carey, S., Surace, J., Willner, S. P., Barmby, P., Wilson, G., Glaccum, W., Lowrance, P., Marengo, M., and Fazio, G. G.: 2005, *PASP* **117**, 978

Reddy, N. A., Pettini, M., Steidel, C. C., Shapley, A. E., Erb, D. K., and Law, D. R.: 2012, *ApJ* **754**, 25

Rieke, G. H.: 1978, *ApJ* **226**, 550

Rieke, G. H., Alonso-Herrero, A., Weiner, B. J., Pérez-González, P. G., Blaylock, M., Donley, J. L., and Marcillac, D.: 2009, *ApJ* **692**, 556

Rieke, G. H. and Lebofsky, M. J.: 1979, *ARA&A* **17**, 477

Rieke, G. H. and Lebofsky, M. J.: 1986, *ApJ* **304**, 326

Rieke, G. H. and Low, F. J.: 1972, *ApJ* **176**, L95

Rieke, G. H., Young, E. T., Engelbracht, C. W., Kelly, D. M., Low, F. J., Haller, E. E., Beeman, J. W., Gordon, K. D., Stansberry, J. A., Misselt, K. A., Cadien, J., Morrison, J. E., Rivlis, G., Latter, W. B., Noriega-Crespo, A., Padgett, D. L., Stapelfeldt, K. R., Hines, D. C., Egami, E., Muzerolle, J., Alonso-Herrero, A., Blaylock, M., Dole, H., Hinz, J. L., Le Floc'h, E., Papovich, C., Pérez-González, P. G., Smith, P. S., Su, K. Y. L., Bennett, L., Frayer, D. T., Henderson, D., Lu, N., Masci, F., Pesenson, M., Rebull, L., Rho, J., Keene, J., Stolovy, S., Wachter, S., Wheaton, W., Werner, M. W., and Richards, P. L.: 2004, *ApJS* **154**, 25

Rodighiero, G., Daddi, E., Baronchelli, I., Cimatti, A., Renzini, A., Aussel, H., Popesso, P., Lutz, D., Andreani, P., Berta, S., Cava, A., Elbaz, D., Feltre, A., Fontana, A., Förster Schreiber, N. M., Franceschini, A., Genzel, R., Grazian, A., Gruppioni, C., Ilbert, O., Le Floch, E., Magdis, G., Magliocchetti, M., Magnelli, B., Maiolino, R., McCracken, H., Nordon, R., Poglitsch, A., Santini, P., Pozzi, F., Riguccini, L., Tacconi, L. J., Wuyts, S., and Zamorani, G.: 2011, *ApJ* **739**, L40

Roseboom, I. G., Oliver, S. J., Kunz, M., Altieri, B., Amblard, A., Arumugam, V., Auld, R., Aussel, H., Babbedge, T., Béthermin, M., Blain, A., Bock, J., Boselli, A., Brisbin, D., Buat, V., Burgarella, D., Castro-Rodríguez, N., Cava, A., Chanial, P., Chapin, E., Clements, D. L., Conley, A., Conversi, L., Cooray, A., Dowell, C. D., Dwek, E., Dye, S., Eales, S., Elbaz, D., Farrah, D., Fox, M., Franceschini, A., Gear, W., Glenn, J., Solares, E. A. G., Griffin, M., Halpern, M., Harwit, M., Hatziminaoglou, E., Huang, J., Ibar, E., Isaak, K., Ivison, R. J., Lagache, G., Levenson, L., Lu, N., Madden, S., Maffei, B., Mainetti, G., Marchetti, L., Marsden, G., Mortier, A. M. J., Nguyen, H. T., O'Halloran, B., Omont, A., Page, M. J., Panuzzo, P., Papageorgiou, A., Patel, H., Pearson, C. P., Pérez-Fournon, I., Pohlen, M., Rawlings, J. I., Raymond, G., Rigopoulou, D., Rizzo, D., Rowan-Robinson, M., Portal, M. S., Schulz, B., Scott, D., Seymour, N., Shupe, D. L., Smith, A. J., Stevens, J. A., Symeonidis, M., Trichas, M., Tugwell, K. E., Vaccari, M., Valtchanov, I., Vieira, J. D., Vigroux, L., Wang, L., Ward, R., Wright, G., Xu, C. K., and Zemcov, M.: 2010, *MNRAS* **409**, 48

Rowan-Robinson, M., Babbedge, T., Surace, J., Shupe, D., Fang, F., Lonsdale, C., Smith, G., Polletta, M., Siana, B., Gonzalez-Solares, E., Xu, K., Owen, F., Davoodi, P., Dole, H., Domingue, D., Efstathiou, A., Farrah, D., Fox, M., Franceschini, A., Frayer, D., Hatziminaoglou, E., Masci, F., Morrison, G., Nandra, K., Oliver, S., Onyett, N., Padgett, D., Perez-Fournon, I., Serjeant, S., Stacey, G., and Vaccari, M.: 2005, *AJ* **129**, 1183

Rowan-Robinson, M., Broadhurst, T., Oliver, S. J., Taylor, A. N., Lawrence, A., McMahon, R. G., Lonsdale, C. J., Hacking, P. B., Conrow, T., Saunders, W., Ellis, R. S., Efstathiou, G. P., and Condon, J. J.: 1991, *Nature* **351**, 719

Rowan-Robinson, M., Lari, C., Perez-Fournon, I., Gonzalez-Solares, E. A., La Franca, F., Vaccari, M., Oliver, S., Gruppioni, C., Ciliegi, P., Héraudeau, P., Serjeant, S., Efstathiou, A., Babbedge, T., Matute, I., Pozzi, F., Franceschini, A., Vaisanen, P., Afonso-Luis, A., Alexander, D. M., Almaini, O., Baker, A. C., Basilakos, S., Barden, M., del Burgo, C., Bellas-Velidis, I., Cabrera-Guerra, F., Carballo, R., Cesarsky, C. J., Clements, D. L., Crockett, H., Danese, L., Dapergolas, A., Drolias, B., Eaton, N., Egami, E., Elbaz, D., Fadda, D., Fox, M., Genzel, R., Goldschmidt, P., Gonzalez-Serrano, J. I., Graham, M., Granato, G. L., Hatziminaoglou, E., Herbstmeier, U., Joshi, M., Kontizas, E., Kontizas, M., Kotilainen, J. K., Kunze, D., Lawrence, A., Lemke, D., Linden-Vørnle, M. J. D., Mann, R. G., Márquez, I., Masegosa, J., McMahon, R. G., Miley, G., Missoulis, V., Mobasher, B., Morel, T., Nørgaard-Nielsen, H., Omont, A., Papadopoulos, P., Puget, J.-L., Rigopoulou, D., Rocca-Volmerange, B., Sedgwick, N., Silva, L., Sumner, T., Surace, C., Vila-Vilaro, B., van der Werf, P., Verma, A., Vigroux, L., Villar-Martin, M., Willott, C. J., Carramiñana, A., and Mujica, R.: 2004, *MNRAS* **351**, 1290

Rowlands, K., Dunne, L., Dye, S., Aragón-Salamanca, A., Maddox, S., da Cunha, E., Smith, D. J. B., Bourne, N., Eales, S., Gomez, H. L., Smail, I., Alpaslan, M., Clark, C. J. R., Driver, S., Ibar, E., Ivison, R. J., Robotham, A., Smith, M. W. L., and Valiante, E.: 2014, *MNRAS* **441**, 1017

Rujopakarn, W., Rieke, G. H., Eisenstein, D. J., and Juneau, S.: 2011, *ApJ* **726**, 93

Salimbeni, S., Fontana, A., Giallongo, E., Grazian, A., Menci, N., Pentericci, L., and Santini, P.: 2009, in G. Giobbi, A. Tornambe, G. Raimondo, M. Limongi, L. A. Antonelli, N. Menci, and E. Brocato (eds.), *American Institute of Physics Conference Series*, Vol. 1111 of *American Institute of Physics Conference Series*, pp 207–211

Salpeter, E. E.: 1955, *ApJ* **121**, 161

Sánchez-Blázquez, P., Peletier, R. F., Jiménez-Vicente, J., Cardiel, N., Cenarro, A. J., Falcón-Barroso, J., Gorgas, J., Selam, S., and Vazdekis, A.: 2006, *MNRAS* **371**, 703

Sanders, D. B. and Mirabel, I. F.: 1996, *ARA&A* **34**, 749

Sanders, D. B., Salvato, M., Aussel, H., Ilbert, O., Scoville, N., Surace, J. A., Frayer, D. T., Sheth, K., Helou, G., Brooke, T., Bhattacharya, B., Yan, L., Kartaltepe, J. S.,

Barnes, J. E., Blain, A. W., Calzetti, D., Capak, P., Carilli, C., Carollo, C. M., Comastri, A., Daddi, E., Ellis, R. S., Elvis, M., Fall, S. M., Franceschini, A., Giavalisco, M., Hasinger, G., Impey, C., Koekemoer, A., Le Fèvre, O., Lilly, S., Liu, M. C., McCracken, H. J., Mobasher, B., Renzini, A., Rich, M., Schinnerer, E., Shopbell, P. L., Taniguchi, Y., Thompson, D. J., Urry, C. M., and Williams, J. P.: 2007, *ApJS* **172**, 86

Sanders, D. B., Soifer, B. T., Elias, J. H., Neugebauer, G., and Matthews, K.: 1988, *ApJ* **328**, L35

Schenker, M. A., Robertson, B. E., Ellis, R. S., Ono, Y., McLure, R. J., Dunlop, J. S., Koekemoer, A., Bowler, R. A. A., Ouchi, M., Curtis-Lake, E., Rogers, A. B., Schneider, E., Charlot, S., Stark, D. P., Furlanetto, S. R., and Cirasuolo, M.: 2013, *ApJ* **768**, 196

Schlegel, D. J., Finkbeiner, D. P., and Davis, M.: 1998, *ApJ* **500**, 525

Silva, L., Granato, G. L., Bressan, A., and Danese, L.: 1998, *ApJ* **509**, 103

Smail, I., Sharp, R., Swinbank, A. M., Akiyama, M., Ueda, Y., Foucaud, S., Almaini, O., and Croom, S.: 2008, *MNRAS* **389**, 407

Smith, A. J., Wang, L., Oliver, S. J., Auld, R., Bock, J., Brisbin, D., Burgarella, D., Chanial, P., Chapin, E., Clements, D. L., Conversi, L., Cooray, A., Dowell, C. D., Eales, S., Farrah, D., Franceschini, A., Glenn, J., Griffin, M., Ivison, R. J., Mortier, A. M. J., Page, M. J., Papageorgiou, A., Pearson, C. P., Pérez-Fournon, I., Pohlen, M., Rawlings, J. I., Raymond, G., Rodighiero, G., Roseboom, I. G., Rowan-Robinson, M., Savage, R., Scott, D., Seymour, N., Symeonidis, M., Tugwell, K. E., Vaccari, M., Valtchanov, I., Vigroux, L., Ward, R., Wright, G., and Zemcov, M.: 2012, *MNRAS* **419**, 377

Soifer, B. T., Rowan-Robinson, M., Houck, J. R., de Jong, T., Neugebauer, G., Aumann, H. H., Beichman, C. A., Boggess, N., Clegg, P. E., Emerson, J. P., Gillett, F. C., Habing, H. J., Hauser, M. G., Low, F. J., Miley, G., and Young, E.: 1984, *ApJ* **278**, L71

Springel, V., White, S. D. M., Jenkins, A., Frenk, C. S., Yoshida, N., Gao, L., Navarro, J., Thacker, R., Croton, D., Helly, J., Peacock, J. A., Cole, S., Thomas, P., Couchman, H., Evrard, A., Colberg, J., and Pearce, F.: 2005, *Nature* **435**, 629

Stickel, M., Bogun, S., Lemke, D., Klaas, U., Toth, L. V., Herbstmeier, U., Richter, G., Assendorp, R., Laureijs, R., Kessler, M. F., Burgdorf, M., Beichman, C. A., Rowan-Robinson, M., and Efstathiou, A.: 1998, *A&A* **336**, 116

Swinbank, A. M., Chapman, S. C., Smail, I., Lindner, C., Borys, C., Blain, A. W., Ivison, R. J., and Lewis, G. F.: 2006, *MNRAS* **371**, 465

Takagi, T., Arimoto, N., and Vansevičius, V.: 1999, *ApJ* **523**, 107

Takeuchi, T. T., Yoshikawa, K., and Ishii, T. T.: 2003, *ApJ* **587**, L89

Tinsley, B. M.: 1972, *A&A* **20**, 383

Toomre, A. and Toomre, J.: 1972, *ApJ* **178**, 623

Tresse, L., Ilbert, O., Zucca, E., Zamorani, G., Bardelli, S., Arnouts, S., Paltani, S., Pozzetti, L., Bottini, D., Garilli, B., Le Brun, V., Le Fèvre, O., Maccagni, D., Picat, J.-P., Scaramella, R., Scodeggio, M., Vettolani, G., Zanichelli, A., Adami, C., Arnaboldi, M., Bolzonella, M., Cappi, A., Charlot, S., Ciliegi, P., Contini, T., Foucaud, S., Franzetti, P., Gavignaud, I., Guzzo, L., Iovino, A., McCracken, H. J., Marano, B., Marinoni, C., Mazure, A., Meneux, B., Merighi, R., Pellò, R., Pollo, A., Radovich, M., Bondi, M., Bongiorno, A., Busarello, G., Cucciati, O., Lamareille, F., Mathez, G., Mellier, Y., Merluzzi, P., and Ripepi, V.: 2007, *A&A* **472**, 403

Tresse, L., Maddox, S. J., Le Fèvre, O., and Cuby, J.-G.: 2002, *MNRAS* **337**, 369

Ueda, Y., Watson, M. G., Stewart, I. M., Akiyama, M., Schwope, A. D., Lamer, G., Ebrero, J., Carrera, F. J., Sekiguchi, K., Yamada, T., Simpson, C., Hasinger, G., and Mateos, S.: 2008, *ApJS* **179**, 124

Utomo, D., Kriek, M., Labbé, I., Conroy, C., and Fumagalli, M.: 2014, *ApJ* **783**, L30

Valdes, F., Gupta, R., Rose, J. A., Singh, H. P., and Bell, D. J.: 2004, *ApJS* **152**, 251

van Breukelen, C., Cotter, G., Rawlings, S., Readhead, T., Bonfield, D., Clewley, L., Ivison, R., Jarvis, M., Simpson, C., and Watson, M.: 2007, *MNRAS* **382**, 971

van der Kruit, P. C.: 1971, *A&A* **15**, 110

Walcher, C. J., Lamareille, F., Vergani, D., Arnouts, S., Buat, V., Charlot, S., Tresse, L., Le Fèvre, O., Bolzonella, M., Brinchmann, J., Pozzetti, L., Zamorani, G., Bottini, D., Garilli, B., Le Brun, V., Maccagni, D., Milliard, B., Scaramella, R., Scodeggio, M., Vettolani, G., Zanichelli, A., Adami, C., Bardelli, S., Cappi, A., Ciliegi, P., Contini, T., Franzetti, P., Foucaud, S., Gavignaud, I., Guzzo, L., Ilbert, O., Iovino, A., McCracken, H. J., Marano, B., Marinoni, C., Mazure, A., Meneux, B., Merighi, R., Paltani, S., Pellò, R., Pollo, A., Radovich, M., Zucca, E., Lonsdale, C., and Martin, C.: 2008, *A&A* **491**, 713

Wang, L., Viero, M., Clarke, C., Bock, J., Buat, V., Conley, A., Farrah, D., Guo, K., Heinis, S., Magdis, G., Marchetti, L., Marsden, G., Norberg, P., Oliver, S. J., Page, M. J., Roehlly, Y., Roseboom, I. G., Schulz, B., Smith, A. J., Vaccari, M., and Zemcov, M.: 2014, *MNRAS* **444**, 2870

Wardlow, J. L., Smail, I., Coppin, K. E. K., Alexander, D. M., Brandt, W. N., Danielson, A. L. R., Luo, B., Swinbank, A. M., Walter, F., Weiß, A., Xue, Y. Q., Zibetti, S., Bertoldi, F., Biggs, A. D., Chapman, S. C., Dannerbauer, H., Dunlop, J. S., Gawiser, E., Ivison, R. J., Knudsen, K. K., Kovács, A., Lacey, C. G., Menten, K. M., Padilla, N., Rix, H.-W., and van der Werf, P. P.: 2011, *MNRAS* **415**, 1479

Werner, M. W., Roellig, T. L., Low, F. J., Rieke, G. H., Rieke, M., Hoffmann, W. F., Young, E., Houck, J. R., Brandl, B., Fazio, G. G., Hora, J. L., Gehrz, R. D., Helou, G., Soifer, B. T., Stauffer, J., Keene, J., Eisenhardt, P., Gallagher, D., Gautier, T. N., Irace, W., Lawrence, C. R., Simmons, L., Van Cleve, J. E., Jura, M., Wright, E. L., and Cruikshank, D. P.: 2004, *ApJS* **154**, 1

Westera, P., Lejeune, T., Buser, R., Cuisinier, F., and Bruzual, G.: 2002, *A&A* **381**, 524

Wieprecht, E., Schreiber, J., de Jong, J., Jacobson, J., Liu, C., Morien, B., Wetzstein, M., Ali, B., Frayer, D., Lutz, D., Okumura, K., Popesso, P., and Sauvage, M.: 2009, in D. A. Bohlender, D. Durand, and P. Dowler (eds.), *Astronomical Data Analysis Software and Systems XVIII*, Vol. 411 of *Astronomical Society of the Pacific Conference Series*, p. 531

Wuyts, S., Förster Schreiber, N. M., Lutz, D., Nordon, R., Berta, S., Altieri, B., Andreani, P., Aussel, H., Bongiovanni, A., Cepa, J., Cimatti, A., Daddi, E., Elbaz, D., Genzel, R., Koekemoer, A. M., Magnelli, B., Maiolino, R., McGrath, E. J., Pérez García, A., Poglitsch, A., Popesso, P., Pozzi, F., Sanchez-Portal, M., Sturm, E., Tacconi, L., and Valtchanov, I.: 2011, *ApJ* **738**, 106

Yagi, Nao, M. S., Yamanoi, H., Furusawa, H., Nakata, F., and Komiyama, Y.: 2013, *PASJ* **65**, 22